MIAMI UNIVERSITY
The Graduate School

Certificate for Approving the Dissertation

We hereby approve the Dissertation

of

Aleksandra J. Gawronska

Candidate for the Degree

DOCTOR OF PHILOSOPHY

_____
Claire McLeod, Director

_____
Mark Krekeler, Reader

_____
Elisabeth Widom, Reader

_____
Barry Shaulis, Reader

_____
Burcin Bayram, Graduate School Representative

ABSTRACT

INVESTIGATING EXTRATERRESTRIAL MAGMATIC PROCESSES: NEW INSIGHTS FROM THE PHYSICAL AND CHEMICAL CHARACTERISTICS OF APOLLO BASALTS.

by

Aleksandra J. Gawronska

Basaltic magmatism is a fundamental process through which rocky objects across the Solar System differentiate and evolve. Basaltic partial melts generated within planetary mantles provide a record of the geologic evolution of mantle source regions, magma storage and ascent dynamics, and the processes through which primary and secondary crusts are established. In terrestrial basaltic systems, comprehensive macro- and microscale investigations that integrate the physical (e.g. crystal size and shape) and chemical (e.g. elemental stratigraphy) properties of crystals have often led to the identification of multiple, petrogenetically distinct crystal populations throughout one mineral phase. This has led to a so-called "paradigm shift" in the field of terrestrial igneous petrology: magmatic systems are "open" in nature. However, the extent to which open system processes exist on other rocky, differentiated planetary objects remains largely unconstrained. Thus, this work targets a suite of basaltic samples collected during the lunar Apollo missions, representing the only direct sampling of basaltic materials from spatially constrained locations on another inner Solar System object. Through a detailed textural, mineralogical, and geochemical investigation this work provides new insights into the emplacement of lava on the lunar surface and new constraints on the evolution of magmatic systems within (and on) the lunar crust. First, X-ray computed tomography (XCT) datasets from a lithologically diverse suite of Apollo basaltic rock chips captured and quantified lunar basalt petrofabrics in 3D. From study of mineral (e.g., ilmenite), and vesicle distributions, resulting textures were found to be broadly consistent with terrestrial pāhoehoe lava flow stratigraphy. Second, petrographic study and *in-situ* geochemical analysis of major and minor silicate phases in thin sections of the same samples indicated the presence of distinct crystal populations within multiple phases. This supports the occurrence of "open" magmatic system processes such as mixing and mafic recharge, similar to many terrestrial counterparts. Third, methods from the previous two studies were combined to evaluate the petrogenesis of the high-K, high-Ti Apollo 11 basalt suite. Results suggest that primary magmas incorporated K-rich material through interaction with a KREEPy component during the later stages of evolution. Overall, this work has advanced our understanding of the emplacement mechanisms through which planetary basaltic crusts are established and indicates that "open" magmatic system processes may occur in basaltic systems on other rocky bodies. Collectively, this provides a geological framework in which the evolution of other differentiated planetary objects which preserve evidence of basaltic volcanism should be considered.

INVESTIGATING EXTRATERRESTRIAL MAGMATIC PROCESSES: NEW INSIGHTS FROM THE PHYSICAL AND CHEMICAL CHARACTERISTICS OF APOLLO BASALTS.

A DISSERTATION

Presented to the Faculty of

Miami University in partial

fulfillment of the requirements

for the degree of

Doctor of Philosophy

Department of Geology and Environmental Earth Science

by

Aleksandra J. Gawronska

The Graduate School
Miami University
Oxford, Ohio

2023

Dissertation Director: Claire L. McLeod

TABLE OF CONTENTS

LIST OF TABLES

LIST OF FIGURES

DEDICATION

I dedicate this work to my dog Charlie, and to my family who have tirelessly supported me throughout this program.

ACKNOWLEDGEMENTS

I acknowledge the collaborators outlined below who have significantly contributed to the improvement of this work, and my committee members whose comments supported constructive discussion of the outlined work. Finally, I acknowledge all those that made the Apollo missions possible allowing for lunar material to be returned to Earth, and all those who have curated these materials ever since allowing for their study decades later. This work was supported by funding from the following funding institutions: the Geological Society of America, the American Geophysical Union, the National Aeronautics and Space Administration, and Miami University.

1. Preface

1.1 Why study the Moon

Humans have long remained fascinated with the Moon. Currently, the Moon presents the easiest extraterrestrial opportunity to study processes that operate across the Solar System, and that may operate elsewhere in our universe. These include internal processes like differentiation and magmatism, and surface processes like impact cratering and weathering via solar wind and galactic radiation. On the Moon, evidence for these processes is clearly preserved, thanks to the lack of plate tectonics mechanisms and liquid water that have erased such evidence on Earth (NRC, 2007). Thanks to this, the lunar surface preserves evidence of processes operating over 4 Ga ago in the Solar System.

In the future, the Moon may also become an important extraterrestrial outpost by 1) providing access to study lunar processes directly on the lunar surface, 2) supporting future Solar System exploratory activities as a refueling outpost, and 3) contributing resources to economic geology efforts on Earth. Such activities will be enhanced by resources currently known to exist at the lunar south pole. There, locations of high topography are illuminated by sunlight all year round which will provide a near-constant source of renewable energy. The lunar south pole also hosts permanently shadowed regions where water ice is believed to exist in recoverable quantities, which would provide oxygen, potable water, and spacecraft propellant (Anand, 2010; Anand et al., 2012; Spudis and Lavoie, 2010). The Moon has also been documented to contain elevated contents of trace elements, including rare earth elements (REE) necessary for technological applications within some basaltic rocks on the lunar near side (within Oceanus Procellarum). Future companies could develop programs to mine these resources on the surface of the Moon, where neither humans nor the environment would be affected (i.e., Anand et al., 2012). This would significantly lessen the burdens associated with resource acquisition on Earth (i.e., mine waste, contamination). Because the Moon is our closest planetary neighbor in space, it is the best location for such extraterrestrial activities (e.g., NRC, 2007).

1.2 How basaltic magmatism relates to planetary science

With improved methods of observation over decades of study, it has become clear that magmatism is an important process for planetary evolution and resurfacing. Magmas generated at depth contribute to local changes in mantle composition by removing material from the mantle via the processes of partial melting. Once generated, some magmas will stall in the crust, but some will eventually erupt at the surface contributing to secondary crusts on planets (BVSP, 1982). Such crusts are often basaltic in composition (<52 wt. % SiO2, <3 wt. % Na_2O+K_2O) across the Solar System (BVSP, 1982). Basaltic magmas are thus important contributors to planet-wide evolutions, both inside and out. Basalt has been found to exist on Earth, the Moon, Mars, Venus, and Jupiter's moon Io. Additionally, asteroids throughout the Solar System can be basaltic in composition, including asteroid Vesta, (Mittlefehldt, 2015). With this in mind, Earth is our best-understood planetary object and remains the best analog for planetary magmatism studies, while the Moon offers the closest opportunity to study extraterrestrial magmatic processes directly.

1.3 How extraterrestrial magmatism has been studied

1.3.1 Remote sensing

For millennia, the only way to study lunar evolution and surface processes was through observation from Earth. While remote sensing does not provide the detail of information that physical sample studies can uncover, remote sensing does allow for much

greater amount of the surface and subsurface to be studied, at least within the context of extraterrestrial science. Along with numerous telescopes on Earth, the spacecraft that have specifically orbited the Moon and contributed critical information regarding it include the National Aeronautics and Space Administration's (NASA) Lunar Reconnaissance Orbiter (LRO), NASA's Clementine mission, NASA's Gravity Recovery And Interior Lab (GRAIL) orbiters, NASA's Lunar Prospector, the Indian Space Research Organisation's (ISRO) Chandrayaan-1 and -2 orbiters, Japan Aerospace Exploration Agency's (JAXA) Selenological and Engineering Explorer (SELENE, also nicknamed Kaguya), and China National Space Agency's (CNSA) Chang'e mission program. Each spacecraft sent to the Moon contains several instruments which independently collected numerous datasets, including images, altimetry data, gravity anomaly data, and compositional data (for more information, the reader is referred to Gawronska and McLeod, 2022, and references therein).

Data collected through these instruments has provided a wealth of information regarding lunar basaltic outflows, known as the maria. Lunar mare basalts are largely confined to the near-side, where they often fill basins formed earlier by giant impacts (i.e, Mare Imbrium, Serenitatis, and Tranquilitatis). The basalts vary widely in composition as exemplified by their TiO_2 content, from less than 1 wt. % TiO_2 to >9 wt. %. The distribution of TiO_2 is continuous, with a mean in the distribution at 3 wt. % (Giguere et al., 2000). Some lunar basalts low in TiO_2 are additionally highly enriched in K, rare earth elements, and P, earning them the name of KREEP basalts; these are largely concentrated in and around Oceanus Procellarum in a region termed the Procellarum KREEP Terrane (Jolliff et al., 2000). Over the years, various authors have used remotely-collected image data and applied crater counting methods in order to gain better insights into the ages of lunar basalts globally, finding that basaltic flows exposed at the surface vary in age from 3.8 to 1.2 Ga (i.e., Hiesinger et al., 2011, and references therein). Imaging of flows has revealed additional features of interest, such as domes, shields, and cones (Head, 1976), channels known as rilles (Hurwitz et al., 2013), flow layering, and pits (i.e., Robinson et al., 2012).

1.3.2 Landed missions and sample return

While remote observations remain important to our understanding of Earth's closest planetary neighbor, the 1960's ushered in a new age of robotic and human exploration. Landed missions to the lunar surface allowed for material to be collected at geographically constrained locations on the lunar surface. These locations are summarized in Fig. 1; see Gawronska and McLeod (2022b) for more detailed information about the material collected at each site. Of the 6 crewed Apollo missions to the surface, 5 explored mare basalt terrain and one explored anorthositic crust; of the three landed robotic Luna missions, 2 explored mare terrain. At the time of writing, the Chang'e 5 mission has also recently returned basaltic material.

The samples returned through both the Apollo and Luna programs 50 years ago, and more recently through the Chang'e program (Li et al., 2021) were thoroughly transformative in the information they provided to researchers, and are used to this day to groundtruth and standardize data collected via remote observations. The more recent sample return through the Chang'e-5 mission has additionally provided a constrain on the length of volcanism on the Moon, by providing samples which are much younger (~2 Ga; Li et al., 2021) than those collected during Apollo and Luna (>3 Ga; i.e., Snape et al., 2016;

2019; see also summary in Gawronska and McLeod, 2022a; 2022b). The samples returned during Apollo and Luna indicated that the Moon was a differentiated body, though its mantle has not been homogenized like Earth's due to processes such as plate tectonics. The samples indicated that the Moon cooled to form a mantle of olivine and pyroxene cumulates, and an anorthite flotation crust sampled primarily during Apollo 16 (Smith et al., 1970; Wood et al., 1970). Eventually, the Moon did experience destabilization of its mantle structure; as late stage oxides such as ilmenite and armalcolite solidified, they sank diapirically, and locally disturbed previous mafic cumulates. A final reservoir enriched in incompatible elements was formed, and eventually named ur-KREEP (Warren and Wasson 1979). This reservoir is believed to be the precursor to the KREEP basalts (collected primarily during Apollo 14 and 15), and a contaminant is some other basaltic suites enriched in K or REEs (i.e., the Apollo 11 high-Ti, high-K suite). Each mission returned samples that have distinct compositional signatures, indicating distinct petrogenetic histories in a heterogeneous lunar mantle. The focus of the dissertation presented here was to investigate in greater, multidisciplinary detail those distinct petrogenetic histories, which were generated as a result of both surface emplacement mechanisms, and subsurface processing during magma transport and ascent through the lunar crust.

1.4 References for this section

Anand, M., 2010. Lunar water: A brief review. Earth Moon Planet. 107, 65–73. https://doi.org/10.1007/s11038-010-9377-9

Anand, M., Crawford, I.A., Balat-Pichelin, M., Abanades, S., van Westrenen, W., Pe´raudeau, G., Jaumann, R., Seboldt, W., 2012. A brief review of chemical and mineralogical resources on the Moon and their potential utilization. Planet. Space Sci. 74 (1), 42–48. https://doi. org/10.1016/j.pss.2012.08.012

Basaltic Volcanism Study Project (BVSP) 1981. Pergamon Press, Inc., New York. 1286 pp.

Gawronska, A. J., McLeod, C. L. 2022a. Moon, Overall Geology. In: Cudink, B. (Eds.) Encyclopedia of Lunar Science. Springer, Cham. https://doi.org/10.1007/978-3-319-05546-6_145-1

Gawronska, A. J., McLeod, C. L. 2022b. Basalt. In: Cudnik, B. (eds.) Encyclopedia of Lunar Science. Springer, Cham. https://doi.org/10.1007/978-3-319-05546-6_135-1

Giguere, T. A., Taylor, G. J., Hawke, B. R., Lucey, P. G. 2000. The titanium contents of lunar mare basalts. Meteoritics and Planetart Science 35, 193-200. https://doi.org/10.1111/j.1945-5100.2000.tb01985.x

Head III, J. W. 1976. Lunar Volcanism in Space and Time. Reviews of Geophysics and Space Physics 14 (2), 265-300.

Hiesinger, H., Head, J.W., Wolf, U., Jaumann, R., Neukum, G., 2011. In: Ambrose, W.A., Williams, D.A. (Eds.), Recent Advances and Current Research Issues in Lunar Stratigraphy, 477. Geological Society of America Special Paper, The Geological Society of America Inc, Boulder, CO, pp. 1–51. https://doi.org/10.1130/2011.2477(01).

Hurwitz, D. M., Head, J. W., Hiesinger, H. 2013. Lunar sinuous rilles :Distribution, characteristics, and implications for their origin. Planetary and Space Science 79-80, 1-38. doi.org/10.1016/j.pss.2012.10.019

Jolliff, B. L., Gillis, J. J., Haskin, L. A., Korotev, R. L., Wieczorek, M, A. 2000. Major lunar crustal terranes: Surface expressions and crust-mantle origins. Journal of Geophysical Research 105 (E2), 4197-4216. https://doi.org/10.1029/1999JE001103

Li, Q.-L., Zhou, Q., Liu, Y., Xiao, Z., Lin, Y., Li, J.-H., Ma, H.-X., et al. 2021. Two-billion-year-old volcanism on the Moon from Chang'e-5 basalts. Nature 600, 54-58. https://doi.org/10.1038/s41586-021-04100-2

Mittlefehldt, D. W. 2015. Asteroid (4) Vesta: I. The howardite-eucrite-diogenite (HED) clan of meteorites. Geochemistry 75 (2), 155-183. doi.org/10.1016/j.chemer.2014.08.002.

National Research Council (NRC), 2007. The Scientific Context for Exploration of the Moon, Final Report, National Academy Press, Washington, D. C.

Robinson, M.S., Ashley, J.W., Boyd, A.K., Wagner, R.V., Speyerer, E.J., Ray Hawke, B., Hiesinger, H., van der Bogert, C.H., 2012. Confirmation of sublunarean voids and thin layering in mare deposits. Planetary and Space Science 69, 18–27. doi:10.1016/j.pss.2012.05.008

Smith, J. V., Anderson, A. T., Newton, r. C., Olsen, E. J., Wyllie, P. J., Crewe, A. V., Isaacson, M. S., Johnson, D. 1970. Petrologic history of the moon inferred from petrography, mineralogy, and petrogenesis of Apollo 11 rocks. Proceedings of the Apollo 11 Lunar Science Conference 1, 897-925.

Snape, J. F., Nemchin, A. A., Bellucci, J. J., Whitehouse, M. J., Tartese, R., Barnes, J. J., Anand, M., Crawford, I. A., Joy, K. H. 2016. Lunar basalt chronology, mantle differentiation and implications for determining the age of the Moon. Earth and Planetary Science Letters 451, 149-158. http://dx.doi.org/10.1016/j.epsl.2016.07.026

Snape, J. F., Nemchin, A. A., Whitehouse, M. J., Merle, R. E., Hopkinson, T., Anand, M. 2019. The timing of basaltic volcanism at the Apollo landing sites. Geochimica et Cosmochimica Acta 266, 29-53. https://doi.org/10.1016/j.gca.2019.07.042

Spudis, P.D., Lavoie, A.R., 2010. Mission and Implementation of an Affordable Lunar Return. Proceedings, Space Manufacturing 14, Space Studies Institute, Princeton NJ

Warren, P. H., Wasson, J. T. 1979. The Origin of KREEP. Reviews of Geophysics and Space Physics 17 (1), 73-88.

Wood, J. A., Dickey Jr., J. S., Marvin, U. B., Powell, B. N. 1970. Lunar anorthosites and a geophysical model of the moon. Proceedings of the Apollo 11 Lunar Science Conference 1, 965-988.

1.5 Figures for this section

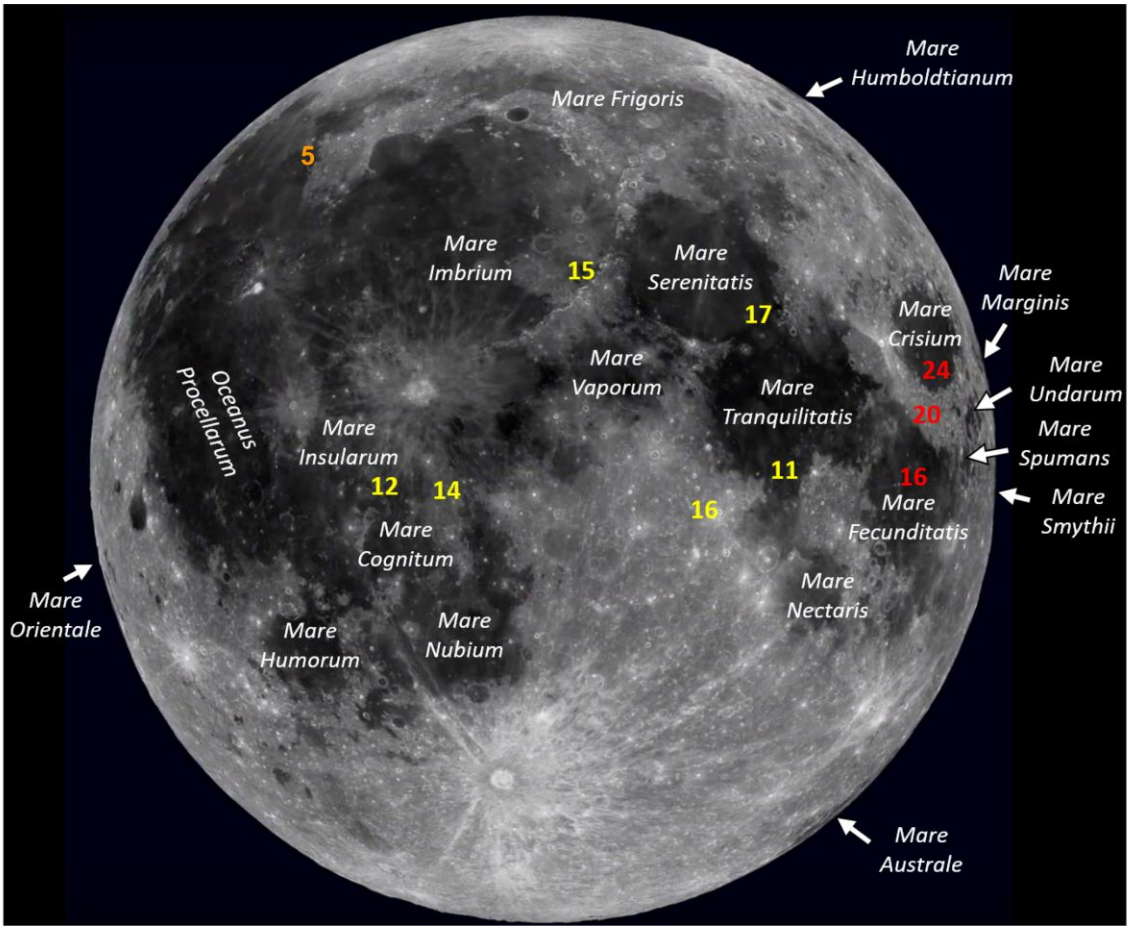

Fig. 1: Summary of mare basalt volcanism and surface mission landing sites; Apollo in yellow, Luna in red, Chang'e in orange. Figure adapted from Gawronska and McLeod (2022b).

2. New interpretations of lunar mare basalt flow emplacement from XCT analysis of Apollo samples

The following chapter is included as a preprint; the final version has been published in the journal Icarus under the following citation:

A. J. Gawronska, C. L. McLeod, E. H. Blumenfeld, R. D. Hanna, R. A. Zeigler (2022) New interpretations of lunar mare basalt flow emplacement from XCT analysis of Apollo samples. *Icarus 388*, 115216. https://doi.org/10.1016/j.icarus.2022.115216

2.1. Introduction

Magmatism is a fundamental process through which rocky objects across our Solar System differentiate and evolve (BVSP, 1981; Wilson and Head, 2018). The Earth's Moon is one of the most comprehensively characterized extraterrestrial objects in our Solar System as a result of over half a century's worth of scientific investigation. This includes insights from remote sensing (e.g., Gillis et al., 2003; 2004; Lemelin et al., 2019), *in-situ* sample return during the Apollo, Luna, and Chang'e 5 missions (e.g., Heiken et al. 1991; Li et al., 2021; Papike et al., 1976; Qian et al., 2021; Taylor, 1982), and the discovery of lunar meteorites on Earth (e.g., Allan Hills 81005, Brum et al., 2020; Gross and Treiman, 2011; Treiman and Drake, 1983). Since *in-situ* sample return, and the identification of basaltic material in lunar meteorites, numerous studies have worked to characterize the microstructural and geochemical diversity that exists within lunar basaltic products (e.g., glassy to microgabbroic textures, Kramer et al., 1977; Ryder, 1985; 1993; Warner, 1970; characteristic Ti, K, and Al contents, Neal and Taylor, 1992, and references therein). As a result, our understanding of lunar basalt petrogeneses and the magmatic processes which operate across rocky planetary objects has greatly advanced (Cone et al., 2020; Neal and Taylor, 1992; Shearer et al., 2006). For example, it is now well established that lunar magmas originated from distinct source regions within the lunar mantle and evolved to produce a petrographically and geochemically diverse suite of basalts. However, questions remain regarding the dynamics of lava emplacement onto the lunar surface (e.g., Gregg, 2017; Hamilton, 2019; Tolometti et al., 2020; Wilson, 2009) and how the crystal and vesicle contents of lunar lavas contributed to flow rheology and emplacement mechanisms (Belousov and Belousova, 2018; Bergantz et al., 2017; Lejeune et al., 1999; Nicolas and Ildefonse, 1996; Paterson et al., 2019; Rumpf et al., 2020; Vernon, 2018).

On Earth, basaltic pāhoehoe lava flows are emplaced through the process of inflation (e.g., Belousov and Belousova, 2018; Keszthelyi and Self, 1998; Rowland and Walker, 1988; Self et al., 1998; Wilson, 2009). During inflation, basaltic lava lobes grow and rupture, generating subsequent lobes. Inflating lava lobes quickly develop a glassy crust that works to trap vesicles as magma continues to be injected into the lobe. This often creates vesicle-rich zones in the lobe crust where the vesicles increase in size but decrease in number inward (e.g., Belousov and Belousova, 2018; Cashman and Kauahikaua, 1997; Hon et al., 1994; Keszthelyi and Self, 1998; Self et al., 1998; Vye-Brown et al., 2013; Thordarson. 1995; Wilmoth and Walker, 1993). The remainder of each lobe is comprised of a relatively insulated core, and a quenched crust at the base of the lobe. On Earth, this base is ~10 cm thick, irrespective of total lobe thickness (Self et al., 1998). The core of the flow lobe can be vesiculated, but it is often vesicle-poor as bubbles rise towards the crust prior to solidification. Furthermore, lavas with higher crystal contents and lower melt fractions have an increased potential to develop mineral flow textures, particularly when only 35 to 40% melt remains (e.g., Paterson et al. 1998; Vernon, 2018). However, recent work also suggests that lava petrofabrics resulting from flow can be far more complex than simple parallel alignment of crystals (see review by Paterson et al., 2019).

Due to their relatively mafic nature (namely <52 wt.% SiO_2), terrestrial basalts have relatively low viscosities. From observational and experimental studies, the viscosities of lunar basaltic lavas were interpreted to likely be one to two orders of magnitude lower than those on Earth (Harris and Allen, 2008; Keszthelyi and Self, 1998; Murase and McBirney,

1970; Rumpf et al., 2020; Taylor et al., 1991; Whitford-Stark et al., 1982). These lower viscosities (~0.13 to 0.87 Pa-s, Rai et al., 2019) suggest that lunar basaltic eruptions may have had high effusion rates and large volumes (e.g., BVSP, 1981; Garry et al., 2012; Head and Wilson, 1992). However, effusion rates also likely varied regionally and temporally and thus created flows of varying thicknesses (e.g., Rumpf et al., 2020). Based on their low viscosities and picritic compositions, the lunar mare basalts were possibly emplaced as pāhoehoe lava flows, and formed inflated lava lobes (Donohue and Neal, 2015; Garry et al., 2012; Keszthelyi and Self, 1998; Li et al., 2021; Roberts and Gregg, 2019; Rumpf et al., 2020; Self et al., 1998; Tolometti et al., 2020; Vye-Brown et al., 2013; Wilson, 2009). The Apollo basalts studied here will be discussed within this framework.

The only field-based study of a lava flow outcrop on the lunar surface to date occurred during the Apollo 15 mission, when flows <1 m to 20 m thick were found to be exposed in the side of Hadley Rille (Howard et al., 1972; Howard and Head, 1972; Swann et al., 1972; Spudis et al, 1988; Vaniman et al., 1991). More recent studies have utilized remote sensing techniques to map lunar flows and investigate their properties (e.g., Head and Wilson, 1992; Hiesinger et al., 2002; Weider et al., 2010; Tolometti et al., 2020). For example, remote work has indicated that several flows are tens to hundreds of meters thick in Mare Tranquilitatis and Humorum (Hiesinger et al., 2002), and in Oceanus Procellarum (Weider et al. 2010). It is, however, challenging to distinguish individual flows from each other within an outcrop from remote sensing alone. The large thicknesses reported by Hiesinger et al. (2002) and Weider et al. (2010) may represent total outcrop thicknesses, and not individual flow thickness (Rumpf et al., 2020; Tolometti et al., 2020; Wilson, 2009). In the absence of lunar field work and in-situ observations of flow characteristics, the work presented here aims to investigate lunar lava flow emplacement via the study of basaltic rock chips from the Apollo 11, 12, 15, and 17 missions.

Advancing our understanding of lunar magmatic systems has historically been supported through traditional petrographic methods and subsequent *in-situ* analysis of samples in 2D via thin section and/or grain mount study (e.g., through electron microscopy and microanalysis, McCubbin et al., 2019). These traditional techniques require some degree of sample destruction, either by slicing, crushing, and/or dissolving. The relative paucity of lunar, and more broadly extraterrestrial, materials available for scientific study necessitates their investigation via non-destructive techniques. X-ray computed tomography (XCT) is one such approach. XCT is an imaging technique that permits measurement and analysis of a sample (and its components) in 3D, thus providing a more accurate record of lunar materials. XCT also provides a comparatively greater amount of material to study when compared to traditional 2D thin section analysis, and works to facilitate sample preservation and curation (e.g., Blumenfeld et al., 2017; 2019; McCubbin et al., 2015; Zeigler et al. 2021). The utility of XCT to advance our understanding of the properties of various materials has been widely demonstrated in numerous fields over the past several decades, including applications in paleontology (Carvalho et al., 2020; Cunningham et al., 2014; Wu and Schepartz, 2009), economic geology (Arif et al., 2021; Gan et al., 2020; Mathews et al., 2017; Wang and Miller, 2020; Zhang et al., 2019), and materials science (du Plessis and Boshoff, 2019; Sanematsu et al., 2019; Vásárhelyi et al., 2020). Within the context of extraterrestrial research, XCT has previously been applied to characterize the petrography, petrofabrics, porosities, and chemistries of chondritic and

Martian meteorites in order to improve understanding of their formation and origin (e.g., Hanna and Ketcham, 2017; Hezel et al., 2013).

Within the context of lunar science, and at the time of writing, the Apollo Next Generation Sample Analysis program is beginning to undertake XCT analyses on Apollo 17 samples opened in the year 2019 (i.e., Zeigler et al., 2021). The work presented here is the first to evaluate lunar basalt petrofabrics and lunar eruptive environments in 3D through the application of XCT. Specifically, textures were observed three-dimensionally for each sample and shape preferred orientations were quantified in order to evaluate whether foliation or lineation was preserved. In addition, particle and vesicle size distributions were quantified in order to determine the cooling history of each sample. Collectively, these data were used to interrogate lava flow stratigraphy and evaluate the emplacement history of lava flows across the lunar surface.

2.2 Methodology

2.2.1 Sample descriptions

Samples studied as part of this work represent much of the textural and chemical diversity that exists throughout the Apollo basalt suite and are associated with the Apollo 11 (sample 10057,19 – 128.7 g), Apollo 12 (sample 12038,7 – 327.5 g; sample 12043,0 – 52.4 g), Apollo 15 (sample 15085,0 – 234.3 g; sample 15556,0 – 619.2 g), and Apollo 17 (sample 70017,8 – 1423.2 g) missions. Hereafter, the samples are only referred to by their parent generic number (e.g., 15556).

Previous studies have provided detailed petrographic summaries of each sample (see Table 1; see also Meyer, 2016, and references therein). Sample 10057 is a fine-grained, vesicular high potassium ilmenite basalt with intergrown subhedral plagioclase, ilmenite, and pyroxene. Sample 12038 is categorized as a coarse-grained hypidiomorphic feldspathic basalt where the feldspars form a loose network. Sample 12043 is a medium-grained pigeonite basalt with pyroxene phenocrysts set in a subophitic groundmass. Sample 15085 is a coarse-grained pigeonite basalt dominated by pyroxene. Sample 15556 is a fine-grained, vesicular olivine-normative basalt with pyroxene subophitically enclosing plagioclase and ilmenite grains. Sample 70017 is a medium-grained, hypidiomorphic, granular, low potassium ilmenite basalt. Previous studies of these samples have also established their modal mineralogies based on 2D thin section analysis (reported in Meyer, 2016, and references therein). Broadly, all samples are comprised of abundant pyroxene and plagioclase feldspar, minor olivine, and trace amounts of accessory phases. Samples 10057 and 70017 are both categorized as high-titanium (~10 to 13 wt. % TiO_2) basalts, and thus have abundant ilmenite, whereas the remaining samples contain low bulk wt. % TiO_2 contents (~2 to 3 wt. %) and have only accessory ilmenite (see Meyer, 2016, and references therein).

The samples studied here vary in vesicle abundances, distributions, and shapes (i.e., Meyer 2016, and references therein). Gas cavities that remain in volcanic materials after crystallization and are often, but not always, rounded will be referred to as vesicles in the work presented here. Relatively small cavities that remain after solidification, are interstitial to crystals, and are bounded by crystal faces will be referred to as vugs. Gas cavities that existed prior to solidification will be referred to as bubbles.

2.2.2 Data extraction

Documentation of XCT methodologies for geologic applications is presented in Cnudde and Boone (2013), Ebel and Rivers (2007), Hanna and Ketcham (2017), and Jerram and Higgins (2007). Five of the six samples studied here were originally scanned as part of the Astromaterials 3D project, a novel effort to create research-grade interior and exterior 3D models of NASA's astromaterials collections for researchers and the public (Blumenfeld et al., 2017). Those five samples (12038, 12043, 15085, 15556, and 70017) were scanned on a North Star Imaging system the University of Texas at Austin High Resolution Computed Tomography Facility (UTCT). The work presented here was selected as a case study for Astromaterials 3D and authors were provided access to the relevant datasets. At the time of writing, three of these samples (12038,7, 15556,0, and 70017,8) can be accessed through the Astromaterials 3D library (https://ares.jsc.nasa.gov/astromaterials3d/). Sample 10057,19 was scanned separately at the Natural History Museum in London, UK on a Nikon Metrology HMX ST 225. Details of the scanning parameters used are summarized in Table S1. Each sample was triple bagged in Teflon for the duration of the scan. As XCT data permits the user to view the sample in more than one direction, sample textures were evaluated while looking down the orthogonal x, y, and z axes (the orthogonal z axis is parallel to the axis of rotation, x and y are the remaining two axes), as shown in Figure 1. Grayscale values vary depending on X-ray attenuation as a result of difference in chemical composition and material density within each voxel (volume element, i.e., a 3D pixel). *ImageJ* (Schneider et al., 2012) was used to adjust the brightness and contrast of the scans to support phase segmentation efforts. *Dragonfly* (version 2021.1, Object Research Systems) was used to generate masks of the area external to each sample (referred to as the "outside" here) so that this area could be segmented away. Any vesicles touching the "outside" component could not be quantified and were therefore discarded as well. The original sample scans (with contrast and brightness values adjusted) had a black "outside" – the applied mask was assigned a value of 255 (white). This approach was taken for all samples except 15556,0, where a mask could not be created due to computational limitations and thus the "outside" and vesicles had the same threshold value. In sample 15556 the "outside" and vesicle components were segmented together as one component, and separated later based on blob volumes (described further below).

Segmentation and separation of sample components was completed using *Blob3D* (Ketcham, 2005), a freely available program developed to extract component information from XCT data. Here, "component" will be used to indicate mineral phases, while "particle" will be used to indicate individual crystals of a mineral phase. Sample components included the mineral phases pyroxene (±olivine), plagioclase feldspar, and oxides (includes all of the brightest phases, namely ilmenite with minor Fe-rich spinels, and sulfides), as well as vesicles, and the "outside." This is an oversimplification of the samples' true mineral assemblage, as accessory minerals overlap in grayscale value with major components. For example, the component "plagioclase feldspar" likely included some K-feldspar and glass. When identified, accessory phases were segmented into an additional "other" category. Most often, this included silica-rich phases like the tridymite found in sample 15085 (described further in section 3.1). Olivine was not segmented because it was indistinguishable from pyroxene. Previous authors have indicated that olivine constitutes a minor component in all samples studied here (~1%, Meyer, 2016 and

references therein). Its presence should therefore not significantly affect the pyroxene abundances reported here.

Voxels were segmented into components based on their grayscale values using the general thresholding option in Blob3D, where a range of grayscale values was chosen for a component, and only voxels with a value within this range were attributed to the component by Blob3D (Figure 2a-b). Occasionally, seeding was used to specifically dictate to *Blob3D* that voxels of certain a greyscale range may only be included in a component if they are touching a voxel of a specified (seed) value. This helped to differentiate phases that partially overlapped in their grayscale values (e.g., bright iron-rich pyroxene rims and bright Fe- and Ti-rich oxide phases, see Figure 3). After segmentation, the next step in *Blob3D* was to separate objects within the same component that are touching, so that the program was able to identify and measure them as discrete objects (Figure 2c).

Separation of particles within sample components followed segmentation. Throughout the studied sample suite, the majority of pyroxene and feldspar grains were in direct contact with several grains of the same phase. While it may be technically possible to manually separate these grains in *Blob3D*, this approach would have been very time intensive due to each sample containing multiple thousands of grains of each phase. Therefore, we analyzed here only the total volumes of pyroxene and plagioclase, and not the shape-preferred orientations of individual grains or the average range in crystal sizes of each mineral phase. Oxide and vesicle data was separated using "No Separation" where each particle or particle cluster was treated as one. Extracting particle characteristics followed. During extraction, a best-fit ellipsoid was fit to each individual oxide and vesicle particle to extract shape and orientation of these objects with respect to the overall sample. While the individual particles were not necessarily ellipsoidal in shape, this approach worked to characterize their shape-preferred orientation. In order to ensure that the smallest distinguishable particles were accounted for, even within the fine-grained samples (10057, 15556), a minimum segmented particle size of seven voxels was chosen. As XCT does not resolve crystallographic axes, particle orientation for the mineral phases discussed here is related to their external shape (i.e., crystal habit). This derived shape and orientation data was used to determine if any foliation and/or lineation fabric was present within the sample volumes using strain analysis described below.

As it was not possible to create a mask for the external portion of sample 15556 due to computational limitations, a different approach was taken to extract vesicles in this sample. The "outside" was segmented and separated as one component with the vesicles, which had similar greyscale values. Once extracted, the particle volumes in the combined "outside"/vesicles component were evaluated to determine the value at which volumes became massive and represented thousands of voxels touching each other "outside" of the sample, not finite vesicles. The blobs determined to be representative of "outside" were discarded. To evaluate the success of this approach, the more vesiculated samples (10057, 12038, and 70017) were analyzed without a mask and compared to their masked versions. In all cases, the vesicularity of the samples changed by ~1%. We are therefore confident that the separation and resulting volumetric analyses of sample 15556 were accurate despite having no mask. All other data from sample 15556 was extracted as described earlier.

2.2.2.1 Investigation of extracted clusters

To evaluate whether including particle clusters without separating them would significantly affect further interpretation, manual separation of oxides in sample 10057 was additionally undertaken. This sample was chosen because 1) it is a high-Ti basalt and thus has one of the highest oxide contents of the samples studied here making it more likely to be affected by clustering, and 2) the 10057 dataset was not as significantly altered by beam hardening as 70017, the other high-Ti sample with similarly high oxide volume (described further below). Using no separation, over 100,000 oxide particles were found to exist in 10057,19. Observing all of them and separating any clusters manually required 2.5 hours per 1% of sample volume traversed. Thus, a representative subset in the center of the sample was cropped to specifically investigate clusters instead. The subset was approximately one tenth of the total sample volume, and was first analyzed using no separation, and then again using manual observation at a rate of 1% completed every ~20 minutes. During manual separation, any simple clusters (see Figure S1) found were separated using the "Pick 3 Points" option where 3 points were selected along a connection between two particles. This generated a plane along which the cluster was split into separate particles. For more information, see Ketcham (2005), and the Blob3D user manual. Complex clusters (Figure S1) were separated when possible, though several (~ 2 to 3% of all particles) were too complicated for this. From this work, the clustered oxides were observed to account for <10% of the data in this high titanium sample. Both datasets were evaluated via *Stereonet* (described in section 2.3 Strain analysis) and size distribution analysis (described in section 2.4 Size distribution analyses), and the results are presented in Figure S2. It was determined that clustering would not significantly influence later textural analyses, and the time involved in manually assessing particles and clusters was not worth the outcome for this study. As a result, manual separation of either oxide or vesicle clusters was not pursued further. All samples were visually examined in Blob3D to ensure that none exhibited more oxide or vesicle clustering than 10057 and to ensure this treatment was appropriate. The only instance where clustering was more significant was in the case of vesicles in 15556. Out of the 91,503 vesicle blobs extracted in 15556 using the methods described in section 2.2, the largest 260 blobs were clusters. These clusters accounted for ~94% of the vesicle volume despite their relatively small frequency. Because clustering here could sway subsequent results, we assessed how removing the 260 particles would change stereographic (see section 2.3; Figure 4) and size distribution (see section 2.4; Figures 5-6) investigations. The results of analyzing data without clusters are presented in Figure S3. The stereonet without clusters (Figure S3) is near identical to the stereonet with clusters (Figure 4). The size distributions, however, do not align – including the 260 clusters indicates vesicle coalescence (Figure 6; described further in sections 3. Results, and 4. Discussion), while excluding those clusters suggests vesicle collapse (e.g., Shea et al., 2010). During collapse, vesicles lose their round shape and become irregular (e.g., Mongrain et al., 2010), which is inconsistent with the spherical texture of vesicles in 15556. For this reason, all discussion of sample 15556 is based on analyses including the clusters. Thus, data collected via "No separation" was used for all datasets, and clusters of oxides/ vesicles were treated as one.

2.2.3 Strain analysis

Previous work has suggested that the long axes of crystals may be aligned parallel to magma flow direction (i.e., Castro et al., 2002; Folkes and Russell, 1980; Martin and

Nokes, 1988; Shaw, 1969), and vesicles may experience elongation due to strain (Lejeune et al., 1999; Okamura et al., 2009; Passey and Bell, 2007; Shea et al., 2010). The role of strain during lava flow and the generation of associated petrofabrics is not completely understood, as there are a number of fabrics beyond lineation and foliation that can be potentially preserved (e.g., Nicolas, 1992; Paterson et al., 1998; 2019). However, parallel alignment of crystals as well as elongation of vesicles in the direction of flow is one of the simplest interpretations of a petrofabric and is one of the most straightforward to quantify. In order to interpret any potential strain imparted on, and recorded by, a lunar lava upon emplacement, extracted shape preferred orientation data was plotted on rose diagrams and on stereographic projections (contoured using Kamb) via *Stereonet 11* (version 11.3, Allmendinger et al., 2012; Cardozo and Allmendinger, 2013) (where particles were treated as unidirectional vectors). Computational limits while using *Stereonet* led to the 10,000 particles of greatest volume being analyzed. It was assumed here that particles of all sizes would have experienced the same degree of strain, and thus our particle volume limitation should have no effect on orientation distribution interpretations. Sample fabrics were further investigated via the methodology outlined by Woodcock and Naylor (1983). Eigenvectors, and associated eigenvalues, of the particle distribution were calculated via *Stereonet 11* using the Bingham Analysis option. Then, the *K*-value and *C*-value were calculated following the method described by Woodcock and Naylor (1983) using the derived eigenvalues. The *K*-value describes the shape of the distribution:

[1] $K = (\ln(S1/S2))/(\ln(S2/S3))$ (Woodcock and Naylor, 1983)

where S1 is the largest eigenvalue, S2 is the intermediate eigenvalue, and S3 is the smallest eigenvalue. If $K>1$, the distribution can be considered as clustered, and if $K<1$, the distribution is girdled. The *C*-value, describes the strength of the fabric (i.e., how tightly the data is oriented in the mean vector direction):

[2] $C = \ln(S1/S3)$ (Woodcock and Naylor, 1983)

Together, these parameters were used to evaluate the stereographic data distributions and the presence of possible fabrics within the samples.

2.2.4 Size distribution analyses

Calculated particle volumes were utilized to examine the particle size distributions (PSDs, e.g., Friedrich et al., 2008; Jerram and Higgins, 2007) of oxides (i.e., ilmenite and spinel). Vesicle size distributions (VSDs, e.g., Shea et al., 2010) were used to examine the vesicle component within each sample. In both cases an X-Y diagram compared the population density (proxy for crystal nucleation rate) with particle/vesicle volumes (proxy for crystal growth rate) in a process similar to crystal size distribution (CSD) analysis (Higgins, 2000; Morgan and Jerram, 2006). Combined, these parameters were used to evaluate the rate of magmatic cooling (e.g., Donohue and Neal, 2015; Morgan and Jerram, 2006; Neal et al., 2015). While CSD analyses rely on estimating a crystal's third dimension (Higgins, 2000), all three dimensions of a particle are defined via XCT. The work of Higgins (2000) and Morgan and Jerram (2006) developed standard methods that are now widely used to generate CSDs based on crystal parameters calculated from 2D observations

(e.g., in a thin section). Here, an Excel spreadsheet called 3DSD (see supplementary materials) was developed based on the work of Higgins (2000) and Morgan and Jerram (2006) to automatically quantify PSD, CSD, and VSD profiles from XCT data. Data was separated into 10 bins based particle axis length. From this, average particle volume, and average particle diameter for each bin was calculated. Volume fraction was also calculated to aid in the visualization of volume fraction size distributions (VFDs). Calculated parameters were then graphed in a series of X-Y diagrams to support evaluation of sample textural characteristics and comparison to CSDs. To support data visualization, log of population density was plotted vs. log of average particle volume. This is different to traditional CSDs. PSDs and VSDs plotted identically to CSDs (ln population density plotted vs. particle volume) can be found in Figure S4. For simplification purposes, only 15,000 particles or vesicles of greatest volume were evaluated. Interpretation of the shape and size of small particles can be challenging (e.g., Donohue and Neal, 2015), therefore omitting this particle population is unlikely to impact data interpretations.

2.3 Results

2.3.1 Mineralogy

The extracted volume-based modal mineralogies of each sample are summarized in Table 1. In summary, all extracted volumetric mineralogies reported here are similar to the ranges of the modal mineralogies reported previously. As expected, there was some variation, as different sample splits were studied here, and not all phases were individually accounted for (e.g., olivine). Nonetheless, the general similarity in modal abundances reported via 2D and 3D indicated that previously reported sample component proportions were accurate. Thanks to its distinct composition and characteristic crystal habit (e.g., Figure 3d), it was even possible to segment tridymite data in sample 15085, which accounts for all of the "other" component in this sample. Vesicle volumes also match previously reported values for samples 10057, 12038, and 15556 (Table S2; Meyer, 2016, and references therein).

Sample 70017 was the largest sample investigated here, and did not initially match modal mineralogies reported by previous authors. The initial oxide volume was 14.5% less (Meyer, 2016, and references therein). To account for its large size relative to other samples (16.5 cm at its widest, as opposed to the other samples which were <10 cm wide), 70017 was scanned at 450 keV, while the remaining samples were all scanned at X-ray energies of <250 keV (Table S1). Higher energy X-rays are necessary to penetrate larger samples, but are less sensitive to changes in sample density and chemistry (Ketcham and Carlson, 2001; Hanna and Ketcham, 2017). This made voxels of different components difficult to distinguish. In addition, the scan of 70017 had a beam hardness artifact due to the sample's large size and density, which prevented the whole sample from being segmented accurately (e.g., Hanna and Ketcham, 2017). To address this, the sample exterior was cropped away, leaving behind ~40% of the interior which was analyzed again via *Blob3D*. By studying only the interior of 70017, much of the variation in grayscale values along the sample rim due to beam hardening was eliminated. This facilitated phase separation despite the challenges associated with a scan energy of 450 keV. The volumetric mineralogies from the interior of sample 70017 matched previously reported modal mineralogies much more closely (Table 1). It was this latter analysis of 70017 that was used in the mask vs. no-mask comparison of 15556 and sample vesicularities described in section 2.2. Based on the

cropping that was necessary, future studies may want to consider scanning smaller sample pieces in order to avoid XCT scanning artifacts and improve analysis (Hanna and Ketcham, 2017). This would also allow the usage of lower energy X-rays, which would aid in component distinction (e.g., Ketcham and Carlson, 2001).

2.3.2 Textural Observations

Sample 10057 is fine-grained (0.1 to 0.3 mm), and vesicular (11.5%). The vesicles in this sample have an aspect ratio of 1.9±0.6, indicating that vesicle shapes vary (Figure 1a-d, Figure S5). Texturally, there was no indication that crystals of any phase in this sample are oriented, which was consistent with the plotted shape preferred orientations (Figure 4; described further in section 3.3). The distribution of vesicles in 10057 was observed to be uniform, except for the region shown at the top of the sample in Figure 1a and detailed in Figure 3a. This region is less vesiculated and visually coarser-grained than the surrounding finer-grained basalt (Figure 3a). The transition between these sample regions is abrupt, thus suggesting that this is an entrained enclave (see Figure 3a for detail). From bulk rock work on sample 10057, Jerde et al. (1992) noted chemical heterogeneity in rare earth elements content; the presence of texturally and mineralogically distinct fragments may, in part, account for this variation.

Sample 12038 is holocrystalline and has an average grain size of ~0.6 mm (Meyer, 2016, and references therein). The vesicles/vugs in this sample have highly irregular shapes, resulting in an average aspect ratio of 2.4±0.8. This sample is dominated by acicular plagioclase feldspar grains which were observed to exhibit subophitic textures and enclose pyroxene grains (Figure S6). This is consistent with its classification as a feldspathic basalt. Much of this sample was found to contain only irregularly shaped vugs that are bound by mineral grains. A small portion of this sample preserves larger cavities that are distinct in their morphology (Figure 3b) and dominate the total vesicularity of this sample (which is 3.7%). The transition between these two regions is gradual, with no clear textural change in the mineralogy of the sample (see Figure 1e-f; see also Figure 3b and Figure S6). The region characterized by small vugs can be described as having diktytaxitic texture (e.g., Wilmoth and Walker, 1993). The significance of this textural characterization is described in greater detail later (see section 4, Discussion).

Sample 12043 is a medium-grained (~1 to 3 mm pyroxene grains in a matrix of ~0.5 mm grains) pigeonite basalt and is holocrystalline. On the basis of the data collected here, some pyroxene crystals were found to be macrocrystic with finer-grained interstitial pyroxene, plagioclase, and rare oxides. This sample also contains small vugs that define a diktytaxitic texture (Wilmoth and Walker, 1993), and a few rounded vesicles all of which are uniformly distributed (Figures 1i-l, 3c, S7). Although this sample is not highly vesiculated (2.7%), it does preserve the highest vesicle aspect ratio of all samples (3.4±1.9). The vugs and vesicles are not oriented in any particular direction indicating the high aspect ratio is likely due to vug shape variation, and not elongation. This is described further in section 3.3.

Sample 15085 is the coarsest grained (~5 mm) sample studied here (Figure 1m-p, and Figure S8), and has previously been described as microgabbroic (e.g., Grove and Walker, 1977). Large euhedral plagioclase and pyroxene crystals are present with finer-grained pyroxene and plagioclase grains present as interstitial. Plagioclase poikilitically

encloses some of the pyroxenes. This sample is also the least vesiculated of all samples studied here (0.6%) with only rare, small vugs dispersed throughout the sample (see Figures 1 and 3d). The average aspect ratio of these vugs is 2.7±1.1, but once again this is attributed to irregular vug shapes, not elongation. This is because elongation mechanisms would align vugs in a specific direction, and this was not observed in the stereonet projection (Figure 4; Passey and Bell, 2007). In addition to being able to distinguish and extract tridymite information, zonation within individual pyroxene grains was revealed (Figure 3d). Here, zonation is normal (i.e., trending towards Fe-rich rims), which, combined with the coarse-grained nature of this sample, indicates that 15085 experienced a slow cooling environment during crystallization, consistent with the conclusions of Grove and Walker (1977) and Takeda et al. (1975).

Sample 15556 is holocrystalline, fine-grained (~0.4 mm, Meyer, 2016, and references therein), and contains minor porphyritic grains of what appeared to be pyroxene, though olivine macrocrysts have also been noted in this sample (Ryder, 1985). This sample is also highly vesiculated (48.0%), but the vesicles have the lowest aspect ratio of all the samples studied here, at 1.5±0.6. The vesicularity reported here for sample 15556 is consistent with previous studies (Table S2, Meyer, 2016, and references therein), although the mineralogy is not. A portion of this sample contains a region with notably smaller vesicles (Figure 3e, S9). This area of interest (on the right in Figure 3e) was cropped and re-analyzed via *Blob3B.* Its vesicularity is ~12%.

Because of the large size of sample 70017, the use of higher energy X-rays was necessitated. This decreased relative attenuation and required a lower imaging resolution. The following observations are based on the cropped evaluation of sample 70017 (see section 3.1). This sample is holocrystalline, medium grained (up to 2 mm), and vesicular (10.1%). The vesicularity of this sample is defined by numerous irregularly shaped vesicles with an average aspect ratio of 2.4±0.8. Some of the largest vesicles were partly filled with chipped sample material (Figure 3f, S10). This likely contributed to irregularity of vesicle shapes and could account for the higher aspect ratio.

2.3.3 Strain evaluation

Shape preferred orientations of oxides and vesicles are summarized as stereographic projections and rose diagrams in Figure 4. Orientation distributions of oxides and vesicles in samples 12038 and 12043 were found to be internally consistent and oriented in cluster distributions (*K*-values >1, see Table S3). In contrast, samples 10057, 15085, 15556, and 70017 were not internally consistent with respect to their oxide and vesicle shape preferred orientations. As summarized by rose diagrams presented in Figure 4, neither oxides nor vesicles are strongly foliated or lineated, suggesting these samples did not experience strain to a degree that imparted a petrofabric. To evaluate this further, the statistical test described by Woodcock and Naylor (1983) was employed to assess the shape (*K*-value, equation [1]) and strength (*C*-value, equation [2]) of each petrofabric. We remind the reader that both parameters are dimensionless units calculated from the eigenvalues of an orientation distribution. From Woodcock and Naylor (1983), a fabric is strong if the *C*-value is near to or greater than 3; a C-value below 3 indicates a weak fabric where particle orientations are close to random. As shown in Table S3, none of the distributions had a *C*-value greater than 1; in fact, most distributions range in *C*-value from 0.1 to 0.4, indicating

that they experienced little strain during emplacement and solidification on the lunar surface. However, it is important to recognize here that the two samples with highest clustering visually (10057 and 70017) in Figure 4 also had the highest *C*-values (0.86 and 0.7, respectively, Table S3) for their oxide distributions. Both samples have K-values of <1 (Table S3) which indicates a girdle distribution. Sample 10057 and 70017 may be the only samples studied here that have preserved some small degree of foliation as a result of emplacement.

2.3.4 Analysis of particle and vesicle size distributions

The size distributions of oxide phases and vesicles are presented in Figures 5 and 6, respectively, and were interpreted based on previously published work (e.g., Higgins, 2000; Morgan and Jerram, 2006). For application specifically to lunar samples, the reader is referred to Donohue and Neal (2015) and Neal et al. (2015). For vesicle distributions, the reader is referred to the work of Shea et al. (2010). The PSDs presented in Figure 5 summarize "oxides" which could comprise several mineral phases with different crystal habits, such as equant ulvöspinel or chromite, and elongated ilmenite. However, phases such as ulvöspinel and chromite typically comprise a minor component in lunar basalts (generally <0.2%; Meyer 2016 and references therein), whereas ilmenite is relatively more abundant and forms larger crystals, particularly in the high-titanium basalts (10057 and 70017). As only the 15,000 particles of greatest volume are represented in Figure 5, it was assumed that phases other than ilmenite would not significantly impact oxide size distributions for any of the samples studied here.

Samples 10057, 12043, 15085, 15556, and 70017 all preserved a "kink" in their oxide PSD (Figure 5; see also Figures S1A-B for an example of the two populations in 10057). 12038 is the only sample where size distributions were close to linear. This sample, however, is a low-titanium basalt and did not contain abundant crystals of ilmenite, hence it was challenging to interpret the oxide distribution (2.7 vol. %, see Table 1). Samples 12043, 15085, and 15556 are also low-titanium basalts and contained minor amounts of oxide particles (1.2%, 4.9%, and 1.2%, respectively), therefore the interpretation of a "kink" is likely not attributable to the samples' entire cooling history. In terms of VSDs, samples 10057 and 15085 record a single stage of growth. Samples 12038 and 12043 preserved a "kink" in their VSDs (Figure 6), indicating the existence of at least two vesicle populations. The vesicles in samples 12043 and 70017 also record some degree of vesicle coalescence. Meanwhile, the vesicle record of sample 15556 (see VFD in Figure 6) preserves clear evidence of vesicle ripening when compared to the work of Mangan and Cashman (1996) and Shea et al. (2010). During ripening, volatile species diffuse between bubbles, increasing bubble size but decreasing bubble number (Mangan and Cashman, 1996). This process likely accounts for the relatively large vesicle sizes in sample 15556 (Figure 1q-t).

At the smallest particle and vesicle sizes, PSDs and VSDs record an upward curved trend in population density. This is opposite to the problem encountered in CSD analyses, where the smallest crystals usually trend downwards in population density due to high uncertainties in their population density calculations (e.g., Cashman, 2020; Castro et al., 2003; Donohue and Neal, 2015). In the PSDs, the upturn is likely the result of a data artifact. The separation methods employed here may have led to the generation of small,

false particles from neighboring voxels of similar grayscales, thus inflating the frequency (and resulting population density) of the smallest particles. Alternatively, these trends may exist because of the incorporation of small crystals of minor phases such as chromite and ulvöspinel into the oxide analyses.

2.4. Discussion

2.4.1 Lunar lava flow morphology

The characteristics of Apollo samples can be compared to pāhoehoe lava stratigraphy seen on Earth (Donohue and Neal, 2015; Garry et al., 2012; Li et al., 2021; Roberts and Gregg, 2019; Rumpf et al., 2020; Tolometti et al., 2020; Wilson, 2009). The samples studied here originated from different magmatic systems and represented flows of distinct compositions, but their textures as characterized via XCT were still consistent with physical characteristics seen at different stratigraphic locations within typical terrestrial pāhoehoe flows. In this framework, samples 10057 (11.5% vesicularity) and 15556 (48.0% vesicularity) were interpreted to generally represent the crust of lunar pāhoehoe lava lobes (Figure 7), consistent with their fine-grained, vesicular textures (Figure 1a-d, q-t). More specifically, vesicle size in the lobe crust generally increases toward the center of a lava lobe until the core is reached (Self et al., 1998), so 15556 was interpreted as having formed deeper inside its lobe crust relative to 10057, considering that the vesicles in 15556 are relatively much larger (see Figures 1, 3, 7). Alternatively, the difference in vesicle shape and size could be related to viscosity differences – this is discussed further in section 4.2. Finally, the zone of relatively low vesicularity identified in sample 15556 (Figure 3e) may represent the transition between a vesicular zone and a less vesicular zone within a lava lobe (Figure 7; De Oliveira et al., 2021).

Pāhoehoe lava lobe crusts consist of more vesiculated and less vesiculated regions (see Figure 7; Self et al., 1998). Within sample 15556, two regions which are vesiculated to different degrees were observed (48.0% vs. 12.1%, Table S2; see Figure 3e, and section 3.2). However, because lava lobe crusts can consist of alternating bands of more and less vesiculated regions, it was challenging to identify specifically which sample region cooled at a stratigraphically higher location (Figure 7; e.g., Self et al., 1998; Vye-Brown et al., 2013). On the Moon, low atmospheric pressures (~1 kPa at 1 m depth) would allow gases to rapidly exsolve, and gases near the surface to potentially explode through the crust (Wilson and Head, 2018). Thus, the nature of 15556 precludes it from originating near the top of a flow crust. As observed, the abundance of well-rounded vesicles are consistent with a cooling environment within a relatively thick lava flow (Figures 1 and 3e; Self et al., 1998), particularly one forming towards the end of an eruption as described by Wilson and Head (2018).

The presence of diktytaxitic textures can record the transition between the crust and core of a pāhoehoe lava lobe (Self et al., 1998; Vye-Brown et al., 2013). The observation of diktytaxitic textures in 12038 (and potentially in 12043) was therefore important within the context of evaluating lunar lava flow lobe stratigraphy, and samples 12038 and 12043 may represent the transition between the lobe crust and core in each of their respective flows. More insulating conditions would exist deeper inside a flow lobe, and would have generated an environment in which bubbles ascend away from the core, consistent with the vesicle size gradation observed in 12038. Specifically, this implies that the larger vesicles

could have formed at a higher stratigraphic location than the remainder of the sample (e.g., De Oliveira et al., 2021). Additionally, insulating conditions deeper in a lobe would have facilitated crystal growth and prolonged crystallization timescales. This would allow crystals to grow into existing bubbles and generate diktytaxitic textures (e.g., Wilmoth and Walker, 1993). It is likely that sample 70017 also formed near the transition between the lobe crust and core. Its medium-grained nature precluded it from having formed in the crust, but its vesicularity (10.1%) indicated that it is unlikely to have formed deep within the lobe core (Self et al., 1998).

Finally, sample 15085 is relatively coarse-grained and less vesiculated (0.6%) relative to the sample suite studied here. Within the context of lava flow architecture, these textural characteristics were consistent with an insulating magmatic cooling environment, such as the core of a lava lobe (Figure 7). The lack of evidence for exsolved gases in this sample also indicated that any bubbles initially present were removed prior to solidification. For typical terrestrial basalt viscosities, bubbles ascend towards the surface of the lava lobe on the order of days to weeks (Aubele et al., 1988; Manga, 1996; McMillan et al., 1989). This leaves behind a dense lobe core, which is consistent with the textures observed in 15085. Previous work has reported slow, nearly linear cooling rates for sample 15085 (Grove and Walker, 1977). These inferences are consistent with the interpretation presented here that 15085 cooled in a pāhoehoe lobe core. PSD results (Figure 5) indicated that 15085 experienced a change in its magmatic environment at some point during its crystallization history, such as an eruption event or a chemical change within the magmatic system. This is discussed further in section 4.3. These scenarios may be investigated further and potentially reconciled with detailed *in-situ* chemical analyses of major silicate phases, but this sample is too coarse-grained to attempt a CSD analysis via thin-section only.

2.4.2 Lunar basalt emplacement

To generate a petrofabric, a small degree of strain is required (Benn, 1994; Paterson et al., 1998). The lower viscosities of lunar magmas would, however, impart less strain during flow and thus would be less likely to align mineral grains (or deform vesicles). There are a couple of scenarios in which vesicles could experience elongation during magmatic ascent or as a result of shear strain (Lejeune et al., 1999; Okamura et al., 2009; Shea et al., 2010). The vesicle populations in the samples studied here did not preserve evidence of either. The lack of significantly strong shape preferred orientations, as indicated by low *C*-values, was consistent with the conclusions of previous authors that lunar magmas had much lower viscosities than terrestrial magmas (e.g., Vernon, 2018; Wilson, 2009). The high aspect ratios reported here (see section 3.2) were therefore attributed to shape irregularity, and not to elongation (e.g., Passey and Bell, 2007). The lack of elongation may also be due to overprinting by other processes, such as bubble coalescence (Shea et al., 2010). This was found to be prevalent in at least three of the samples studied here (10057, 12043, and 70017). In the less vesiculated samples, vesicle/vug fabric formation may not have been preserved. This could be due to 1) efficient initial degassing during eruption leading to the removal of volatile species via rapid exsolution, or 2) an initially lower volatile content in the magma (Wilson, 2009; Wilson and Head, 1981; 2018). This is discussed further in section 4.4.

The XCT datasets and accompanying analyses reported here may also provide some additional insight into lunar lava flow thicknesses. For example, the two Apollo 15 samples studied here were consistent with having crystallized within a relatively thick lava flow. Sample 15556 had the largest vesicles of all samples studied here (Figure 1, 7), consistent with cooling relatively deep inside the crust of a lobe where gases could exsolve and coalesce but could not escape due to the overlying crust (as described in section 4.1; Keszthelyi and Self, 1998; Self et al., 1998; Wilmoth and Walker, 1993; see also Figure 7). Additionally, the microgabbroic nature of sample 15085 was also consistent with slow, insulated cooling occurring inside a relatively thick lava flow (10 to 30 m, Grove and Walker, 1977; Neal and Taylor, 1992; see also Keszthelyi and Self, 1998; Neal et al., 2015; Passey and Bell, 2007; Self et al., 1998; Takeda et al., 1975). Despite these similarities, reported differences in petrography and chemical composition preclude these two Apollo 15 samples from originating from the same flow (e.g., Meyer, 2016, and references therein; Neal and Taylor, 1992).

The low-titanium basalts of Apollo 12 and 15 have on average ~5 wt. % higher bulk SiO_2 content than the high-titanium basalts of the Apollo 11 and 17 sites (e.g., BVSP, 1981; Gawronska and McLeod, 2019; Papike et al., 1976; Papike et al., 1991; Walker et al., 1975). With bulk wt. % SiO_2 content being one of the major controls on basalt viscosity (e.g., Vernon, 2018), the Apollo 12 and 15 basaltic lavas were likely slightly more viscous. More viscous lavas create thicker flows (Rowland and Walker, 1988), which suggests that lava flows near the Apollo 12 and 15 landing sites are potentially thicker than their basaltic counterparts at the Apollo 11 and 17 landing sites.

If this is true, the high TiO_2 and low SiO_2 flows near the Apollo 11 and 17 sites were less viscous and could have been characterized by eruptions with slightly higher effusion rates (BVSP, 1981; Garry et al., 2012; Head and Wilson, 1992; Vernon, 2018). On Earth, basaltic lava flow emplacement that is confined within a lava tube or channel has been demonstrated to lead to increased lava flow rates (Dietterich et al., 2015; Keszthelyi and Self, 1998; Rowland and Walker 1988; 1990). If high effusion rates for lunar volcanism corresponded to rapid emplacement (as has been theorized by Head and Coffin, 2007), this may also induce higher strain (Hon et al., 1994; Keszthelyi and Self, 1998; Passey and Bell, 2007; Rowland and Walker, 1988). Within this context, it could be argued that samples 10057 and 70017, which recorded low, but relatively higher strain as compared to the other samples (Figure 4, Table S3), could have been emplaced more rapidly, for example within a lava tube (Roberts and Gregg, 2019; Spudis et al., 1988; Swann et al., 1972). It is less likely that these samples formed in a channel such as a lunar rille, as lavas traveling in a rille would have a vesicularity close to 0 (Wilson and Head (2018).

2.4.3 Effects of crystal and vesicle cargoes

PSD work presented here indicates that all samples except for 12038 contained two populations of oxides (Figure 5), indicating that crystals have multiple petrogenetic histories. This may correspond to pre-eruptive and post-eruptive cooling episodes resulting in mineral crystallization and gas exsolution (e.g., Donohue and Neal, 2015; Lejeune et al., 1999). Alternatively, multiple crystal populations could correspond to the identification of texturally distinct regions within these samples (e.g., the enclave incorporated in sample

10057). This is important to note because higher crystal contents have the ability to change the internal properties of a lava (Belousov and Belousova, 2018; Bergantz et al., 2017; Lejeune et al., 1999; Nicolas and Ildefonse, 1996; Paterson et al., 2019; Rumpf et al., 2020; Vernon, 2018), which can result in an increase in viscosity (Keszthelyi and Self, 1998; Lejeune et al., 1999; Nicolas, 1992; Nicolas and Ildefonse, 1992; Paterson et al., 1998; 2019; Shaw, 1969; Whitford-Stark, 1982). Vesicles, meanwhile, can either decrease or increase viscosity (Llewellin and Manga, 2005). Altogether, crystal and vesicle content could change the strain experienced by the lava (Nicolas and Ildefonse, 1996; Paterson et al., 2019). The strain recorded by samples studied here is minimal (Figure 4), except perhaps for samples 10057 and 70017 (Figure 4; Table S3). The slightly higher strain recorded by samples 10057 and 70017 could therefore be due to the presence of multiple crystal and vesicle populations (Figures 5 and 6). Overestimation of large particle sizes due to the lack of grain separation may however impact PSD and VSD interpretations (see section 2.2). Nonetheless, crystal and vesicle populations existing prior to solidification in the 10057 and 70017 lavas may have led to increased viscosities, and thus increased strain imparted on these samples during solidification.

It is possible that petrofabrics within lunar lava flows overprint one another, which as been noted on Earth (e.g., Žák et al., 2007). For example, sample 12038 preserved two vesicle/vug populations, which is consistent with vesicle shapes ranging from rounded clusters to interstitial vugs (Figure 3b). However, it was difficult to evaluate the process(es) through which the vesicles formed, as their shapes were overprinted by the later growth of crystals and formation of the diktytaxitic textures (Figure 3b). Meanwhile, sample 12043 records two distinct stages of cooling in both oxide and VSDs (Figures 5 and 6), indicating that this sample experienced two distinct stages of crystal and vesicle growth. The macrocrystic pyroxene crystal population of 12043 existing alongside a population of finer-grained pyroxenes (see Figures 1 and 3c) likely also corresponds to a change in cooling environment. No significant degree of strain is recorded by this sample, indicating that any potential crystal effects associated with strain were either nonexistent, insignificant, overprinted, or too complicated to distinguish here. Additionally, in samples 10057, 15085, 15556, and 70017 the mean planes of oxide and vesicle orientation distributions were not consistent. This may indicate that multiple strain-related mechanisms were involved. For example, strain from buoyancy may have imparted a greater effect on rising bubbles than strain from flow. In this scenario, the original flow fabric would be overprinted (e.g., Aubele et al., 1988; Polacci and Papale, 1997). Alternatively, the samples may have only experienced a minimal amount of strain. The extent to which different components of strain contribute to petrofabrics in lunar basalts, as well as the extent to which petrofabrics are preserved within the Apollo basalt sample suite should therefore be examined further in order to investigate these potential scenarios. Additional Apollo basalt sample characterization must be completed via experimental and analog studies in order to evaluate these emplacement dynamics, particularly for each landing site location. Future *in-situ* sampling of basaltic lava flows on the lunar surface should be informed by knowledge of flow architecture and an understanding of lobe geometry. This would support the collection of sample suites which fully represent the characteristics of lunar lava flows their spatial extent in the field.

2.4.4 Effects of volatiles on lunar eruptions

Within the framework proposed by Wilson and Head (2018), samples 12038 and 12043 may have formed during stage 3 of eruption when vesicularity is low but increasing, while samples 10057 and 70017 may have formed later during their respective eruption events, preserving their volatile content. However, flow rates are minimized during the later stages of the Wilson and Head (2018) model which is not consistent with the low, but relatively higher, strain imparted upon 10057 and 70017 when compared to the other samples, unless they formed in a lava tube as described in section 4.2. Alternatively, 10057 and 70017 may have formed from lavas which were initially volatile-rich. Sample 15085, may have formed during the intermediate stage 2 of the eruption where a high flux of Hawaiian-style effusive flow dominated and vesicularity was near 0 (Wilson and Head, 2018). At this stage, lava lakes are generated and facilitate the formation of coarse-grained textures at stratigraphically low locations (see Figure 7; McCarter et al., 2006). It is not currently possible to measure lava flow thicknesses and properties directly in the field on the Moon, and distinguishing individual lava flows through remote sensing alone proves to be challenging (e.g., Rumpf et al., 2020). From Wilson and Head (2018), lavas with the highest vesicularity are associated with the final stages of eruption and are characterized by Strombolian-style vesicular flow. At this stage, flows that are injected into previous lobes maintain their vesicularity while erupted flows become foams. Sample 15556 cannot be a foam as it contains less than the 60% to 70% vesicles required of foams (Mangan and Cashman, 1996). Instead, the lava which formed 15556 likely intruded into an inflating lobe. This scenario is consistent with the stratigraphic interpretation presented in Figure 7.

The VSD analyses performed here could shed further light on the role of volatiles during lunar lava emplacement. Mangan and Cashman (1996) argue that vesicle ripening is a late-stage effect that post-dates initial volatile exsolution, so the vesicle ripening observed in 15556 could also indicate that this sample was not quenched during eruption on the surface and instead cooled in an environment where ripening was possible. Furthermore, bubble migration due to relatively low lava viscosity could explain the lack of volatile species that is preserved in coarse-grained sample 15085. Alternatively, 15085 was produced by a magma with initially low volatile contents, in contrast to the highly vesiculated nature of 15556. Sample 15085 is a quartz-normative basalt, and 15556 is an olivine-normative basalt, hence they likely originated from distinct sources within the lunar mantle (Neal and Taylor, 1992; Rhodes and Hubbard, 1973). As the lunar mantle is likely heterogeneous with respect to volatile contents (McCubbin et al., 2015), the potentially distinct source regions of 15085 and 15556 could explain the variations in vesicle content of the Apollo 15 lavas. Meanwhile, samples 10057, 12043, and 70017 were found to record evidence of vesicle coalescence (Figure 6; see also Shea et al., 2010). This is consistent with the low viscosities of lunar magmas which would have facilitated bubble migration and coalescence relatively easily compared to higher viscosity magmas (Manga, 1996; Manga and Stone, 1995).

Vesicle volume also has implications for evaluating the volatile load of lunar magmas (e.g., Wilson and Head, 2018). The Moon is generally depleted in volatile species relative to other rocky bodies (e.g., see summaries by McCubbin et al., 2015, and Day and Moynier, 2014). However, volatile species including S, CO, CO_2, H_2O, H_2, F, and Cl have been observed (e.g., Hauri et al., 2015; Wetzel et al., 2015) and modeled (e.g., Newcombe

et al., 2019: Nicholis and Rutherford, 2009) to exist on the Moon. Specifically, CO had long been proposed as the primary volatile species responsible for the generation of pyroclastic deposits and vesicular basalts on the Moon (e.g., Fogel and Rutherford, 1995; Nichols and Rutherford, 2009; Sato, 1979; Wetzel et al., 2015). This necessitates the existence of graphite within the lunar mantle (e.g., Nicholis and Rutherford, 2009), which has only been found in one sample (impact melt breccia 72255).

In 2008, Saal et al. showed that the cores of low-Ti lunar volcanic glass beads contain up to 46 ppm H_2O, 40 ppm, F, and 576 ppm S, with cores of high-Ti beads containing up to 15 ppm H_2O, 15 ppm F, and ~400 ppm S, and the cores of very-low-Ti volcanic glasses containing up to 30 ppm H_2O, 10 ppm F, and 270 ppm S (Saal et al., 2008). Researchers have since argued that the sources of these volatile species in the lunar mantle include residual liquid that remained trapped between lunar mantle cumulates after the solidification of the mantle, and nominally anhydrous minerals that contain trace amounts of volatiles (e.g., Liu et al., 2012; Hui et al., 2013; Mills et al., 2014; McCubbin et al., 2015; Potts et al., 2021). The urKREEP reservoir which formed towards the end of the crystallization of the Lunar Magma Ocean and which is enriched in K, rare earth elements, and P, likely also played a significant role in provide volatile species to lunar magmas. McCubbin et al. (2015) proposed that the primary source of volatiles in lunar magmas is the residual urKREEP reservoir and not the lunar mantle. urKREEP could have contributed to the formation of the vesicular samples studied here. Sample 10057 is a member of the high-K Apollo 11 basalt suite, which is proposed to have formed as a result of mantle-derived magma mixing with a KREEPy assimilant (Jerde et al., 1994, and references therein). The incorporation of KREEP-derived volatiles during the petrogenesis of 10057 is thus a possibility and supported by bulk major element chemistry. Several KREEP basalts were collected during the Apollo 15 mission alongside the highly vesiculated 15556 (Ryder, 1985). This sample, however, does not have a KREEPy geochemical signature and thus it is unlikely that its volatile component is derived from KREEP. Given the lack of graphite observed throughout the lunar mare basalt suite, and the recent findings of elevated H abundance in lunar magmas (e.g., Barnes et al., 2013; Greenwood et al., 2011; McCubbin et al., 2010; Tartèse et al., 2013; 2014), we postulate that the more likely volatile species to have produced the vesicles in 15556 and other basalts studied here is H_2.

2.5 Conclusions

The application of XCT offers planetary geoscientists unparalleled insights into the interior features of extraterrestrial materials. Through the application of XCT to a suite of six basalts from the Apollo 11, 12, 15, and 17 missions it was found that lunar lavas are texturally consistent with terrestrial pāhoehoe lava stratigraphy, indicating that they formed as low-viscosity, effusive flows. This is consistent with the lack of preservation of any strain-induced petrofabric as defined by the oxide or vesicle populations. PSDs indicated that basaltic lunar lavas likely contained crystal loads prior to eruption and emplacement on the lunar surface. Preserved vesicle populations serve as evidence of processes which worked to overprint initial vesicle textures. Specifically, vesicles in several samples record coalescence and ripening. Connectivity modeling of voids within the samples (e.g., Blunt et al., 2013; Moitra and Houghton, 2021; Sok et al., 2009) could shed more light on the textural properties of these vesicles, and the general behavior of bubbles in lunar magmas. Additional work to characterize the role of lunar volatiles would undoubtedly shed more

light on the conditions of lava eruption and flow emplacement mechanisms, as well as the stratigraphic correlations of vesicular samples collected during each Apollo mission. As summarized here, XCT can support remote sensing investigations of lava flows on other planetary bodies by providing general constraints on lava properties.

Within the context of sample preservation and curation, XCT significantly improves documentation practices by curating accurate and precise sample reconstructions (Blumenfeld et al., 2017; 2019; Jerram and Higgins, 2007; McCubbin et al., 2019). By acquiring a 3D scan of a sample, XCT data may better inform researchers on sample heterogeneity (e.g., due to brecciation, Zolensky et al., 2014), as is exemplified by the magmatic enclave found here in sample 10057. XCT datasets can also direct researchers to the most advantageous and representative angle at which a sample should be cut into thin section(s) (e.g., Hanna et al., 2015; Jerram and Higgins, 2007). In short, XCT is a powerful analytical and preservatory technique that continues to prove itself as a critical asset to extraterrestrial sample curation and the planetary science community.

2.6 Acknowledgements

The authors would like to acknowledge the Apollo astronauts for collecting the lunar samples studied here and all those involved in the Apollo program who made this possible. Sincere thanks are extended to Dr. M. Elise Rumpf and Dr. Jessica Barnes for providing detailed, constructive feedback on this manuscript, as well as Dr. Clive Neal and an anonymous reviewer for their comments on an earlier version of this work. Finally, we acknowledge Dr. Vincent Fernandez for providing information regarding parameters used to scan sample 10057 at the National History Museum in London, UK. This research included XCT image data produced by Astromaterials 3D for NASA's Acquisition & Curation Office, funded by NASA Planetary Data Archiving, Restoration, and Tools Program, Proposal No.: 15-PDART15_2-0041.

2.7 References Cited

Allmendinger, R. W., Cardozo, N., and Fisher, D., 2012. Structural geology algorithms: Vectors and tensors in structural geology. Cambridge University Press, New York.

Arif, M., Mahmoud, M., Zhang, Y., Iglauer, S., 2021. X-ray tomography imaging of shale microstructures: A review in the context of multiscale correlative imaging. International Journal of Coal Geology 233, 103641. doi: 10.1016/j.coal.2020.103641

Aubele, J. C., Crumpler, L. S., Elston, W. E., 1988. Vesicle zonation and vertical structure of basalt flows. Journal of Volcanology and Geothermal Research 35, 349-374.

Barnes, J. J., Franci, I. A., Anand, M., Tartèse, R., Starkey, N. A., Koike, M., Sano, Y., Russell, S. S. 2013. Accurate and precise measurements of the D/H ratio and hydroxyl content in lunar apatites using NanoSIMS. Chemical Geology 337-338, 48-55. doi: 10.1016/j.chemgeo.2012.11.015

Basaltic Volcanism Study Project (BVSP), 1981. Basaltic Volcanism on the Terrestrial Planets. Pergamon Press, Inc., New York.

Belousov, A., and Belousova, M., 2018. Dynamics and viscosity of 'a'a and pahoehoe lava flows of the 2012-2013 eruption of Tolbachik volcano, Kamchatka (Russia). Bulletin of Volcanology 80(6). doi:10.1007/s00445-017-1180-2

Benn, K., 1994. Overprinting of magnetic fabrics in granites by small strains: numerical modelling. Tectonophysics 233(3-4), 153-162. doi:10.1016/0040-1951(94)90238-0

Bergantz, G. W., Schleicher, J. M., Burgisser, A., 2017. On the kinematics of crystal-rich systems. Journal of Geophysical Research: Solid Earth 122, 6131-6159. doi:10.1002/2017JB014218

Blumenfeld, E. H., Evans, C. A., Oshel, E. R., Liddle, D. A., Beaulieu, K. R., Zeigler, R. A., Righter, K., Hanna, R. D., Ketcham, R. A., 2017. Research-Grade 3D Virtual Astromaterials Samples: Novel Visualization of NASA's Apollo Lunar Samples and Antarctic Meteorite Samples to benefit Curation, Research, and Education. Houston, Texas, Lunar and Planetary Institute, Lunar and Planetary Science Conference XLVIII, abstract #2874.

Blumenfeld, E. H., Beaulieu, K. R., Thomas, A. B., Evans, C. A., Zeigler, R. A., Oshel, E. R., Liddle, D. A., Righter, K., Hanna, R. D., Ketcham, R. A. 2019. 3D Virtual Astromaterials Samples Collection of NASA's Apollo Lunar and Antarctic Meteorite Samples to be an Online Database to Serve Researchers and the Public.

Houston, Texas, Lunar and Planetary Institute, Lunar and Planetary Science Conference XLVIII, abstract #3056.

Blunt, M. J., Bijeljic, B., Dong, H., Gharbi, O., Iglauer, S., Mostaghimi, P., Paluszny, A., Pentland, C. 2013. Pore-scale imaging and modelling. Advances in Water Resources 51, 197-216. doi: 10.1016/j.advwatres.2012.03.003

Brum, J. T., McLeod, C. L., Shaulis, B., Duley, M., Loocke, M. 2020. Investigating the History of Allan Hills (ALHA) 81005: What a Meteorite's Components Can Tell Us About its Past. Houston, Texas, Lunar and Planetary Institute, Lunar and Planetary Science Conference LII, abstract #2919.

Cardozo, N., and Allmendinger, R.W., 2013, Spherical projections with OSXStereonet: Computers & Geosciences 51, 193-205, doi: 10.1016/j.cageo.2012.07.021

Carvalho, L. E., Fauth, G., Baecker Fauth, S., Krahl, G., Moreira, A. C., Fernandes, C. P., von Wangenheim, A., 2020. Automated Microfossil Identification and Segmentation using a Deep Learning Approach. Marine Micropaleontology 158, 101890. doi: 10.1016/j.marmicro.2020.101890

Cashman, K. V., 2020. Crystal Size Distribution (CSD) Analysis of Volcanic Samples: Advances and Challenges. Frontiers in Earth Science 10. doi:10.3389/feart.2020.00291

Cashman, K. V., and J. P. Kauahikaua, 1997. Re-evaluation of vesicle distributions in basaltic lava flows, Geology 25, 419-422.

Castro, J., Manga, M., Cashman, K., 2002. Dynamics of obsidian flows inferred from microstructures: insights from microlite preferred orientations. Earth and Planetary Science Letters 199, 211-226.

Castro, J. M., Cashman, K. V., Manga, M., 2003. A technique for measuring 3D crystal-size distributions of prismatic microlites in obsidian. American Mineralogist 88, 1230-1240. doi: 10.2138/am-2003-8-906

Cnudde, V., and Boone, M. N., 2013. High-resolution X-ray computed tomography in geosciences: A review of the current technology and applications. Earth-Science Reviews 123, 1-17, doi: 10.1016/j.earscirev.2013.04.003

Cone, K. A., Palin, R. M., Singha, K., 2020. Unsupervised machine learning with petrological database ApolloBasaltDB reveals complexity in lunar basalt major element oxide and mineral distribution patterns. Icarus 346, 113787, doi: 10.1016/j.icarus.2020.113787

Cunningham, J. A., Rahman, I. A., Lautenschlager, S., Rayfield, E. J., Donoghue, P. C. J., 2014. A virtual world of paleontology. Trends in Ecology & Evolution 29(6), 347-357. doi: 10.1016/j.tree.2014.04.004

Day, J. M. D., and Moynier, F. 2014. Evaporative fractionation of volatile stable isotopes and their bearing on the origin of the Moon. Philosophical Transactions of the Royal Society Series A, Mathematical, Physical, and Engineering Sciences 372, 20130259. doi: 10.1098/rsta.2013.0259

De Oliveira, J. H. C., Neal, C. R., Blumenfeld, E. H., 2021. Understanding Orientation and Formation: Using XCT Data to Quantify Void Space in Lunar Sample. Houston, Texas, Lunar and Planetary Institute, Lunar and Planetary Science Conference XII, abstract #2628.

Dietterich, H. R., Cashman, K. V., Rust, A. C., Lev, E., 2015. Diverting lava flows in the lab. Nature Geoscience 8, 494-496. doi: 10.1038/ngeo2470

Donohue, P. H., and Neal, C. R., 2015. Quantitative textural analysis of ilmenite in Apollo 17 high-titanium mare basalts. Geochimica et Cosmochimica Acta 149, 115-130, doi:10.1016/j.gca.2014.11.002

du Plessis, A., and Boshoff, W. P., 2019. A review of X-ray computed tomography of concrete and asphalt construction materials. Construction and Building Materials 199, 637-651. doi: 10.1016/j.conbuildmat.2018.12.049

Ebel, D. S., and Rivers, M. L., 2007. Meteorite 3-D synchrotron microtomography: Methods and applications. Meteoritics & Planetary Science 42(9), 1627-1646, doi:10.1111/j.1945-5100.2007.tb00595.x

Fogel, R. A. and Rutherford, M. J. 1995. Magmatic volatiles in primitive lunar glasses: I. FTIR and EPMA analyses of Apollo 15 green and yellow glasses and revision of the volatile-assisted fire-fountain theory. Geochim. Cosmochim. Acta 59, 201–215.

Folkes, M. J., Russell, D. A. M., 1980. Orientation effects during the flow of short-fibre reinforced thermoplastics. Polymer 21, 1252–1258.

Friedrich, J. M., Macke R. J., Wignarajah D. P., Rivers, M. L., Britt, D. T., Evel, D. S., 2008. Pore size distribution in an uncompacted equilibrated ordinary chondrite. Planetary and Space Science 56(7), 895-900, doi: 10.1016/j.pss.2008.02.002

Gan, M., Zhang, L., Miao, X., Oladyshkin, S., Cheng, X., Wang, Y., Shu, Y., Su, X., Li, X., 2020. Application of computed tomography (CT) in geologic CO_2 utilization and storage research: A critical review. Journal of Natural Gas Science and Engineering 83, 103591. Doi: 10.1016/j.jngse.2020.103591

Garry, W.B., Robinson, M.S., Zimbelman, J.R., Bleacher, J.E., Hawke, B.R., Crumpler, L. S., Braden, S.E., Sato, H., 2012. The origin of Ina: evidence for inflated lava flows on the Moon. Journal of Geophysical Research 117, E00H31. doi: 10.1029/2011JE003981

Gawronska, A. G., and McLeod, C. L., 2019. Basalts: Insights into Planetary Magmatic Processes from the Moon and Earth. Houston, Texas, Lunar and Planetary Institute, Lunar and Planetary Science Conference X, abstract #3271.

Gillis, J. J., Jolliff, B. L., Elphic, R. C. 2003. A revised algorithm for calculating TiO2 from Clementine UVVIS data: A synthesis of rock, soil, and remotely sensed TiO2 concentrations. Journal of Geophysical Research 108 (E2), 1-18. doi: 10.1029/2001JE001515

Gillis, J. J., Jolliff, B. L., Korotev, R. L. 2004. Lunar surface geochemistry: Global concentrations of Th, K., and FeO as derived from lunar prospector and Clementine data. Geochimica et Cosmochimica Acta 68(18):3791-3805. doi: 10.1016/j.gca.2004.03.024

Greenwood, J. P., Itoh, S., Sakamoto, N., Warren, P., Taylor, L., Yurimoto, H. 2011. Hydrogen isotope rations in lunar rocks indicate delivery of cometary water to the Moon. Nature Geoscience 4, 79-82. doi: 10.1038/ngeo1050

Gregg, T., 2017. Patterns and processes: Subaerial lava flow morphologies: A review. Journal of Volcanology and Geothermal Research 342, 3-12. doi: 10.1016/j.jvolgeores.2017.04.022

Gross, J., and Treiman A. H. 2011. Unique spinel-rich lithology in lunar meteorite ALHA 81005: Origin and possible connection to M^3 observations of the farside highlands. Journal of Geophysical Research Letters 116(E10). doi: **10.1029/2011JE003858**

Grove, T. L., and Walker, D., 1977. Cooling histories of Apollo 15 quartz-normative basalts. Proceedings of the 8th Lunar Science Conference, 1501-1520.

Hamilton, C. W., 2019. "Fill and Spill" Lava Flow Emplacement: Implications for Understanding Planetary Flood Basalt Eruptions. In: NASA Technical Memorandum 220139, pp. 47-56.

Hanna, R.D., Ketcham, R.A., Zolensky, M., Behr, W., 2015, Impact-induced brittle deformation, porosity loss, and aqueous alteration in the Murchison CM chondrite: Geochimica et Cosmochimica Acta 171, 256-282, doi:10.1016/j.gca.2015.09.005

Hanna, R. D., and Ketcham, R. A., 2017. X-Ray computed tomography of planetary materials: A primer and review of recent studies. Chemie der Erde 77, 547-572, doi: 10.1016/j.chemer.2017.01.006

Harris, A. J. L., and Allen, J. S., 2008. One-, two- and three-phase viscosity treatments for basaltic lava flows. Journal of Geophysical Research 113, B09212. doi: 10.1029/2007JB005035

Hauri, E. H., Saal, A. E., Rutherford, M. J., Van Orman, J. A. 2015. Water in the Moon's interior: Truth and consequences. Earth and Planetary Science Letters 409, 252-264. doi: 10.1016/j.epsl.2014.10.053

Head, J.W., and Wilson, L., 1992. Lunar mare volcanism: stratigraphy, eruption conditions, and the evolution of secondary crusts. Geochimica and Cosmochimica Acta 56, 2155–2175.

Heiken, G. H., Vaniman, D. T., French, B. M. 1991. The Lunar Sourcebook: A User's Guide to the Moon. Cambridge University Press. 736 p.

Hezel, D. C., Friedrich, J. M., Uesugi, M., 2013. Looking inside: 3D structures of meteorites. Geochimica et Cosmochimica Acta, 116, 1–4, doi: 10.1016/j.gca.2013.01.012

Hiesinger, H., Head III, J.W., Wolf, U., Jaumann, R., Neukum, G., 2002. Lunar mare basalt flow units: thickness determined from crater size-frequency distributions. Geophysical Research Letters 29, 1248. doi: 10.1029/2002GL014847

Higgins, M. D., 2000. Measurement of crystal size distributions. American Mineralogist 85, 1105-1116, doi:10.2138/am-2000-8-901

Hon, K., Kauahikaua, J., Denlinger, R., MacKay, K., 1994. Emplacement and inflation of pahoehoe sheet flows: observations and measurements of active lava flows on Kilauea Volcano, Hawaii. Geological Society of America Bulletin 106, 351–370.

Howard, K. A., and J. W. Head III, 1972. Regional geology of Hadley Rille. In: Apollo 15: Preliminary Science Report. NASA SP-289, 53–58.

Howard, K. A., Head, J. W., Swann, G. A., 1972. Geology of Hadley Rille. In: Proceedings of the 3rd Lunar Science Conference, 1–14.

Hui, H.J., Peslier, A.H., Zhang, Y.X., and Neal, C.R., 2013. Water in lunar anorthosites and evidence for a wet early Moon. Nature Geoscience, 6, 177–180. doi: 10.1038/ngeo1735

Jerde, E. A., Snyder, G. A., Taylor, L. A., Liu, Y. –G., Schmitt, R. A., 1992. Chemical Composition of Apollo 11 Mare Basalt Rocks: Evidence of Sample Heterogeneity in 10057. Abstracts of the Lunar and Planetary Science Conference 23, 613.

Jerde, E. A., Snyder, G. A., Taylor, L. A., Liu, Y.-G., Schmitt, R. A. 1994. The origin and evolution of lunar high-Ti basalts: Periodic melting of a single source at Mare Tranquilitatis. Geochimica et Cosmochimica Acta 58(1), 515-527. doi: 10.1016/0016-7037(94)90480-4

Jerram, D. A., and Higgins, M. D., 2007. 3D Analysis of Rock Textures: Quantifying Igneous Microstructures. Elements 3(4), 239-245, doi: 10.2113/gselements.3.4.239

Keszthelyi, L., Self, S., 1998. Some physical requirements for the emplacement of long basaltic lava flows. Journal of Geophysical Research 103(11), 27,447–27,464.

Ketcham, R. A., and Carlson, W. D., 2001. Acquisition, optimization and interpretation of X-ray computed tomographic imagery: applications to the geosciences. Computers and Geosciences 27(1), 381-400, doi:10.1016/S0098-3004(00)00116-3

Ketcham, R. A., 2005. Computational methods for quantitative analysis of three-dimensional features in geological specimens. Geosphere 1(1), 32-41, doi:10.1130/GES00001.1

Kramer, F. E., Twedell D. B., Walkton Jr., W. J. A., 1977. Apollo-11 Lunar Sample Information Catalogue (Revised). National Aeronautics and Space Administration Johnson Space Center Contribution #12522.

LaSpina, G., Arzilli, F., Llewellin, E. W., Burton, M. R., Clarke, A. B., de'Michieli Vitturi, M., Polacci, M., Hartley, M. E., Di Genova, D., Mader, H. M., 2021. Explosivity of basaltic lava fountains is controlled by magma rheology, ascent rate and outgassing. Earth and Planetary Science Letters 552, 116658. doi: 10.1016/j.epsl.2020.116658

Lemelin, M., Lucey, P. G., Miljković, K., Gaddis, L. R., Hare, T., Ohtake, M. 2019. The compositions of the lunar crust and upper mantle: Spectral analysis of the inner rings of lunar impact basins. Planetary and Space Science 165, 230-243. doi: 10.1016/j.pss.2018.10.003

Li, S., Taylor, G. J., Lentz, R., Needham, D. H., Gaddis, L., Shea, T., 2021. Water Anomalies at Rugged Lava Flows on the Moon. Houston, Texas, Lunar and Planetary Institute, Lunar and Planetary Science Conference XII, abstract #2508.

Li, C., Hu, H., Yang., M-.F., Pei, Z-.Y., Zhou, Q., Ren, X., Liu, B. L., Zeng, X., Zhang, G., Zhang, H., Liu, J., Wang, Q., Deng, X., Xiao, C., Yao, Y., Xue, D., Zuo, W., Su, Y., Wen, W., Ouyang, Z. 2021. Characteristics of the lunar samples returned by Chang'E-5 mission. National Science Review, nwab188, doi:10.1093/nsr/nwab188

Liu, Y., Mosenfelder, J.L., Guan, Y., Rossman, G.R., Eiler, J.M., and Taylor, L.A., 2012. SIMS analysis of water abundances in nominally anhydrous minerals in lunar basalts. Proceedings of the 43rd Lunar and Planetary Science Conference, Woodlands, Texas, 1866.

Llewellin, E. W., Manga, M. 2005. Bubble suspension rheology and implications for conduit flow. Journal of Volcanology and Geothermal Research 143(1-3), 205-217. doi: 10.1016/j.jvolgeores.2004.09.018

Manga, M., 1996. Waves of bubbles in basaltic magmas and lavas. Journal of Geophysical Research 101, 17457-17465.

Manga, M., and Stone, H. A. 1995. Collective hydrodynamics of deformable drops and bubbles in dilute low Reynolds number suspensions: Journal of Fluid Mechanics, v. 300, p. 231–263.

Mangan, M. T., and Cashman, K. V., 1996. The structure of basaltic scoria and reticulite and inferences for vesiculation, foam formation, and fragmentation in lava fountains. Journal of Volcanology and Geothermal Research 73, 1-18. doi:10.1016/0377-0273(96)00018-2

Martin, D., Nokes, R., 1988. Crystal settling in a vigorously convection magma chamber. Nature 332, 534–536.

Mathews, J., Campbell, Q. P., Xu, H., Halleck, P., 2017. A review of the application of X-ray computed tomography to the study of coal. Fuel 209, 10-24. doi: 10.1016/j.fuel.2017.07.079

McCarter, R. L., Fodor, R. V., Trusdell, F. 2006. Perspectives on basaltic magma crystallization and differentiation: Lava-lake blocks erupted at Mauna Loa volcano summit, Hawaii. Lithos 90 (3-4), 187-213. doi: 10.1016/j.lithos.2006.03.005

McCubbin, F. M., Steele, A., Hauri, E. H., Nekvasil, H., Yamashita, S., Hemley, R. J. 2010. Nominally hydrous magmatism on the Moon. Proceedings of the National Academy of Science 107(25), 11223-11228. doi: 10.1073/pnas.100667710

McCubbin, F. M., Vander Kaaden, K. E., Tartèse, R., Klima, R. L., Liu, Y., Mortimer, J., Barnes, J. J., et al. 2015. Magmatic volatiles (H, C, N, F, S, Cl) in the lunar mantle, crust, and regolith: Abundances, distributions, processes, and reservoirs. American Mineralogist 100, 1668-1707. doi: 10.2138/am-2015-4934ccbyncnd

McCubbin, F. M., Herd, C. D. K., Yada, T., Hutzler, A., Calaway, M. J., Allton, J. H., Corrigan, C. M., Fries, M. D., Harrington, A. D., McCoy, T. J., Mitchell, J. L., Regberg, A. B., Righter, K., Snead, C. J., Tait, K. T., Zolensky, M. E., Zeigler, R. A., 2019. Advanced Curation of Astromaterials for Planetary Science. Space Science Reviews 215(48), doi:10.1007/s11214-019-0615-9

McMillan, K., Long, P. E., Cross, R. W., 1989. Vesiculation in Columbia River basalts. See Reidel & Hooper 1989, pp. 157-167

Meyer, C., 2016. The Lunar Sample Compendium Database. Astromaterials Research and Exploration Science. https://curator.jsc.nasa.gov/lunar/lsc/

Mills, R.D., Simon, J.I., Alexander, C.M.O., Wang, J., Christoffersen, R., and Rahman, Z., 2014. Chemical zoning of feldspars in lunar granitoids: Implications for the origins of lunar silicic magmas. 45th Lunar and Planetary Science Conference, The Woodlands, Texas, 1547.

Moitra, P., and Houghton, B. F. 2021. Porosity-permeability relationships in crystal-rich basalts from Plinian eruptions. Bulletin of Volcanology 83, 71. doi: 10.1007/s00445-021-01496-7

Mongrain, J., Larsen, J. F., King, P. L. (2008) Rapid water exsolution, degassing, and bubble collapse observed experimentally in K-phonolite melts. Journal of Volcanology and Geothermal Research 173 (3-4), 178-184. https://doi.org/10.1016/j.jvolgeores.2008.01.026

Morgan, D. J., and Jerram, D. A., 2006. On estimating crystal shape for crystal size distribution analysis. Journal of Volcanology and Geothermal Research 154, 1-7, doi: 10.1016/j.jvolgeores.2005.09.016

Murase, R., and McBirney, A.T., 1970. Viscosity of lunar lavas. Science 167, 1491–1492.

Neal, C. R., and Taylor, L. A., 1992. Petrogenesis of mare basalts: A record of lunar volcanism. Geochimica et Cosmochimica Acta 56, 2177–2211, doi: 10.1016/0016-7037(92)90184-K

Neal, C. R., Donohue, P., Fagan, A. L., O'Sullivan, K., Oshrin, J., Roberts, S., 2015. Distinguishing between basalts produced by endogenic volcanism and impact processes: A non-destructive method using quantitative petrography of lunar basaltic samples. Geochimica et Cosmochimica Acta 148, 62-80, doi: 10.1016/j.gca.2014.08.020

Newcombe, M. E., Beckett, J. R., Baker, M. B., Newman, S., Guan, Y., Eiler, J. M., Stolper, E. M. 2019. Effects of pH2O and fO2 on the diffusion of H-bearing species in lunar basaltic liquid and an iron-free basaltic analog at 1 atm. Geochimica et Cosmochimica Acta 259, 316-343. doi: 10.1016/j.gca.2019.05.033

Nicholis, M. G., and Rutherford, M. J. 2009. Graphite oxidation in the Apollo 17 orange glass magma: Implications for the generation of a lunar volcanic gas phase. Geochimica et Cosmochimica Acta 73(19), 5905-5917. doi: 10.1016/j.gca.2009.06.022

Nicolas, A., 1992. Kinematics in Magmatic Rocks with Special Reference to Gabbros. Journal of Petrology 33(4), 891-915. doi:10.1093/petrology/33.4.891

Nicolas, A., and Ildefonse, B., 1996. Flow mechanisms and viscosity in basaltic magma chambers. Geophysical Research Letters 23(16), 2013-2016. doi: 10.1029/96GL02073

Object Research Systems (ORS) Inc., 2020. Dragonfly 2020.2 [Computer software]. Montreal, Canada; software available at http://www.theobjects.com/dragonfly.

Okamura, S., Nakamura, M., Takeuchi, S., Tsuchiyama, A., Nakano, T., Uesugi, K., 2009. Magma deformation may induce non-explosive volcanism via degassing through bubble networks. Earth and Planetary Science Letters 281, 267-274. doi:10.1016/j.epsl.2009.02.036

Papike, J. J., Hodges, F. N., Bence, A. E., Cameron, M., Rhodes, J. M., 1976. Mare Basalts: Crystal Chemistry, Mineralogy, and Petrology. Reviews of Geophysics and Space Physics 14(4), 475-540.

Papike, J., Taylor, L., Simon, S., 1991. Lunar Minerals. In: Heiken, G.H., Vaniman, D.T., French, B.M. (Eds.), The Lunar Source Book: A User's Guide to the Moon. Cambridge University Press, Cambridge, pp. 121–161.

Passey, S. R., and Bell, B. R., 2007. Morphologies and emplacement mechanisms of the lava flows of the Faroe Islands Basalt Group, Faroe Islands, NE Atlantic Ocean. Bulletin of Volcanology 70, 139-156. doi: 10.1007/s00445-007-0125-6

Paterson, S. R., Fowler, T. K. Jr, Schmidt, K. L., Yoshinobu, A. S., Yuan, E. S., Miller, R. B., 1998. Interpreting magmatic fabric patterns in plutons. Lithos 44, 53-82. doi:10.1016/S0024-4937(98)00022-X

Paterson, S. R., Ardill, K., Vernon, R., Zak, J., 2019. A review of mesoscopic magmatic structures and their potential for evaluating hypersolidus evolution of intrusive complexes. Journal of Structural Geology 125, 134-147. doi:10.1016/j.jsg.2018.04.022

Polacci, M., and Papale, P. 1997. The evolution of lava flows from ephemeral vents at Mount Etna: Insights from vesicle distribution and morphological studies. Journal

of Volcanology and Geothermal Research 76(1-2): 1-17. doi: 10.1016/S0377-0273(96)00070-4

Potts, N. J., Bromiley, G. D., Brooker, R. A., 2021. An experimental investigation of F, Cl and H2O mineral- melt partitioning in a reduced, model lunar system. Geochimica et Cosmochimica Acta 294, 232-254. doi: 10.1016/j.gca.2020.12.003

Qian, Y., Xiao, L., Wang, Q., Head, J. W., Yang, R., Kang, Y., van der Bogert, C. H., Hiesinger, H., Lai, X., Wang, G., Pang, Y., Zhang, N., Yuan, Y., He, Q., Huang, J., Zhao, J., Wang, J., Zhao, S. 2021. China's Chang'e-5 landing site: Geology, stratigraphy, and provenance of materials. Earth and Planetary Science Letters 561, 116855. doi: 10.1016/j.epsl.2021.116855

Rai, N., Perrillat, J.-P., Mezouar, M., Colin, A., Petitgirard, S., van Westrenen, W., 2019. *In situ* Viscometry of Primitive Lunar Magmas at High Pressure and High Temperature. Frontiers in Earth Science 30. doi: 10.3389/feart.2019.00094

Rhodes, J. M., and Hubbard, N. J. 1973. Chemistry, classification, and petrogenesis of Apollo 15 mare basalts. Proceedings of the Fourth Lunar Science Conference (2), 1127-1148.

Roberts, C. E., and Gregg, T. K. P., 2019. Rima Marius, the Moon: Formation of lunar sinuous rilles by constructional and erosional processes. Icarus 317, 682-688. doi: 10.1016/j.icarus.2018.02.033

Robinson, M.S., Ashley, J.W., Boyd, A.K., Wagner, R.V., Speyerer, E.J., Ray Hawke, B., Hiesinger, H., van der Bogert, C.H., 2012. Confirmation of sublunarean voids and thin layering in mare deposits. Planetary and Space Science 69, 18–27. doi:10.1016/j.pss.2012.05.008

Rowland, S. K., and Walker, G. P. L., 1988. Mafic-crystal distributions, viscosities, and lava structures of some Hawaiian lava flows. Journal of Volcanology and Geothermal Research 35, 55-66. doi: 10.1016/0377-0273(88)90005-4

Rowland, S. K., and Walker, G. P. L., 1990. Pahoehoe and aa in Hawaii: volumetric flow rate controls the lava structure. Bulletin of Volcanology 52, 615-628. doi: 10.1007/BF00301212

Rumpf, M. E., Needham, H., Fagents, S. A., 2020. Thicknesses of lava flows in satellite images: Comparison of layered mare units with terrestrial analogs. Icarus 350, 113853. doi:10.1016/j.icarus.2020.113853

Ryder, G., 1985. Catalog of Apollo 15 Rocks. Part 1. National Aeronautics and Space Administration Johnson Space Center Contribution 20787.

Ryder, G., 1993. Catalog of Apollo 17 Rocks. National Aeronautics and Space Administration Johnson Space Center Contribution #26088, 1.

Saal, A. E., Hauri, E. H., Cascio, M. L., Van Orman, J. A., Rutherford, M. C., Cooper, R. F., 2008. Volatile content of lunar volcanic glasses and the presence of water in the Moon's interior. Nature Letters 454, 192-195. doi: 10.1038/nature07047

Sato, M., 1979. The driving mechanism of lunar pyroclastic eruptions inferred from the oxugen fugacity behavior of Apollo 17 orange glass. Proceedings of the 10th Lunar and Planetary Science Conference, Houston, Texas, 311-325.

Schneider, C. A., Rasband, W. S., Eliceiri, K. W., 2012. NIH Image to ImageJ: 25 years of image analysis. Nature methods 9(7), 671-675, doi: 10.1038/nmeth.2089

Sears, D.W.G., Sehlke, A., Friedrich, J. M., Rivers, M. L., Ebel, D. S., 2018. X-ray computed tomography of extraterrestrial rocks eradicates their natural radiation

record and the information it contains. Meteoritic and Planetary Science 53, 2624–2631, doi:10.1111/maps.13183

Self, S., Keszthelyi, L. P., Thordarson, T., 1998. The importance of Pāhoehoe. Annual Reviews in Earth and Planetary Science 26, 81–110.

Shaw, H., 1969. Rheology of basalt in the melting range. Journal of Petrology 10, 510-535.

Shea, T., Houghton, B. F., Gurioli, L., Cashman, K. V., Hammer, J. E., Hobden, B. J., 2010. Textural studies of vesicles in volcanic rocks: An integrated methodology. Journal of Volcanology and Geothermal Research 190, 271-289. doi: 10.1016/j.jvolgeores.2009.12.003

Shearer, C. K., Hess, P. C., Wieczorek, M. A., Pritchard, M. E., Parmentier, E. M., Borg, L. E., Longhi, J., Elkins-Tanton, L. T., Neal, C. R., Antonenko, I., Canup, R. M., Halliday, A. N., Grove, T. L., Hager, B.H., Lee, D-C., Wiechert, U., 2006. Thermal and Magmatic Evolution of the Moon, *in*: Jollif, B. L., Wieczorek, M. A., Shearer, C. K., Neal, C. R., eds., New Views of the Moon. Reviews in Mineralogy & Geochemistry 60(1), 365-518, doi:10.2138/rmg.2006.60.4

Sok, R., Varslot, T. K., Ghous, A., Latham, S., Sheppard, A. P., Knackerstedt, M. 2009. Pore scale characterization of carbonates at multiple scales: Integration of micro-CT, BSEM, and FIBSEM. Petrophysics 51(6).

Spudis, P. D., Swann, G. A., Greeley, R., 1988. The formation of Hadley Rille and implications for the geology of the Apollo 15 region. Proceedings of the Lunar Planetary Science Conference 18, 243–254.

Swann, G.A., et al., 1972. Preliminary geologic investigation of the Apollo 15 landing site. In: Apollo 15: Preliminary Science Report. NASA SP-289, pp. 21–31.

Takeda, H., Miyamoto, M., Ishii, T., Lofgren, G. E., 1975. Relative cooling rates of mare basalts at the Apollo 12 and 15 sites as estimated from pyroxene exsolution data. Proceedings of the 6th Lunar Science Conference, 987-998/

Tartèse, R., Anand, M., Barnes, J. J., Starkey, N. A., Franchi, I. A., Sano, Y. 2013. The abundance, distribution, and isotopic composition of Hydrogen in the Moon as revealed by basaltic lunar samples: Implications for the volatile inventory of the Moon. Geochimica et Cosmochimica Acta 122, 58-74. doi: 10.1016/j.gca.2013.08.014

Tartèse, R., Anand, M., Joy, K. H., Franchi, I. A. 2014. H and Cl isotope systematics of apatite in brecciated lunar meteorites Northwest Africa 4472, Northwest Africa 773, Sayh al Uhaymir 169, and Kalahari 009. Meteoritics and Planetary Science 49(12), 2266-2289. doi: 10.1111/maps.12398

Taylor, S. R. 1982. Planetary Science: A Lunar Perspective. Houston, Texas. Publishers Production International. 481 p.

Taylor, G. J., Warren, P. H., Ryder, G. C., Delano, J. W., Pieters, C. M., Lofgren, G. W., 1991. Lunar rocks. In: Heiken, G.H., Vaniman, D.T., French, B.M. (Eds.), The Lunar Source Book: A User's Guide to the Moon. Cambridge University Press, Cambridge, pp. 183–284.

Thordarson, T. 1995. Volatile release and atmospheric effects of basaltic fissure eruptions. Ph.D. thesis, University of Hawaii, Manoa, Honolulu, 580 pp

Tolometti, G. D., Neish, C. D., Osinski, G. R., Hughes, S. S., Kobs Nawotniak, S. E., 2020. Interpretations of lava flow properties from radar remote sensing data. Planetary and Space Science 190, 104991. doi: 10.1016/j.pss.2020.104991

Treiman, A. H., and Drake M. J. 1983. Origin of lunar meteorite ALHA 81005: Clues from the presence of Terrae clasts and a very low-titanium mare basalt clast. Geophysical Research Letter 10(9), 783-786. doi: **10.1029/GL010i009p00783**

Vaniman, D.T., Reedy, R., Heiken, G.H., Olhoeft, G., Mendell, W.W., 1991. The lunar environment. In: Heiken, G.H., Vaniman, D.T., French, B.M. (Eds.), The Lunar Source Book: A User's Guide to the Moon. Cambridge University Press, Cambridge, pp. 27–60.

Vásárhelyi, L., Kónya, Z., Kukovecz, Á., Vajtai, R., 2020. Microcomputed tomography-based characterization of advanced materials: a review. Materials Today Advances 8, 100084. doi: 10.1016/j.mtadv.2020.100084

Vernon, R. H., 2018. A Practical Guide to Rock Microstructure, 2nd edition. Cambridge University Press, Cambridge. doi: 10.1017/9781108654609

Vye-Brown, C., Self, S., Barry, T. L., 2013. Architecture and emplacement of flood basalt flow fields: case studies from the Columbia River Basalt Group, NW USA. Bulletin of Volcanology 75, 697. doi: 10.1007/s00445-013-0697-2

Walker, D., Longhi, J., Stolper, E. M., Grove, T. L., Hays, J. F., 1975. Origin of titaniferous lunar basalts. Geochimica et Cosmochimica Acta 39(9), 1219-1235. doi: 10.1016/0016-7037(75)90129-5

Wang, Y., and Miller, J. D., 2020. Current developments and applications of micro-CT for the 3D analysis of multiphase mineral systems in geometallurgy. Earth-Science Reviews 211, 103406. Doi: 10.1016/j.earscirev.2020.103406

Warner J., 1970. Apollo 12 Lunar-Sample Information. National Aeronautics and Space Administration Technical Report R-353.

Weider, S.Z., Crawford, I.A., Joy, K.H., 2010. Individual lava flow thicknesses in Oceanus Procellarum and Mare Serenitatis determined from Clementine multi-spectral data. Icarus 209, 323–336.

Wetzel, D. T., Hauri E. H., Saal, A. E. 2015. Carbon content and degassing history of the lunar volcanic glasses. Nature Geoscience 8, 755-758. doi: 10.1038/ngeo2511

Whitford-Stark, J. J., 1982. Factors Influencing the Morphology of Volcanic Landforms: and Earth-Moon Comparison. Earth Science Reviews 18, 109-168.

Wilmoth, R. A., and Walker, G. P. L., 1993. P-type and S-type pahoehoe: a study of vesicle distribution patterns in Hawaiian lava flows. Journal of Volcanology and Geothermal Research 55, 129-142.

Wilson, L., 2009. Volcanism in the Solar System. Nature Geoscience 2, 389-397. doi: 10.1038/ngeo529

Wilson, L., and Head, J. W., 1981. Ascent and Eruption of Basaltic Magma on the Earth and Moon. Journal of Geophysical Research 86, 2971-3001.

Wilson, L., and Head, J. W., 2018. Controls on Lunar Basaltic Volcanic Eruption Structure and Morphology: Gas Release Patterns in Sequential Eruption Phases. Geophysical Research Letters 45(12), 5852-5859, doi: 10.1029/2018GL078327

Woodcock, N. H., and Naylor, M. A., 1983. Randomness testing in three-dimensional orientation data. Journal of Structural Geology 5, 539–548.

Wu, X., Schepartz, L. A., 2009. Application of computed tomography in paleoanthropological research. Progress in Natural Science 19(8), 913-921. doi: 10.1016/j.pnsc.2008.10.009

Žák, J., Patterson, S. R., Memeti, V., 2007. Four magmatic fabrics in the Tuolumne batholith, central Sierra Nevada, California (USA): Implications for interpreting fabric patterns in plutons and evolution of magma chambers in the upper crust. Geological Society of America Bulletin 119, 184-201. doi:10.1130/B25773.1Zeigler, R. A., Eckley, S. A., Hanna, R., Edey, D., Ketcham, R. A., Gross, J., McCubbin, F. M. 2021. Using X-Ray Computed Tomography to Image Apollo Drive Tube 73002. Lunar and Planetary Science Conference LII, abstract #2632.

Zhang, P., Lee, Y. I., Zhang, J., 2019. A review of high-resolution X-ray computed tomography applied to petroleum geology and a case study. Micron 124, 102702. doi: 10.1016/j.micron.2019.102702

Zolensky, M., Mikouchi, T., Fries, M., Bodnar, R., Jenniskens, P., Yin, Q.-z., Hagiya, K., Ohsumi, K., Komatsu, M., Colbert, M., Hanna, R., Maisano, J., Ketcham, R., Kebukawa, Y., Nakamura, T., Matsuoka, M., Sasaki, S., Tsuchiyama, A., Gounelle, M., Le, L., Martinez, J., Ross, K., Rahman, Z., 2014. Mineralogy and petrography of C asteroid regolith: The Sutter's Mill CM meteorite. Meteoritics & Planetary Science 49, 1997-2016, doi: 10.1111/maps.12386

2.8 Figures and Tables

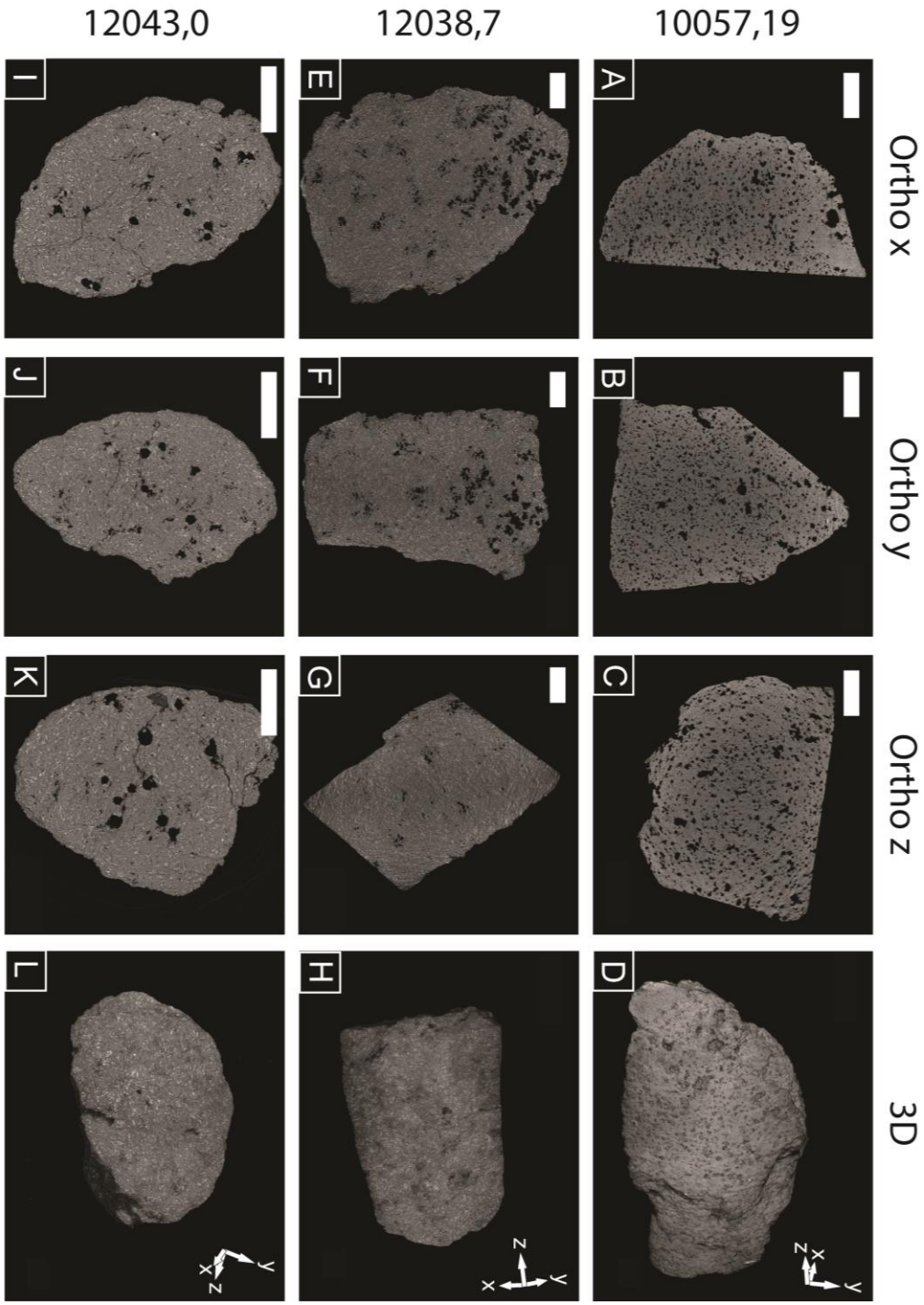

Figure 1: Scan slices at sample center for each of the samples studied here. Scale bars are 1 cm long. The scans were used to create 3D models of samples using Dragonfly (Object Research Systems), seen on the right. Videos of the models can be found in the supplementary materials.

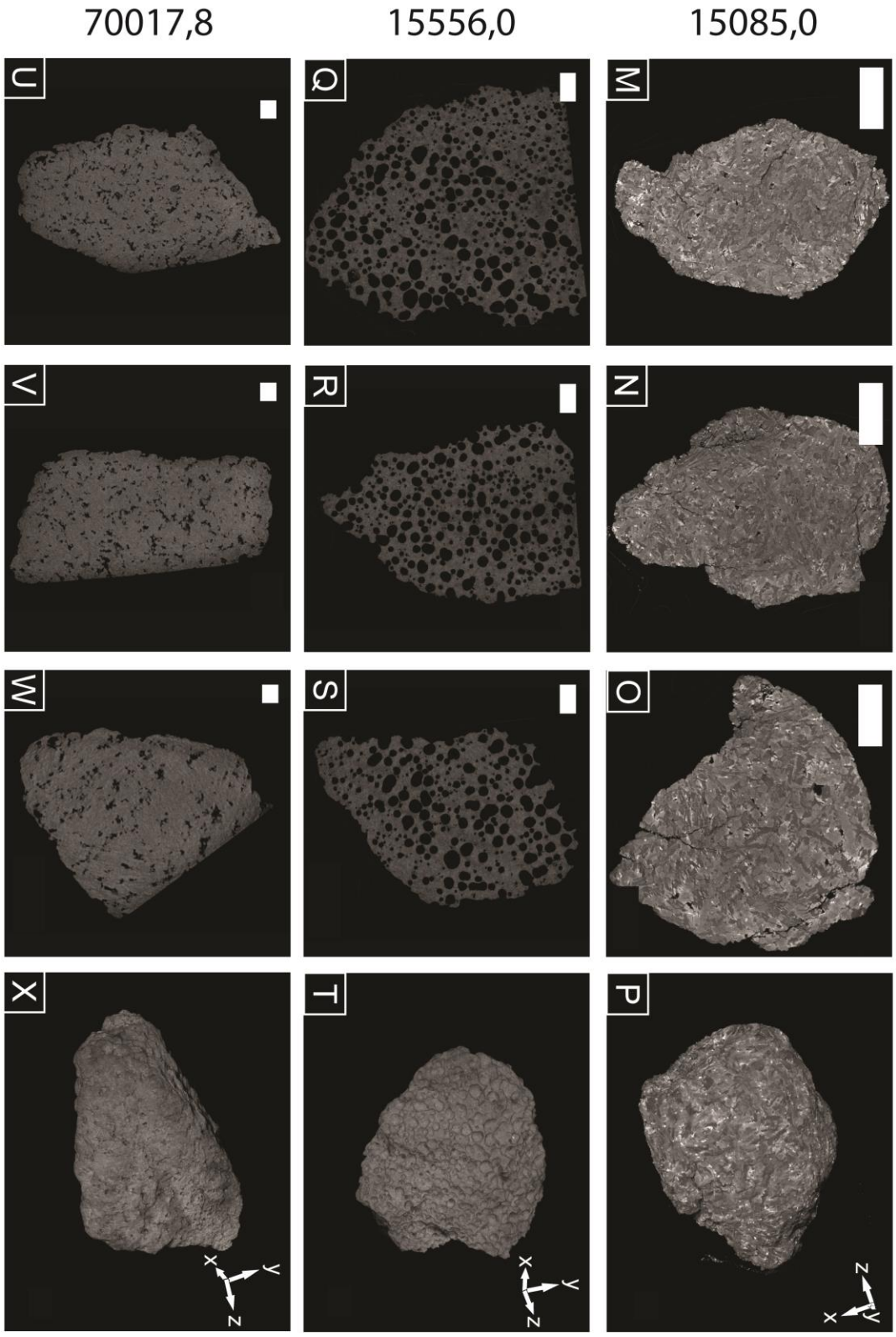

Figure 1 (cont.)

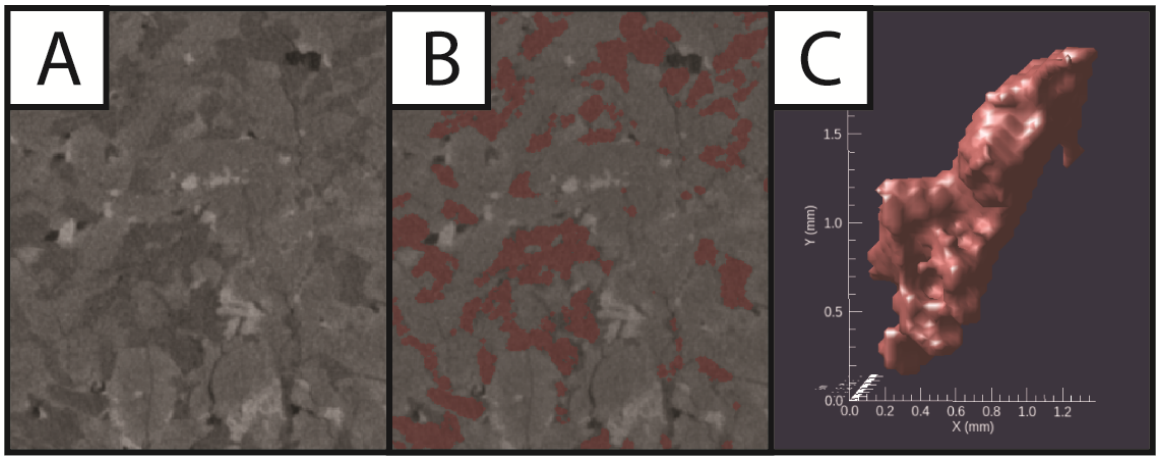

Figure 2: A summary of the steps involved in extracting particle data from XCT scans. A) An example detail of a scan from sample 15085. B) An unseeded grayscale range has been selected to highlight voxels of a specific component (in this case plagioclase feldspar) in the same field of view as panel A, in order to segment them into components using *Blob3D*. C) A "blob" produced from adjacent voxels, representing a distinct particle. The length, width, depth, volume, and orientation with respect to the sample was extracted from such blobs.

TABLE 1. SUMMARY OF SAMPLE MODAL MINERALOGY

Sample Number	Sample description*	Sample texture*	Oxides†		Pyroxene		Plagioclase feldspar		Others§		Vol. % of unassigned voxels#	Total rock volume (mm^3)
			This study (vol. %)	Previous studies*	This study (vol. %)	Previous studies*	This study (vol. %)	Previous studies*	This study (vol. %)	Previous studies*		
10057	High K ilmenite	Fine-grained, vesicular	19.8	15.5-15.7	49.3	50.8-50.9	30.8	19.2-24	N.A.	3.3	0.04	38237
12038	Feldspathic	Coarse-grained, equigranular	2.7	3.46-10	63.5	48.8-55	33.8	30-44	N.A.	2.7-3.4	0.003	101434
12043	Pigeonite	Medium-grained, subophitic	1.2	3.5	76.9	57.7	21.8	32.9	N.A.	4.5	0.02	16380
15085	Pigeonite	Coarse-grained, ophitic	4.9	3-3.5	62.5	40-66	29.5	22-60	2.99	1.6-2.4	0.2	74390
15556	Olivine-normative	Fine-grained, subophitic vesicular	1.2	3-8	38.3	50-57	60.5	30-38	N.A.	1.8-6	N.A.	180768
70017 (full)	Low-K ilmenite	Medium-grained, poikilitic, equigranular	4.7	19.2-22.8	48.2	49.3-57.6	45.4	19.8-26	N.A.	1.6-3	1.7	333627
70017 (cropped)	Low-K ilmenite	Medium-grained, poikilitic, equigranular	21.5	19.2-22.8	42.0	49.3-57.6	36.5	19.8-26	N.A.	1.6-3	N.A.	139782

*Data gathered from the Lunar Sample Compendium (Meyer, 2016, and references therein).

†Oxides include ilmenite, spinels, and Fe-metal.

§Other studies found mesostasis and "silica." Here, it was not possible to separate other sample components except tridymite in 15085,0.

#Voxel is a volume element, a 3D pixel.

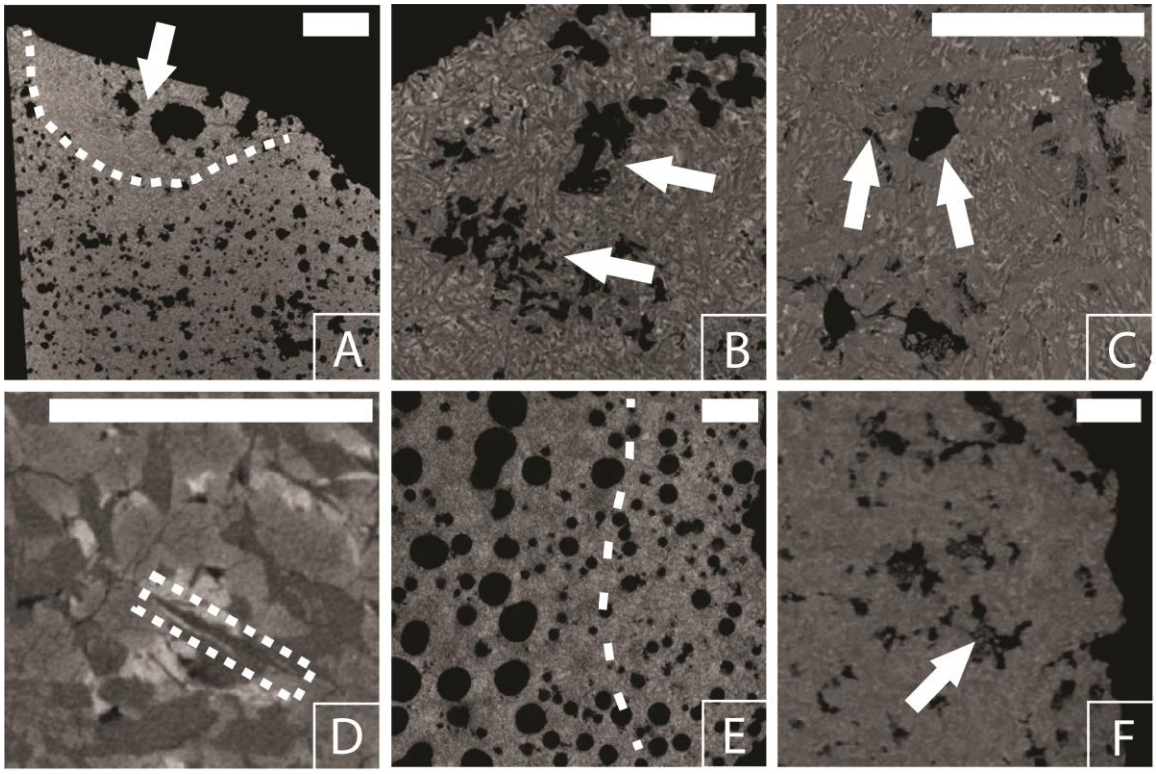

Figure 3: Regions of interest in each of the samples. Scalebars are 5 mm long in all images. A) Area of sample 10057 showing an entrained enclave, outlined and marked by an arrow. B) Area of sample 12038 showing the gradual transition from vesicles (top right) to a more vuggy population (bottom left), indicated by arrows. C) Area of sample 12043 showing two populations of gas cavities – one made up of rounded vesicles, the other made up of interstitial vugs, indicated by arrows. D) Area of sample 15085 showing the accessory phase tridymite (outlined). E) Area of sample 15556 indicating the approximate gradual transition from a highly vesiculated region to a less vesiculated region. F) Area of sample 70017 showing sample material infilling vesicles, indicated by an arrow.

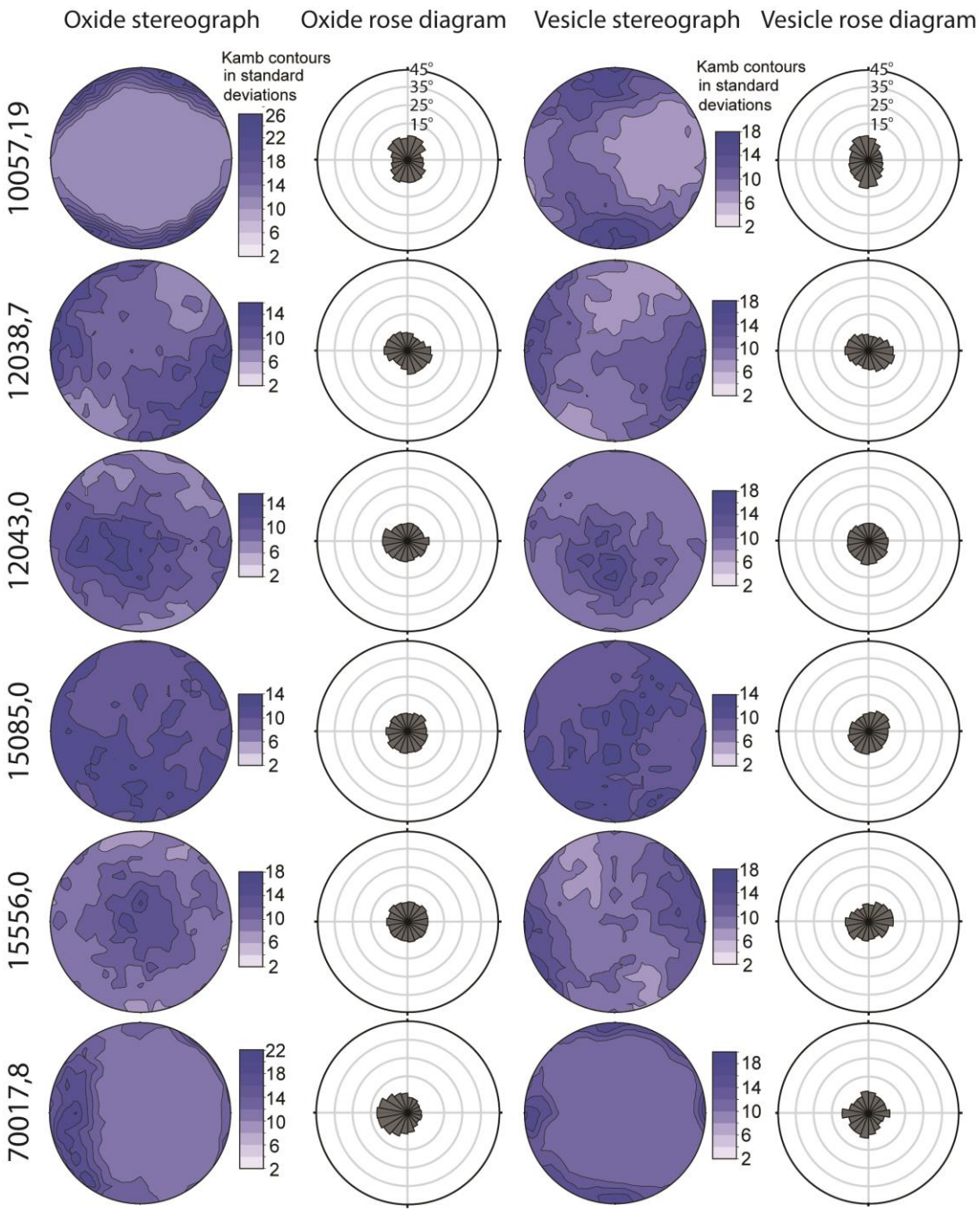

Figure 4: Stereographic projections and rose diagrams generated via *Stereonet 11* (Allmendinger et al., 2012; Cardozo and Allmendinger, 2013) based on the 10,000 particles of greatest volume. Data plotted here is the longest axis of particles or vesicles/vugs. See also Table S3 for *K*-values and *C*-values.

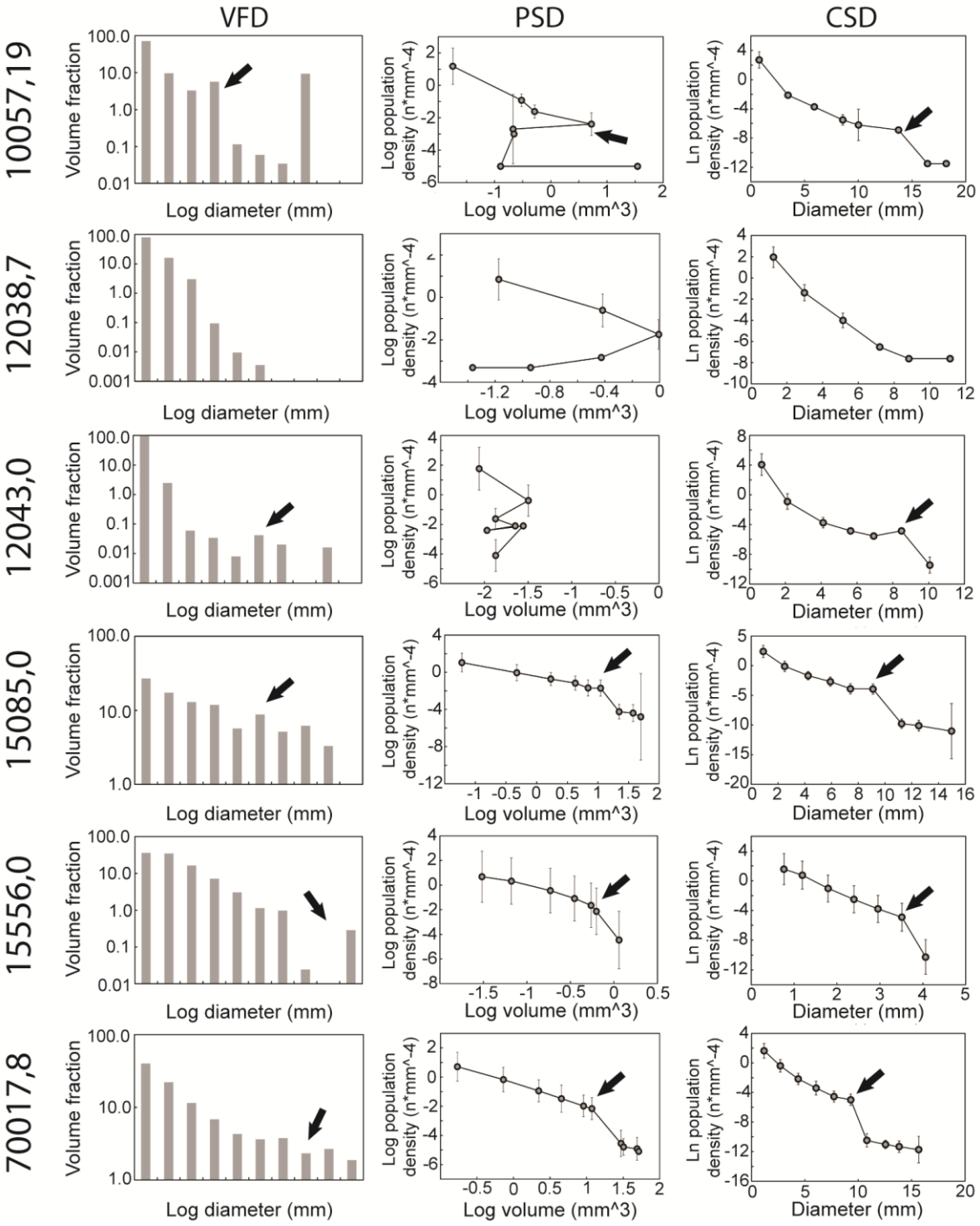

Figure 5: Volume fraction distributions (VFDs, left), particle size distributions (PSDs, center), and crystal size distributions (CSDs, right) for the oxide phases in studied samples based on the 15,000 particles with the greatest volume. Arrows indicate apparent "kinks" which suggest a change in cooling environment. See text for discussion.

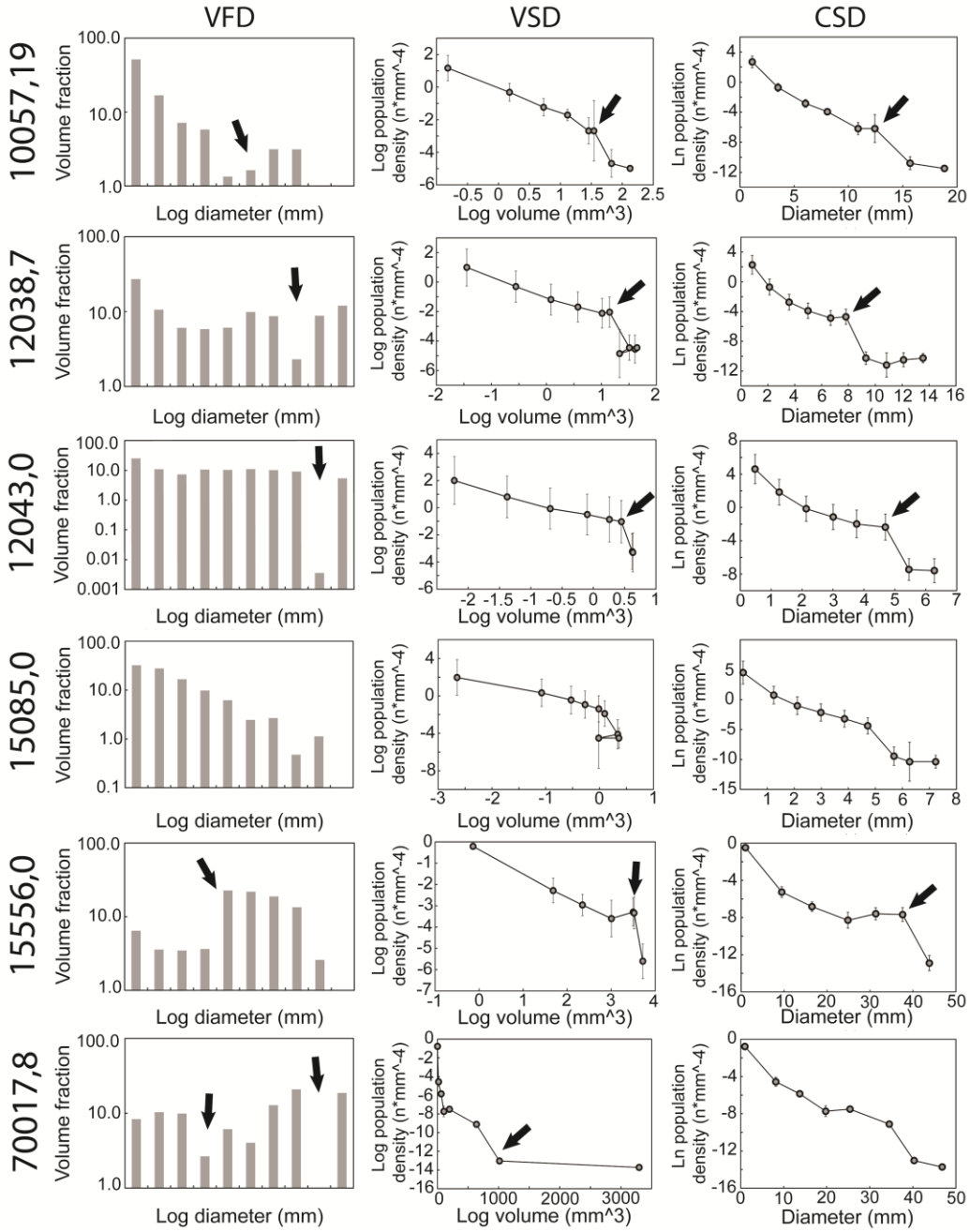

Figure 6: Volume fraction distributions (VFDs, left), vesicle size distributions (VSDs, center), and crystal size distributions (CSDs, right) for the vesicles and/or vugs in studied samples based on the 15,000 particles with the greatest volume. Arrows indicate apparent "kinks" which suggest a change in cooling environment. See text for discussion.

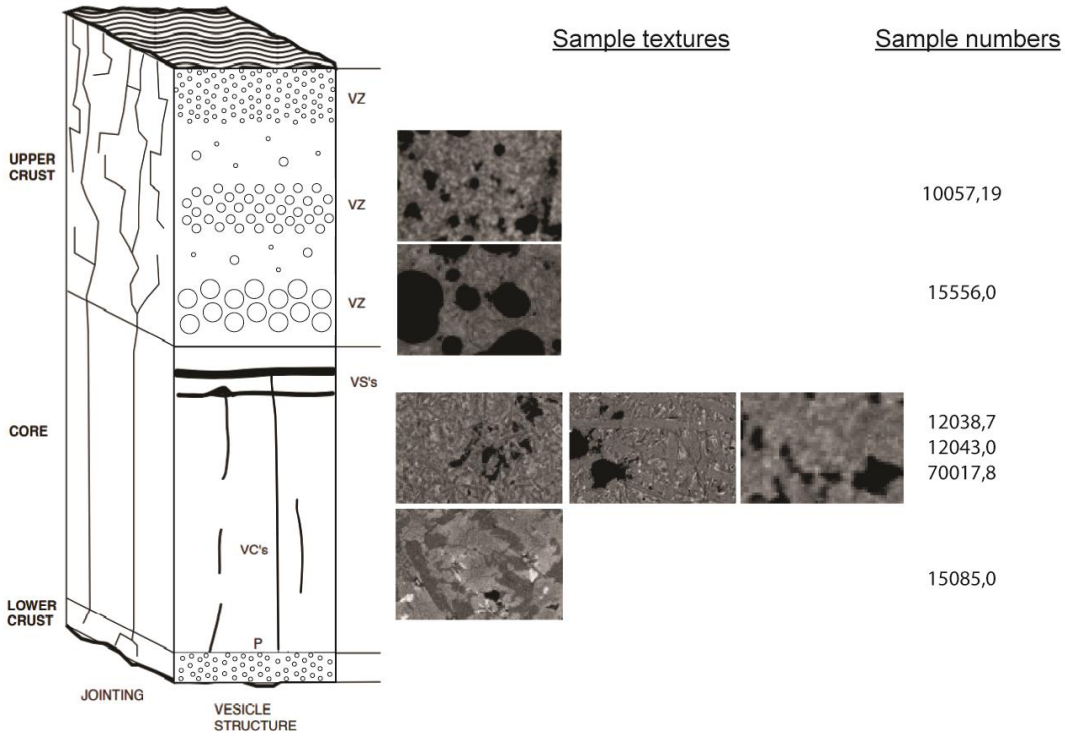

Figure 7: Idealized schematic indicating the likely stratigraphic location where each sample crystallized within its respective lava lobe based on sample textural properties. All images are 1 cm across. While these samples originated from different magmatic systems and had different compositions and volatile loads, based on their textures samples 10057 and 15556 were interpreted to have cooled in the lobe crust; sample 15085 likely cooled in the lobe core; samples 12038, 12043, and 70017 may mark the transition between these two regions. Modified from Self et al. (1998). Highly vesicular zones in the crust are denoted by "VZ"; Self et al. (1998) additionally noted that vesicle sheets (VS's), vesicle cylinders (VC's), and pipe vesicles (P) can exist in the lobe core, but these were not observed in the samples studied here.

2.9 Supplemental Files

TABLE S1. SAMPLE SCAN PARAMETERS

Sample number	Instrument*	Voltage (kV)	Current (mA)	Number projections	Number slices	Resolution (µ/voxel)
10057,19	Nikon† Metrology HMX ST 225	210	0.19	3142	1793	34.3
12038,7	North Star Imaging (NSI) system	220	0.12	3000	1869	43.6
12043,0	NSI system	170	0.14	3000	1896	23.5
15085,0	NSI system	170	0.14	3600	1910	38.6
15556,0	NSI system	170	0.14	2922	1877	55.2
70017,8	NSI system	450	0.8	2110	1914	86.3

*Samples scanned using the NSI system were scanned at the Univesity of Texas at Austin High Resolution Computed Tomography facility.

†Sample scanned using the Nikon scanner was scanned at the Natural History Museum in London, UK.

TABLE S2. SUMMARY OF SAMPLE MINERALOGY INCLUDING VESICLES

Sample Number	Sample description*	Sample texture*	Oxides†		Pyroxene		Plagioclase feldspar		Others§		Unassigned voxels# (vol. %)	Vesicle Volume (vol. %)	Total rock volume (mm^3)
			This study (vol. %)	Previous studies*	This study (vol. %)	Previous studies*	This study (vol. %)	Previous studies*	This study (vol. %)	Previous studies*			
10057	High K ilmenite	Fine-grained, vesicular	17.5	15.5-15.7	43.6	50.8-50.9	27.3	19.2-24	N/A	3.3	0.03	11.5	43205
12038	Feldspathic	Coarse-grained, equigranular	2.6	3.46-10	61.2	48.8-55	32.6	30-44	N/A	2.7-3.4	0.003	3.7	105280
12043	Pigeonite	Medium-grained, subophitic	1.2	3.5	74.9	57.7	21.2	32.9	N/A	4.5	0.02	2.7	16829
15085	Pigeonite	Coarse-grained, ophitic	4.8	3-3.5	62.1	40-66	29.3	22-60	2.97	1.6-2.4	0.2	0.6	74861
15556	Olivine-normative	Fine-grained, subophitic vesicular	0.6	3-8	19.9	50-57	31.5	30-38	N/A	1.8-6	N/A	48.0	347518
70017 (full)	Low-K ilmenite	Medium-grained, poikilitic, equigranular	4.7	19.2-22.8	47.3	49.3-57.6	44.5	19.8-26	N/A	1.6-3	1.6	1.9	340028
70017 (cropped)	Low-K ilmenite	Medium-grained, poikilitic, equigranular	19.3	19.2-22.8	37.7	49.3-57.6	32.8	19.8-26	N/A	1.6-3	N/A	10.1	155558

*Data gathered from the Lunar Sample Compendium (Meyer, 2016).

†Oxides include ilmenite, spinels, and Fe-metal.

§ Other studies found mesostasis and "silica." Here, it was not possible to separate other sample components except tridymite in 15085,0.

#Voxel is a volume element, a 3D pixel.

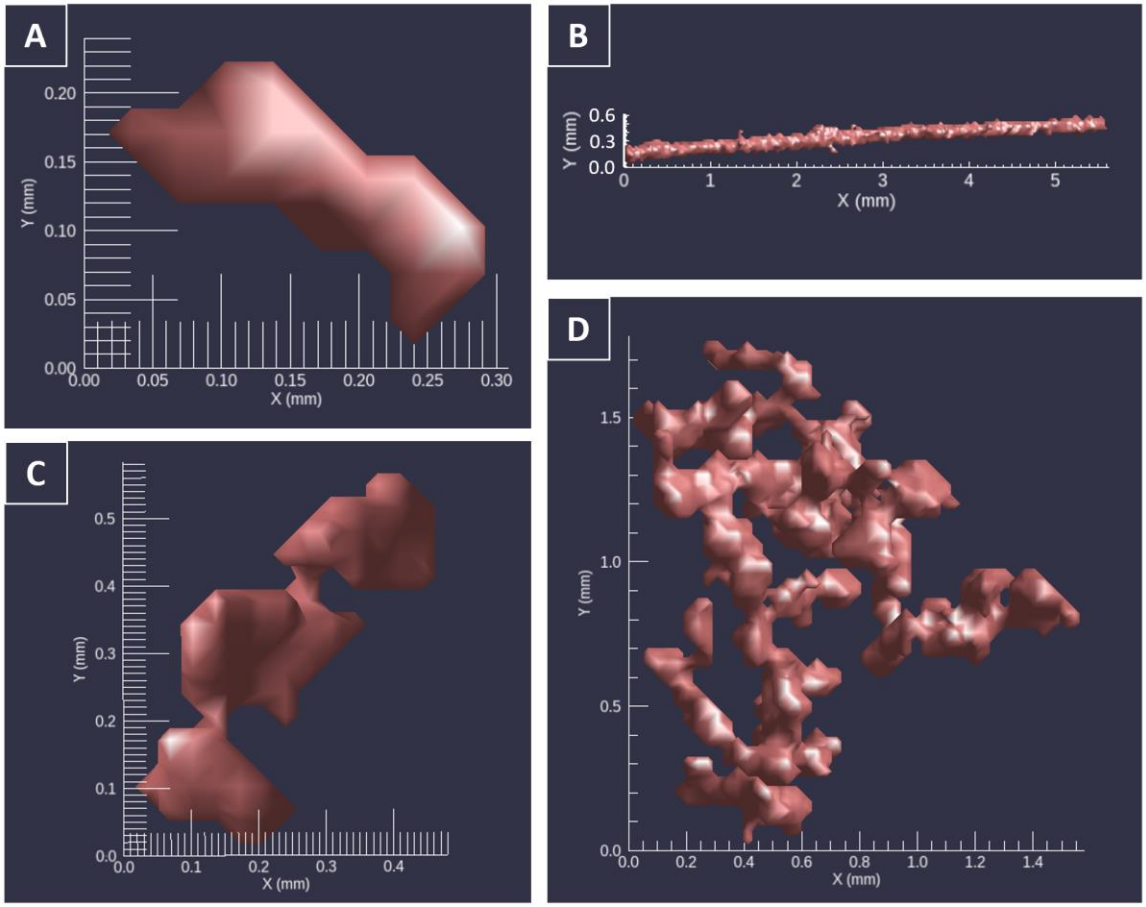

Figure S1: Summary of blobs from Blob3D representing oxide particles in 10057, found during manual separation. A) A blob interpreted to represent one indiviual oxide grain. B) Another blob interpreted as an individual particle – note its different habit and size from the particle shown in panel A. C) A blob interpreted to be a simple cluster of three oxide particles. D) One blob interpreted to represent a complex cluster of several oxide particles.

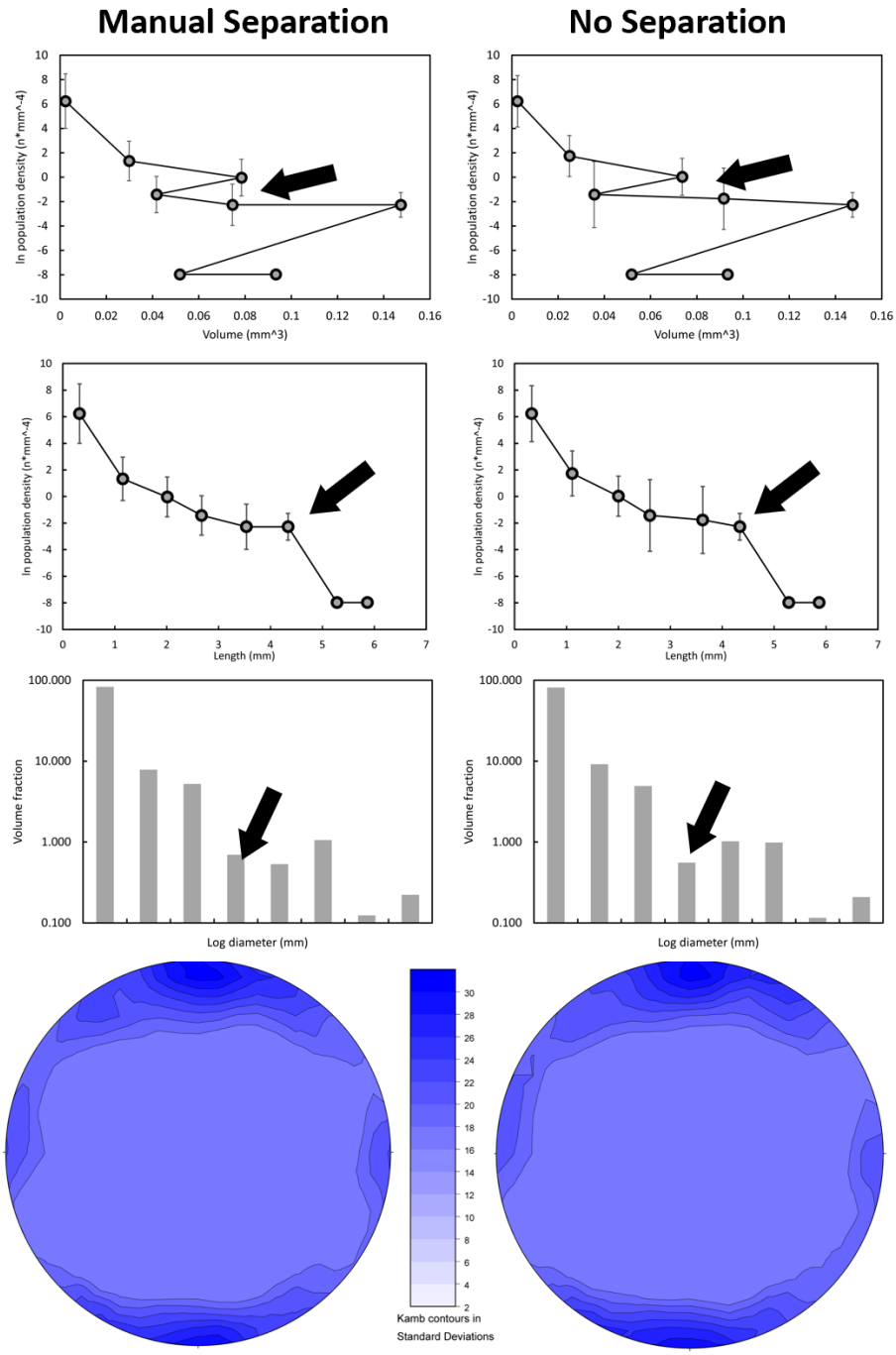

Figure S2: A comparison of the results generated from data that was manually separated vs data that was not separated, both using oxide particles in 10057. The top three panels represent PSD, CSD, and VFD analyses of oxides, the bottom panels are stereonets generated for each datasets. Kamb contour legend between the two stereonets applies to both figures.

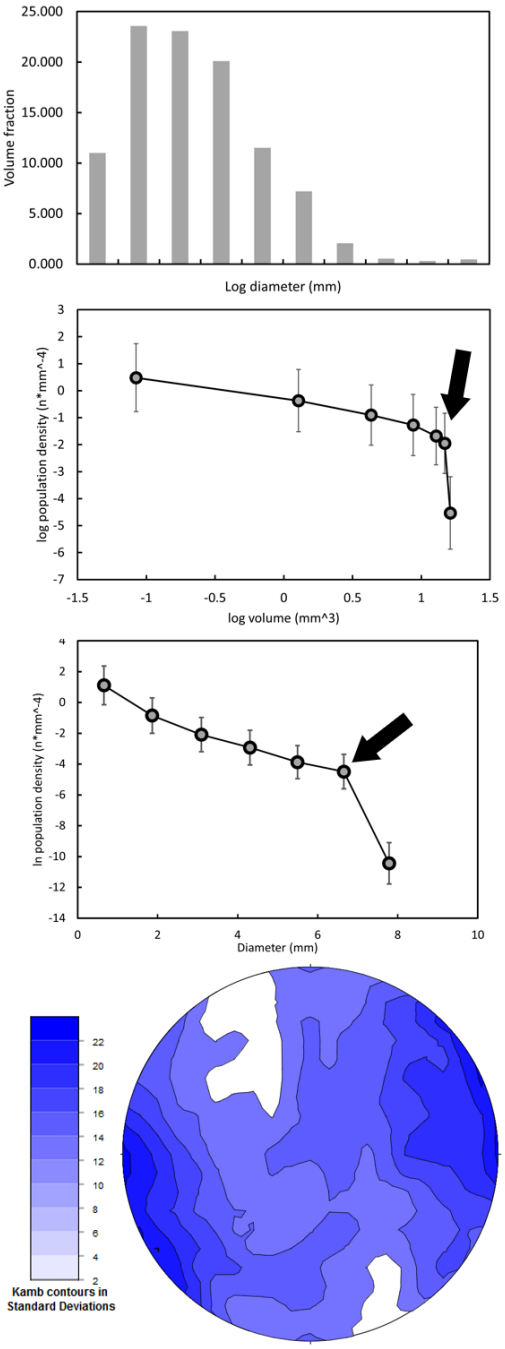

Figure S3: Results of stereographic and size distribution analyses in 15556 with large vesicle clusters excluded. The top three panels represent PSD, CSD, and VFD analyses, respectively, for comparison to Figure 6, the bottom panel is a stereonet generated for the cluster-less data set for comparison with Figure 4.

TABLE S3. SUMMARY OF FABRIC ASSESSMENT.

Sample Numbers	Oxides		Vesicles	
	K*	C†	K	C
10057,19	0.39	0.86	0.86	0.4
12038,7	2.03	0.27	1.93	0.29
12043,0	1.51	0.28	2.86	0.23
15085,0	0.74	0.11	0.34	0.13
15556,0	4.68	0.21	4.63	0.24
70017,8	0.37	0.7	0.39	0.37

*K value is a distribution shape parameter. Cluster distributions are represented by K < 1, girdle by K > 1 (Woodcock and Naylor, 1983).

†C value is a strength parameter, C > 3 indicates a strong fabric (Woodcock and Naylor, 1983).

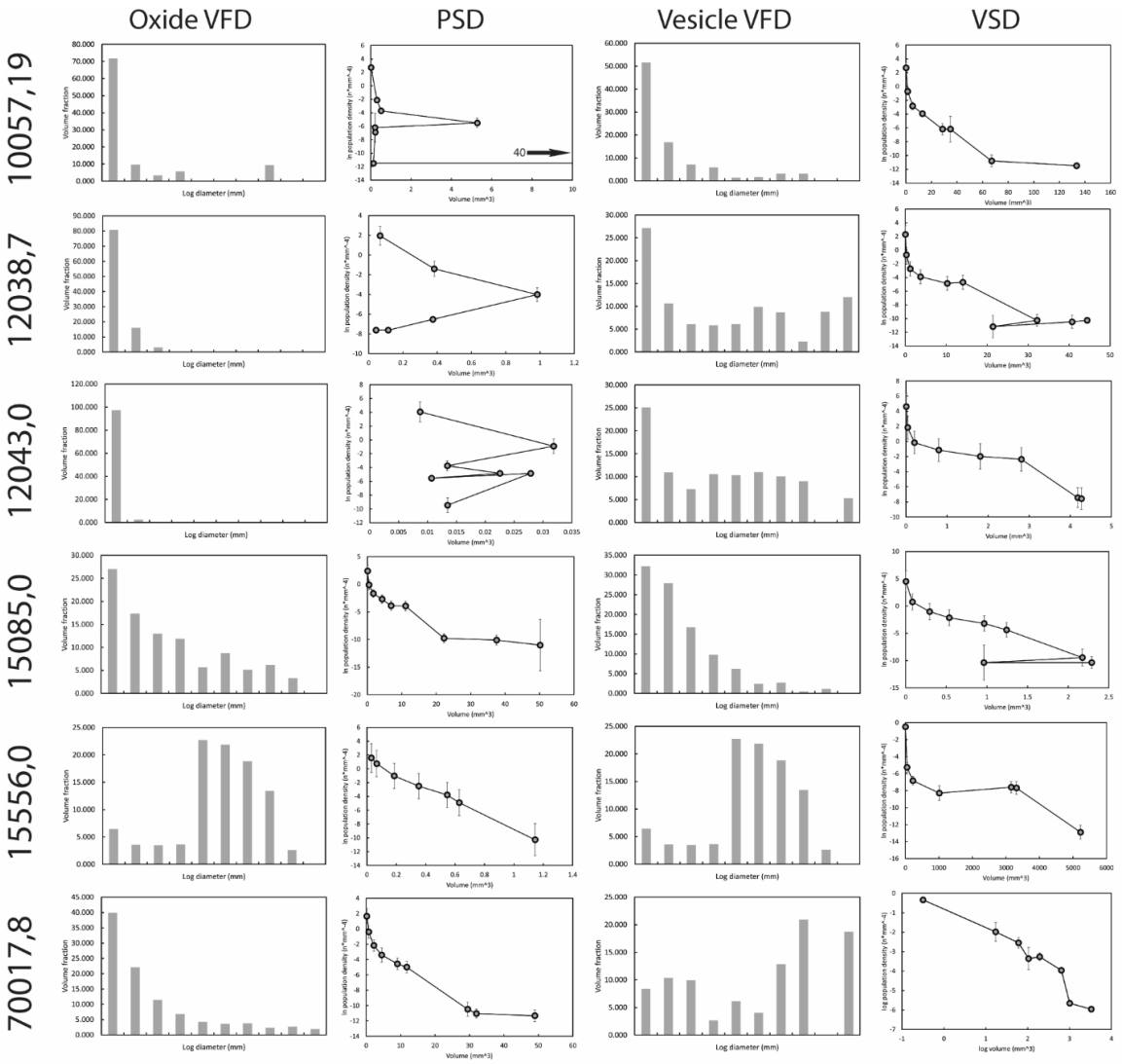

Figure S4: Volume fraction distributions (VFDs) for both oxides and vesicles. Supplemental particle size distributions (PSDs) and vesicle size distributions (VSDs) for each sample are also included. The VFDs, PSDs, and VSDs in this supplemental figure diagram the original calculated parameters, not the log of those parameters as is presented in Figures 5 and 6.

Figure S5: A video of 10057.

Figure S6: A video of 12038.

Figure S7: A video of 12043.

Figure S8: A video of 15085.

Figure S9: A video of 15556.

Figure S10: A video of 70017.

3. The evidence for open magmatic system processes recorded in the crystal cargoes of lunar basalts 10057, 12038, 12043, 15085, 15556, and 70017

The following chapter is currently in preparation for submission to the journal Planetary and Space Science.

3.1 Introduction

3.1.1 Insights from terrestrial systems on basaltic magmatism

Basaltic magmatism is a fundamental process of planetary differentiation, evolution, and crustal (re)surfacing (BVSP, 1981, Wilson, 2009). As direct products of mantle partial melting, basaltic lavas have provided a wealth of information regarding the make-up and evolution of Earth's mantle, the generation of secondary basaltic crusts, and the architecture of magmatic systems and processes operating within them. This has been made possible through decades of detailed mineralogical, textural, geochemical, and geochronological analyses, coupled with observations over a range of temporal and spatial scales thanks to detailed interdisciplinary analyses (BVSP, 1981; Cashman et al., 2015; 2017; Edmonds et al., 2019; Jerram and Davidson, 2007; Lee et al., 2009; Marsh et al., 2009; Middlemost, 2014; Ogawa, 2018; Sparks et al., 2019). Recent 10^2 to 10^3 m-scale geophysical investigations of terrestrial magmatic systems indicate that magmas are generally not stored in large-scale chambers (see recent discussions by Edmonds et al., 2019; Paulatto et al., 2022; Sparks et al., 2019). Recent work suggests this is also true at hotspot volcanoes such as Hawai'i (Wilding et al., 2023), which is often invoked as one of the best analogs for lunar mare eruption dynamics (i.e., Head, 1976; Spudis et al., 2013). Instead, the study of crystal cargoes in magmatic products has recently led to a "paradigm shift" in the field of igneous petrology and an advancement in our understanding of magma plumbing system architecture. Through detailed textural and microgeochemical analysis, researchers have recognized that magmas are stored as distinct batches within lenses, which connect to form trans-crustal magmatic systems (e.g., Cashman et al., 2017; Edmonds et al., 2019; Sparks et al., 2019). In this framework, magma batches evolve separately and produce crystal cargoes which record unique petrogenetic histories. As they cool, melts produce crystal frameworks – the resulting interstitial melts stored in crystal frameworks are defined as "mushes" (Cashman et al., 2017; Sparks et al., 2019). Upon remobilization during transport and ascent, batches have the potential to mix and mingle, exchanging molten (liquid) and solidified (crystals) material to produce a new carrier (or host) magma with a distinct cargo (Fig. 1; i.e., Cashman et al., 2017; Edmonds et al., 2019; Sparks et al., 2019, and references therein). Additional contamination of the carrier magma by surrounding wall rock can further influence final whole rock compositions. As a result, the whole rock compositions of lavas erupted at the surface are not always direct indicators of their source regions but more so of physical mechanisms that work to change magma composition over time (i.e., mixing, assimilation, fractionation; Blundy and Shimizu, 1991; Davidson et al., 2007; Ginibre et al., 2007; Higgins and Roberge, 2007; Jerram and Davidson, 2007; Ogawa, 2018; Ubide et al., 2014; Zellmer, 2021).

3.1.2 Magmatic System Framework

Grain textures along with element partitioning and diffusion behaviors as they relate to temperature, pressure, and melt composition (with or without volatiles) can be used to evaluate the petrogenetic history of a magma's crystal cargo (Blundy and Wood, 1991; Ginibre et al., 2002; 2007; Jerram et al., 2018; Neave and Maclennan, 2020; Ustunisik et al., 2014). One mineral phase that is commonly evaluated is plagioclase feldspar, thanks to its ubiquity in magmatic systems, its compositional simplicity, and the wealth of feldspar geochemical data across different systems (i.e., Blundy and Wood, 1991; Ginigre et al., 2007; Grove et al., 1984). In plagioclase feldspar for example, a temperature increase can lead to rounded habits, a decrease can lead to skeletal and acicular

morphologies potentially with higher An content, while a constant temperature will create near-uniform compositions in plagioclase from core to rim (Ginibre et al., 2007; Lofgren et al., 1974; Mollo et al., 2011). Meanwhile, pressure effects are generally related to decompression during ascent – for example, in plagioclase the albite (Ab) component will more readily resorb during decompression, which can generate reverse zoning (Blundy and Wood, 1991; Ustinusik et al., 2014). Otherwise, resorption without significant chemical change in the crystal can indicate rapid change in temperature or decompression/degassing (Ginibre et al., 2007). With respect to the coupled substitution of Ca-Al by Na-Si in plagioclase feldspar, the rate at which this occurs at subsolidus temperatures compared to exchange of other elements (i.e., Na-K) is slow enough such that An contents are likely primary in nature and not the result of diffusion (Costa and Morgan, 2011; Grove et al., 1984). Evaluation of complementary trace element abundances can help to evaluate crystal cargo petrogenesis further. For example, Sr content in plagioclase is strictly dependent on plagioclase CaO content and not pressure or temperature parameters. An increase in plagioclase Sr content from core to rim will only reflect changes in the composition of the melt due to processes like mixing, and not mechanisms like ascent (i.e., Berlo et al 2007; Bezard et al 2017; Blundy and Wood, 1991; Ginibre et al. 2007). Evaluation of rapidly-diffusing elements like MgO from core to rim in plagioclase can additionally inform recent changes in melt composition (on the order of weeks; Moore et al., 2014). While the above approaches to studying the petrogenetic history of one mineral phase have the potential to inform the evolution of the magma during the growth of that one phase, these inferences are arguably strengthened by considering additional phases within the same erupted or emplaced units whose crystallization windows may potentially combine to span the entire petrogenetic history of the magma.

In pyroxene, decompression during ascent can also trigger crystal breakdown via dissolution (Neave and Maclennan, 2020). In such a case, resorption without chemical change in the remaining portion of the crystal would be recorded, indicating either temperature disturbance or degassing/decompression (Neave and Maclennan, 2020; Streck, 2008). Interactions with hot, compositionally more primitive magmas (i.e., due to mafic recharge) can also cause dissolution in pyroxene, but could additionally be recorded by a subsequent growth zone with increased MgO and Cr content following the influx of primitive magma (Ubide and Kamber, 2018). Interaction with a magma of distinct composition could influence the compositions of new growth zones away from what would otherwise be predicted by closed-system fractional crystallization models (i.e., Lissenberg et al., 2019). An integrated approach which utilizes textural and chemical information across multiple phases has been repeatedly shown to provide new insights and constraints on the physiochemical processes that contribute to the evolution of a magmatic system's crystal cargo (e.g., Davidson et al., 2007; Jerram and Davidson, 2007; Zellmer, 2021). This type of work has been accomplished for samples originating from various tectonic settings including intraplate (Coote and Shane, 2018; Couperthwaite et al. 2020; Ubide et al., 2014), volcanic centers related to subduction zones (Ginibre et al., 2007 and references therein; Kent et al., 2010; Salisbury et al., 2008; Velázquez Santana et al., 2020), and mid-ocean ridges (Bennett et al., 2019; Lissenberg and MacLeod, 2016; Moore et al., 2014). Crystal morphologies as a result of changing conditions have most recently been summarized in Zellmer (2021) who also outlines specific terminology associated with the petrogenetic history of a crystal. This terminology is utilized throughout this work. Briefly, mineral

grains that grew within their host carrier magma are referred to as autocrysts, mineral grains incorporated from distinct but petrogenetically related magmas are referred to as antecrysts, and foreign grains originating from the surrounding wall rock are referred to as xenocrysts (Fig. 1). Antecrysts can generally be identified through observation of reaction textures and unlike autocrysts, can be reversely zoned from core to rim in major and/or trace elements (i.e., Ubide et al., 2014). A grain with only reaction and/or breakdown texture but no accompanying compositional change recorded during growth from core to rim may instead record breakdown during ascent, not mixing or mingling (i.e., Neave and Maclennan, 2016).

3.1.3 Basaltic magmatism beyond Earth

The only direct sampling of extraterrestrial magmatic system products occurred on the Moon during the Apollo and Luna programs between 1969 and 1972 (i.e., Stooke 2017; Yang and Zhao 2018), and recently by Chang'e 5 (i.e., Qian et al., 2021). Collection of lunar meteorites found on Earth provides additional constraints on lunar magmatic system processes from a sample perspective (see Zhou 2017 and references therein). Whole rock composition analysis has been combined with remote sensing evaluation of the physical extents of lunar lava flows to further estimate magma ascent rates and viscosities, with implications for eruption and emplacement mechanisms of extraterrestrial lavas (i.e., Gawronska et al., 2022; Wilson, 2009). Over decades of study, researchers have observed several distinct geochemical differences between suites of lunar basalts. Overall, lunar basalts vary greatly with respect to their whole rock TiO_2 contents; <1 wt. % to 14 wt. %, their whole rock Al_2O_3 contents; 5 wt. % to 20 wt. %, and their whole rock K_2O contents; below detection limit to 15,000 ppm (Neal and Taylor, 1992; Papike et al., 1976; Shearer et al., 2006). These compositional ranges have been interpreted to reflect partial melting of a compositionally stratified lunar mantle characterized by vertical and lateral heterogeneities. Such heterogeneities are believed to have been established during primordial Lunar Magma Ocean (LMO) solidification, which worked to differentiate the Moon into the feldspathic crust, a K-, REEs-, and P-rich reservoir known as urKREEP beneath the lunar crust, and a stratified mantle composed of olivine and pyroxene cumulates with variable amounts of ilmenite and armalcolite (see McLeod and Gawronska, 2022, for a recent summary). Partial melting of these initially stratified, and later overturned cumulates has been proposed to generate the compositional differences in the sampled basaltic samples. However, heterogeneities in lunar basalt compositions may not be wholly representative of their source regions, but may instead reflect the introduction of antecrystic grains which has been documented on Earth (i.e., Ubide et al. 2014). It is thus imperative to investigate the crystallization histories of lunar basalts using the modern terrestrial framework to better understand whether open system magmatic processes such as mixing, mingling, or recharge once operated within lunar magmatic systems. This type of work will provide additional detailed insights regarding the degree to which such processes may have affected the final compositions of basalts sampled at the surface, and thus whether those basalts are representative of their source regions. Here, we begin to evaluate the petrogenesis of lunar magmas through an integrated mineralogical, textural, and geochemical investigation of Apollo lunar basalt samples 10057, 12038, 12043, 15085, 15556, and 70017. Through the characterization of textures and chemistries preserved in mineral grains in a diverse suite of Apollo basalts, we first evaluate whether crystal populations with distinct petrogenetic histories are preserved. Through identifying distinct

crystal populations, we interpret the processes that may have contributed to sample petrogenesis (i.e., open system processes like mixing or closed system processes like convection), discuss the implications for the evolution of magmatic systems on planetary objects which lack plate tectonics, and recommend future directions.

3.1.4 Sample descriptions

Samples were chosen for this study based on their textural and whole rock chemical diversity (see Table S1). Samples include 10057, 12038, 12043, 15085, 15556, and 70017. Detailed descriptions of sample characteristics (textures, mineralogy), ages, and summaries of previous work can be found in Meyer (2016). Brief descriptions are provided here. Sample 10057 is a vesicular to vuggy, fine-grained (Figs. 2-3) high-Ti basalt, and is categorized as an Apollo 11 group A basalt owing to its enrichment in K and the rare earth elements (REEs, e.g., Jerde et al., 1994). This sample is hypocrystalline with a minor mesostasis/glass component (3.3-8.04% modally). Sample 12038 is an Apollo 12 medium grained, granular, low-Ti basalt with a very minor glassy mesostasis component (<1% modally). 12038 is dominated by subhedral to euhedral plagioclase feldspar laths (Fig. 2b), and has been categorized as a feldspathic basalt as a result. Sample 12043 was also collected during Apollo 12, and is classified as a low-Ti pigeonite basalt. It has a porphyritic texture with macrocrystic, zoned pyroxene grains surrounded by a feldspar/pyroxene matrix (Fig. 2c). Sample 15085 is coarse-grained (Fig. 2d), non-vesicular, holocrystalline, and equigranular basalt belonging to the low-Ti quartz-normative group collected during Apollo 15. Sample 15556 is also a low-Ti basalt and represents the olivine-normative Apollo 15 basalts. It is highly vesiculated (~49% by volume, Gawronska et al., 2022) and hypocrystalline with a minor glass component (1 %). 15556 also contains ~2% modally of macrocrystic olivines set in a fine-grained plagioclase/pyroxene matrix (Fig. 2e). Sample 70017 is a medium to coarse grained high-Ti basalt belonging to the Apollo 17 group B, and contains “chains” of ilmenite (Fig. 2f; Meyer, 2016; Paces et al., 1991).

3.2 Methods

3.2.2 Microscopy

We used light and electron microscopy to document sample mineralogy and textural characteristics. Thin sections were first characterized using a Leica DM2700 P polarizing light microscope (PLM). Additional data was collected via a Zeiss Supra 35 VP FEG Scanning Electron Microscope (SEM) in-house at the Miami University Center for Advanced Microscopy and Imaging (CAMI). Characterization via SEM involved acquisition of 1) backscatter electron (BSE) images and 2) energy dispersive X-ray spectroscopy (EDS) elemental maps. Both datasets for each sample were collected at a resolution of 2048 by 1536 pixels, a dwell time of 256 µs, a working distance of 10 mm, and an accelerating voltage of 20 keV. Individual images and maps were stitched together using *Illustrator* (Adobe Inc. ©, version 23.0.1). Finally, *ImageJ* (version 1.52a; Schneider et al., 2012) was used to merge individual elemental maps which supported an initial, qualitative, evaluation of the relationships between mineral textures and chemistries (see Figs. 3, S1).

3.2.3 Crystal Size Distribution Analysis

Imaging via PLM and SEM facilitated identification of phase boundaries. This spatial context permitted crystal size distribution (CSD) analyses to be undertaken in order to evaluate the crystallization history of each sample. The free software GNU Image Manipulation Program (GIMP, version 2.8.18, www.gimp.org) was used to outline each sample, followed by the outlining of individual crystals. During this process, touching crystals remained on separate layers. The outlines were filled, and layers with data were exported from GIMP as images for further analysis. In *ImageJ*, the area of the sample was extracted, along with the areas, lengths, and widths of each grain. This data was next processed through the CSD Slice 2.0 Excel spreadsheet (Morgan and Jerram, 2006), then plotted via the *CSD Corrections* program developed by Higgins (2000). *CSD Corrections* first calculated the most likely three-dimensional shape of each grain, and then determined the natural log of population densities as a function of grain long axes. This process has been documented as successfully quantifying grain cooling histories in both terrestrial and extraterrestrial sample studies (i.e., Donohue and Neal, 2015; Higgins, 2000; Morgan and Jerram, 2006; Neal et al., 2015). Phases investigated via CSD analysis included plagioclase feldspar and ilmenite. To ensure CSDs of a phase with tabular habit (i.e., plagioclase feldspar) are as accurate as possible, 200+ crystals must be outlined (Morgan and Jerram, 2006). For this reason, sample 15085 could not be investigated via CSD. Crystal frequencies are summarized in Table S2, and individual CSDs are reported in Fig. S2. As no sample contained a statistically significant number of olivine grains, olivine was not considered.

3.2.4 Geochemical Analysis

Next, the major element oxide (i.e., SiO_2, CaO, MgO) concentrations of the silicate phases of feldspar, pyroxene, and olivine (where available) were quantified in-situ via electron probe microanalysis (EPMA). This was accomplished on a JEOL JXA-8230 electron microprobe at Louisiana State University via energy dispersive spectrometry. In-situ analyses of trace elements in these phases followed, and were carried out via laser ablation inductively coupled plasma mass spectrometry (LA-ICP-MS) on a NWR193 laser ablation system connected to a Thermo Icap Q ICP-MS at the University of Arkansas. Data was collected as individual spot analyses to ensure that data was "spot-resolved," i.e., the exact location and chemistry of each spot was known and there was no overlap in spots.

3.3 Results and Discussion

3.3.1 Apollo 11 high-Ti basalt 10057

Generally, pyroxene and ilmenite in 10057 are equigranular (~0.2 mm), while the feldspar grains range in size and habit from small (~0.02 to 0.2 mm) anhedral, interstitial grains to larger (~0.3 mm) subhedral/euhedral, tabular grains (Figs. 2-3). Both feldspar and ilmenite CSDs are constant, indicating that neither of these phases records a significant change that would otherwise impact crystallization rate during cooling (Fig. 4). Due to the fine-grained nature of this sample, only three plagioclase feldspar grains could be analyzed via LA-ICP-MS at both the core and rim. Considering major element chemistry, we identified one plagioclase grain that is subhedral and tabular (which is not texturally distinct with respect to other feldspar grains) with reverse zoning in An (core: An_{78}, rim: An_{87}), normal zoning in FeO (core: 0.56, rim: 0.60 wt. %), and an elevated core La/Sm ratio of 4.96, relative to other normally-zoned feldspar crystals (cores: approximately An_{82},

~0.80 wt. % FeO, La/Sm <3.5; rims: <An_{80}, >0.60 wt.% FeO, La/Sm ~2.5 to 3; Fig. 5). The one reversely-zoned also has a ~40 ppm increase in Sr content from core to rim (Fig. 6). Because reverse zoning in major element content corresponds with changing Sr compositions, this grain is interpreted to record a change in its crystallization conditions during growth, likely interaction with a more primitive magma. An additional normally An-zoned crystal also records an increase in Sr at the rim. Both are depleted in other trace elements (e.g., Rb, Sr) relative to a more enriched normally-zoned grain containing elevated REE core contents (Fig. S4) and high La/Y (Fig. S5). Eu/Eu* anomalies were calculated using chondrite-normalized values (after Sun and McDonough, 1989) as Eu/Eu* = $(2*Eu_N)/(Sm_N+Gd_N)$. The Eu/Eu* systematics for this sample record a decrease in Eu/Eu* from core to rim in both of the grains which record an increase in Sr (Fig. S5). The distinct relationship An vs. La/Y and An vs. Eu/Eu* between the reversely-zoned grain and the normally-zoned grains may indicate that these grains all crystallized in distinct magmatic environments. However, these grains are not texturally distinct suggesting they experienced similar cooling histories (consistent with the constant CSD), which may indicate that compositional changes are related to incorporation of material with distinct composition via a process such as mingling, which would not fully homogenize melt composition prior to crystallization. Previous work has proposed that sample 10057 experienced assimilation of KREEPy material during its petrogenesis (Jerde et al., 1994). This is supported by the abundance of K-rich mesostasis, and by approximately half of the feldspar cores analyzed here having elevated trace element contents (i.e., >16 ppm Rb, relative to <5 ppm for the remaining grains, Fig. 6; note that these grains are too small for rim analysis via LA-ICP-MS).

In the pyroxene population, one glomerocryst (Fig. S3) contains larger grains in comparison to all other pyroxene within this sample: ~0.35 mm vs. <0.2 mm long. As mentioned above there are regions of K-rich mesostasis in this sample, and pyroxenes nearby to this mesostasis preserve reaction textures (i.e., resorption). In BSE, pyroxene grains in the glomerocryst display patchy zoning which is distinct from the progressive zoning observed in other pyroxenes. In addition, glomerocrystic pyroxenes contain small ilmenite and feldspar inclusions (Fig. S3). One grain in the glomerocryst has close to constant Mg# (core: 74.1, rim: 72.2), while matrix grains range from Mg# 74.1 to 70.4 in the core and Mg# 56.5 to 17.1 in the rim (i.e., showing normal zoning; Fig. 7). Along with one other matrix grain, the grain analyzed within the glomerocryst has relatively higher CaO values in the core (~17 wt. %) relative to other, non-glomerocrystic cores (<15.5 wt. %; Fig. 7). The glomerocrystic grain is additionally depleted in the trace elements Cr, V, and Sc and elevated in REEs in its core relative to other, non-glomerocrystic grains' cores (Figs. 8, S6-S7). Specifically, the grain within the glomerocryst is reversely zoned in Cr, which is interpreted as recording an influx of primitive magma that was able to effectively mix with the melt initially surrounding this growth, potentially due to recharge (i.e., Costa and Morgan 2011, Ubide and Kamber, 2018, Ubide et al 2019). Thus, based on its distinct texture and geochemistry, the pyroxene glomerocryst is interpreted here as being antecrystic. It is possible that this glomerocryst was plucked from a mushy lens by a hotter, more primitive melt which now represents the remainder of the sample, whereby the change in composition and temperature worked to unlock the mush (see discussion by Neave et al., 2021 and references therein). A change in melt composition due to primitive influx would also generate reverse An and Sr zoning seen in some plagioclase grains. After

rising, this magma with an entrained glomerocryst and reversely-zoned feldspar is inferred to have interacted with a more KREEPy magma batch, generating pyroxene resorption and potentially generating reverse Sc-zoning of one analyzed pyroxene grain that is next to mesostasis (black in Fig. 7). This additionally may have led to incorporation of a distinct feldspar population highly enriched in REEs, and generated the K-rich mesostasis seen in this sample.

3.3.2 Apollo 12 feldspathic basalt 12038

In 12038, both plagioclase and pyroxene are seriate, ranging in size from 0.1 to 10 mm (Fig. 2). Feldspar grains range in habit from euhedral tabular grains to subhedral laths, and some are subophitically contained within pyroxene grains (Fig. S3). CSDs performed here record slight upward curves in both plagioclase and ilmenite (Fig. 4), indicating accumulation and/or coarsening. All feldspar grains analyzed have relatively high CaO wt. % cores (An_{82} to An_{86}), high MgO cores (0.26-0.36 wt. %), and low FeO cores (~0.5 wt. %; Fig. 5). In terms of trace elements, plagioclase cores are low in Eu (~2 ppm), and Sr (292.2 to 306.9 ppm) relative to their respective rims, but the difference from core to rim in Eu is <1 ppm, and in Sr <100 ppm except for one subophitic grain (Figs. 6, S4-S5). Eu/Eu* anomaly values show that all grains preserve similar evolution from core to rim (Fig. S5). Because all analyzed feldspar grains record the same petrogenetic history (as indicated by similar major and trace element signatures from core to rim), geochemical signatures that would otherwise be indicative of open system processes are not evident within the plagioclase population. Crystallization of feldspar is thus inferred to have occurred under closed system conditions, with grains experiencing either accumulation or coarsening during crystallization (as evidenced by CSD work).

All pyroxene grains in 12038 are subhedral to anhedral. Some are sieved near the rim and breaking down to 3-phase symplectite (e.g., Fig. S3). All pyroxenes are normally zoned from core to a mantling zone (Fig. 7; average core: $En_{47.2}Fs_{33.1}Wo_{19.7}$, average mantle: $En_{18.6}Fs_{47.1}Wo_{34.3}$), but three out of seven analyzed grains are reversely zoned after this with higher MgO and lower CaO towards the rim ($En_{28.2}Fs_{39.7}Wo_{32.1}$, as opposed to normally-zoned rims of $En_{7.0}$ $Fs_{70.5}Wo_{22.5}$ of other crystals). One grain is additionally reversely zoned in Al_2O_3 from mantle (2.8 wt. %) to rim (3.8 wt. %) relative to other grains (rims: ≤2 wt. % Al_2O_3; Fig. 7). All grains are normally-zoned in Cr and V, but those with reverse MgO and CaO near their rim also initially increase in Sc by ~20 ppm, and then decrease again in Sc by 60-80 ppm toward the rim to match the Sc core content of a grain with the highest Mg# (52.5) found (Fig. 8). An influx of primitive magma should increase the Cr content at the rim, while mixing with another batch should distinctly affect major and trace element contents, but the element variations here are comparable within and between cores and rims (i.e., Figs. S6-S7). Thus, we conclude that the intragrain geochemical signatures are related to local differences in the melt that may have been produced by movement through a compositional gradient via a process like convection. Pyroxene breakdown can occur from changes in pressure alone during ascent (Neave and Maclennan, 2020), which we invoke here to explain disequilibrium textures (sieving and symplectites; Fig. S3). This sample is currently the only feldspathic basalt in the Apollo 12 suite (i.e., Neal et al., 1994), and is not petrogenetically related to other Apollo 12 basalts based on REE and isotopic contents (Nyquist et al., 1981).

3.3.3 Apollo 12 pigeonite basalt 12043

This porphyritic sample contains pyroxene macrocrysts (1 to 5 mm) in a matrix of feldspar and pyroxene grains that, in certain locations, are radially growing out of points of common nucleation (Fig. S3). Plagioclase grains are seriate (~0.02 to 0.55 mm) and subhedral to euhedral. Some preserve quenched, skeletal textures, and all are oriented along a flow plane and pushed up against pyroxene macrocrysts (Figs. 2-3). There is a kink in the feldspar CSD suggesting a change in cooling parameters, but not in the ilmenite CSD (Fig. 4), which together indicate that a change in the cooling history of this sample may have occurred either prior to ilmenite crystallization, or that the ilmenite crystal population is not large (or abundant) enough to have recorded it. Compositionally, feldspar does not record significant changes in An content, but several feldspar grains are normally zoned from high An cores (An_{93-91}) to lower An rims (An_{91-90}), while others trend reversely from variably low An cores (An_{91-88}) to variably higher An rims (An_{92-89}; Fig. 5). One of the reversely-zoned grains is also reversely zoned in MgO from core to rim (0.19 and 0.39 wt. %, respectively) which could indicate incorporation of a grain which crystallized in a more evolved melt, as opposed to the remaining reverse-An grains which have the opposite correlation (high-MgO cores, lower MgO-rims; Fig. 5). The core of this low-MgO grain is also enriched in Rb (0.36 ppm) relative to other grains (<0.12 ppm Rb in core; Fig. 6), but otherwise is not clearly distinct. There is only limited correlation between Sr values and An content, which may indicate that reverse An is a consequence of rapid decompression during ascent through the system as opposed to changing magma composition. However, Eu/Eu* anomaly values show the opposite relationship between reversely-An zoned and normally-An zoned grains (Fig. S5), perhaps indicating that grains grew in distinct magmatic environments prior to ascent.

Texturally, at least two populations of pyroxene are defined - the coarse-grained (>0.5 mm long), subhedral to euhedral megacrysts, and the smaller (<0.5 mm long) subhedral to anhedral matrix pyroxenes (Figs. 1-3). Most of the macrocrystic pyroxenes have sieved mantles that correspond to an increase in CaO, and are visibly zoned under polarized light (Figs. 2-3). All pyroxenes here are normally zoned, with core Mg# of >57.8, except for a matrix grain that is interpreted to record a later stage of growth (black in Fig. 7). Two analyzed macrocrysts are notably elevated in CaO in their cores (~16 wt. %), while two other grains have mantles that are elevated in CaO (~15 wt. %), but their cores are comparable to other macrocrysts (~4 wt. % core CaO). Of the two grains with high CaO cores, one is also enriched in Sc, Cr, and V (109.7 ppm, 8399.8 ppm, 631.9 ppm, respectively) relative to the cores of other pyroxenes crystals (<85 ppm Sc, <6793 ppm Cr, <476 ppm V). Meanwhile, one of the grains with a high-CaO mantle is also elevated in La/Sm in its core (1.5) relative to its rim (0.6) and to other grains (Fig. 8), and in Ce/Y (0.33 core, 0.18 rim) in its core relative to other grains (Fig. S7). This LREE-enriched grain is the largest (5 mm), tabular pyroxene macrocryst visible in Fig. 2; the high CaO grains represent two macrocrysts, while other macrocrysts plot along matrix pyroxenes.

Between the REE-rich pyroxene macrocryst, the CaO-rich macrocrysts, and matrix pyroxenes, three distinct cooling histories of pyroxene may be recorded. A rising, more primitive magma encountering a mushy lens of more evolved composition could have entrained grains with higher CaO cores, and produced Ca-rich mantles around Mg-rich cores. In this scenario, the Ca-rich cores and mantles are antecrystic, having formed in a

separate crystal mush. Remaining macrocrysts are compositionally similar to matrix pyroxenes in terms of major and trace element contents, but must have formed earlier considering their larger size. Neal et al., (1994) used assimilation and fractional crystallization modeling to show that 12043, and the remaining Apollo 12 pigeonite basalts, likely assimilated crustal materials of varying compositions during their petrogenesis. This work proposed that the assimilants were likely anorthositic in composition, and may therefore have provided additional CaO for pyroxene formation, and generated plagioclase populations with distinct compositional profiles. Meanwhile, transport from depth, between lenses, and/or leading to eruption may have contributed to the observed disequilibrium textures.

3.3.4 Apollo 15 quartz-normative basalt 15085

The grains in this sample are too coarse (average grain size of 1 to 5 mm) to attempt a CSD on any mineral phase. Feldspar grains are generally subhedral and interstitial (Figs. 2-3). Approximately one in ten plagioclase grains in this sample are concentrically zoned under polarized light (Fig. 2). Compositionally, cores of feldspar grains have highly variable An ranging between An_{92} and An_{80}. The majority of the analyzed grains decrease by 2-3 An mol% from core to rim and are thus normally zoned. However, some also display reverse zoning where An increases by 1 to 2 mol from core to rim, while four out of the 18 analyzed grains record no change in An from core to rim (Fig. 5). The normally-zoned grains range in habit from euhedral to anhedral and contain numerous small (<0.5 mm) pyroxene inclusions. The reversely zoned crystals are euhedral to subhedral, relatively large (~3.5 to 4 mm), and typically contain fewer pyroxene inclusions. The MgO contents of cores of normally-zoned An grains are relatively depleted (<0.17 wt. %) when compared to the reversely-zoned population (>0.23 wt. % MgO). In addition, the normally-zoned population records an increase in Sr at the rim (by 50 to 150 ppm) which would be consistent with the introduction of compositionally more primitive magma. This is not observed in the reversely-zoned grains or the no-change grains, neither of which record any change in Sr from core to rim indicating their An change probably comes from Na-Si dissolution during decompression (Ustunisik et al., 2014). As cooling progressed, a final late-stage interstitial population rich in Eu, Rb, Sr, and low in An formed: this additional population of feldspar grains is euhedral to subhedral, low in An (< An_{85}), high in $NaO+K_2O$ (>1.5 wt. %), Eu (>3 ppm), Rb (>0.15 ppm), and Sr (>492 ppm) in their cores relative to the remaining grains (≤ 1 wt. % $NaO+K_2O$, <2 ppm Eu, <0.1 ppm Rb, <300 ppm Sr; see Fig. 6). Thus, this population is interpreted to represent a late stage of growth.. These three feldspar populations have similar trace element, and particularly REE, contents (Figs. S4-S5) suggesting that they did not form in significantly distinct magmatic environments. Eu/Eu* systematics show a complex history of feldspar crystallization, with grains of similar An content having opposite Eu/Eu* values, i.e., some with elevated Eu anomaly values (>60) in their cores relative to their rims, and with others having lower Eu anomaly values in their cores relative to their rims (<40; Fig. S5); the late stage population is distinct on the basis of An values, but not Eu/Eu* values.

Texturally, there are at least three pyroxene populations in sample 15085. The first displays prominent sieve textures which are also associated with discrete compositional zones (Figs. 2-3; Fig. 9). At the rims of these grain, Fs-Fa-SiO_2 symplectites are also present (and, in extreme cases the pyroxenes have been completely replaced by

symplectite, Fig. S3). The second population is characterized by resorbed cores, sieved textures between compositional zones, and displays only minor breakdown to Fs-Fa-Si symplectites. The third population is typically interstitial in nature and comparatively exhibits minimal sieve textures, and no breakdown to symplectite. Generally, pyroxenes in greater textural disequilibrium in 15085 have resorbed MgO- and Cr-rich cores overgrown by Ca-rich mantles, with Fe-rich rims – the transitions between each zone are sieved, and Fe-rich rims are commonly dominated by symplectite. As shown in Fig. 8, the grain mantles coincide with a 9 to 16 wt. % increase in CaO, a 3 wt. % decrease in FeO (Figs. 3,7), and a ~1000 ppm increase in Cr, 45 ppm increase in Sc, and 300 ppm increase in V (Fig. 8). One grain that is texturally similar to the first population (significantly resorbed and has been completely replaced by symplectites at the rim) is compositionally distinct, showing no significant change from core to rim in MgO, and having a core elevated in CaO (~14 wt. %) relative to the remaining cores (<7.5 wt. % CaO), and a mantle elevated in Cr (5432.7 ppm) relative to its core (4802.9 ppm). This grain is not otherwise distinct in trace elements (Fig. 8), but may also preserve evidence of sector zoning which has been partly destroyed by breakdown (Fig. S3).

From La/Sm vs/ Dy/Yb systematics (Fig. 8), there may be potentially three distinct compositions of cores which are not as clearly reflected in other compositional plots. The euhedral to subhedral grains in greatest textural disequilibrium (sieved, with occasional symplectite rims) and the highest core Mg# (>65) and Cr (>4500 ppm) with CaO-rich mantles have generally low La/Sm and Dy/Yb relative to other grains (<0.5, <1, respectively). The CaO-elevated grain described above is associated with this population despite its distinct CaO content. We conclude that this texturally and compositionally distinct pyroxene population represents a relatively early-formed, primitive, antecrystic population within sample 15085, based on definitions by Edmonds et al. (2019) and Zellmer (2021). The second population of resorbing, anhedral grains, some of which have relatively low Al_2O_3 (~1 wt. %) and high Sc (~50 ppm) compared to other populations' cores (>~3 wt. % Al_2O_3 and <40 ppm Sc), have high Dy/Yb (>1) – this may represent crystallization from a chemically distinct, more evolved melt composition. The third group of grains with less extensive sieving have lower Mg# cores (~50), lower Cr (~4000 pm), and higher La/Sm (>0.5) and Ce/Y (Figs. 7-8, S7) values. These are interpreted to represent a later stage of formation based on elevated trace and REE contents in their cores, or may be entirely distinct considering their high Ce/Y values. Moreover, this may be the only population of pyroxenes in 15085 that is in equilibrium with the final carrier magma given the lack of significant sieving or symplectite development.

For 15085 pyroxenes, primitive, early-formed MgO- and Cr-rich cores are interpreted to have been transported to a mushy lens where a compositionally more evolved interstitial melt was present. In this environment, they experienced resorption and subsequently grew CaO-rich mantles, while CaO-rich material (including the CaO-rich core found here) was incorporated. This interstitial, incorporated material was likely not significantly distinct in composition since trace element contents between these two core populations (one CaO-poor, the other CaO-rich) are similar (both with ~250 ppm V, ~23 ppm Sc, ~5000 ppm Cr, La/Sm close to 0). As crystallization continued in this magmatic environment, the interstitial melt would have become more incompatible trace element-enriched (differentiated) as a result of continued crystallization, perhaps generating the

final population with elevated La/Sm and Ce/Y core signatures. These textural and chemical observations are consistent with the conclusions of Vetter et al. (1988) who determined that the Apollo 15 quartz-normative suite which this sample belongs to formed by extensive fractional crystallization of pigeonite, which are now found as phenocrysts throughout the QNB suite; their phenocrystic, early-fractionated pigeonites may be represented here as the early-forming, antecrystic population. Lindstrom and Haskin (1978) additionally argued that mixing of separate magma batches is required to produce the QNB samples, which would account for pyroxene grains with elevated La/Sm and Ce/Y ratios, and plagioclase feldspar grains with distinct Eu/Eu* vs. An relationships. A few pyroxenes in the second (in moderate textural disequilibrium) and third (in minimal textural disequilibrium) populations described here also record an increase in Cr (by 100 to 500 ppm) at the rim, which may correspond to influx of hot primitive magma that would mix with trace element-enriched interstitial melt and unlock and mobilize this cargo. These processes are discussed further in **Section 4**.

3.3.5 Apollo 15 olivine-normative basalt 15556

CSDs of plagioclase record an upwards curve in sample 15556,28 but no change in sample 15556,241. While ilmenite CSDs show a kink in 15556,28, no change is recorded in 15556,241 (Figs. 4, S2). This indicates a potentially complex crystallization history that is not completely recorded by the textural characteristics of these phases. Plagioclase grains are generally equigranular (~0.25 mm), range from subhedral to anhedral, interstitial, and occasionally poikilitically enclose some of the smallest pyroxene grains in this sample (Figs. 3, S3). It is noted here however that some larger feldspar grains (up to 1 mm) do exist in texturally distinct crystal clots throughout this sample (Fig. S3). Some feldspar grains display normal zonation patterns with relatively high An (>An_{91}) and low Na_2O+K_2O (most <0.8 wt. %) cores that decrease by ~2 An and increase by up to 0.5 wt. % Na_2O+K_2O towards the rim, while other feldspar grains record slight reverse zoning from lower-An (generally <An_{90}), higher Na_2O+K_2O (~1.2 wt. %) cores that record a 0.5 An increase and decrease of ~0.3 wt. % Na_2O+K_2O toward the rim. The reverse grains are anhedral, and the normally zoned grains subhedral. All grains increase in FeO from core to rim by 0.1 to 1.5 wt. %. Three out of seven normally An-zoned grains, and two of the four reversely An-zoned grains studied here, increase in Sr (by >60 ppm) and Eu (by 0.5 to 2 ppm) from core to rim. Three out of four reversely An-zoned grains also correspond to an increase in Sr from core to rim, which could indicate an influx of new, compositionally primitive magma. However, changes in the major and trace element contents across all studied grains are small; all grains display similar MgO and FeO systematics, and REE contents are consistent between grains (Figs. S4-S5), thus if any influx of new material into the crystallization environment did occur, it likely had a similar composition. Eu/Eu* anomaly values for plagioclase preserve a range of compositional changes from core to rim, with some grains recording a decrease in Eu/Eu* with decreasing An, some increase in Eu/Eu* with decreasing An, some increase in Eu/Eu* with increasing An, and one showing a decrease in Eu/Eu* with increasing An content. The complex compositional relationships in grains studied here do not correspond to textural differences, but all occur within cm of each other (within this one sample), indicating that melt composition also differed on a small scale. Local differences in the bulk rock composition of 15556 have been attributed to short range unmixing (described further below; Lindstrom and Haskin, 1978).

Pyroxenes are generally euhedral to subhedral, and seriate (0.2 to 0.5 mm long). With the exception of one grain, all analyzed grains (n=13) are normally zoned from cores with Mg# of 62 to 63 and rims of approximately either Mg# 30 or Mg# 13. There is one grain that is interstitial to feldspar, and differs from others with a lower core Mg# (32.9) and higher rim Mg# (34.7, Fig. 7). The core of this grain also has relatively elevated Sc (94.8 ppm), and lower V (122.1 ppm) and Cr (1232.4 ppm) compared to other grain's cores (<81 ppm Sc, >319 ppm V, >3140.4 ppm Cr, Fig. 8). From Sc contents, two groups of pyroxene grains are defined, where several grains are normally zoned from >75 ppm in the cores, to <66 ppm in the rims. The remaining grains (including the low core Mg# grain) have <53 ppm Sc cores and to up to 90 ppm Sc rims (Fig. 8). Grains with relatively low Sc are generally also low in REE contents (Fig. S6), while those with high core Sc have elevated REE contents, with one grain exhibiting a particularly high Ce/Y (Fig. S7). The low-Sc cores also generally correspond to low Dy/Yb core values of ~1.2, while the high Sc cores generally have higher Dy/Yb values of ~2, with some displaying high La/Sm value (>0.4, Fig. 8). Grains that are in textural equilibrium, and grains that are in textural disequilibrium (i.e., lightly sieved and resorbing) exist in both compositional populations (as defined by Sc; see Figs. 2-3, S2). As the name of the sample suite to which 15556 belongs to implies, the compositions of olivine-normative basalts are controlled by olivine growth and fractionation (Ryder and Schuraytz, 2001). Ryder and Schuraytz (2001) found that the within the olivine-normative Apollo 15 basalt suite, sample bulk compositions can vary on a mm- to cm-scale as a result of the addition or removal of olivine. For example, Sc is generally incompatible in olivine (i.e., K_D<0.5, Beattie, 1994) but generally compatible in pyroxene (i.e., K_D>1.0, Hart and Dunn, 1993), thus initial growth and fractionation of olivine would relatively concentrate remaining melt in Sc. Based on the work done here, grain Sc contents are likely related to their proximity to late-stage mesostasis. Grains with elevated Sc contents are not near mesostasis, indicating that they may have formed early when melt remained Sc-enriched following olivine fractionation; grains with low Sc contents generally border mesostasis on at least one side, indicating that they may have crystallized later on. Because core Sc contents form two distinct groups rather than a progressive change, it is possible that pyroxenes crystallized in two-stages, or from a melt that had not efficiently mixed following depletion in Sc as a result of olivine fractionation, likely due to high degrees of undercooling (consistent with plagioclase results). A melt not having effectively homogenized following fractional crystallization is consistent with previous work: Lindstrom and Haskin (1978) determined that compositional changes in the Apollo 15 olivine normative suite resulted from short-range unmixing, where early-formed phases that effectively change the composition of the remaining melt do not effectively fractionate from the melt, thus retaining early-formed grain populations alongside later-formed populations of distinct composition. High degrees of undercooling consistent with this sample's fine-grained nature may have further contributed to preclude efficient element diffusion through melt following olivine fractionation (i.e., Lofgren et al., 1974, Vernon 2018).

Sample 15556 contains olivine macrocrysts, which are skeletal at their rims (as evidenced by incomplete filling between corner growths, Figs. 3, S3), and embayed (as evidenced by irregular crystal faces, Figs. 3, S3). The olivines are normally zoned, some host melt inclusions, but none preserve resorption textures like those observed in pyroxene. The cores of olivine in 15556 are all compositionally strikingly similar, but there are two

compositionally distinct rim compositions. Cores are defined by Mg# >57.5, 0.47 to 0.26 wt. % Cr_2O_3, and 0.046 to 0.27 wt. % NiO. One rim population is characterized by elevated Cr_2O_3 (0.27 to 0.35 wt. %) with no significant change in MnO or CaO toward the rim (Fig. S8) The second population records normal zoning in Cr_2O_3 to rim compositions of <0.12 wt. %, but increases in CaO (from ~0.2 wt. % in the core to >0.3 wt. %), MnO (~0.33 wt. % in the core to >0.5 wt. % in the rim).

3.3.6 Apollo 17 high-Ti basalt 70017

Plagioclase grains in 70017 poikilitically enclose small pyroxene, ilmenite, and olivine grains, and are generally subhedral, ranging from ~0.1 to 2 mm long. From CSDs, ilmenite records a distinct kink (Figs. 4, S2), while the plagioclase feldspar CSD is more complex, recording either multiple kinks in the distribution corresponding to a rapid change in the system, or recording one upwards curve corresponding to crystal accumulation (Fig. 4; i.e., Donohue and Neal, 2015). Compositionally, several grains are variably normally zoned, decreasing by 1 to 5 An mol from core to rim; other grains increase only minimally by ~1 An mol from core to rim (Fig. 5). One normal zoned grain has a compositionally distinct core which is notably low in An (An_{79}) and high in FeO_{total} (0.64 wt. %) relative to other cores (>An_{84} ; <0.45 wt. % FeO_{total}), and likely formed at a later stage, as it is also elevated in total REEs (Fig. S4). Two other grains that are reversely zoned in An are elevated in MgO content (>0.3 wt. % at the core and rim) and alkalis (>1.5 wt. % Na_2O+K_2O in the core) relative to others (<0.25 wt. % MgO in cores and rims; <1.5 wt. % Na_2O+K_2O in cores). With respect to trace elements, the normally-An zoned population is also reversely zoned in compatible Eu and Sr (Fig. 6), though in varying amounts (Fig. 6), while the reversely zoned group preserves only minimal change in Eu or Sr content (<0.5 ppm Eu and <30 ppm Sr change from core to rim; Fig. 6). Some grains that are reversely zoned in An and some that are normally zoned in An show an increase in Eu/Eu* from core to rim, while other reversely-zoned grains and normally-zoned grains show a decreasing Eu/Eu* anomaly from core to rim; neither relationship is related to a particular texture. The reverse An zoning is therefore interpreted as a decompression feature (i.e., Ustunisik et al., 2014) rather than significantly changing magma composition (consistent with the lack of a kink in feldspar CSD analysis). While all feldspar grains in this sample are subhedral, the reversely-zoned grains are generally larger (>1.0 mm long) than the normally zoned populations group (<1.0 mm). Due to their larger size, higher MgO content, and decompression features, these grains likely formed earlier and a greater depth in the system. Their REE contents are however not distinct from the normally zoned population (Figs. S4-S5), thus they may reflect crystallization from partial melting of the same source reservoir.

Pyroxenes in 70017 are subhedral and poikilitically enclose most of the ilmenite present (Figs. 2-3). Based on dihedral angles, it appears that pyroxenes could have experienced textural coarsening (Higgins 2011), which is consistent with recent work by Gawronska et al. (2022). Pyroxene zoning is concentric in smaller crystals (<1 mm), but tends to be patchy in the largest grains (>1 mm; Fig. 2). Pyroxenes have cores relatively high in MgO (Mg# > ~63.5), then mantles/overgrowths with ~1 to 3 wt.% increase in MgO and ~400 ppm increase in Cr, and final Fe-rich rims (Mg# <53). Those mantling zones and patches often correspond to sieve textures (Figs. 1-3, S2). From textural and compositional observations three populations of pyroxene may be present. One population is relatively

primitive in composition with elevated Al_2O_3 (>5.9 wt. %), Sc (>120 ppm), V (>200 ppm), Cr (>6000 ppm) in their cores relative to other populations and is interpreted as having formed before plagioclase. This population is represented by the largest (> ~1.5 mm) pyroxene grains that record both progressive and patchy zoning. A second population is compositionally more evolved. Grain cores are depleted in CaO (<5 wt. %), Sc (<55 ppm), V (<70 ppm), Cr (<3000 ppm), and exhibit lower Dy/Yb values (~1), relative to other cores (Figs. 7-8). This population is made up of the smallest (generally <0.5 mm), euhedral, concentrically zoned crystals. A third population is defined by compositions between these two populations (Figs. 7-8), ranging in size from 1.5 mm to 0.5 mm, and generally recording patchy zoning. Because mantling zones of the first population of grains are in textural disequilibrium, these grains likely represent stages of growth in distinct environments. Three stages of pyroxene growth at different storage locations in the magmatic system are probably represented, which is consistent with select plagioclase grains showing storage at depth prior to ascent (as revealed by reverse An zoning that is not coupled with changing plagioclase Sr content). Resorbed cores of the largest pyroxenes are interpreted as older and antecrystic, eventually being transported by more primitive melt (which imparted sieved mantles that are slightly elevated in MgO, Cr; Figs. 7-8) to a new location where a compositionally more evolved population grew. Evolved, small pyroxenes would represent a population that originate from this lens. Interestingly, the small evolved pyroxenes are reversely zoned in Sc and have distinct core Ce/Y values (Fig. S7), and may thus represent a wholly distinct magma batch that was encountered by a more primitive melt rising with the larger primitive pyroxenes. Prolonged storage in any melt lens, at any stage, may explain the textural coarsening seen documented here and discussed in Gawronska et al. (2022).

Three olivines were analyzed in this sample – two have core Mg# of ~67, Cr_2O_3 <0.2 wt. %, MnO of 0.3 wt. %, while the third has core Mg# of 52.7 wt. %, but Cr_2O_3 of 0.26 wt. %, and MnO of 0.4 wt. %. If interpretations from feldspar and pyroxene elemental stratigraphies are correct, then this third olivine grain may have formed after the proposed two magma batches came in contact.

3.4 Implications for Lunar Magmatic Systems

As documented by the pyroxene and feldspar crystal populations throughout the samples studied here, the Apollo mare basalt crystal cargoes record evidence (Fig. 9) of interactions between materials of distinct compositions at various stages of fractionation. Specifically, samples 10057, 12043, 15085, and 70017 clearly indicate that grains which initially crystallized in compositionally more primitive magmatic environments now coexist with grains that grew in relatively more compositionally differentiated melts. By definition, these types of interactions can only happen in a so-called “open” magmatic system, i.e., one where material can be exchanged through a variety of processes (i.e., Davidson et al., 2007; Ginibre et al., 2007; Jerram and Davidson, 2007; Ogawa, 2018; Ubide et al., 2014; Zellmer, 2021). Thus, it is established that the petrogenesis of at least some lunar basalts is associated with open system processes. Furthermore, magma differentiation likely occurred in distinct lenses within the lunar crust where magma batches were later remobilized and mixed prior to eventual emplacement on the lunar surface. This work suggests that plumbing system architecture evolves similarly across rocky planetary bodies, and may operate similarly on other bodies where magmatism has

operated previously or currently operates, including Mars, Venus, and Jupiter's moon Io (Wilson 2009, and references therein). Below, we outline the major implications this has for our understanding of magmatic systems on the Moon.

3.4.1 Evaluating the potential role of crystal mushes

On Earth, it has been recently recognized that magmatic systems exist as a combination of mushy lenses which can collectively extend vertically throughout the crust (Cashman et al., 2017; Sparks et al., 2019). These so-called "mushes" are continuous networks of crystals through which melt is distributed, and in which rheological properties are controlled by the crystalline network as opposed to magmas, whose rheology is controlled by melt (Cashman et al., 2017; Sparks et al., 2019). The transition between these two domains occurs approximately at 30 to 50% remaining melt (Sparks et al., 2019). Mushes form as magmas incrementally intrude into the crust, pond in lenses, and solidify over time to form crystal-rich networks (i.e., Sparks et al., 2019). Mush crystal frameworks are likely variable in modal proportion and vary on a centimeter to meter scale (i.e., Lissenberg et al., 2019). The igneous crystal cargoes produced throughout these mushy lenses, at any given stage, will crystallize and texturally and chemically trace their magmatic environment(s). Because magmatic systems stored as a network of mushy lenses can be extensive, some crystal populations may form early on (i.e., at depth) in a system's history and later rise (ascend) towards the surface in a carrier magma of distinct composition. Being out of equilibrium with carrier magma, and having crystallization from a chemically distinct source, defines antecrysts (Zellmer 2021). Due to the nature of differentiation and distance from mantle source reservoir, lenses which exist deeper within the crust are more likely to be primitive in composition, while upper lenses are more likely to be characterized by more evolved compositions (Cashman et al., 2017; Jackson et al., 2018). Within this framework, there are plagioclase grains in 10057, 12043, 15085, and 70017 that may be antecrystic in nature based on their more primitive compositions. Furthermore, their decompression features suggest initial growth occurred at depth. Meanwhile, the pyroxene glomerocryst in 10057, pyroxene macrocrysts in 12043, 15085, and 70017 are also antecrysts as evidenced by their disequilibrium textures. This includes resorption in conjunction with changing crystal compositions which likely corresponds to changing melt compositions as a result of mixing between mush melt and intruding primary melts (Fig. 9). Thus, the crystal cargoes from four of six mare basalt samples studied here clearly indicate that lunar magma plumbing systems are similar in architecture to some of their terrestrial counterparts.

3.4.2 Melt Transport Through and From a (Mare) Mush

If lunar magmatic systems operated through a network of mushes, melt transport mechanisms must also be further evaluated. In a melt-dominated system, melts can propagate upwards through a network of dikes and sills (i.e., Lissenberg et al., 2019; Wilding et al., 2023). On the Moon, melt transport may additionally be supported by crustal fracturing as a result of bombardment (Whitford-Stark, 1982). In a system where connected chambers are dominated by mush, it is predicted that melts will migrate through the mush by porous flow over time (McKenzie, 1984; Sparks et al., 2019). As crystallization progresses, the melt will either segregate to generate a secondary, separate eruptible melt lens (or chamber), or will become compacted, and will concentrate into highly porous melt layers within the chamber (Solano et al., 2014). The buoyant melt layers may then escape

upwards due to their buoyancy and establish new lenses at shallower levels, or erupt (i.e., Lissenberg et al., 2019; McKenzie 1984; Solano et al., 2014; Sparks et al., 2019). Besides porous flow, on Earth melts within magmatic systems are also known to be displaced by flow focused in a conduit through a mush. This process is comparatively more rapid (i.e., Lissenberg et al., 2019; Richter and McKenzie, 1984). This displaced flow may eventually reach the surface during an eruption, which occurs due to remobilization of otherwise immobile, solidified components (Sparks et al., 2019). Eruption of crystal-containing melt at the surface can be aided by remobilization of materials through heat, potentially as a result of an intrusion at depth or the influx of a hotter, more mafic magma into a storage region. This occurs during mafic recharge and is commonly invoked as a cause for eruptions on Earth (Huber et al., 2011, Lissenberg and MacLeod, 2016; Sparks et al., 2019; Ubide and Kamber., 2018). In particular, eruptions appear to be common in relatively small systems following recharge, though relatively larger systems may be more buffered against this (Ginibre et al., 2007). The intrusion of hot, primitive magma at depth within a magmatic systems has been shown to be effective at fluidizing crystal mushes, allowing them to rapidly ascend in crystal-poor "chimneys" (Bergantz et al., 2015; Schleicher and Bergantz, 2017; Spera and Bohrson, 2018).

3.4.2.1 Porous Flow of Melt in Mush

As a magma lens continues to evolve and establish a crystal framework, the remaining interstitial melt will become compositionally evolved, and in disequilibrium with grains in the network (Lissenberg et al., 2019). Because of this, recent work on terrestrial magmatic systems at mid-ocean ridge settings suggests that melt coexisting with a mush becomes reactive (Lissenberg and MacLeod, 2016; Lissenberg et al., 2019; Solano et al., 2014) and moves through the mush via reactive porous flow (RPF). Based on compositional modeling of melts at mid-ocean ridge settings, reactive melts can range in composition from primitive (basaltic) to evolved (dacitic) and can thus lead to various interactions with grains in the mush (see discussion by Lissenberg and MacLeod, 2016). Interstitial melts can also become remobilized and mix with any replenishing melt entering the system via a process like recharge. This leads to the possibility of two reactions: one between the mush framework and the increasingly evolved interstitial melt, and one between the mush framework and any hot, primitive, replenishing magma entering the system (Lissenberg and MacLeod 2016; Lissenberg et al., 2019). Such interactions cause crystals within the mush to develop dissolution fronts, ragged grain boundaries, symplectites, and compositions distinct from those otherwise predicted by fractional crystallization models, particularly in terms of trace element contents (i.e., Lissenberg and MacLeod, 2016). The large variety of disequilibrium features observed in terrestrial magmas as a result of RPF are reminiscent of the high degree of textural equilibrium observed in the 15085 pyroxenes (Figs. 3, S3). Pyroxenes in this sample record resorption and in some cases complete breakdown to symplectites. It is however noted here that the 15085 symplectites are defined by ferrosilite, fayalite, and an Si-rich phase, which is different to the clinopyroxene-amphibole symplectites assemblages observed in terrestrial mid-ocean ridge basalts in which RPF studies have primarily been completed (see Lissenberg et al., 2019, and references therein for more information). Resorption, breakdown, and ragged grain boundaries are also seen in pyroxenes in 70017, and to a lesser degree in 12043. At the time of writing, RPF is not a completely understood process in terrestrial systems but it does appear to be a common petrogenetic process operating in

terrestrial magma chambers that are mushy in nature (Lissenberg and MacLeod, 2016), and should be investigated further for potential influence on extraterrestrial magma evolution.

3.4.2.2 Flow of Melt to and from Mush: The Role of Mafic Recharge

RPF can cause melts to rise buoyantly through the crust, and additional mechanisms can work to destabilize this melt further. In particular, minerals with relatively primitive compositions are too refractory to be dissolved and "chemically excavated" by more evolved melts (Neave et al 2014; Ubide and Kamber, 2018), but relatively evolved grains can be more easily entrained from pre-existing shallower zones (i.e., Ganne et al., 2018). Mafic recharge is a particularly effective mechanism for defrosting, unlocking, and destabilizing mush and interstitial melt (Huber et al., 2011, Lissenberg and MacLeod, 2016, Sparks et al., 2019). Intruding primitive hot magma mixes with interstitial melt, and reacts with framework grains, unlocking them. By mixing with interstitial melt and (partly) dissolving framework grains, magma influx leads to homogenization of the melts ultimately derived from mushy lenses and erupted at the surface (i.e., Lissenberg et al., 2019). By unlocking mushes, a replenishing melt traveling through several lenses also has the potential to entrain diverse populations of phenocrysts and glomerocrysts (i.e., Cashman et al. 2017; Lissenberg et al., 2019; Ubide and Kamber, 2018). Dissolution of grains as a result of (mafic) recharge is commonly recognized as a process through which disequilibrium features can be generated (i.e., Ubide and Kamber., 2018). Introduction of primitive, hot magma carries with it a relative influx of MgO and Cr (for example), and can be coupled with disequilibrium features like resorption/dissolution. These textural and chemical features are observed in this study particularly with increased MgO and Sr contents in feldspar populations, and increased MgO, Cr, Sc in pyroxene, coupled with dissolution and sieving clearly seen in pyroxenes. Thus, it is inferred that mafic recharge was also an important process in the evolution of lunar magmatic systems, and should be investigated further as a potential eruption trigger in extraterrestrial settings.

3.5 Conclusions

Altogether, this work indicates that lunar magmatic systems are more complex than previously thought, and carry distinct crystal cargoes which record distinct petrogenetic histories at the crystal scale. This is not unlike their terrestrial counterparts. This suggests that plumbing system architecture evolves similarly across rocky planetary bodies, and may operate similarly on other bodies where magmatism has operated previously or currently operates, including Mars, Venus, and Jupiter's moon Io (Wilson 2009, and references therein). We remind the reader that while the samples were chosen for their textural and chemical diversity for study here, they ultimately represent a random sampling of the mare basalt suite. Detailed investigations of each of the six magmatic systems studied here are warranted, along with detailed evaluations of other mare basalt suites, particularly those from other basalt-generating bodies where possible, in order to fully determine the exact plumbing system architecture and processes involved in magma petrogenesis across the Solar System.

3.6 Acknowledgements

First, we acknowledge the Apollo astronauts for collecting the lunar samples studied here, and all those involved in the Apollo program who made this possible. We also extend our thanks to Matt Duley at the Miami University Center for Advanced Microscopy and Imaging (CAMI) for his support during sample imaging, and Morgan Gillis from the Miami University Department of Geology and Environmental Earth Science (at the time of writing) for her help in carbon coating sample thin sections. This research was funded through a Geological Society of America Graduate Student Research Grant #13203-21 to AG.

3.7 References

Basaltic Volcanism Study Project (BVSP) (1981) Basaltic Volcanism on the Terrestrial Planets. Pergamon Press, Inc., New York. 1286 pp.

Beattie, P. (1994) Systematics and energetics of trace-element partitioning between olivine and silicate melts: Implications for the nature of mineral/melt partitioning. Chemical Geology 117, 57-71.

Bennett, E. N., Lissenberg, C. J., Cashman, K. V. (2019) The significance of plagioclase textures in mid-ocean ridge basalt (Gakkel Ridge, Arctic Ocean). Contributions to Mineralogy and Petrology 174: 49. https://doi.org/10.1007/s00410-019-1587-1

Berlo, K., Blundy, J., Turner, S., Hawkesworth, C., 2007. Textural and chemical variation in plagioclase phenocrysts from the 1980 eruptions of Mount St. Helens, USA. Contrib. Mineral. Petrol. 154, 291–308.Bergantz et al., 2015

Bezard, R., Turner, S., Davidson, J., Schmitt, A.K., Lindsay, J., 2017. Origin and Evolution of Silicic Magmas in Oceanic Arcs; an in situ Study from St Lucia, Lesser Antilles. J. Petrol.58, 1279–1318.

Blundy J. D., Shimizu N. (1991) Trace element evidence for plagioclase recycling in calcalkaline magmas. Earth and Planetary Science Letters 102:2, 178-197.

Blundy, J. D., Wood, B. J. (1991) Crystal-chemical controls on the partitioning of Sr and Ba between plagioclase feldspar, silicate melts, and hydrothermal solutions. Geochimica et Cosmochimica Acta 55, 193-209.

Cashman K. V. (2015) Changing the paradigm – new views on magmatic systems provide new perspectives on volcanic processes. AGU, Fall Meeting 2015.

Cashman K. V., Sparks R. S. J., Blundy J. D. (2017) Vertically extensive and unstable magmatic systems: A unified view of igneous processes. Science 355, 6331. https://doi.org/10.1126/science.aag3055

Coish, R. A., Taylor, L. A. (1979) The Effects of Cooling Rate on Texture and Pyroxene Chemistry in DSDP LEG 34 Basalt: A Microprobe Study. Earth and Planetary Science Letters 42, 389-398.

Coote, A., Shane, P. (2018) Open-system magmatic behaviour beneath monogenetic volcanoes revealed by the geochemistry, texture and thermobarometry of clinopyroxene, Kaikohe-Bay of Islands volcanic field (New Zealand). Journal of Volcanology and Geothermal Research 368, 51-62. https://doi.org/10.1016/j.jvolgeores.2018.11.006

Costa, F., Morgan, D. (2011) Time Constraints from Chemical Equilibration in Magmatic Crystals. In: Dosseto, A., Turner, S. P., Van Orman, J. A. (Eds.) Timescales of Magmatic Processes: From Core to Atmosphere. Blackwell Publishing Ltd.

Couperthwaite, F. K., Thordarson, T., Morgan, D. J., Harvey, J., Wilson, M. (2020) Diffusion Timescales of Magmatic Processes in the Moinui Lava Eruption at Mauna Loa, Hawai'I, as Inferred from Bimodal Olivine Populations. Journal of Petrology 61 (7), egaa058. https://doi.org/10.1093/petrology/egaa058

Davidson J. P., Morgan D. J., Charlier B. L. A., Harlou R., Hora J. M. (2007) Microsampling and Isotopic Analysis of Igneous Rocks: Implications for the Study of Magmatic Systems. Annual Reviews in Earth and Planetary Science 35, 273-311. https://doi.org/10.1146/annurev.earth.35.031306.140211

Donohue P. H., Neal C. R. (2015) Quantitative textural analysis of ilmenite in Apollo 17 high titanium mare basalts. Geochimica et Cosmochimica Acta 149, 115-130. https://doi.org/10.1016/j.gca.2014.11.002

Edmonds, M., Cashman, K. V., Holness, M., Jackson, M. (2019) Architecture and dynamics of magma reservoirs. Philosophical Transactions of the Royal Society A, 377: 20180298. http://dx.doi.org/10.1098/rsta.2018.0298

Gawronska, A. J., McLeod, C. L., Blumenfeld, E. H., Hanna, R. D. Zeigler, R. A. (2022) New interpretations of lunar mare basalt flow emplacement from XCT analysis of Apollo samples. Icarus 388, 115216. https://doi.org/10.1016/j.icarus.2022.115216.

Ginibre C., Worner G., Kronz A. (2007) Crystal Zoning as an Archive for Magma Evolution. Elements 3, 261-266. https://doi.org/10.2113/gselements.3.4.261

Grove, T. L., Baker, M. B., Kinzler, R. J. (1984) Coupled CaAl-NaSi diffusion in plagioclase feldspar: Experiments and applications to cooling rate speedometry. Geochimica et Cosmochimica Acta 48, 2113-2121.

Hart, S. R., Dunn, T. (1993) Experimental cpx/melt partitioning of 24 trace elements. Contributions to Mineralogy and Petrology 113, 1-8.

Head, J. W., (1976) Lunar volcanism in space and time. Reviews of Geophysics 14 (2), 265-300.

Higgins M. D. (2000) Measurement of crystal size distributions. American Mineralogist 85, 1105-1116. https://doi.org/10.2138/am-2000-8-901

Higgins M. D., Roberge J. (2007) Three magmatic components in the 1973 eruption of Eldfell volcano, Iceland: Evidence form plagioclase crystal size distribution (CSD) and geochemistry. Journal of Volcanology and Geothermal Research 161:3, 247-60. https://doi.org/10.1016/j.jvolgeores.2006.12.002

Jackson M, Blundy J, Sparks RSJ. 2018 Chemical differentiation, cold storage and remobilization of magma in the Earth's crust. Nature 355, eaag3055. doi:10.1038/s41586-018-0746-2

Jerde E. A., Snyder G. A., Taylor L. A., Liu Y.-G., Schmitt R. A. (1994) The origin and evolution of lunar high-Ti basalts: Periodic melting of a single source at Mare Tranquilitatis. Geochimica et Cosmochimica Acta 58, 515-527. https://doi.org/10.1016/0016-7037(94)90480-4

Jerram D. A., Davidson J. P. (2007) Frontiers in Textural and Microgeochemical Analysis. Elements 3:4, 235-238. https://doi.org/10.2113/gselements.3.4.235

Kent, A. J. R., Darr, C., Koleszar, A. M., Salisbury, M. J., Cooper, K. M. (2010) Preferential eruption of andesitic magmas through recharge filtering. Nature Geoscience 3, 631-636. https://doi.org/10.1038/ngeo924

Lee C-T. A., Luffi P., Plank T., Dalton H., Leeman W. P. (2009) Constraints on the depths and temperatures of basaltic magma generation on Earth and other terrestrial planets using new thermobarometers for mafic magmas. Earth and Planetary Science Letters 279:1-2, 20-33. https://doi.org/10.1016/j.epsl.2008.12.020

Lindstrom, M. M., Haskin, L. A. (1978) Causes of compositional variations within mare basalt suites. Proceedings of the 9th Lunar and Planetary Science Conference, 465-486.

Lissenberg, C. J., MacLeod, C. J. (2016) A Reactive Porous Flow Control on Mid-ocean Ridge Magmatic Evolution. Journal of Petrology 57 (11&12), 2195-2220. https://doi.org/10.1093/petrology/egw074

Lissenberg, C. J., MacLeod, C. J., Bennett, E. N. (2019) Consequences of a crystal mush-dominated magma plumbing system: a mid-ocean ridge perspective. Philosophical Transactions of the Royal Society A 377: 20180014. http://dx.doi.org/10.1098/rsta.2018.0014

Lofgren, G., Donaldson, C. H., Williams, R. J., Mullins Jr., O., Usselman, T. M. (1974) Experimentally reproduced textures and mineral chemistry of Apollo 15 quartz normative basalts. Proceedings of the Fifth Lunar Conference 5 (1), 549-567.

Marsh B. D. (2009) Dynamics of Magmatic Systems. Elements 2:5, 287-292. https://doi.org/10.2113/gselements.2.5.287

McKenzie, D. (1984) The Generation and Compaction of Partially Molten Rock. Journal of Petrology 25 (3), 713-765.

C. L. McLeod, A. J. Gawronska. (2022) The Lunar Mantle. In: Cudnik, B. (Eds.) Encyclopedia of Lunar Science. Springer, Cham. https://doi.org/10.1007/978-3-319-05546-6_213-1.

Meyer, C., 2016. The Lunar Sample Compendium Database. Astromaterials Research and Exploration Science. https://curator.jsc.nasa.gov/lunar/lsc/

Middlemost E. A. K. (2014) Magmas, Rocks and Planetary Development. Routlege, London. 324 pp

Mollo, S., Putirka, K., Iezzi, G., Del Gaudio, P., Scarlato, P. (2011) Plagioclase-melt (dis)equilibrium due to cooling dynamics: Implications for thermometry, barometry, and hygrometry. Lithos 125, 221-235. doi:10.1016/j.lithos.2011.02.008

Moore, A., Coogan, L. A., Costa, F., Perfit, M. R. (2014) Primitive melt replenishment and crystal-mush disaggregation in the weeks preceding the 2005-2006 eruptions 9°50'N, EPR. Lithos 403 (15-26). https://doi.org/10.1016/j.epsl.2014.06.015

Morgan D. J., Jerram D. A. (2006) On estimating crystal shape for crystal size distribution analysis. Journal of Volcanoly and Geothermal Research 154, 1-7. https://doi.org/10.1016/j.jvolgeores.2005.09.016

National Research Council (2007) The Scientific Context for Exploration of the Moon. Washington, DC: The National Academies Press. https://doi.org/10.17226/11954.

Neal, C. R., Taylor L. A. (1992) Petrogenesis of mare basalts: A record of lunar volcanism. Geochimica et Cosmochimica Acta 56, 2177-2211.

Neal, C. R., Hacker, M. D., Snyder, G. A., Taylor, L. A., Liu, Y.-G., Schmitt , R. A. (1994) Basalt generation at the Apollo 12 site: Part 1: New data, classification, and re-evaluation. Meteoritics 29, 334-348.

Neal C. R., Donohue P., Fagan A. L., O'Sullivan K., Oshrin J., Roberts S. (2015) Distinguishing between basalts produced by endogenic volcanism and impact processes: A non-destructive method using quantitative petrography of lunar basaltic samples. Geochimica et Cosmochimica Acta 148, 6280. https://doi.org/10.1016/j.gca.2014.08.020

Neave, D. A., Maclennan, J., Hartley, M. E., Edmonds, M. & Thordarson, T. (2014) Crystal storage and transfer in basaltic systems: the Skuggafjöll eruption, Iceland. J. Petrol. 55, 2311–2346.

Neave, D. A., Maclennan J. (2020) Clinopyroxene Dissolution Records Rapid Magma Ascent. Frontiers in Earth Science 8, 188. https://doi.org/10.3389/feart.2020.00188

Neave, D. A., Beckmann, P., Behrens, H., Holtz, F. (2021) Mixing between chemically variable primitive basalts creates and modifies crystal cargoes. Nature Communications 12, 5492. https://doi.org/10.1038/s41467-021-25820-z

Nyquist, L. E., Wooden, J. L., Shih, C.-Y., Wiesmann, H., Bansal, B. M. (1981) Isotopic and REE studies of lunar basalt 12038: implications for petrogenesis of aluminous mare basalts. Earth and Planetary Science Letters 55, 335-355.

Ogawa M. (2018) Magmatic differentiation and convective stirring of the mantle in early planets: the effects of the magmatism-mantle upwelling feedback. Geophysical Journal International 215:3, 2144-2155. https://doi.org/10.1093/gji/ggy413

Paces, J. B., Nakai, S., Neal, C. R., Taylor, L. A., Halliday, A. N., Lee, D.-C. (1991) A strontium and neodymium isotopic study of Apollo 17 high-Ti mare baslts: Resolution of ages, evolution of magmas, and origins of source heterogeneities. Geochimica et Cosmochimica Act 55, 2025-2043.

Papike, J. J., Hodges, F. N., Bence, A. E., Cameron, M., Rhodes, J. M. (1976) Mare Basalts: Crystal Chemistry, Mineralogy, and Petrology. Reviews of Geophysics and Space Physics 14 (4), 475-540.

Paulatto, M., Hooft, E. E., Chrapkiewicz, K., Heath, B., Toomey, D. R., Morgan, J. V. (2022) Advances in seismic imaging of magma and crystal mush. Frontiers in Earth Science 10. https://doi.org/10.3389/feart.2022.970131

Qian, Y., Xiao, L., Wang, Q., Head, J. W., Yang, R., Kang, Y., van der Bogert, C. H., Hiesinger, H., Lai, X., Wang, G., Pang, Y., Zhang, N., Yuan, Y., He, Q., Huang, J., Zhao, J., Wang, J., Zhao, S. (2021) China's Chang'e-5 landing site: Geology, stratigraphy, and provenance of materials. Earth and Planetary Science Letters 561, 116855. https://doi.org/10.1016/j.epsl.2021.116855

Richter FM, McKenzie D. (1984) Dynamical models for melt segregation from a deformable matrix. J. Geol. 92, 729–740. (doi:10.1086/628908)

Ryder, G., Schuraytz, B. C. (2001) Chemical variation of the large Apollo 15 olivine-normative mare basalt rock samples. Journal of Geophysical Research 106 (E1), 1435-1451.

Salisbury, M. J., Bohrson, W. A., Clynne, M. A., Ramos, F. C., Hoskin, P. (2008) Multiple Plagioclase Crystal Populations Identified by Crystal Size Distribution and *in situ* Chemical Data: Implications for Timescales of Magma Chamber Processes Associated with the 1915 Eruption of Lassen Peak, CA. Journal of Petrology 49 (10), 1755-1780. doi:10.1093/petrology/egn045

Schleicher J, Bergantz G. (2017) The mechanics and temporal evolution of an open-system magmatic intrusion into a crystal-rich magma. J. Petrol. 58, 1059–1072. doi:10.1093/petrology/egx045

Schneider, C. A., Rasband, W. S., Eliceiri, K. W., (2012). NIH Image to ImageJ: 25 years of image analysis. Nature methods 9(7), 671-675, doi: 10.1038/nmeth.2089

Shearer, C. K., Hess, P. C., Wieczorek, M. A., Pritchard, M. E., Parmentier, E. M., Borg, L. E., Longhi, J., Elkins-Tanton, L. T., Neal, C. R., Antonenko, I., Canup, R. M., Halliday, A. N., Grove, T. L., Hager, B.H., Lee, D-C., Wiechert, U., 2006. Thermal and Magmatic Evolution of the Moon, in: Jollif, B. L., Wieczorek, M. A., Shearer, C. K., Neal, C. R., eds., New Views of the Moon. Reviews in Mineralogy & Geochemistry 60(1), 365-518, doi:10.2138/rmg.2006.60.4

Solano, J. M. S., Jackson, M. D., Sparks, R. S. J., Blundy, J. (2014) Evolution of major and trace element composition during melt migration through crystalline mush: Implications for chemical differentiation in the crust. American Journal of Science 314 (5), 895-939. https://doi.org/10.2475/05.2014.01

Sparks, R. S. J., Annen, C., Blundy, J. D., Cashman, K. V., Rust, A. C., Jackson, D. (2019) Formation and dynamics of magma reservoirs. Philosophical Transactions of the Royal Society A 377, 20180019. http://dx.doi.org/10.1098/rsta.2018.0019

Spera, F. J., Bohrson, W. A. (2018) Rejuvenation of crustal magma mush: A tale of multiply nested processes and timescales. American Journal of Science 318 (1), 90-140. https://doi.org/10.2475/01.2018.05

Spudis, P. D., McGovern, P. J., Kiefer, W. S. (2013) Large shield volcanoes on the Moon. Journal of Geophysical Research: Planets 118 (5), 1063-1081. https://doi.org/10.1002/jgre.20059

Stooke, P. J. (2017) Luna Missions. In: Cudnik, B. (eds) Encyclopedia of Lunar Science. Springer, Cham. https://doi.org/10.1007/978-3-319-05546-6_97-1

Streck, M. J. (2008) Mineral Textures and Zoning as Evidence for Open System Processes. Reviews in Mineralogy and Geochemistry 69, 595-622. https://doi.org/10.2138/rmg.2008.69.15

Sun, S.-s., McDonough, W. F. (1989) Chemical and isotopic systematics of oceanic basalts: implications for mantle composition and processes. In: Saunders, A. D., Norry, M. J. (Eds.) Magmatism in the Ocean Basins. Geological Society Special Publications 42, 313-345 pp.

Ubide T., Gale C., Larrea P., Arranz E., Lago M., Tierz P. (2014) The Relevance of Crystal Transefer to Magma Mixing: A Case Study in Composite Dykes from the Central Pyrenees. Journal of Petrology 55:8, 1535-1559. https://doi.org/10.1093/petrology/egu033

Ubide, T., Kamber, B. S. (2018) Volcanic crystals as time capsules of eruption history. Nature Communications 9: 326. https://doi.org/10.1038/s41467-017-02274-w

Ubide, T., Caulfield, J., Brandt, C., Bussweiler, Y., Mollo, S., Di Stefano, F., Nazzari, M., Scarlato, P. (2019) Deep Magma Storage Revealed by Multi-Method Elemental Mapping of Clinopyroxene Megacrysts at Stromboli Volcano. Frontiers in Earth Science 7:239. doi: 10.3389/feart.2019.00239

Ustunisik, G., Kilinc, A., Nielsen, R. L. (2014) New insights into the processes controlling compositional zoning in plagioclase. Lithos 200-201, 80-93. http://dx.doi.org/10.1016/j.lithos.2014.03.021

Velázquez Santana, L. C., McLeod, C. L., Blakemore, D., Shaulis, B., Hill, T. (2020) Bolivian hornblendite cumulates: Insights into the depths of Central Andean arc magmatic systems. Lithos 370-371, 105618. https://doi.org/10.1016/j.lithos.2020.105618

Vernon, R. H., 2018. A Practical Guide to Rock Microstructure, 2nd edition. Cambridge University Press, Cambridge. doi: 10.1017/9781108654609

Vetter, S. K., Shervais, J. W., Lindstrom, M. M. (1988) Petrology and Geochemistry of Olivine-Normative and Quartz-Normative Basalts from Regolith Breccia 15498: New Diversity in Apollo 15 Mare Basalts. Proceedings of the 18th Lunar and Planetary Science Conference

Whitford-Stark, J. L. (1982) Factors influencing the morphology of volcanic landforms: An earth-moon comparison. Earth-Science Reviews 18 (2), 109-168. https://doi.org/10.1016/0012-8252(82)90050-2

Wilding, J. D., Zhu, W., Ross, Z. E., Jackson, J. M. (2023) The magmatic web beneath Hawai'i. Science 379, 462-468. https://doi.org/10.1126/science.ade5755

Wilson, L. (2009) Volcanism in the Solar System. Nature Geoscience 2, 389-397. https://doi.org/10.1038/ngeo529

Yang, H. and Zhao, W. (2018) Apollo Program. In: Cudnik, B. (eds) Encyclopedia of Lunar Science. Springer, Cham. https://doi.org/10.1007/978-3-319-05546-6_101-1

Zellmer, G. (2021) Gaining acuity on crystal terminology in volcanic rocks. Bulletin of Volcanology 83:77. https://doi.org/10.1007/s00445-021-01505-9

Zhou, Q. (2017) Lunar Meteorites. In: Cudnik, B. (Eds.) Encyclopedia of Lunar Science. Springer, Cham. https://doi.org/10.1007/978-3-319-05546-6_58-1

3.9 Figures

Fig. 1: Schematic of crystal zoning patterns resulting from diverse processes operating in open systems as a result of compositional change. Autocrystic grains can preserve normal and progressive zoning, and/or resorption/dissolution due to changes in melt composition (i.e., Zellmer, 2021; Jerram et al., 2018; Davidson et al., 2007). Phenocrystic populations are expected to preserve normal compositional zoning, while xenocrystic populations can have complex histories (i.e., Zellmer, 2021). Note that physical change like decreasing pressure and depth can generate additional changes in zoning as a result of decompression-induced dissolution (i.e., dissolution of An in plagioclase feldspar, Ustunisik et al., 2014).

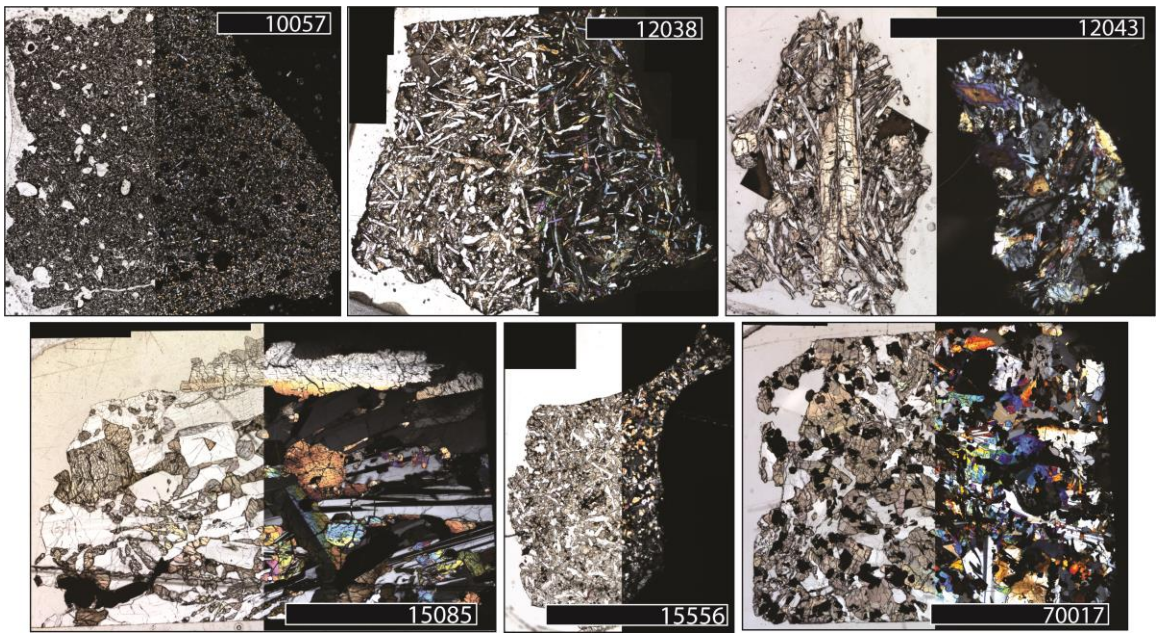

Fig. 2: Photomicrographs of representative thin sections in plane polarized light and cross polarized light for each sample. Scalebars are 5 mm.

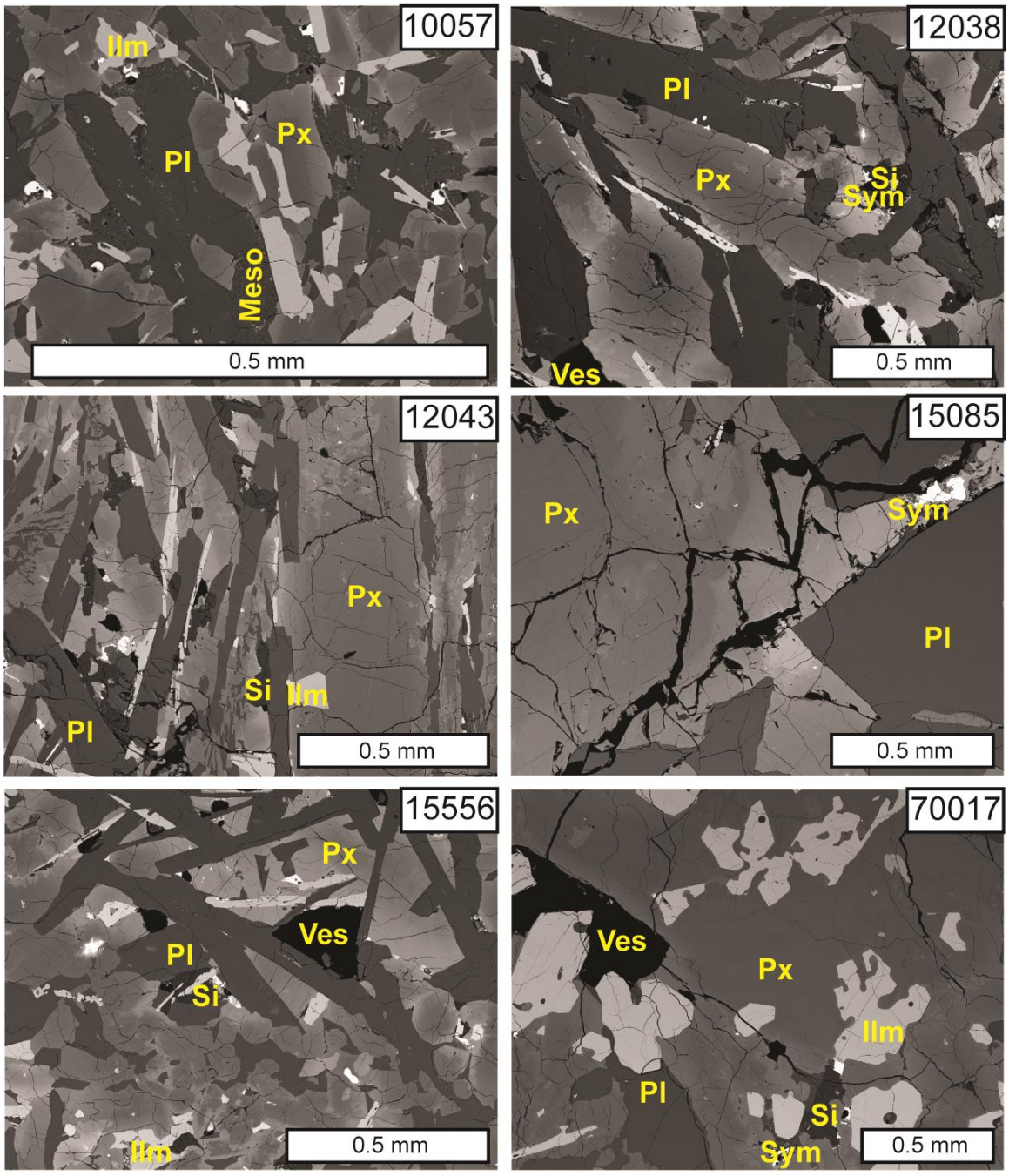

Fig. 3: Detail of sample textures imaged via SEM BSE. Annotations indicate the following components: Pl = plagioclase feldspar, Px = pyroxene, Ilm = ilmenite, Meso = mesostasis, Si = silica-rich phase, Sym = symplectites, Ves = vesicle.

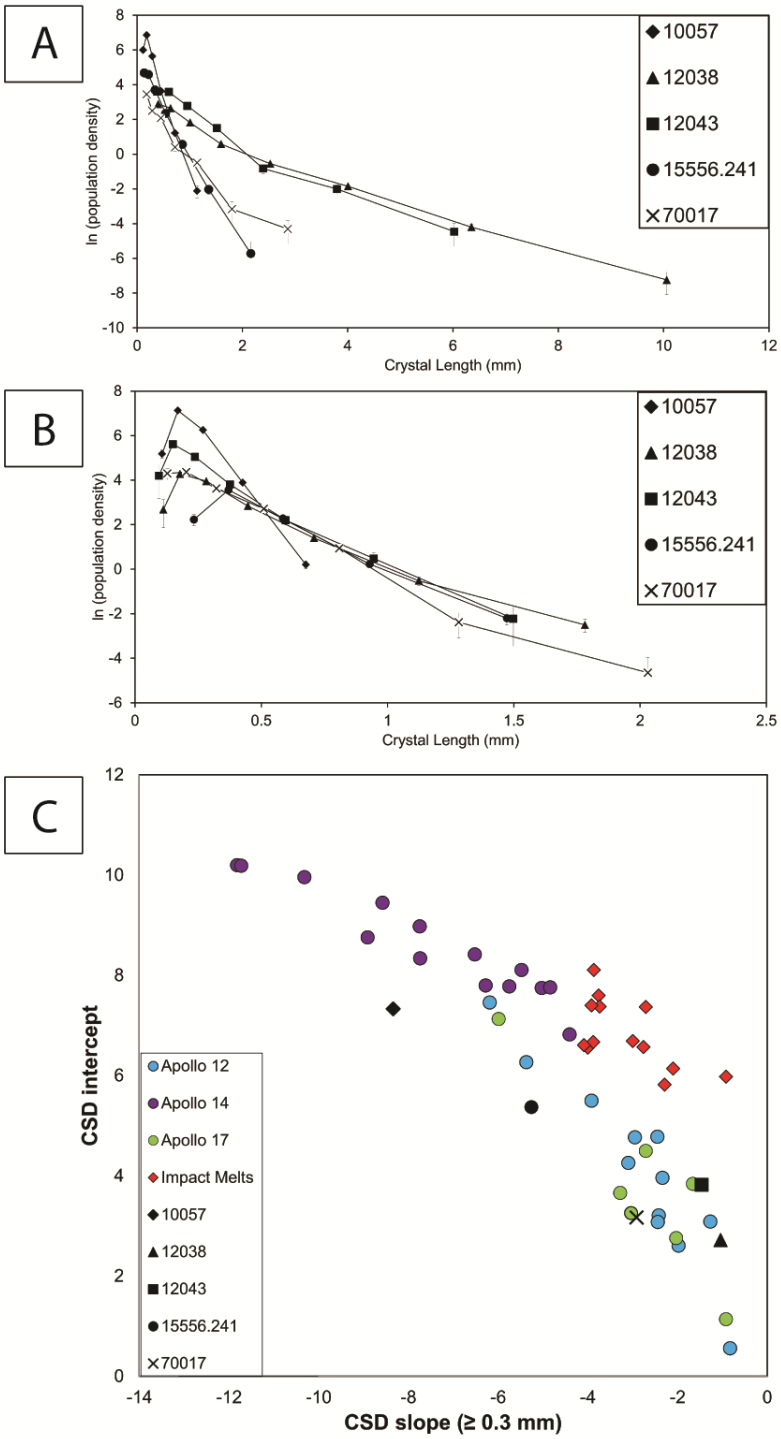

Fig. 4: A) CSDs of plagioclase feldspar in each sample; B) ilmenite CSDs for each of the samples. C) Approximate CSD intercept and slope for each sample is plotted against data collated in Neal et al. (2015).

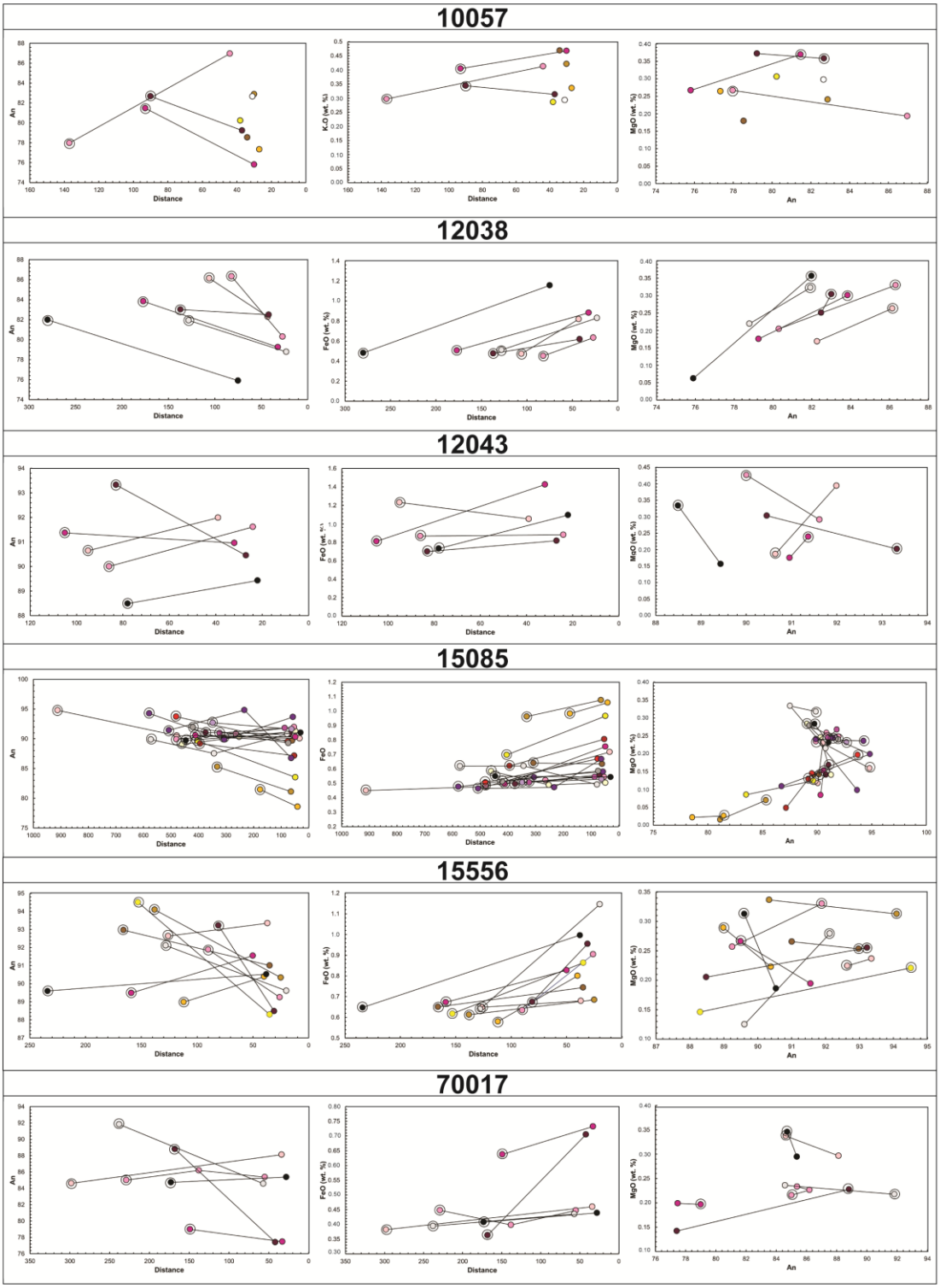

Fig. 5: Select major element data for plagioclase grains studied here. Encircled points denote crystal cores.

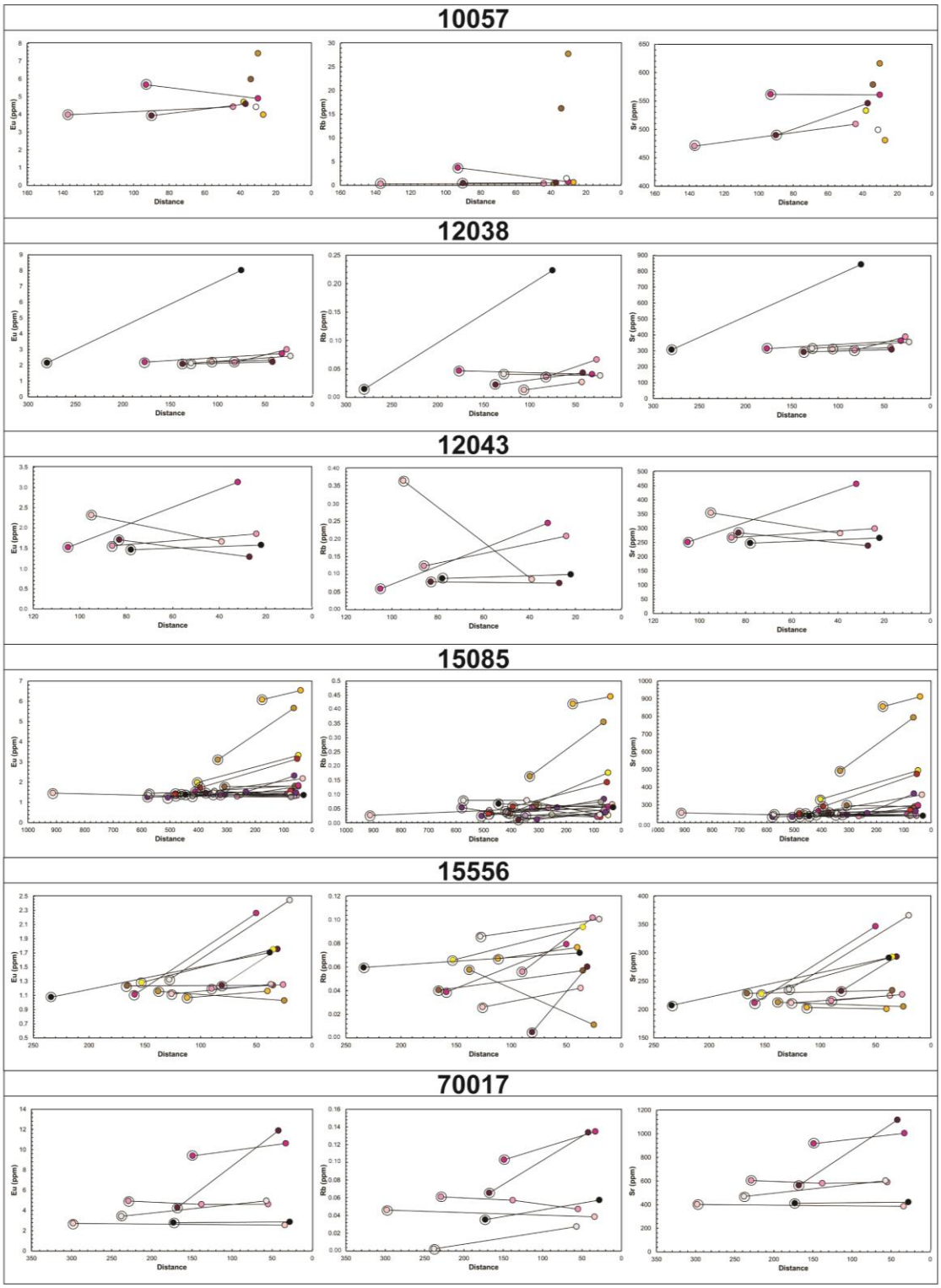

Fig. 6: Select trace element data for plagioclase grains studied here. Encircled points denote crystal cores.

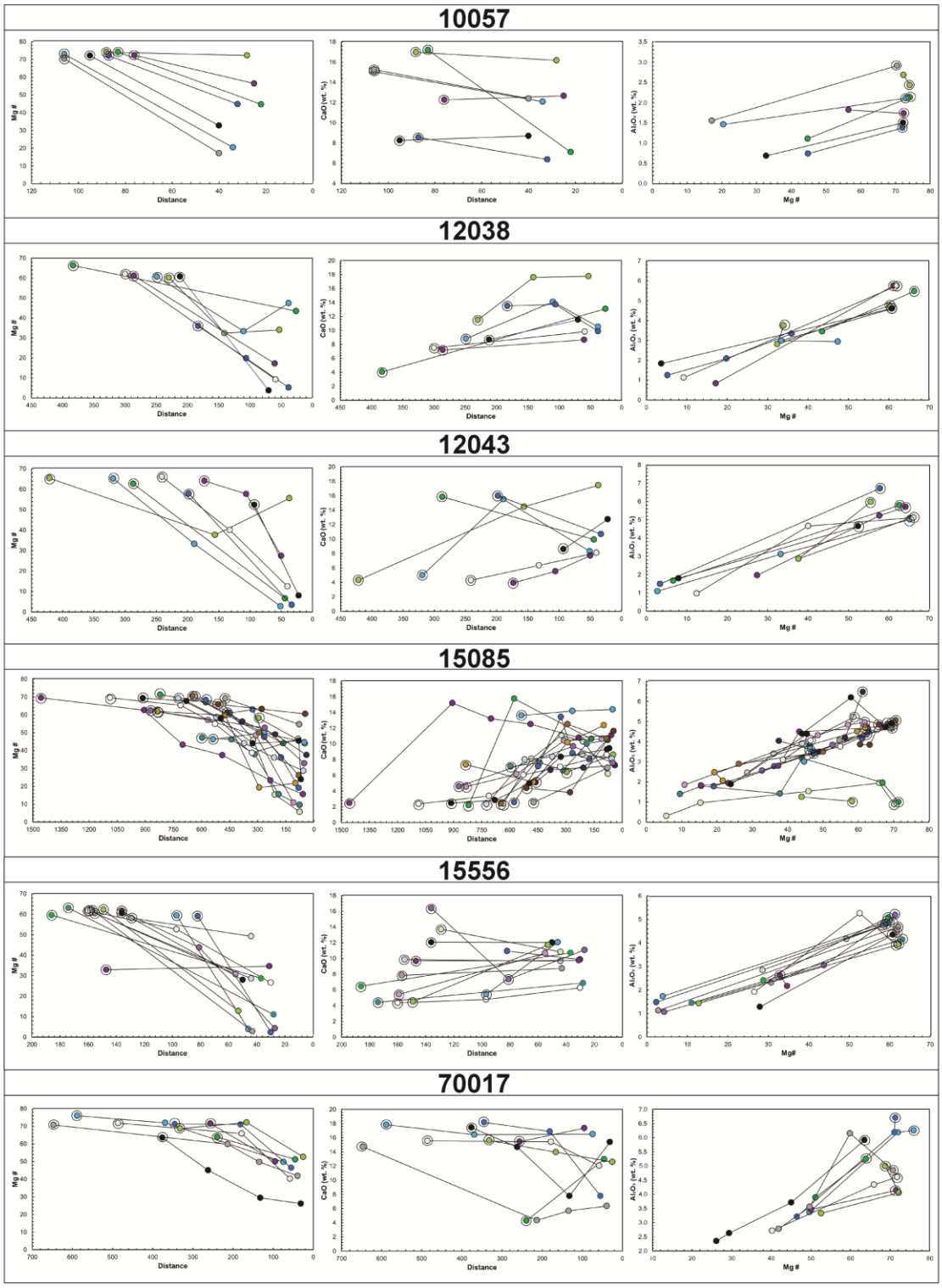

Fig. 7: Select major element data for pyroxene grains studied here. Encircled points denote crystal cores.

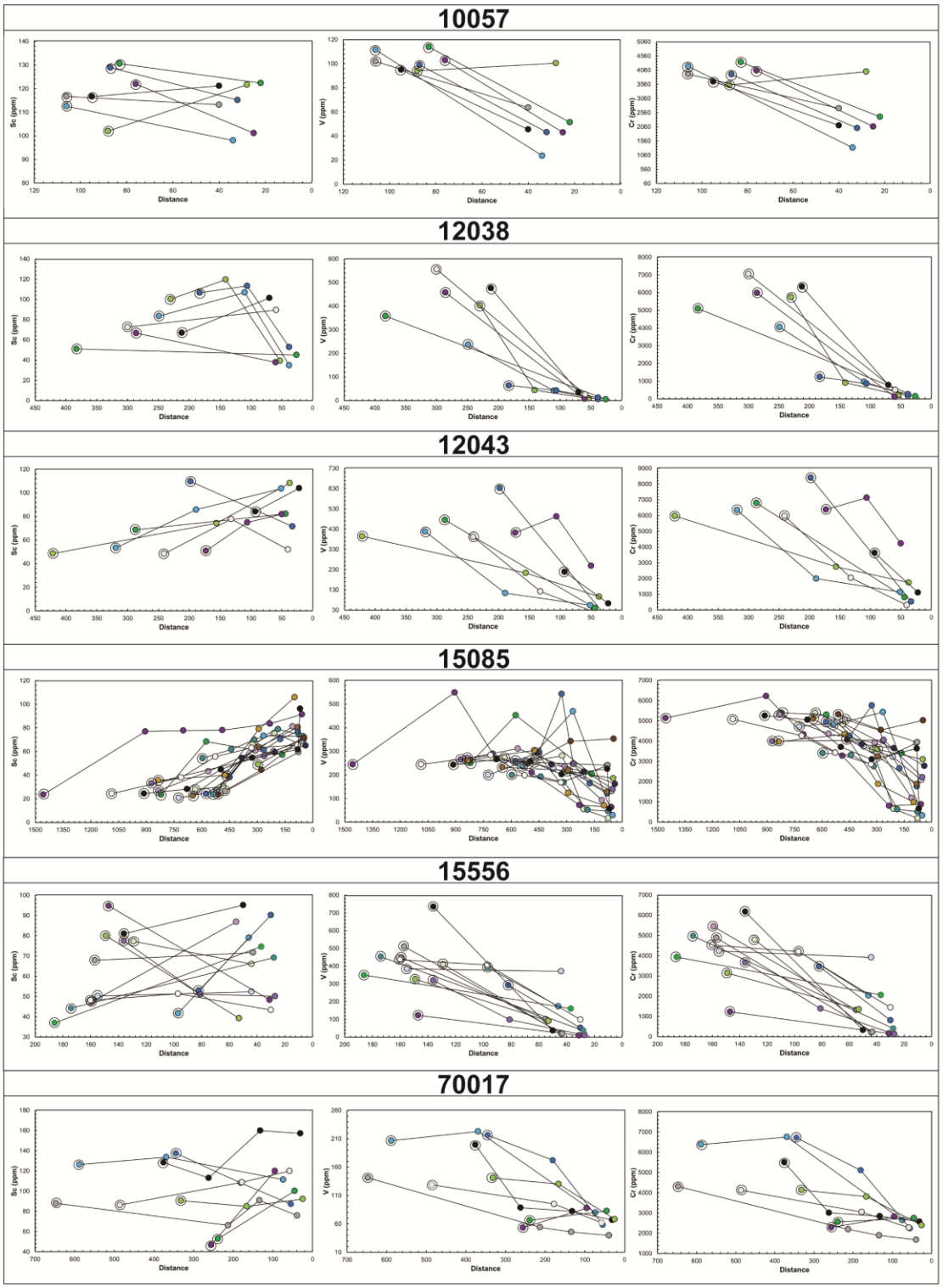

Fig. 8: Select trace element data for pyroxene grains studied here. Encircled points denote crystal cores.

3.10 Supplemental Files

Table S1: Summary of sample characteristics.

Sample	Sampling Location	Dominant Texture	Major Composition	Trace Composition
10057	Mare Tranquilitatis	Fine grained	High Ti	REE enriched
12038	Oceanus Procellarum	Medium grained	Low Ti	not REE enriched
12043	Oceanus Procellarum	Porphyritic	Low Ti	not REE enriched
15085	Mare Imbrium	Coarse grained	Low Ti	not REE enriched
15556	Mare Imbrium	Fine grained	Low Ti	not REE enriched
70017	Mare Serenitatis	Medium grained	High Ti	not REE enriched

Table S2: Summary of plagioclase feldspar CSD parameters plotted in Fig. 4c.

Sample	Slope	Interept
10057	-8.7455	7.7511
12038	-1.0415	2.7218
12043	-1.4895	3.9257
15556,241	-5.2626	5.3809
70017	-2.9172	3.1679

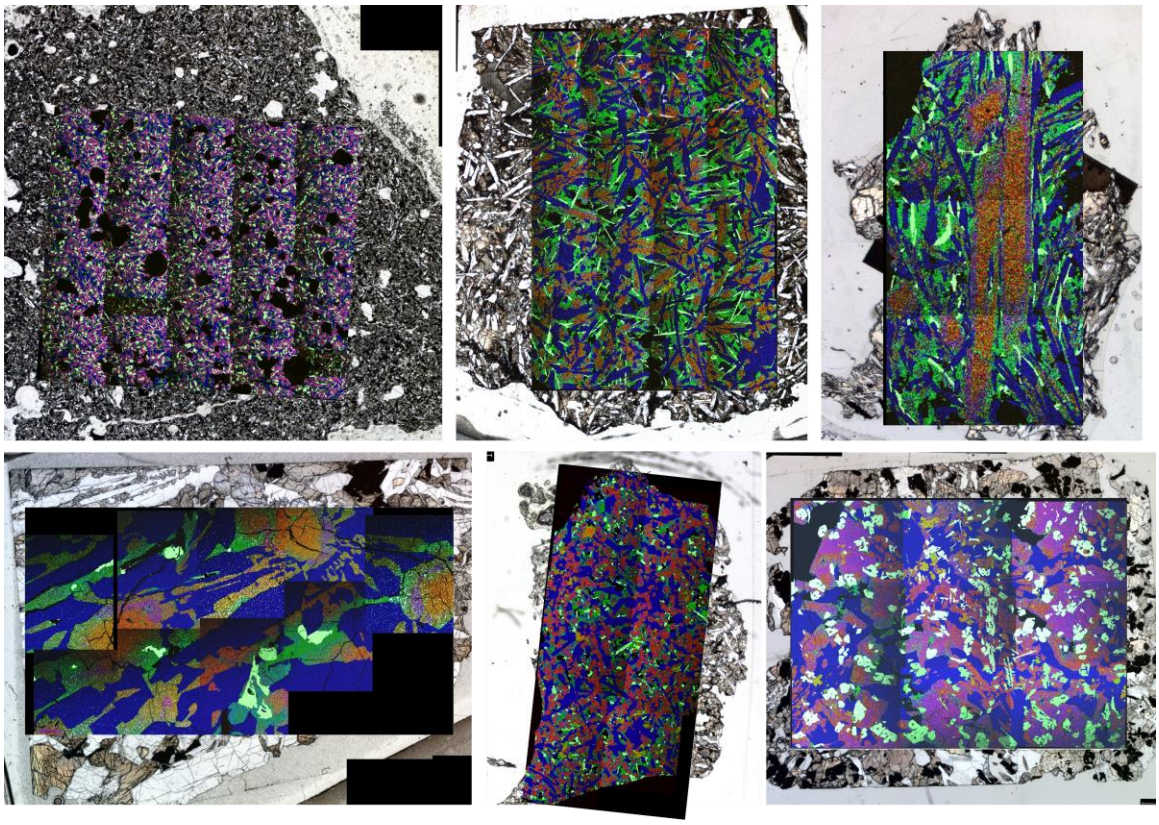

Fig. S1: SEM-EDS major elements maps: red is Mg, green is Fe, blue is Ca, white is Ti.

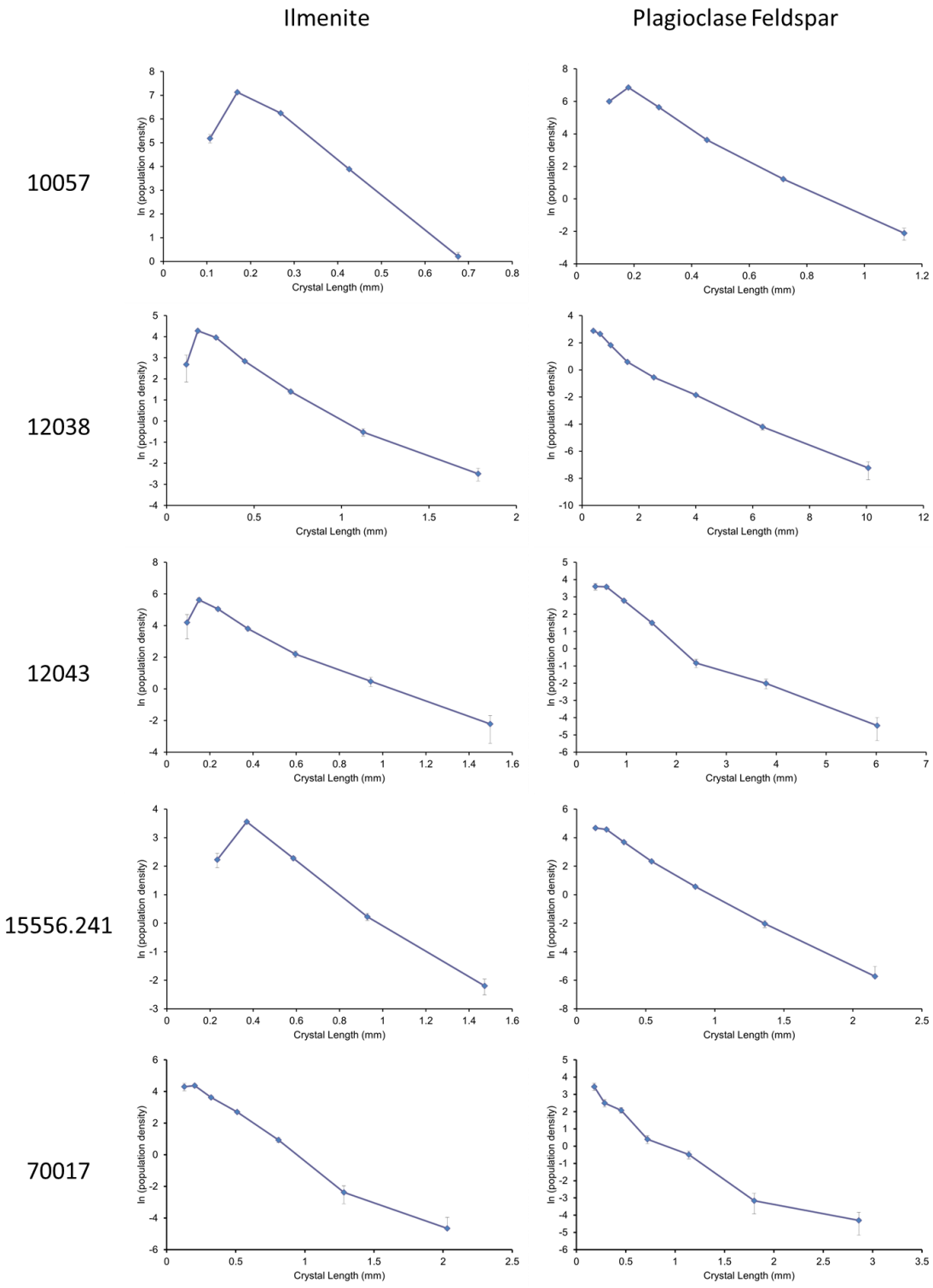

Fig. S2: Individual CSD plots for ilmenite and plagioclase feldspar in the suite.

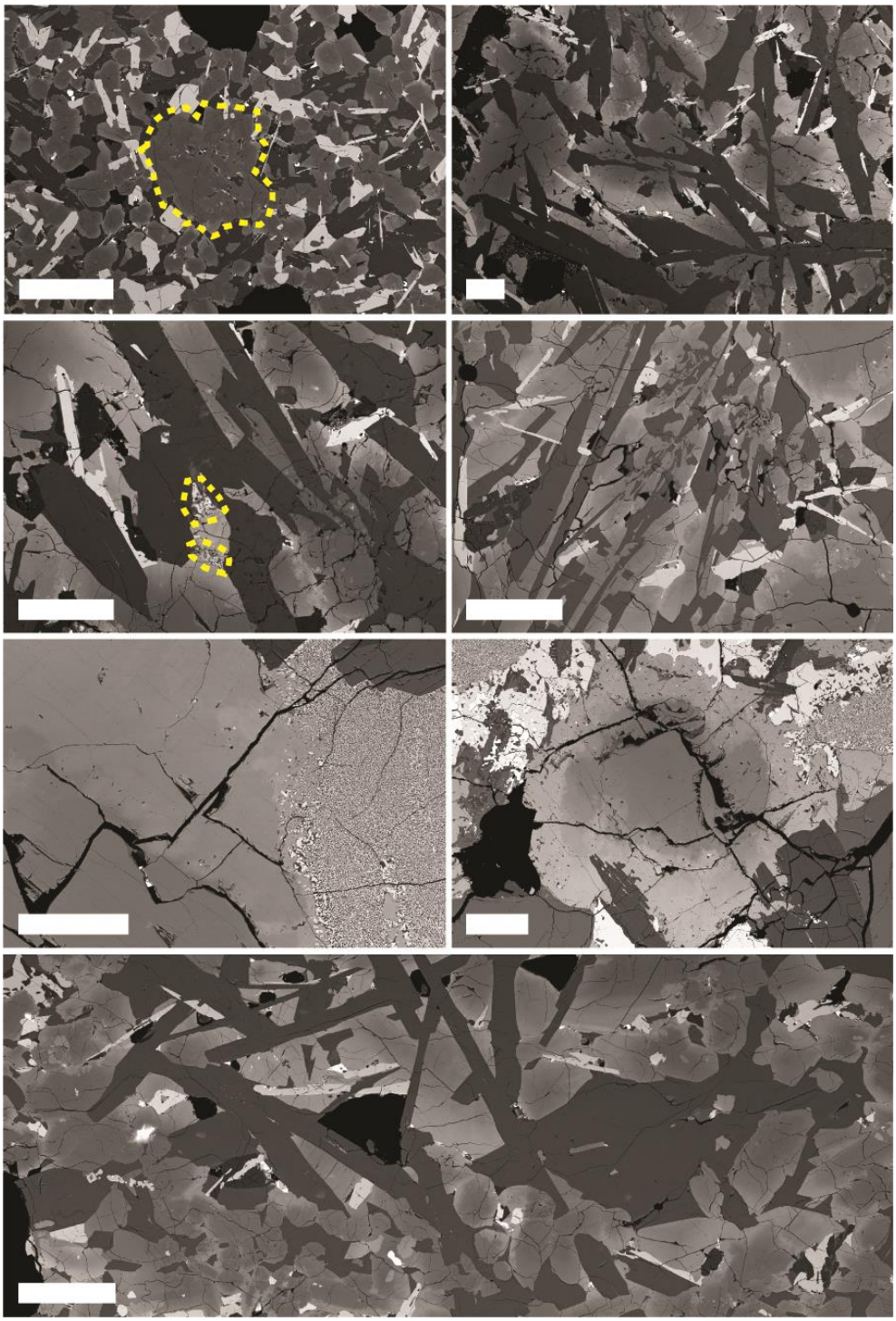

Fig. S3: Exemplary grain textures in the studied samples; all scalebars are 250 µm. a) Glomerocryst in 10057. b) Plagioclase subophitically enclosed in pyroxene in 12038. c) Symplectite along pyroxene rims in 12038. d) Pyroxene and feldspar matrix in 12043. e) Replacement of pyroxene by symplectite in 15085. f) Pyroxene with distinct zoning in 15085. g) Plagioclase feldspar clots in 15556 at top of the image – compared to interstitial texture of feldspar seen at the bottom of the image, typical of this sample.

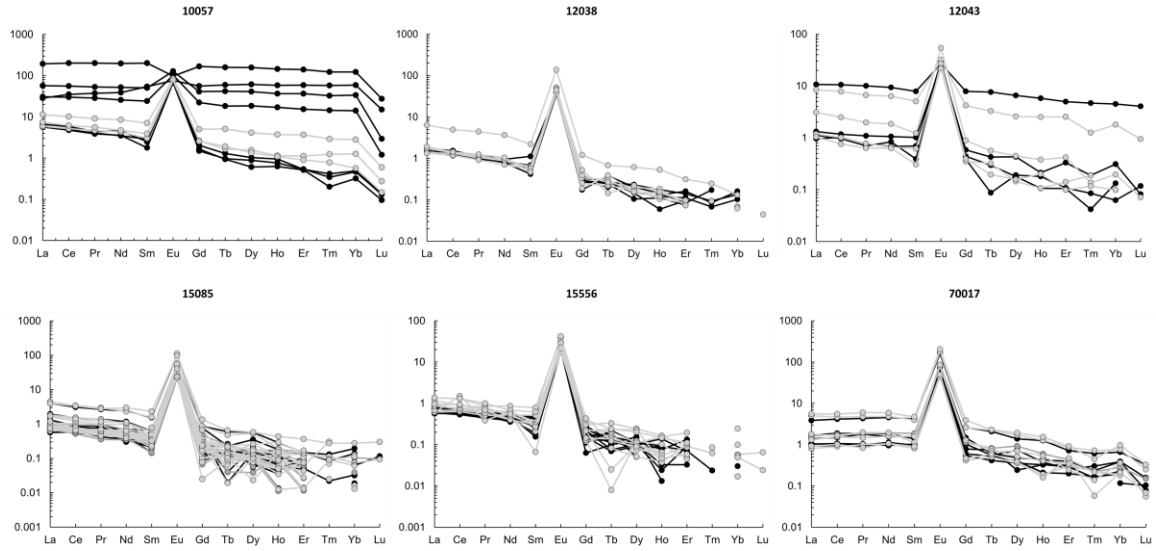

Fig. S4: Chondrite-normalized spidergrams of plagioclase feldspar analyses across the samples studied. Cores in black, rims in light blue.

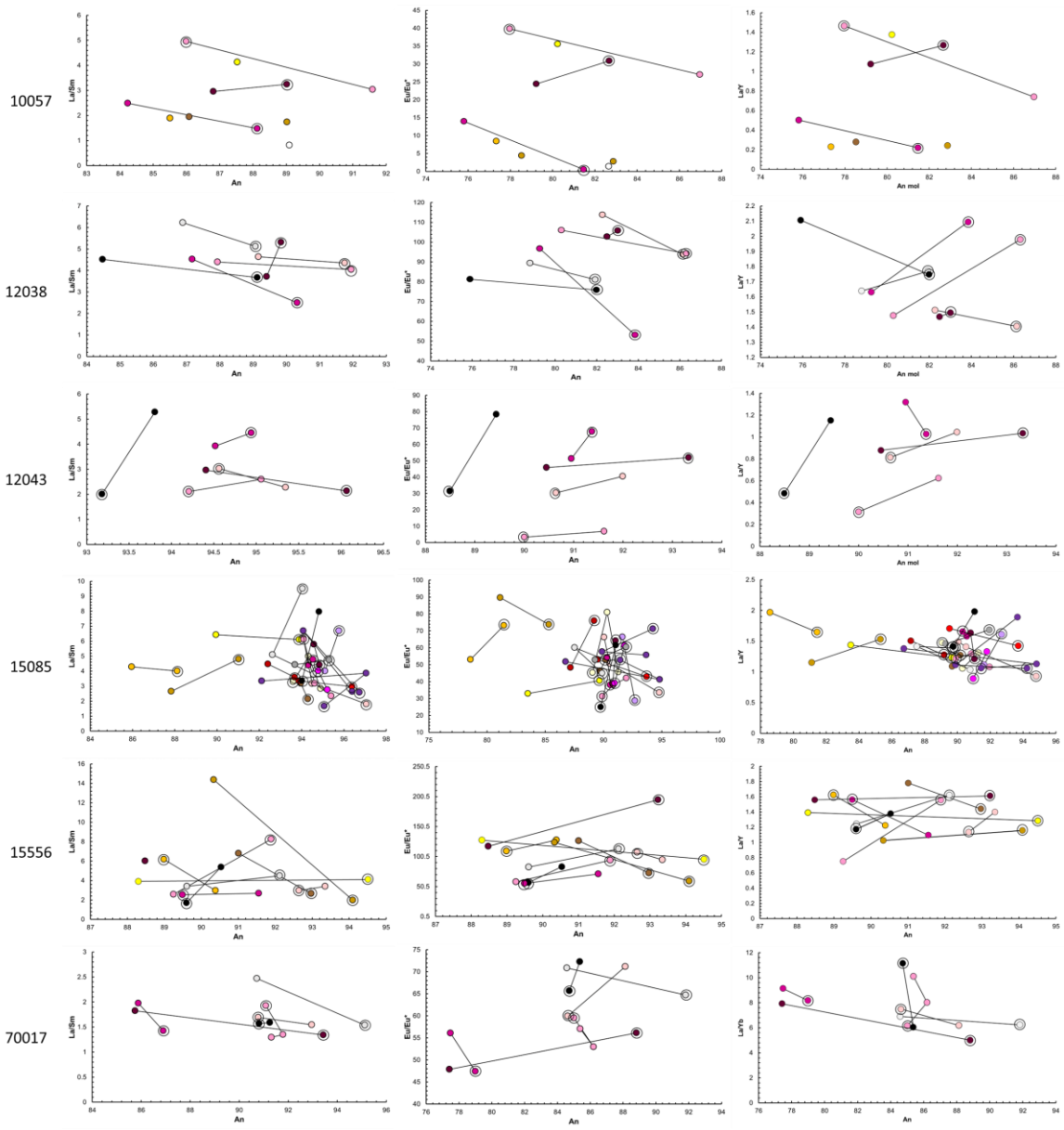

Fig. S5: Trace element ratios in plagioclase feldspar grains studied here. Graphs in the left and center columns match color scheme of figure 5 and 6; plots in the right column depict cores as black, mantles as gray, and rims a white.

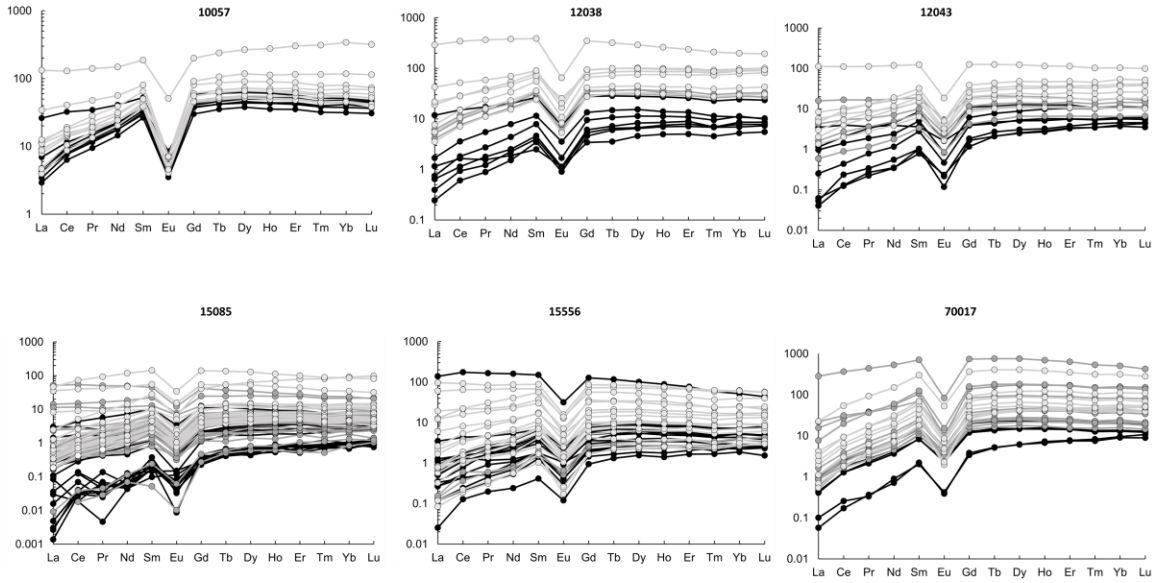

Fig. S6: Chondrite-normalized spidergrams of pyroxene analyses across the samples studied. Core analyses are in black, mantles in dark gray, and rims in light gray.

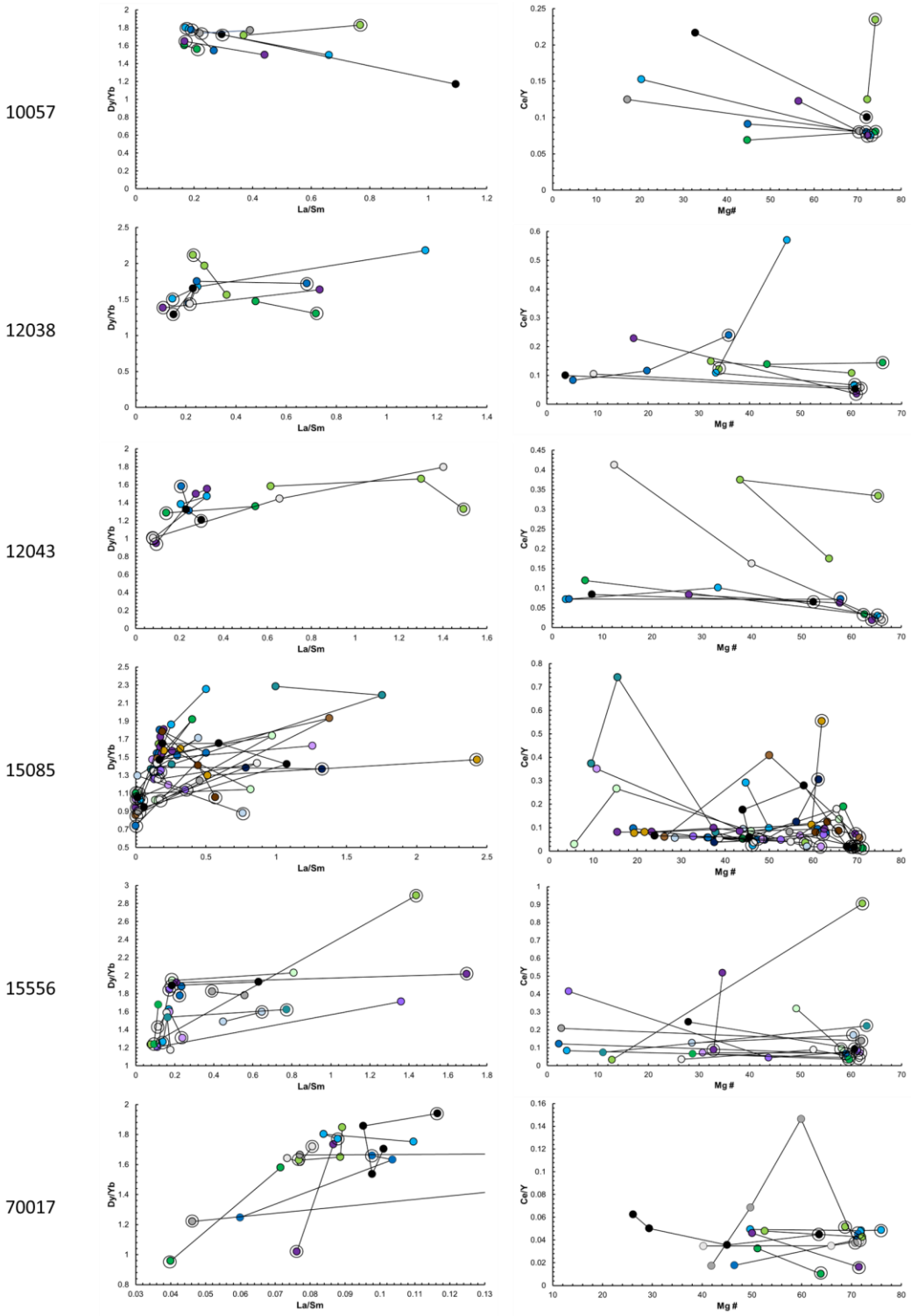

Fig. S7: Trace element ratios in pyroxene grains studied here. Graphs in the left column match color scheme of figure 7 and 8; plots in the right column depict cores as black, mantles as gray, and rims a white.

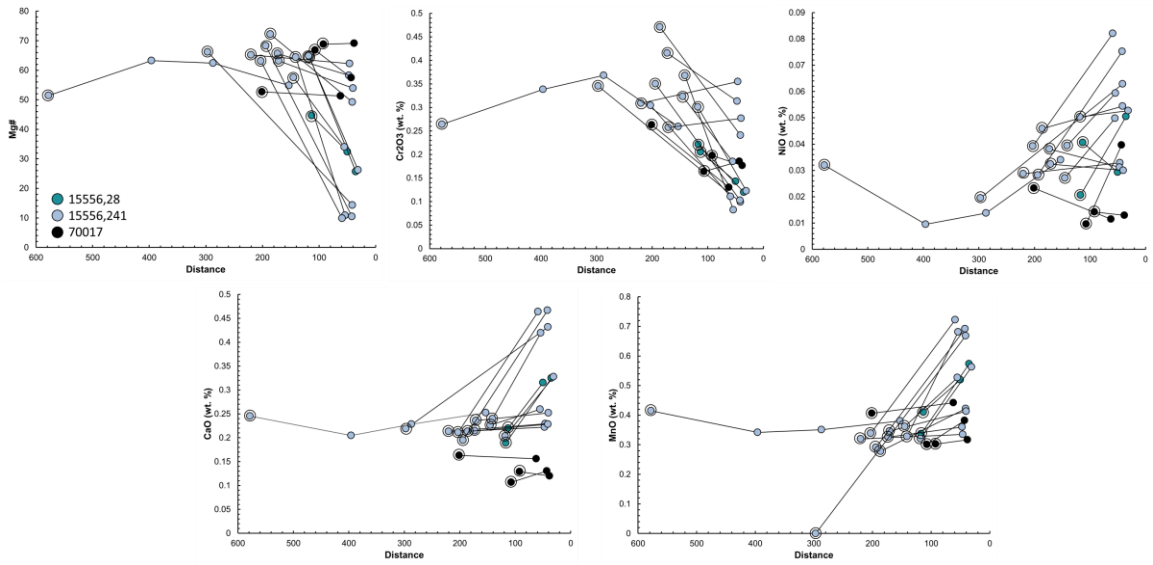

Fig. S8: Major and minor element data for olivine grains studied here. Encircled points mark the core of each grain.

Table S3. Pyroxene major element compositions.

Sample	10057,67	10057,67	10057,67	10057,67	10057,67	10057,67	10057,67	10057,67
Site	67-pyx1	67-pyx1	67-pyx1	67-pyx2	67-pyx2	67-pyx2	67-pyx2	67-pyx2
Line #	62	63	64	65	66	67	68	69
SiO2	50.918	50.439	48.413	50.906	49.115	48.762	50.416	46.772
TiO2	2.051	0.987	0.784	1.877	2.055	1.122	2.013	0.948
Al2O3	2.272	1.288	0.993	2.269	3.233	1.668	2.912	1.556
Cr2O3	0.662	0.243	0.189	0.432	0.448	0.277	0.635	0.135
FeO*	10.959	21.831	31.861	11.558	18.220	26.331	12.418	34.282
FeO	10.959	20.762	30.933	11.519	18.050	26.268	12.273	33.042
Fe2O3	0.000	1.189	1.031	0.043	0.189	0.071	0.161	1.378
MnO	0.211	0.359	0.489	0.220	0.298	0.384	0.226	0.471
MgO	17.288	16.474	10.975	16.916	14.584	8.949	16.569	3.973
CaO	15.969	8.235	5.936	15.719	12.396	12.836	15.263	12.412
Na2O	0.046	0.031	0.000	0.111	0.072	0.040	0.106	0.049
K2O	0.000	0.005	0.000	0.004	0.007	0.027	0.004	0.019
TOTAL	100.375	99.893	99.640	100.011	100.426	100.395	100.562	100.616

Table S3 cont. Pyroxene major element compositions.

Sample	10057,67	10057,67	10057,67	10057,67	10057,67	10057,67	10057,67	10057,67
Site	67-pyx2	67-pyx2	67-pyx2	67-pyx2	67-pyx2	67-pyx3	67-pyx3	67-pyx3
Line #	70	71	72	73	74	75	76	77
SiO2	48.906	50.163	50.918	49.754	49.424	50.513	49.690	50.698
TiO2	2.502	1.587	1.131	1.234	0.593	2.018	0.959	1.952
Al2O3	4.069	2.310	1.622	1.623	0.709	2.664	1.281	2.123
Cr2O3	0.433	0.319	0.264	0.345	0.153	0.542	0.257	0.664
FeO*	11.636	16.845	18.731	22.486	31.000	12.276	25.382	12.011
FeO	11.636	16.361	18.731	22.256	30.475	11.967	24.930	11.577
Fe2O3	0.000	0.538	0.000	0.255	0.584	0.344	0.502	0.482
MnO	0.215	0.299	0.318	0.350	0.466	0.214	0.407	0.224
MgO	14.232	15.002	16.184	12.766	10.686	16.470	11.441	18.251
CaO	17.881	13.685	10.758	11.767	7.406	15.813	11.178	13.778
Na2O	0.057	0.092	0.001	0.028	0.007	0.085	0.036	0.076
K2O	0.013	0.016	0.000	0.012	0.040	0.007	0.019	0.012
TOTAL	99.944	100.317	99.927	100.363	100.483	100.601	100.651	99.788

Table S3 cont. Pyroxene major element compositions.

Sample	10057,67	10057,67	10057,67	10057,67	10057,67	10057,67	10057,67	10057,67
Site	67-pyx3	67-pyx3	67-pyx3	67-pyx3	67-pyx3	67-pyx3	67-pyx3	67-pyx3
Line #	78	79	80	81	82	83	84	85
SiO2	49.857	49.022	52.219	49.986	49.241	50.438	48.877	50.305
TiO2	2.067	1.256	1.332	2.169	1.321	1.866	1.267	2.237
Al2O3	3.374	1.745	1.298	2.846	1.904	2.385	1.802	2.409
Cr2O3	0.561	0.239	0.523	0.346	0.216	0.573	0.174	0.519
FeO*	12.724	23.329	15.500	11.910	22.616	11.722	22.826	10.624
FeO	12.724	22.722	15.126	11.705	22.293	11.495	22.306	9.990
Fe2O3	0.000	0.675	0.415	0.227	0.359	0.252	0.578	0.704
MnO	0.240	0.382	0.243	0.208	0.346	0.195	0.346	0.185
MgO	15.484	11.376	22.183	16.331	12.024	17.001	11.427	16.672
CaO	15.682	12.520	6.742	15.681	12.238	15.374	12.905	17.032
Na2O	0.053	0.057	0.019	0.131	0.055	0.053	0.000	0.097
K2O	0.000	0.021	0.000	0.000	0.021	0.017	0.009	0.000
TOTAL	100.042	99.946	100.057	99.608	99.981	99.624	99.634	100.079

Table S3 cont. Pyroxene major element compositions.

Sample	10057,67	10057,67	10057,67	10057,67	10057,67	10057,67	10057,67	10057,67
Site	67-pyx3	67-pyx3	67-pyx3	67-pyx3	67-pyx4	67-pyx4	67-pyx4	67-pyx4
Line #	86	87	88	89	90	91	92	93
SiO2	50.847	50.051	50.676	48.168	52.313	50.300	49.579	49.044
TiO2	1.046	0.570	2.095	1.229	1.558	2.264	1.893	1.542
Al2O3	1.632	0.655	2.237	1.776	1.651	3.130	3.431	2.011
Cr2O3	0.270	0.072	0.453	0.216	0.572	0.477	0.576	0.325
FeO*	20.637	30.608	9.859	25.470	13.694	10.574	15.374	19.410
FeO	19.730	30.156	9.859	24.503	13.658	10.319	14.601	19.318
Fe2O3	1.007	0.502	0.000	1.075	0.040	0.284	0.860	0.103
MnO	0.328	0.459	0.176	0.330	0.260	0.204	0.261	0.293
MgO	16.958	12.443	16.492	7.084	20.308	15.562	14.891	10.483
CaO	8.677	5.881	17.673	16.267	10.338	18.183	14.853	16.396
Na2O	0.066	0.000	0.000	0.081	0.127	0.134	0.119	0.155
K2O	0.009	0.009	0.000	0.009	0.000	0.000	0.000	0.003
TOTAL	100.469	100.746	99.661	100.629	100.820	100.828	100.976	99.662

Table S3 cont. Pyroxene major element compositions.

Sample	10057,67	10057,67	10057,67	10057,67	10057,67	10057,67	10057,67	10057,67
Site	67-pyx5	67-pyx5	67-pyx5	67-pyx5	67-pyx5	67-pyx5	67-pyx5	67-pyx5
Line #	94	95	96	97	98	99	100	101
SiO2	50.941	48.707	48.298	50.511	49.466	50.556	50.031	47.241
TiO2	2.060	2.425	1.063	1.983	1.430	1.867	0.805	0.638
Al2O3	2.204	4.102	1.482	2.469	2.092	2.337	0.872	0.828
Cr2O3	0.705	0.618	0.175	0.441	0.237	0.297	0.174	0.157
FeO*	11.602	12.945	29.133	11.622	19.583	11.593	26.024	38.981
FeO	10.938	12.872	28.614	11.622	19.309	11.038	25.239	38.173
Fe2O3	0.738	0.081	0.577	0.000	0.304	0.616	0.872	0.898
MnO	0.200	0.214	0.442	0.214	0.305	0.235	0.397	0.527
MgO	18.226	14.503	8.472	16.829	11.557	17.286	12.513	5.769
CaO	14.427	16.517	11.193	15.877	15.551	15.390	9.609	6.283
Na2O	0.129	0.070	0.038	0.000	0.061	0.071	0.064	0.000
K2O	0.019	0.000	0.012	0.000	0.004	0.000	0.000	0.008
TOTAL	100.512	100.100	100.307	99.947	100.285	99.631	100.487	100.432

Table S3 cont. Pyroxene major element compositions.

Sample	10057,67	10057,67	10057,67	10057,67	10057,67	10057,67	10057,67	10057,67
Site	67-pyx5	67-pyx5	67-pyx6	67-pyx6	67-pyx6	67-pyx6	67-pyx6	67-pyx6
Line #	102	103	104	105	106	107	108	109
SiO2	50.685	49.093	50.829	50.908	50.769	49.169	51.163	49.137
TiO2	2.043	1.242	2.137	2.025	2.080	1.457	2.016	2.359
Al2O3	2.299	1.773	2.429	2.454	2.684	1.710	2.133	4.033
Cr2O3	0.667	0.189	0.499	0.363	0.501	0.210	0.511	0.592
FeO*	9.700	23.809	10.344	10.994	11.342	23.877	10.371	11.982
FeO	9.384	22.772	10.344	10.994	11.342	23.751	10.371	11.982
Fe2O3	0.351	1.153	0.000	0.000	0.000	0.140	0.000	0.000
MnO	0.185	0.390	0.197	0.207	0.217	0.360	0.181	0.208
MgO	15.985	11.229	16.611	16.756	16.583	10.666	16.714	13.712
CaO	18.448	12.589	16.971	16.408	16.184	13.172	17.190	18.144
Na2O	0.161	0.099	0.089	0.086	0.099	0.000	0.091	0.134
K2O	0.000	0.017	0.003	0.000	0.010	0.034	0.002	0.000
TOTAL	100.171	100.431	100.108	100.201	100.469	100.656	100.371	100.302

Table S3 cont. Pyroxene major element compositions.

Sample	10057,67	10057,67	10057,67	10057,67	10057,67	10057,67	10057,67	10057,67
Site	67-pyx6	67-pyx6	67-pyx7	67-pyx7	67-pyx7	67-pyx7	67-pyx7	67-pyx7
Line #	110	111	112	113	114	115	116	117
SiO2	49.629	49.387	51.438	49.139	51.065	51.125	46.774	50.518
TiO2	1.702	0.898	1.953	1.454	1.763	0.696	0.992	1.833
Al2O3	2.535	1.109	2.243	2.062	2.108	0.802	1.462	2.098
Cr2O3	0.171	0.218	0.672	0.243	0.522	0.216	0.128	0.455
FeO*	17.227	28.279	11.783	20.375	11.601	24.150	32.974	10.965
FeO	17.039	27.435	11.783	20.307	11.395	23.516	32.395	10.617
Fe2O3	0.209	0.938	0.000	0.075	0.229	0.704	0.644	0.387
MnO	0.000	0.421	0.215	0.303	0.216	0.389	0.466	0.208
MgO	13.185	12.829	17.914	10.527	17.601	16.922	4.745	17.275
CaO	15.610	7.103	14.340	16.064	15.060	5.999	12.090	15.884
Na2O	0.071	0.001	0.008	0.011	0.075	0.000	0.000	0.019
K2O	0.003	0.010	0.003	0.019	0.007	0.000	0.004	0.000
TOTAL	100.133	100.255	100.568	100.197	100.017	100.298	99.633	99.256

Table S3 cont. Pyroxene major element compositions.

Sample	10057,67	10057,67	10057,67	10057,67	10057,67	10057,67	10057,67	10057,67
Site	67-pyx7	67-pyx7	67-pyx7	67-pyx8	67-pyx8	67-pyx8	67-pyx8	67-pyx9
Line #	118	119	120	121	122	123	124	125
SiO2	48.733	48.795	49.202	51.176	49.558	51.798	49.682	51.164
TiO2	1.322	2.918	1.310	1.872	0.841	1.351	0.659	1.623
Al2O3	1.754	3.361	1.898	2.123	1.054	1.377	0.742	1.735
Cr2O3	0.217	0.869	0.352	0.297	0.235	0.515	0.090	0.516
FeO*	24.684	11.573	20.878	11.267	28.144	14.898	29.004	12.824
FeO	24.397	10.933	20.084	10.801	27.493	13.021	27.793	11.785
Fe2O3	0.318	0.711	0.883	0.517	0.724	2.086	1.346	1.154
MnO	0.385	0.225	0.319	0.202	0.451	0.264	0.453	0.221
MgO	10.705	16.546	12.917	17.598	11.290	21.536	13.213	18.858
CaO	12.087	15.386	12.763	15.698	9.203	8.563	6.389	12.273
Na2O	0.017	0.131	0.043	0.085	0.033	0.109	0.000	0.262
K2O	0.009	0.000	0.010	0.000	0.000	0.000	0.004	0.025
TOTAL	99.912	99.802	99.692	100.316	100.808	100.410	100.236	99.501

Table S3 cont. Pyroxene major element compositions.

Sample	10057,67	10057,67	10057,67	10057,67	10057,67	10057,67	10057,67	15085,16
Site	67-pyx9	67-pyx10	67-pyx10	67-pyx10	67-pyx10	67-pyx10	67-pyx10	16-pyx_001
Line #	126	127	128	129	130	131	132	218
SiO2	49.614	51.423	49.831	51.939	48.823	52.386	48.991	45.428
TiO2	1.464	1.693	1.581	1.426	0.703	1.119	1.232	0.429
Al2O3	1.819	2.175	2.031	1.503	0.688	1.217	1.770	0.304
Cr2O3	0.219	0.535	0.318	0.575	0.160	0.386	0.232	0.045
FeO*	19.283	13.160	18.288	14.764	32.247	16.477	24.112	44.154
FeO	17.404	12.907	18.288	13.945	31.693	15.647	23.312	43.436
Fe2O3	2.089	0.281	0.000	0.911	0.615	0.922	0.890	0.797
MnO	0.314	0.224	0.299	0.243	0.472	0.272	0.354	0.659
MgO	14.052	18.117	12.427	21.471	8.807	22.844	11.471	1.499
CaO	12.655	13.435	15.585	8.260	8.699	5.356	11.857	6.192
Na2O	0.358	0.079	0.051	0.068	0.000	0.030	0.073	0.000
K2O	0.000	0.003	0.001	0.009	0.000	0.000	0.015	0.000
TOTAL	99.778	100.842	100.411	100.259	100.600	100.086	100.107	98.710

Table S3 cont. Pyroxene major element compositions.

Sample	15085,16	15085,16	15085,16	15085,16	15085,16	15085,16	15085,16	15085,16
Site	16-pyx_00116-pyx_00116-pyx_00116-pyx_00116-pyx_00116-pyx_00116-pyx_00116-pyx_002							
Line #	219	220	221	222	223	224	225	226
SiO2	46.283	49.454	51.378	53.187	51.371	50.967	48.725	51.211
TiO2	0.846	0.769	0.458	0.217	0.484	0.514	0.768	0.518
Al2O3	0.956	1.532	1.948	0.881	1.893	1.533	1.089	2.231
Cr2O3	0.110	0.272	0.661	0.919	0.633	0.744	0.376	1.021
FeO*	36.305	24.906	17.648	17.830	17.654	22.364	29.274	15.082
FeO	35.608	24.112	16.713	17.830	16.927	21.878	28.937	14.496
Fe2O3	0.774	0.883	1.040	0.000	0.808	0.540	0.374	0.652
MnO	0.449	0.346	0.298	0.277	0.350	0.344	0.422	0.291
MgO	3.689	11.855	19.160	23.537	19.153	16.678	10.915	16.818
CaO	10.300	11.111	8.126	2.397	8.084	7.233	7.842	13.013
Na2O	0.059	0.000	0.037	0.018	0.018	0.033	0.018	0.054
K2O	0.000	0.000	0.032	0.010	0.000	0.011	0.001	0.004
TOTAL	98.997	100.246	99.747	99.275	99.639	100.421	99.430	100.243

Table S3 cont. Pyroxene major element compositions.

Sample	15085,16	15085,16	15085,16	15085,16	15085,16	15085,16	15085,16	15085,16
Site	16-pyx_002	16-pyx_002	16-pyx_002	16-pyx_002	16-pyx_002	16-pyx_003	16-pyx_003	16-pyx_003
Line #	227	228	229	230	231	232	233	234
SiO2	51.955	51.343	49.160	48.850	51.285	50.740	51.181	53.106
TiO2	0.333	0.387	0.727	1.080	0.371	0.590	0.458	0.203
Al2O3	1.521	1.031	1.257	1.165	1.017	1.638	1.955	1.008
Cr2O3	0.745	0.515	0.459	0.422	0.370	0.698	0.744	0.926
FeO*	19.662	22.518	26.957	28.591	22.406	21.515	13.670	17.566
FeO	18.998	21.682	26.774	28.032	21.606	20.926	13.515	16.852
Fe2O3	0.738	0.930	0.203	0.621	0.889	0.655	0.172	0.794
MnO	0.336	0.360	0.395	0.407	0.336	0.326	0.250	0.199
MgO	19.908	17.639	11.848	11.790	18.202	15.810	15.480	24.549
CaO	5.785	6.426	8.620	7.734	5.628	9.058	15.755	2.219
Na2O	0.041	0.005	0.022	0.004	0.000	0.022	0.003	0.000
K2O	0.000	0.000	0.000	0.000	0.018	0.019	0.018	0.009
TOTAL	100.284	100.222	99.443	100.043	99.633	100.416	99.512	99.784

Table S3 cont. Pyroxene major element compositions.

Sample	15085,16	15085,16	15085,16	15085,16	15085,16	15085,16	15085,16	15085,16
Site	16-pyx_003	16-pyx_003	16-pyx_003	16-pyx_004	16-pyx_004	16-pyx_004	16-pyx_004	16-pyx_004
Line #	235	236	237	238	239	240	241	242
SiO2	49.824	49.387	47.831	48.153	48.140	48.882	47.249	46.222
TiO2	0.636	0.667	0.875	0.776	0.675	0.608	1.790	1.028
Al2O3	4.298	4.828	3.192	2.915	3.402	3.783	1.410	1.793
Cr2O3	0.672	0.513	0.494	0.427	0.478	0.432	0.300	0.162
FeO*	18.832	18.473	24.860	28.330	25.702	26.313	30.915	36.635
FeO	18.832	18.473	24.305	28.215	25.068	26.079	30.192	36.130
Fe2O3	0.000	0.000	0.617	0.128	0.704	0.260	0.804	0.562
MnO	0.175	0.270	0.332	0.348	0.343	0.334	0.383	0.401
MgO	11.405	11.422	10.979	10.649	12.900	12.698	10.554	3.786
CaO	14.147	14.013	10.636	8.130	7.136	7.606	6.648	10.027
Na2O	0.015	0.014	0.017	0.060	0.110	0.018	0.018	0.015
K2O	0.000	0.021	0.022	0.011	0.036	0.040	0.038	0.000
TOTAL	100.003	99.607	99.237	99.800	98.922	100.714	99.306	100.068

Table S3 cont. Pyroxene major element compositions.

Sample	15085,16	15085,16	15085,16	15085,16	15085,16	15085,16	15085,16	15085,16
Site	16-pyx_004	16-pyx_005	16-pyx_005	16-pyx_005	16-pyx_005	16-pyx_005	16-pyx_005	16-pyx_005
Line #	243	244	245	246	247	248	249	250
SiO2	46.550	47.288	48.640	49.695	50.886	51.672	49.092	48.128
TiO2	0.900	0.901	0.624	0.462	0.267	0.188	0.261	0.671
Al2O3	1.397	1.918	3.986	4.834	4.700	4.694	5.223	3.911
Cr2O3	0.056	0.008	0.462	0.607	0.739	0.598	0.634	0.514
FeO*	38.070	34.976	26.788	19.650	18.150	17.810	19.808	26.538
FeO	38.070	34.976	26.788	19.650	17.231	17.810	19.808	25.979
Fe2O3	0.000	0.000	0.000	0.000	1.021	0.000	0.000	0.622
MnO	0.409	0.395	0.335	0.260	0.253	0.247	0.253	0.327
MgO	2.262	6.785	12.689	15.916	22.495	22.517	15.768	11.760
CaO	10.498	7.438	6.217	8.473	2.633	2.329	8.029	8.367
Na2O	0.014	0.014	0.055	0.012	0.014	0.038	0.015	0.012
K2O	0.000	0.031	0.040	0.011	0.021	0.016	0.012	0.035
TOTAL	100.155	99.754	99.836	99.921	100.157	100.108	99.095	100.262

Table S3 cont. Pyroxene major element compositions.

Sample	15085,16	15085,16	15085,16	15085,16	15085,16	15085,16	15085,16	15085,16
Site	16-pyx_005	16-pyx_005	16-pyx_006	16-pyx_006	16-pyx_006	16-pyx_006	16-pyx_006	16-pyx_007
Line #	251	252	253	254	255	256	257	258
SiO2	47.981	48.230	48.265	48.361	48.035	49.971	50.594	49.365
TiO2	0.738	0.770	1.076	1.064	1.028	0.431	0.306	0.652
Al2O3	3.398	2.460	3.004	3.503	3.636	4.832	4.829	4.089
Cr2O3	0.451	0.118	0.106	0.586	0.408	0.513	0.431	0.523
FeO*	29.858	32.760	22.396	20.282	21.777	20.986	18.359	24.623
FeO	29.584	32.760	21.687	19.931	21.762	20.017	17.392	24.623
Fe2O3	0.304	0.000	0.788	0.390	0.017	1.076	1.075	0.000
MnO	0.342	0.358	0.303	0.274	0.294	0.262	0.261	0.308
MgO	9.438	7.358	10.151	11.385	10.544	19.594	22.234	11.762
CaO	8.631	8.128	14.389	14.195	13.622	3.702	2.607	9.419
Na2O	0.012	0.007	0.014	0.011	0.013	0.011	0.013	0.013
K2O	0.056	0.044	0.031	0.016	0.000	0.045	0.028	0.000
TOTAL	100.905	100.232	99.736	99.677	99.357	100.346	99.661	100.754

Table S3 cont. Pyroxene major element compositions.

Sample	15085,16	15085,16	15085,16	15085,16	15085,16	15085,16	15085,16	15085,16
Site	16-pyx_007	16-pyx_007	16-pyx_007	16-pyx_007	16-pyx_007	16-pyx_007	16-pyx_007	16-pyx_007
Line #	259	260	261	262	263	264	265	266
SiO2	49.017	49.848	50.497	50.726	50.520	50.007	48.915	46.729
TiO2	0.538	0.327	0.260	0.306	0.349	0.561	0.623	0.862
Al2O3	4.166	4.246	4.692	4.874	4.142	4.530	3.446	2.774
Cr2O3	0.406	0.380	0.647	0.473	0.507	0.702	0.506	0.426
FeO*	22.661	19.868	17.667	18.472	19.594	15.528	24.756	30.991
FeO	21.284	18.420	16.267	17.514	19.594	15.528	24.756	28.338
Fe2O3	1.531	1.609	1.556	1.065	0.000	0.000	0.000	2.948
MnO	0.312	0.276	0.235	0.263	0.280	0.234	0.322	0.363
MgO	16.482	18.185	23.016	22.294	17.223	14.779	12.611	9.866
CaO	6.220	6.711	2.345	2.603	7.158	13.438	8.817	8.043
Na2O	0.014	0.015	0.013	0.016	0.013	0.012	0.013	0.012
K2O	0.027	0.039	0.006	0.000	0.030	0.029	0.005	0.000
TOTAL	99.843	99.894	99.378	100.027	99.815	99.818	100.013	100.068

Table S3 cont. Pyroxene major element compositions.

Sample	15085,16	15085,16	15085,16	15085,16	15085,16	15085,16	15085,16	15085,16
Site	16-pyx_007	16-pyx_008	16-pyx_008	16-pyx_008	16-pyx_008	16-hed	16-hed	16-hed
Line #	267	268	269	270	271	272	273	274
SiO2	46.554	48.533	48.988	49.104	47.577	45.831	45.749	45.847
TiO2	1.169	0.719	0.600	0.616	0.785	1.191	1.427	1.386
Al2O3	1.778	6.473	4.209	3.496	4.038	1.231	1.648	1.532
Cr2O3	0.174	0.422	0.555	0.448	0.437	0.104	0.092	0.106
FeO*	34.645	19.892	22.444	25.277	29.405	32.227	32.204	32.220
FeO	34.371	19.892	21.301	25.277	29.405	31.514	32.053	31.470
Fe2O3	0.305	0.000	1.271	0.000	0.000	0.793	0.168	0.834
MnO	0.375	0.286	0.299	0.334	0.356	0.327	0.274	0.281
MgO	4.596	17.646	16.172	13.634	9.925	0.447	0.774	0.964
CaO	10.589	5.113	6.691	6.965	7.276	18.090	17.223	17.603
Na2O	0.016	0.029	0.014	0.013	0.015	0.013	0.014	0.010
K2O	0.046	0.043	0.017	0.013	0.015	0.000	0.051	0.000
TOTAL	99.943	99.155	99.988	99.900	99.827	99.460	99.455	99.950

Table S3 cont. Pyroxene major element compositions.

Sample	15085,26	15085,26	15085,26	15085,26	15085,26	15085,26	15085,26	15085,26
Site	26-pyx_001	26-pyx_001	26-pyx_001	26-pyx_001	26-pyx_001	26-pyx_001	26-pyx_001	26-pyx_001
Line #	275	276	277	278	279	280	281	282
SiO2	48.578	47.539	48.725	50.563	48.223	46.876	50.892	48.458
TiO2	0.733	0.509	0.246	0.277	0.840	1.183	0.257	0.400
Al2O3	3.947	3.886	4.314	5.059	3.498	2.891	4.794	3.814
Cr2O3	0.535	0.415	0.675	0.634	0.410	0.283	0.687	0.527
FeO*	21.601	21.101	17.022	17.441	21.949	31.477	17.458	20.263
FeO	19.747	12.931	7.842	15.422	19.907	31.477	15.639	14.819
Fe2O3	2.060	9.080	10.202	2.244	2.270	0.000	2.021	6.050
MnO	0.303	0.298	0.231	0.248	0.280	0.376	0.255	0.291
MgO	15.335	20.557	26.505	23.469	12.333	6.270	23.560	19.581
CaO	8.767	5.683	2.266	2.427	12.525	10.622	2.407	6.404
Na2O	0.013	0.018	0.036	0.020	0.014	0.015	0.015	0.017
K2O	0.022	0.020	0.029	0.000	0.044	0.035	0.012	0.000
TOTAL	99.834	100.024	100.050	100.138	100.116	100.027	100.337	99.755

Table S3 cont. Pyroxene major element compositions.

Sample	15085,26	15085,26	15085,26	15085,26	15085,26	15085,26	15085,26	15085,26
Site	26-pyx_001	26-pyx_002	26-pyx_002	26-pyx_002	26-pyx_002	26-pyx_002	26-pyx_002	26-pyx_002
Line #	283	284	285	286	287	288	289	290
SiO2	50.431	52.571	50.361	50.963	49.642	51.331	51.141	51.175
TiO2	0.765	0.254	0.273	0.327	0.549	0.257	0.308	0.327
Al2O3	3.718	5.421	4.729	4.630	4.447	4.855	3.838	3.863
Cr2O3	0.590	0.655	0.457	0.596	0.562	0.503	0.409	0.506
FeO*	21.849	18.043	18.529	19.163	16.582	18.441	20.366	17.528
FeO	21.849	18.043	16.570	19.163	15.484	18.441	20.366	17.528
Fe2O3	0.000	0.000	2.177	0.000	1.220	0.000	0.000	0.000
MnO	0.307	0.245	0.249	0.263	0.257	0.258	0.277	0.253
MgO	13.282	20.110	22.459	20.782	16.312	19.939	19.656	15.097
CaO	9.137	2.627	2.745	3.582	11.636	4.382	3.841	11.628
Na2O	0.014	0.017	0.015	0.015	0.014	0.134	0.018	0.014
K2O	0.000	0.007	0.007	0.019	0.020	0.021	0.018	0.023
TOTAL	100.093	99.948	99.824	100.340	100.020	100.121	99.872	100.415

Table S3 cont. Pyroxene major element compositions.

Sample	15085,26	15085,26	15085,26	15085,26	15085,26	15085,26	15085,26	15085,26
Site	26-pyx_003	26-pyx_003	26-pyx_003	26-pyx_003	26-pyx_003	26-pyx_003	26-pyx_003	26-pyx_004
Line #	291	292	293	294	295	296	297	298
SiO2	50.539	49.542	49.231	50.279	51.453	50.481	48.943	48.906
TiO2	0.678	0.735	0.462	0.306	0.255	0.334	0.433	0.634
Al2O3	4.055	3.101	3.756	4.599	4.651	4.734	3.622	4.078
Cr2O3	0.510	0.377	0.307	0.430	0.721	0.579	0.357	0.540
FeO*	23.953	28.778	23.767	19.769	17.810	18.557	24.572	23.180
FeO	23.953	28.778	22.090	18.336	17.810	18.059	22.474	21.674
Fe2O3	0.000	0.000	1.864	1.593	0.000	0.553	2.332	1.674
MnO	0.324	0.354	0.328	0.268	0.234	0.268	0.338	0.315
MgO	11.703	10.197	16.245	20.962	22.753	20.685	16.221	15.699
CaO	8.607	7.095	6.070	3.381	2.389	4.146	5.538	6.965
Na2O	0.015	0.015	0.016	0.015	0.015	0.015	0.019	0.016
K2O	0.023	0.028	0.017	0.008	0.000	0.026	0.000	0.025
TOTAL	100.408	100.221	100.199	100.017	100.281	99.824	100.044	100.358

Table S3 cont. Pyroxene major element compositions.

Sample	15085,26	15085,26	15085,26	15085,26	15085,26	15085,26	15085,26	15085,26
Site	26-pyx_004	26-pyx_004	26-pyx_005	26-pyx_005	26-pyx_005	26-pyx_005	26-pyx_005	26-pyx_005
Line #	299	300	301	302	303	304	305	306
SiO2	50.852	49.488	48.490	48.847	49.881	50.650	50.809	51.067
TiO2	0.259	0.596	0.665	0.597	0.328	0.255	0.251	0.296
Al2O3	4.682	4.219	3.636	4.134	4.562	4.636	4.910	4.715
Cr2O3	0.533	0.732	0.484	0.513	0.577	0.630	0.684	0.735
FeO*	18.078	15.340	25.328	23.422	20.103	17.281	17.792	18.430
FeO	16.878	14.880	23.589	21.653	18.486	16.318	17.089	18.430
Fe2O3	1.334	0.511	1.933	1.966	1.797	1.071	0.781	0.000
MnO	0.252	0.239	0.316	0.305	0.286	0.252	0.241	0.256
MgO	22.760	14.669	14.580	15.924	20.237	22.715	22.597	21.663
CaO	2.558	14.258	6.650	6.597	3.920	2.860	2.480	2.858
Na2O	0.013	0.016	0.017	0.013	0.015	0.014	0.016	0.016
K2O	0.000	0.034	0.028	0.029	0.000	0.000	0.037	0.000
TOTAL	99.985	99.590	100.193	100.379	99.908	99.293	99.817	100.036

Table S3 cont. Pyroxene major element compositions.

Sample	15085,26	15085,26	15085,26	15085,26	15085,26	15085,26	15085,26	15556,241
Site	26-pyx_00526-pyx_00526-pyx_00526-pyx_00526-pyx_00526-pyx_00526-pyx_00524-pyx_001							
Line #	307	308	309	310	311	312	313	314
SiO2	48.859	48.028	48.223	47.350	51.431	50.854	48.852	50.622
TiO2	0.372	0.923	0.709	1.156	0.264	0.302	1.053	0.481
Al2O3	6.194	4.397	4.381	1.882	4.690	4.160	3.009	3.503
Cr2O3	0.467	0.273	0.366	0.144	0.663	0.469	0.336	0.163
FeO*	21.903	26.038	24.769	33.650	17.901	18.910	26.397	22.916
FeO	21.625	26.038	24.769	33.650	17.901	18.910	26.397	22.916
Fe2O3	0.309	0.000	0.000	0.000	0.000	0.000	0.000	0.000
MnO	0.293	0.323	0.337	0.405	0.241	0.262	0.344	0.305
MgO	16.929	11.487	11.607	5.943	22.222	21.247	11.637	16.581
CaO	4.990	8.349	9.315	9.434	2.404	2.867	8.398	5.491
Na2O	0.037	0.015	0.012	0.012	0.049	0.016	0.035	0.014
K2O	0.032	0.035	0.039	0.055	0.005	0.000	0.053	0.023
TOTAL	100.074	99.866	99.759	100.031	99.869	99.086	100.113	100.099

Table S3 cont. Pyroxene major element compositions.

Sample	15556,241	15556,241	15556,241	15556,241	15556,241	15556,241	15556,241	15556,241
Site	24-pyx_00124-pyx_00124-pyx_00124-pyx_00124-pyx_00124-pyx_00124-pyx_00124-pyx_001							
Line #	315	316	317	318	319	320	321	322
SiO2	46.379	49.413	48.027	50.417	46.990	49.916	46.355	46.432
TiO2	0.936	0.435	1.471	0.544	1.425	0.698	1.249	1.338
Al2O3	1.456	4.568	2.648	4.375	1.685	4.875	2.841	2.765
Cr2O3	0.129	0.422	0.109	0.559	0.191	0.630	0.168	0.138
FeO*	35.900	21.279	28.755	19.611	30.209	18.160	31.778	29.603
FeO	35.783	19.824	28.755	19.611	30.209	18.160	30.797	29.429
Fe2O3	0.130	1.617	0.000	0.000	0.000	0.000	1.090	0.194
MnO	0.396	0.291	0.358	0.290	0.319	0.279	0.370	0.335
MgO	2.601	17.408	7.617	18.503	2.996	15.591	7.150	5.795
CaO	11.990	6.402	11.641	5.645	16.312	9.853	9.668	12.884
Na2O	0.015	0.012	0.014	0.012	0.013	0.011	0.035	0.013
K2O	0.018	0.022	0.012	0.024	0.056	0.012	0.029	0.022
TOTAL	99.820	100.251	100.651	99.980	100.196	100.024	99.645	99.325

Table S3 cont. Pyroxene major element compositions.

Sample	15556,241	15556,241	15556,241	15556,241	15556,241	15556,241	15556,241	15556,241
Site	24-pyx_001	24-pyx_002	24-pyx_002	24-pyx_002	24-pyx_002	24-pyx_002	24-pyx_002	24-pyx_002
Line #	323	324	325	326	327	328	329	330
SiO2	46.406	49.488	47.868	50.238	45.851	47.412	46.369	50.333
TiO2	1.202	0.894	1.478	0.384	1.268	1.435	1.086	0.469
Al2O3	2.135	4.647	2.950	4.902	1.735	2.986	0.967	3.574
Cr2O3	0.181	0.543	0.226	0.475	0.076	0.158	0.000	0.335
FeO*	35.830	16.722	25.906	21.106	38.016	29.776	34.760	24.803
FeO	35.830	16.722	25.906	21.106	38.016	29.776	34.706	24.803
Fe2O3	0.000	0.000	0.000	0.000	0.000	0.000	0.060	0.000
MnO	0.401	0.260	0.313	0.290	0.427	0.365	0.365	0.320
MgO	4.651	14.398	7.866	17.360	0.867	6.147	2.086	15.594
CaO	8.853	12.889	13.212	5.429	12.061	11.863	13.551	5.285
Na2O	0.069	0.012	0.013	0.015	0.015	0.012	0.013	0.013
K2O	0.027	0.006	0.021	0.000	0.038	0.024	0.070	0.020
TOTAL	99.755	99.859	99.851	100.197	100.354	100.178	99.266	100.745

Table S3 cont. Pyroxene major element compositions.

Sample	15556,241	15556,241	15556,241	15556,241	15556,241	15556,241	15556,241	15556,241
Site	24-pyx_002	24-pyx_002	24-pyx_002	24-pyx_002	24-pyx_003	24-pyx_003	24-pyx_003	24-pyx_003
Line #	331	332	333	334	335	336	337	338
SiO2	48.663	44.742	49.311	46.573	49.757	48.307	49.745	46.400
TiO2	0.931	1.219	1.018	1.392	0.533	1.066	0.598	1.331
Al2O3	4.786	1.478	3.612	2.004	4.475	3.920	4.373	2.095
Cr2O3	0.675	0.128	0.816	0.052	0.578	0.492	0.507	0.157
FeO*	18.770	41.478	16.284	33.511	19.594	23.488	19.443	34.144
FeO	17.550	40.282	15.658	33.511	18.199	23.058	18.259	34.144
Fe2O3	1.356	1.329	0.696	0.000	1.550	0.478	1.316	0.000
MnO	0.285	0.430	0.247	0.358	0.285	0.318	0.300	0.377
MgO	15.164	0.556	13.844	3.638	18.943	12.744	18.772	3.531
CaO	10.939	9.878	14.917	12.213	5.940	9.677	6.016	11.938
Na2O	0.013	0.013	0.028	0.087	0.012	0.031	0.051	0.013
K2O	0.027	0.057	0.018	0.041	0.018	0.028	0.016	0.018
TOTAL	100.254	99.980	100.094	99.869	100.135	100.071	99.822	100.004

Table S3 cont. Pyroxene major element compositions.

Sample	15556,241	15556,241	15556,241	15556,241	15556,241	15556,241	15556,241	15556,241
Site	24-pyx_003	24-pyx_003	24-pyx_003	24-pyx_003	24-pyx_003	24-pyx_003	24-pyx_003	24-pyx_004
Line #	339	340	341	342	343	344	345	346
SiO2	51.902	47.362	49.694	46.545	48.706	48.979	45.776	49.615
TiO2	0.354	1.138	0.541	1.542	1.209	0.738	1.009	0.478
Al2O3	3.488	1.273	4.460	2.313	5.192	3.048	1.067	4.400
Cr2O3	0.442	0.000	0.581	0.162	0.848	0.321	0.074	0.589
FeO*	20.726	34.258	20.366	29.935	14.622	27.226	39.889	21.133
FeO	20.726	34.258	19.522	29.574	14.622	27.226	39.065	19.950
Fe2O3	0.000	0.000	0.938	0.402	0.000	0.000	0.915	1.315
MnO	0.274	0.414	0.287	0.390	0.229	0.363	0.424	0.294
MgO	19.317	3.178	18.504	7.450	13.018	11.874	1.003	18.688
CaO	3.820	12.511	5.447	10.665	16.386	7.355	11.081	4.752
Na2O	0.012	0.013	0.012	0.015	0.012	0.084	0.013	0.012
K2O	0.032	0.030	0.025	0.021	0.016	0.030	0.036	0.018
TOTAL	100.366	100.176	99.917	99.038	100.236	100.018	100.370	99.978

Table S3 cont. Pyroxene major element compositions.

Sample	15556,241	15556,241	15556,241	15556,241	15556,241	15556,241	15556,241	15556,241
Site	24-pyx_004	24-pyx_004	24-pyx_004	24-pyx_004	24-pyx_004	24-pyx_004	24-pyx_004	24-pyx_004
Line #	347	348	349	350	351	352	353	354
SiO2	47.317	47.387	49.935	48.569	45.708	46.918	49.170	50.740
TiO2	1.173	1.383	0.481	1.084	1.324	0.787	0.461	0.343
Al2O3	2.175	2.618	4.426	4.431	2.052	1.918	5.261	3.912
Cr2O3	0.094	0.152	0.381	0.552	0.146	0.019	0.213	0.434
FeO*	29.416	30.359	19.931	18.287	37.986	36.269	24.687	20.869
FeO	28.861	30.195	18.356	18.015	37.986	35.123	24.687	20.869
Fe2O3	0.616	0.182	1.751	0.303	0.000	1.273	0.000	0.000
MnO	0.433	0.381	0.300	0.265	0.395	0.400	0.314	0.307
MgO	8.758	8.348	19.555	13.139	1.982	7.359	15.378	18.846
CaO	9.768	9.659	5.044	13.481	10.515	6.285	4.804	4.369
Na2O	0.017	0.016	0.014	0.014	0.014	0.015	0.015	0.013
K2O	0.044	0.000	0.032	0.004	0.021	0.014	0.015	0.028
TOTAL	99.193	100.304	100.099	99.826	100.142	99.984	100.318	99.861

Table S3 cont. Pyroxene major element compositions.

Sample	15556,241	15556,241	15556,241	15556,241	15556,241	15556,241	15556,241	15556,241
Site	24-pyx_004	24-pyx_004	24-pyx_005	24-pyx_005	24-pyx_005	24-pyx_005	24-pyx_005	24-pyx_005
Line #	355	356	357	358	359	360	361	362
SiO2	51.698	45.790	49.949	45.518	47.977	50.065	50.348	48.656
TiO2	0.329	1.257	0.691	1.022	0.758	1.209	0.785	1.164
Al2O3	3.726	1.790	4.689	1.125	2.706	4.622	4.347	1.284
Cr2O3	0.406	0.159	0.631	0.040	0.226	0.081	0.167	0.065
FeO*	20.587	36.793	18.823	42.180	31.442	16.916	17.088	30.662
FeO	20.587	36.503	18.823	42.180	30.875	16.916	17.088	30.662
Fe2O3	0.000	0.322	0.000	0.000	0.630	0.000	0.000	0.000
MnO	0.293	0.386	0.296	0.445	0.371	0.427	0.263	0.387
MgO	18.913	1.727	17.322	0.692	10.281	14.703	14.844	6.663
CaO	4.392	12.318	7.845	8.736	6.081	12.169	12.069	12.037
Na2O	0.019	0.014	0.012	0.018	0.129	0.015	0.072	0.016
K2O	0.028	0.024	0.011	0.035	0.028	0.044	0.024	0.019
TOTAL	100.391	100.256	100.269	99.809	99.999	100.250	100.007	100.953

Table S3 cont. Pyroxene major element compositions.

Sample	15556,241	15556,241	15085,24	15085,24	15085,24	15085,24	15085,24	15085,24
Site	24-pyx_005	24-pyx_005	241-pyx_001	241-pyx_001	241-pyx_001	241-pyx_001	241-pyx_001	241-pyx_001
Line #	363	364	365	366	367	368	369	370
SiO2	49.150	46.653	50.873	49.486	48.570	49.197	51.652	51.691
TiO2	0.629	1.333	0.729	0.792	0.791	0.565	0.256	0.447
Al2O3	4.905	2.245	3.707	4.312	3.542	4.165	4.962	4.836
Cr2O3	0.321	0.159	0.575	0.646	0.456	0.530	0.668	0.438
FeO*	20.047	33.362	21.724	17.146	25.803	21.864	20.211	20.622
FeO	17.146	33.192	21.724	17.146	24.946	20.245	20.211	20.622
Fe2O3	3.224	0.189	0.000	0.000	0.952	1.799	0.000	0.000
MnO	0.285	0.368	0.305	0.258	0.318	0.286	0.258	0.283
MgO	19.516	5.061	12.163	13.029	14.219	17.697	18.345	15.398
CaO	5.498	11.101	9.774	14.421	6.271	5.439	4.553	6.164
Na2O	0.015	0.017	0.015	0.013	0.016	0.014	0.019	0.014
K2O	0.000	0.034	0.000	0.011	0.023	0.074	0.012	0.023
TOTAL	100.366	100.331	99.863	100.115	100.007	99.829	100.937	99.914

Table S3 cont. Pyroxene major element compositions.

Sample	15085,24	15085,24	15085,24	15085,24	15085,24	15085,24	15085,24	15085,24
Site	241-pyx_001	241-pyx_001	241-pyx_001	241-pyx_001	241-pyx_001	241-pyx_001	241-pyx_002	241-pyx_002
Line #	371	372	373	374	375	376	377	378
SiO2	50.998	47.612	49.677	50.669	49.891	48.918	53.056	51.718
TiO2	0.632	1.094	0.340	0.584	0.735	1.072	0.269	0.279
Al2O3	4.319	1.851	4.457	5.080	3.725	2.311	4.381	4.927
Cr2O3	0.377	0.085	0.238	0.634	0.448	0.340	0.693	0.654
FeO*	22.091	35.958	21.344	14.252	18.230	29.941	16.994	17.866
FeO	22.091	35.958	19.671	14.252	18.230	29.941	16.994	17.866
Fe2O3	0.000	0.000	1.859	0.000	0.000	0.000	0.000	0.000
MnO	0.316	0.399	0.278	0.218	0.256	0.340	0.242	0.257
MgO	11.695	2.449	18.541	13.374	12.301	6.116	22.159	22.198
CaO	10.407	10.633	5.167	15.455	14.641	11.071	2.263	2.371
Na2O	0.015	0.015	0.014	0.013	0.015	0.013	0.015	0.073
K2O	0.030	0.000	0.007	0.015	0.015	0.011	0.000	0.000
TOTAL	100.879	100.095	100.061	100.294	100.255	100.133	100.071	100.341

Table S3 cont. Pyroxene major element compositions.

Sample	15085,24	15085,24	15085,24	15085,24	15085,24	15085,24	15085,24	15085,24
Site	241-pyx_002	241-pyx_002	241-pyx_002	241-pyx_002	241-pyx_002	241-pyx_002	241-pyx_003	241-pyx_003
Line #	379	380	381	382	383	384	385	386
SiO2	49.191	49.455	50.442	50.105	49.882	46.930	48.860	50.029
TiO2	0.555	0.716	0.310	0.387	0.696	0.873	0.600	0.362
Al2O3	4.558	4.826	4.353	6.464	3.829	2.556	3.673	7.122
Cr2O3	0.711	0.723	0.389	0.554	0.561	0.263	0.512	0.654
FeO*	15.107	15.032	20.613	20.632	21.468	32.379	24.163	19.438
FeO	14.444	14.703	20.031	20.632	21.468	30.847	22.769	19.438
Fe2O3	0.737	0.366	0.647	0.000	0.000	1.703	1.549	0.000
MnO	0.243	0.234	0.293	0.258	0.297	0.359	0.313	0.276
MgO	14.799	14.331	19.203	16.426	13.422	8.855	14.663	19.008
CaO	14.120	14.998	4.598	4.929	9.684	7.600	7.510	3.433
Na2O	0.014	0.014	0.017	0.015	0.039	0.016	0.013	0.012
K2O	0.032	0.005	0.023	0.025	0.017	0.033	0.020	0.010
TOTAL	99.329	100.334	100.241	99.793	99.894	99.863	100.326	100.343

Table S3 cont. Pyroxene major element compositions.

Sample	15085,24	15085,24	15085,24	15085,24	15085,24	15085,24	15085,24	15085,24
Site	241-pyx_003	241-pyx_003	241-pyx_003	241-pyx_003	241-pyx_003	241-pyx_003	241-pyx_003	241-pyx_003
Line #	387	388	389	390	391	392	393	394
SiO2	51.301	51.093	51.262	49.937	48.961	50.163	49.150	48.249
TiO2	0.259	0.263	0.268	0.669	0.630	0.656	0.844	0.966
Al2O3	7.378	4.871	4.607	4.690	4.842	4.683	4.494	2.799
Cr2O3	0.641	0.652	0.436	0.583	0.465	0.554	0.541	0.402
FeO*	18.095	17.826	19.114	14.969	25.257	14.621	21.960	26.200
FeO	18.095	17.083	19.089	14.969	25.257	14.621	21.960	26.200
Fe2O3	0.000	0.826	0.027	0.000	0.000	0.000	0.000	0.000
MnO	0.251	0.237	0.264	0.227	0.315	0.245	0.294	0.335
MgO	19.482	22.855	21.259	13.937	11.968	13.741	9.413	8.778
CaO	2.417	2.495	3.025	14.989	7.838	15.185	13.211	12.506
Na2O	0.015	0.015	0.089	0.015	0.015	0.017	0.015	0.018
K2O	0.000	0.000	0.000	0.000	0.046	0.002	0.027	0.015
TOTAL	99.837	100.307	100.323	100.015	100.336	99.868	99.948	100.266

Table S3 cont. Pyroxene major element compositions.

Sample	15085,24	15085,24	15085,24	15085,24	15085,24	15085,24	15556,28	15556,28
Site	241-pyx_003	241-pyx_003	241-pyx_004	241-pyx_004	241-pyx_004	241-pyx_004	28-pyx_001	28-pyx_001
Line #	395	396	397	398	399	400	401	402
SiO2	46.535	46.043	50.216	50.793	49.148	47.263	48.299	47.760
TiO2	1.077	1.066	0.486	0.379	0.926	1.160	1.081	1.171
Al2O3	1.939	1.823	4.686	4.509	2.479	2.060	4.752	4.170
Cr2O3	0.145	0.155	0.485	0.548	0.303	0.139	0.690	0.089
FeO*	33.390	35.507	19.057	20.791	31.520	31.978	17.147	22.291
FeO	32.043	34.701	19.057	20.791	31.520	31.978	16.925	22.009
Fe2O3	1.497	0.896	0.000	0.000	0.000	0.000	0.246	0.314
MnO	0.375	0.391	0.000	0.297	0.378	0.353	0.265	0.440
MgO	5.691	3.658	17.429	17.277	4.238	4.977	13.382	12.139
CaO	10.807	11.113	7.379	5.142	10.206	12.374	13.709	10.837
Na2O	0.014	0.013	0.063	0.015	0.016	0.013	0.014	0.014
K2O	0.046	0.034	0.007	0.000	0.054	0.033	0.018	0.041
TOTAL	100.019	99.803	99.808	99.750	99.268	100.351	99.355	98.951

Table S3 cont. Pyroxene major element compositions.

Sample	15556,28	15556,28	15556,28	15556,28	15556,28	15556,28	15556,28	15556,28
Site	28-pyx_001	28-pyx_001	28-pyx_001	28-pyx_001	28-pyx_002	28-pyx_002	28-pyx_002	28-pyx_002
Line #	403	404	405	406	407	408	409	410
SiO2	47.981	47.475	50.079	45.932	47.519	46.300	46.519	51.272
TiO2	0.781	1.232	0.324	1.185	1.248	1.461	1.389	0.581
Al2O3	4.244	4.162	3.941	1.436	3.187	1.997	2.417	5.094
Cr2O3	0.410	0.060	0.370	0.078	0.238	0.085	0.185	0.668
FeO*	23.594	22.537	21.025	36.525	26.926	32.425	31.295	19.465
FeO	22.705	20.908	19.252	35.056	25.965	32.284	29.881	19.465
Fe2O3	0.988	1.810	1.971	1.632	1.068	0.157	1.572	0.000
MnO	0.308	0.495	0.287	0.409	0.339	0.417	0.377	0.276
MgO	11.999	12.192	19.472	3.009	9.910	5.322	7.085	16.149
CaO	10.577	11.405	4.514	11.717	10.818	11.108	10.726	6.477
Na2O	0.014	0.014	0.012	0.018	0.014	0.032	0.012	0.014
K2O	0.019	0.020	0.026	0.022	0.016	0.035	0.061	0.028
TOTAL	99.926	99.592	100.050	100.330	100.215	99.183	100.066	100.022

Table S3 cont. Pyroxene major element compositions.

Sample	15556,28	15556,28	15556,28	15556,28	12038,63	12038,63	12038,63	12038,63
Site	28-pyx_002	28-pyx_002	28-pyx_002	28-pyx_002	63-pyx_001	63-pyx_001	63-pyx_001	63-pyx_001
Line #	411	412	413	414	415	416	417	418
SiO2	50.984	46.954	49.968	47.477	51.635	48.799	49.467	48.277
TiO2	0.649	1.435	0.389	0.989	1.061	1.405	1.259	1.651
Al2O3	4.982	2.688	4.154	1.453	6.251	4.188	4.754	2.812
Cr2O3	0.495	0.227	0.520	0.074	0.827	0.542	0.757	0.160
FeO*	18.847	30.878	20.519	40.095	16.710	20.652	17.255	22.953
FeO	18.847	30.878	18.904	40.095	16.710	20.652	17.255	22.953
Fe2O3	0.000	0.000	1.794	0.000	0.000	0.000	0.000	0.000
MnO	0.279	0.380	0.284	0.445	0.275	0.320	0.258	0.296
MgO	15.885	6.887	19.710	2.798	15.914	13.262	14.634	6.175
CaO	8.187	10.313	4.440	6.888	7.650	11.080	11.507	17.601
Na2O	0.014	0.013	0.011	0.017	0.027	0.012	0.015	0.013
K2O	0.038	0.025	0.011	0.033	0.003	0.011	0.021	0.029
TOTAL	100.359	99.799	100.006	100.267	100.353	100.271	99.927	99.966

Table S3 cont. Pyroxene major element compositions.

Sample	12038,63	12038,63	12038,63	12038,63	12038,63	12038,63	12038,63	12038,63
Site	63-pyx_001	63-pyx_001	63-pyx_001	63-pyx_001	63-pyx_002	63-pyx_002	63-pyx_002	63-pyx_002
Line #	419	420	421	422	423	424	425	426
SiO2	48.267	49.419	48.423	48.984	49.589	45.377	49.194	47.784
TiO2	1.774	0.777	1.601	0.953	0.983	1.186	1.026	1.660
Al2O3	3.752	5.473	3.451	3.987	4.987	1.757	4.591	2.992
Cr2O3	0.028	0.507	0.415	0.053	0.700	0.173	0.495	0.222
FeO*	21.552	18.780	22.981	22.838	17.337	35.451	19.210	25.731
FeO	21.552	17.246	22.981	22.838	17.337	33.991	18.385	25.731
Fe2O3	0.000	1.705	0.000	0.000	0.000	1.623	0.916	0.000
MnO	0.471	0.273	0.300	0.459	0.261	0.408	0.295	0.332
MgO	6.225	20.728	9.920	11.308	17.216	1.980	16.627	7.235
CaO	17.767	4.064	13.086	11.647	8.668	13.462	8.810	14.103
Na2O	0.057	0.012	0.013	0.015	0.011	0.011	0.013	0.016
K2O	0.047	0.020	0.009	0.042	0.031	0.032	0.026	0.027
TOTAL	99.940	100.052	100.199	100.286	99.781	99.837	100.287	100.101

Table S3 cont. Pyroxene major element compositions.

Sample	12038,63	12038,63	12038,63	12038,63	12038,63	12038,63	12038,63	12038,63
Site	63-pyx_002	63-pyx_002	63-pyx_002	63-pyx_003	63-pyx_003	63-pyx_003	63-pyx_003	63-pyx_003
Line #	427	428	429	430	431	432	433	434
SiO2	48.659	49.190	42.244	47.587	46.824	43.223	49.649	45.588
TiO2	0.928	1.761	0.900	1.898	1.274	1.110	0.948	1.158
Al2O3	2.937	4.220	0.833	3.337	2.086	1.252	6.609	1.563
Cr2O3	0.120	0.605	0.109	0.278	0.180	0.139	0.542	0.045
FeO*	23.517	15.696	44.994	25.038	31.276	42.841	18.658	39.326
FeO	23.517	15.696	36.588	25.038	31.276	37.035	18.658	38.255
Fe2O3	0.000	0.000	9.341	0.000	0.000	6.453	0.000	1.191
MnO	0.458	0.235	0.462	0.335	0.386	0.453	0.284	0.459
MgO	11.881	11.191	1.918	7.878	4.331	1.319	15.248	2.141
CaO	10.527	17.304	8.357	13.527	13.744	9.887	8.134	10.058
Na2O	0.015	0.010	0.013	0.025	0.012	0.012	0.013	0.014
K2O	0.056	0.000	0.028	0.008	0.000	0.039	0.002	0.024
TOTAL	99.098	100.212	99.858	99.911	100.113	100.275	100.087	100.376

Table S3 cont. Pyroxene major element compositions.

Sample	12038,63	12038,63	12038,63	12038,63	12038,63	12038,63	12038,63	12038,63
Site	63-pyx_003	63-pyx_003	63-pyx_003	63-pyx_003	63-pyx_004	63-pyx_004	63-pyx_004	63-pyx_004
Line #	435	436	437	438	439	440	441	442
SiO2	49.894	46.206	49.472	43.169	48.956	47.207	52.627	52.976
TiO2	0.894	1.267	0.869	0.941	0.966	1.358	1.011	1.015
Al2O3	4.887	2.010	4.624	0.877	5.784	2.377	5.751	5.594
Cr2O3	0.335	0.043	0.652	0.096	0.898	0.202	0.812	0.768
FeO*	19.328	34.536	19.297	41.935	16.655	29.553	17.087	17.746
FeO	19.328	33.130	19.156	33.613	16.045	29.553	17.087	17.746
Fe2O3	0.000	1.563	0.157	9.249	0.678	0.000	0.000	0.000
MnO	0.286	0.421	0.300	0.425	0.273	0.362	0.259	0.270
MgO	18.025	5.101	17.286	4.540	18.737	5.492	15.096	14.765
CaO	6.197	10.543	7.462	7.934	7.522	13.541	7.200	7.073
Na2O	0.015	0.017	0.013	0.013	0.011	0.017	0.012	0.013
K2O	0.001	0.052	0.015	0.036	0.000	0.007	0.020	0.016
TOTAL	99.862	100.196	99.989	99.966	99.803	100.115	99.874	100.235

Table S3 cont. Pyroxene major element compositions.

Sample	12038,63	12038,63	12038,63	12038,63	12038,63	12038,63	12038,63	12043,15
Site	63-pyx_004	63-pyx_004	63-pyx_005	63-pyx_005	63-pyx_005	63-pyx_005	63-pyx_005	15-pyx_001
Line #	443	444	445	446	447	448	449	450
SiO2	48.171	43.222	52.253	47.639	44.254	51.305	47.689	47.686
TiO2	1.256	0.880	1.023	1.501	1.042	1.092	1.344	1.464
Al2O3	3.707	0.836	5.749	3.489	1.128	4.609	1.829	2.717
Cr2O3	0.318	0.085	0.790	0.348	0.097	0.683	0.017	0.178
FeO*	25.097	41.477	17.044	24.329	40.897	17.913	36.458	27.106
FeO	24.500	32.261	17.044	23.489	36.509	17.913	36.458	27.106
Fe2O3	0.664	10.242	0.000	0.933	4.877	0.000	0.000	0.000
MnO	0.337	0.438	0.270	0.340	0.449	0.274	0.425	0.347
MgO	12.943	4.828	15.593	11.157	2.335	15.603	0.781	7.447
CaO	8.332	8.655	7.500	11.341	9.819	8.695	11.526	12.928
Na2O	0.011	0.015	0.011	0.013	0.012	0.012	0.013	0.034
K2O	0.030	0.003	0.021	0.002	0.032	0.020	0.013	0.017
TOTAL	100.203	100.439	100.254	100.157	100.065	100.205	100.095	99.923

Table S3 cont. Pyroxene major element compositions.

Sample	12043,15	12043,15	12043,15	12043,15	12043,15	12043,15	12043,15	12043,15
Site	15-pyx_001	15-pyx_001	15-pyx_001	15-pyx_001	15-pyx_001	15-pyx_001	15-pyx_001	15-pyx_001
Line #	451	452	453	454	455	456	457	458
SiO2	49.386	49.239	47.846	49.334	48.273	45.500	47.236	48.862
TiO2	0.763	0.706	1.517	1.966	1.623	1.106	0.872	1.833
Al2O3	5.157	5.104	2.864	5.984	5.797	1.667	2.607	5.858
Cr2O3	0.865	0.833	0.250	0.862	1.034	0.186	0.266	0.812
FeO*	19.144	19.327	24.404	14.071	13.957	39.400	30.782	13.217
FeO	18.102	17.094	24.404	14.071	13.957	39.304	28.726	13.217
Fe2O3	1.159	2.482	0.000	0.000	0.000	0.107	2.285	0.000
MnO	0.281	0.277	0.326	0.201	0.236	0.448	0.377	0.224
MgO	19.294	20.475	8.276	9.863	13.118	1.571	10.214	11.389
CaO	5.337	4.328	14.485	17.467	15.832	9.934	7.645	17.884
Na2O	0.013	0.014	0.013	0.013	0.012	0.013	0.015	0.013
K2O	0.020	0.011	0.029	0.021	0.000	0.020	0.031	0.003
TOTAL	100.259	100.313	100.010	99.782	99.881	99.845	100.043	100.095

Table S3 cont. Pyroxene major element compositions.

Sample	12043,15	12043,15	12043,15	12043,15	12043,15	12043,15	12043,15	12043,15
Site	15-pyx_002	15-pyx_002	15-pyx_002	15-pyx_002	15-pyx_002	15-pyx_002	15-pyx_002	15-pyx_002
Line #	459	460	461	462	463	464	465	466
SiO2	47.106	49.504	49.257	47.282	49.938	46.803	47.367	42.966
TiO2	1.722	0.831	0.798	1.129	0.723	1.275	1.426	0.965
Al2O3	2.744	5.193	5.194	3.184	5.138	2.948	2.748	0.959
Cr2O3	0.264	0.633	0.807	0.350	0.879	0.295	0.194	0.050
FeO*	29.949	18.097	18.059	28.483	18.551	28.683	28.747	42.882
FeO	29.949	17.441	15.288	25.650	18.107	28.367	28.747	35.882
Fe2O3	0.000	0.729	3.080	3.148	0.493	0.351	0.000	7.779
MnO	0.380	0.283	0.286	0.367	0.265	0.354	0.366	0.432
MgO	7.311	19.134	21.386	12.428	20.501	6.832	7.353	1.815
CaO	10.760	6.174	4.505	7.019	4.139	12.583	11.893	9.833
Na2O	0.070	0.032	0.013	0.059	0.017	0.015	0.012	0.014
K2O	0.043	0.016	0.028	0.037	0.021	0.006	0.027	0.011
TOTAL	100.349	99.896	100.333	100.338	100.172	99.795	100.132	99.924

Table S3 cont. Pyroxene major element compositions.

Sample	12043,15	12043,15	12043,15	12043,15	12043,15	12043,15	12043,15	12043,15
Site	15-pyx_002	15-pyx_002	15-pyx_003	15-pyx_003	15-pyx_003	15-pyx_003	15-pyx_003	15-pyx_003
Line #	467	468	469	470	471	472	473	474
SiO2	46.740	43.397	49.783	47.447	43.774	49.040	47.569	42.582
TiO2	1.868	0.832	0.728	1.879	1.137	0.814	1.777	0.872
Al2O3	3.198	0.798	5.015	3.120	1.093	5.140	2.973	0.859
Cr2O3	0.250	0.061	0.776	0.305	0.076	0.831	0.204	0.071
FeO*	25.457	46.435	18.630	24.671	44.607	19.653	25.658	45.332
FeO	24.732	41.264	18.452	24.671	40.849	17.937	25.658	37.246
Fe2O3	0.807	5.746	0.198	0.000	4.176	1.907	0.000	8.986
MnO	0.330	0.495	0.290	0.309	0.458	0.282	0.325	0.446
MgO	8.071	0.904	19.609	6.903	0.710	19.142	6.716	1.995
CaO	14.067	7.127	4.998	15.508	8.324	5.416	14.732	8.081
Na2O	0.011	0.015	0.015	0.013	0.014	0.017	0.017	0.015
K2O	0.015	0.022	0.004	0.025	0.020	0.004	0.019	0.010
TOTAL	100.007	100.086	99.847	100.179	100.213	100.337	99.988	100.263

Table S3 cont. Pyroxene major element compositions.

Sample	12043,15	12043,15	12043,15	12043,15	12043,15	12043,15	12043,15	12043,15
Site	15-pyx_003	15-pyx_003	15-pyx_003	15-pyx_003	15-pyx_003	15-pyx_003	15-pyx_004	15-pyx_004
Line #	475	476	477	478	479	480	481	482
SiO2	47.556	47.606	42.995	43.766	47.453	48.482	51.458	52.494
TiO2	1.481	1.297	1.229	1.216	1.402	1.660	0.690	0.762
Al2O3	4.044	3.985	1.290	1.490	3.356	6.722	5.710	5.225
Cr2O3	0.390	0.268	0.134	0.158	0.292	0.924	0.725	0.744
FeO*	24.813	30.125	42.753	41.680	26.759	14.741	18.520	19.699
FeO	23.409	30.125	37.596	37.297	25.417	14.741	18.520	19.699
Fe2O3	1.561	0.000	5.731	4.871	1.491	0.000	0.000	0.000
MnO	0.343	0.374	0.446	0.453	0.358	0.240	0.273	0.289
MgO	13.619	9.017	0.386	0.823	11.039	11.345	18.587	15.076
CaO	7.880	7.498	10.658	10.689	9.677	15.988	3.935	5.521
Na2O	0.015	0.034	0.015	0.085	0.010	0.014	0.016	0.014
K2O	0.001	0.025	0.021	0.039	0.034	0.009	0.043	0.021
TOTAL	100.142	100.228	99.926	100.399	100.379	100.125	99.957	99.842

Table S3 cont. Pyroxene major element compositions.

Sample	12043,15	12043,15	12043,15	12043,15	12043,15	12043,15	12043,15	12043,15
Site	15-pyx_004	15-pyx_005	15-pyx_005	15-pyx_005	15-pyx_005	15-pyx_005	15-pyx_005	15-pyx_005
Line #	483	484	485	486	487	488	489	490
SiO2	46.816	49.728	49.508	44.333	50.082	47.036	45.376	47.927
TiO2	0.884	0.708	1.088	0.880	1.630	1.684	1.458	1.467
Al2O3	1.963	5.126	4.662	0.968	2.844	2.675	1.802	4.648
Cr2O3	0.153	0.612	0.409	0.101	0.154	0.154	0.173	0.525
FeO*	34.725	18.861	27.365	41.810	27.030	26.957	36.400	22.691
FeO	33.193	17.388	27.365	36.894	27.030	26.957	35.543	21.943
Fe2O3	1.702	1.637	0.000	5.463	0.000	0.000	0.952	0.831
MnO	0.417	0.272	0.381	0.445	0.337	0.309	0.412	0.320
MgO	7.364	20.661	10.250	3.337	3.846	4.608	1.768	14.014
CaO	7.718	4.298	6.366	8.119	14.236	16.940	12.740	8.614
Na2O	0.016	0.013	0.039	0.014	0.013	0.013	0.014	0.053
K2O	0.025	0.013	0.021	0.015	0.027	0.020	0.025	0.032
TOTAL	100.080	100.291	100.088	100.022	100.198	100.395	100.168	100.291

Table S3 cont. Pyroxene major element compositions.

Sample	12043,15	70017,123	70017,123	70017,123	70017,123	70017,123	70017,123	70017,123
Site	15-pyx_005	123-pyx_001	123-pyx_001	123-pyx_001	123-pyx_001	123-pyx_001	123-pyx_002	123-pyx_002
Line #	491	492	493	494	495	496	497	498
SiO2	47.353	48.964	49.905	51.891	49.857	48.186	49.275	51.993
TiO2	1.411	1.160	1.623	1.746	0.964	2.957	1.657	0.835
Al2O3	3.395	3.330	4.055	5.000	2.863	6.086	4.250	5.253
Cr2O3	0.394	0.306	0.486	0.516	0.256	0.714	0.436	0.294
FeO*	27.577	20.718	12.040	11.244	26.731	9.097	16.554	18.614
FeO	26.768	19.981	11.636	11.244	26.731	9.097	16.554	18.614
Fe2O3	0.900	0.819	0.449	0.000	0.000	0.000	0.000	0.000
MnO	0.351	0.325	0.206	0.219	0.396	0.180	0.283	0.282
MgO	10.946	12.895	17.544	13.877	9.545	14.552	12.757	18.468
CaO	8.684	12.583	13.979	15.626	9.447	18.527	14.539	4.308
Na2O	0.014	0.013	0.013	0.012	0.017	0.014	0.056	0.040
K2O	0.022	0.039	0.015	0.032	0.036	0.013	0.007	0.020
TOTAL	100.148	100.330	99.866	100.164	100.112	100.324	99.812	100.105

Table S3 cont. Pyroxene major element compositions.

Sample	70017,123	70017,123	70017,123	70017,123	70017,123	70017,123	70017,123	70017,123
Site	123-pyx_002	123-pyx_002	123-pyx_002	123-pyx_002	123-pyx_003	123-pyx_003	123-pyx_003	123-pyx_003
Line #	499	500	501	502	503	504	505	506
SiO2	50.594	48.701	48.247	45.242	48.199	48.884	49.571	48.433
TiO2	1.208	1.423	2.661	3.288	1.630	1.524	2.068	1.377
Al2O3	3.893	3.371	6.190	6.259	4.142	3.462	5.025	3.470
Cr2O3	0.374	0.387	0.770	0.781	0.368	0.315	0.351	0.400
FeO*	19.376	18.917	10.374	9.639	12.588	17.914	12.507	21.363
FeO	19.376	18.917	10.374	3.416	7.384	17.914	12.507	20.701
Fe2O3	0.000	0.000	0.000	6.915	5.783	0.000	0.000	0.736
MnO	0.309	0.286	0.204	0.188	0.214	0.272	0.224	0.325
MgO	11.395	10.477	14.932	17.102	17.724	10.075	14.249	11.970
CaO	12.986	16.515	16.441	17.852	15.448	17.361	16.171	13.036
Na2O	0.014	0.011	0.011	0.011	0.012	0.015	0.029	0.011
K2O	0.015	0.019	0.000	0.015	0.020	0.007	0.028	0.012
TOTAL	100.165	100.107	99.829	100.376	100.344	99.829	100.223	100.398

Table S3 cont. Pyroxene major element compositions.

Sample	70017,123	70017,123	70017,123	70017,123	70017,123	70017,123	70017,123	70017,123
Site	123-pyx_003	123-pyx_003	123-pyx_003	123-pyx_004	123-pyx_004	123-pyx_004	123-pyx_004	123-pyx_004
Line #	507	508	509	510	511	512	513	514
SiO2	47.800	48.646	48.124	47.412	47.710	50.009	48.496	48.332
TiO2	3.393	2.731	1.040	1.055	1.859	1.723	2.733	1.221
Al2O3	6.708	6.192	3.217	2.715	4.339	4.610	5.988	2.915
Cr2O3	0.805	0.712	0.351	0.266	0.493	0.503	0.825	0.373
FeO*	9.455	10.414	26.425	26.212	14.326	11.314	9.800	21.788
FeO	9.455	10.414	25.035	24.130	10.812	11.314	9.800	21.788
Fe2O3	0.000	0.000	1.545	2.314	3.905	0.000	0.000	0.000
MnO	0.183	0.207	0.399	0.360	0.230	0.208	0.196	0.332
MgO	13.165	14.334	12.864	9.906	15.550	16.160	14.406	8.446
CaO	18.195	16.899	7.799	12.049	15.419	15.551	17.871	16.533
Na2O	0.055	0.049	0.013	0.012	0.029	0.013	0.016	0.015
K2O	0.027	0.011	0.019	0.000	0.022	0.007	0.005	0.026
TOTAL	99.786	100.196	100.250	99.986	99.978	100.097	100.334	99.980

Table S3 cont. Pyroxene major element compositions.

Sample	70017,123	70017,123	70017,123	70017,123	70017,123	70017,123	70017,123	70017,123
Site	123-pyx_005	123-pyx_005	123-pyx_005	123-pyx_005	123-pyx_005	123-pyx_005	123-pyx_005	123-pyx_005
Line #	515	516	517	518	519	520	521	522
SiO2	48.093	46.431	52.059	47.990	50.423	48.303	51.608	52.185
TiO2	0.735	0.827	0.766	1.069	1.694	2.778	2.661	1.441
Al2O3	2.780	3.561	6.157	2.655	4.848	6.154	5.916	3.712
Cr2O3	0.264	0.204	0.322	0.312	0.389	0.733	0.475	0.348
FeO*	29.525	27.700	19.523	25.131	11.766	10.428	10.832	18.697
FeO	28.151	21.054	19.523	24.963	11.766	10.428	10.832	18.697
Fe2O3	1.527	7.385	0.000	0.186	0.000	0.000	0.000	0.000
MnO	0.426	0.393	0.274	0.386	0.219	0.184	0.205	0.290
MgO	11.928	15.358	16.343	7.986	15.969	14.665	10.588	8.593
CaO	6.374	5.665	4.337	14.508	14.750	16.896	17.447	14.684
Na2O	0.016	0.013	0.013	0.015	0.033	0.014	0.012	0.014
K2O	0.028	0.039	0.023	0.034	0.029	0.044	0.021	0.034
TOTAL	100.168	100.190	99.819	100.085	100.120	100.197	99.766	99.998

Table S3 cont. Pyroxene major element compositions.

Sample	70017,123	70017,123
Site	123-pyx_005	123-pyx_005
Line #	523	524
SiO2	50.370	48.867
TiO2	0.963	1.091
Al2O3	2.626	2.351
Cr2O3	0.210	0.387
FeO*	30.508	26.370
FeO	30.508	26.370
Fe2O3	0.000	0.000
MnO	0.434	0.365
MgO	7.117	5.243
CaO	7.784	15.404
Na2O	0.019	0.014
K2O	0.018	0.027
TOTAL	100.047	100.117

Table S4: Pyroxene trace element compositions.

Sample	10057	10057	10057	10057	10057	10057	10057	10057
Site	67-PYX-1.64	67-PYX-2.67	67-PYX-2.68	67-PYX-2.69	67-PYX-3.82	67-PYX-3.83	67-PYX-3.85	67-PYX-4.90
Si29_ppm_mean	484125.000	487622.000	504159.000	467724.000	492414.000	504375.000	503049.000	523130.000
Si29_ppm_2SE(int)	0.000	0.000	0.000	0.000	0.000	0.000	0.000	0.000
Ca43_ppm_mean	86558.116	155758.119	152983.299	137316.926	149421.474	154513.906	143007.558	155676.434
Ca43_ppm_2SE(int)	1333.368	2206.480	3073.748	2733.993	3156.858	2821.139	2301.572	2736.323
Sc45_ppm_mean	87.956	155.039	116.723	113.187	116.586	127.934	123.783	120.713
Sc45_ppm_2SE(int)	1.343	2.289	2.677	3.337	2.718	2.517	2.730	2.203
Ti47_ppm_mean	5674.246	12103.253	12679.766	9528.844	11302.224	11957.844	10551.471	11621.010
Ti47_ppm_2SE(int)	89.686	253.102	315.210	231.336	244.584	260.003	198.355	246.532
V51_ppm_mean	31.766	64.242	101.907	63.620	90.187	90.205	72.170	89.923
V51_ppm_2SE(int)	0.549	1.393	2.134	1.506	1.800	1.597	1.664	2.534
Cr52_ppm_mean	1573.914	2862.085	3917.224	2716.422	3492.173	3617.931	2932.751	3523.813
Cr52_ppm_2SE(int)	29.270	53.137	80.097	57.530	48.847	68.646	58.887	63.968
Mn55_ppm_mean	2968.525	2371.315	1881.499	2170.207	1940.804	2165.976	2318.303	2118.629
Mn55_ppm_2SE(int)	44.196	54.240	37.795	40.467	40.987	44.546	37.438	36.167
Co59_ppm_mean	23.441	19.175	19.662	17.862	19.494	19.825	19.952	20.942
Co59_ppm_2SE(int)	0.454	0.438	0.617	0.476	0.471	0.536	0.486	0.576
Ni60_ppm_mean	0.614	0.491	1.017	0.730	0.972	0.910	0.648	1.173
Ni60_ppm_2SE(int)	0.125	0.113	0.178	0.135	0.168	0.201	0.146	0.184
Cu63_ppm_mean	0.200	0.482	0.488	0.654	0.289	1.094	0.391	0.536
Cu63_ppm_2SE(int)	0.052	0.080	0.077	0.123	0.076	0.117	0.084	0.105
Zn66_ppm_mean	3.793	2.455	2.513	2.850	2.066	3.157	2.738	2.468
Zn66_ppm_2SE(int)	0.587	0.516	0.673	0.680	0.543	0.589	0.715	0.577
Rb85_ppm_mean	0.075	0.026	0.035	0.649	0.018	0.055	0.021	0.155
Rb85_ppm_2SE(int)	0.029	0.017	0.019	0.101	0.015	0.023	0.015	0.033
Sr88_ppm_mean	5.998	12.788	22.311	18.462	9.861	10.293	9.522	13.404
Sr88_ppm_2SE(int)	0.740	0.339	1.477	1.213	0.343	0.342	0.270	0.386
Y89_ppm_mean	73.494	124.065	60.157	87.072	67.688	79.842	76.657	70.954
Y89_ppm_2SE(int)	5.232	3.502	1.456	4.903	1.480	2.858	2.922	1.303
Zr90_ppm_mean	68.721	83.388	39.588	66.820	37.416	57.997	46.393	49.412
Zr90_ppm_2SE(int)	22.128	2.400	1.306	5.660	0.866	4.447	2.068	1.329
Nb93_ppm_mean	3.889	0.577	0.209	0.756	0.095	0.606	0.090	0.429
Nb93_ppm_2SE(int)	2.246	0.180	0.054	0.143	0.022	0.179	0.022	0.060
Hf178_ppm_mean	3.400	4.957	2.488	3.698	2.351	3.180	3.037	2.914
Hf178_ppm_2SE(int)	0.894	0.231	0.140	0.311	0.121	0.225	0.143	0.129
Ta181_ppm_mean	0.178	0.033	0.020	0.050	0.009	0.039	0.010	0.030
Ta181_ppm_2SE(int)	0.103	0.009	0.006	0.011	0.003	0.011	0.004	0.007
Pb208_ppm_mean	0.945	0.233	0.801	0.959	0.124	1.128	0.068	0.367
Pb208_ppm_2SE(int)	0.476	0.048	0.073	0.132	0.051	0.066	0.020	0.164
Th232_ppm_mean	1.485	0.127	0.024	0.276	0.014	0.129	0.013	0.133
Th232_ppm_2SE(int)	0.925	0.050	0.007	0.051	0.004	0.034	0.004	0.024
U238_ppm_mean	0.281	0.021	0.005	0.063	0.004	0.057	0.006	0.041
U238_ppm_2SE(int)	0.176	0.007	0.002	0.013	0.002	0.019	0.002	0.008

Table S4 cont.: Pyroxene trace element compositions.

Sample	10057	10057	10057	10057	10057	10057	10057	10057
Site	67-PYX-5.94	67-PYX-5.102	67-PYX-6.104	67-PYX-6.106	67-PYX-6.108	67-PYX-6.111	67-PYX-7.114	67-PYX-7.116
Si29_ppm_mean	509414.000	506846.000	508293.000	507685.000	511627.000	493867.000	510653.000	467737.000
Si29_ppm_2SE(int)	0.000	0.000	0.000	0.000	0.000	0.000	0.000	0.000
Ca43_ppm_mean	150948.216	158023.423	147672.969	160460.198	157446.512	126006.973	153300.954	94965.146
Ca43_ppm_2SE(int)	3294.854	2709.739	3114.721	3185.550	4304.623	3522.424	3737.782	1403.940
Sc45_ppm_mean	124.298	119.600	102.043	121.686	130.607	122.334	112.565	98.025
Sc45_ppm_2SE(int)	2.932	2.237	2.316	2.983	3.293	2.840	2.144	2.231
Ti47_ppm_mean	12107.050	12070.459	11583.474	13325.428	49054.636	8731.859	12132.273	5404.612
Ti47_ppm_2SE(int)	373.578	298.177	295.681	291.593	2756.612	243.141	321.717	108.568
V51_ppm_mean	96.899	97.166	94.059	100.530	113.915	51.384	111.523	23.605
V51_ppm_2SE(int)	3.361	2.030	2.925	1.910	4.001	1.496	2.545	0.670
Cr52_ppm_mean	3830.283	3685.406	3536.908	4008.776	4349.768	2411.322	4193.700	1322.146
Cr52_ppm_2SE(int)	104.133	64.877	93.985	76.344	140.866	62.562	112.220	30.206
Mn55_ppm_mean	2149.504	1904.115	1997.545	1905.955	2355.597	2636.346	1872.502	3335.050
Mn55_ppm_2SE(int)	51.702	37.920	41.012	35.320	71.318	55.619	34.682	56.626
Co59_ppm_mean	19.952	19.147	19.816	18.737	20.377	21.329	20.287	22.598
Co59_ppm_2SE(int)	0.602	0.535	0.653	0.396	0.667	0.564	0.699	0.570
Ni60_ppm_mean	1.102	0.969	1.086	1.320	0.981	0.652	1.172	0.531
Ni60_ppm_2SE(int)	0.191	0.164	0.237	0.343	0.199	0.161	0.201	0.135
Cu63_ppm_mean	0.524	0.640	0.446	1.159	2.198	0.391	0.789	0.750
Cu63_ppm_2SE(int)	0.093	0.102	0.093	0.140	0.242	0.067	0.138	0.126
Zn66_ppm_mean	2.894	3.339	3.028	2.700	4.417	3.730	2.108	4.926
Zn66_ppm_2SE(int)	0.628	0.655	0.850	0.626	0.835	0.696	0.697	0.574
Rb85_ppm_mean	0.027	0.029	0.593	0.198	0.049	0.025	0.022	0.237
Rb85_ppm_2SE(int)	0.017	0.015	0.064	0.039	0.026	0.018	0.017	0.054
Sr88_ppm_mean	9.939	10.903	22.558	14.096	10.480	8.966	10.450	14.765
Sr88_ppm_2SE(int)	0.276	0.305	1.195	0.399	0.329	0.291	0.266	1.735
Y89_ppm_mean	72.293	58.293	84.057	70.481	68.293	93.080	50.971	163.059
Y89_ppm_2SE(int)	2.029	1.609	5.587	1.632	1.315	1.979	0.920	15.296
Zr90_ppm_mean	41.765	34.976	89.654	58.861	134.295	53.254	28.810	241.697
Zr90_ppm_2SE(int)	1.012	1.062	8.487	1.712	8.448	1.504	0.912	39.717
Nb93_ppm_mean	0.107	0.142	2.475	0.980	5.072	0.077	0.047	5.075
Nb93_ppm_2SE(int)	0.024	0.027	0.285	0.113	0.515	0.017	0.015	1.082
Hf178_ppm_mean	2.638	2.202	3.827	3.099	4.843	3.155	1.821	8.808
Hf178_ppm_2SE(int)	0.140	0.107	0.294	0.156	0.278	0.147	0.095	1.088
Ta181_ppm_mean	0.011	0.013	0.150	0.071	0.356	0.012	0.007	0.335
Ta181_ppm_2SE(int)	0.004	0.005	0.022	0.020	0.044	0.004	0.004	0.076
Pb208_ppm_mean	0.400	1.289	0.444	0.368	0.072	0.601	0.928	0.901
Pb208_ppm_2SE(int)	0.069	0.105	0.048	0.083	0.015	0.045	0.084	0.137
Th232_ppm_mean	0.015	0.022	0.727	0.169	0.084	0.016	0.022	1.773
Th232_ppm_2SE(int)	0.004	0.007	0.134	0.023	0.015	0.005	0.009	0.334
U238_ppm_mean	0.006	0.009	0.189	0.055	0.053	0.006	0.007	0.611
U238_ppm_2SE(int)	0.002	0.003	0.039	0.010	0.008	0.002	0.003	0.132

Table S4 cont.: Pyroxene trace element compositions.

Sample	10057	10057	10057	10057	10057	10057	12039	12039
Site	67-PYX-8.123	67-PYX-8.124	67-PYX-9.125	67-PYX-9.126	67-PYX-10.129	67-PYX-10.130	63-PYX-1.417	63-PYX-1.418
Si29_ppm_mean	517976.000	496823.000	511639.000	496141.000	519393.000	488229.000	494669.000	482767.000
Si29_ppm_2SE(int)	0.000	0.000	0.000	0.000	0.000	0.000	0.000	0.000
Ca43_ppm_mean	167020.682	117336.129	146797.650	108632.117	165200.745	132897.859	150675.155	163146.302
Ca43_ppm_2SE(int)	2833.070	2060.779	2704.767	1755.512	4011.340	2392.346	3177.890	2548.805
Sc45_ppm_mean	128.877	115.195	122.001	101.179	116.591	121.148	100.306	119.595
Sc45_ppm_2SE(int)	2.708	1.968	2.631	1.946	2.982	3.103	2.353	1.889
Ti47_ppm_mean	12852.897	7432.963	12989.363	8057.105	11739.957	10147.896	9384.457	7351.727
Ti47_ppm_2SE(int)	301.431	131.629	345.545	175.033	266.493	303.818	187.188	128.933
V51_ppm_mean	99.100	43.072	102.977	42.911	94.939	45.539	402.540	44.090
V51_ppm_2SE(int)	2.674	1.082	2.135	1.342	2.628	0.910	7.238	1.087
Cr52_ppm_mean	3908.649	2018.752	4050.809	2066.877	3655.440	2111.274	5749.069	912.376
Cr52_ppm_2SE(int)	86.085	36.354	87.735	48.518	72.693	42.760	101.690	21.430
Mn55_ppm_mean	1978.722	2807.066	2103.331	2758.446	1967.166	2732.358	2248.298	3152.386
Mn55_ppm_2SE(int)	42.238	51.286	38.340	47.578	37.896	58.696	43.936	52.051
Co59_ppm_mean	18.561	21.479	21.217	22.629	19.640	39.656	30.944	36.228
Co59_ppm_2SE(int)	0.400	0.556	0.620	0.589	0.639	2.397	0.672	0.745
Ni60_ppm_mean	0.845	0.341	1.319	0.867	1.316	10.940	1.231	1.047
Ni60_ppm_2SE(int)	0.162	0.124	0.203	0.162	0.293	1.175	0.208	0.197
Cu63_ppm_mean	0.631	0.283	0.435	1.268	4.251	26.293	0.580	0.391
Cu63_ppm_2SE(int)	0.101	0.078	0.109	0.165	0.820	3.302	0.096	0.080
Zn66_ppm_mean	2.723	3.853	3.177	3.574	2.197	5.373	1.618	1.666
Zn66_ppm_2SE(int)	0.755	0.621	0.697	0.612	0.666	0.745	0.473	0.549
Rb85_ppm_mean	0.036	1.547	0.032	0.604	0.277	0.922	0.008	0.026
Rb85_ppm_2SE(int)	0.015	0.184	0.017	0.129	0.050	0.119	0.011	0.014
Sr88_ppm_mean	19.790	19.787	8.863	22.489	36.608	199.061	9.283	19.602
Sr88_ppm_2SE(int)	2.733	0.753	0.267	0.713	0.866	3.561	0.253	0.443
Y89_ppm_mean	74.026	99.903	62.427	78.626	70.117	365.692	20.217	47.639
Y89_ppm_2SE(int)	3.199	2.522	1.050	1.354	3.545	50.458	0.512	1.032
Zr90_ppm_mean	45.180	72.200	39.442	64.620	48.840	1217.116	18.318	50.288
Zr90_ppm_2SE(int)	2.077	3.246	0.783	2.141	3.302	234.601	0.602	1.085
Nb93_ppm_mean	0.110	0.712	0.079	1.502	0.778	123.180	0.025	0.045
Nb93_ppm_2SE(int)	0.024	0.102	0.020	0.110	0.110	24.794	0.011	0.014
Hf178_ppm_mean	2.815	4.035	2.544	3.137	2.990	52.274	0.986	2.528
Hf178_ppm_2SE(int)	0.169	0.190	0.123	0.132	0.245	8.906	0.073	0.111
Ta181_ppm_mean	0.008	0.042	0.013	0.088	0.035	5.887	0.004	0.005
Ta181_ppm_2SE(int)	0.004	0.010	0.005	0.011	0.008	1.150	0.003	0.002
Pb208_ppm_mean	0.121	1.013	0.757	3.180	0.620	9.768	0.484	1.642
Pb208_ppm_2SE(int)	0.022	0.151	0.215	0.306	0.156	1.785	0.103	0.139
Th232_ppm_mean	0.025	0.151	0.012	0.272	0.270	25.342	0.002	0.002
Th232_ppm_2SE(int)	0.006	0.033	0.004	0.028	0.041	5.766	0.002	0.002
U238_ppm_mean	0.011	0.043	0.004	0.073	0.037	8.205	0.000	0.000
U238_ppm_2SE(int)	0.003	0.009	0.002	0.010	0.008	1.404	0.001	0.000

Pyroxene trace element compositions.

Sample	12039	12039	12039	12039	12039	12039	12039	12039
Site	63-PYX-1.419	63-PYX-1.420	63-PYX-1.421	63-PYX-2.425	63-PYX-2.426	63-PYX-2.427	63-PYX-3.430	63-PYX-3.431
Si29_ppm_mean	482668.000	494188.000	484231.000	491940.000	477838.000	486588.000	475872.000	468240.000
Si29_ppm_2SE(int)	0.000	0.000	0.000	0.000	0.000	0.000	0.000	0.000
Ca43_ppm_mean	92310.978	41444.925	95023.152	102181.506	128053.432	103037.434	127715.630	135211.764
Ca43_ppm_2SE(int)	1385.261	938.817	1405.336	2109.444	2318.259	2768.599	2050.535	1888.286
Sc45_ppm_mean	39.295	51.101	45.012	83.623	106.812	34.812	106.568	113.389
Sc45_ppm_2SE(int)	0.708	0.844	0.814	1.907	1.764	0.883	1.648	1.955
Ti47_ppm_mean	4633.909	4176.019	4995.780	7977.033	6981.895	4608.762	7320.165	6797.300
Ti47_ppm_2SE(int)	65.612	74.544	66.656	167.431	98.268	72.018	134.095	99.336
V51_ppm_mean	8.773	358.335	4.712	236.845	41.459	5.894	63.899	42.705
V51_ppm_2SE(int)	0.274	7.354	0.241	5.272	1.060	0.285	1.630	0.904
Cr52_ppm_mean	214.153	5096.380	137.966	4054.546	962.288	161.300	1233.446	851.654
Cr52_ppm_2SE(int)	4.787	101.434	3.885	101.837	24.680	5.784	31.979	15.787
Mn55_ppm_mean	4334.783	2505.128	4265.981	2986.714	3572.953	4539.236	3395.869	3669.433
Mn55_ppm_2SE(int)	52.067	47.465	61.434	54.357	49.837	81.932	55.439	64.302
Co59_ppm_mean	22.808	40.591	23.863	36.967	38.300	23.427	37.460	37.162
Co59_ppm_2SE(int)	0.560	0.816	0.666	1.290	0.715	0.541	0.795	0.803
Ni60_ppm_mean	0.111	3.768	0.160	1.368	0.929	0.298	1.075	0.734
Ni60_ppm_2SE(int)	0.096	0.517	0.091	0.207	0.203	0.126	0.183	0.151
Cu63_ppm_mean	0.539	0.451	1.305	0.342	0.258	2.545	1.311	0.274
Cu63_ppm_2SE(int)	0.115	0.147	0.225	0.081	0.069	0.321	0.215	0.085
Zn66_ppm_mean	4.762	1.193	5.183	2.277	2.969	8.159	3.252	2.583
Zn66_ppm_2SE(int)	0.692	0.673	0.684	0.585	0.606	0.702	0.606	0.615
Rb85_ppm_mean	0.048	0.028	0.075	0.004	0.005	0.191	0.409	0.021
Rb85_ppm_2SE(int)	0.015	0.025	0.023	0.012	0.012	0.037	0.056	0.013
Sr88_ppm_mean	16.002	4.106	72.846	4.222	11.011	69.254	17.979	14.340
Sr88_ppm_2SE(int)	0.542	0.461	4.330	0.152	0.194	9.877	0.786	0.264
Y89_ppm_mean	143.323	7.004	124.932	16.527	43.254	371.816	38.589	51.730
Y89_ppm_2SE(int)	2.001	0.206	2.391	0.405	1.118	38.314	0.961	1.059
Zr90_ppm_mean	162.605	7.594	155.019	11.872	37.870	329.448	56.929	50.985
Zr90_ppm_2SE(int)	4.129	0.461	5.293	0.445	1.030	39.061	2.554	1.207
Nb93_ppm_mean	0.634	0.121	1.356	0.023	0.033	5.380	1.136	0.053
Nb93_ppm_2SE(int)	0.111	0.030	0.171	0.010	0.011	2.286	0.255	0.014
Hf178_ppm_mean	7.052	0.303	6.697	0.568	1.822	11.963	2.012	2.410
Hf178_ppm_2SE(int)	0.203	0.035	0.260	0.056	0.093	0.932	0.151	0.094
Ta181_ppm_mean	0.047	0.013	0.071	0.001	0.003	0.229	0.058	0.004
Ta181_ppm_2SE(int)	0.010	0.005	0.013	0.001	0.002	0.082	0.011	0.002
Pb208_ppm_mean	1.604	0.011	3.968	0.009	0.265	22.901	4.443	0.084
Pb208_ppm_2SE(int)	0.091	0.009	0.301	0.006	0.056	1.317	0.776	0.097
Th232_ppm_mean	0.118	0.008	0.224	0.000	0.002	5.263	0.121	0.005
Th232_ppm_2SE(int)	0.021	0.003	0.038	0.000	0.002	1.263	0.018	0.003
U238_ppm_mean	0.028	0.012	0.034	0.003	0.019	1.535	0.039	0.001
U238_ppm_2SE(int)	0.006	0.017	0.007	0.004	0.035	0.248	0.007	0.001

Table S4 cont.: Pyroxene trace element compositions.

Sample	12039	12039	12039	12039	12039	12039	12039	12043
Site	63-PYX-3.432	63-PYX-4.441	63-PYX-4.444	63-PYX-5.445	63-PYX-5.447	63-PYX-5.448	63-PYX-5.449	15-PYX.1.452
Si29_ppm_mean	432225.000	526267.000	432224.000	522533.000	442539.000	513052.000	476888.000	492387.000
Si29_ppm_2SE(int)	0.000	0.000	0.000	0.000	0.000	0.000	0.000	0.000
Ca43_ppm_mean	82179.958	62214.163	85469.308	68168.746	110844.379	65747.873	117199.155	38809.149
Ca43_ppm_2SE(int)	1154.645	1204.605	1294.845	1161.084	1661.757	1189.933	1642.833	847.896
Sc45_ppm_mean	52.868	66.682	37.790	72.627	89.554	67.054	101.369	48.584
Sc45_ppm_2SE(int)	1.033	1.317	0.655	1.520	1.361	1.110	1.401	0.977
Ti47_ppm_mean	4969.835	5241.608	4704.635	5873.230	6064.879	5471.930	6767.016	4279.420
Ti47_ppm_2SE(int)	65.431	89.936	78.342	113.983	85.740	93.469	99.369	137.638
V51_ppm_mean	12.013	457.885	7.011	556.094	25.249	475.828	35.246	394.120
V51_ppm_2SE(int)	0.339	11.198	0.217	12.519	2.082	9.154	0.686	7.522
Cr52_ppm_mean	263.985	5982.720	109.618	7047.264	499.229	6341.359	776.354	5971.675
Cr52_ppm_2SE(int)	6.242	92.100	2.884	106.684	9.212	121.520	10.514	115.099
Mn55_ppm_mean	4059.959	2760.785	4066.253	2597.811	3779.590	2560.713	3895.593	2415.285
Mn55_ppm_2SE(int)	56.882	44.009	55.321	46.295	52.675	41.433	45.759	40.664
Co59_ppm_mean	24.021	41.189	21.332	39.035	34.423	38.422	39.217	47.597
Co59_ppm_2SE(int)	0.641	0.915	0.469	0.930	0.614	0.695	0.689	1.458
Ni60_ppm_mean	0.140	2.768	0.127	3.242	0.737	2.827	0.867	6.725
Ni60_ppm_2SE(int)	0.079	0.296	0.085	0.317	0.155	0.270	0.169	0.632
Cu63_ppm_mean	0.160	0.432	3.168	3.770	0.681	0.447	0.219	2.585
Cu63_ppm_2SE(int)	0.060	0.065	0.588	0.234	0.094	0.082	0.066	0.361
Zn66_ppm_mean	3.941	2.659	3.547	3.645	2.742	2.154	2.542	2.164
Zn66_ppm_2SE(int)	0.610	0.644	0.588	0.562	0.588	0.650	0.547	0.709
Rb85_ppm_mean	0.027	0.022	0.153	0.042	0.020	0.003	0.016	0.903
Rb85_ppm_2SE(int)	0.015	0.013	0.032	0.018	0.011	0.014	0.013	0.079
Sr88_ppm_mean	9.426	1.483	30.581	2.207	11.489	1.774	9.934	7.206
Sr88_ppm_2SE(int)	0.216	0.074	2.842	0.160	0.237	0.113	0.227	0.580
Y89_ppm_mean	110.211	10.303	139.694	12.134	62.051	10.842	43.925	7.323
Y89_ppm_2SE(int)	2.274	0.263	2.891	0.327	1.128	0.225	0.805	0.257
Zr90_ppm_mean	113.023	6.630	205.137	10.005	59.333	7.880	39.544	13.677
Zr90_ppm_2SE(int)	2.863	0.274	11.125	0.441	1.066	0.344	0.936	0.763
Nb93_ppm_mean	0.128	0.029	3.211	0.045	0.051	0.037	0.055	0.844
Nb93_ppm_2SE(int)	0.022	0.011	0.381	0.017	0.014	0.014	0.016	0.083
Hf178_ppm_mean	5.378	0.312	7.800	0.511	2.934	0.425	1.882	0.393
Hf178_ppm_2SE(int)	0.209	0.040	0.322	0.049	0.100	0.051	0.102	0.042
Ta181_ppm_mean	0.008	0.000	0.172	0.002	0.005	0.006	0.006	0.043
Ta181_ppm_2SE(int)	0.003	0.000	0.025	0.002	0.003	0.003	0.003	0.009
Pb208_ppm_mean	0.707	41.341	0.153	3.310	0.341	2.593	0.030	0.114
Pb208_ppm_2SE(int)	0.060	5.176	0.027	0.122	0.070	0.296	0.013	0.018
Th232_ppm_mean	0.005	0.000	0.456	0.000	0.006	0.000	0.002	0.117
Th232_ppm_2SE(int)	0.002	0.000	0.067	0.000	0.003	0.000	0.001	0.017
U238_ppm_mean	0.003	0.001	0.129	0.000	0.002	0.000	0.002	0.033
U238_ppm_2SE(int)	0.001	0.001	0.022	0.000	0.001	0.000	0.001	0.005

Table S4 cont.: Pyroxene trace element compositions.

Sample	12043	12043	12043	12043	12043	12043	12043	12043
Site	15-PYX-1.453	15-PYX-1.454	15-PYX-1.455	15-PYX-1.456	15-PYX-3.469	15-PYX-3.470	15-PYX-3.471	15-PYX-3.478
Si29_ppm_mean	478458.000	493344.000	482726.000	455003.000	497828.000	474470.000	437741.000	437664.000
Si29_ppm_2SE(int)	0.000	0.000	0.000	0.000	0.000	0.000	0.000	0.000
Ca43_ppm_mean	104775.568	131080.264	70499.422	96593.244	42988.841	111017.520	101939.606	85128.565
Ca43_ppm_2SE(int)	3964.060	2127.766	2548.703	1872.421	1004.462	1871.861	1793.110	1338.844
Sc45_ppm_mean	74.243	108.319	68.636	82.343	53.376	85.780	103.640	71.652
Sc45_ppm_2SE(int)	1.909	1.833	1.418	1.786	1.162	1.694	1.623	1.126
Ti47_ppm_mean	8213.831	8592.896	4930.689	5483.627	3643.970	7647.817	7198.218	4798.631
Ti47_ppm_2SE(int)	163.252	136.632	113.278	101.619	57.670	112.848	103.544	62.710
V51_ppm_mean	212.870	96.118	475.360	40.448	417.269	114.082	53.600	26.624
V51_ppm_2SE(int)	8.319	1.933	8.449	1.058	8.273	2.059	1.497	0.650
Cr52_ppm_mean	2748.975	1747.099	6792.283	812.496	6345.823	1999.153	1142.016	530.795
Cr52_ppm_2SE(int)	115.710	29.066	133.648	20.581	151.361	31.323	29.506	8.447
Mn55_ppm_mean	2988.991	3274.929	2482.048	3847.026	2528.149	3156.446	3507.753	4056.421
Mn55_ppm_2SE(int)	53.914	50.365	33.331	76.156	46.086	53.026	54.838	86.497
Co59_ppm_mean	38.184	39.676	36.293	35.974	41.818	39.415	36.795	36.710
Co59_ppm_2SE(int)	1.352	0.974	0.702	0.810	0.863	0.826	0.829	0.680
Ni60_ppm_mean	2.680	2.239	2.901	0.910	4.613	1.908	1.207	0.932
Ni60_ppm_2SE(int)	0.306	0.285	0.299	0.177	0.516	0.283	0.184	0.163
Cu63_ppm_mean	5.260	0.912	0.219	0.448	0.255	0.496	0.230	0.272
Cu63_ppm_2SE(int)	1.597	0.352	0.058	0.079	0.078	0.086	0.065	0.067
Zn66_ppm_mean	1.339	1.751	1.858	2.100	2.136	2.226	1.658	2.208
Zn66_ppm_2SE(int)	0.542	0.638	0.581	0.546	0.895	0.522	0.392	0.452
Rb85_ppm_mean	0.428	0.200	0.006	0.224	0.017	0.049	0.008	0.031
Rb85_ppm_2SE(int)	0.061	0.046	0.010	0.227	0.017	0.018	0.012	0.015
Sr88_ppm_mean	22.008	11.597	1.219	9.708	0.428	5.915	5.531	6.123
Sr88_ppm_2SE(int)	1.829	1.073	0.111	0.915	0.039	0.266	0.158	0.205
Y89_ppm_mean	27.346	26.256	7.956	52.225	4.865	16.397	34.168	45.211
Y89_ppm_2SE(int)	0.947	0.684	0.309	1.223	0.143	0.311	0.612	0.691
Zr90_ppm_mean	61.579	29.126	4.742	61.953	2.479	15.052	27.786	35.116
Zr90_ppm_2SE(int)	5.038	1.655	0.303	6.322	0.153	0.709	0.627	0.734
Nb93_ppm_mean	2.968	0.749	0.026	1.552	0.019	0.168	0.043	0.100
Nb93_ppm_2SE(int)	0.345	0.140	0.011	0.317	0.008	0.036	0.011	0.023
Hf178_ppm_mean	1.978	1.323	0.273	2.655	0.136	0.749	1.544	1.887
Hf178_ppm_2SE(int)	0.146	0.092	0.038	0.213	0.026	0.063	0.099	0.094
Ta181_ppm_mean	0.173	0.040	0.000	0.070	0.000	0.010	0.004	0.008
Ta181_ppm_2SE(int)	0.024	0.011	0.000	0.018	0.001	0.004	0.002	0.003
Pb208_ppm_mean	0.172	0.059	0.013	0.092	0.011	0.080	0.012	0.019
Pb208_ppm_2SE(int)	0.024	0.015	0.006	0.032	0.006	0.128	0.008	0.015
Th232_ppm_mean	0.484	0.143	0.000	0.317	0.000	0.028	0.004	0.020
Th232_ppm_2SE(int)	0.046	0.022	0.000	0.085	0.000	0.008	0.002	0.005
U238_ppm_mean	0.138	0.036	0.000	0.184	0.000	0.007	0.003	0.007
U238_ppm_2SE(int)	0.018	0.007	0.000	0.148	0.000	0.003	0.002	0.003

Table S4 cont.: Pyroxene trace element compositions.

Sample	12043	12043	12043	12043	12043	12043	12043	12043
Site	15-PYX-3.480	15-PYX-4.481	15-PYX-4.482	15-PYX-4.483	15-PYX-5.484	15-PYX-5.485	15-PYX-4.486	15-PYX-4.489
Si29_ppm_mean	484816.000	514583.000	524935.000	468157.000	497283.000	495075.000	443325.000	453764.000
Si29_ppm_2SE(int)	0.000	0.000	0.000	0.000	0.000	0.000	0.000	0.000
Ca43_ppm_mean	157248.003	35484.183	80018.614	104778.755	36665.521	93466.495	80764.875	122682.049
Ca43_ppm_2SE(int)	2755.273	711.070	3689.733	2095.041	700.478	1470.132	1389.485	2132.324
Sc45_ppm_mean	109.674	50.867	74.965	82.016	48.539	77.809	52.021	104.017
Sc45_ppm_2SE(int)	1.794	0.918	2.139	1.742	0.918	1.350	0.938	3.932
Ti47_ppm_mean	9191.987	3510.568	5547.647	7723.953	3323.457	6756.510	4652.147	118552.763
Ti47_ppm_2SE(int)	117.760	54.309	207.856	128.602	53.143	109.636	96.175	23222.953
V51_ppm_mean	631.946	412.239	492.505	248.475	392.132	121.906	15.230	62.803
V51_ppm_2SE(int)	12.546	7.242	9.288	8.360	6.236	2.752	0.484	5.720
Cr52_ppm_mean	8399.838	6375.486	7136.061	4223.952	5974.980	2042.849	314.244	1112.864
Cr52_ppm_2SE(int)	130.196	104.479	139.894	105.585	108.042	52.538	5.278	82.284
Mn55_ppm_mean	2160.313	2462.995	2606.342	2623.494	2414.176	3464.637	4139.247	4475.822
Mn55_ppm_2SE(int)	34.051	35.781	32.976	51.605	43.511	43.012	62.909	182.697
Co59_ppm_mean	28.383	45.840	39.809	34.040	44.124	41.222	28.322	38.189
Co59_ppm_2SE(int)	0.566	0.982	0.866	0.620	0.937	0.590	0.844	1.789
Ni60_ppm_mean	2.218	6.708	3.265	1.673	5.563	1.845	0.380	1.158
Ni60_ppm_2SE(int)	0.256	0.478	0.345	0.237	0.501	0.224	0.149	0.286
Cu63_ppm_mean	0.380	0.129	0.315	0.360	0.196	1.725	14.589	2.139
Cu63_ppm_2SE(int)	0.083	0.057	0.090	0.100	0.066	0.188	5.253	0.474
Zn66_ppm_mean	1.484	1.837	1.976	1.829	2.215	1.313	2.488	6.606
Zn66_ppm_2SE(int)	0.584	0.430	0.643	0.552	0.543	0.692	0.461	1.219
Rb85_ppm_mean	0.003	0.008	0.052	0.029	0.017	0.157	0.118	0.038
Rb85_ppm_2SE(int)	0.014	0.011	0.025	0.015	0.012	0.027	0.029	0.019
Sr88_ppm_mean	5.290	0.348	2.459	7.307	0.377	8.480	29.249	10.580
Sr88_ppm_2SE(int)	0.150	0.037	0.263	1.264	0.034	0.531	1.034	0.407
Y89_ppm_mean	17.439	4.157	8.777	14.802	4.200	20.188	164.724	65.703
Y89_ppm_2SE(int)	0.306	0.136	0.404	0.336	0.144	0.569	6.382	1.607
Zr90_ppm_mean	15.378	1.889	6.492	12.495	2.019	25.102	529.511	157.047
Zr90_ppm_2SE(int)	0.450	0.136	0.448	0.448	0.125	1.337	57.100	18.484
Nb93_ppm_mean	0.048	0.022	0.076	0.135	0.017	0.810	10.011	36.575
Nb93_ppm_2SE(int)	0.015	0.011	0.018	0.034	0.009	0.085	1.700	5.707
Hf178_ppm_mean	1.007	0.131	0.356	0.765	0.134	0.988	16.309	6.246
Hf178_ppm_2SE(int)	0.078	0.025	0.045	0.064	0.026	0.070	1.447	0.597
Ta181_ppm_mean	0.008	0.000	0.003	0.008	0.001	0.030	0.688	2.540
Ta181_ppm_2SE(int)	0.003	0.000	0.002	0.004	0.001	0.007	0.106	0.412
Pb208_ppm_mean	0.004	0.006	0.036	0.052	0.017	0.045	1.860	0.042
Pb208_ppm_2SE(int)	0.005	0.005	0.011	0.011	0.006	0.010	0.229	0.012
Th232_ppm_mean	0.004	0.000	0.004	0.025	0.000	0.154	4.953	0.087
Th232_ppm_2SE(int)	0.002	0.000	0.002	0.008	0.001	0.022	0.358	0.015
U238_ppm_mean	0.002	0.000	0.001	0.011	0.000	0.030	1.825	0.081
U238_ppm_2SE(int)	0.002	0.000	0.001	0.004	0.000	0.006	0.221	0.014

Table S4 cont.: Pyroxene trace element compositions.

Sample	12043	15085	15085	15085	15085	15085	15085	15085
Site	15-PYX-4.490	16-PYX-1.218	16-PYX-1.219	16-PYX-1.220	16-PYX-1.221	16-PYX-1.222	16-PYX-2.226	16-PYX-2.227
Si29_ppm_mean	479269.000	454277.000	462830.000	494544.000	513783.000	531874.000	512114.000	519548.000
Si29_ppm_2SE(int)	0.000	0.000	0.000	0.000	0.000	0.000	0.000	0.000
Ca43_ppm_mean	75663.692	74617.176	93150.537	93451.031	28367.694	22701.645	118825.588	61521.159
Ca43_ppm_2SE(int)	1484.679	2441.080	1587.924	1882.872	738.096	532.200	2988.571	1131.184
Sc45_ppm_mean	84.248	66.806	75.687	66.385	30.383	27.830	66.711	47.849
Sc45_ppm_2SE(int)	1.433	1.224	1.208	1.324	0.809	0.701	1.501	1.078
Ti47_ppm_mean	7557.539	3125.429	5794.875	4145.104	1556.859	1242.132	3034.457	2616.472
Ti47_ppm_2SE(int)	100.376	103.321	259.687	65.852	38.428	18.015	68.742	48.809
V51_ppm_mean	219.079	16.454	54.562	281.426	259.912	273.405	558.961	306.949
V51_ppm_2SE(int)	4.141	0.785	1.270	4.756	5.121	4.856	13.352	6.445
Cr52_ppm_mean	3631.003	186.252	658.921	3585.400	4825.313	5391.853	6261.085	4307.816
Cr52_ppm_2SE(int)	66.263	9.896	17.842	60.201	89.884	106.049	122.788	93.990
Mn55_ppm_mean	3048.836	4446.106	3614.161	3078.312	2422.953	2398.745	2361.386	2827.599
Mn55_ppm_2SE(int)	49.728	77.310	50.041	57.459	38.609	49.152	51.293	72.865
Co59_ppm_mean	38.279	25.233	38.193	43.881	52.158	55.874	36.710	44.500
Co59_ppm_2SE(int)	0.782	0.613	0.949	0.823	0.985	1.131	0.980	0.994
Ni60_ppm_mean	1.990	0.710	3.884	7.340	18.062	33.459	8.785	7.379
Ni60_ppm_2SE(int)	0.243	0.167	0.758	0.570	0.964	1.153	0.630	0.570
Cu63_ppm_mean	0.275	0.532	7.104	0.640	0.732	0.210	0.286	0.461
Cu63_ppm_2SE(int)	0.068	0.393	2.561	0.105	0.177	0.076	0.076	0.091
Zn66_ppm_mean	1.628	3.088	3.075	1.488	1.242	1.480	1.105	1.428
Zn66_ppm_2SE(int)	0.469	0.592	0.630	0.639	0.720	0.732	0.567	0.618
Rb85_ppm_mean	0.040	0.039	0.528	0.007	0.012	-0.004	0.008	0.148
Rb85_ppm_2SE(int)	0.024	0.015	0.064	0.015	0.014	0.013	0.013	0.075
Sr88_ppm_mean	2.699	6.259	24.041	3.876	1.652	0.164	3.555	1.973
Sr88_ppm_2SE(int)	0.381	0.245	2.505	0.266	0.212	0.024	0.146	0.499
Y89_ppm_mean	13.408	107.414	34.519	8.576	2.202	1.254	6.565	4.897
Y89_ppm_2SE(int)	0.336	3.488	1.561	0.241	0.132	0.081	0.235	0.199
Zr90_ppm_mean	10.570	32.094	61.339	5.797	2.430	0.535	3.658	4.089
Zr90_ppm_2SE(int)	0.628	0.923	6.994	0.359	0.240	0.081	0.215	0.574
Nb93_ppm_mean	0.133	0.118	1.957	0.134	0.103	0.013	0.020	0.159
Nb93_ppm_2SE(int)	0.035	0.032	0.470	0.033	0.029	0.008	0.009	0.052
Hf178_ppm_mean	0.630	1.361	2.091	0.253	0.097	0.015	0.205	0.170
Hf178_ppm_2SE(int)	0.064	0.079	0.244	0.039	0.024	0.009	0.034	0.033
Ta181_ppm_mean	0.010	0.007	0.114	0.005	0.003	0.000	0.001	0.008
Ta181_ppm_2SE(int)	0.004	0.003	0.025	0.003	0.002	0.000	0.001	0.004
Pb208_ppm_mean	0.018	0.258	0.135	0.060	0.140	0.209	0.085	0.078
Pb208_ppm_2SE(int)	0.007	0.022	0.023	0.044	0.023	0.025	0.018	0.024
Th232_ppm_mean	0.023	0.015	0.362	0.012	0.005	0.000	0.002	0.008
Th232_ppm_2SE(int)	0.009	0.007	0.054	0.006	0.003	0.000	0.002	0.004
U238_ppm_mean	0.008	0.003	0.085	0.003	0.003	0.000	0.000	0.005
U238_ppm_2SE(int)	0.003	0.002	0.018	0.002	0.002	0.000	0.000	0.006

Table S4 cont.: Pyroxene trace element compositions.

Sample	15085	15085	15085	15085	15085	15085	15085	15085
Site	16-PYX-2.228	16-PYX-2.229	16-PYX-2.230	16-PYX-3.233	16-PYX-3.234	16-PYX-3.237	16-PYX-4.239	16-PYX-4.240
Si29_ppm_mean	513426.000	491597.000	488504.000	511807.000	531057.000	478305.000	481402.000	488817.000
Si29_ppm_2SE(int)	0.000	0.000	0.000	0.000	0.000	0.000	0.000	0.000
Ca43_ppm_mean	64772.219	86214.194	150760.176	142394.670	19356.962	82322.757	68872.485	68481.941
Ca43_ppm_2SE(int)	1334.977	1353.584	2795.108	2709.859	577.370	1739.504	1423.568	1195.073
Sc45_ppm_mean	49.069	70.204	80.796	68.400	23.457	57.197	54.262	61.885
Sc45_ppm_2SE(int)	0.977	1.529	1.668	1.683	0.777	1.210	1.097	1.152
Ti47_ppm_mean	2657.507	4346.587	4597.832	6214.928	1099.380	3459.515	3262.446	3748.757
Ti47_ppm_2SE(int)	45.792	84.907	79.583	169.464	25.322	79.370	83.290	64.241
V51_ppm_mean	216.937	185.304	433.737	452.720	249.902	203.100	199.298	192.739
V51_ppm_2SE(int)	4.269	4.165	9.718	12.043	7.384	5.031	5.312	3.717
Cr52_ppm_mean	3590.131	3099.065	5633.480	5308.344	5400.211	3407.603	3408.822	3312.060
Cr52_ppm_2SE(int)	90.541	76.263	124.405	104.984	147.085	76.366	82.140	67.616
Mn55_ppm_mean	2974.881	3289.760	2095.681	2239.818	2258.091	2922.771	3009.491	3214.029
Mn55_ppm_2SE(int)	61.474	61.880	42.038	42.923	65.955	70.188	63.899	56.450
Co59_ppm_mean	46.607	47.154	31.628	31.295	58.294	44.403	45.442	48.201
Co59_ppm_2SE(int)	1.487	1.421	0.912	0.826	1.716	1.016	0.991	1.089
Ni60_ppm_mean	7.731	6.880	6.096	6.285	45.111	7.172	7.331	8.110
Ni60_ppm_2SE(int)	0.574	0.537	0.450	0.538	1.612	0.462	0.457	0.593
Cu63_ppm_mean	0.150	0.459	0.604	0.456	0.165	0.285	0.356	0.273
Cu63_ppm_2SE(int)	0.057	0.071	0.105	0.119	0.063	0.077	0.086	0.066
Zn66_ppm_mean	2.203	1.390	2.400	2.677	1.659	1.828	1.460	2.096
Zn66_ppm_2SE(int)	0.651	0.459	0.604	0.811	0.662	0.594	0.604	0.683
Rb85_ppm_mean	-0.010	-0.006	0.034	1.118	-0.004	0.012	0.001	0.109
Rb85_ppm_2SE(int)	0.013	0.013	0.022	0.176	0.016	0.025	0.014	0.215
Sr88_ppm_mean	1.000	2.388	7.146	11.292	0.141	2.087	1.556	1.394
Sr88_ppm_2SE(int)	0.062	0.104	0.507	0.623	0.025	0.093	0.134	0.068
Y89_ppm_mean	4.953	7.879	11.012	14.316	0.955	6.591	5.958	6.574
Y89_ppm_2SE(int)	0.191	0.192	0.257	0.362	0.060	0.190	0.221	0.187
Zr90_ppm_mean	1.871	3.967	9.662	23.922	0.367	3.037	3.010	2.823
Zr90_ppm_2SE(int)	0.146	0.216	0.633	0.834	0.062	0.183	0.266	0.154
Nb93_ppm_mean	0.006	0.015	0.314	0.625	0.021	0.016	0.033	0.011
Nb93_ppm_2SE(int)	0.005	0.008	0.117	0.117	0.011	0.008	0.017	0.007
Hf178_ppm_mean	0.089	0.189	0.415	0.865	0.020	0.180	0.143	0.156
Hf178_ppm_2SE(int)	0.021	0.028	0.049	0.071	0.011	0.023	0.031	0.027
Ta181_ppm_mean	0.001	0.000	0.016	0.043	0.000	0.000	0.005	0.000
Ta181_ppm_2SE(int)	0.001	0.000	0.006	0.013	0.000	0.000	0.003	0.000
Pb208_ppm_mean	0.022	0.085	0.060	0.073	0.050	0.024	0.004	0.018
Pb208_ppm_2SE(int)	0.010	0.027	0.013	0.021	0.017	0.010	0.004	0.008
Th232_ppm_mean	0.000	0.000	0.016	0.056	0.000	0.002	0.002	0.000
Th232_ppm_2SE(int)	0.000	0.001	0.007	0.025	0.000	0.003	0.002	0.000
U238_ppm_mean	0.001	0.000	0.006	0.014	0.000	0.179	0.001	0.000
U238_ppm_2SE(int)	0.001	0.000	0.003	0.006	0.000	0.248	0.001	0.000

Table S4 cont.: Pyroxene trace element compositions.

Sample	15085	15085	15085	15085	15085	15085	15085	15085
Site	16-PYX-4.241	16-PYX-4.242	16-PYX-4.243	16-PYX-5.248	16-PYX-5.249	16-PYX-5.250	16-PYX-5.251	16-PYX-5.252
Si29_ppm_mean	472494.000	462219.000	465500.000	516721.000	490922.000	481283.000	479811.000	482301.000
Si29_ppm_2SE(int)	0.000	0.000	0.000	0.000	0.000	0.000	0.000	0.000
Ca43_ppm_mean	76740.364	96287.515	109632.826	19141.348	22791.269	68812.954	87158.792	86732.940
Ca43_ppm_2SE(int)	1576.462	1645.907	1911.696	481.084	587.259	1236.058	2054.250	1942.083
Sc45_ppm_mean	69.951	78.830	74.409	20.670	26.568	53.927	60.294	69.252
Sc45_ppm_2SE(int)	1.392	1.393	1.439	0.572	0.606	1.091	1.457	1.342
Ti47_ppm_mean	4502.383	4931.100	5351.404	867.186	1206.652	3235.012	3644.351	4642.800
Ti47_ppm_2SE(int)	83.898	82.332	82.813	19.046	20.393	50.337	83.352	97.758
V51_ppm_mean	168.958	52.325	46.709	200.266	258.826	225.683	196.602	131.434
V51_ppm_2SE(int)	3.415	0.855	0.955	4.083	5.596	4.653	3.720	3.207
Cr52_ppm_mean	2755.740	630.684	511.217	4711.651	4936.063	3734.229	3221.667	2074.217
Cr52_ppm_2SE(int)	55.013	11.994	11.017	103.810	108.668	61.108	68.011	55.083
Mn55_ppm_mean	3352.459	3531.807	3395.668	2265.708	2268.627	2829.930	2926.732	3395.993
Mn55_ppm_2SE(int)	59.349	54.983	58.733	43.968	47.277	49.184	53.229	71.162
Co59_ppm_mean	45.413	37.874	32.650	55.889	51.112	43.724	43.752	46.657
Co59_ppm_2SE(int)	1.073	0.737	0.832	1.410	1.274	1.048	0.875	1.004
Ni60_ppm_mean	6.676	4.318	3.366	45.453	25.220	8.368	7.564	7.685
Ni60_ppm_2SE(int)	0.506	0.386	0.389	1.581	1.327	1.016	0.532	0.626
Cu63_ppm_mean	0.672	0.730	0.571	0.153	0.137	1.195	0.405	0.437
Cu63_ppm_2SE(int)	0.163	0.156	0.168	0.083	0.070	0.472	0.107	0.114
Zn66_ppm_mean	1.645	3.009	3.430	1.204	0.999	1.032	2.369	2.745
Zn66_ppm_2SE(int)	0.602	0.544	0.655	0.619	0.732	0.744	0.693	0.693
Rb85_ppm_mean	0.007	1.995	1.454	0.020	0.034	0.112	0.101	0.024
Rb85_ppm_2SE(int)	0.012	0.274	0.366	0.013	0.033	0.030	0.168	0.017
Sr88_ppm_mean	2.959	58.934	42.825	0.122	0.178	4.259	2.483	2.617
Sr88_ppm_2SE(int)	0.220	7.245	6.920	0.021	0.042	0.548	0.114	0.121
Y89_ppm_mean	9.315	45.184	65.984	0.839	1.149	6.115	7.065	8.500
Y89_ppm_2SE(int)	0.220	2.981	2.742	0.074	0.058	0.163	0.238	0.267
Zr90_ppm_mean	6.677	112.193	132.812	0.251	0.461	4.526	3.141	4.142
Zr90_ppm_2SE(int)	0.340	11.687	14.780	0.047	0.062	0.269	0.249	0.211
Nb93_ppm_mean	0.121	2.908	4.163	0.005	0.019	0.220	0.015	0.018
Nb93_ppm_2SE(int)	0.025	0.385	0.486	0.005	0.011	0.042	0.009	0.009
Hf178_ppm_mean	0.282	2.989	4.421	0.009	0.019	0.214	0.188	0.168
Hf178_ppm_2SE(int)	0.040	0.304	0.411	0.007	0.010	0.031	0.028	0.029
Ta181_ppm_mean	0.005	0.195	0.232	0.000	0.017	0.007	0.001	0.000
Ta181_ppm_2SE(int)	0.002	0.028	0.037	0.000	0.032	0.004	0.001	0.000
Pb208_ppm_mean	0.054	0.718	0.350	0.047	0.083	0.032	0.127	0.098
Pb208_ppm_2SE(int)	0.011	0.135	0.104	0.013	0.015	0.011	0.021	0.016
Th232_ppm_mean	0.012	1.265	0.793	0.000	0.002	0.015	0.000	0.000
Th232_ppm_2SE(int)	0.005	0.227	0.160	0.000	0.003	0.005	0.000	0.000
U238_ppm_mean	0.001	0.357	0.279	0.000	0.204	0.006	0.000	0.001
U238_ppm_2SE(int)	0.001	0.067	0.205	0.000	0.283	0.003	0.000	0.001

Table S4 cont.: Pyroxene trace element compositions.

Sample	15085	15085	15085	15085	15085	15085	15085	15085
Site	16-PYX-6.253	16-PYX-6.254	16-PYX-6.255	16-PYX-7.262	16-PYX-7.263	16-PYX-7.264	16-PYX-7.265	16-PYX-7.266
Si29_ppm_mean	482651.000	483614.000	480350.000	507262.000	505203.000	500070.000	489147.000	467292.000
Si29_ppm_2SE(int)	0.000	0.000	0.000	0.000	0.000	0.000	0.000	0.000
Ca43_ppm_mean	185555.686	138164.676	19602.156	20470.591	50086.777	122277.422	82662.360	82212.367
Ca43_ppm_2SE(int)	3164.667	2496.452	460.324	513.775	1138.569	2595.104	1586.374	1834.184
Sc45_ppm_mean	72.889	73.371	23.753	24.247	38.239	62.461	61.349	70.352
Sc45_ppm_2SE(int)	1.647	1.640	0.645	0.641	1.072	1.729	1.286	1.766
Ti47_ppm_mean	7427.392	4015.932	1095.883	1148.069	1807.361	2917.689	3716.622	4572.653
Ti47_ppm_2SE(int)	143.002	94.938	24.556	25.387	46.494	62.131	74.065	109.127
V51_ppm_mean	29.659	469.313	235.895	259.201	296.068	542.802	246.592	163.827
V51_ppm_2SE(int)	0.709	9.151	4.907	6.385	6.923	15.930	5.640	4.008
Cr52_ppm_mean	329.671	5432.723	4802.866	4949.211	4257.133	5760.360	3998.760	2650.908
Cr52_ppm_2SE(int)	6.531	135.663	94.605	109.416	83.583	134.772	88.319	63.700
Mn55_ppm_mean	2645.542	2176.385	2145.021	2283.539	2513.534	2205.323	2911.367	3176.065
Mn55_ppm_2SE(int)	49.630	46.361	41.452	33.842	63.127	58.969	58.951	65.653
Co59_ppm_mean	18.711	32.464	51.710	54.496	42.811	34.601	45.067	44.303
Co59_ppm_2SE(int)	0.534	0.837	1.054	1.373	1.450	1.225	1.030	1.082
Ni60_ppm_mean	0.817	6.225	30.560	29.489	9.517	7.994	8.282	7.103
Ni60_ppm_2SE(int)	0.184	0.412	1.117	1.299	0.730	0.674	0.614	0.515
Cu63_ppm_mean	0.835	0.530	0.199	0.113	0.284	0.131	0.154	0.228
Cu63_ppm_2SE(int)	0.144	0.193	0.074	0.070	0.105	0.066	0.065	0.076
Zn66_ppm_mean	2.828	1.616	1.726	1.875	1.355	1.443	1.265	0.814
Zn66_ppm_2SE(int)	0.727	0.687	0.623	0.588	0.609	0.723	0.742	0.568
Rb85_ppm_mean	0.072	0.016	0.014	0.028	0.041	0.041	0.017	0.013
Rb85_ppm_2SE(int)	0.022	0.014	0.012	0.017	0.019	0.019	0.027	0.017
Sr88_ppm_mean	65.244	5.521	0.147	0.139	2.064	3.595	2.009	2.454
Sr88_ppm_2SE(int)	1.349	0.201	0.025	0.020	0.195	0.167	0.093	0.115
Y89_ppm_mean	152.982	8.967	0.970	1.120	2.993	6.239	6.995	8.245
Y89_ppm_2SE(int)	2.546	0.253	0.066	0.083	0.132	0.205	0.231	0.267
Zr90_ppm_mean	314.224	6.550	0.363	0.448	2.108	3.424	3.333	4.266
Zr90_ppm_2SE(int)	5.459	0.334	0.060	0.067	0.212	0.221	0.223	0.212
Nb93_ppm_mean	0.629	0.065	0.013	0.009	0.073	0.021	0.018	0.015
Nb93_ppm_2SE(int)	0.142	0.021	0.010	0.007	0.021	0.010	0.010	0.008
Hf178_ppm_mean	14.212	0.337	0.019	0.017	0.085	0.184	0.181	0.213
Hf178_ppm_2SE(int)	0.430	0.047	0.009	0.009	0.022	0.030	0.036	0.035
Ta181_ppm_mean	0.051	0.002	0.000	0.000	0.007	0.000	0.000	0.000
Ta181_ppm_2SE(int)	0.013	0.002	0.001	0.000	0.004	0.000	0.000	0.000
Pb208_ppm_mean	2.211	0.036	0.069	0.004	0.029	0.186	0.090	0.002
Pb208_ppm_2SE(int)	0.119	0.010	0.012	0.005	0.010	0.027	0.016	0.004
Th232_ppm_mean	0.100	0.003	0.000	0.000	0.004	0.001	0.000	0.000
Th232_ppm_2SE(int)	0.025	0.002	0.001	0.000	0.002	0.001	0.000	0.000
U238_ppm_mean	0.030	0.001	0.000	0.000	0.003	0.000	0.001	0.001
U238_ppm_2SE(int)	0.009	0.001	0.000	0.000	0.002	0.000	0.001	0.001

Table S4 cont.: Pyroxene trace element compositions.

Sample	15085	15085	15085	15085	15085	15085	15085	15085
Site	16-PYX-7.267	16-PYX-8.268	16-PYX-8.269	16-PYX-8.270	16-PYX-8.271	24-PYX-1.369	24-PYX-1.370	24-PYX-1.371
Si29_ppm_mean	465536.000	485325.000	489884.000	491038.000	475765.000	516524.000	516910.000	509975.000
Si29_ppm_2SE(int)	0.000	0.000	0.000	0.000	0.000	0.000	0.000	0.000
Ca43_ppm_mean	84776.584	47802.398	61311.080	76532.966	65462.050	21804.165	54972.213	78504.377
Ca43_ppm_2SE(int)	1794.642	1172.236	1145.451	1514.865	1149.413	532.898	943.217	1178.885
Sc45_ppm_mean	77.226	39.349	54.526	59.345	64.985	26.949	43.180	60.701
Sc45_ppm_2SE(int)	1.977	0.962	0.867	1.299	1.317	0.591	0.996	1.213
Ti47_ppm_mean	5439.578	2061.295	3345.244	3498.293	4103.680	1252.222	2046.001	3556.115
Ti47_ppm_2SE(int)	110.451	56.513	48.320	61.202	71.774	22.171	40.358	53.269
V51_ppm_mean	121.162	294.941	244.307	213.979	161.315	270.562	311.227	235.044
V51_ppm_2SE(int)	2.537	5.751	4.685	4.152	3.106	4.261	5.454	3.623
Cr52_ppm_mean	1762.096	4055.855	3842.941	3653.191	2770.398	5303.660	4363.153	3913.533
Cr52_ppm_2SE(int)	40.960	62.399	69.449	72.943	49.434	93.273	70.104	61.254
Mn55_ppm_mean	3227.039	2516.656	2814.639	2987.226	3335.459	2298.975	2700.384	3034.127
Mn55_ppm_2SE(int)	72.582	42.870	46.327	49.698	57.956	49.281	54.220	40.784
Co59_ppm_mean	42.189	42.319	44.017	45.687	47.313	55.305	43.559	46.057
Co59_ppm_2SE(int)	1.085	0.916	0.870	0.853	0.978	1.059	1.201	0.816
Ni60_ppm_mean	6.217	11.318	8.398	7.138	7.325	34.420	9.597	8.145
Ni60_ppm_2SE(int)	0.567	1.504	0.723	0.635	0.509	1.197	0.623	0.598
Cu63_ppm_mean	0.255	0.881	0.472	0.374	0.168	0.868	0.525	0.455
Cu63_ppm_2SE(int)	0.087	0.344	0.147	0.175	0.063	0.127	0.109	0.129
Zn66_ppm_mean	2.276	2.065	1.448	1.203	2.621	2.212	2.127	2.086
Zn66_ppm_2SE(int)	0.693	0.690	0.775	0.589	0.657	0.691	0.575	0.538
Rb85_ppm_mean	0.021	0.063	0.043	-0.001	0.033	0.008	0.025	0.002
Rb85_ppm_2SE(int)	0.015	0.025	0.020	0.014	0.054	0.015	0.015	0.012
Sr88_ppm_mean	2.987	6.837	3.990	1.784	1.345	0.184	1.088	1.666
Sr88_ppm_2SE(int)	0.121	0.563	0.583	0.101	0.076	0.073	0.136	0.081
Y89_ppm_mean	11.860	3.575	6.278	6.479	6.717	1.096	3.409	6.365
Y89_ppm_2SE(int)	0.483	0.167	0.213	0.219	0.168	0.064	0.129	0.198
Zr90_ppm_mean	8.983	5.483	6.063	3.176	3.085	0.456	1.964	3.012
Zr90_ppm_2SE(int)	0.641	0.626	0.500	0.227	0.159	0.059	0.176	0.200
Nb93_ppm_mean	0.064	0.423	0.261	0.019	0.020	0.033	0.036	0.019
Nb93_ppm_2SE(int)	0.021	0.062	0.044	0.011	0.012	0.041	0.014	0.010
Hf178_ppm_mean	0.331	0.177	0.226	0.126	0.137	0.017	0.078	0.183
Hf178_ppm_2SE(int)	0.041	0.043	0.036	0.026	0.031	0.009	0.016	0.032
Ta181_ppm_mean	0.001	0.024	0.020	0.001	0.000	0.000	0.002	0.000
Ta181_ppm_2SE(int)	0.002	0.007	0.006	0.001	0.001	0.000	0.002	0.000
Pb208_ppm_mean	0.045	0.062	0.027	0.084	0.054	0.154	0.288	0.120
Pb208_ppm_2SE(int)	0.012	0.021	0.009	0.016	0.103	0.019	0.061	0.020
Th232_ppm_mean	0.014	0.038	0.022	0.001	0.000	0.000	0.000	0.000
Th232_ppm_2SE(int)	0.005	0.007	0.007	0.001	0.001	0.000	0.000	0.000
U238_ppm_mean	0.003	0.012	0.012	0.001	0.001	0.000	0.022	0.001
U238_ppm_2SE(int)	0.002	0.004	0.009	0.001	0.001	0.000	0.042	0.002

Table S4 cont.: Pyroxene trace element compositions.

Sample	15085	15085	15085	15085	15085	15085	15085	15085
Site	24-PYX-1.372	24-PYX-2.377	24-PYX-2.379	24-PYX-2.381	24-PYX-2.383	24-PYX-2.384	24-PYX-3.388	24-PYX-3.392
Si29_ppm_mean	476118.000	530556.000	491913.000	504424.000	498823.000	469295.000	510926.000	501625.000
Si29_ppm_2SE(int)	0.000	0.000	0.000	0.000	0.000	0.000	0.000	0.000
Ca43_ppm_mean	99023.415	19241.766	144739.373	40426.050	76286.604	84550.821	19813.835	154273.722
Ca43_ppm_2SE(int)	1659.525	606.764	2367.641	930.166	1635.794	1483.068	508.018	3028.578
Sc45_ppm_mean	81.190	27.362	79.593	33.041	56.028	71.049	23.624	76.901
Sc45_ppm_2SE(int)	1.440	0.797	1.450	0.856	1.363	1.385	0.588	1.547
Ti47_ppm_mean	5955.540	1287.581	4263.522	1706.236	3253.054	4907.036	1122.982	3904.501
Ti47_ppm_2SE(int)	93.398	28.480	69.435	39.514	63.430	86.096	25.392	67.527
V51_ppm_mean	93.368	289.688	485.677	265.595	246.004	139.910	244.417	549.059
V51_ppm_2SE(int)	1.703	5.792	9.610	5.550	5.634	2.173	4.734	9.213
Cr52_ppm_mean	1197.559	5878.595	5926.918	3994.893	4059.434	2217.619	5134.120	6221.254
Cr52_ppm_2SE(int)	27.018	133.339	110.032	81.422	71.121	37.326	104.952	132.602
Mn55_ppm_mean	3379.808	2162.715	2092.865	2545.649	2817.897	3328.355	2225.401	2014.941
Mn55_ppm_2SE(int)	51.418	42.554	36.476	46.411	50.299	61.792	45.011	39.011
Co59_ppm_mean	43.086	57.429	32.183	44.740	43.095	45.375	54.079	30.557
Co59_ppm_2SE(int)	0.874	1.526	0.756	0.965	1.002	0.892	1.015	0.723
Ni60_ppm_mean	5.919	71.628	6.713	9.389	7.848	7.416	43.008	6.951
Ni60_ppm_2SE(int)	0.539	2.320	0.614	0.519	0.527	0.497	1.625	0.435
Cu63_ppm_mean	2.549	0.272	1.405	0.517	0.521	0.232	0.283	0.627
Cu63_ppm_2SE(int)	0.839	0.102	0.122	0.110	0.114	0.064	0.119	0.101
Zn66_ppm_mean	2.022	1.689	1.592	2.836	2.063	1.869	1.631	1.184
Zn66_ppm_2SE(int)	0.500	0.544	0.560	0.893	0.583	0.462	0.661	0.538
Rb85_ppm_mean	0.270	0.089	0.033	0.037	0.008	0.010	0.012	0.007
Rb85_ppm_2SE(int)	0.041	0.095	0.013	0.043	0.012	0.011	0.011	0.014
Sr88_ppm_mean	21.125	0.137	5.230	1.087	1.648	2.573	0.135	5.614
Sr88_ppm_2SE(int)	2.718	0.025	0.168	0.212	0.074	0.102	0.021	0.220
Y89_ppm_mean	15.998	1.242	9.664	2.693	5.792	8.504	1.044	8.693
Y89_ppm_2SE(int)	1.157	0.079	0.227	0.122	0.176	0.244	0.065	0.257
Zr90_ppm_mean	25.936	0.547	6.457	1.849	2.823	4.224	0.387	5.534
Zr90_ppm_2SE(int)	5.113	0.079	0.265	0.214	0.189	0.220	0.048	0.267
Nb93_ppm_mean	0.617	0.009	0.014	0.058	0.021	0.016	0.010	0.025
Nb93_ppm_2SE(int)	0.151	0.006	0.008	0.021	0.010	0.008	0.006	0.012
Hf178_ppm_mean	0.776	0.019	0.325	0.079	0.132	0.187	0.016	0.295
Hf178_ppm_2SE(int)	0.143	0.008	0.046	0.020	0.021	0.032	0.008	0.032
Ta181_ppm_mean	0.049	0.000	0.001	0.002	0.001	0.000	0.000	0.001
Ta181_ppm_2SE(int)	0.016	0.001	0.001	0.002	0.001	0.000	0.000	0.001
Pb208_ppm_mean	0.331	0.018	0.297	0.074	0.047	-0.001	0.034	0.557
Pb208_ppm_2SE(int)	0.030	0.010	0.028	0.015	0.010	0.003	0.023	0.052
Th232_ppm_mean	0.181	0.000	0.001	0.004	0.002	0.000	0.000	0.001
Th232_ppm_2SE(int)	0.036	0.000	0.001	0.003	0.003	0.000	0.000	0.001
U238_ppm_mean	0.045	0.000	0.000	0.002	0.001	0.002	0.094	0.001
U238_ppm_2SE(int)	0.012	0.000	0.000	0.001	0.001	0.002	0.185	0.001

Table S4 cont.: Pyroxene trace element compositions.

Sample	15085	15085	15085	15085	15085	15085	15085	15085
Site	24-PYX-3.393	24-PYX-3.394	24-PYX-3.395	24-PYX-3.396	24-PYX-4.397	24-PYX-4.298	24-PYX-4.399	24-PYX-4.400
Si29_ppm_mean	491503.000	482488.000	465351.000	460433.000	502159.000	507932.000	491476.000	472633.000
Si29_ppm_2SE(int)	0.000	0.000	0.000	0.000	0.000	0.000	0.000	0.000
Ca43_ppm_mean	134253.652	113634.991	115268.813	103926.237	44520.072	46472.108	100661.146	119764.879
Ca43_ppm_2SE(int)	2269.623	2476.002	1907.613	1864.866	1077.381	922.152	1784.243	1826.743
Sc45_ppm_mean	77.833	78.126	83.546	91.473	35.682	40.058	79.091	106.031
Sc45_ppm_2SE(int)	1.300	1.646	1.677	1.845	0.892	0.745	1.149	1.463
Ti47_ppm_mean	4843.381	5057.449	5966.113	5512.830	1999.465	2067.972	5195.243	6163.823
Ti47_ppm_2SE(int)	73.329	91.226	96.913	119.704	76.025	28.215	73.854	80.032
V51_ppm_mean	290.189	209.997	72.622	63.918	261.829	304.718	123.811	71.149
V51_ppm_2SE(int)	6.969	4.727	1.765	1.345	5.954	4.570	2.897	1.111
Cr52_ppm_mean	4324.126	3276.372	803.715	873.885	3977.153	4337.429	1884.039	983.291
Cr52_ppm_2SE(int)	91.685	67.443	19.596	18.065	79.134	60.523	30.082	21.091
Mn55_ppm_mean	2617.273	3053.605	3104.818	3385.235	2548.677	2651.353	3428.736	3322.469
Mn55_ppm_2SE(int)	46.929	55.964	57.560	55.346	46.672	34.150	47.693	46.988
Co59_ppm_mean	39.567	42.868	39.881	39.020	43.828	44.407	44.725	39.838
Co59_ppm_2SE(int)	0.897	1.067	0.934	0.823	1.016	0.810	0.738	0.757
Ni60_ppm_mean	7.595	7.279	6.071	5.870	8.556	8.216	6.981	5.990
Ni60_ppm_2SE(int)	0.491	0.533	0.352	0.387	0.457	0.480	0.403	0.450
Cu63_ppm_mean	1.847	1.295	0.725	1.592	0.532	1.630	1.528	1.439
Cu63_ppm_2SE(int)	0.205	0.173	0.093	0.160	0.126	0.146	0.279	0.156
Zn66_ppm_mean	1.282	2.422	2.226	2.300	1.573	1.810	1.856	1.552
Zn66_ppm_2SE(int)	0.549	0.567	0.467	0.478	0.529	0.636	0.584	0.517
Rb85_ppm_mean	0.005	0.027	0.001	0.011	0.132	0.045	0.027	0.014
Rb85_ppm_2SE(int)	0.016	0.018	0.011	0.013	0.030	0.016	0.015	0.012
Sr88_ppm_mean	5.442	5.018	5.493	6.371	15.303	2.097	4.533	6.695
Sr88_ppm_2SE(int)	0.139	0.229	0.144	0.212	2.244	0.281	0.286	0.171
Y89_ppm_mean	9.831	9.510	12.209	20.491	3.289	3.229	11.765	19.623
Y89_ppm_2SE(int)	0.281	0.262	0.274	0.509	0.229	0.126	0.296	0.409
Zr90_ppm_mean	5.803	6.293	6.943	12.997	6.710	3.315	7.267	12.646
Zr90_ppm_2SE(int)	0.235	0.302	0.235	0.419	1.141	0.271	0.289	0.373
Nb93_ppm_mean	0.019	0.114	0.019	0.023	0.781	0.085	0.055	0.031
Nb93_ppm_2SE(int)	0.008	0.035	0.014	0.009	0.145	0.024	0.020	0.012
Hf178_ppm_mean	0.308	0.315	0.353	0.729	0.157	0.130	0.368	0.640
Hf178_ppm_2SE(int)	0.037	0.035	0.036	0.053	0.032	0.025	0.042	0.046
Ta181_ppm_mean	0.000	0.001	0.002	0.002	0.040	0.008	0.003	0.000
Ta181_ppm_2SE(int)	0.001	0.001	0.001	0.002	0.010	0.003	0.002	0.000
Pb208_ppm_mean	0.282	0.350	0.142	0.194	0.164	0.264	0.183	0.121
Pb208_ppm_2SE(int)	0.028	0.031	0.023	0.022	0.023	0.027	0.027	0.017
Th232_ppm_mean	0.000	0.005	0.000	0.005	0.067	0.009	0.010	0.000
Th232_ppm_2SE(int)	0.000	0.002	0.001	0.007	0.015	0.004	0.004	0.000
U238_ppm_mean	0.000	0.005	0.001	0.002	0.020	0.004	0.020	0.001
U238_ppm_2SE(int)	0.000	0.003	0.001	0.001	0.005	0.003	0.035	0.001

Table S4 cont.: Pyroxene trace element compositions.

Sample	15085	15085	15085	15085	15085	15085	15085	15085
Site	26-PYX-1.277	26-PYX-1.278	26-PYX-1.279	26-PYX-1.280	26-PYX-2.288	26-PYX-2.289	26-PYX-2.290	26-PYX-3.291
Si29_ppm_mean	487248.000	505626.000	482233.000	468761.000	513308.000	511413.000	511753.000	505391.000
Si29_ppm_2SE(int)	0.000	0.000	0.000	0.000	0.000	0.000	0.000	0.000
Ca43_ppm_mean	17064.772	18317.266	110756.992	93151.978	18978.176	66614.291	122389.081	74141.601
Ca43_ppm_2SE(int)	484.840	544.163	2431.115	1791.568	552.619	1287.038	2306.731	1062.456
Sc45_ppm_mean	22.705	22.636	63.739	80.642	23.555	44.538	71.935	65.469
Sc45_ppm_2SE(int)	0.735	0.658	1.135	1.295	0.666	0.864	1.611	0.950
Ti47_ppm_mean	1042.172	1047.236	5940.843	5651.992	1102.046	2177.050	4098.470	3781.709
Ti47_ppm_2SE(int)	29.044	24.727	336.823	89.223	27.176	42.166	65.018	46.854
V51_ppm_mean	242.783	232.494	218.832	127.978	247.714	342.409	352.861	239.105
V51_ppm_2SE(int)	5.558	5.079	6.429	2.651	6.228	6.244	6.738	4.122
Cr52_ppm_mean	5078.675	5113.494	3231.373	1883.617	5323.486	4551.198	5021.157	3912.055
Cr52_ppm_2SE(int)	137.574	101.244	102.525	33.394	100.490	84.989	93.713	53.714
Mn55_ppm_mean	2037.616	2126.218	2763.012	3239.578	2206.900	2585.497	2559.655	2959.074
Mn55_ppm_2SE(int)	44.910	42.422	62.339	52.075	45.975	51.815	46.265	39.923
Co59_ppm_mean	53.649	53.926	43.565	43.761	55.725	42.605	39.515	45.966
Co59_ppm_2SE(int)	1.357	1.347	2.626	1.003	1.508	1.004	0.848	0.869
Ni60_ppm_mean	48.160	48.058	9.106	7.019	48.588	7.715	7.144	7.889
Ni60_ppm_2SE(int)	1.796	1.762	1.672	0.537	1.690	0.586	0.508	0.469
Cu63_ppm_mean	0.809	0.930	6.003	0.506	2.102	1.157	1.539	0.626
Cu63_ppm_2SE(int)	0.159	0.130	1.678	0.084	0.189	0.142	0.142	0.131
Zn66_ppm_mean	2.109	2.088	3.157	2.248	3.899	2.373	3.399	2.436
Zn66_ppm_2SE(int)	0.675	0.618	3.354	0.616	0.719	0.614	0.706	0.503
Rb85_ppm_mean	0.014	0.006	4.393	0.008	0.005	0.075	0.013	0.009
Rb85_ppm_2SE(int)	0.012	0.013	0.524	0.012	0.014	0.028	0.012	0.012
Sr88_ppm_mean	0.143	0.145	38.781	3.552	0.174	2.395	3.952	1.476
Sr88_ppm_2SE(int)	0.025	0.036	3.575	0.380	0.028	0.282	0.124	0.092
Y89_ppm_mean	0.918	0.962	17.626	10.415	0.974	3.937	9.016	7.130
Y89_ppm_2SE(int)	0.090	0.065	1.794	0.263	0.081	0.170	0.239	0.204
Zr90_ppm_mean	0.446	0.358	41.346	5.857	0.541	3.731	5.562	3.685
Zr90_ppm_2SE(int)	0.080	0.063	5.878	0.234	0.095	0.560	0.241	0.201
Nb93_ppm_mean	0.020	0.010	2.747	0.050	0.013	0.225	0.041	0.010
Nb93_ppm_2SE(int)	0.012	0.007	0.306	0.035	0.008	0.066	0.015	0.006
Hf178_ppm_mean	0.015	0.024	1.282	0.325	0.022	0.128	0.310	0.216
Hf178_ppm_2SE(int)	0.010	0.011	0.197	0.037	0.009	0.027	0.039	0.033
Ta181_ppm_mean	0.001	0.000	0.217	0.000	0.002	0.008	0.003	0.001
Ta181_ppm_2SE(int)	0.001	0.000	0.079	0.000	0.002	0.003	0.002	0.001
Pb208_ppm_mean	0.972	0.363	0.240	0.285	2.925	1.095	1.045	0.042
Pb208_ppm_2SE(int)	0.443	0.161	0.085	0.352	0.143	0.490	0.579	0.011
Th232_ppm_mean	0.002	0.000	0.321	0.002	0.000	0.008	0.000	0.000
Th232_ppm_2SE(int)	0.002	0.000	0.044	0.002	0.000	0.004	0.000	0.001
U238_ppm_mean	0.012	0.001	0.065	0.001	0.001	0.004	0.001	0.001
U238_ppm_2SE(int)	0.021	0.001	0.011	0.001	0.001	0.002	0.001	0.001

Table S4 cont.: Pyroxene trace element compositions.

Sample	15085	15085	15085	15085	15085	15085	15085	15085
Site	26-PYX-3.292	26-PYX-3.293	26-PYX-3.294	26-PYX-3.295	26-PYX-4.298	26-PYX-4.299	26-PYX-5.305	26-PYX-5.306
Si29_ppm_mean	495423.000	492305.000	502791.000	514534.000	489063.000	508517.000	508090.000	510665.000
Si29_ppm_2SE(int)	0.000	0.000	0.000	0.000	0.000	0.000	0.000	0.000
Ca43_ppm_mean	77589.652	69238.226	42308.916	20627.920	70355.958	22132.901	19426.393	24652.380
Ca43_ppm_2SE(int)	1106.567	1143.932	1007.634	349.033	1172.835	460.397	471.889	623.300
Sc45_ppm_mean	63.085	55.595	38.059	24.401	59.428	26.468	24.320	28.169
Sc45_ppm_2SE(int)	1.142	1.027	0.876	0.654	1.023	0.588	0.509	0.621
Ti47_ppm_mean	4899.842	3228.481	2156.164	1133.958	3326.887	1194.827	1099.848	1288.535
Ti47_ppm_2SE(int)	64.076	38.544	73.560	18.319	51.086	18.393	20.433	21.191
V51_ppm_mean	167.704	198.249	283.752	244.496	241.165	253.134	243.316	266.084
V51_ppm_2SE(int)	2.300	3.043	4.551	4.084	4.692	5.089	3.851	4.419
Cr52_ppm_mean	2847.108	3424.704	4259.552	5077.433	3944.098	5074.791	5258.049	5052.187
Cr52_ppm_2SE(int)	47.643	45.830	74.242	76.096	73.123	82.440	92.441	79.357
Mn55_ppm_mean	3085.014	2918.983	2543.517	2222.130	2783.587	2240.906	2153.400	2289.144
Mn55_ppm_2SE(int)	44.959	37.948	43.808	34.033	44.786	36.160	38.548	38.893
Co59_ppm_mean	47.622	44.845	44.956	55.056	43.544	53.921	55.201	53.577
Co59_ppm_2SE(int)	0.853	0.748	0.730	1.097	0.823	1.146	1.038	1.003
Ni60_ppm_mean	7.928	7.702	8.732	43.611	7.183	30.633	54.477	25.889
Ni60_ppm_2SE(int)	0.532	0.530	0.653	1.302	0.473	1.133	1.505	1.034
Cu63_ppm_mean	0.669	0.377	0.651	0.497	0.454	0.240	0.443	0.337
Cu63_ppm_2SE(int)	0.166	0.082	0.113	0.089	0.144	0.080	0.083	0.073
Zn66_ppm_mean	2.014	2.461	2.243	3.078	1.680	1.921	2.474	1.913
Zn66_ppm_2SE(int)	0.593	0.488	0.722	0.542	0.461	0.536	0.639	0.627
Rb85_ppm_mean	0.050	0.000	0.384	0.008	0.113	0.022	0.019	0.029
Rb85_ppm_2SE(int)	0.047	0.013	0.048	0.013	0.029	0.016	0.013	0.013
Sr88_ppm_mean	2.520	1.330	3.112	0.160	2.629	0.156	0.130	0.171
Sr88_ppm_2SE(int)	0.164	0.079	0.195	0.024	0.372	0.023	0.019	0.025
Y89_ppm_mean	10.483	6.061	3.819	1.106	6.456	1.169	1.072	1.287
Y89_ppm_2SE(int)	0.289	0.183	0.252	0.076	0.222	0.070	0.068	0.080
Zr90_ppm_mean	7.914	2.706	5.782	0.379	4.361	0.445	0.404	0.477
Zr90_ppm_2SE(int)	0.480	0.149	0.649	0.059	0.269	0.067	0.052	0.071
Nb93_ppm_mean	0.081	0.035	0.249	0.024	0.219	0.011	0.015	0.017
Nb93_ppm_2SE(int)	0.024	0.023	0.042	0.016	0.058	0.007	0.008	0.008
Hf178_ppm_mean	0.341	0.152	0.191	0.016	0.190	0.011	0.017	0.024
Hf178_ppm_2SE(int)	0.038	0.028	0.034	0.008	0.031	0.007	0.009	0.010
Ta181_ppm_mean	0.008	0.000	0.016	0.000	0.011	0.001	0.001	0.000
Ta181_ppm_2SE(int)	0.004	0.000	0.005	0.000	0.004	0.001	0.001	0.000
Pb208_ppm_mean	0.057	0.541	0.101	0.119	0.029	0.010	0.106	0.055
Pb208_ppm_2SE(int)	0.012	1.025	0.028	0.024	0.012	0.006	0.017	0.011
Th232_ppm_mean	0.002	0.000	0.015	0.000	0.009	0.000	0.000	0.000
Th232_ppm_2SE(int)	0.002	0.000	0.005	0.001	0.004	0.000	0.000	0.000
U238_ppm_mean	0.001	0.034	0.023	0.001	0.004	0.001	0.002	0.000
U238_ppm_2SE(int)	0.001	0.062	0.025	0.001	0.002	0.001	0.001	0.001

Table S4 cont.: Pyroxene trace element compositions.

Sample	15085	15085	15085	15085	15556	15556	15556	15556
Site	26-PYX-5.307	26-PYX-5.308	26-PYX-5.309	26-PYX-5.310	28-PYX-1.401	28-PYX-1.402	28-PYX-1.405	28-PYX-1.406
Si29_ppm_mean	488589.000	480279.000	482229.000	473501.000	482990.000	477597.000	500791.000	459316.000
Si29_ppm_2SE(int)	0.000	0.000	0.000	0.000	0.000	0.000	0.000	0.000
Ca43_ppm_mean	57604.457	66403.692	97579.941	105485.815	130469.398	95974.952	144718.947	48221.697
Ca43_ppm_2SE(int)	1047.593	985.062	1638.264	1754.348	2480.179	2156.619	3176.197	1192.978
Sc45_ppm_mean	44.827	54.580	61.735	96.307	77.273	66.031	79.999	39.299
Sc45_ppm_2SE(int)	0.843	0.950	1.156	1.472	2.073	1.697	1.751	1.036
Ti47_ppm_mean	2808.835	3587.518	3596.048	6524.213	5794.688	5551.046	8726.758	2935.485
Ti47_ppm_2SE(int)	96.585	71.755	61.897	74.970	146.528	129.795	350.166	58.302
V51_ppm_mean	257.152	202.483	225.506	57.436	410.413	19.910	326.591	90.542
V51_ppm_2SE(int)	4.805	4.072	4.595	1.165	14.015	1.313	10.503	2.291
Cr52_ppm_mean	3701.233	3097.670	3630.583	673.019	4786.515	204.473	3140.418	1352.694
Cr52_ppm_2SE(int)	72.540	47.841	78.254	11.692	129.627	10.585	77.665	34.279
Mn55_ppm_mean	2523.984	2949.137	2750.026	3449.573	2385.209	3945.936	2885.553	3099.585
Mn55_ppm_2SE(int)	41.360	43.190	40.831	49.522	50.483	74.938	58.850	57.378
Co59_ppm_mean	40.272	45.105	42.383	41.595	39.677	45.012	38.103	51.168
Co59_ppm_2SE(int)	0.844	0.803	0.908	0.855	1.343	1.147	1.129	1.140
Ni60_ppm_mean	7.500	5.665	7.087	6.079	14.747	9.800	12.430	16.192
Ni60_ppm_2SE(int)	0.757	0.424	0.502	0.485	0.746	0.780	0.879	0.762
Cu63_ppm_mean	1.169	1.078	0.593	0.481	0.510	0.879	1.024	0.379
Cu63_ppm_2SE(int)	0.280	0.192	0.119	0.103	0.102	0.184	0.166	0.087
Zn66_ppm_mean	2.189	2.086	1.641	1.919	1.591	3.076	1.726	1.490
Zn66_ppm_2SE(int)	0.556	0.511	0.616	0.521	0.525	0.591	0.572	0.594
Rb85_ppm_mean	0.083	0.531	0.008	0.018	0.018	0.158	3.813	0.033
Rb85_ppm_2SE(int)	0.020	0.152	0.012	0.012	0.015	0.069	0.440	0.026
Sr88_ppm_mean	8.824	3.216	2.843	4.935	4.708	8.478	55.775	0.672
Sr88_ppm_2SE(int)	0.573	0.366	0.105	0.157	0.151	1.549	6.784	0.057
Y89_ppm_mean	5.649	10.958	7.338	16.140	8.619	41.758	118.603	3.546
Y89_ppm_2SE(int)	0.261	0.375	0.217	0.341	0.318	10.063	14.531	0.127
Zr90_ppm_mean	10.562	16.415	3.301	9.503	6.576	96.958	213.685	1.466
Zr90_ppm_2SE(int)	0.840	1.396	0.185	0.252	0.269	50.396	30.741	0.129
Nb93_ppm_mean	0.655	0.135	0.010	0.018	0.040	1.724	5.947	0.001
Nb93_ppm_2SE(int)	0.078	0.044	0.006	0.009	0.015	1.135	0.845	0.002
Hf178_ppm_mean	0.309	0.579	0.188	0.427	0.416	2.687	6.337	0.084
Hf178_ppm_2SE(int)	0.046	0.064	0.036	0.052	0.045	1.065	0.898	0.019
Ta181_ppm_mean	0.038	0.006	0.000	0.001	0.002	0.257	0.502	0.000
Ta181_ppm_2SE(int)	0.009	0.003	0.000	0.001	0.002	0.178	0.070	0.000
Pb208_ppm_mean	0.121	0.326	0.147	0.443	0.155	1.035	1.425	0.034
Pb208_ppm_2SE(int)	0.024	0.071	0.020	0.032	0.082	0.433	0.209	0.019
Th232_ppm_mean	0.054	0.057	0.000	0.000	0.001	0.489	3.224	0.000
Th232_ppm_2SE(int)	0.008	0.021	0.000	0.000	0.001	0.293	0.479	0.000
U238_ppm_mean	0.012	0.017	0.070	0.000	0.002	0.196	1.228	0.000
U238_ppm_2SE(int)	0.003	0.005	0.136	0.000	0.002	0.135	0.176	0.000

Table S4 cont.: Pyroxene trace element compositions.

Sample	15556	15556	15556	15556	15556	15556	15556	15556
Site	28-PYX-2.407	28-PYX-2.408	28-PYX-2.409	28-PYX-2.410	28-PYX-2.413	28-PYX-2.414	241-PYX-1.314	241-PYX-1.320
Si29_ppm_mean	475187.000	462998.000	465186.000	512716.000	499677.000	474770.000	506221.000	499159.000
Si29_ppm_2SE(int)	0.000	0.000	0.000	0.000	0.000	0.000	0.000	0.000
Ca43_ppm_mean	86929.313	99723.365	81078.748	46030.827	52101.136	81785.406	90596.012	66004.193
Ca43_ppm_2SE(int)	1604.681	1795.284	2251.229	1115.421	1441.218	1900.695	1626.925	1362.994
Sc45_ppm_mean	78.096	91.179	74.676	36.989	44.262	69.239	71.651	50.238
Sc45_ppm_2SE(int)	1.431	2.058	1.866	0.944	1.375	1.817	1.595	1.326
Ti47_ppm_mean	6290.596	7793.508	5927.443	2161.882	3143.597	5863.917	5636.074	4100.544
Ti47_ppm_2SE(int)	96.653	136.634	123.582	48.492	83.705	149.300	107.103	143.270
V51_ppm_mean	106.191	93.808	160.203	349.264	453.803	36.520	259.945	384.836
V51_ppm_2SE(int)	3.359	3.600	3.739	9.205	16.491	0.891	5.568	7.813
Cr52_ppm_mean	1359.395	1074.823	2063.294	3938.224	4976.485	405.896	3208.739	4236.130
Cr52_ppm_2SE(int)	44.365	51.578	37.794	112.962	122.520	10.519	53.819	71.722
Mn55_ppm_mean	3376.546	3258.010	3192.930	2756.185	2733.175	3801.452	3027.461	2741.010
Mn55_ppm_2SE(int)	60.141	58.409	51.869	82.358	63.962	78.994	56.222	43.680
Co59_ppm_mean	51.093	49.679	50.221	49.174	48.717	54.947	48.556	47.191
Co59_ppm_2SE(int)	1.076	1.072	1.206	1.398	1.247	1.383	1.177	1.076
Ni60_ppm_mean	16.170	16.026	16.177	20.038	19.772	17.140	14.857	17.865
Ni60_ppm_2SE(int)	0.892	0.895	0.721	0.867	1.314	0.932	0.792	0.857
Cu63_ppm_mean	0.279	0.365	0.640	0.363	0.931	0.734	0.326	0.684
Cu63_ppm_2SE(int)	0.087	0.108	0.112	0.079	0.198	0.102	0.092	0.122
Zn66_ppm_mean	2.412	2.549	3.252	2.109	4.312	3.524	1.825	2.089
Zn66_ppm_2SE(int)	0.620	0.572	1.098	0.522	0.965	0.825	0.565	0.584
Rb85_ppm_mean	0.037	0.022	0.009	0.005	0.134	0.024	0.008	0.078
Rb85_ppm_2SE(int)	0.017	0.027	0.014	0.013	0.029	0.017	0.017	0.050
Sr88_ppm_mean	3.824	3.809	2.311	0.504	4.336	2.970	2.413	5.225
Sr88_ppm_2SE(int)	0.199	0.127	0.107	0.049	0.523	0.127	0.090	0.504
Y89_ppm_mean	11.099	12.461	8.950	2.256	3.657	10.816	7.599	5.590
Y89_ppm_2SE(int)	0.363	0.317	0.304	0.105	0.161	0.361	0.176	0.294
Zr90_ppm_mean	10.044	9.973	6.095	1.049	7.037	8.211	4.966	7.305
Zr90_ppm_2SE(int)	0.471	0.338	0.310	0.109	1.747	0.362	0.202	0.658
Nb93_ppm_mean	0.152	0.035	0.018	0.008	0.241	0.021	0.017	0.349
Nb93_ppm_2SE(int)	0.033	0.012	0.010	0.006	0.038	0.009	0.009	0.062
Hf178_ppm_mean	0.506	0.515	0.300	0.061	0.271	0.415	0.278	0.268
Hf178_ppm_2SE(int)	0.048	0.042	0.035	0.017	0.046	0.053	0.047	0.047
Ta181_ppm_mean	0.009	0.028	0.001	0.000	0.014	0.000	0.001	0.022
Ta181_ppm_2SE(int)	0.004	0.044	0.001	0.000	0.005	0.000	0.001	0.007
Pb208_ppm_mean	0.226	0.250	1.165	0.158	11.521	0.180	0.013	0.034
Pb208_ppm_2SE(int)	0.230	0.163	0.445	0.028	7.345	0.110	0.008	0.010
Th232_ppm_mean	0.013	0.002	0.000	0.000	0.020	0.000	0.000	0.028
Th232_ppm_2SE(int)	0.005	0.002	0.000	0.000	0.006	0.000	0.000	0.006
U238_ppm_mean	0.003	0.005	0.001	0.001	0.010	0.001	0.001	0.008
U238_ppm_2SE(int)	0.002	0.004	0.001	0.001	0.005	0.001	0.001	0.003

Table S4 cont.: Pyroxene trace element compositions.

Sample	15556	15556	15556	15556	15556	15556	15556	15556
Site	241-PYX-1.321	241-PYX-2.326	241-PYX-2.327	241-PYX-2.328	241-PYX-2.329	241-PYX-2.330	241-PYX-2.331	241-PYX-2.332
Si29_ppm_mean	463551.000	502380.000	458509.000	474118.000	463691.000	503330.000	486633.000	447416.000
Si29_ppm_2SE(int)	0.000	0.000	0.000	0.000	0.000	0.000	0.000	0.000
Ca43_ppm_mean	70468.293	53215.569	102048.149	127021.436	83044.215	95508.748	71147.167	114346.090
Ca43_ppm_2SE(int)	1443.833	1160.688	2182.345	2587.762	1713.098	1661.077	1339.968	2391.474
Sc45_ppm_mean	52.370	41.745	79.035	102.985	73.376	70.476	52.946	90.258
Sc45_ppm_2SE(int)	0.954	0.906	1.702	2.154	1.290	1.566	1.183	1.553
Ti47_ppm_mean	4121.958	2540.162	6606.174	8744.154	6305.892	6026.844	3731.502	6998.031
Ti47_ppm_2SE(int)	87.427	65.067	114.626	180.791	137.300	108.597	82.858	145.185
V51_ppm_mean	371.140	392.876	173.915	93.706	95.850	155.813	292.702	51.458
V51_ppm_2SE(int)	8.679	12.809	7.526	2.707	2.189	2.845	9.323	1.792
Cr52_ppm_mean	3914.705	4212.829	2038.220	1135.234	1140.269	2146.352	3473.174	807.246
Cr52_ppm_2SE(int)	93.850	85.477	88.379	23.445	29.121	42.725	77.548	27.732
Mn55_ppm_mean	2499.480	2599.771	2993.537	2997.247	3206.045	3308.248	2767.699	3249.207
Mn55_ppm_2SE(int)	48.706	51.300	54.372	58.895	55.660	70.001	50.372	70.725
Co59_ppm_mean	42.521	46.895	44.113	45.994	48.643	48.227	45.745	42.502
Co59_ppm_2SE(int)	0.954	1.016	0.815	0.932	0.956	1.411	0.961	0.921
Ni60_ppm_mean	15.397	19.177	13.691	15.126	14.760	12.453	14.020	9.394
Ni60_ppm_2SE(int)	0.783	1.102	0.746	0.952	0.712	0.736	0.639	0.694
Cu63_ppm_mean	0.787	0.234	0.193	0.741	0.326	0.929	0.683	0.778
Cu63_ppm_2SE(int)	0.133	0.082	0.067	0.131	0.078	0.161	0.091	0.928
Zn66_ppm_mean	2.044	1.947	1.711	2.741	2.385	1.636	1.515	2.065
Zn66_ppm_2SE(int)	0.747	0.597	0.628	0.838	0.504	0.523	0.605	0.574
Rb85_ppm_mean	0.049	0.019	-0.003	0.015	0.025	0.056	0.011	0.032
Rb85_ppm_2SE(int)	0.023	0.017	0.010	0.013	0.016	0.021	0.014	0.017
Sr88_ppm_mean	3.372	0.795	4.309	6.690	3.268	6.476	1.603	8.164
Sr88_ppm_2SE(int)	0.328	0.058	0.121	0.184	0.291	0.353	0.102	0.232
Y89_ppm_mean	5.538	2.828	13.965	16.179	9.451	14.844	4.909	26.971
Y89_ppm_2SE(int)	0.157	0.122	0.430	0.357	0.357	0.420	0.218	0.718
Zr90_ppm_mean	5.686	1.541	11.324	15.774	8.165	16.666	3.243	31.186
Zr90_ppm_2SE(int)	0.335	0.118	0.472	0.617	0.768	0.695	0.243	0.898
Nb93_ppm_mean	0.166	0.016	0.017	0.028	0.140	0.193	0.043	0.055
Nb93_ppm_2SE(int)	0.040	0.009	0.009	0.011	0.047	0.042	0.014	0.017
Hf178_ppm_mean	0.269	0.071	0.569	0.821	0.417	0.733	0.183	1.655
Hf178_ppm_2SE(int)	0.036	0.017	0.058	0.059	0.040	0.063	0.032	0.087
Ta181_ppm_mean	0.012	0.000	0.006	0.005	0.007	0.009	0.000	0.003
Ta181_ppm_2SE(int)	0.005	0.001	0.004	0.003	0.003	0.005	0.000	0.002
Pb208_ppm_mean	0.027	0.012	0.004	0.018	0.031	0.039	0.021	0.011
Pb208_ppm_2SE(int)	0.009	0.006	0.005	0.008	0.009	0.011	0.008	0.008
Th232_ppm_mean	0.018	0.000	0.000	0.000	0.015	0.038	0.000	0.003
Th232_ppm_2SE(int)	0.005	0.000	0.000	0.000	0.006	0.020	0.001	0.002
U238_ppm_mean	0.004	0.000	0.020	0.001	0.004	0.005	0.002	0.004
U238_ppm_2SE(int)	0.002	0.000	0.038	0.001	0.002	0.002	0.001	0.002

Table S4 cont.: Pyroxene trace element compositions.

Sample	15556	15556	15556	15556	15556	15556	15556	15556
Site	241-PYX-3.339	241-PYX-3.340	241-PYX-3.341	241-PYX-3.342	241-PYX-3.343	241-PYX-3.344	241-PYX-3.345	241-PYX-4.347
Si29_ppm_mean	519021.000	473619.000	496938.000	465447.000	487060.000	489794.000	457557.000	473170.000
Si29_ppm_2SE(int)	0.000	0.000	0.000	0.000	0.000	0.000	0.000	0.000
Ca43_ppm_mean	55198.872	112275.417	63764.648	97242.462	119351.028	68822.606	89864.845	92625.672
Ca43_ppm_2SE(int)	1520.822	2346.931	1484.955	1702.329	3481.976	1472.065	1886.841	1578.695
Sc45_ppm_mean	44.606	92.470	47.499	86.845	77.453	51.056	50.187	48.386
Sc45_ppm_2SE(int)	1.069	1.855	1.040	1.444	1.431	1.376	0.937	0.826
Ti47_ppm_mean	2918.001	7403.948	3077.383	7143.285	5974.082	4018.180	4950.855	5832.356
Ti47_ppm_2SE(int)	60.939	133.523	74.646	139.111	114.206	79.208	88.522	79.652
V51_ppm_mean	402.515	89.862	448.175	100.088	319.399	97.753	10.905	8.565
V51_ppm_2SE(int)	8.392	8.784	16.180	2.077	23.028	2.917	0.448	0.319
Cr52_ppm_mean	4474.392	1035.616	5440.583	1316.046	3662.507	1387.691	120.798	154.154
Cr52_ppm_2SE(int)	82.853	123.022	400.331	28.748	183.976	59.177	5.297	3.526
Mn55_ppm_mean	2665.314	3369.474	2636.895	3242.524	2687.166	3382.549	4055.125	4114.624
Mn55_ppm_2SE(int)	44.063	68.846	64.716	58.554	52.468	64.261	60.960	59.104
Co59_ppm_mean	49.440	48.201	45.918	48.678	43.159	52.444	39.174	33.059
Co59_ppm_2SE(int)	1.359	1.023	1.167	0.951	1.095	1.224	0.893	0.769
Ni60_ppm_mean	20.046	14.447	17.573	13.732	13.377	15.064	4.513	1.143
Ni60_ppm_2SE(int)	0.972	0.811	0.958	0.791	0.851	0.808	0.541	0.184
Cu63_ppm_mean	0.407	0.586	0.591	0.420	0.395	0.310	3.414	1.288
Cu63_ppm_2SE(int)	0.104	0.102	0.102	0.087	0.104	0.069	1.210	0.239
Zn66_ppm_mean	2.065	2.895	1.242	1.491	0.820	1.745	2.897	3.275
Zn66_ppm_2SE(int)	0.635	0.713	0.598	0.621	0.550	0.486	0.571	0.593
Rb85_ppm_mean	0.017	0.007	0.028	0.005	0.007	0.003	0.093	0.240
Rb85_ppm_2SE(int)	0.015	0.013	0.014	0.014	0.014	0.012	0.031	0.067
Sr88_ppm_mean	1.307	6.149	1.201	3.462	4.015	1.261	18.375	19.201
Sr88_ppm_2SE(int)	0.108	0.289	0.084	0.123	0.178	0.079	1.952	2.984
Y89_ppm_mean	3.365	20.288	3.735	13.534	8.473	5.129	95.852	109.166
Y89_ppm_2SE(int)	0.146	0.998	0.143	0.268	0.265	0.228	9.400	11.345
Zr90_ppm_mean	2.538	18.949	2.274	10.569	6.275	2.495	353.694	285.409
Zr90_ppm_2SE(int)	0.206	1.201	0.118	0.334	0.261	0.159	95.978	54.972
Nb93_ppm_mean	0.080	0.078	0.028	0.016	0.042	0.000	11.709	13.461
Nb93_ppm_2SE(int)	0.022	0.024	0.012	0.009	0.035	0.000	3.433	2.743
Hf178_ppm_mean	0.139	0.851	0.147	0.616	0.341	0.135	10.219	8.965
Hf178_ppm_2SE(int)	0.023	0.077	0.031	0.053	0.043	0.028	2.462	1.167
Ta181_ppm_mean	0.007	0.004	0.001	0.000	0.004	0.000	0.944	0.561
Ta181_ppm_2SE(int)	0.003	0.002	0.002	0.000	0.003	0.000	0.289	0.096
Pb208_ppm_mean	0.015	0.138	0.023	0.017	0.009	0.016	0.629	0.688
Pb208_ppm_2SE(int)	0.007	0.030	0.008	0.007	0.007	0.011	0.151	0.183
Th232_ppm_mean	0.008	0.011	0.002	0.002	0.006	0.000	1.691	2.285
Th232_ppm_2SE(int)	0.006	0.005	0.003	0.001	0.006	0.000	0.505	0.582
U238_ppm_mean	0.000	0.004	0.018	0.001	0.001	0.000	0.291	0.422
U238_ppm_2SE(int)	0.000	0.002	0.030	0.001	0.001	0.000	0.061	0.120

Table S4 cont.: Pyroxene trace element compositions.

Sample	15556	15556	15556	15556	15556	15556	15556	15556
Site	241-PYX-4.348	241-PYX-4.352	241-PYX-4.353	241-PYX-4.354	241-PYX-5.357	241-PYX-5.358	241-PYX-5.359	241-PYX-5.360
Si29_ppm_mean	473870.000	469179.000	491704.000	507396.000	499488.000	455177.000	479766.000	500645.000
Si29_ppm_2SE(int)	0.000	0.000	0.000	0.000	0.000	0.000	0.000	0.000
Ca43_ppm_mean	113014.671	51508.108	72692.445	62451.420	105116.545	106539.479	88199.100	171622.873
Ca43_ppm_2SE(int)	2823.480	1066.204	1780.079	1960.354	2161.918	1705.311	2410.438	2799.172
Sc45_ppm_mean	94.785	43.384	51.403	48.125	67.906	71.710	73.586	98.100
Sc45_ppm_2SE(int)	2.192	0.952	1.559	1.553	1.780	1.704	1.677	1.831
Ti47_ppm_mean	8281.214	3334.328	3172.246	2939.115	4816.490	6370.017	6496.294	9241.115
Ti47_ppm_2SE(int)	174.567	57.021	101.138	70.337	91.972	132.375	154.427	164.310
V51_ppm_mean	122.112	98.023	407.537	435.509	509.594	19.195	104.400	18.114
V51_ppm_2SE(int)	4.820	2.275	9.505	9.203	13.233	0.521	2.759	0.550
Cr52_ppm_mean	1232.359	1443.998	4204.007	4525.634	4883.344	233.075	1231.363	245.601
Cr52_ppm_2SE(int)	70.279	30.060	91.114	91.032	121.082	4.269	33.508	7.132
Mn55_ppm_mean	3081.839	3199.321	2580.518	2632.248	2570.661	3595.998	3333.337	3485.507
Mn55_ppm_2SE(int)	52.610	58.590	52.327	47.807	59.853	70.337	59.957	59.767
Co59_ppm_mean	47.450	50.802	43.593	47.102	43.069	41.701	49.864	29.992
Co59_ppm_2SE(int)	1.144	0.982	1.000	1.051	1.147	0.859	1.096	0.611
Ni60_ppm_mean	13.695	13.639	15.237	18.406	15.487	7.678	14.418	2.115
Ni60_ppm_2SE(int)	0.673	0.686	0.824	0.957	0.848	0.578	0.850	0.275
Cu63_ppm_mean	0.409	0.372	0.399	0.341	1.073	1.520	1.334	0.827
Cu63_ppm_2SE(int)	0.071	0.142	0.117	0.090	0.125	0.126	0.259	0.140
Zn66_ppm_mean	1.680	2.093	2.106	1.066	0.932	1.892	1.921	1.959
Zn66_ppm_2SE(int)	0.483	0.577	0.557	0.658	0.712	0.557	0.682	0.750
Rb85_ppm_mean	0.014	0.020	0.016	0.011	0.024	0.108	0.154	0.092
Rb85_ppm_2SE(int)	0.016	0.014	0.018	0.016	0.017	0.031	0.033	0.030
Sr88_ppm_mean	4.918	0.922	1.407	0.960	3.746	11.509	10.500	30.373
Sr88_ppm_2SE(int)	0.225	0.085	0.097	0.068	0.207	0.823	0.710	0.820
Y89_ppm_mean	11.933	3.923	4.171	3.563	7.645	23.850	11.396	64.071
Y89_ppm_2SE(int)	0.358	0.152	0.220	0.187	0.314	0.521	0.406	0.983
Zr90_ppm_mean	9.673	1.828	2.526	1.863	7.738	31.303	17.211	133.983
Zr90_ppm_2SE(int)	0.464	0.120	0.206	0.152	0.628	1.184	0.838	2.832
Nb93_ppm_mean	0.031	0.004	0.014	0.020	0.143	0.586	0.554	0.519
Nb93_ppm_2SE(int)	0.015	0.004	0.008	0.009	0.032	0.097	0.085	0.120
Hf178_ppm_mean	0.556	0.113	0.148	0.105	0.376	1.288	0.659	6.728
Hf178_ppm_2SE(int)	0.058	0.026	0.027	0.025	0.049	0.080	0.058	0.280
Ta181_ppm_mean	0.003	0.000	0.001	0.000	0.008	0.027	0.035	0.040
Ta181_ppm_2SE(int)	0.002	0.000	0.002	0.000	0.004	0.008	0.008	0.010
Pb208_ppm_mean	0.008	0.014	0.008	0.018	0.023	0.030	0.045	0.033
Pb208_ppm_2SE(int)	0.005	0.010	0.007	0.006	0.008	0.008	0.011	0.009
Th232_ppm_mean	0.004	0.000	0.000	0.000	0.015	0.074	0.083	0.055
Th232_ppm_2SE(int)	0.002	0.000	0.000	0.001	0.007	0.019	0.014	0.014
U238_ppm_mean	0.000	0.001	0.001	0.084	0.007	0.020	0.020	0.014
U238_ppm_2SE(int)	0.000	0.001	0.001	0.165	0.003	0.006	0.005	0.004

Table S4 cont.: Pyroxene trace element compositions.

Sample	15556	15556	70017	70017	70017	70017	70017	70017
Site	241-PYX-5.361	241-PYX-5.362	123-PYX-1.492	123-PYX-1.493	123-PYX-1.494	123-PYX-2.498	123-PYX-2.499	123-PYX-2.500
Si29_ppm_mean	503482.000	486555.000	489638.000	499050.000	518908.000	519925.000	505939.000	487008.000
Si29_ppm_2SE(int)	0.000	0.000	0.000	0.000	0.000	0.000	0.000	0.000
Ca43_ppm_mean	125433.798	141009.821	100143.566	137149.236	158058.275	41987.833	131656.599	116684.542
Ca43_ppm_2SE(int)	3197.195	2157.914	2115.215	2762.961	3460.936	944.541	2316.892	2429.583
Sc45_ppm_mean	81.003	95.144	92.160	85.045	90.654	52.746	100.153	111.469
Sc45_ppm_2SE(int)	2.323	2.099	1.829	1.911	1.996	1.287	1.828	2.338
Ti47_ppm_mean	5464.758	8672.436	6941.899	9438.745	10906.988	5196.617	6920.150	6680.133
Ti47_ppm_2SE(int)	128.549	153.394	728.407	163.585	252.338	104.199	111.974	121.063
V51_ppm_mean	734.765	36.195	68.259	130.466	141.068	66.220	82.846	79.749
V51_ppm_2SE(int)	25.144	1.355	1.876	2.792	2.893	1.689	1.701	1.885
Cr52_ppm_mean	6179.457	322.139	2394.224	3810.057	4133.238	2562.891	2752.724	2650.336
Cr52_ppm_2SE(int)	192.693	14.217	54.054	71.385	91.624	48.265	49.864	60.516
Mn55_ppm_mean	2321.040	3460.617	3077.887	1998.780	1955.000	2715.533	2924.126	3072.064
Mn55_ppm_2SE(int)	64.322	61.337	58.639	37.925	45.147	49.624	46.696	61.748
Co59_ppm_mean	38.462	40.752	13.621	12.289	13.694	17.557	12.679	14.992
Co59_ppm_2SE(int)	1.116	0.931	0.448	0.400	0.508	0.538	0.333	0.494
Ni60_ppm_mean	14.356	9.383	0.227	0.588	0.764	0.501	0.305	0.343
Ni60_ppm_2SE(int)	1.018	0.634	0.098	0.296	0.196	0.375	0.116	0.121
Cu63_ppm_mean	0.566	0.693	1.187	0.291	0.453	0.171	0.331	0.550
Cu63_ppm_2SE(int)	0.229	0.156	0.145	0.089	0.104	0.078	0.071	0.121
Zn66_ppm_mean	1.204	2.565	74.226	4.431	19.866	11.142	118.948	1646.176
Zn66_ppm_2SE(int)	0.571	0.632	2.255	0.773	1.089	1.096	6.134	304.944
Rb85_ppm_mean	0.010	0.167	0.027	0.009	0.003	0.016	0.033	0.071
Rb85_ppm_2SE(int)	0.011	0.038	0.016	0.014	0.017	0.015	0.018	0.019
Sr88_ppm_mean	3.817	15.982	9.040	8.812	9.138	0.837	10.999	17.524
Sr88_ppm_2SE(int)	0.147	1.001	0.333	0.246	0.257	0.066	0.297	0.489
Y89_ppm_mean	7.466	39.905	70.484	23.579	21.033	10.164	56.893	115.570
Y89_ppm_2SE(int)	0.254	1.350	3.350	0.579	0.586	0.324	0.977	2.384
Zr90_ppm_mean	6.193	58.033	19.051	9.996	9.689	3.224	18.716	42.634
Zr90_ppm_2SE(int)	0.259	4.096	0.933	0.455	0.387	0.195	0.542	1.297
Nb93_ppm_mean	0.034	1.181	0.324	0.027	0.044	0.019	0.040	0.403
Nb93_ppm_2SE(int)	0.014	0.259	0.196	0.012	0.017	0.010	0.012	0.070
Hf178_ppm_mean	0.368	2.497	1.213	0.730	0.668	0.251	1.238	2.687
Hf178_ppm_2SE(int)	0.053	0.156	0.095	0.074	0.055	0.036	0.077	0.124
Ta181_ppm_mean	0.002	0.071	0.039	0.006	0.005	0.001	0.003	0.031
Ta181_ppm_2SE(int)	0.002	0.018	0.024	0.003	0.003	0.001	0.002	0.007
Pb208_ppm_mean	0.009	0.107	0.017	0.092	0.018	0.016	0.004	0.308
Pb208_ppm_2SE(int)	0.005	0.026	0.009	0.171	0.010	0.008	0.005	0.090
Th232_ppm_mean	0.001	0.235	0.015	0.000	0.000	0.000	0.000	0.023
Th232_ppm_2SE(int)	0.001	0.064	0.006	0.000	0.000	0.000	0.000	0.006
U238_ppm_mean	0.052	0.040	0.006	0.007	0.000	0.170	0.001	0.040
U238_ppm_2SE(int)	0.099	0.009	0.003	0.012	0.000	0.338	0.001	0.063

Table S4 cont.: Pyroxene trace element compositions.

Sample	70017	70017	70017	70017	70017	70017	70017	70017
Site	123-PYX-2.501	123-PYX-2.502	123-PYX-3.507	123-PYX-3.508	123-PYX-3.509	123-PYX-3.503	123-PYX-3.504	123-PYX-4.510
Si29_ppm_mean	482472.000	452419.000	477998.000	486457.000	481235.000	481986.000	488837.000	474118.000
Si29_ppm_2SE(int)	0.000	0.000	0.000	0.000	0.000	0.000	0.000	0.000
Ca43_ppm_mean	175101.947	162368.736	177167.694	138721.613	63187.317	41752.123	128606.944	105675.115
Ca43_ppm_2SE(int)	3425.851	3555.386	3564.050	2579.320	1084.584	786.736	2337.660	1618.103
Sc45_ppm_mean	133.809	126.187	137.584	108.107	87.247	46.591	119.960	119.953
Sc45_ppm_2SE(int)	3.094	2.798	3.616	2.244	1.364	0.987	2.416	1.799
Ti47_ppm_mean	20704.512	20410.291	22030.955	14056.213	5466.052	4599.290	7652.508	5454.338
Ti47_ppm_2SE(int)	396.304	413.017	506.408	336.553	75.772	80.279	133.153	89.885
V51_ppm_mean	222.821	206.534	216.322	172.003	58.484	53.202	87.691	62.118
V51_ppm_2SE(int)	4.042	4.952	5.197	3.718	1.033	1.237	1.668	1.268
Cr52_ppm_mean	6752.271	6385.084	6720.436	5113.408	2240.000	2283.152	2820.803	2273.075
Cr52_ppm_2SE(int)	141.310	117.772	148.357	98.600	34.956	42.034	56.325	55.826
Mn55_ppm_mean	1782.567	1615.043	1700.517	2033.522	3548.172	2503.434	2831.965	3571.556
Mn55_ppm_2SE(int)	32.429	30.745	39.879	38.607	47.762	52.608	48.227	68.234
Co59_ppm_mean	12.760	12.116	12.370	12.824	16.893	13.328	14.210	12.953
Co59_ppm_2SE(int)	0.602	0.380	0.503	0.430	0.402	0.355	0.458	0.462
Ni60_ppm_mean	0.667	1.091	0.858	0.448	0.305	0.167	0.444	0.298
Ni60_ppm_2SE(int)	0.223	0.209	0.226	0.175	0.100	0.083	0.141	0.136
Cu63_ppm_mean	0.393	0.351	0.443	0.560	0.319	0.654	0.424	0.188
Cu63_ppm_2SE(int)	0.099	0.092	0.096	0.101	0.062	0.124	0.094	0.065
Zn66_ppm_mean	2.391	1.434	2.044	3.082	6.179	32.956	10.476	3.918
Zn66_ppm_2SE(int)	0.738	0.587	0.561	0.649	0.799	2.336	1.022	0.670
Rb85_ppm_mean	0.014	0.005	0.032	0.035	0.020	0.013	0.037	0.044
Rb85_ppm_2SE(int)	0.023	0.018	0.018	0.020	0.015	0.015	0.022	0.014
Sr88_ppm_mean	12.129	11.302	12.182	9.424	3.652	1.082	17.011	15.238
Sr88_ppm_2SE(int)	0.307	0.288	0.352	0.453	0.119	0.062	0.450	0.336
Y89_ppm_mean	33.787	30.881	33.646	29.389	59.637	9.649	86.772	164.430
Y89_ppm_2SE(int)	0.754	0.777	0.859	0.771	1.031	0.237	1.336	2.552
Zr90_ppm_mean	23.444	22.731	25.512	18.622	18.023	3.047	36.191	50.089
Zr90_ppm_2SE(int)	0.720	0.651	0.721	0.669	0.541	0.181	0.862	1.233
Nb93_ppm_mean	0.093	0.099	0.081	0.292	0.079	0.016	0.068	0.157
Nb93_ppm_2SE(int)	0.027	0.025	0.023	0.067	0.018	0.008	0.021	0.039
Hf178_ppm_mean	1.702	1.663	1.834	1.265	1.129	0.216	2.361	3.015
Hf178_ppm_2SE(int)	0.115	0.106	0.090	0.085	0.077	0.032	0.115	0.186
Ta181_ppm_mean	0.009	0.014	0.016	0.017	0.003	0.000	0.016	0.018
Ta181_ppm_2SE(int)	0.003	0.005	0.005	0.006	0.002	0.000	0.015	0.006
Pb208_ppm_mean	0.008	-0.006	0.012	0.064	0.055	0.004	0.016	0.010
Pb208_ppm_2SE(int)	0.006	0.004	0.007	0.012	0.012	0.005	0.012	0.006
Th232_ppm_mean	0.000	0.000	0.001	0.006	0.001	0.000	0.005	0.002
Th232_ppm_2SE(int)	0.000	0.000	0.001	0.003	0.001	0.000	0.003	0.002
U238_ppm_mean	0.000	0.000	0.000	0.001	0.002	0.000	0.005	0.001
U238_ppm_2SE(int)	0.000	0.000	0.000	0.001	0.001	0.001	0.002	0.001

Table S4 cont.: Pyroxene trace element compositions.

Sample	70017	70017	70017	70017	70017	70017	70017	70017
Site	123-PYX-4.511	123-PYX-4.512	123-PYX-5.515	123-PYX-5.516	123-PYX-5.517	123-PYX-5.518	123-PYX-5.519	123-PYX-5.520
Si29_ppm_mean	477102.000	500087.000	480928.000	464308.000	520592.000	479899.000	504227.000	483027.000
Si29_ppm_2SE(int)	0.000	0.000	0.000	0.000	0.000	0.000	0.000	0.000
Ca43_ppm_mean	127741.728	153480.301	63800.448	65158.702	52242.884	94338.350	143550.852	158057.735
Ca43_ppm_2SE(int)	2543.427	2721.104	1062.226	1694.469	1876.907	2576.380	2769.826	2413.663
Sc45_ppm_mean	108.763	86.280	75.935	90.882	66.266	99.351	87.892	125.500
Sc45_ppm_2SE(int)	2.119	1.842	1.359	2.006	2.029	2.421	1.717	2.686
Ti47_ppm_mean	8712.769	11004.062	3874.062	4405.214	5654.557	5977.273	11188.135	17516.612
Ti47_ppm_2SE(int)	171.498	259.931	57.348	63.070	182.928	127.595	229.011	382.232
V51_ppm_mean	95.084	128.922	39.872	45.854	53.862	48.120	141.243	213.132
V51_ppm_2SE(int)	2.030	2.727	1.117	0.996	1.413	1.648	3.944	4.442
Cr52_ppm_mean	3044.102	4123.299	1682.912	1892.792	2188.041	1793.787	4312.109	6016.503
Cr52_ppm_2SE(int)	62.548	86.786	36.197	39.267	52.803	44.839	94.235	108.515
Mn55_ppm_mean	2526.476	1949.464	3799.724	3696.597	3231.323	2950.519	2019.188	1894.264
Mn55_ppm_2SE(int)	47.311	44.875	61.490	52.369	66.694	72.885	42.311	39.053
Co59_ppm_mean	12.301	13.942	14.559	13.667	16.890	9.459	14.291	11.716
Co59_ppm_2SE(int)	0.404	0.338	0.375	0.353	0.586	0.394	0.476	0.404
Ni60_ppm_mean	0.235	1.049	0.173	0.207	0.457	0.517	0.696	0.493
Ni60_ppm_2SE(int)	0.115	0.226	0.109	0.123	0.128	0.270	0.147	0.160
Cu63_ppm_mean	0.235	0.357	0.548	0.370	0.959	0.288	0.749	0.497
Cu63_ppm_2SE(int)	0.074	0.178	0.123	0.122	0.243	0.074	0.153	0.092
Zn66_ppm_mean	7.662	1.774	57.491	20.978	3.751	5.195	4.275	5.948
Zn66_ppm_2SE(int)	0.919	0.609	10.075	1.147	0.690	0.807	0.705	0.909
Rb85_ppm_mean	0.006	0.020	0.025	0.246	0.534	14.618	0.109	0.012
Rb85_ppm_2SE(int)	0.014	0.051	0.014	0.057	0.124	1.044	0.174	0.015
Sr88_ppm_mean	11.134	7.807	4.040	14.624	24.123	118.361	7.554	10.292
Sr88_ppm_2SE(int)	0.266	0.216	0.122	1.428	4.058	7.066	0.252	0.249
Y89_ppm_mean	54.823	20.007	62.999	237.958	130.709	920.475	20.915	33.275
Y89_ppm_2SE(int)	1.009	0.548	1.057	9.656	11.570	85.163	0.523	0.777
Zr90_ppm_mean	23.058	9.031	14.300	89.022	105.345	1699.071	9.048	21.881
Zr90_ppm_2SE(int)	0.750	0.413	0.455	5.995	16.152	224.451	0.361	0.696
Nb93_ppm_mean	0.077	0.026	0.047	1.647	4.570	85.775	0.044	0.085
Nb93_ppm_2SE(int)	0.026	0.012	0.013	0.346	0.866	11.512	0.016	0.023
Hf178_ppm_mean	1.513	0.692	0.839	5.019	4.364	62.125	0.676	1.572
Hf178_ppm_2SE(int)	0.095	0.058	0.056	0.334	0.644	7.110	0.062	0.092
Ta181_ppm_mean	0.005	0.004	0.002	0.127	0.364	6.736	0.004	0.008
Ta181_ppm_2SE(int)	0.002	0.003	0.002	0.027	0.072	0.886	0.003	0.004
Pb208_ppm_mean	0.007	0.022	0.010	0.097	0.148	3.842	0.113	0.053
Pb208_ppm_2SE(int)	0.005	0.032	0.006	0.021	0.028	0.449	0.019	0.061
Th232_ppm_mean	0.000	0.000	0.000	0.144	0.317	8.789	0.000	0.000
Th232_ppm_2SE(int)	0.000	0.000	0.001	0.035	0.060	1.162	0.000	0.000
U238_ppm_mean	0.000	0.000	0.000	0.038	0.098	3.459	0.000	0.000
U238_ppm_2SE(int)	0.000	0.000	0.001	0.011	0.018	0.526	0.000	0.000

Table S4 cont.: Pyroxene trace element compositions.

Sample	70017	70017	70017	70017
Site	123-PYX-5.521	123-PYX-5.522	123-PYX-5.523	123-PYX-5.524
Si29_ppm_mean	516080.000	521847.000	503703.000	488665.000
Si29_ppm_2SE(int)	0.000	0.000	0.000	0.000
Ca43_ppm_mean	158317.691	131233.058	140342.633	141133.689
Ca43_ppm_2SE(int)	3037.224	2773.841	3562.222	3183.959
Sc45_ppm_mean	128.339	113.104	159.900	157.108
Sc45_ppm_2SE(int)	2.664	2.444	3.748	3.865
Ti47_ppm_mean	16155.709	8486.351	7133.920	5701.921
Ti47_ppm_2SE(int)	419.138	203.905	156.248	111.072
V51_ppm_mean	199.505	88.609	82.281	66.953
V51_ppm_2SE(int)	5.077	2.102	1.978	1.846
Cr52_ppm_mean	5500.489	3013.770	2844.690	2569.131
Cr52_ppm_2SE(int)	102.933	57.258	61.900	48.503
Mn55_ppm_mean	2021.123	3012.550	3485.359	3595.427
Mn55_ppm_2SE(int)	44.491	67.612	73.076	69.875
Co59_ppm_mean	12.980	14.009	11.482	8.663
Co59_ppm_2SE(int)	0.328	0.591	0.446	0.302
Ni60_ppm_mean	0.465	0.164	0.237	0.167
Ni60_ppm_2SE(int)	0.142	0.097	0.111	0.091
Cu63_ppm_mean	0.685	0.163	0.418	0.331
Cu63_ppm_2SE(int)	0.140	0.061	0.091	0.095
Zn66_ppm_mean	20.208	2.786	4.847	37.633
Zn66_ppm_2SE(int)	1.234	0.713	0.715	2.963
Rb85_ppm_mean	0.003	0.023	0.051	1.608
Rb85_ppm_2SE(int)	0.016	0.017	0.022	0.184
Sr88_ppm_mean	11.803	11.857	29.800	135.185
Sr88_ppm_2SE(int)	0.314	0.333	0.764	11.076
Y89_ppm_mean	37.911	65.510	240.982	523.829
Y89_ppm_2SE(int)	0.961	1.437	5.257	11.873
Zr90_ppm_mean	22.519	25.848	93.872	217.829
Zr90_ppm_2SE(int)	0.699	0.802	1.666	3.451
Nb93_ppm_mean	0.094	0.155	0.302	1.339
Nb93_ppm_2SE(int)	0.022	0.057	0.059	0.191
Hf178_ppm_mean	1.585	1.454	5.719	12.977
Hf178_ppm_2SE(int)	0.090	0.088	0.199	0.305
Ta181_ppm_mean	0.010	0.013	0.035	0.141
Ta181_ppm_2SE(int)	0.005	0.005	0.007	0.017
Pb208_ppm_mean	0.026	0.219	0.072	0.060
Pb208_ppm_2SE(int)	0.008	0.292	0.015	0.013
Th232_ppm_mean	0.003	0.005	0.013	0.089
Th232_ppm_2SE(int)	0.002	0.003	0.005	0.016
U238_ppm_mean	0.000	0.001	0.010	0.038
U238_ppm_2SE(int)	0.000	0.001	0.005	0.007

Table S5: Pyroxene rare earth element compositions.

Sample	10057	10057	10057	10057	10057	10057	10057	10057
Site	67-PYX-1.64	67-PYX-2.67	67-PYX-2.68	67-PYX-2.69	67-PYX-3.82	67-PYX-3.83	67-PYX-3.85	67-PYX-4.90
La139_ppm_mean	1.826	2.719	1.006	2.982	0.864	1.378	0.933	1.870
La139_ppm_2SE(int)	0.550	0.287	0.056	0.436	0.047	0.128	0.067	0.184
Ce140_ppm_mean	7.204	11.668	4.883	10.879	4.803	6.475	5.368	8.421
Ce140_ppm_2SE(int)	1.747	0.888	0.157	1.135	0.215	0.316	0.229	0.558
Pr141_ppm_mean	1.445	2.670	1.170	2.212	1.201	1.426	1.242	1.718
Pr141_ppm_2SE(int)	0.300	0.138	0.057	0.213	0.052	0.074	0.064	0.099
Nd146_ppm_mean	9.088	18.167	8.306	14.560	8.957	10.321	9.398	11.675
Nd146_ppm_2SE(int)	1.517	0.783	0.301	1.207	0.378	0.501	0.569	0.534
Sm147_ppm_mean	5.179	9.934	4.575	7.616	5.136	6.381	5.335	6.149
Sm147_ppm_2SE(int)	0.646	0.515	0.248	0.627	0.306	0.358	0.365	0.315
Eu153_ppm_mean	0.175	0.390	0.329	0.411	0.232	0.244	0.242	0.283
Eu153_ppm_2SE(int)	0.025	0.032	0.025	0.042	0.021	0.026	0.022	0.024
Gd157_ppm_mean	8.364	16.640	7.649	11.397	8.563	9.856	9.253	9.727
Gd157_ppm_2SE(int)	0.774	0.497	0.356	0.840	0.386	0.470	0.514	0.437
Tb159_ppm_mean	1.780	3.246	1.571	2.363	1.756	1.996	1.965	1.902
Tb159_ppm_2SE(int)	0.170	0.126	0.061	0.152	0.066	0.081	0.108	0.062
Dy163_ppm_mean	12.958	22.954	11.111	16.761	12.394	14.637	13.977	13.398
Dy163_ppm_2SE(int)	0.998	0.689	0.321	1.053	0.365	0.600	0.640	0.328
Ho165_ppm_mean	2.936	5.092	2.447	3.668	2.760	3.223	3.112	2.899
Ho165_ppm_2SE(int)	0.223	0.170	0.083	0.223	0.078	0.151	0.158	0.084
Er166_ppm_mean	8.504	14.481	6.899	10.126	7.856	8.973	8.687	8.131
Er166_ppm_2SE(int)	0.655	0.451	0.252	0.575	0.233	0.407	0.399	0.212
Tm169_ppm_mean	1.323	2.009	0.974	1.438	1.109	1.302	1.239	1.106
Tm169_ppm_2SE(int)	0.112	0.080	0.051	0.078	0.047	0.075	0.077	0.044
Yb172_ppm_mean	9.218	13.579	6.389	9.459	7.209	8.828	8.305	7.558
Yb172_ppm_2SE(int)	0.636	0.515	0.203	0.511	0.211	0.407	0.398	0.273
Lu175_ppm_mean	1.373	1.875	0.922	1.321	1.067	1.213	1.241	1.074
Lu175_ppm_2SE(int)	0.089	0.088	0.047	0.079	0.041	0.061	0.064	0.045

Table S5 cont.: Pyroxene rare earth element compositions.

Sample	10057	10057	10057	10057	10057	10057	10057	10057
Site	67-PYX-5.94	67-PYX-5.102	67-PYX-6.104	67-PYX-6.106	67-PYX-6.108	67-PYX-6.111	67-PYX-7.114	67-PYX-7.116
La139_ppm_mean	0.937	0.878	6.186	2.187	1.093	1.105	0.693	8.113
La139_ppm_2SE(int)	0.042	0.044	0.832	0.179	0.068	0.062	0.047	2.831
Ce140_ppm_mean	5.324	4.670	19.724	8.795	5.517	6.415	3.854	24.895
Ce140_ppm_2SE(int)	0.150	0.145	2.234	0.461	0.153	0.180	0.155	7.379
Pr141_ppm_mean	1.270	1.060	3.277	1.727	1.229	1.568	0.900	4.520
Pr141_ppm_2SE(int)	0.059	0.049	0.328	0.091	0.052	0.064	0.046	1.182
Nd146_ppm_mean	9.505	7.744	19.136	11.601	9.023	11.403	6.757	26.191
Nd146_ppm_2SE(int)	0.363	0.273	1.955	0.483	0.385	0.333	0.315	5.884
Sm147_ppm_mean	5.712	4.418	8.059	5.921	5.208	6.636	4.064	12.271
Sm147_ppm_2SE(int)	0.296	0.219	0.704	0.290	0.292	0.290	0.260	1.929
Eu153_ppm_mean	0.235	0.221	0.433	0.308	0.230	0.263	0.204	0.418
Eu153_ppm_2SE(int)	0.023	0.025	0.048	0.029	0.027	0.027	0.020	0.042
Gd157_ppm_mean	9.126	7.445	12.173	9.367	8.354	11.395	6.158	18.779
Gd157_ppm_2SE(int)	0.388	0.365	0.998	0.407	0.393	0.432	0.335	2.460
Tb159_ppm_mean	1.834	1.496	2.269	1.867	1.722	2.322	1.317	3.973
Tb159_ppm_2SE(int)	0.078	0.056	0.178	0.066	0.064	0.086	0.063	0.426
Dy163_ppm_mean	13.229	10.854	15.858	13.148	12.723	16.787	9.614	29.941
Dy163_ppm_2SE(int)	0.505	0.376	1.160	0.444	0.373	0.513	0.344	2.829
Ho165_ppm_mean	2.864	2.372	3.449	2.797	2.779	3.672	2.003	6.378
Ho165_ppm_2SE(int)	0.094	0.085	0.244	0.099	0.086	0.107	0.076	0.583
Er166_ppm_mean	8.336	6.679	9.446	7.955	7.995	10.832	5.807	19.140
Er166_ppm_2SE(int)	0.281	0.266	0.683	0.254	0.306	0.311	0.178	1.397
Tm169_ppm_mean	1.152	0.951	1.305	1.136	1.180	1.512	0.810	2.942
Tm169_ppm_2SE(int)	0.061	0.046	0.107	0.051	0.055	0.055	0.038	0.216
Yb172_ppm_mean	7.876	6.289	8.660	7.670	8.157	10.464	5.339	20.055
Yb172_ppm_2SE(int)	0.280	0.257	0.605	0.334	0.371	0.292	0.235	1.174
Lu175_ppm_mean	1.061	0.870	1.201	0.962	1.139	1.494	0.777	2.891
Lu175_ppm_2SE(int)	0.049	0.039	0.091	0.045	0.064	0.063	0.047	0.132

Table S5 cont.: Pyroxene rare earth element compositions.

Sample	10057	10057	10057	10057	10057	10057	12039	12039
Site	67-PYX-8.123	67-PYX-8.124	67-PYX-9.125	67-PYX-9.126	67-PYX-10.129	67-PYX-10.130	63-PYX-1.417	63-PYX-1.418
La139_ppm_mean	1.126	2.070	0.811	2.610	1.638	31.374	0.401	1.441
La139_ppm_2SE(int)	0.075	0.199	0.041	0.139	0.140	10.093	0.025	0.063
Ce140_ppm_mean	5.917	9.094	4.688	9.655	7.038	79.242	2.190	7.097
Ce140_ppm_2SE(int)	0.268	0.514	0.128	0.390	0.459	22.461	0.073	0.141
Pr141_ppm_mean	1.397	1.898	1.093	1.824	1.508	13.371	0.520	1.564
Pr141_ppm_2SE(int)	0.066	0.093	0.049	0.075	0.103	3.623	0.035	0.049
Nd146_ppm_mean	10.237	13.544	8.230	11.382	10.493	69.413	3.666	10.772
Nd146_ppm_2SE(int)	0.541	0.638	0.287	0.508	0.691	16.652	0.166	0.351
Sm147_ppm_mean	5.921	7.743	4.833	5.915	5.566	28.663	1.755	5.246
Sm147_ppm_2SE(int)	0.354	0.394	0.252	0.296	0.400	5.348	0.130	0.196
Eu153_ppm_mean	0.399	0.420	0.205	0.400	0.489	2.961	0.205	0.488
Eu153_ppm_2SE(int)	0.044	0.044	0.025	0.037	0.040	0.134	0.024	0.036
Gd157_ppm_mean	9.515	12.384	7.849	9.382	8.834	41.140	2.777	7.445
Gd157_ppm_2SE(int)	0.513	0.518	0.320	0.422	0.644	6.799	0.173	0.326
Tb159_ppm_mean	1.952	2.531	1.572	1.965	1.852	8.949	0.555	1.368
Tb159_ppm_2SE(int)	0.113	0.100	0.059	0.073	0.104	1.368	0.030	0.049
Dy163_ppm_mean	14.183	18.379	11.613	14.168	13.204	67.494	3.922	9.575
Dy163_ppm_2SE(int)	0.696	0.670	0.304	0.348	0.761	9.509	0.186	0.329
Ho165_ppm_mean	2.916	3.981	2.483	3.104	2.813	15.661	0.794	1.880
Ho165_ppm_2SE(int)	0.145	0.149	0.071	0.086	0.180	2.176	0.043	0.066
Er166_ppm_mean	8.607	11.896	7.300	9.138	8.347	50.042	2.250	5.104
Er166_ppm_2SE(int)	0.404	0.395	0.222	0.281	0.477	7.087	0.094	0.207
Tm169_ppm_mean	1.167	1.719	1.009	1.340	1.167	7.930	0.291	0.679
Tm169_ppm_2SE(int)	0.065	0.061	0.039	0.051	0.079	1.036	0.021	0.032
Yb172_ppm_mean	7.986	11.893	7.048	9.458	7.652	57.784	1.851	4.865
Yb172_ppm_2SE(int)	0.399	0.418	0.275	0.364	0.545	7.285	0.096	0.176
Lu175_ppm_mean	1.079	1.741	0.965	1.323	1.065	8.043	0.261	0.690
Lu175_ppm_2SE(int)	0.063	0.066	0.037	0.061	0.079	0.901	0.019	0.037

Table S5 cont.: Pyroxene rare earth element compositions.

Sample	12039	12039	12039	12039	12039	12039	12039	12039
Site	63-PYX-1.419	63-PYX-1.420	63-PYX-1.421	63-PYX-2.425	63-PYX-2.426	63-PYX-2.427	63-PYX-3.430	63-PYX-3.431
La139_ppm_mean	4.509	0.275	5.147	0.176	0.964	68.912	2.798	1.205
La139_ppm_2SE(int)	0.335	0.034	0.620	0.022	0.050	10.697	0.234	0.053
Ce140_ppm_mean	17.469	1.008	17.343	1.112	4.701	211.771	9.249	6.006
Ce140_ppm_2SE(int)	0.948	0.202	1.377	0.055	0.113	30.986	0.632	0.139
Pr141_ppm_mean	3.698	0.149	3.458	0.260	1.089	34.679	1.642	1.425
Pr141_ppm_2SE(int)	0.148	0.020	0.184	0.020	0.045	5.209	0.108	0.046
Nd146_ppm_mean	24.944	0.886	22.160	2.053	7.801	177.651	9.450	9.494
Nd146_ppm_2SE(int)	0.767	0.113	1.030	0.159	0.288	25.965	0.476	0.285
Sm147_ppm_mean	12.409	0.382	10.760	1.201	3.907	59.629	4.098	4.937
Sm147_ppm_2SE(int)	0.456	0.063	0.432	0.114	0.201	8.500	0.270	0.298
Eu153_ppm_mean	0.980	0.065	1.484	0.098	0.351	3.759	0.421	0.458
Eu153_ppm_2SE(int)	0.049	0.016	0.080	0.014	0.028	0.519	0.039	0.031
Gd157_ppm_mean	19.030	0.707	15.752	1.947	6.005	72.294	5.720	7.170
Gd157_ppm_2SE(int)	0.525	0.091	0.473	0.150	0.293	9.395	0.275	0.355
Tb159_ppm_mean	3.725	0.133	3.187	0.402	1.155	12.056	1.065	1.360
Tb159_ppm_2SE(int)	0.086	0.012	0.094	0.025	0.047	1.465	0.053	0.059
Dy163_ppm_mean	25.961	1.162	22.189	2.909	7.978	74.011	7.150	9.635
Dy163_ppm_2SE(int)	0.529	0.090	0.534	0.138	0.281	8.666	0.255	0.279
Ho165_ppm_mean	5.603	0.281	4.893	0.640	1.686	14.851	1.546	2.042
Ho165_ppm_2SE(int)	0.109	0.021	0.113	0.030	0.061	1.538	0.056	0.065
Er166_ppm_mean	16.360	0.830	14.263	1.801	4.766	39.504	4.302	5.744
Er166_ppm_2SE(int)	0.293	0.060	0.356	0.096	0.202	3.963	0.170	0.204
Tm169_ppm_mean	2.356	0.117	2.056	0.242	0.668	5.373	0.578	0.766
Tm169_ppm_2SE(int)	0.055	0.012	0.056	0.020	0.036	0.481	0.027	0.039
Yb172_ppm_mean	16.619	0.892	15.059	1.928	4.760	33.927	4.147	5.502
Yb172_ppm_2SE(int)	0.322	0.085	0.462	0.140	0.190	2.628	0.204	0.191
Lu175_ppm_mean	2.573	0.141	2.303	0.254	0.696	4.919	0.595	0.835
Lu175_ppm_2SE(int)	0.060	0.015	0.070	0.020	0.033	0.351	0.034	0.039

Table S5 cont.: Pyroxene rare earth element compositions.

Sample	12039	12039	12039	12039	12039	12039	12039	12043
Site	63-PYX-3.432	63-PYX-4.441	63-PYX-4.444	63-PYX-5.445	63-PYX-5.447	63-PYX-5.448	63-PYX-5.449	15-PYX.1.452
La139_ppm_mean	1.796	0.058	10.119	0.153	1.305	0.094	0.844	0.830
La139_ppm_2SE(int)	0.072	0.013	1.114	0.025	0.052	0.013	0.039	0.089
Ce140_ppm_mean	9.159	0.373	31.977	0.699	6.495	0.572	4.386	2.446
Ce140_ppm_2SE(int)	0.207	0.025	3.071	0.050	0.160	0.037	0.279	0.207
Pr141_ppm_mean	2.246	0.085	5.579	0.170	1.519	0.116	1.057	0.348
Pr141_ppm_2SE(int)	0.075	0.013	0.421	0.018	0.048	0.013	0.041	0.032
Nd146_ppm_mean	15.829	0.714	32.592	1.179	10.757	1.057	7.201	1.821
Nd146_ppm_2SE(int)	0.458	0.085	2.194	0.136	0.282	0.115	0.236	0.191
Sm147_ppm_mean	8.496	0.535	13.788	0.706	5.508	0.617	3.694	0.556
Sm147_ppm_2SE(int)	0.318	0.073	0.669	0.092	0.236	0.071	0.208	0.072
Eu153_ppm_mean	0.630	0.053	1.187	0.065	0.481	0.061	0.310	0.094
Eu153_ppm_2SE(int)	0.040	0.011	0.081	0.013	0.032	0.012	0.032	0.020
Gd157_ppm_mean	13.642	0.943	19.344	1.256	8.486	1.098	5.658	0.837
Gd157_ppm_2SE(int)	0.427	0.078	0.788	0.126	0.335	0.129	0.245	0.085
Tb159_ppm_mean	2.709	0.227	3.729	0.269	1.647	0.246	1.194	0.176
Tb159_ppm_2SE(int)	0.080	0.023	0.120	0.018	0.054	0.022	0.048	0.015
Dy163_ppm_mean	19.242	1.642	25.220	2.106	11.348	1.706	8.329	1.287
Dy163_ppm_2SE(int)	0.604	0.104	0.670	0.117	0.253	0.096	0.229	0.089
Ho165_ppm_mean	4.289	0.398	5.421	0.483	2.428	0.428	1.766	0.292
Ho165_ppm_2SE(int)	0.134	0.027	0.137	0.023	0.070	0.029	0.062	0.020
Er166_ppm_mean	12.360	1.178	15.502	1.490	7.117	1.315	5.076	0.931
Er166_ppm_2SE(int)	0.340	0.069	0.341	0.094	0.226	0.068	0.186	0.072
Tm169_ppm_mean	1.869	0.174	2.219	0.176	0.994	0.181	0.703	0.138
Tm169_ppm_2SE(int)	0.058	0.016	0.059	0.015	0.045	0.016	0.034	0.012
Yb172_ppm_mean	13.316	1.187	15.421	1.461	6.945	1.323	5.041	0.968
Yb172_ppm_2SE(int)	0.391	0.102	0.302	0.098	0.184	0.118	0.160	0.075
Lu175_ppm_mean	2.080	0.186	2.379	0.219	1.086	0.198	0.789	0.139
Lu175_ppm_2SE(int)	0.068	0.014	0.056	0.018	0.043	0.018	0.028	0.014

Table S5 cont.: Pyroxene rare earth element compositions.

Sample	12043	12043	12043	12043	12043	12043	12043	12043
Site	15-PYX-1.453	15-PYX-1.454	15-PYX-1.455	15-PYX-1.456	15-PYX-3.469	15-PYX-3.470	15-PYX-3.471	15-PYX-3.478
La139_ppm_mean	3.748	1.356	0.060	1.984	0.013	0.383	0.485	0.708
La139_ppm_2SE(int)	0.308	0.182	0.010	0.394	0.005	0.041	0.031	0.045
Ce140_ppm_mean	10.251	4.587	0.269	6.231	0.145	1.658	2.443	3.272
Ce140_ppm_2SE(int)	0.806	0.438	0.027	0.847	0.047	0.114	0.063	0.097
Pr141_ppm_mean	1.582	0.833	0.075	1.220	0.032	0.345	0.592	0.749
Pr141_ppm_2SE(int)	0.122	0.061	0.011	0.173	0.008	0.030	0.030	0.031
Nd146_ppm_mean	8.092	4.917	0.542	7.591	0.259	2.263	4.465	5.468
Nd146_ppm_2SE(int)	0.554	0.317	0.072	0.500	0.049	0.149	0.205	0.260
Sm147_ppm_mean	2.880	2.204	0.431	3.637	0.158	1.182	2.350	2.919
Sm147_ppm_2SE(int)	0.223	0.152	0.062	0.215	0.043	0.121	0.146	0.185
Eu153_ppm_mean	0.314	0.171	0.027	0.255	0.013	0.111	0.148	0.187
Eu153_ppm_2SE(int)	0.036	0.027	0.008	0.029	0.007	0.014	0.016	0.018
Gd157_ppm_mean	3.964	3.611	0.800	6.034	0.378	1.981	4.098	5.221
Gd157_ppm_2SE(int)	0.234	0.202	0.089	0.279	0.073	0.156	0.185	0.239
Tb159_ppm_mean	0.788	0.692	0.163	1.243	0.102	0.414	0.836	1.086
Tb159_ppm_2SE(int)	0.042	0.034	0.016	0.045	0.013	0.024	0.042	0.042
Dy163_ppm_mean	5.109	4.911	1.345	9.325	0.780	3.013	6.105	8.181
Dy163_ppm_2SE(int)	0.229	0.193	0.097	0.271	0.075	0.136	0.183	0.221
Ho165_ppm_mean	1.124	1.046	0.327	2.043	0.183	0.662	1.291	1.856
Ho165_ppm_2SE(int)	0.049	0.050	0.022	0.073	0.016	0.028	0.048	0.055
Er166_ppm_mean	3.050	2.988	0.940	6.087	0.626	1.903	4.182	5.590
Er166_ppm_2SE(int)	0.133	0.114	0.065	0.174	0.060	0.088	0.160	0.150
Tm169_ppm_mean	0.424	0.437	0.142	0.946	0.109	0.279	0.608	0.833
Tm169_ppm_2SE(int)	0.031	0.024	0.014	0.037	0.013	0.019	0.033	0.031
Yb172_ppm_mean	3.067	3.101	1.045	6.853	0.776	2.047	4.410	6.241
Yb172_ppm_2SE(int)	0.171	0.152	0.087	0.255	0.066	0.111	0.175	0.180
Lu175_ppm_mean	0.413	0.458	0.154	1.042	0.115	0.284	0.666	0.964
Lu175_ppm_2SE(int)	0.025	0.025	0.012	0.049	0.014	0.023	0.032	0.033

Table S5 cont.: Pyroxene rare earth element compositions.

Sample	12043	12043	12043	12043	12043	12043	12043	12043
Site	15-PYX-3.480	15-PYX-4.481	15-PYX-4.482	15-PYX-4.483	15-PYX-5.484	15-PYX-5.485	15-PYX-4.486	15-PYX-4.489
La139_ppm_mean	0.273	0.015	0.140	0.319	0.010	1.012	26.531	1.134
La139_ppm_2SE(int)	0.028	0.006	0.023	0.057	0.004	0.088	1.734	0.071
Ce140_ppm_mean	1.258	0.076	0.544	1.236	0.080	3.285	67.956	5.515
Ce140_ppm_2SE(int)	0.062	0.012	0.063	0.138	0.013	0.250	4.249	0.240
Pr141_ppm_mean	0.314	0.021	0.110	0.266	0.026	0.558	10.574	1.268
Pr141_ppm_2SE(int)	0.022	0.005	0.017	0.028	0.007	0.040	0.584	0.062
Nd146_ppm_mean	2.137	0.161	0.833	1.815	0.165	3.300	55.498	8.818
Nd146_ppm_2SE(int)	0.145	0.037	0.110	0.139	0.037	0.242	3.011	0.522
Sm147_ppm_mean	1.307	0.157	0.510	0.980	0.121	1.541	18.917	4.934
Sm147_ppm_2SE(int)	0.125	0.040	0.079	0.107	0.036	0.141	0.961	0.332
Eu153_ppm_mean	0.097	0.007	0.049	0.096	0.014	0.140	1.071	0.291
Eu153_ppm_2SE(int)	0.015	0.004	0.011	0.018	0.005	0.019	0.069	0.033
Gd157_ppm_mean	2.295	0.342	0.865	1.733	0.241	2.382	25.816	7.958
Gd157_ppm_2SE(int)	0.151	0.070	0.103	0.126	0.039	0.170	1.139	0.392
Tb159_ppm_mean	0.441	0.079	0.196	0.381	0.078	0.502	4.687	1.644
Tb159_ppm_2SE(int)	0.028	0.010	0.023	0.023	0.012	0.033	0.224	0.073
Dy163_ppm_mean	3.225	0.651	1.658	2.770	0.639	3.565	31.476	12.116
Dy163_ppm_2SE(int)	0.136	0.053	0.123	0.134	0.059	0.168	1.230	0.478
Ho165_ppm_mean	0.705	0.164	0.370	0.601	0.154	0.766	6.448	2.653
Ho165_ppm_2SE(int)	0.033	0.017	0.031	0.032	0.015	0.036	0.248	0.086
Er166_ppm_mean	2.072	0.565	1.098	1.766	0.542	2.401	18.646	7.875
Er166_ppm_2SE(int)	0.096	0.057	0.091	0.096	0.042	0.097	0.671	0.295
Tm169_ppm_mean	0.267	0.088	0.167	0.261	0.089	0.338	2.619	1.155
Tm169_ppm_2SE(int)	0.021	0.010	0.015	0.020	0.011	0.023	0.101	0.056
Yb172_ppm_mean	2.037	0.685	1.107	1.783	0.635	2.466	17.529	9.151
Yb172_ppm_2SE(int)	0.116	0.072	0.096	0.100	0.064	0.131	0.503	0.332
Lu175_ppm_mean	0.282	0.111	0.169	0.259	0.090	0.364	2.506	1.309
Lu175_ppm_2SE(int)	0.019	0.013	0.018	0.019	0.011	0.026	0.084	0.053

Table S5 cont.: Pyroxene rare earth element compositions.

Sample	12043	15085	15085	15085	15085	15085	15085	15085
Site	15-PYX-4.490	16-PYX-1.218	16-PYX-1.219	16-PYX-1.220	16-PYX-1.221	16-PYX-1.222	16-PYX-2.226	16-PYX-2.227
La139_ppm_mean	0.231	0.587	3.327	0.164	0.100	0.001	0.093	0.061
La139_ppm_2SE(int)	0.057	0.037	0.447	0.032	0.023	0.001	0.018	0.015
Ce140_ppm_mean	0.872	3.142	9.170	0.729	0.299	0.019	0.514	0.267
Ce140_ppm_2SE(int)	0.143	0.112	1.082	0.064	0.070	0.007	0.037	0.040
Pr141_ppm_mean	0.179	0.816	1.556	0.146	0.042	0.002	0.124	0.063
Pr141_ppm_2SE(int)	0.022	0.035	0.160	0.024	0.009	0.002	0.015	0.013
Nd146_ppm_mean	1.128	6.706	8.644	1.023	0.274	0.044	0.833	0.431
Nd146_ppm_2SE(int)	0.138	0.261	0.787	0.103	0.054	0.023	0.090	0.053
Sm147_ppm_mean	0.770	4.222	3.424	0.562	0.122	0.038	0.445	0.304
Sm147_ppm_2SE(int)	0.080	0.206	0.314	0.081	0.030	0.019	0.078	0.061
Eu153_ppm_mean	0.048	0.377	0.440	0.066	0.024	0.002	0.050	0.027
Eu153_ppm_2SE(int)	0.010	0.030	0.046	0.014	0.009	0.002	0.012	0.008
Gd157_ppm_mean	1.266	8.390	5.044	0.933	0.239	0.058	0.842	0.465
Gd157_ppm_2SE(int)	0.122	0.310	0.425	0.115	0.058	0.022	0.096	0.078
Tb159_ppm_mean	0.289	1.992	0.922	0.221	0.042	0.019	0.172	0.100
Tb159_ppm_2SE(int)	0.023	0.067	0.066	0.020	0.009	0.005	0.020	0.013
Dy163_ppm_mean	2.235	15.938	6.417	1.506	0.358	0.184	1.310	0.741
Dy163_ppm_2SE(int)	0.117	0.602	0.390	0.094	0.054	0.036	0.097	0.071
Ho165_ppm_mean	0.558	4.026	1.367	0.332	0.075	0.046	0.274	0.176
Ho165_ppm_2SE(int)	0.027	0.143	0.078	0.028	0.013	0.011	0.023	0.020
Er166_ppm_mean	1.717	13.113	4.035	0.956	0.292	0.160	0.768	0.619
Er166_ppm_2SE(int)	0.097	0.510	0.245	0.070	0.041	0.030	0.070	0.052
Tm169_ppm_mean	0.255	2.070	0.539	0.150	0.036	0.031	0.100	0.075
Tm169_ppm_2SE(int)	0.018	0.092	0.033	0.016	0.008	0.007	0.013	0.009
Yb172_ppm_mean	1.853	15.536	3.689	0.970	0.313	0.167	0.696	0.509
Yb172_ppm_2SE(int)	0.133	0.581	0.182	0.083	0.048	0.038	0.066	0.060
Lu175_ppm_mean	0.266	2.476	0.544	0.136	0.035	0.023	0.082	0.087
Lu175_ppm_2SE(int)	0.017	0.102	0.032	0.015	0.008	0.006	0.011	0.013

Table S5 cont.: Pyroxene rare earth element compositions.

Sample	15085	15085	15085	15085	15085	15085	15085	15085
Site	16-PYX-2.228	16-PYX-2.229	16-PYX-2.230	16-PYX-3.233	16-PYX-3.234	16-PYX-3.237	16-PYX-4.239	16-PYX-4.240
La139_ppm_mean	0.026	0.080	0.215	0.648	0.000	0.060	0.058	0.038
La139_ppm_2SE(int)	0.007	0.012	0.026	0.143	0.000	0.011	0.021	0.011
Ce140_ppm_mean	0.173	0.416	1.157	2.708	0.011	0.339	0.293	0.243
Ce140_ppm_2SE(int)	0.022	0.035	0.053	0.380	0.005	0.028	0.042	0.027
Pr141_ppm_mean	0.049	0.098	0.253	0.539	0.003	0.080	0.070	0.071
Pr141_ppm_2SE(int)	0.009	0.015	0.021	0.051	0.002	0.012	0.012	0.009
Nd146_ppm_mean	0.371	0.742	1.807	3.392	0.033	0.622	0.583	0.472
Nd146_ppm_2SE(int)	0.055	0.090	0.141	0.249	0.018	0.068	0.074	0.069
Sm147_ppm_mean	0.186	0.483	0.895	1.612	0.008	0.351	0.341	0.354
Sm147_ppm_2SE(int)	0.041	0.072	0.101	0.184	0.009	0.064	0.063	0.067
Eu153_ppm_mean	0.022	0.043	0.090	0.196	0.001	0.038	0.029	0.033
Eu153_ppm_2SE(int)	0.008	0.011	0.015	0.044	0.001	0.010	0.009	0.008
Gd157_ppm_mean	0.442	0.862	1.613	2.266	0.056	0.674	0.669	0.591
Gd157_ppm_2SE(int)	0.065	0.091	0.129	0.191	0.022	0.073	0.078	0.075
Tb159_ppm_mean	0.110	0.183	0.312	0.419	0.019	0.155	0.131	0.155
Tb159_ppm_2SE(int)	0.012	0.017	0.021	0.029	0.006	0.014	0.013	0.017
Dy163_ppm_mean	0.831	1.404	2.189	2.654	0.154	1.151	1.050	1.135
Dy163_ppm_2SE(int)	0.088	0.096	0.103	0.149	0.031	0.087	0.080	0.078
Ho165_ppm_mean	0.203	0.299	0.456	0.527	0.034	0.271	0.241	0.254
Ho165_ppm_2SE(int)	0.023	0.022	0.033	0.036	0.007	0.021	0.019	0.018
Er166_ppm_mean	0.582	0.861	1.261	1.500	0.091	0.800	0.735	0.771
Er166_ppm_2SE(int)	0.055	0.064	0.076	0.105	0.021	0.060	0.069	0.070
Tm169_ppm_mean	0.090	0.131	0.172	0.202	0.013	0.111	0.104	0.116
Tm169_ppm_2SE(int)	0.012	0.016	0.016	0.020	0.004	0.014	0.012	0.012
Yb172_ppm_mean	0.639	0.854	1.252	1.383	0.140	0.760	0.784	0.830
Yb172_ppm_2SE(int)	0.062	0.082	0.105	0.109	0.032	0.074	0.076	0.060
Lu175_ppm_mean	0.090	0.141	0.158	0.180	0.026	0.119	0.094	0.129
Lu175_ppm_2SE(int)	0.010	0.015	0.018	0.016	0.007	0.013	0.014	0.014

Table S5 cont.: Pyroxene rare earth element compositions.

Sample	15085	15085	15085	15085	15085	15085	15085	15085
Site	16-PYX-4.241	16-PYX-4.242	16-PYX-4.243	16-PYX-5.248	16-PYX-5.249	16-PYX-5.250	16-PYX-5.251	16-PYX-5.252
La139_ppm_mean	0.171	12.179	8.374	0.020	0.001	0.165	0.066	0.079
La139_ppm_2SE(int)	0.027	2.039	1.346	0.040	0.001	0.028	0.013	0.013
Ce140_ppm_mean	0.741	33.482	24.653	0.011	0.022	0.569	0.405	0.473
Ce140_ppm_2SE(int)	0.082	5.511	3.121	0.005	0.008	0.055	0.036	0.034
Pr141_ppm_mean	0.139	4.762	4.003	0.000	0.004	0.100	0.080	0.126
Pr141_ppm_2SE(int)	0.017	0.745	0.422	0.001	0.003	0.015	0.011	0.015
Nd146_ppm_mean	0.971	23.154	21.957	0.020	0.049	0.729	0.715	0.788
Nd146_ppm_2SE(int)	0.081	3.299	2.046	0.014	0.020	0.086	0.117	0.110
Sm147_ppm_mean	0.665	6.940	8.413	0.026	0.051	0.372	0.458	0.518
Sm147_ppm_2SE(int)	0.080	0.796	0.621	0.018	0.029	0.071	0.080	0.092
Eu153_ppm_mean	0.061	0.703	0.902	0.004	0.006	0.048	0.047	0.038
Eu153_ppm_2SE(int)	0.014	0.088	0.094	0.003	0.004	0.013	0.013	0.011
Gd157_ppm_mean	1.037	8.645	11.098	0.050	0.110	0.691	0.753	0.952
Gd157_ppm_2SE(int)	0.108	0.835	0.754	0.023	0.035	0.083	0.094	0.111
Tb159_ppm_mean	0.223	1.395	2.001	0.018	0.024	0.134	0.143	0.204
Tb159_ppm_2SE(int)	0.014	0.114	0.118	0.006	0.006	0.017	0.015	0.017
Dy163_ppm_mean	1.612	8.829	13.487	0.111	0.204	1.141	1.172	1.481
Dy163_ppm_2SE(int)	0.096	0.654	0.644	0.029	0.037	0.087	0.101	0.109
Ho165_ppm_mean	0.358	1.711	2.664	0.035	0.046	0.220	0.269	0.349
Ho165_ppm_2SE(int)	0.024	0.112	0.126	0.007	0.010	0.020	0.025	0.030
Er166_ppm_mean	1.065	4.649	7.211	0.085	0.164	0.637	0.842	0.988
Er166_ppm_2SE(int)	0.077	0.315	0.335	0.024	0.026	0.065	0.064	0.070
Tm169_ppm_mean	0.159	0.621	0.919	0.018	0.024	0.118	0.120	0.142
Tm169_ppm_2SE(int)	0.019	0.046	0.051	0.005	0.006	0.011	0.013	0.013
Yb172_ppm_mean	1.134	4.037	5.899	0.126	0.157	0.666	0.811	1.031
Yb172_ppm_2SE(int)	0.087	0.225	0.269	0.033	0.034	0.068	0.084	0.083
Lu175_ppm_mean	0.177	0.527	0.806	0.022	0.035	0.103	0.111	0.141
Lu175_ppm_2SE(int)	0.015	0.029	0.043	0.007	0.007	0.014	0.014	0.015

Table S5 cont.: Pyroxene rare earth element compositions.

Sample	15085	15085	15085	15085	15085	15085	15085	15085
Site	16-PYX-6.253	16-PYX-6.254	16-PYX-6.255	16-PYX-7.262	16-PYX-7.263	16-PYX-7.264	16-PYX-7.265	16-PYX-7.266
La139_ppm_mean	10.943	0.188	0.001	0.000	0.082	0.079	0.059	0.086
La139_ppm_2SE(int)	0.382	0.026	0.002	0.000	0.014	0.017	0.013	0.015
Ce140_ppm_mean	44.603	0.873	0.023	0.019	0.279	0.490	0.338	0.469
Ce140_ppm_2SE(int)	1.283	0.056	0.007	0.006	0.034	0.039	0.025	0.038
Pr141_ppm_mean	8.806	0.204	0.013	0.005	0.048	0.110	0.085	0.111
Pr141_ppm_2SE(int)	0.230	0.019	0.015	0.003	0.009	0.015	0.012	0.014
Nd146_ppm_mean	54.606	1.426	0.029	0.031	0.303	0.899	0.670	0.830
Nd146_ppm_2SE(int)	1.447	0.131	0.015	0.017	0.066	0.099	0.092	0.081
Sm147_ppm_mean	21.806	0.741	0.032	0.024	0.165	0.461	0.387	0.566
Sm147_ppm_2SE(int)	0.737	0.107	0.020	0.016	0.047	0.080	0.068	0.090
Eu153_ppm_mean	1.986	0.105	0.001	0.005	0.023	0.066	0.056	0.047
Eu153_ppm_2SE(int)	0.089	0.018	0.001	0.004	0.008	0.017	0.012	0.012
Gd157_ppm_mean	28.508	1.214	0.082	0.074	0.271	0.704	0.780	0.891
Gd157_ppm_2SE(int)	0.763	0.118	0.032	0.032	0.057	0.105	0.080	0.098
Tb159_ppm_mean	5.086	0.268	0.017	0.018	0.057	0.169	0.162	0.196
Tb159_ppm_2SE(int)	0.137	0.022	0.005	0.006	0.010	0.023	0.018	0.017
Dy163_ppm_mean	32.841	1.690	0.161	0.136	0.562	1.200	1.168	1.365
Dy163_ppm_2SE(int)	0.809	0.124	0.048	0.033	0.069	0.094	0.089	0.097
Ho165_ppm_mean	6.331	0.361	0.046	0.045	0.112	0.257	0.272	0.326
Ho165_ppm_2SE(int)	0.159	0.025	0.009	0.009	0.014	0.021	0.022	0.026
Er166_ppm_mean	16.484	1.046	0.121	0.138	0.389	0.685	0.784	0.916
Er166_ppm_2SE(int)	0.393	0.076	0.022	0.028	0.044	0.064	0.058	0.083
Tm169_ppm_mean	2.256	0.155	0.022	0.021	0.058	0.095	0.112	0.134
Tm169_ppm_2SE(int)	0.071	0.016	0.006	0.006	0.010	0.013	0.015	0.013
Yb172_ppm_mean	14.573	0.908	0.157	0.184	0.363	0.666	0.757	0.977
Yb172_ppm_2SE(int)	0.402	0.072	0.026	0.036	0.051	0.083	0.080	0.085
Lu175_ppm_mean	2.062	0.131	0.026	0.025	0.059	0.091	0.117	0.155
Lu175_ppm_2SE(int)	0.065	0.017	0.006	0.007	0.009	0.012	0.014	0.018

Table S5 cont.: Pyroxene rare earth element compositions.

Sample	15085	15085	15085	15085	15085	15085	15085	15085
Site	16-PYX-7.267	16-PYX-8.268	16-PYX-8.269	16-PYX-8.270	16-PYX-8.271	24-PYX-1.369	24-PYX-1.370	24-PYX-1.371
La139_ppm_mean	0.238	0.336	0.273	0.070	0.045	0.000	0.041	0.041
La139_ppm_2SE(int)	0.025	0.045	0.050	0.015	0.014	0.000	0.013	0.009
Ce140_ppm_mean	1.141	1.092	0.779	0.311	0.251	0.020	0.226	0.314
Ce140_ppm_2SE(int)	0.081	0.104	0.099	0.029	0.024	0.007	0.092	0.024
Pr141_ppm_mean	0.233	0.155	0.135	0.086	0.062	0.003	0.042	0.077
Pr141_ppm_2SE(int)	0.023	0.021	0.023	0.016	0.009	0.002	0.009	0.011
Nd146_ppm_mean	1.653	0.769	0.784	0.641	0.456	0.028	0.261	0.524
Nd146_ppm_2SE(int)	0.175	0.095	0.133	0.077	0.066	0.016	0.051	0.063
Sm147_ppm_mean	0.807	0.254	0.349	0.432	0.354	0.057	0.176	0.346
Sm147_ppm_2SE(int)	0.095	0.055	0.061	0.074	0.062	0.042	0.039	0.058
Eu153_ppm_mean	0.073	0.067	0.043	0.032	0.036	0.002	0.018	0.034
Eu153_ppm_2SE(int)	0.017	0.013	0.014	0.010	0.010	0.002	0.007	0.010
Gd157_ppm_mean	1.397	0.482	0.691	0.608	0.631	0.094	0.352	0.701
Gd157_ppm_2SE(int)	0.158	0.084	0.086	0.094	0.070	0.032	0.058	0.101
Tb159_ppm_mean	0.306	0.079	0.148	0.140	0.150	0.025	0.075	0.138
Tb159_ppm_2SE(int)	0.026	0.011	0.017	0.017	0.016	0.008	0.010	0.014
Dy163_ppm_mean	2.091	0.595	0.992	1.097	1.125	0.185	0.511	1.119
Dy163_ppm_2SE(int)	0.162	0.066	0.067	0.098	0.082	0.031	0.059	0.108
Ho165_ppm_mean	0.452	0.142	0.272	0.239	0.250	0.050	0.132	0.251
Ho165_ppm_2SE(int)	0.029	0.018	0.023	0.024	0.019	0.007	0.017	0.020
Er166_ppm_mean	1.358	0.376	0.743	0.741	0.768	0.127	0.398	0.762
Er166_ppm_2SE(int)	0.096	0.043	0.063	0.052	0.065	0.021	0.049	0.061
Tm169_ppm_mean	0.205	0.071	0.111	0.121	0.112	0.024	0.060	0.110
Tm169_ppm_2SE(int)	0.016	0.011	0.013	0.015	0.013	0.005	0.008	0.012
Yb172_ppm_mean	1.379	0.435	0.717	0.789	0.852	0.178	0.428	0.760
Yb172_ppm_2SE(int)	0.097	0.059	0.089	0.079	0.084	0.035	0.057	0.075
Lu175_ppm_mean	0.201	0.065	0.112	0.113	0.132	0.031	0.068	0.120
Lu175_ppm_2SE(int)	0.018	0.009	0.016	0.015	0.018	0.005	0.010	0.013

Table S5 cont.: Pyroxene rare earth element compositions.

Sample	15085	15085	15085	15085	15085	15085	15085	15085
Site	24-PYX-1.372	24-PYX-2.377	24-PYX-2.379	24-PYX-2.381	24-PYX-2.383	24-PYX-2.384	24-PYX-3.388	24-PYX-3.392
La139_ppm_mean	1.955	0.029	0.142	0.046	0.044	0.091	0.000	0.145
La139_ppm_2SE(int)	0.418	0.049	0.019	0.016	0.010	0.013	0.000	0.019
Ce140_ppm_mean	5.604	0.024	0.834	0.188	0.278	0.525	0.076	0.815
Ce140_ppm_2SE(int)	1.133	0.007	0.043	0.056	0.022	0.033	0.115	0.050
Pr141_ppm_mean	0.859	0.010	0.230	0.040	0.076	0.127	0.004	0.196
Pr141_ppm_2SE(int)	0.169	0.008	0.024	0.011	0.012	0.014	0.002	0.020
Nd146_ppm_mean	4.399	0.028	1.496	0.216	0.497	0.819	0.059	1.359
Nd146_ppm_2SE(int)	0.806	0.014	0.126	0.046	0.066	0.075	0.023	0.129
Sm147_ppm_mean	1.555	0.037	0.835	0.131	0.334	0.506	0.022	0.722
Sm147_ppm_2SE(int)	0.275	0.017	0.094	0.041	0.077	0.076	0.013	0.089
Eu153_ppm_mean	0.292	0.005	0.084	0.008	0.037	0.049	0.009	0.071
Eu153_ppm_2SE(int)	0.046	0.003	0.016	0.004	0.010	0.009	0.008	0.013
Gd157_ppm_mean	2.062	0.100	1.325	0.231	0.629	0.916	0.060	1.133
Gd157_ppm_2SE(int)	0.261	0.036	0.127	0.045	0.076	0.088	0.022	0.110
Tb159_ppm_mean	0.413	0.019	0.272	0.064	0.139	0.196	0.017	0.239
Tb159_ppm_2SE(int)	0.043	0.004	0.020	0.010	0.016	0.018	0.004	0.021
Dy163_ppm_mean	2.978	0.184	1.947	0.433	0.976	1.476	0.159	1.643
Dy163_ppm_2SE(int)	0.259	0.033	0.131	0.046	0.076	0.096	0.033	0.111
Ho165_ppm_mean	0.644	0.046	0.398	0.107	0.223	0.344	0.037	0.359
Ho165_ppm_2SE(int)	0.050	0.008	0.029	0.013	0.016	0.022	0.006	0.023
Er166_ppm_mean	1.758	0.167	1.033	0.303	0.743	0.963	0.139	0.955
Er166_ppm_2SE(int)	0.141	0.026	0.066	0.036	0.053	0.064	0.030	0.071
Tm169_ppm_mean	0.261	0.028	0.145	0.054	0.095	0.143	0.018	0.127
Tm169_ppm_2SE(int)	0.026	0.006	0.015	0.009	0.010	0.012	0.005	0.011
Yb172_ppm_mean	1.830	0.201	0.946	0.380	0.778	1.090	0.170	0.909
Yb172_ppm_2SE(int)	0.151	0.039	0.072	0.044	0.058	0.089	0.030	0.088
Lu175_ppm_mean	0.259	0.028	0.146	0.061	0.107	0.146	0.023	0.103
Lu175_ppm_2SE(int)	0.022	0.006	0.017	0.009	0.012	0.013	0.006	0.010

Table S5 cont.: Pyroxene rare earth element compositions.

Sample	15085	15085	15085	15085	15085	15085	15085	15085
Site	24-PYX-3.393	24-PYX-3.394	24-PYX-3.395	24-PYX-3.396	24-PYX-4.397	24-PYX-4.298	24-PYX-4.399	24-PYX-4.400
La139_ppm_mean	0.150	0.188	0.187	0.289	0.724	0.102	0.249	0.303
La139_ppm_2SE(int)	0.017	0.033	0.020	0.023	0.111	0.018	0.033	0.027
Ce140_ppm_mean	0.833	0.931	1.000	1.659	1.823	0.360	0.900	1.595
Ce140_ppm_2SE(int)	0.041	0.083	0.039	0.070	0.255	0.048	0.068	0.052
Pr141_ppm_mean	0.204	0.201	0.247	0.394	0.234	0.064	0.199	0.389
Pr141_ppm_2SE(int)	0.019	0.019	0.023	0.023	0.043	0.012	0.019	0.025
Nd146_ppm_mean	1.446	1.321	1.823	2.715	1.006	0.420	1.345	2.786
Nd146_ppm_2SE(int)	0.102	0.117	0.110	0.147	0.180	0.079	0.112	0.146
Sm147_ppm_mean	0.853	0.721	1.071	1.566	0.298	0.200	0.778	1.509
Sm147_ppm_2SE(int)	0.099	0.084	0.095	0.125	0.068	0.052	0.083	0.104
Eu153_ppm_mean	0.097	0.085	0.100	0.155	0.131	0.022	0.088	0.136
Eu153_ppm_2SE(int)	0.016	0.014	0.016	0.018	0.025	0.009	0.014	0.018
Gd157_ppm_mean	1.306	1.286	1.587	2.515	0.437	0.314	1.323	2.433
Gd157_ppm_2SE(int)	0.117	0.122	0.124	0.157	0.080	0.057	0.110	0.165
Tb159_ppm_mean	0.267	0.236	0.307	0.557	0.087	0.071	0.301	0.542
Tb159_ppm_2SE(int)	0.021	0.017	0.021	0.030	0.016	0.010	0.022	0.030
Dy163_ppm_mean	1.872	1.676	2.350	3.842	0.629	0.527	2.183	3.659
Dy163_ppm_2SE(int)	0.113	0.090	0.124	0.162	0.076	0.052	0.127	0.156
Ho165_ppm_mean	0.401	0.366	0.481	0.796	0.131	0.122	0.474	0.815
Ho165_ppm_2SE(int)	0.022	0.020	0.026	0.037	0.017	0.014	0.025	0.037
Er166_ppm_mean	1.119	1.098	1.426	2.323	0.471	0.399	1.302	2.161
Er166_ppm_2SE(int)	0.084	0.064	0.081	0.116	0.056	0.048	0.065	0.096
Tm169_ppm_mean	0.158	0.140	0.199	0.352	0.060	0.047	0.200	0.309
Tm169_ppm_2SE(int)	0.017	0.012	0.012	0.019	0.011	0.009	0.019	0.021
Yb172_ppm_mean	1.085	1.068	1.457	2.493	0.427	0.406	1.368	2.325
Yb172_ppm_2SE(int)	0.079	0.076	0.106	0.112	0.055	0.052	0.088	0.123
Lu175_ppm_mean	0.158	0.154	0.216	0.374	0.073	0.074	0.208	0.332
Lu175_ppm_2SE(int)	0.015	0.014	0.017	0.023	0.010	0.008	0.016	0.023

Table S5 cont.: Pyroxene rare earth element compositions.

Sample	15085	15085	15085	15085	15085	15085	15085	15085
Site	26-PYX-1.277	26-PYX-1.278	26-PYX-1.279	26-PYX-1.280	26-PYX-2.288	26-PYX-2.289	26-PYX-2.290	26-PYX-3.291
La139_ppm_mean	0.004	0.000	2.712	0.104	0.008	0.126	0.130	0.044
La139_ppm_2SE(int)	0.003	0.000	0.279	0.014	0.005	0.036	0.020	0.018
Ce140_ppm_mean	0.043	0.054	7.206	0.631	0.083	0.489	0.720	0.257
Ce140_ppm_2SE(int)	0.017	0.038	0.775	0.038	0.016	0.109	0.045	0.023
Pr141_ppm_mean	0.002	0.005	1.022	0.162	0.005	0.085	0.162	0.061
Pr141_ppm_2SE(int)	0.002	0.004	0.123	0.019	0.003	0.020	0.016	0.011
Nd146_ppm_mean	0.040	0.053	5.520	1.168	0.021	0.540	1.354	0.564
Nd146_ppm_2SE(int)	0.023	0.023	0.718	0.122	0.014	0.095	0.122	0.079
Sm147_ppm_mean	0.030	0.014	1.969	0.669	0.015	0.283	0.685	0.338
Sm147_ppm_2SE(int)	0.017	0.011	0.298	0.091	0.013	0.051	0.072	0.064
Eu153_ppm_mean	0.002	0.033	0.393	0.069	0.007	0.031	0.062	0.040
Eu153_ppm_2SE(int)	0.003	0.051	0.050	0.014	0.004	0.008	0.011	0.010
Gd157_ppm_mean	0.046	0.082	2.596	1.314	0.066	0.410	1.107	0.783
Gd157_ppm_2SE(int)	0.023	0.036	0.332	0.110	0.028	0.074	0.115	0.109
Tb159_ppm_mean	0.015	0.014	0.520	0.242	0.015	0.077	0.236	0.161
Tb159_ppm_2SE(int)	0.005	0.004	0.061	0.018	0.005	0.012	0.020	0.018
Dy163_ppm_mean	0.123	0.137	3.317	1.837	0.121	0.716	1.643	1.114
Dy163_ppm_2SE(int)	0.032	0.030	0.355	0.117	0.029	0.074	0.108	0.081
Ho165_ppm_mean	0.030	0.036	0.681	0.414	0.042	0.164	0.404	0.276
Ho165_ppm_2SE(int)	0.009	0.008	0.067	0.028	0.011	0.015	0.028	0.022
Er166_ppm_mean	0.117	0.121	2.009	1.188	0.096	0.468	1.060	0.823
Er166_ppm_2SE(int)	0.033	0.024	0.215	0.071	0.024	0.045	0.068	0.067
Tm169_ppm_mean	0.020	0.021	0.245	0.164	0.021	0.071	0.149	0.112
Tm169_ppm_2SE(int)	0.005	0.006	0.030	0.014	0.006	0.009	0.016	0.013
Yb172_ppm_mean	0.154	0.160	1.716	1.235	0.115	0.507	0.921	0.829
Yb172_ppm_2SE(int)	0.039	0.032	0.167	0.096	0.026	0.052	0.082	0.069
Lu175_ppm_mean	0.019	0.025	0.226	0.191	0.025	0.074	0.145	0.130
Lu175_ppm_2SE(int)	0.007	0.007	0.027	0.016	0.007	0.011	0.013	0.014

Table S5 cont.: Pyroxene rare earth element compositions.

Sample	15085	15085	15085	15085	15085	15085	15085	15085
Site	26-PYX-3.292	26-PYX-3.293	26-PYX-3.294	26-PYX-3.295	26-PYX-4.298	26-PYX-4.299	26-PYX-5.305	26-PYX-5.306
La139_ppm_mean	0.104	0.042	0.231	0.007	0.152	0.001	0.000	0.002
La139_ppm_2SE(int)	0.016	0.008	0.029	0.013	0.037	0.001	0.001	0.002
Ce140_ppm_mean	0.563	0.242	0.685	0.011	0.526	0.025	0.017	0.024
Ce140_ppm_2SE(int)	0.041	0.022	0.075	0.005	0.090	0.007	0.007	0.007
Pr141_ppm_mean	0.145	0.055	0.131	0.007	0.091	0.003	0.006	0.004
Pr141_ppm_2SE(int)	0.015	0.010	0.018	0.003	0.014	0.002	0.003	0.002
Nd146_ppm_mean	1.094	0.469	0.797	0.024	0.567	0.055	0.024	0.054
Nd146_ppm_2SE(int)	0.101	0.075	0.108	0.014	0.095	0.025	0.013	0.019
Sm147_ppm_mean	0.694	0.269	0.268	0.041	0.333	0.032	0.026	0.037
Sm147_ppm_2SE(int)	0.087	0.052	0.062	0.022	0.060	0.016	0.017	0.019
Eu153_ppm_mean	0.059	0.029	0.047	0.004	0.044	0.003	0.004	0.004
Eu153_ppm_2SE(int)	0.012	0.008	0.013	0.004	0.011	0.002	0.003	0.003
Gd157_ppm_mean	1.148	0.551	0.514	0.086	0.635	0.071	0.072	0.096
Gd157_ppm_2SE(int)	0.108	0.082	0.086	0.031	0.086	0.027	0.027	0.033
Tb159_ppm_mean	0.246	0.141	0.088	0.016	0.141	0.023	0.018	0.022
Tb159_ppm_2SE(int)	0.021	0.016	0.014	0.005	0.014	0.009	0.005	0.006
Dy163_ppm_mean	1.779	0.942	0.658	0.168	1.002	0.162	0.158	0.209
Dy163_ppm_2SE(int)	0.117	0.077	0.068	0.029	0.078	0.032	0.031	0.035
Ho165_ppm_mean	0.396	0.219	0.132	0.040	0.246	0.042	0.051	0.047
Ho165_ppm_2SE(int)	0.027	0.018	0.017	0.007	0.022	0.008	0.009	0.009
Er166_ppm_mean	1.270	0.707	0.415	0.140	0.798	0.140	0.141	0.173
Er166_ppm_2SE(int)	0.081	0.057	0.049	0.024	0.062	0.022	0.026	0.027
Tm169_ppm_mean	0.169	0.105	0.064	0.022	0.116	0.023	0.021	0.028
Tm169_ppm_2SE(int)	0.018	0.012	0.009	0.006	0.013	0.005	0.005	0.006
Yb172_ppm_mean	1.243	0.751	0.459	0.164	0.808	0.181	0.150	0.221
Yb172_ppm_2SE(int)	0.094	0.069	0.066	0.033	0.064	0.029	0.028	0.045
Lu175_ppm_mean	0.189	0.116	0.063	0.029	0.111	0.029	0.036	0.031
Lu175_ppm_2SE(int)	0.017	0.013	0.010	0.006	0.012	0.006	0.008	0.006

Table S5 cont.: Pyroxene rare earth element compositions.

Sample	15085	15085	15085	15085	15556	15556	15556	15556
Site	26-PYX-5.307	26-PYX-5.308	26-PYX-5.309	26-PYX-5.310	28-PYX-1.401	28-PYX-1.402	28-PYX-1.405	28-PYX-1.406
La139_ppm_mean	0.579	0.554	0.082	0.196	0.142	4.549	32.958	0.020
La139_ppm_2SE(int)	0.054	0.185	0.015	0.022	0.019	2.531	4.853	0.006
Ce140_ppm_mean	1.578	1.923	0.436	1.052	0.821	13.284	107.478	0.115
Ce140_ppm_2SE(int)	0.121	0.505	0.037	0.053	0.052	6.970	15.712	0.014
Pr141_ppm_mean	0.237	0.318	0.113	0.252	0.201	2.101	15.662	0.030
Pr141_ppm_2SE(int)	0.022	0.069	0.013	0.026	0.022	0.880	2.314	0.007
Nd146_ppm_mean	1.311	2.001	0.768	2.033	1.420	11.785	74.590	0.274
Nd146_ppm_2SE(int)	0.147	0.334	0.090	0.135	0.120	4.764	10.653	0.050
Sm147_ppm_mean	0.539	0.935	0.425	1.161	0.758	5.620	22.922	0.260
Sm147_ppm_2SE(int)	0.075	0.147	0.053	0.100	0.101	1.908	3.098	0.051
Eu153_ppm_mean	0.085	0.048	0.061	0.107	0.072	0.315	1.832	0.010
Eu153_ppm_2SE(int)	0.017	0.011	0.012	0.013	0.013	0.084	0.260	0.004
Gd157_ppm_mean	0.757	1.408	0.838	1.936	1.200	7.315	26.175	0.349
Gd157_ppm_2SE(int)	0.097	0.169	0.102	0.138	0.113	2.219	3.494	0.058
Tb159_ppm_mean	0.135	0.292	0.179	0.408	0.256	1.271	4.363	0.080
Tb159_ppm_2SE(int)	0.017	0.026	0.017	0.027	0.019	0.335	0.545	0.011
Dy163_ppm_mean	0.954	1.985	1.308	2.936	1.705	8.660	25.632	0.573
Dy163_ppm_2SE(int)	0.084	0.125	0.073	0.118	0.118	2.417	3.028	0.061
Ho165_ppm_mean	0.224	0.435	0.286	0.648	0.352	1.887	4.982	0.138
Ho165_ppm_2SE(int)	0.019	0.025	0.017	0.033	0.029	0.526	0.566	0.015
Er166_ppm_mean	0.652	1.349	0.850	1.848	0.924	4.746	12.697	0.378
Er166_ppm_2SE(int)	0.065	0.094	0.068	0.087	0.076	1.086	1.360	0.038
Tm169_ppm_mean	0.087	0.184	0.109	0.272	0.120	0.591	1.477	0.058
Tm169_ppm_2SE(int)	0.013	0.017	0.012	0.021	0.014	0.135	0.149	0.008
Yb172_ppm_mean	0.671	1.200	0.792	1.996	0.876	4.267	8.871	0.464
Yb172_ppm_2SE(int)	0.057	0.088	0.066	0.119	0.069	0.854	0.836	0.070
Lu175_ppm_mean	0.100	0.173	0.127	0.291	0.125	0.539	1.107	0.073
Lu175_ppm_2SE(int)	0.010	0.013	0.017	0.020	0.017	0.082	0.096	0.010

Table S5 cont.: Pyroxene rare earth element compositions.

Sample	15556	15556	15556	15556	15556	15556	15556	15556
Site	28-PYX-2.407	28-PYX-2.408	28-PYX-2.409	28-PYX-2.410	28-PYX-2.413	28-PYX-2.414	241-PYX-1.314	241-PYX-1.320
La139_ppm_mean	0.274	0.177	0.077	0.006	0.209	0.134	0.083	0.301
La139_ppm_2SE(int)	0.033	0.025	0.015	0.003	0.032	0.020	0.014	0.043
Ce140_ppm_mean	1.042	0.960	0.600	0.078	0.813	0.801	0.475	0.951
Ce140_ppm_2SE(int)	0.097	0.053	0.061	0.014	0.081	0.048	0.037	0.090
Pr141_ppm_mean	0.208	0.223	0.146	0.019	0.112	0.186	0.171	0.175
Pr141_ppm_2SE(int)	0.021	0.019	0.017	0.006	0.019	0.017	0.132	0.024
Nd146_ppm_mean	1.590	1.641	0.856	0.112	0.584	1.392	0.840	0.951
Nd146_ppm_2SE(int)	0.124	0.137	0.072	0.035	0.072	0.114	0.088	0.099
Sm147_ppm_mean	0.814	0.938	0.660	0.064	0.271	0.824	0.589	0.466
Sm147_ppm_2SE(int)	0.102	0.082	0.092	0.024	0.065	0.099	0.085	0.079
Eu153_ppm_mean	0.089	0.088	0.066	0.007	0.060	0.070	0.053	0.060
Eu153_ppm_2SE(int)	0.016	0.015	0.014	0.004	0.025	0.012	0.014	0.014
Gd157_ppm_mean	1.407	1.558	1.057	0.194	0.441	1.315	0.768	0.729
Gd157_ppm_2SE(int)	0.131	0.118	0.099	0.052	0.090	0.105	0.091	0.091
Tb159_ppm_mean	0.279	0.337	0.217	0.049	0.091	0.295	0.187	0.134
Tb159_ppm_2SE(int)	0.022	0.026	0.020	0.008	0.015	0.023	0.015	0.017
Dy163_ppm_mean	2.051	2.361	1.620	0.394	0.680	1.830	1.363	1.009
Dy163_ppm_2SE(int)	0.131	0.129	0.104	0.048	0.065	0.119	0.091	0.102
Ho165_ppm_mean	0.441	0.466	0.347	0.079	0.154	0.394	0.317	0.230
Ho165_ppm_2SE(int)	0.027	0.026	0.025	0.010	0.017	0.026	0.019	0.022
Er166_ppm_mean	1.265	1.459	1.038	0.273	0.412	1.226	0.886	0.617
Er166_ppm_2SE(int)	0.083	0.095	0.080	0.035	0.046	0.075	0.062	0.061
Tm169_ppm_mean	0.187	0.211	0.135	0.043	0.069	0.166	0.112	0.084
Tm169_ppm_2SE(int)	0.017	0.019	0.015	0.009	0.012	0.014	0.012	0.010
Yb172_ppm_mean	1.352	1.325	0.965	0.318	0.419	1.190	0.910	0.632
Yb172_ppm_2SE(int)	0.088	0.085	0.085	0.047	0.053	0.103	0.080	0.067
Lu175_ppm_mean	0.203	0.220	0.155	0.039	0.063	0.185	0.125	0.087
Lu175_ppm_2SE(int)	0.018	0.017	0.018	0.006	0.011	0.016	0.014	0.012

Table S5 cont.: Pyroxene rare earth element compositions.

Sample	15556	15556	15556	15556	15556	15556	15556	15556
Site	241-PYX-1.321	241-PYX-2.326	241-PYX-2.327	241-PYX-2.328	241-PYX-2.329	241-PYX-2.330	241-PYX-2.331	241-PYX-2.332
La139_ppm_mean	0.177	0.028	0.199	0.340	0.203	0.509	0.063	0.625
La139_ppm_2SE(int)	0.027	0.007	0.022	0.039	0.035	0.050	0.012	0.034
Ce140_ppm_mean	0.703	0.130	1.159	1.692	0.907	2.301	0.328	3.269
Ce140_ppm_2SE(int)	0.062	0.019	0.059	0.075	0.124	0.167	0.030	0.131
Pr141_ppm_mean	0.134	0.032	0.301	0.390	0.171	0.456	0.086	0.771
Pr141_ppm_2SE(int)	0.017	0.009	0.020	0.022	0.023	0.038	0.015	0.033
Nd146_ppm_mean	0.806	0.248	1.897	2.745	1.267	2.806	0.505	5.232
Nd146_ppm_2SE(int)	0.088	0.055	0.154	0.161	0.160	0.191	0.070	0.229
Sm147_ppm_mean	0.395	0.199	1.171	1.471	0.755	1.317	0.278	2.652
Sm147_ppm_2SE(int)	0.062	0.044	0.116	0.125	0.096	0.131	0.051	0.162
Eu153_ppm_mean	0.061	0.017	0.099	0.141	0.072	0.144	0.029	0.209
Eu153_ppm_2SE(int)	0.012	0.007	0.015	0.017	0.013	0.017	0.008	0.021
Gd157_ppm_mean	0.883	0.300	1.932	2.244	1.213	2.005	0.609	4.121
Gd157_ppm_2SE(int)	0.344	0.048	0.161	0.167	0.109	0.170	0.082	0.214
Tb159_ppm_mean	0.147	0.062	0.377	0.471	0.218	0.393	0.126	0.782
Tb159_ppm_2SE(int)	0.015	0.011	0.021	0.028	0.021	0.026	0.014	0.036
Dy163_ppm_mean	0.927	0.477	2.561	3.148	1.693	2.772	0.890	5.321
Dy163_ppm_2SE(int)	0.067	0.059	0.129	0.140	0.099	0.167	0.076	0.220
Ho165_ppm_mean	0.218	0.101	0.558	0.653	0.360	0.579	0.190	1.105
Ho165_ppm_2SE(int)	0.019	0.012	0.034	0.030	0.024	0.035	0.021	0.045
Er166_ppm_mean	0.638	0.338	1.555	1.855	1.088	1.620	0.553	3.132
Er166_ppm_2SE(int)	0.047	0.040	0.084	0.098	0.076	0.085	0.049	0.151
Tm169_ppm_mean	0.078	0.061	0.221	0.245	0.141	0.230	0.077	0.430
Tm169_ppm_2SE(int)	0.012	0.009	0.017	0.017	0.016	0.018	0.011	0.025
Yb172_ppm_mean	0.623	0.378	1.578	1.767	1.046	1.605	0.501	2.833
Yb172_ppm_2SE(int)	0.067	0.041	0.104	0.105	0.082	0.104	0.060	0.175
Lu175_ppm_mean	0.091	0.060	0.221	0.222	0.160	0.228	0.077	0.438
Lu175_ppm_2SE(int)	0.011	0.011	0.017	0.016	0.015	0.017	0.011	0.027

Table S5 cont.: Pyroxene rare earth element compositions.

Sample	15556	15556	15556	15556	15556	15556	15556	15556
Site	241-PYX-3.339	241-PYX-3.340	241-PYX-3.341	241-PYX-3.342	241-PYX-3.343	241-PYX-3.344	241-PYX-3.345	241-PYX-4.347
La139_ppm_mean	0.078	0.396	0.063	0.186	0.119	0.033	14.157	22.922
La139_ppm_2SE(int)	0.020	0.040	0.014	0.024	0.019	0.009	3.471	5.814
Ce140_ppm_mean	0.261	2.051	0.267	0.971	0.688	0.224	39.761	56.554
Ce140_ppm_2SE(int)	0.033	0.177	0.031	0.050	0.040	0.021	8.955	13.840
Pr141_ppm_mean	0.053	0.450	0.051	0.238	0.158	0.056	6.239	7.916
Pr141_ppm_2SE(int)	0.010	0.039	0.010	0.018	0.018	0.009	1.302	1.751
Nd146_ppm_mean	0.349	3.134	0.465	1.747	1.225	0.393	32.049	40.187
Nd146_ppm_2SE(int)	0.057	0.249	0.061	0.125	0.115	0.066	5.744	8.225
Sm147_ppm_mean	0.227	1.675	0.264	1.066	0.693	0.299	10.405	13.518
Sm147_ppm_2SE(int)	0.054	0.151	0.058	0.102	0.087	0.053	1.373	2.258
Eu153_ppm_mean	0.031	0.145	0.024	0.081	0.072	0.030	0.736	0.917
Eu153_ppm_2SE(int)	0.009	0.020	0.007	0.013	0.013	0.008	0.082	0.144
Gd157_ppm_mean	0.440	2.827	0.393	1.697	1.113	0.505	14.790	17.712
Gd157_ppm_2SE(int)	0.062	0.240	0.069	0.163	0.113	0.068	1.853	2.350
Tb159_ppm_mean	0.080	0.545	0.086	0.342	0.213	0.118	2.741	3.173
Tb159_ppm_2SE(int)	0.012	0.039	0.013	0.019	0.016	0.015	0.303	0.380
Dy163_ppm_mean	0.577	3.845	0.566	2.521	1.645	0.838	18.106	20.856
Dy163_ppm_2SE(int)	0.058	0.248	0.057	0.130	0.120	0.084	1.783	2.369
Ho165_ppm_mean	0.135	0.789	0.145	0.531	0.334	0.190	3.901	4.269
Ho165_ppm_2SE(int)	0.015	0.047	0.013	0.030	0.025	0.017	0.404	0.442
Er166_ppm_mean	0.415	2.269	0.436	1.525	1.000	0.624	10.960	11.673
Er166_ppm_2SE(int)	0.039	0.153	0.052	0.087	0.075	0.050	1.080	1.140
Tm169_ppm_mean	0.051	0.299	0.066	0.210	0.124	0.087	1.464	1.594
Tm169_ppm_2SE(int)	0.009	0.028	0.011	0.017	0.013	0.011	0.162	0.137
Yb172_ppm_mean	0.433	2.204	0.432	1.579	0.893	0.695	10.576	10.339
Yb172_ppm_2SE(int)	0.060	0.168	0.049	0.096	0.082	0.070	0.990	0.796
Lu175_ppm_mean	0.059	0.340	0.066	0.208	0.119	0.108	1.440	1.410
Lu175_ppm_2SE(int)	0.010	0.032	0.008	0.017	0.012	0.013	0.123	0.088

Table S5 cont.: Pyroxene rare earth element compositions.

Sample	15556	15556	15556	15556	15556	15556	15556	15556
Site	241-PYX-4.348	241-PYX-4.352	241-PYX-4.353	241-PYX-4.354	241-PYX-5.357	241-PYX-5.358	241-PYX-5.359	241-PYX-5.360
La139_ppm_mean	0.212	0.028	0.037	0.028	0.260	1.428	0.819	3.046
La139_ppm_2SE(int)	0.026	0.009	0.010	0.009	0.041	0.191	0.069	0.130
Ce140_ppm_mean	1.057	0.136	0.371	0.149	1.055	4.959	2.648	13.514
Ce140_ppm_2SE(int)	0.068	0.017	0.267	0.022	0.133	0.372	0.191	0.495
Pr141_ppm_mean	0.253	0.034	0.057	0.043	0.224	0.937	0.441	2.926
Pr141_ppm_2SE(int)	0.023	0.008	0.010	0.008	0.029	0.072	0.039	0.092
Nd146_ppm_mean	1.685	0.261	0.346	0.324	1.299	5.728	2.496	18.846
Nd146_ppm_2SE(int)	0.156	0.048	0.053	0.058	0.133	0.291	0.198	0.565
Sm147_ppm_mean	1.010	0.157	0.231	0.249	0.663	2.559	1.053	8.559
Sm147_ppm_2SE(int)	0.128	0.037	0.047	0.067	0.119	0.185	0.142	0.384
Eu153_ppm_mean	0.111	0.015	0.038	0.024	0.069	0.289	0.139	0.801
Eu153_ppm_2SE(int)	0.019	0.005	0.010	0.009	0.015	0.025	0.016	0.095
Gd157_ppm_mean	1.760	0.332	0.548	0.411	1.078	3.586	1.559	11.551
Gd157_ppm_2SE(int)	0.161	0.066	0.084	0.061	0.132	0.248	0.155	0.485
Tb159_ppm_mean	0.335	0.085	0.104	0.083	0.214	0.697	0.320	2.093
Tb159_ppm_2SE(int)	0.028	0.011	0.016	0.013	0.021	0.035	0.026	0.078
Dy163_ppm_mean	2.347	0.624	0.700	0.634	1.580	4.686	2.191	13.393
Dy163_ppm_2SE(int)	0.142	0.072	0.077	0.072	0.127	0.205	0.152	0.341
Ho165_ppm_mean	0.483	0.143	0.155	0.148	0.317	0.951	0.443	2.699
Ho165_ppm_2SE(int)	0.031	0.015	0.020	0.017	0.024	0.040	0.032	0.084
Er166_ppm_mean	1.370	0.429	0.449	0.433	0.831	2.623	1.307	7.090
Er166_ppm_2SE(int)	0.094	0.043	0.045	0.058	0.062	0.106	0.073	0.202
Tm169_ppm_mean	0.187	0.063	0.070	0.057	0.127	0.381	0.179	0.926
Tm169_ppm_2SE(int)	0.017	0.008	0.010	0.010	0.014	0.026	0.015	0.050
Yb172_ppm_mean	1.222	0.532	0.442	0.443	0.866	2.631	1.215	6.713
Yb172_ppm_2SE(int)	0.098	0.070	0.067	0.054	0.093	0.139	0.098	0.257
Lu175_ppm_mean	0.204	0.076	0.079	0.061	0.126	0.388	0.196	1.010
Lu175_ppm_2SE(int)	0.019	0.011	0.011	0.012	0.014	0.023	0.021	0.048

Table S5 cont.: Pyroxene rare earth element compositions.

Sample	15556	15556	70017	70017	70017	70017	70017	70017
Site	241-PYX-5.361	241-PYX-5.362	123-PYX-1.492	123-PYX-1.493	123-PYX-1.494	123-PYX-2.498	123-PYX-2.499	123-PYX-2.500
La139_ppm_mean	0.121	2.896	0.465	0.148	0.124	0.014	0.265	0.982
La139_ppm_2SE(int)	0.017	0.520	0.044	0.023	0.021	0.007	0.024	0.087
Ce140_ppm_mean	0.688	9.752	3.373	1.007	1.087	0.105	1.850	5.699
Ce140_ppm_2SE(int)	0.043	1.300	0.130	0.051	0.439	0.015	0.066	0.269
Pr141_ppm_mean	0.154	1.822	0.930	0.253	0.260	0.035	0.588	1.616
Pr141_ppm_2SE(int)	0.019	0.215	0.048	0.021	0.025	0.007	0.033	0.085
Nd146_ppm_mean	1.043	10.614	8.022	2.117	2.109	0.333	4.711	12.740
Nd146_ppm_2SE(int)	0.111	0.912	0.488	0.145	0.158	0.059	0.224	0.532
Sm147_ppm_mean	0.654	4.596	5.218	1.665	1.618	0.339	3.704	8.958
Sm147_ppm_2SE(int)	0.087	0.316	0.395	0.131	0.151	0.072	0.202	0.394
Eu153_ppm_mean	0.074	0.411	0.233	0.163	0.167	0.023	0.280	0.466
Eu153_ppm_2SE(int)	0.012	0.036	0.024	0.025	0.021	0.007	0.026	0.038
Gd157_ppm_mean	1.040	6.623	8.877	3.001	2.550	0.782	6.640	14.684
Gd157_ppm_2SE(int)	0.123	0.407	0.514	0.203	0.189	0.082	0.316	0.506
Tb159_ppm_mean	0.206	1.235	1.851	0.612	0.566	0.195	1.450	3.093
Tb159_ppm_2SE(int)	0.020	0.065	0.094	0.040	0.032	0.020	0.054	0.078
Dy163_ppm_mean	1.393	7.970	13.338	4.472	3.767	1.545	10.454	22.529
Dy163_ppm_2SE(int)	0.116	0.340	0.745	0.196	0.161	0.097	0.314	0.608
Ho165_ppm_mean	0.281	1.608	2.850	0.968	0.895	0.409	2.392	4.918
Ho165_ppm_2SE(int)	0.023	0.070	0.146	0.057	0.049	0.024	0.062	0.135
Er166_ppm_mean	0.796	4.356	7.867	2.573	2.403	1.285	6.723	13.443
Er166_ppm_2SE(int)	0.081	0.222	0.412	0.133	0.124	0.077	0.228	0.373
Tm169_ppm_mean	0.109	0.611	1.063	0.388	0.345	0.212	0.988	1.866
Tm169_ppm_2SE(int)	0.013	0.036	0.055	0.028	0.024	0.017	0.046	0.074
Yb172_ppm_mean	0.737	4.128	7.221	2.711	2.311	1.614	6.618	12.857
Yb172_ppm_2SE(int)	0.080	0.180	0.351	0.188	0.145	0.096	0.259	0.419
Lu175_ppm_mean	0.097	0.622	1.038	0.366	0.325	0.273	0.970	1.729
Lu175_ppm_2SE(int)	0.014	0.033	0.055	0.027	0.024	0.021	0.044	0.059

Table S5 cont.: Pyroxene rare earth element compositions.

Sample	70017	70017	70017	70017	70017	70017	70017	70017
Site	123-PYX-2.501	123-PYX-2.502	123-PYX-3.507	123-PYX-3.508	123-PYX-3.509	123-PYX-3.503	123-PYX-3.504	123-PYX-4.510
La139_ppm_mean	0.211	0.198	0.245	0.204	0.164	0.024	0.585	0.772
La139_ppm_2SE(int)	0.023	0.019	0.025	0.030	0.022	0.007	0.037	0.045
Ce140_ppm_mean	1.629	1.505	1.521	1.180	1.061	0.156	3.997	5.712
Ce140_ppm_2SE(int)	0.065	0.071	0.065	0.061	0.047	0.018	0.103	0.195
Pr141_ppm_mean	0.429	0.432	0.394	0.319	0.343	0.031	1.158	1.636
Pr141_ppm_2SE(int)	0.030	0.033	0.029	0.022	0.026	0.007	0.050	0.068
Nd146_ppm_mean	3.692	3.322	3.630	2.644	3.113	0.419	9.183	14.376
Nd146_ppm_2SE(int)	0.202	0.181	0.210	0.177	0.188	0.059	0.383	0.483
Sm147_ppm_mean	2.520	2.251	2.505	1.973	2.738	0.311	6.755	10.507
Sm147_ppm_2SE(int)	0.192	0.170	0.176	0.148	0.202	0.063	0.309	0.379
Eu153_ppm_mean	0.223	0.238	0.220	0.187	0.114	0.024	0.400	0.493
Eu153_ppm_2SE(int)	0.027	0.023	0.024	0.022	0.016	0.008	0.035	0.041
Gd157_ppm_mean	4.377	4.054	4.377	3.381	5.349	0.697	10.932	18.770
Gd157_ppm_2SE(int)	0.216	0.258	0.241	0.226	0.287	0.083	0.370	0.639
Tb159_ppm_mean	0.919	0.841	0.938	0.746	1.292	0.192	2.318	4.176
Tb159_ppm_2SE(int)	0.044	0.037	0.052	0.039	0.047	0.019	0.071	0.114
Dy163_ppm_mean	6.700	5.978	6.271	5.468	10.118	1.554	16.628	30.948
Dy163_ppm_2SE(int)	0.231	0.259	0.277	0.257	0.288	0.119	0.337	0.676
Ho165_ppm_mean	1.418	1.341	1.370	1.222	2.385	0.379	3.592	6.953
Ho165_ppm_2SE(int)	0.058	0.049	0.053	0.057	0.061	0.030	0.101	0.137
Er166_ppm_mean	3.857	3.524	3.892	3.503	7.352	1.245	9.936	19.692
Er166_ppm_2SE(int)	0.166	0.140	0.178	0.167	0.226	0.070	0.259	0.512
Tm169_ppm_mean	0.527	0.508	0.538	0.496	1.137	0.192	1.358	2.693
Tm169_ppm_2SE(int)	0.031	0.029	0.032	0.029	0.047	0.022	0.050	0.079
Yb172_ppm_mean	3.717	3.376	3.778	3.350	8.108	1.524	9.583	18.856
Yb172_ppm_2SE(int)	0.185	0.123	0.202	0.159	0.229	0.120	0.303	0.493
Lu175_ppm_mean	0.515	0.467	0.506	0.454	1.248	0.225	1.348	2.779
Lu175_ppm_2SE(int)	0.037	0.027	0.028	0.026	0.041	0.019	0.055	0.079

Table S5 cont.: Pyroxene rare earth element compositions.

Sample	70017	70017	70017	70017	70017	70017	70017	70017
Site	123-PYX-4.511	123-PYX-4.512	123-PYX-5.515	123-PYX-5.516	123-PYX-5.517	123-PYX-5.518	123-PYX-5.519	123-PYX-5.520
La139_ppm_mean	0.264	0.105	0.127	3.662	5.233	66.954	0.097	0.200
La139_ppm_2SE(int)	0.025	0.015	0.015	0.753	0.919	13.282	0.015	0.023
Ce140_ppm_mean	1.917	0.782	1.094	16.297	19.140	222.243	0.783	1.410
Ce140_ppm_2SE(int)	0.079	0.043	0.047	2.722	3.057	37.649	0.042	0.060
Pr141_ppm_mean	0.542	0.202	0.384	3.630	3.558	41.803	0.222	0.411
Pr141_ppm_2SE(int)	0.029	0.023	0.026	0.478	0.558	6.871	0.021	0.027
Nd146_ppm_mean	4.775	1.695	3.358	26.344	22.627	250.560	1.891	3.325
Nd146_ppm_2SE(int)	0.220	0.123	0.155	2.949	3.384	39.319	0.133	0.152
Sm147_ppm_mean	3.415	1.300	2.744	16.155	10.564	108.995	1.258	2.301
Sm147_ppm_2SE(int)	0.184	0.148	0.189	1.191	1.369	13.525	0.119	0.178
Eu153_ppm_mean	0.273	0.134	0.132	0.572	0.591	4.818	0.145	0.188
Eu153_ppm_2SE(int)	0.023	0.020	0.015	0.059	0.105	0.203	0.023	0.024
Gd157_ppm_mean	6.502	2.448	5.838	28.398	16.960	151.528	2.683	4.164
Gd157_ppm_2SE(int)	0.274	0.161	0.251	1.799	2.072	17.638	0.176	0.259
Tb159_ppm_mean	1.388	0.505	1.360	5.972	3.429	28.291	0.513	0.888
Tb159_ppm_2SE(int)	0.058	0.032	0.052	0.307	0.370	2.781	0.028	0.044
Dy163_ppm_mean	10.042	3.782	10.644	43.970	24.205	192.721	3.718	6.312
Dy163_ppm_2SE(int)	0.228	0.218	0.314	2.091	2.411	19.298	0.203	0.219
Ho165_ppm_mean	2.299	0.848	2.556	9.671	5.246	39.325	0.819	1.342
Ho165_ppm_2SE(int)	0.068	0.047	0.081	0.381	0.508	3.674	0.045	0.062
Er166_ppm_mean	6.548	2.353	7.866	28.042	15.043	105.494	2.343	3.867
Er166_ppm_2SE(int)	0.213	0.126	0.215	1.184	1.333	9.167	0.120	0.173
Tm169_ppm_mean	0.898	0.322	1.209	3.823	2.083	13.572	0.328	0.527
Tm169_ppm_2SE(int)	0.041	0.023	0.058	0.154	0.175	1.058	0.023	0.028
Yb172_ppm_mean	6.211	2.199	8.720	26.846	14.181	86.268	2.234	3.758
Yb172_ppm_2SE(int)	0.231	0.125	0.242	0.871	1.183	6.281	0.141	0.169
Lu175_ppm_mean	0.867	0.311	1.286	3.841	2.032	10.780	0.331	0.498
Lu175_ppm_2SE(int)	0.044	0.021	0.053	0.132	0.153	0.717	0.020	0.032

Table S5 cont.: Pyroxene rare earth element compositions.

Sample	70017	70017	70017	70017
Site	123-PYX-5.521	123-PYX-5.522	123-PYX-5.523	123-PYX-5.524
La139_ppm_mean	0.250	0.382	1.806	5.331
La139_ppm_2SE(int)	0.030	0.037	0.091	0.174
Ce140_ppm_mean	1.695	2.332	12.108	32.734
Ce140_ppm_2SE(int)	0.075	0.152	0.440	0.681
Pr141_ppm_mean	0.438	0.685	3.444	8.823
Pr141_ppm_2SE(int)	0.024	0.041	0.102	0.194
Nd146_ppm_mean	3.547	5.717	27.775	69.627
Nd146_ppm_2SE(int)	0.190	0.292	0.710	1.730
Sm147_ppm_mean	2.479	3.906	18.959	45.767
Sm147_ppm_2SE(int)	0.201	0.202	0.576	1.259
Eu153_ppm_mean	0.228	0.302	0.870	3.048
Eu153_ppm_2SE(int)	0.028	0.030	0.057	0.186
Gd157_ppm_mean	4.706	7.476	32.508	74.814
Gd157_ppm_2SE(int)	0.255	0.321	0.815	1.758
Tb159_ppm_mean	1.000	1.587	6.726	15.197
Tb159_ppm_2SE(int)	0.047	0.058	0.166	0.397
Dy163_ppm_mean	7.081	11.646	46.315	102.992
Dy163_ppm_2SE(int)	0.263	0.342	1.095	2.236
Ho165_ppm_mean	1.547	2.635	9.999	21.804
Ho165_ppm_2SE(int)	0.061	0.098	0.228	0.489
Er166_ppm_mean	4.278	7.411	27.265	57.883
Er166_ppm_2SE(int)	0.168	0.266	0.621	1.330
Tm169_ppm_mean	0.581	1.056	3.715	7.999
Tm169_ppm_2SE(int)	0.037	0.044	0.103	0.179
Yb172_ppm_mean	4.154	7.581	24.945	53.081
Yb172_ppm_2SE(int)	0.225	0.257	0.491	1.247
Lu175_ppm_mean	0.542	1.031	3.475	7.161
Lu175_ppm_2SE(int)	0.032	0.040	0.092	0.179

Table S6: Plagioclase feldspar major element compositions.

Sample	10057,67	10057,67	10057,67	10057,67	10057,67	10057,67	10057,67	10057,67
Site	67-plag1	67-plag1	67-plag1	67-plag1	67-plag2	67-plag2	67-plag2	67-plag2
Line #	6	7	8	9	10	11	12	13
SiO2	49.915	48.842	49.395	77.711	49.471	49.390	50.384	49.267
Al2O3	30.712	30.986	31.032	10.617	31.164	31.584	30.968	31.303
FeO	0.614	0.759	0.980	2.601	0.586	0.730	0.646	0.778
MnO	0.010	0.003	0.000	0.022	0.000	0.026	0.000	0.010
MgO	0.259	0.306	0.182	0.026	0.261	0.246	0.264	0.185
CaO	14.974	15.451	15.535	1.567	15.506	15.973	15.135	15.380
BaO	0.000	0.000	0.037	0.808	0.017	0.043	0.027	0.019
Na2O	2.041	1.915	1.204	0.533	1.961	1.802	2.230	1.715
K2O	0.319	0.286	0.460	6.143	0.239	0.326	0.336	0.198
TOTAL	98.844	98.548	98.826	100.028	99.205	100.119	99.989	98.855

Table S6 cont.: Plagioclase feldspar major element compositions.

Sample	10057,67	10057,67	10057,67	10057,67	10057,67	10057,67	10057,67	10057,67
Site	67-plag3	67-plag3	67-plag3	67-plag4	67-plag4	67-plag4	67-plag5	67-plag5
Line #	14	15	16	18	19	20	21	22
SiO2	49.486	48.968	49.599	50.328	51.511	49.399	49.290	50.088
Al2O3	31.339	31.578	30.827	30.379	30.382	30.962	31.280	30.784
FeO	0.657	0.603	0.561	0.785	0.602	0.705	0.741	0.906
MnO	0.013	0.000	0.017	0.012	0.001	0.004	0.009	0.013
MgO	0.251	0.252	0.267	0.370	0.267	0.273	0.210	0.381
CaO	15.658	15.843	15.055	15.313	14.785	15.555	15.725	15.377
BaO	0.033	0.009	0.000	0.032	0.000	0.018	0.000	0.035
Na2O	1.860	1.844	2.155	1.659	2.300	1.148	1.803	1.879
K2O	0.300	0.270	0.297	0.405	0.467	0.249	0.388	0.426
TOTAL	99.597	99.367	98.777	99.281	100.315	98.313	99.446	99.889

Table S6 cont.: Plagioclase feldspar major element compositions.

Sample	10057,67	10057,67	10057,67	10057,67	10057,67	10057,67	10057,67	10057,67
Site	67-plag5	67-plag5	67-plag5	67-plag5	67-plag6	67-plag6	67-plag6	67-plag6
Line #	23	24	25	26	27	28	29	30
SiO2	50.257	50.333	49.178	49.082	49.452	49.976	49.325	49.678
Al2O3	30.583	30.798	30.794	31.206	31.050	31.320	31.174	31.118
FeO	1.012	0.686	0.784	0.902	0.782	0.752	0.710	0.710
MnO	0.000	0.009	0.000	0.000	0.012	0.001	0.000	0.000
MgO	0.371	0.248	0.289	0.281	0.297	0.181	0.241	0.184
CaO	15.628	15.029	15.430	15.761	15.764	15.569	15.812	15.418
BaO	0.017	0.020	0.016	0.046	0.034	0.008	0.000	0.014
Na2O	1.971	2.093	1.450	1.785	0.729	1.741	1.529	1.906
K2O	0.435	0.484	0.354	0.423	0.398	0.344	0.421	0.463
TOTAL	100.273	99.700	98.296	99.487	98.517	99.891	99.212	99.490

Table S6 cont.: Plagioclase feldspar major element compositions.

Sample	10057,67	10057,67	10057,67	10057,67	10057,67	10057,67	10057,67	10057,67
Site	67-plag7	67-plag7	67-plag7	67-plag7	67-plag8	67-plag8	67-plag8	67-plag8
Line #	31	32	33	34	35	36	37	38
SiO2	49.419	49.932	50.420	50.047	50.341	50.825	50.684	50.611
Al2O3	31.008	30.771	30.506	30.543	30.885	30.888	31.001	30.597
FeO	0.738	0.898	0.760	0.838	0.854	0.881	0.671	0.775
MnO	0.025	0.026	0.016	0.014	0.006	0.018	0.000	0.000
MgO	0.337	0.179	0.372	0.358	0.298	0.213	0.300	0.323
CaO	15.631	15.196	15.255	15.501	15.426	15.303	15.535	15.303
BaO	0.003	0.050	0.014	0.000	0.021	0.048	0.014	0.012
Na2O	1.853	1.987	2.004	1.569	1.596	2.035	1.629	2.013
K2O	0.342	0.469	0.313	0.344	0.293	0.488	0.308	0.374
TOTAL	99.357	99.508	99.658	99.214	99.719	100.698	100.143	100.008

Table S6 cont.: Plagioclase feldspar major element compositions.

Sample	10057,67	10057,67	10057,67	10057,67	10057,67	10057,67	10057,67	10057,67
Site	67-plag8	67-plag9	67-plag9	67-plag9	67-plag9	67-plag9	67-plag10	67-plag10
Line #	39	40	41	42	43	44	45	46
SiO2	48.724	49.137	49.842	50.282	50.538	49.833	49.617	49.603
Al2O3	31.963	31.666	30.851	30.688	30.520	31.218	31.224	31.157
FeO	0.735	0.779	0.835	0.850	0.644	0.812	0.761	0.735
MnO	0.007	0.000	0.000	0.032	0.002	0.004	0.000	0.021
MgO	0.163	0.138	0.178	0.357	0.288	0.298	0.267	0.331
CaO	16.378	16.080	15.701	15.403	14.653	15.604	15.759	15.680
BaO	0.022	0.018	0.011	0.024	0.000	0.064	0.037	0.022
Na2O	1.320	1.654	1.061	1.552	2.223	1.912	1.927	1.865
K2O	0.383	0.259	0.478	0.389	0.285	0.375	0.405	0.292
TOTAL	99.693	99.731	98.957	99.579	99.154	100.122	99.997	99.706

Table S6 cont.: Plagioclase feldspar major element compositions.

Sample	15085,16	15085,16	15085,16	15085,16	15085,16	15085,16	15085,16	15085,16
Site	16-plag_1	16-plag_1	16-plag_1	16-plag_1	16-plag_1	16-plag_1	16-plag_2	16-plag_2
Line #	4	5	6	7	8	9	10	11
SiO2	45.833	45.125	45.997	46.224	45.823	45.143	45.360	45.727
Al2O3	34.679	34.939	33.974	33.728	34.315	34.730	34.414	34.174
FeO	0.489	0.491	0.541	0.584	0.489	0.504	0.500	0.503
MnO	0.034	0.000	0.013	0.009	0.007	0.002	0.002	0.000
MgO	0.233	0.141	0.266	0.284	0.245	0.141	0.221	0.225
CaO	18.562	18.589	18.343	17.985	18.305	18.482	18.467	18.347
BaO	0.000	0.000	0.003	0.000	0.005	0.011	0.000	0.009
Na2O	0.760	0.995	1.152	1.202	1.054	0.941	0.694	0.555
K2O	0.000	0.042	0.014	0.028	0.047	0.052	0.000	0.023
TOTAL	100.591	100.323	100.302	100.043	100.291	100.007	99.659	99.563

Table S6 cont.: Plagioclase feldspar major element compositions.

Sample	15085,16	15085,16	15085,16	15085,16	15085,16	15085,16	15085,16	15085,16
Site	16-plag_2	16-plag_2	16-plag_2	16-plag_2	16-plag_2	16-plag_2	16-plag_3	16-plag_3
Line #	12	13	14	15	16	17	18	19
SiO2	48.454	48.022	47.341	47.821	47.953	48.240	48.690	48.259
Al2O3	31.970	32.808	33.281	32.654	32.368	31.960	31.840	32.164
FeO	1.035	0.791	0.696	0.796	0.903	0.966	1.059	0.982
MnO	0.002	0.014	0.042	0.005	0.031	0.003	0.005	0.010
MgO	0.075	0.113	0.124	0.122	0.127	0.085	0.022	0.026
CaO	16.378	17.086	17.282	17.051	16.833	16.733	15.888	16.242
BaO	0.004	0.007	0.000	0.003	0.000	0.005	0.029	0.015
Na2O	1.969	1.171	1.053	1.545	1.681	1.744	2.006	1.765
K2O	0.071	0.066	0.074	0.088	0.120	0.125	0.588	0.425
TOTAL	99.957	100.079	99.894	100.084	100.017	99.861	100.128	99.887

Table S6 cont.: Plagioclase feldspar major element compositions.

Sample	15085,16	15085,16	15085,16	15085,16	15085,16	15085,16	15085,16	15085,16
Site	16-plag_3	16-plag_4	16-plag_4	16-plag_4	16-plag_5	16-plag_5	16-plag_5	16-plag_5
Line #	20	21	22	23	24	25	26	27
SiO2	48.909	48.342	48.181	48.192	46.283	46.307	46.455	48.103
Al2O3	31.264	31.959	31.885	32.236	34.218	33.838	33.653	32.182
FeO	1.409	1.076	1.030	0.963	0.634	0.640	0.663	1.022
MnO	0.000	0.005	0.009	0.000	0.000	0.000	0.000	0.000
MgO	0.020	0.016	0.057	0.070	0.141	0.142	0.128	0.077
CaO	15.933	16.212	16.399	16.656	17.981	18.084	17.858	16.802
BaO	0.094	0.035	0.000	0.000	0.000	0.000	0.000	0.010
Na2O	1.983	1.775	1.421	1.476	1.118	1.077	1.257	1.433
K2O	0.771	0.470	0.400	0.167	0.038	0.016	0.066	0.113
TOTAL	100.383	99.890	99.382	99.759	100.412	100.105	100.079	99.743

Table S6 cont.: Plagioclase feldspar major element compositions.

Sample	15085,26	15085,26	15085,26	15085,26	15085,26	15085,26	15085,26	15085,26
Site	26-plag_1	26-plag_1	26-plag_1	26-plag_1	26-plag_1	26-plag_1	26-plag_2	26-plag_2
Line #	28	29	30	31	32	33	34	35
SiO2	45.994	45.884	45.605	45.592	45.845	46.130	45.138	45.790
Al2O3	33.937	33.848	34.073	34.341	34.254	34.124	34.847	33.835
FeO	0.506	0.530	0.544	0.507	0.501	0.554	0.580	0.541
MnO	0.000	0.005	0.000	0.014	0.000	0.007	0.007	0.004
MgO	0.232	0.245	0.267	0.244	0.242	0.267	0.098	0.241
CaO	18.012	18.223	18.242	18.330	18.272	18.291	18.276	17.963
BaO	0.000	0.000	0.000	0.000	0.000	0.000	0.000	0.003
Na2O	0.763	0.888	0.869	1.003	0.721	0.953	0.683	1.094
K2O	0.033	0.049	0.048	0.007	0.040	0.046	0.000	0.036
TOTAL	99.478	99.672	99.647	100.037	99.874	100.372	99.628	99.507

Table S6 cont.: Plagioclase feldspar major element compositions.

Sample	15085,26	15085,26	15085,26	15085,26	15085,26	15085,26	15085,26	15085,26
Site	26-plag_2	26-plag_2	26-plag_2	26-plag_2	26-plag_3	26-plag_3	26-plag_3	26-plag_3
Line #	36	37	38	39	40	41	42	43
SiO2	45.268	45.178	45.614	46.812	45.474	45.388	47.001	47.079
Al2O3	34.536	34.774	34.933	33.354	34.351	34.330	33.017	33.184
FeO	0.476	0.464	0.472	0.667	0.678	0.520	0.619	0.642
MnO	0.000	0.000	0.004	0.019	0.015	0.000	0.045	0.006
MgO	0.236	0.244	0.199	0.109	0.127	0.262	0.318	0.343
CaO	18.534	18.465	18.673	17.342	18.140	18.414	17.497	17.721
BaO	0.000	0.000	0.000	0.010	0.000	0.009	0.000	0.012
Na2O	0.623	0.950	0.555	1.426	1.169	0.906	1.047	1.387
K2O	0.003	0.008	0.012	0.059	0.061	0.036	0.062	0.055
TOTAL	99.676	100.082	100.461	99.798	100.015	99.864	99.606	100.428

Table S6 cont.: Plagioclase feldspar major element compositions.

Sample	15085,26	15085,26	15085,26	15085,26	15085,26	15085,26	15085,26	15085,26
Site	26-plag_3	26-plag_3	26-plag_3	26-plag_4	26-plag_4	26-plag_4	26-plag_4	26-plag_4
Line #	44	45	46	47	48	49	50	51
SiO2	47.165	47.317	45.534	45.931	46.429	46.196	46.415	46.274
Al2O3	32.878	32.730	34.427	34.105	33.614	33.677	33.584	33.685
FeO	0.620	0.621	0.492	0.512	0.586	0.515	0.607	0.637
MnO	0.013	0.018	0.000	0.007	0.002	0.000	0.006	0.000
MgO	0.350	0.334	0.215	0.240	0.279	0.256	0.289	0.272
CaO	17.478	17.507	18.344	18.182	18.007	17.947	17.691	17.999
BaO	0.004	0.008	0.000	0.000	0.024	0.000	0.010	0.000
Na2O	1.372	1.350	0.980	0.848	1.156	1.137	1.361	1.219
K2O	0.066	0.045	0.075	0.049	0.058	0.041	0.037	0.009
TOTAL	99.946	99.927	100.067	99.874	100.155	99.769	100.000	100.094

Table S6 cont.: Plagioclase feldspar major element compositions.

Sample	15085,26	15085,26	15085,26	15085,26	15085,26	15085,26	15085,26	15556,241
Site	26-plag_4	26-plag_5	26-plag_5	26-plag_5	26-plag_5	26-plag_5	26-plag_5	241-plag_1
Line #	52	53	54	55	56	57	58	59
SiO2	47.002	46.641	46.115	46.719	46.033	46.324	45.535	45.907
Al2O3	33.238	33.220	33.711	33.862	33.909	34.004	34.367	33.744
FeO	0.635	0.589	0.561	0.607	0.549	0.574	0.544	0.651
MnO	0.000	0.005	0.022	0.000	0.008	0.000	0.002	0.000
MgO	0.330	0.319	0.293	0.292	0.284	0.314	0.232	0.253
CaO	17.653	17.767	17.911	17.823	17.967	17.967	18.308	18.178
BaO	0.008	0.000	0.000	0.000	0.019	0.000	0.008	0.002
Na2O	1.281	0.902	0.916	0.907	1.115	1.076	0.984	0.738
K2O	0.078	0.062	0.000	0.038	0.030	0.019	0.017	0.033
TOTAL	100.225	99.505	99.528	100.247	99.912	100.278	99.996	99.504

Table S6 cont.: Plagioclase feldspar major element compositions.

Sample	15556,241	15556,241	15556,241	15556,241	15556,241	15556,241	15556,241	15556,241
Site	241-plag_1	241-plag_1	241-plag_1	241-plag_2	241-plag_2	241-plag_2	241-plag_2	241-plag_2
Line #	60	61	62	63	64	65	66	67
SiO2	46.635	46.118	46.174	46.619	46.535	46.406	46.785	46.409
Al2O3	33.279	33.911	33.833	33.651	33.573	33.509	33.285	33.837
FeO	0.744	0.649	0.679	0.645	0.768	0.725	0.668	0.689
MnO	0.004	0.000	0.002	0.043	0.006	0.000	0.004	0.021
MgO	0.266	0.225	0.237	0.283	0.299	0.337	0.289	0.300
CaO	17.920	18.072	18.299	17.832	17.905	18.054	17.632	17.851
BaO	0.000	0.031	0.000	0.029	0.000	0.020	0.000	0.016
Na2O	0.944	0.793	0.711	0.979	1.232	1.053	1.183	0.848
K2O	0.053	0.000	0.014	0.038	0.020	0.054	0.023	0.000
TOTAL	99.844	99.798	99.948	100.118	100.337	100.157	99.870	99.971

Table S6 cont.: Plagioclase feldspar major element compositions.

Sample	15556,241	15556,241	15556,241	15556,241	15556,241	15556,241	15556,241	15556,241
Site	241-plag_3	241-plag_3	241-plag_3	241-plag_3	241-plag_3	241-plag_3	241-plag_3	241-plag_3
Line #	68	69	70	71	72	73	74	75
SiO2	46.246	46.471	46.407	46.380	46.322	46.347	45.826	46.332
Al2O3	33.338	33.550	33.462	33.408	33.629	33.297	34.116	33.228
FeO	0.905	0.634	0.673	0.827	0.720	0.705	0.675	0.955
MnO	0.006	0.000	0.012	0.008	0.014	0.014	0.008	0.016
MgO	0.257	0.330	0.266	0.195	0.259	0.368	0.255	0.205
CaO	17.943	17.869	17.963	17.904	17.739	18.018	18.537	17.709
BaO	0.000	0.000	0.000	0.000	0.051	0.002	0.001	0.000
Na2O	1.157	0.871	1.125	0.894	0.867	0.946	0.734	1.233
K2O	0.056	0.000	0.062	0.028	0.046	0.038	0.017	0.063
TOTAL	99.908	99.725	99.969	99.643	99.644	99.734	100.169	99.740

Table S6 cont.: Plagioclase feldspar major element compositions.

Sample	15556,241	15556,241	15556,241	15556,241	15556,241	15556,241	15556,241	15556,241
Site	241-plag_4	241-plag_4	241-plag_4	241-plag_4	241-plag_4	241-plag_4	241-plag_5	241-plag_5
Line #	76	77	78	79	80	81	82	83
SiO2	46.324	46.001	47.287	46.003	47.261	46.182	45.763	46.047
Al2O3	33.566	33.878	32.605	34.132	32.647	33.910	34.290	33.901
FeO	0.757	0.640	1.146	0.607	1.160	0.751	0.647	0.688
MnO	0.023	0.011	0.000	0.006	0.024	0.004	0.009	0.000
MgO	0.310	0.279	0.125	0.283	0.107	0.227	0.259	0.305
CaO	17.952	17.954	17.369	18.363	17.491	17.860	18.407	18.226
BaO	0.000	0.001	0.000	0.013	0.000	0.010	0.007	0.003
Na2O	1.048	0.798	1.041	1.031	0.966	1.166	0.775	0.797
K2O	0.049	0.077	0.110	0.046	0.098	0.060	0.027	0.036
TOTAL	100.027	99.640	99.682	100.483	99.754	100.168	100.184	100.003

Table S6 cont.: Plagioclase feldspar major element compositions.

Sample	15556,241	15556,241	15556,241	15556,241	15085,24	15085,24	15085,24	15085,24
Site	241-plag_5	241-plag_5	241-plag_5	241-plag_5	24-plag_1	24-plag_1	24-plag_1	24-plag_1
Line #	84	85	86	87	88	89	90	91
SiO2	46.817	46.890	46.253	46.205	46.353	45.585	45.745	45.526
Al2O3	32.960	33.224	33.700	33.827	34.215	34.698	34.336	34.750
FeO	0.997	0.897	0.647	0.829	0.716	0.543	0.478	0.480
MnO	0.018	0.007	0.002	0.008	0.001	0.006	0.003	0.015
MgO	0.186	0.223	0.313	0.226	0.117	0.150	0.230	0.211
CaO	17.541	17.583	18.096	18.071	17.932	18.492	18.172	18.506
BaO	0.015	0.000	0.027	0.000	0.000	0.000	0.000	0.000
Na2O	0.962	1.241	1.147	0.830	1.032	0.959	1.036	0.723
K2O	0.079	0.054	0.022	0.053	0.094	0.030	0.023	0.041
TOTAL	99.574	100.118	100.206	100.048	100.461	100.463	100.022	100.251

Table S6 cont.: Plagioclase feldspar major element compositions.

Sample	15085,24	15085,24	15085,24	15085,24	15085,24	15085,24	15085,24	15085,24
Site	24-plag_1	24-plag_1	24-plag_1	24-plag_2	24-plag_2	24-plag_2	24-plag_2	24-plag_2
Line #	92	93	94	95	96	97	98	99
SiO2	44.695	45.111	46.133	45.803	45.245	46.067	46.435	45.598
Al2O3	35.050	34.733	34.218	34.280	34.606	33.913	33.905	34.470
FeO	0.450	0.494	0.569	0.552	0.474	0.485	0.522	0.545
MnO	0.009	0.004	0.000	0.000	0.018	0.000	0.003	0.000
MgO	0.159	0.167	0.242	0.215	0.230	0.234	0.258	0.247
CaO	18.840	18.556	18.176	18.114	18.370	18.005	17.866	18.121
BaO	0.000	0.000	0.000	0.000	0.000	0.012	0.006	0.000
Na2O	0.571	0.681	1.131	1.060	0.858	1.099	0.950	0.875
K2O	0.000	0.019	0.021	0.000	0.013	0.031	0.067	0.000
TOTAL	99.774	99.764	100.489	100.023	99.815	99.845	100.012	99.857

Table S6 cont.: Plagioclase feldspar major element compositions.

Sample	15085,24	15085,24	15085,24	15085,24	15085,24	15085,24	15085,24	15085,24
Site	24-plag_3	24-plag_3	24-plag_3	24-plag_3	24-plag_3	24-plag_3	24-plag_3	24-plag_4
Line #	100	101	102	103	104	105	106	107
SiO2	47.018	45.377	45.348	45.991	45.808	46.668	46.190	45.396
Al2O3	33.219	34.766	34.964	34.230	34.499	33.781	34.246	34.453
FeO	0.863	0.515	0.493	0.755	0.570	0.568	0.519	0.560
MnO	0.000	0.000	0.019	0.027	0.008	0.033	0.015	0.026
MgO	0.058	0.166	0.153	0.085	0.142	0.259	0.236	0.141
CaO	17.137	18.284	18.475	17.829	18.203	17.781	17.992	18.342
BaO	0.000	0.000	0.004	0.022	0.000	0.000	0.015	0.030
Na2O	1.464	0.957	1.051	1.021	1.172	0.899	1.152	0.977
K2O	0.160	0.017	0.017	0.054	0.016	0.012	0.010	0.075
TOTAL	99.919	100.082	100.524	100.013	100.416	100.000	100.376	99.999

Table S6 cont.: Plagioclase feldspar major element compositions.

Sample	15085,24	15085,24	15085,24	15085,24	15085,24	15085,24	15085,24	15085,24
Site	24-plag_4	24-plag_4	24-plag_4	24-plag_4	24-plag_4	24-plag_4	24-plag_4	24-plag_5
Line #	108	109	110	111	112	113	114	115
SiO2	45.616	45.147	45.391	45.742	45.619	45.459	45.379	45.652
Al2O3	34.645	34.639	34.534	34.248	34.357	34.407	34.319	34.148
FeO	0.516	0.495	0.539	0.580	0.652	0.523	0.595	0.669
MnO	0.015	0.015	0.004	0.014	0.011	0.000	0.008	0.028
MgO	0.158	0.169	0.171	0.158	0.146	0.181	0.178	0.145
CaO	18.470	18.384	18.296	18.414	18.095	18.383	18.430	18.107
BaO	0.018	0.034	0.000	0.000	0.010	0.000	0.000	0.000
Na2O	0.717	0.999	0.967	0.578	1.148	0.935	0.930	1.151
K2O	0.025	0.001	0.043	0.014	0.000	0.025	0.046	0.031
TOTAL	100.181	99.881	99.945	99.747	100.037	99.912	99.885	99.931

Table S6 cont.: Plagioclase feldspar major element compositions.

Sample	15085,24	15085,24	15085,24	15085,24	15085,24	15085,24	15085,24	15556,28
Site	24-plag_5	24-plag_5	24-plag_5	24-plag_5	24-plag_5	24-plag_5	24-plag_5	28-plag_1
Line #	116	117	118	119	120	121	122	123
SiO2	45.189	45.308	45.358	46.033	46.188	46.174	46.578	46.021
Al2O3	34.729	34.774	34.341	33.983	34.037	33.923	33.540	33.965
FeO	0.497	0.507	0.535	0.631	0.620	0.665	0.806	0.668
MnO	0.003	0.015	0.004	0.025	0.002	0.000	0.013	0.000
MgO	0.194	0.197	0.154	0.132	0.129	0.131	0.048	0.262
CaO	18.568	18.448	18.279	17.834	17.834	17.742	17.409	18.183
BaO	0.000	0.000	0.000	0.000	0.000	0.000	0.005	0.001
Na2O	0.986	0.667	0.992	1.173	1.170	1.227	1.390	1.072
K2O	0.033	0.026	0.041	0.015	0.037	0.067	0.041	0.052
TOTAL	100.201	99.941	99.704	99.827	100.018	99.929	99.830	100.224

Table S6 cont.: Plagioclase feldspar major element compositions.

Sample	15556,28	15556,28	15556,28	15556,28	15556,28	15556,28	15556,28	15556,28
Site	28-plag_1	28-plag_1	28-plag_1	28-plag_1	28-plag_1	28-plag_1	28-plag_1	28-plag_2
Line #	124	125	126	127	128	129	130	131
SiO2	45.957	45.432	46.146	46.158	46.519	46.286	46.386	46.002
Al2O3	33.860	33.909	33.739	34.264	33.651	33.968	33.662	34.055
FeO	0.631	0.731	0.575	0.618	0.863	0.571	0.874	0.584
MnO	0.015	0.000	0.000	0.028	0.000	0.000	0.013	0.028
MgO	0.346	0.227	0.257	0.221	0.146	0.289	0.188	0.286
CaO	18.033	18.188	18.138	18.135	17.641	17.963	17.848	18.080
BaO	0.000	0.010	0.000	0.009	0.000	0.004	0.000	0.018
Na2O	0.861	0.996	1.067	0.554	1.228	1.044	1.111	1.099
K2O	0.041	0.103	0.009	0.043	0.097	0.070	0.083	0.000
TOTAL	99.745	99.596	99.931	100.028	100.145	100.195	100.165	100.152

Table S6 cont.: Plagioclase feldspar major element compositions.

Sample	15556,28	15556,28	15556,28	15556,28	15556,28	15556,28	15556,28	15556,28
Site	28-plag_2	28-plag_2	28-plag_2	28-plag_2	28-plag_2	28-plag_3	28-plag_3	28-plag_3
Line #	132	133	134	135	136	137	138	139
SiO2	45.835	46.822	44.765	46.494	46.282	46.054	46.671	46.150
Al2O3	33.952	33.267	35.591	33.674	33.495	33.647	33.480	33.846
FeO	0.703	0.618	0.801	0.579	0.687	0.672	0.884	0.684
MnO	0.000	0.000	0.030	0.007	0.000	0.010	0.011	0.019
MgO	0.244	0.324	0.223	0.289	0.350	0.208	0.148	0.337
CaO	17.921	17.729	17.302	17.827	17.940	18.067	17.753	18.025
BaO	0.000	0.000	0.015	0.000	0.004	0.008	0.000	0.000
Na2O	1.035	1.013	0.986	1.191	0.957	1.115	1.215	1.048
K2O	0.076	0.042	0.047	0.042	0.041	0.059	0.020	0.027
TOTAL	99.767	99.814	99.759	100.103	99.757	99.839	100.182	100.137

Table S6 cont.: Plagioclase feldspar major element compositions.

Sample	15556,28	15556,28	15556,28	12038,63	12038,63	12038,63	12038,63	12038,63
Site	28-plag_3	28-plag_3	28-plag_3	63-plag_1	63-plag_1	63-plag_1	63-plag_1	63-plag_2
Line #	140	141	142	143	144	145	146	147
SiO2	46.133	45.818	48.970	47.740	47.747	49.082	47.285	47.855
Al2O3	34.101	34.042	31.685	32.800	32.637	31.737	32.996	32.724
FeO	0.613	0.686	1.560	0.518	0.557	0.819	0.473	0.452
MnO	0.003	0.014	0.011	0.008	0.005	0.002	0.000	0.000
MgO	0.313	0.159	0.062	0.333	0.248	0.169	0.264	0.330
CaO	17.894	18.180	16.831	16.987	16.766	15.968	17.024	16.735
BaO	0.006	0.000	0.004	0.000	0.000	0.000	0.016	0.000
Na2O	0.620	0.988	0.875	1.500	2.071	1.821	1.478	1.465
K2O	0.000	0.063	0.184	0.064	0.068	0.121	0.053	0.000
TOTAL	99.682	99.951	100.182	99.951	100.098	99.719	99.588	99.561

Table S6 cont.: Plagioclase feldspar major element compositions.

Sample	12038,63	12038,63	12038,63	12038,63	12038,63	12038,63	12038,63	12038,63
Site	63-plag_2	63-plag_2	63-plag_2	63-plag_2	63-plag_3	63-plag_3	63-plag_3	63-plag_3
Line #	148	149	150	151	152	153	154	155
SiO2	48.571	49.026	47.568	48.414	46.798	47.060	48.196	47.556
Al2O3	32.020	31.751	32.849	32.028	33.364	32.904	32.169	32.946
FeO	0.634	0.882	0.506	0.668	0.376	0.445	0.567	0.478
MnO	0.003	0.014	0.043	0.000	0.000	0.008	0.022	0.000
MgO	0.204	0.176	0.301	0.167	0.311	0.317	0.243	0.305
CaO	16.170	15.896	16.845	16.058	17.399	16.942	16.414	16.854
BaO	0.033	0.000	0.000	0.021	0.000	0.016	0.000	0.000
Na2O	2.139	2.220	1.774	2.276	1.742	1.735	1.560	1.906
K2O	0.081	0.120	0.031	0.099	0.044	0.046	0.070	0.000
TOTAL	99.855	100.084	99.917	99.730	100.033	99.472	99.239	100.043

Table S6 cont.: Plagioclase feldspar major element compositions.

Sample	12038,63	12038,63	12038,63	12038,63	12038,63	12038,63	12038,63	12038,63
Site	63-plag_3	63-plag_4	63-plag_4	63-plag_4	63-plag_4	63-plag_4	63-plag_4	63-plag_4
Line #	156	157	158	159	160	161	162	163
SiO2	47.553	47.847	48.589	48.002	47.793	48.294	50.021	48.007
Al2O3	32.944	32.617	31.942	32.729	32.564	31.956	30.667	32.460
FeO	0.619	0.480	0.925	0.627	0.512	0.831	1.156	0.482
MnO	0.003	0.010	0.019	0.019	0.000	0.000	0.023	0.026
MgO	0.251	0.357	0.162	0.206	0.323	0.219	0.062	0.357
CaO	16.731	16.609	16.096	16.701	16.803	16.100	15.255	16.753
BaO	0.000	0.007	0.000	0.004	0.000	0.003	0.011	0.004
Na2O	1.924	2.064	2.123	1.891	2.018	2.329	2.431	2.014
K2O	0.058	0.050	0.110	0.071	0.044	0.101	0.373	0.030
TOTAL	100.084	100.042	99.966	100.249	100.057	99.832	99.997	100.132

Table S6 cont.: Plagioclase feldspar major element compositions.

Sample	12038,63	12043,15	12043,15	12043,15	12043,15	12043,15	12043,15	12043,15
Site	63-plag_4	15-plag_1	15-plag_1	15-plag_1	15-plag_1	15-plag_2	15-plag_2	15-plag_2
Line #	164	165	166	167	168	169	170	171
SiO2	48.680	46.770	46.231	47.244	47.736	46.669	47.759	48.107
Al2O3	31.686	32.761	33.620	32.163	31.808	33.059	32.211	31.977
FeO	0.921	0.842	0.717	0.915	1.081	0.909	1.232	1.053
MnO	0.023	0.019	0.002	0.000	0.020	0.008	0.014	0.019
MgO	0.201	0.354	0.278	0.400	0.483	0.266	0.187	0.394
CaO	15.773	18.069	18.226	17.663	17.464	17.673	17.417	17.416
BaO	0.000	0.001	0.006	0.000	0.002	0.009	0.000	0.015
Na2O	2.407	1.003	0.736	0.817	1.170	1.004	0.978	0.814
K2O	0.127	0.069	0.020	0.001	0.006	0.069	0.023	0.036
TOTAL	99.819	99.888	99.836	99.202	99.769	99.665	99.821	99.830

Table S6 cont.: Plagioclase feldspar major element compositions.

Sample	12043,15	12043,15	12043,15	12043,15	12043,15	12043,15	12043,15	12043,15
Site	15-plag_2	15-plag_2	15-plag_2	15-plag_3	15-plag_3	15-plag_3	15-plag_3	15-plag_3
Line #	172	173	174	175	176	177	178	179
SiO2	46.212	47.482	48.338	45.244	47.678	47.784	47.561	47.169
Al2O3	33.543	32.167	31.939	34.543	31.929	32.015	32.206	32.822
FeO	0.783	1.129	1.005	0.667	1.002	1.247	0.866	0.880
MnO	0.016	0.033	0.000	0.005	0.000	0.023	0.000	0.011
MgO	0.295	0.362	0.346	0.193	0.412	0.181	0.426	0.291
CaO	18.038	17.658	17.062	18.640	17.441	17.421	17.533	17.867
BaO	0.000	0.000	0.000	0.010	0.000	0.000	0.022	0.000
Na2O	0.983	0.828	1.273	0.733	1.134	1.051	1.072	0.854
K2O	0.073	0.103	0.065	0.073	0.095	0.081	0.006	0.075
TOTAL	99.942	99.763	100.027	100.108	99.691	99.802	99.692	99.968

Table S6 cont.: Plagioclase feldspar major element compositions.

Sample	12043,15	12043,15	12043,15	12043,15	12043,15	12043,15	12043,15	12043,15
Site	15-plag_4	15-plag_4	15-plag_4	15-plag_4	15-plag_4	15-plag_5	15-plag_5	15-plag_5
Line #	180	181	182	183	184	185	186	187
SiO2	47.326	46.927	46.356	48.402	47.175	46.452	45.395	46.927
Al2O3	32.890	33.306	33.527	31.586	32.711	32.832	34.147	32.885
FeO	0.774	0.911	0.811	1.425	0.743	0.685	0.700	0.816
MnO	0.000	0.000	0.021	0.006	0.003	0.015	0.000	0.003
MgO	0.287	0.189	0.239	0.175	0.315	0.300	0.202	0.303
CaO	17.508	17.967	18.056	17.224	17.598	17.771	18.509	17.876
BaO	0.000	0.000	0.000	0.000	0.000	0.000	0.000	0.000
Na2O	0.874	0.899	0.904	0.845	1.125	1.069	0.680	1.011
K2O	0.096	0.040	0.058	0.154	0.054	0.001	0.078	0.048
TOTAL	99.755	100.239	99.973	99.819	99.724	99.123	99.711	99.869

Table S6 cont.: Plagioclase feldspar major element compositions.

Sample	12043,15	12043,15	70017,123	70017,123	70017,123	70017,123	70017,123	70017,123
Site	15-plag_5	15-plag_5	123-plag_1	123-plag_1	123-plag_1	123-plag_1	123-plag_1	123-plag_2
Line #	188	189	190	191	192	193	194	195
SiO2	47.744	47.153	46.494	46.877	47.244	46.760	46.750	47.190
Al2O3	32.299	32.756	34.022	33.292	33.188	33.454	33.492	33.308
FeO	1.095	0.732	0.317	0.412	0.383	0.308	0.460	0.448
MnO	0.012	0.015	0.020	0.005	0.025	0.036	0.000	0.000
MgO	0.156	0.334	0.284	0.326	0.338	0.274	0.296	0.216
CaO	17.286	17.572	17.565	17.388	17.167	17.277	17.345	17.121
BaO	0.000	0.011	0.000	0.005	0.006	0.000	0.000	0.000
Na2O	1.103	1.217	1.481	1.674	1.685	1.649	1.247	1.658
K2O	0.039	0.069	0.059	0.097	0.059	0.073	0.066	0.017
TOTAL	99.734	99.858	100.242	100.076	100.094	99.832	99.657	99.957

Table S6 cont.: Plagioclase feldspar major element compositions.

Sample	70017,123	70017,123	70017,123	70017,123	70017,123	70017,123	70017,123	70017,123
Site	123-plag_2	123-plag_2	123-plag__3	123-plag__3	123-plag__3	123-plag__3	123-plag__3	123-plag__3
Line #	196	197	198	199	200	201	202	203
SiO2	46.377	46.829	48.964	49.154	49.371	46.357	48.485	47.004
Al2O3	33.795	33.480	31.807	31.455	31.256	33.861	32.243	33.423
FeO	0.398	0.447	0.638	0.732	0.705	0.364	0.615	0.445
MnO	0.000	0.000	0.000	0.014	0.000	0.000	0.003	0.002
MgO	0.226	0.233	0.197	0.199	0.142	0.228	0.169	0.238
CaO	17.563	17.258	15.922	15.748	15.591	17.749	16.330	17.266
BaO	0.003	0.021	0.000	0.014	0.027	0.000	0.002	0.004
Na2O	1.521	1.616	2.222	2.416	2.363	1.212	1.929	1.664
K2O	0.050	0.025	0.178	0.173	0.228	0.036	0.087	0.080
TOTAL	99.933	99.909	99.927	99.904	99.683	99.806	99.862	100.126

Table S6 cont.: Plagioclase feldspar major element compositions.

Sample	70017,123	70017,123	70017,123	70017,123	70017,123
Site	123-plag__3	123-plag_4	123-plag_4	123-plag_4	123-plag_4
Line #	204	205	206	207	208
SiO2	47.150	46.480	47.059	46.963	46.954
Al2O3	33.365	33.765	33.396	33.112	33.279
FeO	0.501	0.394	0.435	0.408	0.440
MnO	0.000	0.007	0.035	0.015	0.005
MgO	0.204	0.218	0.236	0.346	0.295
CaO	17.029	17.575	17.089	17.326	17.264
BaO	0.000	0.000	0.000	0.000	0.000
Na2O	1.729	0.799	1.672	1.671	1.596
K2O	0.129	0.101	0.075	0.082	0.060
TOTAL	100.106	99.337	99.996	99.923	99.891

Table S7: Plagioclase feldspar trace element compositions.

Sample	10057	10057	10057	10057	10057	10057	10057	10057
Site	67-PLAG-1.7	67-PLAG-2.10	67-PLAG-2.11	67-PLAG-2.12	67-PLAG-3.16	67-PLAG-3.17	67-PLAG-4.18	67-PLAG-4.19
Si29_ppm_mean	488421.000	494707.000	493900.000	503836.000	495992.000	484813.000	503282.000	515113.000
Si29_ppm_2SE(int)	0.000	0.000	0.000	0.000	0.000	0.000	0.000	0.000
Ca43_ppm_mean	149946.071	148313.975	149261.397	150529.226	146287.388	152148.637	159331.066	155637.878
Ca43_ppm_2SE(int)	2420.264	2468.716	2667.632	2778.140	2767.253	2479.015	3324.228	2690.103
Sc45_ppm_mean	4.023	3.987	4.159	12.323	4.033	5.488	6.291	4.592
Sc45_ppm_2SE(int)	0.295	0.273	0.238	1.455	0.249	0.249	0.651	0.284
Ti47_ppm_mean	649.120	673.510	649.302	1641.687	863.375	701.382	1977.023	896.317
Ti47_ppm_2SE(int)	13.131	25.933	13.797	89.101	26.743	24.625	362.991	39.549
V51_ppm_mean	0.365	0.448	0.327	3.694	0.384	0.961	0.523	0.505
V51_ppm_2SE(int)	0.175	0.154	0.159	0.658	0.145	0.187	0.191	0.147
Cr52_ppm_mean	3.832	2.672	3.511	155.668	3.797	36.626	12.623	2.611
Cr52_ppm_2SE(int)	0.860	0.891	0.818	28.591	0.788	2.369	3.816	0.952
Mn55_ppm_mean	58.071	55.463	55.933	275.648	51.611	95.565	132.610	69.422
Mn55_ppm_2SE(int)	1.168	1.351	0.930	37.987	1.507	2.604	18.032	1.767
Co59_ppm_mean	0.628	0.535	0.622	2.364	0.568	0.868	1.246	0.648
Co59_ppm_2SE(int)	0.090	0.085	0.084	0.326	0.089	0.111	0.178	0.093
Ni60_ppm_mean	0.276	0.393	0.271	0.324	0.345	0.290	0.394	0.262
Ni60_ppm_2SE(int)	0.164	0.138	0.166	0.165	0.168	0.153	0.178	0.164
Cu63_ppm_mean	0.609	0.672	0.628	0.979	0.616	0.460	2.022	0.929
Cu63_ppm_2SE(int)	0.150	0.145	0.170	0.164	0.119	0.116	0.323	0.158
Zn66_ppm_mean	0.583	1.303	0.658	0.632	0.189	0.647	1.323	1.085
Zn66_ppm_2SE(int)	1.056	0.974	0.907	0.889	1.046	0.881	1.064	1.147
Rb85_ppm_mean	0.443	0.363	0.376	0.606	0.339	0.367	3.709	0.708
Rb85_ppm_2SE(int)	0.055	0.048	0.050	0.079	0.056	0.049	0.226	0.070
Sr88_ppm_mean	532.983	471.937	490.510	480.837	470.431	509.445	561.805	560.679
Sr88_ppm_2SE(int)	8.723	7.099	5.965	10.537	8.482	7.445	14.027	7.713
Y89_ppm_mean	1.149	1.307	1.170	10.052	0.924	1.901	206.591	5.358
Y89_ppm_2SE(int)	0.083	0.126	0.092	0.757	0.067	0.123	56.307	0.553
Zr90_ppm_mean	0.087	0.971	0.075	15.504	0.170	0.711	673.996	7.337
Zr90_ppm_2SE(int)	0.036	0.333	0.029	0.884	0.049	0.099	207.764	0.945
Nb93_ppm_mean	0.006	0.084	0.013	0.652	0.012	0.005	31.224	0.412
Nb93_ppm_2SE(int)	0.007	0.032	0.009	0.097	0.009	0.006	8.019	0.084
Hf178_ppm_mean	0.000	0.012	0.000	0.568	0.000	0.031	21.442	0.169
Hf178_ppm_2SE(int)	0.000	0.010	0.000	0.071	0.000	0.015	6.509	0.046
Ta181_ppm_mean	0.000	0.000	0.000	0.036	0.000	0.000	1.816	0.018
Ta181_ppm_2SE(int)	0.000	0.000	0.000	0.011	0.000	0.000	0.526	0.007
Pb208_ppm_mean	1.493	0.208	0.161	0.632	0.083	0.041	5.288	1.962
Pb208_ppm_2SE(int)	0.072	0.032	0.056	0.066	0.020	0.014	0.468	0.117
Th232_ppm_mean	0.000	0.009	0.000	0.134	0.001	0.000	6.891	0.067
Th232_ppm_2SE(int)	0.000	0.005	0.000	0.021	0.002	0.000	1.712	0.017
U238_ppm_mean	0.000	0.002	0.000	0.028	0.000	0.000	2.617	0.014
U238_ppm_2SE(int)	0.001	0.002	0.000	0.007	0.000	0.000	0.739	0.005

Table S7 cont.: Plagioclase feldspar trace element compositions.

Sample	10057	10057	10057	10057	10057	10057	10057	12038
Site	67-PLAG-5.21	67-PLAG-6.29	67-PLAG-7.32	67-PLAG-7.33	67-PLAG-7.34	67-PLAG-8.35	67-PLAG-8.36	63-PLAG-1.145
Si29_ppm_mean	492901.000	493252.000	499324.000	504198.000	500470.000	503405.000	508252.000	490819.000
Si29_ppm_2SE(int)	0.000	0.000	0.000	0.000	0.000	0.000	0.000	0.000
Ca43_ppm_mean	149124.242	109558.924	127336.912	154209.801	150624.133	150737.116	145218.177	163626.263
Ca43_ppm_2SE(int)	2460.935	3530.525	2069.979	2448.276	2657.026	3247.458	2225.834	2600.589
Sc45_ppm_mean	4.791	5.686	4.712	4.115	4.170	17.491	52.324	3.839
Sc45_ppm_2SE(int)	0.261	0.329	0.254	0.249	0.270	3.566	2.812	0.308
Ti47_ppm_mean	1176.016	2115.592	1019.226	849.058	877.340	2040.293	3615.203	419.387
Ti47_ppm_2SE(int)	40.591	238.015	21.642	18.748	18.420	270.264	138.411	9.852
V51_ppm_mean	0.350	0.466	0.061	0.446	0.715	1.200	18.298	3.356
V51_ppm_2SE(int)	0.150	0.148	0.132	0.158	0.189	0.218	0.681	0.240
Cr52_ppm_mean	6.240	18.961	3.415	2.747	4.487	36.786	786.217	8.190
Cr52_ppm_2SE(int)	1.138	2.813	1.118	1.213	1.711	8.873	33.503	1.176
Mn55_ppm_mean	103.745	134.415	89.618	61.332	57.938	740.014	1226.169	62.302
Mn55_ppm_2SE(int)	4.045	5.570	1.262	0.905	2.600	178.503	74.887	1.237
Co59_ppm_mean	0.806	0.805	0.685	0.747	0.573	2.958	9.510	0.996
Co59_ppm_2SE(int)	0.099	0.088	0.081	0.093	0.094	0.669	0.530	0.122
Ni60_ppm_mean	0.254	0.240	0.192	0.411	0.108	0.234	0.435	0.502
Ni60_ppm_2SE(int)	0.157	0.127	0.144	0.210	0.152	0.134	0.180	0.207
Cu63_ppm_mean	0.962	0.940	0.754	0.656	0.599	1.028	1.297	2.229
Cu63_ppm_2SE(int)	0.165	0.147	0.181	0.147	0.136	0.211	0.193	0.287
Zn66_ppm_mean	-0.063	1.221	1.756	1.102	-0.056	1.851	1.535	1.869
Zn66_ppm_2SE(int)	0.915	0.870	1.130	1.001	0.932	0.945	0.903	1.106
Rb85_ppm_mean	2.797	27.726	16.208	0.507	0.430	1.425	0.338	0.027
Rb85_ppm_2SE(int)	0.190	1.998	0.741	0.068	0.066	0.343	0.058	0.028
Sr88_ppm_mean	521.066	615.806	578.583	545.769	489.766	499.150	443.259	320.025
Sr88_ppm_2SE(int)	7.751	9.233	8.729	6.619	7.014	16.369	7.715	4.950
Y89_ppm_mean	102.919	55.607	25.832	1.650	1.130	83.674	43.643	0.214
Y89_ppm_2SE(int)	16.125	3.809	1.127	0.127	0.122	22.344	3.565	0.043
Zr90_ppm_mean	100.738	285.344	121.283	1.372	0.175	137.980	25.190	0.028
Zr90_ppm_2SE(int)	7.235	25.158	5.379	0.253	0.050	40.853	2.230	0.019
Nb93_ppm_mean	3.668	9.686	3.112	0.088	0.004	3.340	0.307	0.000
Nb93_ppm_2SE(int)	0.429	1.116	0.204	0.029	0.005	1.147	0.067	0.000
Hf178_ppm_mean	2.780	9.471	3.872	0.050	0.000	6.026	1.410	0.000
Hf178_ppm_2SE(int)	0.228	0.930	0.237	0.022	0.000	1.731	0.145	0.000
Ta181_ppm_mean	0.203	0.604	0.203	0.000	0.000	0.202	0.020	0.000
Ta181_ppm_2SE(int)	0.034	0.075	0.022	0.000	0.000	0.070	0.008	0.000
Pb208_ppm_mean	0.769	1.377	0.851	0.410	0.323	1.680	8.176	14.914
Pb208_ppm_2SE(int)	0.072	0.114	0.059	0.043	0.058	0.400	0.528	1.695
Th232_ppm_mean	1.910	1.966	0.661	0.011	0.000	0.794	0.040	0.000
Th232_ppm_2SE(int)	0.256	0.171	0.046	0.007	0.000	0.309	0.011	0.000
U238_ppm_mean	0.459	0.549	0.181	0.002	0.000	0.223	0.018	0.000
U238_ppm_2SE(int)	0.045	0.051	0.018	0.002	0.000	0.094	0.005	0.001

Table S7 cont.: Plagioclase feldspar trace element compositions.

Sample	12038	12038	12038	12038	12038	12038	12038	12038
Site	63-PLAG-1.146	63-PLAG-2.147	63-PLAG-2.148	63-PLAG-2.149	63-PLAG-2.150	63-PLAG-3.155	63-PLAG-3.156	63-PLAG-4.160
Si29_ppm_mean	472846.000	478551.000	485708.000	490255.000	475678.000	475555.000	475526.000	477929.000
Si29_ppm_2SE(int)	0.000	0.000	0.000	0.000	0.000	0.000	0.000	0.000
Ca43_ppm_mean	163832.572	161317.801	154344.311	149746.137	160689.038	159063.088	163785.743	158423.174
Ca43_ppm_2SE(int)	2444.083	2921.045	2449.023	3492.398	2914.433	2545.763	3055.783	2375.166
Sc45_ppm_mean	3.854	3.873	3.798	3.976	3.726	3.655	3.626	3.572
Sc45_ppm_2SE(int)	0.205	0.211	0.226	0.275	0.268	0.239	0.202	0.215
Ti47_ppm_mean	414.952	404.908	441.993	458.797	413.565	408.490	417.626	451.462
Ti47_ppm_2SE(int)	11.623	13.506	12.571	13.738	11.228	10.002	10.743	10.027
V51_ppm_mean	4.451	4.559	1.551	1.991	4.184	5.129	3.918	4.523
V51_ppm_2SE(int)	0.220	0.249	0.161	0.229	0.248	0.303	0.278	0.283
Cr52_ppm_mean	11.830	10.994	3.266	4.771	9.151	10.457	8.436	10.029
Cr52_ppm_2SE(int)	1.098	1.048	1.050	1.157	1.055	1.101	0.893	1.170
Mn55_ppm_mean	60.516	61.154	63.773	63.024	61.200	59.700	60.167	62.349
Mn55_ppm_2SE(int)	1.117	1.233	1.098	1.154	1.167	1.167	1.026	1.086
Co59_ppm_mean	0.942	0.803	0.868	0.861	0.910	0.893	0.802	1.227
Co59_ppm_2SE(int)	0.117	0.122	0.107	0.117	0.125	0.110	0.121	0.146
Ni60_ppm_mean	0.240	0.166	0.446	0.411	0.234	0.218	0.345	0.352
Ni60_ppm_2SE(int)	0.180	0.131	0.171	0.213	0.146	0.191	0.157	0.166
Cu63_ppm_mean	2.113	0.388	0.481	0.556	0.666	0.396	8.893	1.017
Cu63_ppm_2SE(int)	0.242	0.115	0.123	0.134	0.141	0.151	0.702	0.161
Zn66_ppm_mean	0.543	0.389	-0.104	0.714	0.960	1.242	0.476	0.429
Zn66_ppm_2SE(int)	0.883	1.036	0.878	1.355	0.968	1.037	0.942	1.020
Rb85_ppm_mean	0.013	0.036	0.066	0.040	0.047	0.022	0.043	0.041
Rb85_ppm_2SE(int)	0.026	0.029	0.029	0.029	0.028	0.023	0.025	0.025
Sr88_ppm_mean	309.020	303.250	387.756	362.759	314.060	292.316	308.248	315.457
Sr88_ppm_2SE(int)	4.539	4.751	7.432	6.607	5.124	4.357	4.958	4.403
Y89_ppm_mean	0.232	0.194	0.290	0.249	0.206	0.227	0.216	0.233
Y89_ppm_2SE(int)	0.038	0.033	0.040	0.040	0.028	0.038	0.043	0.039
Zr90_ppm_mean	0.033	0.018	0.017	0.000	0.017	0.014	0.019	0.056
Zr90_ppm_2SE(int)	0.019	0.015	0.015	0.000	0.015	0.013	0.015	0.026
Nb93_ppm_mean	0.000	0.000	0.000	0.000	0.000	0.000	0.000	0.004
Nb93_ppm_2SE(int)	0.000	0.000	0.000	0.000	0.000	0.000	0.000	0.005
Hf178_ppm_mean	0.000	0.000	0.000	0.000	0.000	0.000	0.000	0.000
Hf178_ppm_2SE(int)	0.000	0.000	0.000	0.000	0.000	0.000	0.000	0.000
Ta181_ppm_mean	0.000	0.000	0.000	0.000	0.000	0.000	0.000	0.000
Ta181_ppm_2SE(int)	0.000	0.000	0.000	0.000	0.000	0.000	0.000	0.000
Pb208_ppm_mean	1.231	0.019	0.037	1.109	1.319	0.022	1.423	9.515
Pb208_ppm_2SE(int)	0.130	0.010	0.017	0.294	0.100	0.014	0.258	3.626
Th232_ppm_mean	0.000	0.000	0.000	0.000	0.000	0.000	0.000	0.000
Th232_ppm_2SE(int)	0.000	0.000	0.000	0.000	0.000	0.000	0.000	0.000
U238_ppm_mean	0.001	0.000	0.000	0.000	0.000	0.000	0.000	0.000
U238_ppm_2SE(int)	0.001	0.000	0.000	0.000	0.000	0.001	0.000	0.000

Table S7 cont.: Plagioclase feldspar trace element compositions.

Sample	12038	12038	12038	12043	12043	12043	12043	12043
Site	63-PLAG-4.161	63-PLAG-4.162	63-PLAG-4.163	15-PLAG-2.170	15-PLAG-2.171	15-PLAG-3.178	15-PLAG-3.179	15-PLAG-4.182
Si29_ppm_mean	482941.000	500206.000	480067.000	477588.000	481067.000	475613.000	471687.000	463562.000
Si29_ppm_2SE(int)	0.000	0.000	0.000	0.000	0.000	0.000	0.000	0.000
Ca43_ppm_mean	157392.673	147517.450	159558.888	175043.700	173358.700	173780.386	179696.143	177588.522
Ca43_ppm_2SE(int)	2669.824	2460.120	2395.751	2313.402	3035.413	2762.885	2378.447	2952.375
Sc45_ppm_mean	3.636	3.933	3.751	3.830	3.591	3.765	3.770	3.634
Sc45_ppm_2SE(int)	0.253	0.198	0.244	0.305	0.244	0.272	0.287	0.291
Ti47_ppm_mean	465.103	209.298	440.322	319.191	542.077	673.456	447.923	402.369
Ti47_ppm_2SE(int)	12.151	7.602	10.250	13.550	13.022	28.045	15.209	11.801
V51_ppm_mean	2.107	0.085	4.187	0.708	2.700	2.471	1.604	2.346
V51_ppm_2SE(int)	0.213	0.131	0.246	0.198	0.221	0.264	0.242	0.216
Cr52_ppm_mean	6.208	0.786	9.583	2.625	5.762	8.346	5.502	6.271
Cr52_ppm_2SE(int)	0.912	1.038	0.977	1.210	1.011	1.332	1.403	0.971
Mn55_ppm_mean	63.634	75.644	61.141	90.971	91.201	110.201	89.653	80.974
Mn55_ppm_2SE(int)	1.169	1.599	1.125	1.980	1.611	2.859	3.557	1.482
Co59_ppm_mean	0.960	1.210	0.979	1.380	1.554	1.881	5.831	1.408
Co59_ppm_2SE(int)	0.109	0.117	0.122	0.130	0.159	0.189	1.536	0.108
Ni60_ppm_mean	0.094	0.218	0.323	0.224	0.347	0.336	-0.014	0.101
Ni60_ppm_2SE(int)	0.164	0.171	0.151	0.207	0.157	0.220	0.241	0.166
Cu63_ppm_mean	0.935	0.675	0.402	0.415	0.489	1.512	21.439	0.711
Cu63_ppm_2SE(int)	0.175	0.139	0.122	0.142	0.129	0.313	5.782	0.134
Zn66_ppm_mean	-1.173	0.661	-0.845	0.566	0.293	-0.250	-1.033	0.276
Zn66_ppm_2SE(int)	0.767	0.855	0.950	0.949	1.139	1.076	1.153	0.974
Rb85_ppm_mean	0.038	0.223	0.015	0.364	0.086	0.124	0.208	0.059
Rb85_ppm_2SE(int)	0.024	0.044	0.024	0.082	0.032	0.038	0.073	0.028
Sr88_ppm_mean	354.554	841.804	306.924	354.960	282.673	266.922	298.965	251.452
Sr88_ppm_2SE(int)	5.063	18.728	3.932	11.631	3.906	3.861	8.774	4.381
Y89_ppm_mean	0.276	0.721	0.220	0.782	0.350	8.028	3.209	0.259
Y89_ppm_2SE(int)	0.041	0.073	0.039	0.100	0.053	1.069	1.061	0.046
Zr90_ppm_mean	0.032	0.116	0.000	1.777	0.041	24.832	6.486	0.031
Zr90_ppm_2SE(int)	0.019	0.039	0.000	0.383	0.023	3.962	2.152	0.024
Nb93_ppm_mean	0.000	0.006	0.008	0.114	0.000	1.755	0.211	0.000
Nb93_ppm_2SE(int)	0.000	0.007	0.009	0.039	0.000	0.360	0.075	0.000
Hf178_ppm_mean	0.000	0.000	0.038	0.022	0.000	0.609	0.166	0.000
Hf178_ppm_2SE(int)	0.000	0.000	0.071	0.013	0.000	0.120	0.074	0.000
Ta181_ppm_mean	0.000	0.000	0.000	0.005	0.000	0.086	0.008	0.000
Ta181_ppm_2SE(int)	0.000	0.000	0.000	0.005	0.000	0.020	0.005	0.000
Pb208_ppm_mean	11.128	0.135	0.038	0.062	0.022	0.084	0.366	0.027
Pb208_ppm_2SE(int)	1.198	0.043	0.015	0.016	0.010	0.022	0.080	0.011
Th232_ppm_mean	0.000	0.000	0.000	0.028	0.000	0.310	0.311	0.000
Th232_ppm_2SE(int)	0.000	0.000	0.000	0.012	0.000	0.047	0.137	0.000
U238_ppm_mean	0.000	0.001	0.000	0.012	0.000	0.077	0.050	0.000
U238_ppm_2SE(int)	0.000	0.001	0.001	0.005	0.000	0.014	0.018	0.001

Table S7 cont.: Plagioclase feldspar trace element compositions.

Sample	12043	12043	12043	12043	12043	15085	15085	15085
Site	15-PLAG-4.183	15-PLAG-5.186	15-PLAG-5.187	15-PLAG-5.188	15-PLAG-5.189	16-PLAG-1.7	16-PLAG-1.8	16-PLAG-1.9
Si29_ppm_mean	484024.000	453953.000	469269.000	477442.000	471530.000	462241.000	458229.000	451431.000
Si29_ppm_2SE(int)	0.000	0.000	0.000	0.000	0.000	0.000	0.000	0.000
Ca43_ppm_mean	175742.124	170163.777	170580.131	176577.575	173034.962	169872.472	172640.157	166862.367
Ca43_ppm_2SE(int)	2282.504	3243.999	2705.600	2486.784	2598.411	2825.480	2411.671	2109.858
Sc45_ppm_mean	3.668	3.419	3.727	3.393	3.606	3.401	3.392	3.332
Sc45_ppm_2SE(int)	0.239	0.224	0.267	0.268	0.304	0.248	0.260	0.251
Ti47_ppm_mean	288.871	263.022	446.060	372.225	589.808	240.583	214.481	182.398
Ti47_ppm_2SE(int)	8.422	10.859	20.801	12.207	16.062	8.457	6.576	7.677
V51_ppm_mean	0.621	1.228	2.782	1.533	2.296	3.410	3.449	1.577
V51_ppm_2SE(int)	0.218	0.176	0.303	0.188	0.230	0.300	0.317	0.203
Cr52_ppm_mean	2.288	3.092	11.273	4.119	9.144	7.108	8.976	3.766
Cr52_ppm_2SE(int)	1.005	0.926	2.777	1.401	1.398	1.270	1.365	1.202
Mn55_ppm_mean	101.139	74.110	86.353	77.794	91.008	65.703	63.559	57.887
Mn55_ppm_2SE(int)	1.820	1.466	3.915	1.145	1.640	0.929	1.152	1.002
Co59_ppm_mean	1.796	1.185	1.477	1.099	1.355	1.083	0.911	0.615
Co59_ppm_2SE(int)	0.141	0.118	0.147	0.123	0.140	0.158	0.120	0.114
Ni60_ppm_mean	0.185	0.162	-0.009	-0.026	-0.046	0.327	0.012	0.043
Ni60_ppm_2SE(int)	0.178	0.192	0.154	0.166	0.190	0.211	0.166	0.170
Cu63_ppm_mean	0.773	0.806	0.814	0.638	0.771	0.499	0.428	0.334
Cu63_ppm_2SE(int)	0.129	0.132	0.152	0.160	0.209	0.188	0.141	0.130
Zn66_ppm_mean	0.514	0.463	-0.088	0.654	0.308	0.338	1.628	0.996
Zn66_ppm_2SE(int)	0.816	1.093	0.862	1.134	1.142	1.300	1.188	1.201
Rb85_ppm_mean	0.244	0.079	0.075	0.100	0.088	-0.005	0.029	0.027
Rb85_ppm_2SE(int)	0.046	0.027	0.034	0.042	0.034	0.026	0.035	0.027
Sr88_ppm_mean	456.515	284.598	238.437	265.916	247.641	251.142	242.299	294.634
Sr88_ppm_2SE(int)	7.512	5.046	2.859	3.792	2.814	3.854	2.659	3.827
Y89_ppm_mean	0.555	0.220	0.319	0.214	0.643	0.152	0.177	0.150
Y89_ppm_2SE(int)	0.060	0.038	0.052	0.046	0.076	0.036	0.042	0.036
Zr90_ppm_mean	0.026	0.000	0.076	0.008	1.074	0.000	0.000	0.000
Zr90_ppm_2SE(int)	0.018	0.000	0.036	0.012	0.155	0.000	0.000	0.000
Nb93_ppm_mean	0.000	0.000	0.002	0.000	0.071	0.000	0.000	0.000
Nb93_ppm_2SE(int)	0.000	0.000	0.004	0.000	0.025	0.000	0.000	0.000
Hf178_ppm_mean	0.000	0.000	0.000	0.000	0.032	0.000	0.000	0.000
Hf178_ppm_2SE(int)	0.000	0.000	0.000	0.000	0.017	0.000	0.000	0.000
Ta181_ppm_mean	0.000	0.000	0.000	0.000	0.000	0.000	0.000	0.000
Ta181_ppm_2SE(int)	0.000	0.000	0.000	0.000	0.000	0.000	0.000	0.000
Pb208_ppm_mean	0.018	0.016	0.009	0.367	0.034	0.010	-0.008	-0.005
Pb208_ppm_2SE(int)	0.011	0.011	0.009	0.657	0.017	0.013	0.010	0.011
Th232_ppm_mean	0.000	0.000	0.000	0.000	0.009	0.000	0.000	0.000
Th232_ppm_2SE(int)	0.000	0.000	0.000	0.000	0.005	0.000	0.000	0.000
U238_ppm_mean	0.000	0.000	0.000	0.000	0.000	0.000	0.000	0.000
U238_ppm_2SE(int)	0.000	0.000	0.000	0.000	0.000	0.000	0.000	0.000

Table S7 cont.: Plagioclase feldspar trace element compositions.

Sample	15085	15085	15085	15085	15085	15085	15085	15085
Site	16-PLAG-2.14	16-PLAG-2.17	16-PLAG-3.18	16-PLAG-3.19	16-PLAG-4.21	16-PLAG-4.23	16-PLAG-5.24	16-PLAG-5.25
Si29_ppm_mean	473412.000	482400.000	486898.000	482586.000	483421.000	481922.000	462832.000	463073.000
Si29_ppm_2SE(int)	0.000	0.000	0.000	0.000	0.000	0.000	0.000	0.000
Ca43_ppm_mean	166526.445	162865.935	157067.219	160986.795	159404.214	163672.477	172219.559	171745.744
Ca43_ppm_2SE(int)	2604.684	2537.826	2196.853	1975.404	2623.547	2566.007	2785.626	2984.057
Sc45_ppm_mean	3.614	3.436	3.405	3.456	3.434	2.929	3.276	3.279
Sc45_ppm_2SE(int)	0.240	0.301	0.241	0.292	0.236	0.257	0.225	0.211
Ti47_ppm_mean	261.145	229.169	166.744	170.219	163.619	226.569	233.986	235.985
Ti47_ppm_2SE(int)	9.536	8.499	6.669	7.843	7.092	8.432	8.473	7.847
V51_ppm_mean	1.347	0.314	0.072	0.289	0.167	0.440	2.010	1.693
V51_ppm_2SE(int)	0.222	0.160	0.125	0.134	0.148	0.188	0.254	0.224
Cr52_ppm_mean	3.856	0.625	0.740	3.375	2.573	0.103	4.691	4.439
Cr52_ppm_2SE(int)	1.375	1.361	1.630	1.418	1.460	1.314	1.407	1.321
Mn55_ppm_mean	65.167	66.709	58.293	64.354	63.231	70.641	62.584	64.264
Mn55_ppm_2SE(int)	1.222	1.318	1.330	1.084	1.068	1.116	1.055	1.260
Co59_ppm_mean	1.102	0.947	0.617	0.759	0.919	1.153	0.884	0.970
Co59_ppm_2SE(int)	0.152	0.141	0.115	0.137	0.145	0.126	0.113	0.137
Ni60_ppm_mean	0.364	0.273	0.333	0.181	0.454	0.004	0.038	0.186
Ni60_ppm_2SE(int)	0.243	0.235	0.254	0.236	0.262	0.204	0.236	0.236
Cu63_ppm_mean	0.171	0.415	0.451	0.397	0.465	0.379	0.308	0.441
Cu63_ppm_2SE(int)	0.131	0.170	0.177	0.156	0.198	0.167	0.130	0.135
Zn66_ppm_mean	0.543	-0.094	1.567	-0.373	-2.245	-0.976	0.313	0.667
Zn66_ppm_2SE(int)	1.433	1.205	1.381	1.455	1.119	1.335	1.192	1.197
Rb85_ppm_mean	0.033	0.177	0.445	0.419	0.355	0.164	0.055	0.062
Rb85_ppm_2SE(int)	0.031	0.042	0.064	0.072	0.071	0.049	0.034	0.033
Sr88_ppm_mean	331.494	494.083	912.330	856.354	794.661	492.185	290.800	296.451
Sr88_ppm_2SE(int)	4.386	6.931	12.696	9.940	11.670	6.379	3.393	4.557
Y89_ppm_mean	0.178	0.299	0.530	0.572	0.818	0.298	0.166	0.166
Y89_ppm_2SE(int)	0.041	0.057	0.087	0.069	0.188	0.047	0.038	0.040
Zr90_ppm_mean	0.000	0.000	0.014	0.000	1.227	0.004	0.004	0.000
Zr90_ppm_2SE(int)	0.000	0.000	0.016	0.000	0.704	0.008	0.007	0.000
Nb93_ppm_mean	0.000	0.000	0.000	0.000	0.059	0.000	0.000	0.000
Nb93_ppm_2SE(int)	0.000	0.000	0.000	0.000	0.033	0.000	0.000	0.000
Hf178_ppm_mean	0.000	0.000	0.000	0.000	0.032	0.000	0.000	0.000
Hf178_ppm_2SE(int)	0.000	0.000	0.000	0.000	0.029	0.000	0.000	0.000
Ta181_ppm_mean	0.000	0.000	0.000	0.000	0.000	0.000	0.000	0.000
Ta181_ppm_2SE(int)	0.000	0.000	0.000	0.000	0.000	0.000	0.000	0.000
Pb208_ppm_mean	-0.006	0.007	0.044	0.044	0.085	0.002	0.015	0.014
Pb208_ppm_2SE(int)	0.012	0.012	0.019	0.016	0.026	0.010	0.019	0.012
Th232_ppm_mean	0.000	0.000	0.000	0.000	0.007	0.000	0.000	0.000
Th232_ppm_2SE(int)	0.000	0.000	0.000	0.000	0.006	0.000	0.000	0.000
U238_ppm_mean	0.000	0.000	0.000	0.000	0.002	0.000	0.000	0.000
U238_ppm_2SE(int)	0.000	0.000	0.000	0.000	0.002	0.000	0.000	0.000

Table S7 cont.: Plagioclase feldspar trace element compositions.

Sample	15085	15085	15085	15085	15085	15085	15085	15085
Site	24-PLAG-1.88	24-PLAG-1.90	24-PLAG-1.92	24-PLAG-2.97	24-PLAG-2.98	24-PLAG-2.99	24-PLAG-3.100	24-PLAG-3.102
Si29_ppm_mean	463531.000	457453.000	446952.000	460666.000	464351.000	455978.000	470184.000	453483.000
Si29_ppm_2SE(int)	0.000	0.000	0.000	0.000	0.000	0.000	0.000	0.000
Ca43_ppm_mean	163739.693	173792.581	180939.130	173340.495	166671.850	170100.103	158461.279	168245.648
Ca43_ppm_2SE(int)	2977.666	2942.639	3004.761	2431.427	2548.757	2930.337	2477.749	3249.152
Sc45_ppm_mean	3.176	3.151	3.156	3.480	3.112	3.252	3.197	3.100
Sc45_ppm_2SE(int)	0.240	0.255	0.219	0.276	0.234	0.227	0.239	0.252
Ti47_ppm_mean	262.090	219.427	166.109	209.488	247.239	222.843	205.858	191.679
Ti47_ppm_2SE(int)	7.528	6.482	6.309	6.602	8.183	7.394	6.911	6.905
V51_ppm_mean	0.914	3.300	3.258	3.807	3.324	4.668	0.481	2.481
V51_ppm_2SE(int)	0.180	0.248	0.279	0.505	0.230	2.441	0.125	0.191
Cr52_ppm_mean	2.083	7.511	5.666	6.898	8.787	5.869	1.020	3.821
Cr52_ppm_2SE(int)	1.091	0.925	1.169	0.996	1.006	1.139	0.914	1.020
Mn55_ppm_mean	62.389	62.375	58.301	60.761	62.281	60.616	61.390	58.824
Mn55_ppm_2SE(int)	1.358	1.315	1.227	1.178	1.035	1.250	1.272	1.275
Co59_ppm_mean	0.929	1.106	0.976	0.659	0.715	0.618	0.868	0.876
Co59_ppm_2SE(int)	0.111	0.135	0.130	0.093	0.093	0.096	0.116	0.101
Ni60_ppm_mean	0.145	0.383	0.144	0.408	0.359	0.347	0.451	0.296
Ni60_ppm_2SE(int)	0.148	0.183	0.187	0.201	0.198	0.161	0.215	0.190
Cu63_ppm_mean	0.279	1.497	0.451	0.326	0.313	0.261	0.345	0.248
Cu63_ppm_2SE(int)	0.122	0.214	0.157	0.130	0.113	0.113	0.115	0.108
Zn66_ppm_mean	0.689	-0.416	0.619	1.117	1.042	0.448	0.317	0.497
Zn66_ppm_2SE(int)	0.947	0.913	1.016	0.971	1.002	1.001	0.886	0.886
Rb85_ppm_mean	0.064	0.044	0.026	0.033	0.052	0.043	0.102	0.035
Rb85_ppm_2SE(int)	0.028	0.030	0.026	0.023	0.028	0.025	0.033	0.023
Sr88_ppm_mean	357.834	241.106	255.317	234.187	236.371	238.410	426.175	264.631
Sr88_ppm_2SE(int)	5.366	4.141	3.583	3.379	3.048	4.175	7.341	4.676
Y89_ppm_mean	0.169	0.127	0.146	0.111	0.137	0.137	0.223	0.098
Y89_ppm_2SE(int)	0.033	0.032	0.031	0.026	0.029	0.031	0.036	0.025
Zr90_ppm_mean	0.011	0.032	0.000	0.000	0.024	0.008	0.063	0.000
Zr90_ppm_2SE(int)	0.013	0.020	0.000	0.000	0.017	0.011	0.034	0.000
Nb93_ppm_mean	0.000	0.006	0.000	0.004	0.000	0.000	0.016	0.000
Nb93_ppm_2SE(int)	0.000	0.007	0.000	0.006	0.000	0.000	0.013	0.000
Hf178_ppm_mean	0.000	0.000	0.000	0.000	0.000	0.000	0.000	0.000
Hf178_ppm_2SE(int)	0.000	0.000	0.000	0.000	0.000	0.000	0.000	0.000
Ta181_ppm_mean	0.000	0.000	0.000	0.000	0.000	0.001	0.000	0.000
Ta181_ppm_2SE(int)	0.000	0.000	0.000	0.000	0.000	0.001	0.000	0.000
Pb208_ppm_mean	0.014	0.135	0.019	0.005	0.005	-0.005	0.002	0.006
Pb208_ppm_2SE(int)	0.009	0.024	0.014	0.008	0.008	0.006	0.008	0.009
Th232_ppm_mean	0.000	0.000	0.000	0.000	0.000	0.000	0.001	0.000
Th232_ppm_2SE(int)	0.000	0.000	0.000	0.000	0.000	0.000	0.002	0.000
U238_ppm_mean	0.000	0.000	0.000	0.039	0.000	0.000	0.001	0.000
U238_ppm_2SE(int)	0.000	0.000	0.000	0.077	0.000	0.000	0.001	0.000

Table S7 cont.: Plagioclase feldspar trace element compositions.

Sample	15085	15085	15085	15085	15085	15085	15085	15085
Site	24-PLAG-3.103	24-PLAG-4.107	24-PLAG-4.109	24-PLAG-4.111	24-PLAG-4.112	24-PLAG-5.115	24-PLAG-5.117	24-PLAG-5.120
Si29_ppm_mean	459912.000	453962.000	451470.000	457415.000	456189.000	456524.000	453084.000	461884.000
Si29_ppm_2SE(int)	0.000	0.000	0.000	0.000	0.000	0.000	0.000	0.000
Ca43_ppm_mean	166168.134	167440.364	165628.918	166257.644	161243.218	170640.276	174006.709	169901.647
Ca43_ppm_2SE(int)	2603.750	3176.318	3149.071	2793.729	2248.504	2611.210	3207.341	2990.781
Sc45_ppm_mean	3.015	3.107	3.195	2.996	3.055	3.522	3.051	3.282
Sc45_ppm_2SE(int)	0.218	0.203	0.217	0.244	0.193	0.218	0.220	0.249
Ti47_ppm_mean	211.700	186.520	186.232	191.886	209.587	201.230	192.019	217.428
Ti47_ppm_2SE(int)	8.508	7.425	7.801	7.373	7.523	8.481	5.651	7.039
V51_ppm_mean	1.765	2.904	2.945	2.287	2.018	2.235	3.168	1.987
V51_ppm_2SE(int)	0.185	0.366	0.249	0.228	0.163	0.227	0.264	0.145
Cr52_ppm_mean	2.967	4.308	6.176	4.062	2.008	4.464	5.346	2.614
Cr52_ppm_2SE(int)	0.789	1.069	1.083	1.017	0.801	1.070	1.180	1.119
Mn55_ppm_mean	59.383	59.823	58.283	60.297	57.835	62.914	59.662	62.383
Mn55_ppm_2SE(int)	1.067	1.037	1.452	1.209	1.247	1.028	1.136	1.268
Co59_ppm_mean	0.763	0.713	0.772	0.717	0.623	0.804	0.801	0.819
Co59_ppm_2SE(int)	0.108	0.100	0.116	0.104	0.092	0.107	0.110	0.099
Ni60_ppm_mean	0.184	0.220	0.466	0.413	0.530	0.531	0.327	0.421
Ni60_ppm_2SE(int)	0.181	0.150	0.429	0.193	0.197	0.202	0.195	0.201
Cu63_ppm_mean	0.361	0.329	0.360	0.367	0.271	0.345	0.354	0.428
Cu63_ppm_2SE(int)	0.117	0.125	0.135	0.128	0.105	0.113	0.120	0.107
Zn66_ppm_mean	-0.265	0.292	-0.449	0.071	0.100	0.120	0.949	-0.227
Zn66_ppm_2SE(int)	0.973	0.966	1.025	0.953	0.872	0.847	0.942	0.811
Rb85_ppm_mean	0.057	0.036	0.010	0.022	0.021	0.021	0.031	0.057
Rb85_ppm_2SE(int)	0.030	0.027	0.025	0.023	0.028	0.025	0.027	0.028
Sr88_ppm_mean	297.865	261.299	257.059	267.830	277.544	268.018	253.689	291.918
Sr88_ppm_2SE(int)	4.449	4.465	5.506	5.027	4.394	4.117	4.093	5.357
Y89_ppm_mean	0.135	0.113	0.133	0.127	0.117	0.098	0.135	0.139
Y89_ppm_2SE(int)	0.032	0.027	0.033	0.032	0.032	0.025	0.034	0.028
Zr90_ppm_mean	0.000	0.000	0.026	0.015	0.000	0.004	0.004	0.000
Zr90_ppm_2SE(int)	0.000	0.000	0.019	0.014	0.000	0.007	0.008	0.000
Nb93_ppm_mean	0.000	0.000	0.000	0.002	0.000	0.000	0.000	0.000
Nb93_ppm_2SE(int)	0.000	0.000	0.000	0.004	0.000	0.000	0.000	0.000
Hf178_ppm_mean	0.000	0.000	0.000	0.000	0.000	0.000	0.000	0.000
Hf178_ppm_2SE(int)	0.000	0.000	0.000	0.000	0.000	0.000	0.000	0.000
Ta181_ppm_mean	0.000	0.000	0.023	0.000	0.000	0.000	0.000	0.000
Ta181_ppm_2SE(int)	0.000	0.000	0.031	0.000	0.000	0.000	0.000	0.000
Pb208_ppm_mean	0.009	0.030	0.010	0.026	0.011	0.017	0.013	0.010
Pb208_ppm_2SE(int)	0.009	0.049	0.008	0.016	0.008	0.010	0.009	0.009
Th232_ppm_mean	0.000	0.000	0.000	0.000	0.001	0.000	0.000	0.000
Th232_ppm_2SE(int)	0.000	0.000	0.000	0.000	0.001	0.000	0.000	0.000
U238_ppm_mean	0.000	0.000	0.000	0.000	0.000	0.000	0.000	0.000
U238_ppm_2SE(int)	0.000	0.000	0.000	0.001	0.001	0.000	0.000	0.001

Table S7 cont.: Plagioclase feldspar trace element compositions.

Sample	15085	15085	15085	15085	15085	15085	15085	15085
Site	24-PLAG-5.122	26-PLAG-1.28	26-PLAG-1.29	26-PLAG-1.30	26-PLAG-1.31	26-PLAG-2.34	26-PLAG-2.35	26-PLAG-2.36
Si29_ppm_mean	465781.000	459942.000	458839.000	456050.000	455924.000	451376.000	457899.000	452684.000
Si29_ppm_2SE(int)	0.000	0.000	0.000	0.000	0.000	0.000	0.000	0.000
Ca43_ppm_mean	167165.051	170864.524	173308.561	177683.926	176122.586	180677.733	171762.374	175750.369
Ca43_ppm_2SE(int)	3014.125	3463.442	2613.048	3042.634	2325.751	2701.064	2993.333	2441.896
Sc45_ppm_mean	2.938	3.009	3.116	3.181	3.282	3.114	3.165	2.889
Sc45_ppm_2SE(int)	0.239	0.276	0.266	0.257	0.254	0.257	0.285	0.235
Ti47_ppm_mean	160.557	227.367	226.293	218.862	214.828	150.748	222.283	179.261
Ti47_ppm_2SE(int)	6.226	8.416	9.066	9.706	7.628	6.207	9.791	7.306
V51_ppm_mean	0.378	3.108	3.314	3.168	3.361	2.860	3.062	3.634
V51_ppm_2SE(int)	0.115	0.301	0.339	0.266	0.275	0.248	0.233	0.284
Cr52_ppm_mean	1.185	6.426	6.428	8.520	7.575	5.196	8.197	7.163
Cr52_ppm_2SE(int)	1.021	0.870	1.178	1.426	1.173	1.178	1.202	1.155
Mn55_ppm_mean	64.818	60.074	60.710	61.794	61.247	58.753	61.667	58.937
Mn55_ppm_2SE(int)	1.088	1.182	1.152	1.124	1.177	0.960	1.124	1.154
Co59_ppm_mean	0.649	0.873	0.857	0.814	0.786	0.511	0.745	0.720
Co59_ppm_2SE(int)	0.094	0.111	0.114	0.110	0.132	0.096	0.137	0.128
Ni60_ppm_mean	0.319	0.204	0.166	0.396	-0.037	0.258	0.244	0.489
Ni60_ppm_2SE(int)	0.159	0.152	0.199	0.215	0.185	0.196	0.194	0.236
Cu63_ppm_mean	1.353	0.337	0.490	0.192	0.580	0.177	0.420	0.427
Cu63_ppm_2SE(int)	0.220	0.137	0.124	0.119	0.158	0.121	0.135	0.168
Zn66_ppm_mean	1.003	-0.939	-1.268	1.145	0.660	-0.733	0.073	0.433
Zn66_ppm_2SE(int)	1.112	0.880	0.994	1.093	1.085	1.099	0.964	1.019
Rb85_ppm_mean	0.143	0.025	0.045	0.021	0.053	0.037	0.012	0.054
Rb85_ppm_2SE(int)	0.041	0.031	0.029	0.033	0.025	0.027	0.034	0.033
Sr88_ppm_mean	473.807	244.912	246.065	247.074	243.169	264.755	243.408	232.374
Sr88_ppm_2SE(int)	7.204	4.541	3.907	3.550	3.291	3.175	3.653	3.395
Y89_ppm_mean	0.268	0.125	0.161	0.134	0.206	0.088	0.134	0.146
Y89_ppm_2SE(int)	0.041	0.029	0.037	0.033	0.039	0.025	0.032	0.029
Zr90_ppm_mean	0.007	0.000	0.000	0.000	0.000	0.000	0.000	0.000
Zr90_ppm_2SE(int)	0.010	0.000	0.000	0.000	0.000	0.000	0.000	0.000
Nb93_ppm_mean	0.000	0.000	0.000	0.024	0.000	0.000	0.000	0.000
Nb93_ppm_2SE(int)	0.000	0.000	0.000	0.038	0.000	0.000	0.000	0.000
Hf178_ppm_mean	0.000	0.000	0.000	0.000	0.000	0.000	0.000	0.000
Hf178_ppm_2SE(int)	0.000	0.000	0.000	0.000	0.000	0.000	0.000	0.000
Ta181_ppm_mean	0.000	0.000	0.000	0.000	0.000	0.000	0.000	0.000
Ta181_ppm_2SE(int)	0.000	0.000	0.000	0.000	0.000	0.000	0.000	0.000
Pb208_ppm_mean	0.137	0.008	0.005	0.005	0.007	0.007	0.022	0.015
Pb208_ppm_2SE(int)	0.024	0.007	0.010	0.010	0.012	0.009	0.012	0.012
Th232_ppm_mean	0.000	0.000	0.000	0.000	0.000	0.002	0.000	0.000
Th232_ppm_2SE(int)	0.000	0.000	0.000	0.000	0.000	0.002	0.000	0.000
U238_ppm_mean	0.000	0.000	0.000	0.001	0.000	0.000	0.000	0.000
U238_ppm_2SE(int)	0.000	0.000	0.000	0.001	0.000	0.000	0.000	0.000

Table S7 cont.: Plagioclase feldspar trace element compositions.

Sample	15085	15085	15085	15085	15085	15085	15085	15085
Site	26-PLAG-2.37	26-PLAG-2.38	26-PLAG-2.39	26-PLAG-3.42	26-PLAG-3.45	26-PLAG-3.46	26-PLAG-4.47	26-PLAG-4.48
Si29_ppm_mean	451779.000	456137.000	468121.000	470013.000	473166.000	455342.000	459314.000	464294.000
Si29_ppm_2SE(int)	0.000	0.000	0.000	0.000	0.000	0.000	0.000	0.000
Ca43_ppm_mean	174580.531	177173.035	165251.644	167326.496	169389.299	172555.048	172664.255	167405.380
Ca43_ppm_2SE(int)	2772.977	2686.653	2319.557	2558.362	2439.901	2470.934	3162.945	2946.016
Sc45_ppm_mean	2.967	3.161	3.294	2.921	3.121	3.085	3.205	2.982
Sc45_ppm_2SE(int)	0.256	0.255	0.276	0.251	0.269	0.300	0.263	0.207
Ti47_ppm_mean	194.998	168.259	233.693	286.828	289.674	220.095	209.348	240.055
Ti47_ppm_2SE(int)	5.789	7.919	9.790	9.729	8.021	8.977	6.970	7.948
V51_ppm_mean	3.649	3.125	0.553	3.544	3.527	3.294	3.019	3.193
V51_ppm_2SE(int)	0.248	0.241	0.153	0.265	0.264	0.254	0.270	0.266
Cr52_ppm_mean	8.853	6.059	3.093	7.311	10.294	9.474	7.349	5.898
Cr52_ppm_2SE(int)	1.347	1.208	1.098	1.181	1.257	3.513	1.081	1.043
Mn55_ppm_mean	60.185	59.881	60.764	70.093	73.145	62.416	62.275	62.734
Mn55_ppm_2SE(int)	1.048	1.143	1.230	1.211	1.282	1.269	1.315	1.367
Co59_ppm_mean	0.477	0.615	0.598	1.414	1.417	0.905	0.927	1.050
Co59_ppm_2SE(int)	0.089	0.098	0.108	0.161	0.151	0.111	0.121	0.125
Ni60_ppm_mean	0.242	0.224	0.347	0.349	0.151	0.380	0.335	0.404
Ni60_ppm_2SE(int)	0.190	0.220	0.233	0.208	0.203	0.197	0.221	0.179
Cu63_ppm_mean	0.305	0.360	0.391	0.370	0.371	0.357	0.473	0.512
Cu63_ppm_2SE(int)	0.154	0.127	0.138	0.150	0.150	0.146	0.120	0.122
Zn66_ppm_mean	0.915	1.459	0.742	0.053	-0.486	-1.671	-0.409	-0.026
Zn66_ppm_2SE(int)	1.237	1.000	1.157	1.291	1.314	1.101	0.864	0.979
Rb85_ppm_mean	0.024	0.054	0.084	0.079	0.079	0.029	0.040	0.073
Rb85_ppm_2SE(int)	0.026	0.029	0.029	0.032	0.035	0.032	0.028	0.034
Sr88_ppm_mean	232.000	253.515	363.414	247.952	252.561	238.329	243.670	239.840
Sr88_ppm_2SE(int)	3.722	2.831	5.454	4.077	3.955	3.192	3.956	4.334
Y89_ppm_mean	0.143	0.146	0.182	0.225	0.188	0.197	0.145	0.150
Y89_ppm_2SE(int)	0.040	0.033	0.041	0.049	0.042	0.041	0.031	0.031
Zr90_ppm_mean	0.000	0.005	0.028	0.000	0.000	0.059	0.008	0.011
Zr90_ppm_2SE(int)	0.000	0.009	0.022	0.000	0.000	0.030	0.011	0.012
Nb93_ppm_mean	0.000	0.000	0.000	0.000	0.000	0.000	0.000	0.000
Nb93_ppm_2SE(int)	0.000	0.000	0.000	0.000	0.000	0.000	0.000	0.000
Hf178_ppm_mean	0.000	0.000	0.000	0.000	0.000	0.000	0.000	0.000
Hf178_ppm_2SE(int)	0.000	0.000	0.000	0.000	0.000	0.000	0.000	0.000
Ta181_ppm_mean	0.000	0.000	0.000	0.000	0.000	0.000	0.000	0.000
Ta181_ppm_2SE(int)	0.000	0.000	0.000	0.000	0.000	0.000	0.000	0.000
Pb208_ppm_mean	0.025	0.031	0.023	0.014	0.006	0.001	0.027	0.001
Pb208_ppm_2SE(int)	0.018	0.013	0.015	0.012	0.011	0.010	0.010	0.008
Th232_ppm_mean	0.000	0.000	0.000	0.000	0.000	0.000	0.000	0.000
Th232_ppm_2SE(int)	0.000	0.000	0.000	0.000	0.000	0.000	0.000	0.000
U238_ppm_mean	0.000	0.000	0.000	0.000	0.000	0.000	0.000	0.000
U238_ppm_2SE(int)	0.000	0.000	0.000	0.000	0.000	0.000	0.000	0.000

Table S7 cont.: Plagioclase feldspar trace element compositions.

Sample	15085	15085	15085	15085	15556	15556	15556	15556
Site	26-PLAG-5.53	26-PLAG-5.55	26-PLAG-5.56	26-PLAG-5.58	28-PLAG-1.127	28-PLAG-1.128	28-PLAG-2.134	28-PLAG-2.135
Si29_ppm_mean	466411.000	467190.000	460329.000	455354.000	461581.000	465187.000	447652.000	464935.000
Si29_ppm_2SE(int)	0.000	0.000	0.000	0.000	0.000	0.000	0.000	0.000
Ca43_ppm_mean	168686.330	175595.692	163984.983	172814.717	173629.249	171211.384	160052.916	167521.786
Ca43_ppm_2SE(int)	2713.294	2605.678	2805.362	2736.309	3335.230	2935.130	3502.589	2857.195
Sc45_ppm_mean	2.882	2.866	3.149	3.151	2.904	3.058	2.935	3.098
Sc45_ppm_2SE(int)	0.232	0.223	0.255	0.335	0.251	0.263	0.245	0.232
Ti47_ppm_mean	249.487	228.995	265.825	213.667	308.601	319.130	289.967	310.660
Ti47_ppm_2SE(int)	7.944	7.890	8.791	8.741	10.521	11.799	10.214	9.233
V51_ppm_mean	3.545	3.460	3.412	3.657	3.587	1.396	3.586	4.710
V51_ppm_2SE(int)	0.263	0.290	0.249	0.271	0.287	0.547	0.239	0.250
Cr52_ppm_mean	7.037	8.065	8.681	6.670	6.705	3.645	11.845	9.478
Cr52_ppm_2SE(int)	1.321	1.509	1.129	1.233	1.200	1.208	1.026	0.952
Mn55_ppm_mean	64.616	63.136	64.651	59.781	69.065	69.001	67.054	70.352
Mn55_ppm_2SE(int)	1.345	0.827	1.112	1.131	1.264	1.633	1.189	1.373
Co59_ppm_mean	1.434	0.936	1.388	0.862	1.363	1.284	1.071	1.323
Co59_ppm_2SE(int)	0.152	0.115	0.171	0.126	0.175	0.119	0.119	0.135
Ni60_ppm_mean	0.249	0.340	0.169	0.270	0.493	0.347	0.533	0.237
Ni60_ppm_2SE(int)	0.193	0.206	0.151	0.202	0.202	0.197	0.291	0.195
Cu63_ppm_mean	0.414	0.408	0.373	0.416	0.771	0.764	0.989	0.733
Cu63_ppm_2SE(int)	0.131	0.140	0.129	0.205	0.175	0.139	0.186	0.139
Zn66_ppm_mean	-1.209	-0.698	0.414	0.854	0.286	0.670	3.988	2.872
Zn66_ppm_2SE(int)	0.943	1.277	0.999	0.955	1.053	1.055	1.276	0.848
Rb85_ppm_mean	0.063	0.047	0.067	0.055	0.066	0.094	0.077	0.067
Rb85_ppm_2SE(int)	0.030	0.030	0.028	0.030	0.029	0.042	0.042	0.028
Sr88_ppm_mean	249.248	239.985	236.896	239.217	227.657	293.064	200.832	203.567
Sr88_ppm_2SE(int)	3.604	2.977	3.262	3.547	4.102	4.898	3.927	3.255
Y89_ppm_mean	0.163	0.179	0.162	0.142	0.137	0.151	0.116	0.106
Y89_ppm_2SE(int)	0.041	0.041	0.039	0.032	0.031	0.036	0.030	0.026
Zr90_ppm_mean	0.000	0.000	0.039	0.004	0.000	0.009	0.358	0.015
Zr90_ppm_2SE(int)	0.000	0.000	0.023	0.008	0.000	0.013	0.117	0.014
Nb93_ppm_mean	0.000	0.000	0.000	0.000	0.000	0.000	0.000	0.000
Nb93_ppm_2SE(int)	0.000	0.000	0.000	0.000	0.000	0.000	0.000	0.000
Hf178_ppm_mean	0.000	0.000	0.000	0.000	0.000	0.000	0.000	0.000
Hf178_ppm_2SE(int)	0.000	0.000	0.000	0.000	0.000	0.000	0.000	0.000
Ta181_ppm_mean	0.000	0.000	0.000	0.000	0.000	0.000	0.000	0.000
Ta181_ppm_2SE(int)	0.000	0.000	0.000	0.000	0.000	0.000	0.000	0.000
Pb208_ppm_mean	0.009	0.019	0.016	0.011	0.014	0.008	1.979	0.043
Pb208_ppm_2SE(int)	0.008	0.009	0.011	0.012	0.013	0.010	0.551	0.014
Th232_ppm_mean	0.000	0.000	0.000	0.000	0.000	0.000	0.004	0.000
Th232_ppm_2SE(int)	0.000	0.000	0.000	0.000	0.000	0.000	0.004	0.000
U238_ppm_mean	0.000	0.000	0.000	0.002	0.000	0.000	0.003	0.000
U238_ppm_2SE(int)	0.000	0.000	0.000	0.002	0.000	0.000	0.003	0.000

Table S7 cont.: Plagioclase feldspar trace element compositions.

Sample	15556	15556	15556	15556	15556	15556	15556	15556
Site	28-PLAG-3.139	28-PLAG-3.140	241-PLAG-1.59	241-PLAG-1.60	241-PLAG-1.61	241-PLAG-1.62	241-PLAG-2.68	241-PLAG-2.69
Si29_ppm_mean	461502.000	461328.000	459066.000	466346.000	461180.000	461735.000	462460.000	464705.000
Si29_ppm_2SE(int)	0.000	0.000	0.000	0.000	0.000	0.000	0.000	0.000
Ca43_ppm_mean	175819.635	172528.424	164504.404	165192.907	167368.837	167043.044	166566.118	170242.212
Ca43_ppm_2SE(int)	3045.199	2891.313	3589.330	2799.960	3279.942	2921.123	2547.143	2266.860
Sc45_ppm_mean	3.124	3.045	2.968	3.073	2.912	2.843	3.561	2.899
Sc45_ppm_2SE(int)	0.233	0.255	0.244	0.250	0.255	0.216	0.259	0.224
Ti47_ppm_mean	317.265	307.507	304.954	344.090	286.781	301.746	368.178	325.332
Ti47_ppm_2SE(int)	10.535	9.613	10.142	8.332	9.521	9.572	16.529	8.367
V51_ppm_mean	5.417	4.326	3.249	3.570	3.432	3.350	3.606	4.039
V51_ppm_2SE(int)	0.328	0.349	0.247	0.255	0.210	0.253	0.348	0.235
Cr52_ppm_mean	10.408	5.996	6.920	7.245	6.593	5.709	15.208	7.432
Cr52_ppm_2SE(int)	1.260	1.285	1.113	1.058	0.971	0.786	1.411	1.212
Mn55_ppm_mean	70.296	70.576	69.626	71.070	70.648	68.073	111.534	69.847
Mn55_ppm_2SE(int)	1.150	1.156	1.756	1.999	1.216	1.313	5.745	1.198
Co59_ppm_mean	1.136	1.339	1.429	1.430	1.156	1.160	1.837	1.393
Co59_ppm_2SE(int)	0.121	0.138	0.174	0.130	0.119	0.126	0.206	0.135
Ni60_ppm_mean	0.040	0.186	0.373	0.362	0.293	0.188	0.360	0.136
Ni60_ppm_2SE(int)	0.189	0.162	0.173	0.178	0.172	0.152	0.233	0.158
Cu63_ppm_mean	0.889	0.746	0.871	0.837	0.709	0.598	0.703	0.913
Cu63_ppm_2SE(int)	0.199	0.183	0.154	0.145	0.186	0.144	0.202	0.162
Zn66_ppm_mean	-0.081	-0.322	-0.549	0.188	1.148	-0.546	0.921	0.164
Zn66_ppm_2SE(int)	1.189	1.116	0.856	0.892	1.110	0.937	1.112	0.926
Rb85_ppm_mean	0.011	0.058	0.040	0.057	0.026	0.042	0.102	0.056
Rb85_ppm_2SE(int)	0.029	0.032	0.032	0.031	0.026	0.025	0.038	0.028
Sr88_ppm_mean	205.388	212.963	228.470	233.852	211.685	224.461	226.629	215.662
Sr88_ppm_2SE(int)	2.658	3.384	4.496	2.867	3.827	5.086	2.969	3.583
Y89_ppm_mean	0.142	0.128	0.127	0.122	0.119	0.116	0.271	0.126
Y89_ppm_2SE(int)	0.028	0.031	0.031	0.025	0.030	0.025	0.049	0.028
Zr90_ppm_mean	0.054	0.000	0.004	0.000	0.000	0.043	0.341	0.015
Zr90_ppm_2SE(int)	0.047	0.000	0.007	0.000	0.000	0.024	0.101	0.014
Nb93_ppm_mean	0.000	0.000	0.000	0.000	0.002	0.008	0.030	0.000
Nb93_ppm_2SE(int)	0.000	0.000	0.000	0.000	0.004	0.008	0.019	0.000
Hf178_ppm_mean	0.000	0.000	0.000	0.000	0.000	0.000	0.000	0.000
Hf178_ppm_2SE(int)	0.000	0.000	0.000	0.000	0.000	0.000	0.000	0.000
Ta181_ppm_mean	0.000	0.000	0.001	0.000	0.000	0.000	0.000	0.000
Ta181_ppm_2SE(int)	0.000	0.000	0.003	0.000	0.000	0.000	0.000	0.000
Pb208_ppm_mean	0.311	0.039	0.005	0.014	0.016	0.012	0.053	0.005
Pb208_ppm_2SE(int)	0.216	0.018	0.010	0.009	0.011	0.009	0.022	0.007
Th232_ppm_mean	0.000	0.000	0.000	0.000	0.000	0.000	0.000	0.000
Th232_ppm_2SE(int)	0.000	0.000	0.000	0.000	0.000	0.000	0.000	0.000
U238_ppm_mean	0.000	0.000	0.000	0.028	0.016	0.001	0.004	0.000
U238_ppm_2SE(int)	0.000	0.000	0.000	0.053	0.031	0.001	0.003	0.000

Table S7 cont.: Plagioclase feldspar trace element compositions.

Sample	15556	15556	15556	15556	15556	15556	15556	15556
Site	241-PLAG-2.70	241-PLAG-2.71	241-PLAG-2.74	241-PLAG-2.75	241-PLAG-3.77	241-PLAG-3.78	241-PLAG-4.84	241-PLAG-4.86
Si29_ppm_mean	464066.000	463798.000	458259.000	463321.000	460009.000	472866.000	468172.000	462525.000
Si29_ppm_2SE(int)	0.000	0.000	0.000	0.000	0.000	0.000	0.000	0.000
Ca43_ppm_mean	163859.768	158631.607	168071.228	176294.788	169670.038	166141.946	162512.361	168757.943
Ca43_ppm_2SE(int)	2684.490	2112.539	2572.197	2202.429	2913.925	2373.236	2051.576	3112.778
Sc45_ppm_mean	3.253	3.037	2.908	3.112	2.901	3.123	2.922	2.942
Sc45_ppm_2SE(int)	0.227	0.183	0.242	0.214	0.169	0.216	0.215	0.228
Ti47_ppm_mean	316.673	293.011	304.658	360.432	298.713	304.436	338.213	323.115
Ti47_ppm_2SE(int)	12.401	13.798	10.561	11.910	9.077	8.612	8.340	8.857
V51_ppm_mean	3.433	0.766	2.859	1.843	3.368	0.501	0.871	4.443
V51_ppm_2SE(int)	0.217	0.139	0.292	0.222	0.239	0.121	0.168	0.324
Cr52_ppm_mean	6.752	3.393	6.139	4.225	6.705	1.746	2.017	7.647
Cr52_ppm_2SE(int)	1.143	1.256	1.129	1.150	1.030	0.873	0.979	0.968
Mn55_ppm_mean	70.558	84.833	68.470	72.162	68.662	81.837	75.261	73.961
Mn55_ppm_2SE(int)	1.182	4.646	1.310	1.232	1.362	1.603	1.325	1.421
Co59_ppm_mean	1.356	1.726	1.331	1.379	1.306	1.874	1.560	1.449
Co59_ppm_2SE(int)	0.149	0.164	0.154	0.145	0.123	0.162	0.135	0.152
Ni60_ppm_mean	0.457	0.192	0.125	0.282	0.422	0.081	0.160	0.020
Ni60_ppm_2SE(int)	0.184	0.175	0.170	0.175	0.177	0.169	0.208	0.143
Cu63_ppm_mean	0.698	0.805	0.679	0.671	0.884	0.844	1.066	0.693
Cu63_ppm_2SE(int)	0.150	0.155	0.163	0.170	0.176	0.141	0.195	0.168
Zn66_ppm_mean	0.428	0.911	0.806	1.374	0.067	1.091	0.681	0.138
Zn66_ppm_2SE(int)	0.817	0.826	1.084	0.983	0.838	0.899	0.827	0.775
Rb85_ppm_mean	0.039	0.079	0.005	0.060	0.086	0.100	0.072	0.060
Rb85_ppm_2SE(int)	0.027	0.024	0.026	0.036	0.034	0.036	0.035	0.035
Sr88_ppm_mean	211.437	346.583	232.702	293.297	235.427	365.926	291.540	207.321
Sr88_ppm_2SE(int)	3.669	6.803	3.603	3.987	3.500	8.065	4.779	3.076
Y89_ppm_mean	0.111	0.292	0.111	0.176	0.104	0.259	0.163	0.119
Y89_ppm_2SE(int)	0.029	0.066	0.029	0.035	0.024	0.033	0.034	0.029
Zr90_ppm_mean	0.000	0.128	0.004	0.000	0.000	0.010	0.007	0.000
Zr90_ppm_2SE(int)	0.000	0.059	0.008	0.000	0.000	0.011	0.010	0.000
Nb93_ppm_mean	0.000	0.004	0.000	0.000	0.000	0.000	0.000	0.000
Nb93_ppm_2SE(int)	0.000	0.006	0.000	0.000	0.000	0.000	0.000	0.000
Hf178_ppm_mean	0.000	0.000	0.000	0.000	0.000	0.000	0.000	0.000
Hf178_ppm_2SE(int)	0.000	0.000	0.000	0.000	0.000	0.000	0.000	0.000
Ta181_ppm_mean	0.000	0.000	0.000	0.001	0.000	0.000	0.000	0.000
Ta181_ppm_2SE(int)	0.000	0.000	0.000	0.002	0.000	0.000	0.000	0.000
Pb208_ppm_mean	0.008	0.008	0.020	0.018	0.005	0.009	0.023	0.010
Pb208_ppm_2SE(int)	0.009	0.008	0.014	0.011	0.007	0.008	0.010	0.008
Th232_ppm_mean	0.000	0.001	0.000	0.000	0.000	0.000	0.000	0.000
Th232_ppm_2SE(int)	0.000	0.002	0.000	0.000	0.000	0.000	0.000	0.000
U238_ppm_mean	0.000	0.000	0.000	0.000	0.000	0.000	0.000	0.000
U238_ppm_2SE(int)	0.000	0.000	0.000	0.000	0.000	0.000	0.000	0.000

Table S7 cont.: Plagioclase feldspar trace element compositions.

Sample	70017	70017	70017	70017	70017	70017	70017	70017
Site	123-PLAG-1.192	123-PLAG-1.194	123-PLAG-2.195	123-PLAG-2.196	123-PLAG-2.197	123-PLAG-3.198	123-PLAG-3.199	123-PLAG-3.200
Si29_ppm_mean	472435.000	467500.000	471897.000	463768.000	468290.000	489641.000	491541.000	493713.000
Si29_ppm_2SE(int)	0.000	0.000	0.000	0.000	0.000	0.000	0.000	0.000
Ca43_ppm_mean	168308.102	165429.080	164574.668	167155.226	168113.606	158580.720	158588.676	158067.641
Ca43_ppm_2SE(int)	2832.933	2780.375	3143.036	3035.648	3006.669	2828.406	2832.954	2329.405
Sc45_ppm_mean	3.353	3.192	3.022	3.160	2.957	3.266	3.274	3.202
Sc45_ppm_2SE(int)	0.245	0.188	0.222	0.226	0.203	0.262	0.224	0.251
Ti47_ppm_mean	865.555	797.894	497.730	568.111	528.843	429.807	423.661	406.426
Ti47_ppm_2SE(int)	21.183	18.764	12.076	14.575	14.290	10.628	11.006	12.699
V51_ppm_mean	1.352	1.520	1.041	1.042	0.855	0.629	0.634	0.589
V51_ppm_2SE(int)	0.176	0.189	0.177	0.158	0.143	0.171	0.130	0.141
Cr52_ppm_mean	8.801	6.255	4.025	4.432	3.516	3.325	2.182	2.492
Cr52_ppm_2SE(int)	0.982	1.142	1.052	1.079	1.038	0.922	0.907	1.028
Mn55_ppm_mean	55.979	50.376	59.842	56.467	53.769	65.440	63.690	64.742
Mn55_ppm_2SE(int)	1.094	0.870	1.281	1.032	1.149	1.416	1.174	1.117
Co59_ppm_mean	0.300	0.275	0.298	0.316	0.279	0.235	0.340	0.328
Co59_ppm_2SE(int)	0.072	0.069	0.062	0.075	0.086	0.070	0.070	0.075
Ni60_ppm_mean	0.235	0.209	0.283	0.256	0.289	0.207	0.366	0.196
Ni60_ppm_2SE(int)	0.156	0.191	0.163	0.155	0.199	0.170	0.202	0.155
Cu63_ppm_mean	0.339	0.469	0.364	0.141	0.317	0.458	0.437	0.455
Cu63_ppm_2SE(int)	0.148	0.158	0.128	0.105	0.108	0.151	0.143	0.129
Zn66_ppm_mean	5.797	22.446	0.217	0.188	0.325	-0.225	1.523	1.003
Zn66_ppm_2SE(int)	1.339	1.852	0.989	0.845	0.882	0.836	0.943	0.841
Rb85_ppm_mean	0.046	0.039	0.061	0.057	0.047	0.103	0.135	0.134
Rb85_ppm_2SE(int)	0.030	0.025	0.030	0.030	0.028	0.031	0.031	0.034
Sr88_ppm_mean	402.803	385.656	605.151	581.091	589.410	917.462	1004.694	1118.038
Sr88_ppm_2SE(int)	6.830	5.272	11.561	8.214	9.639	16.321	17.435	17.909
Y89_ppm_mean	0.468	0.416	0.806	0.720	0.718	1.658	1.941	2.054
Y89_ppm_2SE(int)	0.056	0.059	0.069	0.061	0.060	0.123	0.140	0.131
Zr90_ppm_mean	0.041	0.048	0.048	0.053	0.023	0.082	0.043	0.134
Zr90_ppm_2SE(int)	0.023	0.025	0.024	0.025	0.018	0.034	0.023	0.049
Nb93_ppm_mean	0.000	0.000	0.000	0.000	0.000	0.000	0.009	0.005
Nb93_ppm_2SE(int)	0.000	0.000	0.000	0.000	0.000	0.000	0.008	0.007
Hf178_ppm_mean	0.000	0.000	0.000	0.000	0.000	0.000	0.002	0.000
Hf178_ppm_2SE(int)	0.000	0.000	0.000	0.000	0.000	0.000	0.005	0.000
Ta181_ppm_mean	0.001	0.000	0.000	0.000	0.000	0.000	0.000	0.000
Ta181_ppm_2SE(int)	0.002	0.000	0.000	0.000	0.000	0.000	0.000	0.000
Pb208_ppm_mean	0.011	0.020	-0.006	0.012	0.011	0.029	0.012	0.011
Pb208_ppm_2SE(int)	0.011	0.013	0.007	0.010	0.007	0.013	0.010	0.010
Th232_ppm_mean	0.000	0.000	0.000	0.000	0.000	0.000	0.000	0.000
Th232_ppm_2SE(int)	0.000	0.000	0.000	0.000	0.000	0.000	0.000	0.000
U238_ppm_mean	0.000	0.001	0.000	0.000	0.000	0.001	0.000	0.000
U238_ppm_2SE(int)	0.000	0.002	0.000	0.001	0.000	0.001	0.001	0.000

Table S7 cont.: Plagioclase feldspar trace element compositions.

Sample	70017	70017	70017	70017	70017
Site	123-PLAG-3.201	123-PLAG-4.205	123-PLAG-4.206	123-PLAG-4.207	123-PLAG-4.208
Si29_ppm_mean	463572.000	464799.000	470587.000	469629.000	469537.000
Si29_ppm_2SE(int)	0.000	0.000	0.000	0.000	0.000
Ca43_ppm_mean	168204.089	169142.803	165658.753	165764.309	166134.409
Ca43_ppm_2SE(int)	2825.726	2748.524	3040.350	2826.994	2852.684
Sc45_ppm_mean	3.065	3.082	2.935	2.953	3.241
Sc45_ppm_2SE(int)	0.190	0.252	0.263	0.266	0.266
Ti47_ppm_mean	582.739	609.760	490.016	896.341	802.172
Ti47_ppm_2SE(int)	17.588	16.037	13.150	22.312	18.056
V51_ppm_mean	1.015	1.088	0.950	1.507	1.132
V51_ppm_2SE(int)	0.176	0.189	0.160	0.188	0.192
Cr52_ppm_mean	3.270	5.287	6.048	7.840	6.346
Cr52_ppm_2SE(int)	1.065	1.126	1.161	1.319	1.396
Mn55_ppm_mean	58.435	53.582	56.540	56.027	53.444
Mn55_ppm_2SE(int)	1.020	1.040	1.110	0.978	0.913
Co59_ppm_mean	0.228	0.247	0.316	0.306	0.308
Co59_ppm_2SE(int)	0.073	0.072	0.071	0.082	0.083
Ni60_ppm_mean	0.320	0.427	0.321	0.312	0.269
Ni60_ppm_2SE(int)	0.186	0.198	0.189	0.213	0.144
Cu63_ppm_mean	0.369	0.326	0.325	0.539	0.345
Cu63_ppm_2SE(int)	0.115	0.147	0.121	0.160	0.164
Zn66_ppm_mean	14.316	7.807	1.430	13.688	-0.191
Zn66_ppm_2SE(int)	1.776	1.461	1.059	1.653	1.221
Rb85_ppm_mean	0.066	0.002	0.027	0.035	0.057
Rb85_ppm_2SE(int)	0.028	0.027	0.050	0.038	0.038
Sr88_ppm_mean	563.130	469.573	603.635	411.149	421.017
Sr88_ppm_2SE(int)	8.059	6.870	7.920	6.076	6.989
Y89_ppm_mean	0.625	0.524	0.809	0.479	0.460
Y89_ppm_2SE(int)	0.066	0.065	0.097	0.067	0.061
Zr90_ppm_mean	0.039	0.035	0.046	0.014	0.020
Zr90_ppm_2SE(int)	0.025	0.023	0.026	0.015	0.017
Nb93_ppm_mean	0.002	0.005	0.000	0.000	0.000
Nb93_ppm_2SE(int)	0.004	0.007	0.000	0.000	0.000
Hf178_ppm_mean	0.000	0.000	0.000	0.000	0.000
Hf178_ppm_2SE(int)	0.000	0.000	0.000	0.000	0.000
Ta181_ppm_mean	0.000	0.000	0.002	0.000	0.000
Ta181_ppm_2SE(int)	0.000	0.000	0.003	0.000	0.000
Pb208_ppm_mean	0.010	0.009	0.029	0.020	-0.002
Pb208_ppm_2SE(int)	0.010	0.009	0.049	0.013	0.011
Th232_ppm_mean	0.000	0.000	0.000	0.000	0.000
Th232_ppm_2SE(int)	0.000	0.000	0.000	0.000	0.000
U238_ppm_mean	0.000	0.000	0.000	0.001	0.000
U238_ppm_2SE(int)	0.000	0.000	0.000	0.001	0.000

Table S8: Plagioclase feldspar rare earth element contents.

Sample	10057	10057	10057	10057	10057	10057	10057	10057
Site	67-PLAG-1.7	67-PLAG-2.10	67-PLAG-2.11	67-PLAG-2.12	67-PLAG-3.16	67-PLAG-3.17	67-PLAG-4.18	67-PLAG-4.19
La139_ppm_mean	1.582	1.340	1.460	2.320	1.355	1.406	45.781	2.695
La139_ppm_2SE(int)	0.089	0.088	0.075	0.115	0.077	0.067	12.667	0.158
Ce140_ppm_mean	3.562	3.124	3.112	5.421	2.921	3.173	123.988	6.188
Ce140_ppm_2SE(int)	0.133	0.104	0.100	0.248	0.126	0.108	34.532	0.330
Pr141_ppm_mean	0.420	0.383	0.414	0.817	0.369	0.442	19.107	0.862
Pr141_ppm_2SE(int)	0.041	0.030	0.029	0.054	0.040	0.037	5.453	0.073
Nd146_ppm_mean	2.131	1.616	1.836	3.795	1.666	2.006	92.586	3.969
Nd146_ppm_2SE(int)	0.173	0.182	0.177	0.224	0.149	0.193	25.995	0.360
Sm147_ppm_mean	0.383	0.364	0.348	1.224	0.273	0.463	31.032	1.082
Sm147_ppm_2SE(int)	0.091	0.070	0.086	0.148	0.066	0.097	8.771	0.158
Eu153_ppm_mean	4.697	3.972	4.147	3.987	3.984	4.434	5.676	4.898
Eu153_ppm_2SE(int)	0.152	0.132	0.141	0.146	0.134	0.163	0.265	0.186
Gd157_ppm_mean	0.421	0.305	0.290	1.718	0.342	0.539	34.529	1.030
Gd157_ppm_2SE(int)	0.082	0.073	0.084	0.235	0.062	0.100	9.983	0.168
Tb159_ppm_mean	0.049	0.048	0.053	0.259	0.035	0.062	5.946	0.190
Tb159_ppm_2SE(int)	0.010	0.012	0.013	0.030	0.010	0.012	1.688	0.029
Dy163_ppm_mean	0.262	0.293	0.261	1.908	0.155	0.398	39.835	1.053
Dy163_ppm_2SE(int)	0.058	0.051	0.045	0.190	0.041	0.066	11.261	0.142
Ho165_ppm_mean	0.054	0.052	0.042	0.406	0.035	0.065	8.214	0.211
Ho165_ppm_2SE(int)	0.013	0.012	0.010	0.042	0.009	0.012	2.312	0.029
Er166_ppm_mean	0.088	0.079	0.077	1.070	0.086	0.185	23.260	0.607
Er166_ppm_2SE(int)	0.023	0.027	0.024	0.125	0.026	0.043	6.463	0.091
Tm169_ppm_mean	0.011	0.006	0.010	0.157	0.005	0.032	3.149	0.074
Tm169_ppm_2SE(int)	0.005	0.003	0.005	0.022	0.003	0.009	0.871	0.014
Yb172_ppm_mean	0.083	0.103	0.072	1.195	0.055	0.215	20.847	0.479
Yb172_ppm_2SE(int)	0.029	0.032	0.023	0.155	0.023	0.042	5.635	0.079
Lu175_ppm_mean	0.006	0.004	0.005	0.154	0.003	0.022	2.582	0.065
Lu175_ppm_2SE(int)	0.004	0.003	0.003	0.028	0.002	0.007	0.693	0.015

Table S8 cont.: Plagioclase feldspar rare earth element contents.

Sample	10057	10057	10057	10057	10057	10057	10057	12038
Site	67-PLAG-5.21	67-PLAG-6.29	67-PLAG-7.32	67-PLAG-7.33	67-PLAG-7.34	67-PLAG-8.35	67-PLAG-8.36	63-PLAG-1.145
La139_ppm_mean	21.798	13.498	7.247	1.774	1.433	6.806	2.961	0.323
La139_ppm_2SE(int)	3.284	0.748	0.284	0.086	0.087	1.804	0.162	0.039
Ce140_ppm_mean	61.444	34.177	18.362	3.778	3.002	21.504	7.678	0.815
Ce140_ppm_2SE(int)	9.454	1.535	0.611	0.147	0.126	6.099	0.361	0.069
Pr141_ppm_mean	9.782	5.050	2.724	0.535	0.385	3.544	1.325	0.098
Pr141_ppm_2SE(int)	1.575	0.261	0.118	0.041	0.033	0.987	0.107	0.018
Nd146_ppm_mean	50.109	24.239	12.078	2.205	1.642	18.209	8.139	0.476
Nd146_ppm_2SE(int)	8.062	1.373	0.497	0.195	0.146	4.813	0.616	0.074
Sm147_ppm_mean	16.874	7.742	3.718	0.599	0.441	8.318	3.843	0.070
Sm147_ppm_2SE(int)	2.797	0.606	0.315	0.118	0.093	2.165	0.330	0.031
Eu153_ppm_mean	4.553	7.437	5.985	4.588	3.927	4.418	4.652	2.333
Eu153_ppm_2SE(int)	0.171	0.216	0.159	0.167	0.148	0.178	0.148	0.147
Gd157_ppm_mean	18.378	8.448	4.565	0.526	0.308	11.545	6.060	0.052
Gd157_ppm_2SE(int)	3.129	0.622	0.311	0.111	0.075	3.232	0.527	0.028
Tb159_ppm_mean	3.210	1.568	0.686	0.072	0.036	2.232	1.110	0.008
Tb159_ppm_2SE(int)	0.540	0.120	0.051	0.014	0.010	0.594	0.094	0.004
Dy163_ppm_mean	20.129	10.478	4.683	0.345	0.226	15.537	7.825	0.045
Dy163_ppm_2SE(int)	3.165	0.760	0.236	0.055	0.045	4.052	0.726	0.020
Ho165_ppm_mean	3.888	2.083	0.965	0.061	0.043	3.301	1.818	0.006
Ho165_ppm_2SE(int)	0.595	0.148	0.058	0.012	0.009	0.874	0.167	0.004
Er166_ppm_mean	10.111	6.071	2.552	0.149	0.089	9.778	5.089	0.014
Er166_ppm_2SE(int)	1.530	0.439	0.198	0.030	0.029	2.584	0.464	0.010
Tm169_ppm_mean	1.347	0.834	0.368	0.020	0.009	1.469	0.718	0.000
Tm169_ppm_2SE(int)	0.203	0.082	0.033	0.007	0.005	0.377	0.070	0.000
Yb172_ppm_mean	8.306	5.707	2.395	0.096	0.079	9.971	5.069	0.012
Yb172_ppm_2SE(int)	1.142	0.458	0.180	0.031	0.031	2.513	0.452	0.011
Lu175_ppm_mean	0.941	0.769	0.318	0.006	0.005	1.458	0.665	0.000
Lu175_ppm_2SE(int)	0.128	0.074	0.031	0.004	0.003	0.384	0.054	0.000

Table S8 cont.: Plagioclase feldspar rare earth element contents.

Sample	12038	12038	12038	12038	12038	12038	12038	12038
Site	63-PLAG-1.146	63-PLAG-2.147	63-PLAG-2.148	63-PLAG-2.149	63-PLAG-2.150	63-PLAG-3.155	63-PLAG-3.156	63-PLAG-4.160
La139_ppm_mean	0.325	0.383	0.428	0.405	0.431	0.339	0.317	0.412
La139_ppm_2SE(int)	0.036	0.044	0.052	0.035	0.049	0.036	0.045	0.042
Ce140_ppm_mean	0.722	0.762	0.885	0.843	0.848	0.710	0.725	0.946
Ce140_ppm_2SE(int)	0.047	0.064	0.051	0.057	0.051	0.052	0.055	0.191
Pr141_ppm_mean	0.094	0.091	0.100	0.110	0.098	0.096	0.087	0.107
Pr141_ppm_2SE(int)	0.016	0.016	0.017	0.021	0.015	0.015	0.015	0.015
Nd146_ppm_mean	0.456	0.387	0.409	0.426	0.448	0.368	0.328	0.468
Nd146_ppm_2SE(int)	0.088	0.077	0.071	0.081	0.081	0.074	0.061	0.075
Sm147_ppm_mean	0.075	0.095	0.097	0.090	0.172	0.064	0.085	0.080
Sm147_ppm_2SE(int)	0.038	0.042	0.041	0.038	0.050	0.030	0.033	0.039
Eu153_ppm_mean	2.212	2.172	3.005	2.743	2.198	2.079	2.217	2.134
Eu153_ppm_2SE(int)	0.071	0.099	0.131	0.114	0.101	0.119	0.119	0.081
Gd157_ppm_mean	0.067	0.036	0.070	0.081	0.062	0.054	0.039	0.078
Gd157_ppm_2SE(int)	0.036	0.023	0.035	0.036	0.031	0.027	0.023	0.039
Tb159_ppm_mean	0.011	0.014	0.011	0.010	0.008	0.010	0.015	0.010
Tb159_ppm_2SE(int)	0.005	0.005	0.005	0.005	0.004	0.005	0.006	0.006
Dy163_ppm_mean	0.039	0.052	0.038	0.051	0.058	0.037	0.040	0.059
Dy163_ppm_2SE(int)	0.017	0.023	0.017	0.026	0.023	0.017	0.017	0.023
Ho165_ppm_mean	0.007	0.008	0.008	0.011	0.010	0.003	0.007	0.008
Ho165_ppm_2SE(int)	0.004	0.005	0.004	0.006	0.004	0.003	0.004	0.004
Er166_ppm_mean	0.018	0.014	0.015	0.012	0.023	0.016	0.000	0.027
Er166_ppm_2SE(int)	0.011	0.010	0.010	0.010	0.012	0.010	0.000	0.014
Tm169_ppm_mean	0.002	0.004	0.000	0.000	0.002	0.000	0.002	0.002
Tm169_ppm_2SE(int)	0.002	0.003	0.000	0.000	0.002	0.000	0.002	0.002
Yb172_ppm_mean	0.018	0.000	0.011	0.000	0.023	0.000	0.000	0.027
Yb172_ppm_2SE(int)	0.013	0.000	0.010	0.000	0.014	0.000	0.000	0.015
Lu175_ppm_mean	0.000	0.000	0.000	0.000	0.000	0.000	0.001	0.000
Lu175_ppm_2SE(int)	0.000	0.000	0.000	0.000	0.000	0.000	0.002	0.000

Table S8 cont.: Plagioclase feldspar rare earth element contents.

Sample	12038	12038	12038	12043	12043	12043	12043	12043
Site	63-PLAG-4.161	63-PLAG-4.162	63-PLAG-4.163	15-PLAG-2.170	15-PLAG-2.171	15-PLAG-3.178	15-PLAG-3.179	15-PLAG-4.182
La139_ppm_mean	0.452	1.520	0.384	0.636	0.366	2.542	2.000	0.266
La139_ppm_2SE(int)	0.043	0.089	0.041	0.077	0.051	0.291	0.600	0.040
Ce140_ppm_mean	0.867	3.010	0.832	1.477	0.749	6.455	4.760	0.589
Ce140_ppm_2SE(int)	0.059	0.141	0.056	0.155	0.045	0.698	1.483	0.050
Pr141_ppm_mean	0.119	0.420	0.108	0.199	0.101	0.951	0.634	0.066
Pr141_ppm_2SE(int)	0.020	0.042	0.014	0.031	0.017	0.115	0.188	0.012
Nd146_ppm_mean	0.489	1.705	0.385	0.723	0.360	4.355	2.963	0.388
Nd146_ppm_2SE(int)	0.088	0.140	0.077	0.127	0.088	0.620	0.955	0.073
Sm147_ppm_mean	0.073	0.336	0.105	0.210	0.160	1.205	0.771	0.060
Sm147_ppm_2SE(int)	0.034	0.077	0.038	0.081	0.048	0.207	0.280	0.029
Eu153_ppm_mean	2.584	8.026	2.157	2.316	1.664	1.562	1.851	1.525
Eu153_ppm_2SE(int)	0.102	0.287	0.090	0.159	0.093	0.093	0.113	0.086
Gd157_ppm_mean	0.107	0.248	0.061	0.258	0.075	1.619	0.864	0.079
Gd157_ppm_2SE(int)	0.044	0.064	0.029	0.067	0.037	0.286	0.304	0.036
Tb159_ppm_mean	0.005	0.025	0.009	0.033	0.015	0.286	0.122	0.003
Tb159_ppm_2SE(int)	0.003	0.007	0.005	0.010	0.007	0.047	0.042	0.003
Dy163_ppm_mean	0.056	0.157	0.027	0.181	0.133	1.660	0.656	0.048
Dy163_ppm_2SE(int)	0.024	0.041	0.015	0.044	0.046	0.253	0.219	0.021
Ho165_ppm_mean	0.009	0.030	0.006	0.030	0.010	0.326	0.142	0.010
Ho165_ppm_2SE(int)	0.005	0.008	0.004	0.010	0.005	0.052	0.042	0.006
Er166_ppm_mean	0.016	0.052	0.012	0.078	0.015	0.824	0.419	0.018
Er166_ppm_2SE(int)	0.010	0.022	0.009	0.028	0.010	0.154	0.140	0.011
Tm169_ppm_mean	0.000	0.006	0.000	0.016	0.000	0.119	0.032	0.002
Tm169_ppm_2SE(int)	0.000	0.003	0.000	0.007	0.000	0.025	0.011	0.002
Yb172_ppm_mean	0.000	0.022	0.012	0.080	0.013	0.761	0.304	0.011
Yb172_ppm_2SE(int)	0.000	0.014	0.010	0.031	0.011	0.147	0.112	0.010
Lu175_ppm_mean	0.000	0.000	0.000	0.007	0.000	0.103	0.024	0.003
Lu175_ppm_2SE(int)	0.000	0.000	0.000	0.004	0.000	0.025	0.012	0.003

Table S8 cont.: Plagioclase feldspar rare earth element contents.

Sample	12043	12043	12043	12043	12043	15085	15085	15085
Site	15-PLAG-4.183	15-PLAG-5.186	15-PLAG-5.187	15-PLAG-5.188	15-PLAG-5.189	16-PLAG-1.7	16-PLAG-1.8	16-PLAG-1.9
La139_ppm_mean	0.732	0.228	0.280	0.247	0.312	0.225	0.188	0.197
La139_ppm_2SE(int)	0.062	0.033	0.034	0.038	0.045	0.037	0.028	0.034
Ce140_ppm_mean	1.513	0.620	0.616	0.464	0.716	0.488	0.412	0.458
Ce140_ppm_2SE(int)	0.096	0.046	0.048	0.044	0.060	0.041	0.041	0.048
Pr141_ppm_mean	0.187	0.073	0.074	0.060	0.104	0.052	0.057	0.056
Pr141_ppm_2SE(int)	0.023	0.015	0.014	0.014	0.017	0.012	0.014	0.013
Nd146_ppm_mean	0.861	0.315	0.310	0.295	0.491	0.282	0.228	0.265
Nd146_ppm_2SE(int)	0.124	0.083	0.065	0.074	0.103	0.071	0.059	0.067
Sm147_ppm_mean	0.186	0.106	0.095	0.047	0.155	0.068	0.038	0.069
Sm147_ppm_2SE(int)	0.051	0.044	0.042	0.031	0.060	0.035	0.029	0.036
Eu153_ppm_mean	3.130	1.708	1.288	1.578	1.461	1.405	1.364	1.783
Eu153_ppm_2SE(int)	0.129	0.096	0.072	0.086	0.097	0.082	0.075	0.106
Gd157_ppm_mean	0.182	0.090	0.071	0.080	0.120	0.023	0.044	0.061
Gd157_ppm_2SE(int)	0.054	0.035	0.033	0.039	0.049	0.022	0.031	0.034
Tb159_ppm_mean	0.021	0.011	0.012	0.007	0.016	0.000	0.000	0.003
Tb159_ppm_2SE(int)	0.007	0.005	0.005	0.004	0.006	0.000	0.000	0.003
Dy163_ppm_mean	0.113	0.045	0.036	0.040	0.109	0.014	0.029	0.024
Dy163_ppm_2SE(int)	0.032	0.021	0.018	0.021	0.036	0.013	0.018	0.017
Ho165_ppm_mean	0.021	0.006	0.006	0.011	0.012	0.006	0.006	0.000
Ho165_ppm_2SE(int)	0.007	0.004	0.004	0.006	0.006	0.004	0.004	0.000
Er166_ppm_mean	0.069	0.017	0.023	0.016	0.055	0.016	0.004	0.007
Er166_ppm_2SE(int)	0.021	0.012	0.013	0.013	0.021	0.013	0.006	0.008
Tm169_ppm_mean	0.003	0.001	0.005	0.003	0.005	0.000	0.000	0.000
Tm169_ppm_2SE(int)	0.003	0.001	0.003	0.004	0.004	0.000	0.000	0.000
Yb172_ppm_mean	0.033	0.022	0.000	0.017	0.053	0.003	0.000	0.000
Yb172_ppm_2SE(int)	0.016	0.014	0.000	0.014	0.028	0.006	0.000	0.000
Lu175_ppm_mean	0.002	0.000	0.000	0.000	0.002	0.000	0.000	0.000
Lu175_ppm_2SE(int)	0.002	0.000	0.000	0.000	0.002	0.000	0.000	0.000

Table S8 cont.: Plagioclase feldspar rare earth element contents.

Sample	15085	15085	15085	15085	15085	15085	15085	15085
Site	16-PLAG-2.14	16-PLAG-2.17	16-PLAG-3.18	16-PLAG-3.19	16-PLAG-4.21	16-PLAG-4.23	16-PLAG-5.24	16-PLAG-5.25
La139_ppm_mean	0.220	0.430	1.042	0.942	0.944	0.457	0.181	0.211
La139_ppm_2SE(int)	0.032	0.053	0.089	0.185	0.106	0.048	0.028	0.033
Ce140_ppm_mean	0.509	0.937	2.086	1.892	2.071	0.920	0.465	0.461
Ce140_ppm_2SE(int)	0.048	0.070	0.134	0.096	0.205	0.077	0.043	0.050
Pr141_ppm_mean	0.070	0.128	0.282	0.254	0.264	0.131	0.054	0.069
Pr141_ppm_2SE(int)	0.013	0.023	0.031	0.028	0.037	0.022	0.013	0.014
Nd146_ppm_mean	0.332	0.480	1.071	1.109	1.395	0.545	0.262	0.332
Nd146_ppm_2SE(int)	0.085	0.107	0.162	0.156	0.243	0.109	0.067	0.079
Sm147_ppm_mean	0.036	0.067	0.243	0.235	0.355	0.095	0.057	0.098
Sm147_ppm_2SE(int)	0.028	0.040	0.068	0.073	0.109	0.050	0.033	0.045
Eu153_ppm_mean	1.985	3.332	6.541	6.081	5.660	3.104	1.804	1.773
Eu153_ppm_2SE(int)	0.104	0.151	0.231	0.178	0.169	0.116	0.114	0.108
Gd157_ppm_mean	0.041	0.070	0.174	0.177	0.277	0.157	0.023	0.071
Gd157_ppm_2SE(int)	0.033	0.039	0.059	0.061	0.090	0.054	0.022	0.037
Tb159_ppm_mean	0.005	0.009	0.018	0.022	0.024	0.009	0.004	0.002
Tb159_ppm_2SE(int)	0.004	0.005	0.008	0.008	0.010	0.005	0.003	0.002
Dy163_ppm_mean	0.036	0.064	0.136	0.146	0.147	0.090	0.029	0.053
Dy163_ppm_2SE(int)	0.021	0.027	0.047	0.043	0.058	0.034	0.018	0.025
Ho165_ppm_mean	0.010	0.017	0.011	0.016	0.025	0.010	0.001	0.004
Ho165_ppm_2SE(int)	0.005	0.007	0.006	0.007	0.010	0.005	0.001	0.003
Er166_ppm_mean	0.020	0.024	0.010	0.024	0.060	0.024	0.002	0.000
Er166_ppm_2SE(int)	0.014	0.015	0.010	0.015	0.032	0.015	0.005	0.000
Tm169_ppm_mean	0.000	0.000	0.008	0.003	0.007	0.002	0.000	0.000
Tm169_ppm_2SE(int)	0.000	0.000	0.005	0.003	0.005	0.002	0.000	0.000
Yb172_ppm_mean	0.000	0.021	0.000	0.033	0.047	0.024	0.000	0.000
Yb172_ppm_2SE(int)	0.000	0.017	0.000	0.020	0.023	0.017	0.000	0.000
Lu175_ppm_mean	0.000	0.000	0.000	0.000	0.008	0.000	0.000	0.000
Lu175_ppm_2SE(int)	0.000	0.000	0.000	0.000	0.005	0.000	0.000	0.000

Table S8 cont.: Plagioclase feldspar rare earth element contents.

Sample	15085	15085	15085	15085	15085	15085	15085	15085
Site	24-PLAG-1.88	24-PLAG-1.90	24-PLAG-1.92	24-PLAG-2.97	24-PLAG-2.98	24-PLAG-2.99	24-PLAG-3.100	24-PLAG-3.102
La139_ppm_mean	0.252	0.178	0.135	0.135	0.178	0.148	0.380	0.154
La139_ppm_2SE(int)	0.031	0.029	0.024	0.022	0.024	0.023	0.054	0.028
Ce140_ppm_mean	0.623	0.393	0.453	0.355	0.367	0.429	0.747	0.380
Ce140_ppm_2SE(int)	0.053	0.038	0.041	0.038	0.030	0.040	0.060	0.039
Pr141_ppm_mean	0.088	0.053	0.059	0.080	0.046	0.067	0.093	0.040
Pr141_ppm_2SE(int)	0.016	0.012	0.012	0.048	0.012	0.014	0.015	0.009
Nd146_ppm_mean	0.227	0.232	0.217	0.221	0.209	0.237	0.455	0.162
Nd146_ppm_2SE(int)	0.056	0.064	0.056	0.058	0.050	0.055	0.087	0.057
Sm147_ppm_mean	0.041	0.056	0.075	0.022	0.056	0.063	0.089	0.032
Sm147_ppm_2SE(int)	0.025	0.032	0.037	0.019	0.028	0.036	0.037	0.023
Eu153_ppm_mean	2.181	1.314	1.457	1.311	1.290	1.340	2.737	1.528
Eu153_ppm_2SE(int)	0.115	0.091	0.085	0.078	0.073	0.079	0.122	0.087
Gd157_ppm_mean	0.076	0.014	0.000	0.036	0.049	0.043	0.060	0.018
Gd157_ppm_2SE(int)	0.035	0.015	0.000	0.024	0.027	0.025	0.035	0.018
Tb159_ppm_mean	0.003	0.006	0.005	0.006	0.000	0.006	0.008	0.005
Tb159_ppm_2SE(int)	0.003	0.004	0.003	0.004	0.000	0.004	0.004	0.003
Dy163_ppm_mean	0.033	0.014	0.018	0.040	0.030	0.029	0.047	0.000
Dy163_ppm_2SE(int)	0.018	0.013	0.013	0.023	0.016	0.016	0.020	0.000
Ho165_ppm_mean	0.005	0.000	0.002	0.003	0.003	0.003	0.007	0.004
Ho165_ppm_2SE(int)	0.003	0.000	0.002	0.003	0.003	0.003	0.004	0.003
Er166_ppm_mean	0.012	0.000	0.000	0.000	0.010	0.007	0.021	0.002
Er166_ppm_2SE(int)	0.009	0.000	0.000	0.000	0.009	0.007	0.011	0.004
Tm169_ppm_mean	0.000	0.000	0.000	0.000	0.000	0.000	0.003	0.000
Tm169_ppm_2SE(int)	0.000	0.000	0.000	0.000	0.000	0.000	0.002	0.000
Yb172_ppm_mean	0.011	0.000	0.000	0.000	0.018	0.013	0.013	0.011
Yb172_ppm_2SE(int)	0.010	0.000	0.000	0.000	0.013	0.011	0.011	0.010
Lu175_ppm_mean	0.000	0.000	0.000	0.000	0.002	0.000	0.002	0.003
Lu175_ppm_2SE(int)	0.000	0.000	0.000	0.000	0.002	0.000	0.002	0.003

Table S8 cont.: Plagioclase feldspar rare earth element contents.

Sample	15085	15085	15085	15085	15085	15085	15085	15085
Site	24-PLAG-3.103	24-PLAG-4.107	24-PLAG-4.109	24-PLAG-4.111	24-PLAG-4.112	24-PLAG-5.115	24-PLAG-5.117	24-PLAG-5.120
La139_ppm_mean	0.224	0.185	0.162	0.198	0.189	0.167	0.192	0.178
La139_ppm_2SE(int)	0.031	0.028	0.031	0.032	0.024	0.030	0.027	0.026
Ce140_ppm_mean	0.455	0.406	0.442	0.425	0.383	0.409	0.336	0.430
Ce140_ppm_2SE(int)	0.043	0.045	0.143	0.042	0.033	0.041	0.039	0.038
Pr141_ppm_mean	0.054	0.048	0.056	0.048	0.051	0.049	0.046	0.049
Pr141_ppm_2SE(int)	0.012	0.009	0.014	0.009	0.010	0.010	0.011	0.011
Nd146_ppm_mean	0.210	0.227	0.239	0.311	0.257	0.247	0.188	0.244
Nd146_ppm_2SE(int)	0.057	0.061	0.065	0.077	0.050	0.067	0.061	0.053
Sm147_ppm_mean	0.051	0.032	0.037	0.061	0.077	0.050	0.064	0.049
Sm147_ppm_2SE(int)	0.030	0.023	0.024	0.033	0.041	0.027	0.030	0.027
Eu153_ppm_mean	1.836	1.545	1.462	1.615	1.666	1.551	1.432	1.728
Eu153_ppm_2SE(int)	0.097	0.089	0.068	0.099	0.077	0.087	0.094	0.105
Gd157_ppm_mean	0.048	0.036	0.023	0.031	0.047	0.043	0.028	0.054
Gd157_ppm_2SE(int)	0.026	0.024	0.020	0.022	0.026	0.025	0.021	0.028
Tb159_ppm_mean	0.006	0.006	0.006	0.006	0.002	0.003	0.005	0.004
Tb159_ppm_2SE(int)	0.004	0.003	0.004	0.005	0.002	0.003	0.003	0.003
Dy163_ppm_mean	0.020	0.026	0.028	0.020	0.027	0.029	0.038	0.031
Dy163_ppm_2SE(int)	0.013	0.015	0.015	0.013	0.014	0.016	0.021	0.016
Ho165_ppm_mean	0.003	0.002	0.004	0.003	0.007	0.005	0.003	0.001
Ho165_ppm_2SE(int)	0.003	0.002	0.003	0.003	0.004	0.003	0.003	0.001
Er166_ppm_mean	0.000	0.011	0.000	0.016	0.012	0.018	0.008	0.000
Er166_ppm_2SE(int)	0.000	0.009	0.000	0.010	0.009	0.011	0.007	0.000
Tm169_ppm_mean	0.002	0.000	0.000	0.000	0.000	0.000	0.000	0.000
Tm169_ppm_2SE(int)	0.002	0.000	0.000	0.000	0.000	0.000	0.000	0.000
Yb172_ppm_mean	0.000	0.000	0.005	0.003	0.002	0.000	0.011	0.003
Yb172_ppm_2SE(int)	0.000	0.000	0.007	0.005	0.004	0.000	0.010	0.005
Lu175_ppm_mean	0.000	0.000	0.000	0.000	0.000	0.000	0.000	0.000
Lu175_ppm_2SE(int)	0.000	0.000	0.000	0.000	0.000	0.000	0.000	0.000

Table S8 cont.: Plagioclase feldspar rare earth element contents.

Sample	15085	15085	15085	15085	15085	15085	15085	15085
Site	24-PLAG-5.122	26-PLAG-1.28	26-PLAG-1.29	26-PLAG-1.30	26-PLAG-1.31	26-PLAG-2.34	26-PLAG-2.35	26-PLAG-2.36
La139_ppm_mean	0.404	0.201	0.180	0.178	0.184	0.166	0.149	0.154
La139_ppm_2SE(int)	0.042	0.036	0.032	0.029	0.033	0.029	0.024	0.025
Ce140_ppm_mean	0.856	0.402	0.373	0.408	0.380	0.351	0.393	0.335
Ce140_ppm_2SE(int)	0.055	0.040	0.036	0.046	0.039	0.043	0.032	0.039
Pr141_ppm_mean	0.111	0.046	0.053	0.065	0.046	0.044	0.047	0.049
Pr141_ppm_2SE(int)	0.016	0.013	0.012	0.012	0.012	0.012	0.012	0.014
Nd146_ppm_mean	0.514	0.234	0.264	0.229	0.219	0.200	0.180	0.225
Nd146_ppm_2SE(int)	0.079	0.061	0.069	0.073	0.058	0.066	0.057	0.057
Sm147_ppm_mean	0.090	0.030	0.045	0.064	0.046	0.063	0.022	0.060
Sm147_ppm_2SE(int)	0.041	0.023	0.030	0.034	0.030	0.034	0.022	0.034
Eu153_ppm_mean	3.150	1.386	1.314	1.418	1.362	1.476	1.381	1.253
Eu153_ppm_2SE(int)	0.141	0.085	0.087	0.109	0.089	0.092	0.100	0.084
Gd157_ppm_mean	0.138	0.036	0.020	0.016	0.038	0.005	0.049	0.061
Gd157_ppm_2SE(int)	0.052	0.026	0.019	0.018	0.027	0.010	0.031	0.033
Tb159_ppm_mean	0.003	0.005	0.004	0.005	0.003	0.003	0.003	0.000
Tb159_ppm_2SE(int)	0.003	0.004	0.003	0.004	0.003	0.003	0.003	0.000
Dy163_ppm_mean	0.046	0.026	0.030	0.067	0.030	0.029	0.025	0.029
Dy163_ppm_2SE(int)	0.019	0.016	0.017	0.031	0.018	0.018	0.017	0.018
Ho165_ppm_mean	0.010	0.007	0.000	0.006	0.000	0.000	0.001	0.001
Ho165_ppm_2SE(int)	0.005	0.004	0.000	0.004	0.000	0.000	0.001	0.001
Er166_ppm_mean	0.024	0.014	0.000	0.000	0.000	0.007	0.000	0.000
Er166_ppm_2SE(int)	0.012	0.010	0.000	0.000	0.000	0.008	0.000	0.000
Tm169_ppm_mean	0.002	0.000	0.001	0.000	0.000	0.000	0.000	0.000
Tm169_ppm_2SE(int)	0.002	0.000	0.001	0.000	0.000	0.000	0.000	0.000
Yb172_ppm_mean	0.019	0.000	0.000	0.000	0.000	0.000	0.000	0.000
Yb172_ppm_2SE(int)	0.013	0.000	0.000	0.000	0.000	0.000	0.000	0.000
Lu175_ppm_mean	0.000	0.000	0.000	0.000	0.000	0.000	0.000	0.000
Lu175_ppm_2SE(int)	0.000	0.000	0.000	0.000	0.000	0.000	0.000	0.000

Table S8 cont.: Plagioclase feldspar rare earth element contents.

Sample	15085	15085	15085	15085	15085	15085	15085	15085
Site	26-PLAG-2.37	26-PLAG-2.38	26-PLAG-2.39	26-PLAG-3.42	26-PLAG-3.45	26-PLAG-3.46	26-PLAG-4.47	26-PLAG-4.48
La139_ppm_mean	0.152	0.165	0.251	0.312	0.266	0.204	0.244	0.218
La139_ppm_2SE(int)	0.027	0.031	0.035	0.045	0.039	0.037	0.039	0.038
Ce140_ppm_mean	0.342	0.319	0.478	0.543	0.560	0.381	0.382	0.461
Ce140_ppm_2SE(int)	0.039	0.030	0.045	0.057	0.049	0.043	0.042	0.046
Pr141_ppm_mean	0.058	0.034	0.054	0.085	0.093	0.049	0.048	0.043
Pr141_ppm_2SE(int)	0.014	0.010	0.012	0.017	0.017	0.013	0.012	0.011
Nd146_ppm_mean	0.140	0.162	0.345	0.316	0.317	0.181	0.280	0.243
Nd146_ppm_2SE(int)	0.048	0.051	0.075	0.070	0.086	0.060	0.070	0.065
Sm147_ppm_mean	0.091	0.043	0.075	0.033	0.052	0.054	0.051	0.049
Sm147_ppm_2SE(int)	0.043	0.028	0.038	0.025	0.032	0.033	0.032	0.028
Eu153_ppm_mean	1.233	1.519	2.319	1.448	1.550	1.383	1.307	1.265
Eu153_ppm_2SE(int)	0.103	0.090	0.119	0.080	0.104	0.099	0.083	0.080
Gd157_ppm_mean	0.027	0.053	0.061	0.098	0.096	0.054	0.047	0.041
Gd157_ppm_2SE(int)	0.023	0.034	0.034	0.045	0.056	0.037	0.028	0.027
Tb159_ppm_mean	0.006	0.002	0.008	0.001	0.009	0.008	0.006	0.008
Tb159_ppm_2SE(int)	0.004	0.002	0.005	0.001	0.005	0.005	0.004	0.004
Dy163_ppm_mean	0.021	0.010	0.035	0.039	0.039	0.047	0.029	0.043
Dy163_ppm_2SE(int)	0.015	0.011	0.019	0.020	0.020	0.022	0.017	0.019
Ho165_ppm_mean	0.002	0.007	0.005	0.007	0.008	0.005	0.000	0.008
Ho165_ppm_2SE(int)	0.003	0.004	0.004	0.004	0.005	0.004	0.000	0.004
Er166_ppm_mean	0.000	0.000	0.002	0.010	0.024	0.002	0.000	0.028
Er166_ppm_2SE(int)	0.000	0.000	0.004	0.009	0.014	0.004	0.000	0.014
Tm169_ppm_mean	0.001	0.000	0.000	0.000	0.000	0.002	0.000	0.000
Tm169_ppm_2SE(int)	0.001	0.000	0.000	0.000	0.000	0.003	0.000	0.000
Yb172_ppm_mean	0.000	0.013	0.000	0.003	0.007	0.011	0.000	0.000
Yb172_ppm_2SE(int)	0.000	0.013	0.000	0.006	0.009	0.012	0.000	0.000
Lu175_ppm_mean	0.000	0.000	0.000	0.000	0.000	0.000	0.000	0.000
Lu175_ppm_2SE(int)	0.000	0.000	0.000	0.000	0.000	0.000	0.000	0.000

Table S8 cont.: Plagioclase feldspar rare earth element contents.

Sample	15085	15085	15085	15085	15556	15556	15556	15556
Site	26-PLAG-5.53	26-PLAG-5.55	26-PLAG-5.56	26-PLAG-5.58	28-PLAG-1.127	28-PLAG-1.128	28-PLAG-2.134	28-PLAG-2.135
La139_ppm_mean	0.228	0.178	0.228	0.281	0.176	0.210	0.142	0.173
La139_ppm_2SE(int)	0.034	0.032	0.038	0.175	0.025	0.033	0.029	0.026
Ce140_ppm_mean	0.478	0.482	0.482	0.399	0.352	0.440	0.919	0.378
Ce140_ppm_2SE(int)	0.050	0.041	0.042	0.043	0.038	0.041	0.128	0.035
Pr141_ppm_mean	0.050	0.059	0.047	0.066	0.045	0.062	0.037	0.047
Pr141_ppm_2SE(int)	0.012	0.015	0.011	0.013	0.013	0.015	0.010	0.013
Nd146_ppm_mean	0.216	0.181	0.311	0.293	0.203	0.296	0.295	0.220
Nd146_ppm_2SE(int)	0.054	0.054	0.062	0.080	0.062	0.064	0.077	0.056
Sm147_ppm_mean	0.034	0.119	0.068	0.035	0.043	0.054	0.048	0.028
Sm147_ppm_2SE(int)	0.026	0.058	0.034	0.027	0.028	0.030	0.035	0.021
Eu153_ppm_mean	1.412	1.354	1.377	1.364	1.283	1.750	1.161	1.067
Eu153_ppm_2SE(int)	0.087	0.105	0.079	0.092	0.084	0.080	0.077	0.068
Gd157_ppm_mean	0.037	0.049	0.044	0.034	0.037	0.025	0.000	0.031
Gd157_ppm_2SE(int)	0.026	0.032	0.027	0.026	0.027	0.021	0.000	0.022
Tb159_ppm_mean	0.009	0.001	0.010	0.004	0.004	0.006	0.003	0.003
Tb159_ppm_2SE(int)	0.005	0.001	0.006	0.003	0.004	0.004	0.003	0.003
Dy163_ppm_mean	0.037	0.025	0.032	0.006	0.039	0.019	0.013	0.023
Dy163_ppm_2SE(int)	0.021	0.018	0.018	0.008	0.019	0.014	0.012	0.014
Ho165_ppm_mean	0.003	0.003	0.007	0.008	0.001	0.004	0.002	0.005
Ho165_ppm_2SE(int)	0.003	0.003	0.004	0.005	0.001	0.003	0.002	0.003
Er166_ppm_mean	0.015	0.012	0.008	0.005	0.000	0.000	0.000	0.000
Er166_ppm_2SE(int)	0.011	0.011	0.008	0.006	0.000	0.000	0.000	0.000
Tm169_ppm_mean	0.000	0.000	0.001	0.000	0.000	0.000	0.002	0.000
Tm169_ppm_2SE(int)	0.000	0.000	0.001	0.000	0.000	0.000	0.002	0.000
Yb172_ppm_mean	0.000	0.010	0.006	0.000	0.000	0.003	0.000	0.000
Yb172_ppm_2SE(int)	0.000	0.012	0.008	0.000	0.000	0.006	0.000	0.000
Lu175_ppm_mean	0.000	0.000	0.000	0.000	0.000	0.000	0.000	0.000
Lu175_ppm_2SE(int)	0.000	0.000	0.000	0.000	0.000	0.000	0.000	0.000

Table S8 cont.: Plagioclase feldspar rare earth element contents.

Sample	15556	15556	15556	15556	15556	15556	15556	15556
Site	28-PLAG-3.139	28-PLAG-3.140	241-PLAG-1.59	241-PLAG-1.60	241-PLAG-1.61	241-PLAG-1.62	241-PLAG-2.68	241-PLAG-2.69
La139_ppm_mean	0.146	0.148	0.184	0.217	0.135	0.162	0.204	0.196
La139_ppm_2SE(int)	0.032	0.025	0.030	0.032	0.025	0.025	0.037	0.034
Ce140_ppm_mean	0.390	0.360	0.455	0.452	0.352	0.420	0.472	0.414
Ce140_ppm_2SE(int)	0.050	0.042	0.045	0.036	0.034	0.042	0.052	0.042
Pr141_ppm_mean	0.048	0.046	0.047	0.064	0.041	0.055	0.073	0.041
Pr141_ppm_2SE(int)	0.014	0.014	0.011	0.017	0.011	0.012	0.015	0.010
Nd146_ppm_mean	0.249	0.189	0.166	0.194	0.216	0.187	0.248	0.232
Nd146_ppm_2SE(int)	0.067	0.056	0.051	0.051	0.049	0.064	0.064	0.060
Sm147_ppm_mean	0.010	0.075	0.069	0.032	0.045	0.048	0.079	0.024
Sm147_ppm_2SE(int)	0.014	0.047	0.033	0.023	0.026	0.026	0.043	0.020
Eu153_ppm_mean	1.028	1.157	1.235	1.242	1.122	1.255	1.250	1.195
Eu153_ppm_2SE(int)	0.085	0.083	0.082	0.074	0.071	0.086	0.095	0.063
Gd157_ppm_mean	0.045	0.036	0.027	0.027	0.013	0.030	0.046	0.058
Gd157_ppm_2SE(int)	0.030	0.026	0.021	0.021	0.014	0.021	0.028	0.029
Tb159_ppm_mean	0.001	0.006	0.005	0.000	0.004	0.005	0.008	0.005
Tb159_ppm_2SE(int)	0.002	0.004	0.003	0.001	0.003	0.003	0.005	0.003
Dy163_ppm_mean	0.026	0.030	0.027	0.031	0.033	0.026	0.028	0.021
Dy163_ppm_2SE(int)	0.017	0.017	0.015	0.016	0.018	0.014	0.017	0.014
Ho165_ppm_mean	0.004	0.004	0.002	0.006	0.000	0.003	0.009	0.005
Ho165_ppm_2SE(int)	0.003	0.003	0.002	0.004	0.000	0.003	0.006	0.003
Er166_ppm_mean	0.000	0.022	0.005	0.008	0.000	0.015	0.032	0.012
Er166_ppm_2SE(int)	0.000	0.014	0.006	0.007	0.000	0.010	0.016	0.009
Tm169_ppm_mean	0.000	0.000	0.000	0.000	0.000	0.002	0.000	0.001
Tm169_ppm_2SE(int)	0.000	0.000	0.000	0.000	0.000	0.002	0.000	0.001
Yb172_ppm_mean	0.000	0.005	0.000	0.000	0.000	0.000	0.042	0.000
Yb172_ppm_2SE(int)	0.000	0.007	0.000	0.000	0.000	0.000	0.026	0.000
Lu175_ppm_mean	0.000	0.000	0.000	0.000	0.000	0.000	0.000	0.000
Lu175_ppm_2SE(int)	0.000	0.000	0.000	0.000	0.000	0.000	0.000	0.000

Table S8 cont.: Plagioclase feldspar rare earth element contents.

Sample	15556	15556	15556	15556	15556	15556	15556	15556
Site	241-PLAG-2.70	241-PLAG-2.71	241-PLAG-2.74	241-PLAG-2.75	241-PLAG-3.77	241-PLAG-3.78	241-PLAG-4.84	241-PLAG-4.86
La139_ppm_mean	0.173	0.321	0.179	0.274	0.169	0.323	0.225	0.140
La139_ppm_2SE(int)	0.031	0.038	0.026	0.036	0.027	0.038	0.030	0.025
Ce140_ppm_mean	0.380	0.795	0.361	0.558	0.437	0.795	0.572	0.328
Ce140_ppm_2SE(int)	0.049	0.064	0.042	0.045	0.032	0.050	0.045	0.037
Pr141_ppm_mean	0.054	0.081	0.041	0.075	0.053	0.095	0.066	0.042
Pr141_ppm_2SE(int)	0.012	0.014	0.011	0.013	0.012	0.015	0.013	0.009
Nd146_ppm_mean	0.244	0.401	0.221	0.238	0.283	0.316	0.259	0.178
Nd146_ppm_2SE(int)	0.055	0.090	0.069	0.065	0.074	0.072	0.059	0.037
Sm147_ppm_mean	0.068	0.119	0.000	0.046	0.038	0.095	0.042	0.082
Sm147_ppm_2SE(int)	0.031	0.058	0.000	0.031	0.024	0.040	0.025	0.037
Eu153_ppm_mean	1.112	2.260	1.239	1.753	1.322	2.444	1.706	1.077
Eu153_ppm_2SE(int)	0.084	0.108	0.080	0.108	0.087	0.107	0.079	0.074
Gd157_ppm_mean	0.050	0.063	0.045	0.045	0.032	0.081	0.089	0.023
Gd157_ppm_2SE(int)	0.027	0.028	0.028	0.027	0.023	0.033	0.034	0.020
Tb159_ppm_mean	0.004	0.012	0.003	0.009	0.007	0.009	0.005	0.008
Tb159_ppm_2SE(int)	0.003	0.005	0.003	0.005	0.004	0.004	0.003	0.004
Dy163_ppm_mean	0.026	0.061	0.025	0.059	0.013	0.052	0.023	0.028
Dy163_ppm_2SE(int)	0.015	0.023	0.016	0.028	0.011	0.022	0.014	0.018
Ho165_ppm_mean	0.008	0.009	0.001	0.002	0.000	0.008	0.003	0.005
Ho165_ppm_2SE(int)	0.004	0.005	0.002	0.002	0.000	0.004	0.003	0.003
Er166_ppm_mean	0.011	0.014	0.015	0.017	0.008	0.018	0.010	0.000
Er166_ppm_2SE(int)	0.009	0.009	0.011	0.011	0.008	0.011	0.008	0.000
Tm169_ppm_mean	0.000	0.000	0.000	0.000	0.000	0.000	0.000	0.000
Tm169_ppm_2SE(int)	0.000	0.000	0.000	0.000	0.000	0.000	0.000	0.000
Yb172_ppm_mean	0.000	0.010	0.000	0.009	0.000	0.017	0.008	0.000
Yb172_ppm_2SE(int)	0.000	0.009	0.000	0.010	0.000	0.012	0.009	0.000
Lu175_ppm_mean	0.000	0.002	0.000	0.000	0.000	0.000	0.001	0.000
Lu175_ppm_2SE(int)	0.000	0.002	0.000	0.000	0.000	0.000	0.001	0.000

Table S8 cont.: Plagioclase feldspar rare earth element contents.

Sample	70017	70017	70017	70017	70017	70017	70017	70017
Site	123-PLAG-1.192	123-PLAG-1.194	123-PLAG-2.195	123-PLAG-2.196	123-PLAG-2.197	123-PLAG-3.198	123-PLAG-3.199	123-PLAG-3.200
La139_ppm_mean	0.251	0.193	0.409	0.386	0.313	0.916	1.190	1.305
La139_ppm_2SE(int)	0.034	0.032	0.038	0.044	0.037	0.058	0.076	0.086
Ce140_ppm_mean	0.611	0.551	1.152	1.078	0.949	2.553	2.851	3.374
Ce140_ppm_2SE(int)	0.045	0.049	0.060	0.063	0.062	0.097	0.097	0.115
Pr141_ppm_mean	0.093	0.095	0.176	0.172	0.138	0.413	0.449	0.570
Pr141_ppm_2SE(int)	0.013	0.015	0.022	0.024	0.022	0.040	0.033	0.047
Nd146_ppm_mean	0.529	0.486	0.862	0.909	0.749	2.127	2.266	2.774
Nd146_ppm_2SE(int)	0.090	0.086	0.104	0.124	0.102	0.168	0.205	0.201
Sm147_ppm_mean	0.148	0.125	0.212	0.286	0.242	0.641	0.602	0.716
Sm147_ppm_2SE(int)	0.045	0.047	0.057	0.070	0.066	0.124	0.128	0.108
Eu153_ppm_mean	2.718	2.541	4.937	4.588	4.610	9.401	10.631	11.892
Eu153_ppm_2SE(int)	0.117	0.104	0.178	0.162	0.121	0.259	0.308	0.270
Gd157_ppm_mean	0.123	0.085	0.303	0.230	0.248	0.543	0.535	0.799
Gd157_ppm_2SE(int)	0.046	0.042	0.076	0.076	0.076	0.112	0.110	0.127
Tb159_ppm_mean	0.020	0.019	0.023	0.031	0.029	0.078	0.083	0.087
Tb159_ppm_2SE(int)	0.010	0.007	0.007	0.011	0.009	0.016	0.016	0.015
Dy163_ppm_mean	0.103	0.089	0.122	0.236	0.131	0.353	0.430	0.488
Dy163_ppm_2SE(int)	0.035	0.030	0.031	0.049	0.036	0.067	0.070	0.065
Ho165_ppm_mean	0.012	0.011	0.024	0.034	0.023	0.071	0.073	0.087
Ho165_ppm_2SE(int)	0.005	0.005	0.008	0.009	0.008	0.014	0.017	0.015
Er166_ppm_mean	0.033	0.051	0.065	0.071	0.057	0.119	0.142	0.149
Er166_ppm_2SE(int)	0.018	0.021	0.022	0.023	0.021	0.030	0.032	0.033
Tm169_ppm_mean	0.004	0.006	0.006	0.006	0.006	0.016	0.018	0.012
Tm169_ppm_2SE(int)	0.003	0.004	0.003	0.003	0.003	0.006	0.006	0.007
Yb172_ppm_mean	0.033	0.031	0.066	0.048	0.031	0.112	0.130	0.165
Yb172_ppm_2SE(int)	0.017	0.017	0.028	0.022	0.018	0.038	0.037	0.042
Lu175_ppm_mean	0.000	0.000	0.004	0.004	0.000	0.008	0.006	0.008
Lu175_ppm_2SE(int)	0.000	0.000	0.003	0.003	0.000	0.004	0.004	0.004

Table S8 cont.: Plagioclase feldspar rare earth element contents.

Sample	70017	70017	70017	70017	70017
Site	123-PLAG-3.201	123-PLAG-4.205	123-PLAG-4.206	123-PLAG-4.207	123-PLAG-4.208
La139_ppm_mean	0.328	0.244	0.428	0.222	0.218
La139_ppm_2SE(int)	0.039	0.036	0.046	0.031	0.036
Ce140_ppm_mean	0.911	0.653	1.023	0.591	0.619
Ce140_ppm_2SE(int)	0.063	0.043	0.073	0.053	0.049
Pr141_ppm_mean	0.169	0.099	0.187	0.088	0.079
Pr141_ppm_2SE(int)	0.026	0.021	0.029	0.017	0.015
Nd146_ppm_mean	0.734	0.443	0.906	0.494	0.496
Nd146_ppm_2SE(int)	0.118	0.086	0.135	0.087	0.096
Sm147_ppm_mean	0.244	0.159	0.173	0.141	0.138
Sm147_ppm_2SE(int)	0.073	0.057	0.055	0.059	0.053
Eu153_ppm_mean	4.274	3.431	4.950	2.786	2.861
Eu153_ppm_2SE(int)	0.156	0.138	0.167	0.141	0.124
Gd157_ppm_mean	0.212	0.162	0.262	0.110	0.096
Gd157_ppm_2SE(int)	0.064	0.053	0.078	0.042	0.043
Tb159_ppm_mean	0.021	0.028	0.025	0.016	0.022
Tb159_ppm_2SE(int)	0.008	0.010	0.010	0.007	0.010
Dy163_ppm_mean	0.188	0.062	0.179	0.091	0.098
Dy163_ppm_2SE(int)	0.041	0.027	0.048	0.036	0.033
Ho165_ppm_mean	0.021	0.019	0.030	0.018	0.009
Ho165_ppm_2SE(int)	0.007	0.008	0.009	0.008	0.005
Er166_ppm_mean	0.043	0.048	0.040	0.052	0.078
Er166_ppm_2SE(int)	0.018	0.020	0.022	0.022	0.029
Tm169_ppm_mean	0.008	0.004	0.004	0.000	0.001
Tm169_ppm_2SE(int)	0.004	0.003	0.003	0.000	0.002
Yb172_ppm_mean	0.065	0.039	0.062	0.020	0.036
Yb172_ppm_2SE(int)	0.026	0.022	0.029	0.015	0.019
Lu175_ppm_mean	0.002	0.000	0.001	0.003	0.002
Lu175_ppm_2SE(int)	0.002	0.000	0.002	0.003	0.002

Table S9: Olivine major element contents.

Sample	15085,16	15085,16	15085,16	15556,241	15556,241	15556,241	15556,241	15556,241
Site	16-ol	16-ol	16-ol	241-ol_001	241-ol_001	241-ol_001	241-ol_001	241-ol_001
Line #	534	535	536	537	538	539	540	541
SiO2	30.031	29.878	29.649	35.242	35.446	36.495	36.585	35.007
TiO2	0.207	0.413	0.166	0.056	0.056	0.045	0.025	0.041
Al2O3	0.000	0.000	0.000	0.009	0.009	0.011	0.011	0.008
Cr2O3	0.083	0.058	0.066	0.205	0.260	0.368	0.339	0.264
FeO	68.138	67.281	67.985	38.492	37.555	32.226	31.634	39.811
NiO	0.046	0.050	0.043	0.031	0.034	0.014	0.010	0.032
MnO	0.926	0.893	0.897	0.374	0.380	0.351	0.342	0.415
MgO	0.932	1.176	0.353	24.786	25.572	30.044	30.540	23.679
CaO	0.415	0.406	0.405	0.241	0.253	0.228	0.205	0.245
TOTAL	100.778	100.156	99.563	99.435	99.563	99.783	99.690	99.502

Table S9 cont.: Olivine major element contents.

Sample	15556,241	15556,241	15556,241	15556,241	15556,241	15556,241	15556,241	15556,241
Site	241-ol_001	241-ol_001	241-ol_001	241-ol_001	241-ol_001	241-ol_002	241-ol_002	241-ol_002
Line #	542	543	544	545	546	547	548	549
SiO2	36.869	36.806	36.338	36.694	36.614	37.940	37.698	34.731
TiO2	0.031	0.022	0.047	0.042	0.054	0.031	0.019	0.079
Al2O3	0.012	0.011	0.010	0.011	0.011	0.014	0.013	0.008
Cr2O3	0.419	0.366	0.300	0.340	0.317	0.471	0.342	0.241
FeO	30.356	30.625	32.914	31.158	31.582	24.891	25.901	41.279
NiO	0.033	0.046	0.012	0.014	0.025	0.046	0.050	0.054
MnO	0.312	0.335	0.352	0.376	0.352	0.278	0.285	0.422
MgO	31.613	31.388	29.467	30.940	30.584	36.200	35.352	22.447
CaO	0.238	0.240	0.215	0.207	0.237	0.213	0.194	0.228
TOTAL	99.884	99.838	99.654	99.783	99.776	100.083	99.852	99.490

Table S9 cont.: Olivine major element contents.

Sample	15556,241	15556,241	15556,241	15556,241	15556,241	15556,241	15556,241	15556,241
Site	241-ol_002	241-ol_002	241-ol_002	241-ol_003	241-ol_003	241-ol_003	241-ol_003	241-ol_003
Line #	550	551	552	553	554	555	556	557
SiO2	35.336	36.577	35.638	34.629	34.105	35.808	32.932	30.507
TiO2	0.045	0.052	0.043	0.069	0.059	0.040	0.080	0.133
Al2O3	0.009	0.011	0.010	0.008	0.007	0.010	0.005	0.002
Cr2O3	0.277	0.257	0.329	0.279	0.195	0.323	0.185	0.083
FeO	38.153	31.685	36.630	41.685	44.367	35.699	50.574	63.355
NiO	0.030	0.032	0.022	0.018	0.072	0.027	0.050	0.059
MnO	0.413	0.347	0.382	0.392	0.409	0.361	0.527	0.682
MgO	25.070	30.498	26.348	22.106	19.856	27.129	14.647	4.320
CaO	0.252	0.236	0.248	0.178	0.212	0.227	0.260	0.419
TOTAL	99.585	99.696	99.650	99.363	99.281	99.624	99.259	99.560

Table S9 cont.: Olivine major element contents.

Sample	15556,241	15556,241	15556,241	15556,241	15556,241	15556,241	15556,241	15556,241
Site	241-ol_003	241-ol_004	241-ol_004	241-ol_004	241-ol_004	241-ol_004	241-ol_004	241-ol_004
Line #	558	559	560	561	562	563	564	565
SiO2	36.777	36.564	30.474	36.816	32.081	37.308	30.539	32.568
TiO2	0.020	0.033	0.151	0.029	0.078	0.031	0.182	0.078
Al2O3	0.012	0.011	0.001	0.011	0.004	0.012	0.001	0.004
Cr2O3	0.368	0.304	0.111	0.301	0.123	0.350	0.103	0.184
FeO	30.760	31.754	63.741	30.434	54.975	27.912	63.415	52.434
NiO	0.039	0.039	0.082	0.050	0.053	0.028	0.075	0.030
MnO	0.328	0.339	0.722	0.321	0.563	0.291	0.692	0.534
MgO	31.274	30.440	3.896	31.548	10.953	33.664	4.171	13.086
CaO	0.240	0.211	0.464	0.203	0.328	0.195	0.467	0.277
TOTAL	99.817	99.695	99.642	99.713	99.156	99.792	99.645	99.194

Table S9 cont.: Olivine major element contents.

Sample	15556,241	15556,241	15556,241	15556,241	15556,241	15556,241	15556,241	15556,241
Site	241-ol_004	241-ol_004	241-ol_005	241-ol_005	241-ol_005	241-ol_005	241-ol_005	241-ol_005
Line #	566	567	568	569	570	571	572	573
SiO2	37.088	35.408	36.886	36.828	36.853	36.458	36.959	35.900
TiO2	0.041	0.028	0.028	0.026	0.030	0.027	0.031	0.044
Al2O3	0.012	0.009	0.011	0.011	0.011	0.011	0.011	0.010
Cr2O3	0.399	0.262	0.338	0.324	0.309	0.355	0.416	0.313
FeO	29.182	37.576	30.078	30.379	30.240	32.376	29.883	35.216
NiO	0.019	0.000	0.031	0.029	0.029	0.033	0.038	0.031
MnO	0.317	0.366	0.300	0.297	0.320	0.335	0.326	0.360
MgO	32.599	25.555	31.847	31.594	31.711	29.919	32.010	27.535
CaO	0.218	0.209	0.202	0.231	0.213	0.229	0.215	0.222
TOTAL	99.874	99.412	99.721	99.719	99.715	99.742	99.888	99.631

Table S9 cont.: Olivine major element contents.

Sample	15556,241	15556,241	15556,241	15556,241	15556,28	15556,28	15556,28	15556,28
Site	241-ol_006	241-ol_006	241-ol_006	241-ol_006	28-ol_001	28-ol_001	28-ol_001	28-ol_001
Line #	574	575	576	577	578	579	580	581
SiO2	36.946	37.022	36.001	30.880	34.781	32.512	34.153	32.744
TiO2	0.042	0.044	0.026	0.137	0.048	0.085	0.100	0.094
Al2O3	0.012	0.012	0.010	0.002	0.008	0.004	0.007	0.005
Cr2O3	0.345	0.345	0.274	0.099	0.203	0.229	0.206	0.143
FeO	29.486	29.463	34.544	61.484	40.842	52.839	44.188	51.541
NiO	0.020	0.027	0.011	0.063	0.005	0.057	0.041	0.029
MnO	0.000	0.323	0.338	0.668	0.406	0.532	0.411	0.519
MgO	32.343	32.363	28.099	5.791	22.813	12.746	20.005	13.835
CaO	0.219	0.220	0.216	0.432	0.247	0.276	0.220	0.316
TOTAL	99.413	99.819	99.520	99.555	99.352	99.280	99.329	99.226

Table S9 cont.: Olivine major element contents.

Sample	15556,28	15556,28	15556,28	15556,28	15556,28	15556,28	15556,28	15556,28
Site	28-ol_002	28-ol_002	28-ol_002	28-ol_002	28-ol_002	28-ol_003	28-ol_003	28-ol_003
Line #	582	583	584	585	586	587	588	589
SiO2	30.046	29.974	29.666	29.535	29.727	32.044	36.497	36.742
TiO2	0.155	0.200	0.239	0.145	0.175	0.125	0.027	0.029
Al2O3	0.001	0.001	0.000	0.000	0.000	0.004	0.011	0.011
Cr2O3	0.068	0.072	0.045	0.059	0.070	0.120	0.182	0.222
FeO	65.817	66.391	68.112	68.461	67.675	55.256	31.784	30.648
NiO	0.061	0.054	0.086	0.042	0.078	0.051	0.035	0.021
MnO	0.735	0.763	0.782	0.784	0.780	0.574	0.332	0.337
MgO	1.955	1.673	0.719	0.364	0.795	10.718	30.415	31.369
CaO	0.431	0.499	0.528	0.453	0.508	0.325	0.139	0.189
TOTAL	99.268	99.626	100.178	99.843	99.807	99.214	99.422	99.567

Table S9 cont.: Olivine major element contents.

Sample	70017,123	70017,123	70017,123	70017,123	70017,123	70017,123	70017,123	70017,123
Site	123-Ol_001	123-Ol_001	123-Ol_002	123-Ol_002	123-Ol_002	123-Ol_002	123-Ol_002	123-Ol_002
Line #	590	591	592	593	594	595	596	597
SiO2	36.886	36.862	35.780	37.030	37.350	37.383	37.325	37.291
TiO2	0.105	0.093	0.147	0.084	0.105	0.081	0.100	0.145
Al2O3	0.012	0.012	0.010	0.012	0.013	0.013	0.013	0.013
Cr2O3	0.140	0.160	0.186	0.164	0.198	0.177	0.204	0.208
FeO	29.829	29.969	35.751	29.022	27.514	27.266	27.681	27.911
NiO	0.019	0.009	0.040	0.010	0.014	0.013	0.008	0.000
MnO	0.311	0.302	0.382	0.301	0.302	0.317	0.323	0.311
MgO	32.055	31.938	27.086	32.733	33.998	34.207	33.859	33.665
CaO	0.137	0.160	0.130	0.107	0.129	0.120	0.149	0.137
TOTAL	99.495	99.505	99.511	99.462	99.623	99.575	99.661	99.680

Table S9 cont.: Olivine major element contents.

Sample	70017,123	70017,123	70017,123	70017,123
Site	123-Ol_003	123-Ol_003	123-Ol_003	123-Ol_003
Line #	598	599	600	601
SiO2	35.153	35.198	34.934	35.587
TiO2	0.085	0.194	0.086	0.159
Al2O3	0.009	0.009	0.008	0.009
Cr2O3	0.132	0.263	0.130	0.146
FeO	38.772	38.992	39.947	36.679
NiO	0.008	0.023	0.012	0.005
MnO	0.406	0.406	0.442	0.381
MgO	24.551	24.366	23.564	26.307
CaO	0.150	0.163	0.156	0.148
TOTAL	99.265	99.614	99.279	99.421

Table S10: Olivine trace element contents.

Sample	15556	15556	15556	15556	15556	15556	15556	15556
Site	28-OL-1.578	28-OL-1.579	28-OL-1.580	28-OL-1.581	28-OL-2.582	28-OL-2.584	28-OL-3.587	28-OL-3.589
Si29_ppm_mean	347811.000	325124.000	341526.000	327438.000	300459.000	296661.000	320438.000	367421.000
Si29_ppm_2SE(int)	0.000	0.000	0.000	0.000	0.000	0.000	0.000	0.000
Ca43_ppm_mean	4205.543	2995.083	26240.238	3057.563	23692.325	7523.786	2534.307	3043.754
Ca43_ppm_2SE(int)	432.660	146.926	1620.893	143.560	3774.762	257.662	210.054	251.194
Sc45_ppm_mean	11.206	9.952	24.540	10.194	21.521	9.617	9.122	9.458
Sc45_ppm_2SE(int)	0.340	0.308	0.852	0.383	2.034	0.275	0.475	0.401
Ti47_ppm_mean	2335.939	327.704	1840.903	278.564	1613.950	973.369	240.357	222.653
Ti47_ppm_2SE(int)	132.269	30.345	87.141	6.913	199.782	62.864	12.975	7.618
V51_ppm_mean	429.230	68.385	40.466	29.543	16.064	2.130	52.262	100.463
V51_ppm_2SE(int)	24.707	5.434	0.966	0.682	2.514	0.153	2.648	2.630
Cr52_ppm_mean	16609.213	1571.590	712.322	524.214	201.203	51.397	992.267	2216.401
Cr52_ppm_2SE(int)	1051.918	249.709	14.627	8.910	22.557	1.236	68.761	75.257
Mn55_ppm_mean	3569.856	3153.717	3411.228	3601.503	4731.701	5715.852	3073.479	2718.087
Mn55_ppm_2SE(int)	56.177	53.253	71.405	68.165	168.775	74.494	101.494	62.117
Co59_ppm_mean	112.611	104.011	82.081	102.947	54.360	53.520	113.285	129.081
Co59_ppm_2SE(int)	2.409	1.934	2.992	2.174	1.524	1.140	4.291	3.590
Ni60_ppm_mean	71.170	66.779	33.625	47.871	8.908	7.442	152.941	137.317
Ni60_ppm_2SE(int)	1.883	2.068	2.133	1.640	1.163	1.268	6.863	4.110
Cu63_ppm_mean	0.808	0.250	0.603	0.495	9.930	4.347	0.984	0.557
Cu63_ppm_2SE(int)	0.165	0.068	0.115	0.097	2.780	1.635	0.268	0.142
Zn66_ppm_mean	5.049	3.633	2.489	3.567	4.281	3.093	4.588	3.397
Zn66_ppm_2SE(int)	0.752	0.554	0.695	0.640	0.625	0.570	1.352	0.914
Rb85_ppm_mean	0.035	0.023	0.001	-0.001	0.405	0.573	0.017	0.009
Rb85_ppm_2SE(int)	0.022	0.016	0.013	0.014	0.093	0.164	0.020	0.024
Sr88_ppm_mean	2.348	0.027	3.626	0.018	5.646	5.645	0.034	0.014
Sr88_ppm_2SE(int)	0.812	0.009	0.457	0.007	1.441	1.450	0.017	0.010
Y89_ppm_mean	1.388	0.376	9.218	0.916	13.354	16.865	0.610	0.197
Y89_ppm_2SE(int)	0.150	0.039	0.850	0.056	1.383	0.743	0.068	0.034
Zr90_ppm_mean	2.872	0.093	8.300	0.075	26.750	18.483	0.188	0.078
Zr90_ppm_2SE(int)	1.083	0.034	0.894	0.024	5.319	3.951	0.166	0.038
Nb93_ppm_mean	0.142	0.011	0.043	0.000	0.846	0.793	0.006	0.000
Nb93_ppm_2SE(int)	0.036	0.007	0.016	0.000	0.197	0.172	0.007	0.000
Hf178_ppm_mean	0.089	0.000	0.420	0.001	0.963	0.465	0.000	0.000
Hf178_ppm_2SE(int)	0.034	0.000	0.061	0.003	0.200	0.103	0.000	0.000
Ta181_ppm_mean	0.009	0.000	0.005	0.003	0.074	0.046	0.000	0.000
Ta181_ppm_2SE(int)	0.004	0.000	0.003	0.006	0.018	0.012	0.000	0.000
Pb208_ppm_mean	4.276	0.049	0.032	0.055	0.150	0.109	1.214	0.148
Pb208_ppm_2SE(int)	4.372	0.012	0.010	0.014	0.083	0.023	0.921	0.058
Th232_ppm_mean	0.014	0.000	0.053	0.000	0.125	0.113	0.000	0.000
Th232_ppm_2SE(int)	0.006	0.000	0.011	0.000	0.031	0.027	0.000	0.000
U238_ppm_mean	0.006	0.012	0.006	0.000	0.036	0.035	0.000	0.002
U238_ppm_2SE(int)	0.003	0.023	0.003	0.000	0.010	0.010	0.000	0.002

Table S10 cont.: Olivine trace element contents.

Sample	15556	15556	15556	15556	15556	15556	70017	70017
Site	241-OL-5.570	241-OL-5.571	241-OL-5.572	241-OL-5.573	241-OL-6.574	241-OL-5.577	123-OL-1.591	123-OL-2.592
Si29_ppm_mean	368527.000	364576.000	369585.000	359002.000	369464.000	308798.000	368618.000	357796.000
Si29_ppm_2SE(int)	0.000	0.000	0.000	0.000	0.000	0.000	0.000	0.000
Ca43_ppm_mean	2833.493	2812.570	2715.836	2705.997	2804.113	2444.135	2182.303	1626.951
Ca43_ppm_2SE(int)	167.489	168.557	147.300	160.895	136.784	102.976	147.510	117.851
Sc45_ppm_mean	8.904	9.079	9.108	9.471	8.998	8.938	14.692	13.499
Sc45_ppm_2SE(int)	0.290	0.318	0.324	0.311	0.403	0.284	0.436	0.498
Ti47_ppm_mean	181.735	184.318	183.487	188.234	181.918	201.884	608.166	444.294
Ti47_ppm_2SE(int)	7.373	6.087	6.074	5.750	5.177	4.765	11.078	16.478
V51_ppm_mean	105.456	102.271	106.857	101.005	99.777	47.739	20.896	18.886
V51_ppm_2SE(int)	2.560	2.120	2.046	1.553	2.493	0.963	0.543	0.613
Cr52_ppm_mean	2396.900	2310.347	2552.451	2265.001	2285.258	901.358	955.290	809.741
Cr52_ppm_2SE(int)	71.048	53.079	48.976	40.223	60.198	17.873	22.118	12.822
Mn55_ppm_mean	2634.186	2692.739	2599.880	2683.475	2562.582	2965.086	2613.813	2661.734
Mn55_ppm_2SE(int)	54.012	49.192	51.581	46.674	67.540	37.738	49.236	42.453
Co59_ppm_mean	122.357	119.974	121.493	119.075	124.893	94.059	53.336	52.467
Co59_ppm_2SE(int)	2.580	2.484	2.540	2.206	3.351	1.497	1.202	0.989
Ni60_ppm_mean	139.535	136.736	138.374	134.407	147.721	79.413	3.091	0.973
Ni60_ppm_2SE(int)	3.372	3.699	2.970	3.005	3.884	2.168	0.305	0.196
Cu63_ppm_mean	0.386	0.416	0.241	0.413	0.271	0.440	0.051	0.448
Cu63_ppm_2SE(int)	0.087	0.102	0.067	0.111	0.074	0.076	0.051	0.089
Zn66_ppm_mean	2.686	2.502	2.628	2.126	2.302	2.581	5.109	36.074
Zn66_ppm_2SE(int)	0.610	0.654	0.664	0.599	0.578	0.519	0.694	2.343
Rb85_ppm_mean	0.022	0.015	0.016	0.015	0.029	0.012	-0.007	0.018
Rb85_ppm_2SE(int)	0.017	0.026	0.016	0.018	0.014	0.012	0.014	0.015
Sr88_ppm_mean	0.005	0.003	0.005	0.002	0.003	0.005	0.006	0.001
Sr88_ppm_2SE(int)	0.005	0.003	0.004	0.003	0.003	0.003	0.004	0.001
Y89_ppm_mean	0.130	0.194	0.166	0.191	0.187	0.494	1.521	1.841
Y89_ppm_2SE(int)	0.022	0.029	0.025	0.027	0.024	0.045	0.093	0.108
Zr90_ppm_mean	0.043	0.066	0.058	0.053	0.041	0.017	0.155	0.158
Zr90_ppm_2SE(int)	0.018	0.027	0.023	0.018	0.019	0.010	0.041	0.040
Nb93_ppm_mean	0.000	0.000	0.005	0.010	0.004	0.002	0.000	0.000
Nb93_ppm_2SE(int)	0.000	0.000	0.005	0.007	0.005	0.003	0.000	0.000
Hf178_ppm_mean	0.003	0.000	0.000	0.000	0.003	0.002	0.000	0.000
Hf178_ppm_2SE(int)	0.004	0.000	0.000	0.000	0.004	0.003	0.000	0.000
Ta181_ppm_mean	0.000	0.000	0.000	0.000	0.000	0.000	0.000	0.000
Ta181_ppm_2SE(int)	0.000	0.000	0.000	0.000	0.000	0.000	0.000	0.000
Pb208_ppm_mean	0.014	0.018	0.006	0.001	0.003	0.018	-0.002	0.010
Pb208_ppm_2SE(int)	0.006	0.006	0.004	0.004	0.006	0.007	0.004	0.007
Th232_ppm_mean	0.000	0.000	0.000	0.000	0.000	0.000	0.000	0.000
Th232_ppm_2SE(int)	0.000	0.000	0.001	0.000	0.000	0.000	0.000	0.000
U238_ppm_mean	0.001	0.003	0.000	0.000	0.001	0.000	0.000	0.007
U238_ppm_2SE(int)	0.001	0.005	0.000	0.000	0.001	0.000	0.000	0.014

Table S10 cont.: Olivine trace element contents.

Sample	70017	70017	70017	70017	70017
Site	123-OL-2.593	123-OL-2.594	123-OL-2.595	123-OL-3.599	123-OL-3.600
Si29_ppm_mean	370299.000	373495.000	373829.000	351976.000	349337.000
Si29_ppm_2SE(int)	0.000	0.000	0.000	0.000	0.000
Ca43_ppm_mean	1461.133	1844.440	1736.525	2005.934	1977.792
Ca43_ppm_2SE(int)	113.219	116.229	126.065	135.474	126.801
Sc45_ppm_mean	14.319	13.277	13.506	15.181	17.053
Sc45_ppm_2SE(int)	0.506	0.467	0.456	0.416	0.525
Ti47_ppm_mean	404.899	597.428	562.781	408.134	440.710
Ti47_ppm_2SE(int)	12.475	16.631	19.485	9.901	10.065
V51_ppm_mean	19.816	19.507	19.689	14.442	14.824
V51_ppm_2SE(int)	0.822	0.832	0.642	0.522	0.439
Cr52_ppm_mean	742.536	1043.255	1111.667	640.497	646.159
Cr52_ppm_2SE(int)	15.363	30.749	27.801	13.105	12.142
Mn55_ppm_mean	2403.010	2596.442	2580.742	3197.114	3392.072
Mn55_ppm_2SE(int)	52.428	64.643	49.095	62.243	73.869
Co59_ppm_mean	64.662	43.604	44.220	42.686	40.294
Co59_ppm_2SE(int)	1.344	1.323	1.380	0.993	1.019
Ni60_ppm_mean	1.106	0.984	1.017	0.818	0.714
Ni60_ppm_2SE(int)	0.188	0.227	0.201	0.195	0.166
Cu63_ppm_mean	0.239	0.661	0.783	0.878	0.018
Cu63_ppm_2SE(int)	0.084	0.271	0.124	0.147	0.054
Zn66_ppm_mean	19.805	30.752	35.421	39.140	5.774
Zn66_ppm_2SE(int)	3.079	1.543	1.998	4.031	0.700
Rb85_ppm_mean	0.157	0.038	0.008	0.000	0.014
Rb85_ppm_2SE(int)	0.221	0.045	0.015	0.013	0.018
Sr88_ppm_mean	0.005	0.004	0.025	0.008	0.000
Sr88_ppm_2SE(int)	0.004	0.003	0.009	0.005	0.000
Y89_ppm_mean	1.257	1.247	1.306	3.659	4.658
Y89_ppm_2SE(int)	0.077	0.072	0.097	0.129	0.166
Zr90_ppm_mean	0.179	0.403	0.266	0.466	0.718
Zr90_ppm_2SE(int)	0.043	0.069	0.048	0.061	0.091
Nb93_ppm_mean	0.017	0.006	0.005	0.001	0.000
Nb93_ppm_2SE(int)	0.032	0.009	0.005	0.002	0.000
Hf178_ppm_mean	0.012	0.012	0.013	0.010	0.018
Hf178_ppm_2SE(int)	0.007	0.007	0.007	0.007	0.009
Ta181_ppm_mean	0.000	0.000	0.000	0.000	0.002
Ta181_ppm_2SE(int)	0.000	0.000	0.001	0.000	0.002
Pb208_ppm_mean	0.009	0.000	0.060	0.011	0.001
Pb208_ppm_2SE(int)	0.006	0.004	0.020	0.006	0.006
Th232_ppm_mean	0.004	0.000	0.000	0.000	0.000
Th232_ppm_2SE(int)	0.009	0.000	0.000	0.000	0.000
U238_ppm_mean	0.021	0.001	0.026	0.000	0.001
U238_ppm_2SE(int)	0.030	0.001	0.052	0.000	0.001

Table S11: Olivine rare earth element contents.

Sample	15556	15556	15556	15556	15556	15556	15556	15556
Site	28-OL-1.578	28-OL-1.579	28-OL-1.580	28-OL-1.581	28-OL-2.582	28-OL-2.584	28-OL-3.587	28-OL-3.589
La139_ppm_mean	0.114	0.001	0.225	0.000	1.005	0.881	0.004	0.000
La139_ppm_2SE(int)	0.037	0.001	0.028	0.000	0.233	0.212	0.004	0.000
Ce140_ppm_mean	0.399	0.009	0.869	0.010	2.824	2.373	0.094	0.004
Ce140_ppm_2SE(int)	0.113	0.005	0.080	0.006	0.650	0.540	0.130	0.004
Pr141_ppm_mean	0.041	0.001	0.181	0.002	0.465	0.355	0.001	0.000
Pr141_ppm_2SE(int)	0.014	0.001	0.023	0.002	0.106	0.088	0.002	0.000
Nd146_ppm_mean	0.208	0.000	1.286	0.024	2.859	1.702	0.026	0.000
Nd146_ppm_2SE(int)	0.071	0.000	0.173	0.014	0.622	0.396	0.029	0.000
Sm147_ppm_mean	0.066	0.000	0.714	0.005	1.008	0.582	0.000	0.000
Sm147_ppm_2SE(int)	0.026	0.000	0.104	0.007	0.224	0.132	0.000	0.000
Eu153_ppm_mean	0.015	0.000	0.061	0.001	0.096	0.089	0.000	0.000
Eu153_ppm_2SE(int)	0.007	0.000	0.013	0.001	0.024	0.023	0.000	0.000
Gd157_ppm_mean	0.137	0.011	1.104	0.024	1.648	1.054	0.020	0.000
Gd157_ppm_2SE(int)	0.043	0.010	0.133	0.015	0.334	0.170	0.018	0.000
Tb159_ppm_mean	0.025	0.003	0.245	0.009	0.318	0.272	0.006	0.001
Tb159_ppm_2SE(int)	0.007	0.002	0.027	0.003	0.055	0.030	0.005	0.002
Dy163_ppm_mean	0.182	0.051	1.575	0.132	2.179	2.198	0.093	0.033
Dy163_ppm_2SE(int)	0.047	0.016	0.176	0.029	0.298	0.173	0.027	0.020
Ho165_ppm_mean	0.052	0.011	0.375	0.035	0.504	0.618	0.016	0.009
Ho165_ppm_2SE(int)	0.011	0.004	0.042	0.007	0.065	0.035	0.007	0.005
Er166_ppm_mean	0.130	0.044	1.069	0.120	1.582	2.252	0.096	0.021
Er166_ppm_2SE(int)	0.025	0.014	0.119	0.021	0.144	0.124	0.029	0.016
Tm169_ppm_mean	0.025	0.008	0.151	0.023	0.251	0.411	0.010	0.005
Tm169_ppm_2SE(int)	0.006	0.003	0.018	0.006	0.022	0.024	0.005	0.004
Yb172_ppm_mean	0.216	0.099	1.005	0.155	1.868	3.135	0.101	0.045
Yb172_ppm_2SE(int)	0.034	0.025	0.104	0.032	0.122	0.144	0.027	0.022
Lu175_ppm_mean	0.030	0.012	0.162	0.025	0.300	0.534	0.021	0.010
Lu175_ppm_2SE(int)	0.006	0.004	0.022	0.007	0.018	0.023	0.007	0.005

Table S11 cont.: Olivine rare earth element contents.

Sample	15556	15556	15556	15556	15556	15556	70017	70017
Site	241-OL-5.570	241-OL-5.571	241-OL-5.572	241-OL-5.573	241-OL-6.574	241-OL-5.577	123-OL-1.591	123-OL-2.592
La139_ppm_mean	0.001	0.000	0.000	0.000	0.000	0.000	0.000	0.000
La139_ppm_2SE(int)	0.001	0.000	0.000	0.000	0.000	0.000	0.000	0.000
Ce140_ppm_mean	0.000	0.001	0.000	0.000	0.000	0.000	0.006	0.001
Ce140_ppm_2SE(int)	0.000	0.001	0.000	0.000	0.000	0.000	0.010	0.001
Pr141_ppm_mean	0.000	0.000	0.000	0.000	0.000	0.000	0.000	0.000
Pr141_ppm_2SE(int)	0.001	0.000	0.000	0.000	0.000	0.000	0.000	0.000
Nd146_ppm_mean	0.000	0.005	0.000	0.007	0.010	0.000	0.005	0.002
Nd146_ppm_2SE(int)	0.000	0.007	0.000	0.010	0.012	0.000	0.007	0.004
Sm147_ppm_mean	0.000	0.000	0.000	0.000	0.000	0.000	0.016	0.000
Sm147_ppm_2SE(int)	0.000	0.000	0.000	0.000	0.000	0.000	0.013	0.000
Eu153_ppm_mean	0.001	0.002	0.000	0.000	0.000	0.000	0.000	0.001
Eu153_ppm_2SE(int)	0.001	0.003	0.000	0.000	0.000	0.000	0.000	0.001
Gd157_ppm_mean	0.008	0.000	0.000	0.000	0.000	0.015	0.031	0.023
Gd157_ppm_2SE(int)	0.008	0.000	0.000	0.000	0.000	0.011	0.017	0.015
Tb159_ppm_mean	0.000	0.000	0.000	0.001	0.000	0.009	0.016	0.016
Tb159_ppm_2SE(int)	0.001	0.000	0.000	0.001	0.001	0.003	0.004	0.005
Dy163_ppm_mean	0.013	0.020	0.014	0.027	0.010	0.062	0.217	0.158
Dy163_ppm_2SE(int)	0.009	0.010	0.009	0.012	0.007	0.016	0.035	0.028
Ho165_ppm_mean	0.006	0.006	0.002	0.005	0.002	0.020	0.056	0.063
Ho165_ppm_2SE(int)	0.003	0.003	0.002	0.002	0.002	0.006	0.011	0.012
Er166_ppm_mean	0.031	0.029	0.018	0.031	0.015	0.062	0.248	0.259
Er166_ppm_2SE(int)	0.012	0.012	0.009	0.012	0.007	0.015	0.037	0.037
Tm169_ppm_mean	0.006	0.007	0.005	0.006	0.005	0.011	0.055	0.042
Tm169_ppm_2SE(int)	0.002	0.004	0.003	0.003	0.002	0.003	0.011	0.007
Yb172_ppm_mean	0.039	0.048	0.048	0.031	0.043	0.089	0.455	0.451
Yb172_ppm_2SE(int)	0.016	0.016	0.017	0.011	0.015	0.018	0.049	0.055
Lu175_ppm_mean	0.005	0.006	0.010	0.009	0.013	0.018	0.088	0.082
Lu175_ppm_2SE(int)	0.002	0.003	0.004	0.003	0.004	0.005	0.011	0.011

Table S11 cont.: Olivine rare earth element contents.

Sample	70017	70017	70017	70017	70017
Site	123-OL-2.593	123-OL-2.594	123-OL-2.595	123-OL-3.599	123-OL-3.600
La139_ppm_mean	0.002	0.000	0.000	0.000	0.000
La139_ppm_2SE(int)	0.002	0.000	0.000	0.000	0.000
Ce140_ppm_mean	0.001	0.004	0.000	0.000	0.005
Ce140_ppm_2SE(int)	0.002	0.003	0.001	0.000	0.003
Pr141_ppm_mean	0.000	0.000	0.000	0.000	0.001
Pr141_ppm_2SE(int)	0.001	0.000	0.001	0.001	0.001
Nd146_ppm_mean	0.005	0.024	0.000	0.011	0.000
Nd146_ppm_2SE(int)	0.007	0.033	0.000	0.011	0.000
Sm147_ppm_mean	0.000	0.000	0.000	0.016	0.013
Sm147_ppm_2SE(int)	0.000	0.000	0.000	0.012	0.011
Eu153_ppm_mean	0.001	0.000	0.000	0.000	0.000
Eu153_ppm_2SE(int)	0.002	0.000	0.000	0.000	0.000
Gd157_ppm_mean	0.028	0.040	0.028	0.118	0.141
Gd157_ppm_2SE(int)	0.015	0.023	0.016	0.038	0.038
Tb159_ppm_mean	0.010	0.013	0.011	0.036	0.043
Tb159_ppm_2SE(int)	0.004	0.005	0.004	0.006	0.010
Dy163_ppm_mean	0.103	0.146	0.146	0.432	0.486
Dy163_ppm_2SE(int)	0.025	0.031	0.034	0.050	0.058
Ho165_ppm_mean	0.042	0.040	0.041	0.135	0.152
Ho165_ppm_2SE(int)	0.007	0.007	0.008	0.017	0.017
Er166_ppm_mean	0.162	0.176	0.192	0.493	0.609
Er166_ppm_2SE(int)	0.029	0.027	0.031	0.042	0.052
Tm169_ppm_mean	0.036	0.037	0.034	0.086	0.122
Tm169_ppm_2SE(int)	0.007	0.008	0.007	0.011	0.016
Yb172_ppm_mean	0.350	0.309	0.328	0.758	0.911
Yb172_ppm_2SE(int)	0.049	0.040	0.054	0.070	0.075
Lu175_ppm_mean	0.070	0.065	0.056	0.138	0.158
Lu175_ppm_2SE(int)	0.010	0.010	0.009	0.013	0.016

Table S12: Silica and glass major element contents.

Sample	10057,67	10057,67	10057,67	10057,67	10057,67	10057,67	10057,67
Site	67-Glass1	67-Glass1	67-Glass1	67-Glass1	67-Glass2	67-Glass2	67-Glass2
Line #	148	149	150	151	152	153	154
SiO2	97.046	77.074	68.348	96.536	97.310	59.989	77.574
TiO2	0.328	0.785	1.974	0.325	0.258	0.464	1.203
Al2O3	1.613	10.564	10.580	1.695	1.221	20.971	9.241
Cr2O3	0.000	0.015	0.000	0.000	0.000	0.000	0.007
FeO	0.000	2.148	8.589	0.000	0.000	1.707	3.934
MnO	0.242	0.027	0.092	0.281	0.386	0.001	0.042
MgO	0.000	0.447	1.925	0.000	0.000	0.750	1.342
CaO	0.473	2.617	2.365	0.489	0.324	10.349	1.220
Na2O	0.450	0.965	0.828	0.582	0.297	2.079	0.568
K2O	0.000	5.397	5.931	0.011	0.023	2.808	4.635
P2O5	0.184	0.066	0.152	0.180	0.184	0.020	0.034
SO3	0.003	0.021	0.113	0.017	0.000	0.038	0.005
TOTAL	100.338	100.125	100.898	100.115	100.003	99.174	99.804

Table S12 cont.: Silica and glass major element contents.

Sample	10057,67	15085,16	15085,16	15085,16	15085,16	15085,16	15085,16
Site	67-Glass2	16-silica	16-silica	16-silica2	16-silica2	16-silica2	16-silica2
Line #	155	609	610	611	612	613	614
SiO2	74.472	95.750	95.722	96.163	96.240	74.684	75.636
TiO2	0.664	0.517	0.364	0.230	0.348	0.673	0.607
Al2O3	12.981	1.425	1.448	1.427	1.521	11.969	11.617
Cr2O3	0.000	0.000	0.000	0.005	0.017	0.000	0.024
FeO	2.788	0.154	0.031	0.133	0.051	1.983	1.957
MnO	0.031	0.000	0.000	0.000	0.002	0.023	0.007
MgO	0.254	0.078	0.093	0.075	0.135	0.059	0.084
CaO	3.901	0.013	0.009	0.057	0.022	2.597	6.540
Na2O	0.897	1.493	1.346	1.368	1.845	1.866	1.775
K2O	4.713	0.357	0.311	0.390	0.368	6.408	2.016
P2O5	0.030	0.000	0.000	0.000	0.000	0.000	0.000
SO3	0.021	0.009	0.000	0.015	0.000	0.000	0.030
TOTAL	100.752	99.797	99.324	99.863	100.548	100.262	100.293

4. New Insights Into Magma Storage and Ascent on the Moon: An Integrated Textural, Mineralogical, and Geochemical Study of Apollo 11 High Potassium Basalts

The following chapter is currently in preparation for submission to the journal Geochimica et Cosmochimica Acta.

4.1 Introduction

Basaltic magmatism is a fundamental process through which rocky planetary objects differentiate and evolve (BVSP, 1981; Middlemost, 2014; Wilson; 2009). This is due to the generation of primary partial melts within planetary mantles, which, upon ascent and eruption, contribute to the establishment of primary and secondary planetary crusts (BVSP, 1981; Gounelle et al., 2009; Lee et al., 2009; Li et al., 2022; Middlemost; 2014; Wilson, 2009). In addition, these erupted products provide a record of the thermal and chemical history of their source regions (BVSP, 1981; Lee et al., 2009; Middlemost, 2014; Ogawa, 2018; Shearer and Papike, 1999; Wilson and Head, 2017). Extruded magmatic products possess distinct physical and chemical attributes which, through the application and integration of appropriate petrological datasets, can be comprehensively interrogated to provide new insights into the geologic processes that drive their evolution (e.g., magma mixing, magma mingling, crustal contamination; Blundy and Shimizu, 1991; Ginibre et al., 2002; Higgins and Roberge, 2007; Jerram and Davidson, 2007; Jerram et al., 2018; Marsh, 2009; Singer et al., 1995; Ubide et al., 2014).

Within the context of basaltic systems on Earth, these processes have been studied for decades across a range of tectonic settings and over a range of temporal and spatial scales (Cashman, 2015; Cashman et al., 2017; Edmonds et al., 2019; Jerram and Davidson, 2007; Lee et al., 2009; Marsh et al., 2009; Middlemost, 2014; Ogawa, 2018; Sparks et al., 2019). Advancing our knowledge of the processes which operate at depth beneath these volcanic edifices often requires detailed examination of the textural, mineralogical, and geochemical relationships within and between the systems components. From this, crystal populations with distinct petrogenetic histories have been observed (e.g., autocrysts, antecrysts, xenocrysts; Davidson et al., 2007; Zellmer, 2021). The existence of multiple crystal populations throughout one phase (i.e., plagioclase feldspar) in a single eruptive unit (i.e., a lava flow), and our ability to examine their physical and chemical properties at the macro- and microscale, has led to the identification of so-called "open system" processes (Ginibre et al., 2007; Ubide et al., 2019). In short, this has led to a "paradigm shift" in our understanding of how terrestrial magmatic systems are established within the lithosphere and subsequently evolve (Cashman, 2015; Cashman et al., 2017). However, this integrated approach to advancing our understanding of magma system dynamics and the role this play in the evolution of other differentiated rocky bodies within our Solar System remains largely unexplored. For context Mercury, Venus, the Moon, Mars, and Earth all have vast lava plains across their surfaces (Byrne, 2020; Wilson, 2009). Within the context of composition, flows on Mars, Earth, and the Moon have been confirmed as basaltic in nature through direct sample analysis and/or remote sensing (Byrne, 2020; Greeley and Spudis, 1981; Middlemost, 1975; Papike et al., 1976; Shearer and Papike 1999; Wilson 2009). While no samples have been collected or identified within the meteorite collection from Venus, remote sensing analyses also suggest that some lava flows on Venus may be basaltic (i.e., Cutler et al., 2020; MacLellan et al., 2021). Meanwhile, many meteorites found on Earth also suggest that at least some of the asteroids withing the asteroid belt contain basaltic flows and intrusions (i.e., Taylor et al., 1993); specifically, Eucrite meteorites are all basaltic and are understood to originate from the asteroid Vesta (see review by Mittlefehldt, 2015). Finally, considering the outer Solar System, Jupiter's moon Io is also understood to host potentially young volcanic plains considering its generally smooth (not heavily cratered) surface (i.e., Johnson et al., 1979). Thus,

investigating magmatic processes via analysis of extraterrestrial basaltic systems has the potential to fundamentally advance our knowledge and understanding of magma dynamics across the Solar System.

From the documented ability of detailed, spatially resolved petrological studies of crystal populations to advance knowledge and understanding of magmatic systems on Earth, this work applies this approach to the Moon and a suite of Apollo basalts. This study builds on previous work by Gawronska et al. (2022) which utilized computed tomography (CT) to investigate emplacement mechanisms of lunar lava flows, within a terrestrial framework of pāhoehoe flow evolution. Here, the re-evaluation of the Apollo 11 high titanium (Ti), high potassium (K) basalts (known as the Apollo 11 group A basalts) provides new insights in to the petrogenesis of lunar magmas and ultimately the formation of the Moons secondary basaltic crust.

4.1.1 Magmatism on the Moon

The lunar mare basalts cover approximately 17% of the lunar surface (Fig. 1; Head, 1976). The sampling of basaltic materials during the during the Apollo 11 mission marked the first time that rocks were directly and intentionally gathered from another planetary object. Following their return and curation on Earth, bulk chemical analyses led to the postulation of the widely recognized Lunar Magma Ocean (LMO) theory (e.g., Smith et al., 1970; Wood et al., 1970; for more information see Shearer et al., 2006, and references therein). This theory describes the stages of Moon-wide cooling of the mantle and primary anorthositic crust production prior to complete solidification of the Moon. During the initial stages of lunar differentiation, olivine and pyroxene cumulates are proposed to have sunk towards the lunar interior, with a feldspathic flotation crust forming as Ca-rich plagioclase became a liquidus phase. The remaining melt proceeded to crystallize denser oxide phases (i.e., ilmenite and armalcolite) that sunk diapirically in the mantle, generating lateral and vertical heterogeneities and establishing the ilmenite-bearing cumulates, or IBCs (Hess and Parmentier, 1995; Li et al., 2019; Ringwood and Kesson, 1976). The final stages of the LMO theory propose that an incompatible-element-rich reservoir formed at the base of the lunar crust. This primordial geochemical reservoir is proposed to be enriched in K, REEs, and P, and as a result is referred to as ur-KREEP (Warren and Wasson, 1979). In the decades since the Apollo missions, lunar basalt samples (in addition to basaltic materials identified in meteoritic materials), have been classified, grouped, and split based on a variety of textural and/or chemical features.

One of the primary approaches to classifying the mare basalts within the context of their chemical signatures, is whole rock wt. % TiO_2. As a collective suite, the mare basalts range from very low titanium (<1 wt. % TiO_2) to high titanium (>6 wt. % TiO_2; Giguere et al., 2000; Neal and Taylor, 1992). The basalts collected during Apollo 11, 17, and Chang'e 5 define the high-Ti groups, while Apollo 12, 14, 15, Luna 16, and 24 samples broadly define the low-Ti group (Che et al., 2021; Gawronska and McLeod 2022; Neal and Taylor, 1992; Papike et al., 1976; Qian et al., 2021). However, it is important to note that mare units on the lunar surface are unimodal in Ti content and do not support the sample bimodality of "high" vs. "low" contents (Giguere et al., 2000). Collectively, lunar basalts also vary in bulk composition with respect to wt. % Al_2O_3 content (i.e., the Apollo 14 high alumina basalts) and elevated wt. % K_2O contents (i.e., the Apollo 11 group A, and Apollo

14 and 15 KREEP basalts; Gawronska and McLeod, 2022; Neal and Taylor, 1992; Papike et al., 1976). Within this framework, lunar basalts represent partial melts of the olivine and pyroxene lunar mantle, where the high titanium basalts represent partial melting of mantle source regions which are additionally characterized by the presence of ilmenite ($(Fe,Ti)_2O_3$) and armalcolite ($(Fe,Mg)Ti_2O_5$) cumulates, thus producing the so-called high-Ti mare basalts (Papike et al., 1976; Shearer et al., 2006, and references therein). Furthermore, is has been proposed that several of the lunar basalts also incorporated geochemically more evolved material during transport through the crust, thus producing additional compositional variations. Lunar mare basalts which are classified as being both high Ti and high K have only been collected at the Apollo 11 landing site, and are hypothesized to have formed as ascending magmas assimilated KREEPy material en route to the surface (Jerde et al., 1994). This suite forms the basis of this study.

4.1.2 Motivation

While the physical characteristics of extrusive lunar mare rocks preserve crucial of their emplacement conditions (Gawronska et al., 2022; Head and Wilson, 2017; Wilson and Head, 2017; Wilson and Head, 2018), their chemical characteristics can provide evidence of the processes which governed their petrogenesis within the lunar interior (e.g., fractional crystallization, assimilation). Such processes are likely recorded by the minerals within their crystal cargoes as has been demonstrated in terrestrial basaltic systems (see discussion earlier; Blundy and Shimizu, 1991; Jerram et al., 2018; Ubide et al., 2014). Gawronska et al. (in prep; chapter 3 of this dissertation) recently evaluated the presence of crystals with distinct petrogenetic histories in lunar basalts 10057, 12038, 12043, 15085, 15556, and 70017. They investigated the presence of autocrysts which formed in the carrier magma, antecrysts which formed in a separate, petrogenetically related magma, and/or xenocrysts that are not petrogenetically related to the carrier magma (Davidson et al., 2007; see also Zellmer, 2021, for a recent review). For example, pyroxene grains crystallizing from a melt in a closed system as autocrysts would be expected to record normal zoning from core to rim with Mg decreasing and Fe increasing. If, however, a pyroxene grain was transferred to a new magmatic environment, that grain could either react and preserve a resorption texture, or continue to grow but record a distinct chemical zone with a "step" in its Mg-Fe profile (an antecryst: Cashman et al., 2017; Jerram and Davidson, 2007; Jerram et al., 2018). Gawronska et al. (in prep; Chapter 3) identified antecrystic pyroxene populations in at least 4 of the 6 samples they studied. Given the location of these studied samples, they represent different magmatic systems which operated at different times across the lunar surface.

On the lunar surface, the upper layers of basaltic flows have been destroyed through continuous weathering by meteoroid and solar wind bombardment, and are now covered by regolith spanning from meter sized boulders to sub-millimeter sized dust (Lucey et al. 2000; Lucey et al 2006; McKay et al 1991;). As a result, it is challenging to near impossible to study most of the lunar lava flows directly in the field by either well-planned extravehicular astronaut activity, or by robotic spacecraft. For this reason, it is important to evaluate any samples returned from the lunar surface using modern methodologies, and novel frameworks of understanding. The work completed here aimed to expand on the recent application of XCT by Gawronska et al. (2022), and the evaluation of distinct crystal populations by Gawronska et al. (in prep; chapter 3 of this dissertation) in order to evaluate

a specific mare basalt suite in greater detail. Through this, we traced the petrogenetic history of this sample suite from surface to source by first evaluating 3D microstructures via X-ray computed tomography (XCT). This approach investigated basaltic lava flow emplacement mechanisms. Seeing as rocks are three dimensional objects, they can be (and should be) analyzed and interpreted as such, particularly when rare samples are the focus of study. Previous studies have demonstrated the utility of this technique within the context of studying terrestrial (Blundy and Cashman, 2008; Cnudde and Boone, 2013; Ketcham and Carlson, 2001; Withers et al., 2021) and extraterrestrial systems (Friedrich et al., 2008; Hanna and Ketcham, 2017; Hanna et al., 2015; Uesugi et al., 2010). Next, we applied traditional petrographic and geochemical approaches to characterize melt solidification regimes and evaluate the magmatic processes operating during crystal growth (i.e., assimilation). In-situ major element data was integrated with trace element to assess the petrogenetic histories of each mineral phase; for example, crystallization of pyroxene from a more Mg-rich, mafic melt would be complemented by lower concentrations in light REEs, compared to crystallization in a more compositionally evolved (Si-rich, Mg-poor) melt. The investigation of trace elements also permitted us to evaluate whether potential growth zones of fast-diffusing elements (e.g., Mg-Fe in olivine and pyroxene) were obscured by diffusion, but were otherwise preserved by slow-diffusing elements (e.g., Ti in pyroxene, Cherniak and Liang, 2012).

4.2 Methods

4.2.1 Site description

All samples collected during the Apollo 11 mission were collected from the weathered surface of Mare Tranquilitatis on the near side of the Moon (Fig. 1a). Mare Tranquilitatis is one of the major lunar basaltic outflows which fill a basin generated earlier by impact processes. While Mare Tranquilitatis lava flows range in age from 3.39 to 4.23 Ga, most have been dated to between 3.6 and 3.7 Ga (Hiesinger et al. 2011). All sampled flows from the Apollo 11 mission can be classified as high-Ti (> ~6 wt. %; see Sato et al., 2017 for more information), and have lower abundances of radiogenic elements (e.g., Th) than mare basalts on the western lunar near side (see Lawrence et al., 2002; 2007). The Apollo 11 mission landed on the southwestern edge of Mare Tranquilitatis, approximately 50 km from the nearest lunar highlands materials and ~400 m west of the aptly named West Crater (Hess and Calio, 1969). Specifically, the lunar module landed between rays of ejecta from West Crater in an area relatively free of coarse blocks (~5 m); the site was covered by regolith ranging from dust-sized materials to blocky craters ~1 m in diameter (Shoemaker et al., 1969). Materials found included "fine-grained vesicular crystalline igneous rock," "medium-grained crystalline igneous rock," "breccia," and "fines" (Hess and Calio, 1969).

4.2.2 Sample descriptions and previous work

The Apollo 11 high Ti, high-K suite (also referred to as the Apollo 11 group A basalts) was specifically chosen for this study. This group includes the following samples: 10017, 10022, 10024, 10049, 10057, 10069, 10071, 10072. This chemically distinct suite is made up of fine grained to very fine grained vesicular rocks. All exhibit whole rock wt. % TiO_2 >8 wt. %, (e.g., Jerde et al., 1994). They are also the only high-Ti basalts which preserve elevated K contents (> ~0.2 wt. % K_2O, e.g., Jerde et al., 1994) relative to other mare basalts collected during the Apollo, Luna, or Chang'e 5 missions. Beaty and Albee

(1978) describe the Apollo 11 group A basalts as "isotopically, petrologically, chemically, and texturally " distinct from the remaining Apollo 11 samples. Papanastassiou et al. (1977) additionally showed that, based on Rb-Sr systematis, the Apollo 11 group A originated from a geochemically distinct mantle source region, and erupted at a later time relative to other Apollo 11 samples; they have been dated to ~3.59 Ga (summarized in Snyder et al., 1994). Based on this, it has been previously theorized that group A basalts are all petrogenetically related and originated from one magmatic system (Fig. 1b). Thus, they offer a unique opportunity to investigate a suite of petrogenetically related lunar magmas which potentially experienced KREEP assimilation prior to emplacement on the lunar surface (e.g., Jerde et al., 1994). This provides and important framework for the investigation of lava flow properties and crystallization histories via XCT (described further below).

During Apollo 11, West crater (33 m in diameter and 6 m in depth), was visited by astronaut Armstrong near the end of the mission. This is the only crater that was found to have a pile of blocks on the crater floor, which were later taken to indicate that the floor of this crater lies near the base of the regolith (LSPET, 1969) and thus may be close to the original lava flows. In turn, this was also taken to suggest that the depth of regolith at the Apollo 11 landing site is up to 6 m. Because all other craters visited during this mission were ≤1 m in depth, little information regarding field context for the lava flows sampled during Apollo 11 exists.

4.2.3 Petrophysical characteristics

Two methods were used to investigate and characterize the petrophysical characteristics of the Apollo 11 group A basalts: XCT and polarized light microscopy. XCT allowed for the evaluation of sample volumetric mineralogies and vesicularities, potential foliations/lineations, and the size distributions of select phases (e.g., oxides and vesicles). XCT has been widely used on a variety of terrestrial and extraterrestrial materials with the method recently optimized for the specific study of lunar samples (Gawronska et al., 2022). For additional information see Cnudde and Boone (2013), Hanna and Ketcham (2017), and Withers et al. (2021).

Briefly, as a sample is scanned, X-rays interact more with relatively heavier elements with dense electron clouds (e.g., Fe, Ti). These in turn attenuate X-rays at a rate greater than other elements (i.e., Hanna and Ketcham, 2017). As a result, these elements produce higher grayscale values at corresponding voxels (volume elements; essentially 3D pixels) in the acquired images. This allows for voxels to be assigned distinct components using the Blob3D program (i.e., mineral phases, see Gawronska et al. 2022; Ketcham, 2005). Once segmented, the voxels in each component are separated into individual particles whose three-dimensional attributes were then extracted (i.e., volume, shape-preferred orientation). From this, volumetric mineralogies and vesicularities were calculated. Particle volumes were then used to calculate particle size distributions (PSDs, Bergantz et al., 2017; Friedrich et al., 2008). This was completed using the worksheet 3DSD and following the process described by Gawronska et al. (2022; chapter 2 of this dissertation). PSDs determined from 3D data can be readily compared to crystal size distributions (CSDs) generated from 2D thin section analysis in order to 1) evaluate the cooling regime of a sample and 2) assess how crystal and vesicle contents may have

influenced lava emplacement (e.g., Bergantz et al., 2017; Higgins 2000; Morgan and Jerram 2006). For a given mineral phase, (e.g., oxides) PSDs were established by plotting crystal (or vesicle) size vs. population density as proxies for crystal (or vesicle) growth and nucleation rates, respectively (Higgins, 2000; Morgan and Jerram, 2006). The resulting plot facilitates the identification of cooling regime change(s). If the plotted slope is constant, no change was experienced. However, if the slope is kinked, this is indicative of a change in the magmatic environment. For example, a cooling magma may experience a sudden change in either chemistry (i.e., due to mixing with another magma in an open magmatic system) or cooling environment (i.e., due to eruption; Donohue and Neal, 2015; Magee et al., 2010; Morgan and Jerram, 2006; Pupier et al., 2007). Alternatively, if the PSD profile is curved, then the magma experienced a change due to crystal fractionation or accumulation. Both of these can occur in closed magmatic systems (e.g., Donohue and Neal, 2015; Neal et al., 2015; Pankhurst et al., 2018). Meanwhile, a rapid change in either chemistry or cooling regime will result in a kink in PSDs.

Light microscopy (LM) and scanning electron microscopy (SEM) were subsequently used to evaluate sample textures and mineralogies. LM was performed on a Leica DM2700 P polarizing light microscope in-house at the Miami University Department of Geology and Environmental Earth Science, while SEM work was conducted on a Zeiss Supra 35 VP FEG SEM at the Center for Advanced Microscopy and Imaging (CAMI), also at Miami University. The SEM was used to collect backscatter electron (BSE) images of entire sample thin sections to assess textural details not visible through LM, and to acquire elemental maps of major and minor species (e.g., MgO, FeO, SiO_2, CaO, Al_2O_3, NaO, K_2O, TiO_2) via energy dispersive spectroscopy (EDS). In both cases, a current of 25 nA and accelerating voltage of 25 keV at a working distance of 8 mm were used. Combined, these techniques allowed for comprehensive characterization of textural features not visible via LM, and for the qualitative assessment of major (and minor) elemental abundances within the context of textural features.

4.2.4 Geochemistry (EPMA+LAICPMS)

In-situ quantification of major silicate phase elemental contents followed study by LM and SEM. LM and SEM investigations were used to identify texturally distinct crystal populations (i.e., those with resorbed contacts between growth zones, and those without) for subsequent geochemical analysis. In situ quantification of major element abundances in representative plagioclase feldspar and pyroxene crystal populations were collected via electron probe microanalysis (EPMA) on a CAMECA SX-100 at the University of Notre Dame. Representative crystals of appropriate size (>100 µm to accommodate laser spot size) were further investigated via laser ablation inductively coupled plasma mass spectrometry (LAICPMS) at the University of Arkansas TRace element And Radiogenic Isotope Laboratory (TRAIL) using a NWR193 excimer-based laser system coupled to a Thermo Icap Q ICPMS, using a spot size of 50 µm. These techniques follow standard methods established for analysis of silicate materials.

4.3 Results

4.3.1 Petrography

The Apollo 11 group A basalts vary in texture from very fine grained (average grain size of ~50 µm) to fine grained (average grain size of ~ 500 µm; Fig. 2). Specifically,

samples 10049 and 10069 both have an average grain size of ~50 microns, with regions of slightly coarser-grained material (Fig. 3). Samples 10022, 10024, and 10072 are relatively coarser grained with an average grain size of up to 500 µm in maximum length. The average grain sizes of samples 10017 and 10071 lie in between these two. All samples studied are vesicular, vuggy, and hypocrystalline containing ~5% mesostasis. The grains range in texture on a mm to cm scale, such that most samples preserve up to three texturally distinct domains (Fig. 3). Generally, one domain in each sample is dominated by tabular, embayed grains of ilmenite, interstitial feldspar, and notably larger pyroxene (up to 200-300 µm; Fig. 2a-b); this domain will be referred to a "region 1" hereafter. Samples 10022, 10024, 10049, 10071 and 10072 also contain domains associated with a higher component of mesostasis, acicular ilmenite, feldspar grains that range from columnar/acicular to equant and euhedral in habit (Fig. 3c-d), which will be referred to as "region 2". We found sample 10071 to additionally preserve a clear igneous contact with a separate component made up of greater mesostasis and acicular grains, which previous authors named "iota" (Beaty and Albee, 1978; Fig. 3e-f). In samples 10049 and 10069, a third texturally distinct domain exists that appears to be a finer-grained matrix version of the texture with tabular ilmenite/feldspar and little mesostasis (Fig. 3g-h), though modally it may contain more ilmenite than the primary domain. This matrix domain will be referred to as "matrix 1" hereafter (Fig. 3). There is an additional, even finer-grained region in 10069 which we will refer to as "matrix 2" (Fig. 3). In region 2, mesostasis is interstitial (i.e., Fig. 4a-b), and grains which are nearby the mesostasis have rare pyroxene/feldspar coronas (Fig. 4c-d). The gradation between these texturally distinct regions is not gradual (see Fig. 4), and XCT analysis indicates that they permeate the samples and do not define a stratification (Fig. 5). Instead, there may be a stratification from the finer-grained region we term "matrix" which doesn't appear to exist in the coarser-grained regions, and vice-versa the coarser "region 1" is rarely represented in the finer grained samples (i.e., bottom of Fig. 5d).

From XCT analysis, it was also possible to assess sample volumetric modal content, which broadly supports previous work for the coarser samples (10017, 10022, 10024, 10071, and 10072; Table S1). It was not possible to separate mesostasis from feldspar due to their similar grayscale values (i.e., Fig. 5), thus variation in numbers reported in Table S1 for those samples stems from the challenges encountered in separating glass from other components. Samples 10049 and 10069, meanwhile, may be too fine grained for accurate component analysis – both returned numbers that are inconsistent with previous work (Table S1). In all Apollo 11 group A samples, ilmenite is often poikilitically hosted within pyroxene. In the case of XCT work as it pertains to finer grained samples, such ilmenite may not have been individually distinguished, but rather included in the pyroxene component, incorrectly summarizing sample modal proportions. Nonetheless, the remaining samples accurately summarize sample components, which we interpret as confirmation that particles were successfully segmented, separated, and extracted. This allowed for further analysis of PSDs (Fig. S1). Pyroxene and feldspar are generally highly intergrown in the sample and could not be analyzed via PSD, but it was possible to investigate ilmenite which generally grew as individual grains, in samples 10017, 10024, 10071, and 10072. From PSD analysis, the volume fraction of ilmenite in these samples is split into two populations, one that is larger in diameter and one that is smaller (Fig. S1). Including both populations in PSDs generated by 3DSD (Gawronska et al., 2022; the second chapter of this dissertation) generates bin sizes that are too large to effectively

investigate the size distribution of the smaller particle sizes. Thus, the most voluminous particles/clusters were removed for PSD analysis (n<10 removed in all samples). The resulting PSD plots of the smaller population are presented in Fig. S1 – all samples preserve an upwards curve which represents either accumulation or textural coarsening (Donohue and Neal, 2015; Marsh, 1998; discussed further in section 4.4).

Pyroxene is seriate in the coarser samples (10022, 10024, 10072); the relatively largest pyroxene grains are also incorporated into the finer-grained samples as either phenocrysts (10049) or glomerocrysts (10057; Gawronska et al., chapter 3 of this dissertation). The largest pyroxene grains (>200 μm) range in texture from normally zoned grains with core ilmenite inclusions (Figs. 2-4), to grains that preserve evidence of resorption/reaction (Fig. 4c-d). Smaller matrix grains (<100 μm) similarly range from grains that appear to be unassociated with mesostasis to grains that preserve small-scale evidence of reaction through ragged contacts between growth zones. Small pyroxene grains (<50 μm) are also occasionally antiophitically included in feldspar grains as chadacrysts (Fig. 2).

The habit of plagioclase feldspar ranges greatly throughout the sample suite. The largest (up to 700 μm) plagioclase grains are subhedral to tabular and contain inclusions of ilmenite or pyroxene (Fig. 2c-d). Smaller grains (~100 μm) exist as acicular rods in mesostasis (Fig. 3c-d), as euhedral, equant tabular grains that are also associated with region 2 (bottom of Fig. 3c-d; top of Fig. 4c-d). Plagioclase feldspar grains are rarely associated with mesostasis, but when they are, they are sometimes intergrown with silica in myrmekitic/micrographic assemblages (Fig. 6).

Mesostasis throughout this suite is interstitial and ranges from cryptocrystalline to glassy (Figs. 3-4). It is clearly associated with ilmenite that displays tabular and embayed habits. As revealed by SEM-EDS, the mesostasis is K-rich and associated with trace phosphate and troilite (Fig. 6). Additionally, SEM-EDS study reveals that some pyroxenes contain relic Mg-rich olivine cores and complex zoning patterns, with initial growth later overgrown by a slightly lower Ca compositions, and final Fe-rims (i.e., Fig. 6a-b). From SEM-EDS work, no significant compositional change in plagioclase feldspar, of any texture, was observed here.

4.3.2 Geochemistry

Major element analyses of pyroxene compositions throughout this suite indicate that pyroxene compositions range from pigeonite to augite (Fig. 7). The pigeonites tend to be larger in size (up to 500 μm) in medium grained samples (10024, 10072). In finer grained sample 10049, three pigeonite grains are distinctly coarser grained than the remaining pyroxene population in 10049 and associated with the domain “matrix 1” (seen in Fig. 2a-b) and are interpreted to be either autocrysts or antecrysts (see discussion later). Specifically, these pigeonites in 10049 are >200 microns, while matrix pyroxenes are 50 to 100 microns. From LA-ICP-MS, pigeonite grains are low in Sc (<60 ppm) relative to all other analyzed grains in this sample suite (>80 ppm), and are relatively depleted in all REE’s (Fig. 7) but are not otherwise compositionally distinct from augitic pyroxenes. The only pyroxene chadacryst (grain poikilitically enclosed in a feldspar) analyzed in this work is also of pigeonite composition. Of the 68 pyroxene grains whose trace element content was analyzed, 38 were large enough for rim analysis (all representing the largest textures).

Rims of all grains are generally augitic in composition, with few grading into the pyroxene "forbidden zone" (Lindsley, 1983). Rims of all grains regardless of region are generally variably lower in Mg# and higher in P_2O_5 than their cores. All grains analyzed also decrease variably in Cr and Sc from core to rim, except for the pigeonite cores, which have low Sc core contents and increase by ~40 ppm at the rim (Fig. 7). The coarser pigeonite grains from 10049 are depleted in REEs in their cores relative to all other grains analyzed here as part of the Apollo 11 group A suite (Fig. 7). Throughout the studied suite, pyroxene grains otherwise do not preserve any correlation between their observed textures and their major and/or trace element signatures (Fig. S2). In terms of their relation to the regions described above (section 4.3.1), region 1 consistently contains grains that are generally more primitive. Most (but not all) pyroxenes in this region cluster around Mg# 70, 0.6 wt. % Cr_2O_3, 15.5 wt. % CaO, and and highly variably trace element contents (i.e., 33 to 147 ppm Sc, 7.3 to 277.8 ppm Y, and 1 to >20 ppm Hf; Fig. 7), with Eu/Eu* values ranging from 0.44 to 0.05, with an average of 0.15 and median of 0.13 (n=37). Grains from "iota" in 10071 are somewhat more evolved, with generally lower Mg# (all <63), Cr_2O_5 (all <0.4 wt. %), CaO (group average of 12.2 wt. %), trace element contents that are comparable to the first region (i.e., 90.0 to 148.6 ppm Sc, 106.8 to 278.6 ppm Y, and 4.7 to 12.6 ppm Hf; Fig. 7), and Eu/Eu* ranging from 0.27 to 0.08, with an average of 0.12 and median of 0.08 (n=5). Pyroxenes from the remaining texturally distinct regions (region 2, matrix 1 and 2) range in composition between region 1 and "iota", thus, no pyroxenes associated with any domain are compositionally distinct, except for the pigeonites. The largest pyroxene grains in at least sample samples 10024, 10071, and 10072 also host rare relic olivine (Fo_{52-68}) cores.

When evaluated within the context of the grain textures described in section 4.3.1, no clear relationships exist between texture and either major or trace element contents in plagioclase feldspar. With the exception of grains intergrown with silica (n=9), all feldspars analyzed (n=75) are generally low in K_2O (<0.4 wt. %), Ba (<500 ppm), and Sr (<1000 ppm; Fig. 8). Plagioclase feldspar grains intergrown with silica are elevated in K_2O by ~0.5 wt. % and are generally lower in An (most $<An_{75}$) relative to other grains. Out of the 84 grains analyzed via EPMA and LA-ICP-MS, 26 were large enough for core and rim analyses via LA-ICP-MS (representing only the largest feldspar grains). From feldspar Ab-An systematics, at least two compositionally distinct populations of plagioclase feldspar are preserved in at least samples 10017, 10024, 10049, 10069, and 10071 – one normally zoned, and one reversely zoned (Fig. S3). The reverse population is generally composed of the largest plagioclase feldspar grains (100 to 200 microns) that poikilitically to sub-poikilitically enclose small pyroxenes. Both the normal and reverse An groups increase in variable amounts of Sr from core to rim. Otherwise, rim analyses indicate that grains preserve complex relationships from core to rim that generally do not appear to be associated with documented textures or sizes. For example, some grains decrease by up to ~0.4 wt. % MgO while others increase by up to 0.8 wt.% from core to rim. Some grains increase by 50 to 100 ppm Ba from core to rim, while others decrease by ~50 ppm Ba. When considered within the context of the regions described above, however, some spatially-related compositional differences emerge. Namely, feldspar grains in region 1 cluster at An_{80} and are generally poor in K_2O (most ~0.2 wt. %), Ba (most ~125 ppm), and Rb (most ~0.25 ppm; Fig. 8). These grains also have elevated positive Eu anomalies at an average value of 11.5, a median of 12.7 (n=31), though many cluster around a value of ~20

(Fig.8). Grains in the "iota" domain defined by Beaty and Albee (1978) preserve the opposite story – they average An_{76}, and are relatively elevated in K_2O (most >0.5 wt. %), Ba (all analyzed >350 ppm), and Rb (all analyzed >2.6 ppm), with an average Eu anomaly of 0.33 and a median of 0.12 (n=6; Fig. 8). Grains in region 2 compositionally range between these two domains (Fig. 8), and have positive Eu anomaly values of 4.7, at a median of 1.8 (n=14). Grains from the finer-grained matrix 1 domain existing in 10049 and 10069 similarly range between those two domains (Eu/Eu* average = 4.7, median 1.8, n=14; Fig. 8). Chondrite-normalized (after Sun and McDonough, 1989) spidergrams in Fig. 8 additionally indicate that feldspar grains in "iota" are elevated in REEs relative to most grains from region 1, while grains associated with region 2 range in composition between the compositions of feldspars from the other two domains. Interestingly, a number of plagioclase feldspar grains investigated record negative Eu anomalies (Fig. 8).

It was also possible to analyze the Si-rich phase in samples 10017, 10022, 10069, and 10071 via EPMA (n=13). Based on these analyses, the Si-rich phase in the Apollo 11 group A suite has an average composition of 96 wt. % SiO_2, 1.3 wt. % Al_2O_3, 0.3 wt. % CaO, and 0.3 wt. % TiO_2 and FeO, and 0.2 wt. % Na_2O (Fig. S4). Two Si-rich grains were large enough (>35 um) for trace element analysis. While both of these grains are Si-rich (96 and 97 wt. % SiO_2), the latter has triple the K_2O content (0.012 vs. 0.004 wt. %) – this elevated K_2O content is consistent with corresponding trace elements which are all also systematically higher. This relatively high-K grain is proximal to nearby mesostasis.

Based on 31 analyses across the samples studied, the mesostasis in this suite ranges in composition (Fig. S4), but has an average composition of 65 wt. % SiO_2, 20 wt. % Al_2O_3, 9 wt. % CaO, 2 wt. % FeO, 2 wt. % Na_2O, 1 wt. % K_2O, and 0.2 wt. % P_2O_5. Notably, K2O and P2O5 contents are positively correlated (Fig. S4). 11 locations of mesostasis were large enough for analysis via LA-ICP-MS; K_2O is positively correlated with Rb and Ba, with all REEs (La through Lu), and with Th and U.

4.4 Discussion

4.4.Textural insights into petrogenesis

Expanding on previous studies, which were based on 2D examinations of thin sections (i.e., Beaty and Albee, 1978; Xue et al., 2021), comprehensive textural investigations in both 2D and 3D significantly expand our understanding and ability to document texturally distinct regions within the Apollo 11 group A basalt suite in this work. If samples are indeed from one flow, this work indicates that 10049 and 10069 make up the crust of the flow, while remaining samples make up the core of the flow. In Fig. 5b, we have outlined a portion of 10069 where two regions are distinct – one to the left with no vugs, and one to the right that may be minimally coarser grained and contains diktytaxitic voids, which exist partially between grains. This distinction permeates the sample. Diktytaxitic voids are generally associated with the transition between the crust and the core of a lava flow lobe (Hon et al., 1994; Self et al., 1998), thus this distinction in 10069 may represent a transitional portion of this sample. Such voids are not clearly distinguishable in any other sample studied here via XCT. Meanwhile 10049 is slightly finer grained than 10069, so we interpret it having formed at a higher stratigraphic locations within the context of the lava flow (not necessarily in the same location laterally). Remaining samples must represent the flow core – they are coarser grained, and preserve

rare well-rounded vesicles indicating that there was time for gas to collect and for grains to crystallize (i.e., Gawronska et al., 2022; Rumpf et al., 2020). Interestingly, 10049 may host an enclave, as a sharp contact is seen in Fig. 5d. This is consistent with recent work of Gawronska et al. (2022) who found an enclave in 10057, a member of the Apollo 1 group A suite that was not analyzed as part of the present study.

By comparing thin section analysis with XCT, the work presented here significantly expands on this by identifying distinct domains within the suite. Specifically, we identify at least four texturally distinct domains in the Apollo 11 group A basalts which exist within at least two or more samples: one texture that is relatively coarser than the other two (region 1 in 10017, 10022, 10024, 10071, 10072), one texture that is fine grained but not dominated by acicular grains (matrix in 10049 and 10069), and one texture that is dominated by acicular grains, and contains greater mesostasis (region 2 in 10022, 10024, 10071, and 10072), in addition to "iota" identified by Beaty and Albee (1978) and also documented here. As previous workers have pointed out, these regions are "mappable" as shown in figure of this (Figs. 3 and 5). The coarser region 1 is interpreted as having cooled relatively slowly, as it is defined by subhedral to euhedral tabular grains (i.e., Usselman et al., 1975). From Beaty and Albee (1978), a distinct fine-grained region exists in sample 10024, and contains a modally greater proportion of ilmenite; this region is compositionally more primitive (i.e., higher plagioclase An content, and higher pyroxene Mg#). Such a region was not found here. It is important to note that only the samples interpreted to represent the core preserve any evidence of region 2 – samples 10049 and 10069 were not found to contain this domain, even though their grain size varies otherwise (i.e., Figs 2-3). The significance of this is discussed in 4.4.3.

Region 2 composed of acicular grains, which is present throughout 4 of the 7 studied samples, is interpreted here as having cooled relatively rapidly based on acicular crystal habits (Usselman et al., 1975). Of the Apollo 11 samples studied by Beaty and Albee (1978), this distinct region was only identified in sample 10022 (see Fig. 5c here), and identified on the basis of ilmenite habit and a greater modal proportion of mesostasis compared to other samples: 9.9% vs. ~5%. We suggest that this region occurs in other suite samples, as the correlation between the occurrences of acicular ilmenite, plagioclase, and mesostasis alongside reaction contacts in pyroxene is unlikely to be a coincidence. Specifically, this textural domain is present in samples 10022, 10024, 10049, 10071 (not near "iota"), and in 10072 , and is documented here both in 2D and in 3D. We suggest that the presence of this domain is therefore a significant feature of the Apollo 11 group A basalts suite and should be considered in the future when evaluating potentially petrogenetically linked samples, and in the characterization of basaltic clasts in lunar meteorites.

The textures associated with the relatively mesostasis-dominated domains (region 2) appear similar to the "unique" igneous contact identified in 10071 (Fig. e-f; see also Drake and Weill, 1971), named "iota" by Beaty and Albee (1978), who found that grains within this region (Fig. 3e-f) are compositionally more evolved than those throughout the remaining sample. As reported by Beaty and Albee (1978), the composition of "iota" can be related to the remainder of 10071 through 40% fractional crystallization of early forming phases. Prior to that work, Drake and Weill (1971) had postulated that "iota" may represent

an “intermediate liquid” that was injected into an already-solidified lava flow or crustal lava pond. Their hypothesis may potentially explain a plastically-deformed pyroxene grain identified in this study (see Fig. 2g-h). However, because only one contact is seen in either thin section (Fig. 3e-f) or XCT (potentially the top of Fig. 5h), it is impossible to distinguish whether this contact marks an injection, an enclave, or a xenolith. From the work of Usselman et al. (1975), “iota” cooled far more quickly than region 1 of the remaining samples and Beaty and Albee (1978) later argued that if “iota” had been injected while the original lava was still cooling, then the two would have similar cooling histories, thus “iota” must be a later injection or potentially an enclave.

More recently, Xue et al. (2021) summarized that the textures of all Apollo 11 basaltic groups (of which there are 5; i.e., Jerde et al., 1994) can be accounted for through a complex interplay between cooling rate, bulk composition, and nucleation density during crystallization. Within the context of the samples studies here, Xue et al. (2021) found that group A (with the exception of 10072), preserved the fastest cooling rates of all the Apollo 11 samples. For sample 10072, using evidence of coarsening in plagioclase feldspar along with relatively slower cooling rate (based on feldspar and ilmenite CSDs), Xue et al. (2021) concluded that the Apollo 11 group A must have cooled in a relatively thick flow to produce the textures seen 10072. This generated a continuous range in grain sizes across the suite (ranging from 30 to 250 μm), which is consistent with the work presented here and with previous work (i.e., Beaty and Albee, 1978). As presented in the results, PSDs completed here on samples 10017, 10024, 10071, and 10072 all preserve two populations of ilmenite based on the fraction of ilmenite volume associated with given grain length (Fig. S1). The populations with smaller diameters were plotted via PSD and all four samples may preserve evidence of coarsening, expanding on the work of Xue et al. (2021). PSD’s were completed here on >10,000 particles per sample, thus providing more robust datasets which may have preserved a more complete record of Apollo 11 group A sample cooling histories.

4.4.2 Geochemical insights into petrogenesis

In Beaty and Albee (1978), bulk rock compositions of the Apollo 11 group A samples were used to evaluate their potential association through closed system fractionation. They found that the fractionation of either ilmenite/armalcolite or pyroxene/olivine accounts for all samples, and further argued that cooling rate of the Apollo 11 group A basalts as determined by grain size is independent of the fractionation trend. This indicates that differentiation must have occurred at depth prior to final emplacement. The authors further argued that such a system could be achieved in a shallow chamber that was continuously fractionating material during the eruption, so that the collected samples represent lateral variation away from the vent as melt compositions continued to change.

Plagioclase feldspar displays a variety of textures throughout this sample suite. However, Xue et al. (2021) recently found that feldspar CSDs preserve lower slopes than ilmenite indicating that feldspar may have cooled more slowly, which could account for the variety of sizes and textures. This is consistent with experimental work of Grove and Beaty (1980). Furthermore, Xue et al. (2021) found that plagioclase feldspar in 10072 and 10017 preserves evidence of coarsening, suggesting that both of these samples likely crystallized over a longer period of time, near the flow core, which is consistent with out

ilmenite PSDs. Overall, grain compositions as they relate to texture were not found here to be chemically dissimilar, while grains in distinct domains are not significantly distinct either in major or trace element content (other than Eu/Eu* in plagioclase feldspar). This is consistent with the work of Beaty and Albee (1978) who used EPMA analysis to conclude that sample cooling rates (as determined by crystal sizes) are independent of bulk compositions. Based on feldspar compositions, it is apparent that some K-rich material worked to enrich some of the feldspar rims in K_2O relative to other grains, but plagioclase feldspar was not generally affected otherwise. The only feldspar grains whose core compositions are markedly different are those intergrown with silica. Such intergrowths are related to interstitial mesostasis and domains of blady ilmenite, further indicating the distinct nature of these domains. Additionally, this may suggest that incorporation of the K-rich material concentrated in mesostasis occurred after plagioclase feldspar and pyroxene had mostly crystallized, which would be consistent with the infiltration hypothesis of Drake and Weill (1971). Note that Beaty and Albee (1978) refer to the Si component as cristobalite.

Pyroxene grains, meanwhile, do not appear to have been affected by the K-rich material during growth, instead preserving evidence of later reaction (i.e., Fig. 4). Pyroxenes are not clearly distinct when related to either grain texture or domain, other than the large pigeonite grains which are more primitive (i.e., elevated Mg# and low CaO; Fig. 7). Because the pyroxene chadacryst analyzed here is also pigeonitic in composition, the pigeonites are generally interpreted to represent an early stage of crystallization. As a result, it is noted here that the pigeonites may be characterized as antecrysts based on the work of Zellmer (2021). Meanwhile rare olivine cores contained in some pyroxenes were found to be in equilibrium with the host melt by Beaty and Albee (1978), consistent with them having formed earlier in the melt and the melt preserving evidence of a single cooling history in a closed system. Interestingly, some matrix pyroxenes (i.e., in 10049) also have pigeonite compositions, but most are augitic. Importantly, both large and small augite grains that appear to have reacted with mesostasis-related melt have the same core compositions as those grains which do not appear to have been affected by such an interaction, again indicating that augite and pigeonite compositional differences are not the result of incorporation or interaction with K-rich material. The few pigeonites found here have augite rims, and thus grew in a changing magmatic environment likely as a result of typical fractionating processes. Interestingly, a few augitic core grains did develop pigeonite rims, which may indicate some inhomogeneity in the melt during growth, and crystals moving through said regions of inhomogeneous composition.

By definition, early-formed grains (i.e., pigeonites) should be removed from the remaining melt in a fractionating system. However, a few of the pigeonites found here were primarily found as having been incorporated into 10049 and 10069 (Figs. 2a-b, 5a-b,e). Sample 10049 is the most evolved basalt collected as part of the group A suite, according to the work of Beaty and Albee (1978). Thus, physical mechanisms associated with the generation of this suite may be more complicated, having led to the incorporation of an earlier crystal generation into a later-formed lava. Neave and Maclennan (2020) argue that it is more difficult to mobilize earlier-formed, relatively more refractory grains by relatively more evolved melts, relative to the ability of primitive melts to mobilize more evolved crystal cargoes. Interestingly, while the pyroxene record here does not show a

reversal in compositions from core to rim, the grains of all samples preserve a decrease in the compositional change recorded from core to rim, so that some grains change drastically in composition from core to rim, while others only minimally (Fig. 7). This change is not tied to a textural region. Instead, it may be motivated by a minor change in the melt, which could theoretically be explained by processes such as convection or minor replenishment from below with more primitive magma (not necessarily recharge since compositions between grains are not significantly distinct). Due to the fine-grained nature of this sample suite it is difficult to evaluate fine-scale compositional changes that could result from a process such as convection. On the other hand, introduction of a minor amount of more primitive melt could generate pockets of primary material which would address the finer-grained, Mg-rich material that Beaty and Albee (1978) found in 10024, which was not found here. This would also be consistent with the findings of Gawronska et al. (in prep, chapter 3) who found a pyroxene glomerocryst that was reversely zoned in Cr, and interpreted to represent a distinct stage of growth in an evolved environment, being plucked from a mushy lens by more mafic melt (Gawronska et al., chapter 3 of this dissertation). Introduction of primitive melt is often invoked on Earth as an eruption trigger in small systems (Huber et al., 2011, Lissenberg and MacLeod, 2016; Sparks et al., 2019; Ubide and Kamber., 2018), so this would also provide a potential eruption trigger for this lava.

4.4.3 Incorporation of KREEPy material

Using bulk rock compositions, Beaty and Albee (1978) were able to relate all members of the Apollo 11 group A by fractionation. They argued that 10049 is the most evolved sample, while 10024 is the most primitive. 10049 can be derived from 10024 by fractionation of about 10% armalcolite and/or ilmenite, along with olivine and/or pyroxene. Rocks 10024, 10071, 10017, 10057, and 10049 also plot similarly in in terms of their CaO and TiO_2 content. Meanwhile, 10022 and 10072 can be related to the group by additional fractionation of armalcolite/ilmenite, while 10069 can be related by fractionations of pyroxene/olivine. Rb-Sr work by Papanastassiou et al. (1977) supports the group A distinction from the remainder of the Apollo 11 basalts. A simple explanation may be a differentiated lava flow, but this would suggest that sample composition can be tied to stratigraphic location in the flow as it relates to texture, which has been demonstrated to not be the case here and elsewhere (Beaty and Albee, 1978). This is specifically because XCT confirms the stratigraphic locations of 10049 and 10069 with relation to the coarser samples, but their mineral compositions are not sample-distinct despite any inferred stratigraphy (Figs. 7-8). Thus, differentiation must have occurred prior to emplacement. From this, Beaty and Albee (1978) argued that the Apollo 11 group A samples may have formed by continuous differentiation of a shallow magma chamber where phases were progressively fractionating out to produce the subsequently more evolved basalts.

More recently, Jerde et al. (1994) evaluated Apollo 11 group A basalt bulk rock compositions (collected via instrumental neutron activation analysis, or INAA) to further evaluate the incorporation of KREEPy material. They found that while the Apollo 11 group A samples indeed likely form one lava flow whose mantle source region is distinct from the remaining Apollo 11 rocks, based on bulk rock rare earth element contents (which were not analyzed in-situ by Beaty and Albee, 1978), this suite must have incorporated a KREEPy component. They term this component neu-KREEP, and suggest that it may have originated as an evolved cap to a Mg-suite pluton (examples of plutonic activity were also

collected during Apollo 11; Jerde et al., 1994). However, is such melt was incorporated at depth, and if these flows crystallized primarily on the lunar surface as was proposed by Xue et al. (2021), then K-rich compositions should be reflected in the growing feldspar and pyroxene populations, for example as elevated K_2O and P_2O_5 content, which is not the case here. Instead, K-rich/KREEPy material is relegated to "iota" and to interstitial pockets of mesostasis with distinct cooling histories as has been discussed above. The work of Beaty and Albee (1978) shows that feldspar and pyroxene compositions indicate that the magma which formed the Apollo 11 group A suite likely differentiated, if not crystallized to some degree, in several stages at depth prior to emplacement to produce the progressively more evolved basalts. Thus, we suggest that the Apollo 11 group A magma differentiated and crystallized in different stages within distinct lenses at depth, some of which were mushy according to the findings of Gawronska et al. (chapter 3 of this dissertation). Specifically in this framework, the magmas may have continued to fractionate at depth to produce mushy lenses with increasingly crystalline proportions, where melt lenses periodically collected and rose closer toward the surface (i.e., Lissenberg et al., 2019; Solano et al., 2014; Wilding et al., 2023). Thus, more primitive, crystallizing magma from below could move upwards to more evolved, but fully petrogenetically related magmas, combining components from different stages (i.e., pigeonites in 10049 and glomerocryst in 10057).

At some point, this system came in contact with KREEPy melt. Because amounts of K-rich material is low and grains associated with it are petrogenetically related to grains not associated, it may be most likely that a small amount of this material was incorporated as a partial melt generated through heating of the intruding magma, and not incorporated as a distinct liquid. Thus, the K-rich material did not permeate the primary magma. Alternatively, KREEPy melt may have been incorporated even later, via intrusion into an already-existing Apollo 11 group A lava flow. Plagioclase feldspar and pyroxene compositions are similar to other Apollo sample suites (Fig. 9) and are not dissimilar in the way that KREEP materials generally are (see the elevated K_2O contents of some Apollo 15 feldspars in Fig. 9). This late-stage incorporation/intrusion would be consistent with the hypothesis of Drake and Weill (1971) who studied "iota." Either way, incorporation of K-rich material was a late stage process. Finally, a few plagioclase feldspar grains preserve negative Eu/Eu*, which has been previously attributed to being generated through impact-related processes. It may be possible that an impact mobilized KREEPy "iota" melt and allowed it to enter the initially more pristine Apollo 11 group A flow, but future work must be done to evaluate this further. There is precedent for incorporation of K-rich material through impact-related processes in the Apollo 14 very high potassium (VHK) basalt suite, a portion of which is understood to have incorporated granitic material on the surface following impact (Roberts et al., 2019).

4.5 Conclusions and Implications

In this work, we provide new insights into the specific mechanisms involved in the petrogenesis of Apollo 11 group A basalts by providing detailed in situ analysis of major and trace element contents of silicate phases to supplement previous work on this suite. Here, texture of individual phases does not appear to have resulted from generation in compositionally distinct environments, as grains of plagioclase feldspar and pyroxene which are texturally distinct (i.e., of different sizes or habits) are not necessarily distinct. Rather, minor changes in bulk composition as a result of fractionation and KREEP

incorporation, and maybe addition of more primitive melt, have led to texturally distinct regions in the samples. Such regions range from coarser grained with little mesostasis, to finer grained matrix-type regions, to finer grained regions with distinct crystal habits and relatively more KREEPy mesostasis. This is specifically indicated by the change in grain size and habit between distinct regions, and the amount of mesostasis present in different regions. Because grains of pyroxene do not preserve evidence of changing melt composition as a result of changing melt composition, and because plagioclase feldspar only preserves distinct compositions where intergrown with silica, we argue that incorporation of KREEPy material was a late-stage process. Because this is only preserved in texturally distinct regions, we also argue that KREEPy melt did not completely homogenize or mix with the pre-existing host melt. This is supported by the fact that mesostasis primarily exists interstitially to more acicular grains within finer grained regions. As a result, this work supports previous work that shows mare basalt textures result from the interplay of bulk compositions and cooling rates (i.e., Xue et al., 2021, others). The Apollo 11 group A suite also demonstrates how inhomogeneities on the 1 mm-scale may be preserved in samples, generating local textural differences. This can be generated simply by shifting the crystals around slightly (as in the short-range unmixing theory of Lindstrom and Haskin, 1978).

4.6 Acknowledgements

We thank Dr. Ryan Zeigler and Scott Eckley at NASA Johnson Space Center for collecting the XCT datasets that were later used to interpret flow properties here. Thanks are extended to Morgan Gillis and Matt Dulley of Miami University for their support in sample carbon coating and SEM imaging, respectively, to Dr. Karl Cronberger at the University of Notre Dame for EPMA support, and to Dr. Barry Shaulis at the University of Arkansas for LAICPMS support. This work was funded in part through a GSA graduate student research grant (#13203-21) and an AGU Lawrence A. Taylor Research Fund (#19486) to AG. AG was supported by a NASA FINESST award (#21-PLANET21-0151) during this work.

4.7 References

Basaltic Volcanism Study Project (BVSP) (1981) Basaltic Volcanism on the Terrestrial Planets. Pergamon Press, Inc., New York. 1286 pp.

Bergantz, G. W., Schleicher, J. M., Burgisser, A., (2017) On the kinematics of crystal-rich systems. Journal of Geophysical Research: Solid Earth 122, 6131-6159. https://doi.org/10.1002/2017JB014218

Beaty, D. W., Albee, A. L. (1978) Comparative petrology and possible genetic relations among the Apollo 11 basalts. Proceedings of the 9th Lunar and Planetary Science Conference, 359-463.

Blundy J. D., Shimizu N. (1991) Trace element evidence for plagioclase recycling in calcalkaline magmas. Earth and Planetary Science Letters 102:2, 178-197.

Blundy J. and Cashman K. (2008) Petrologic Reconstruction of Magmatic System Variables and Processes. Reviews in Mineralogy and Geochemistry 69, 179-239. https://doi.org/10.2138/rmg.2008.69.6

Byrne, P. K. (2020) A comparison of inner Solar System volcanism. Nature Astronomy 4, 321-327. https://doi.org/10.1038/s41550-019-0944-3

Cashman K. V. (2015) Changing the paradigm – new views on magmatic systems provide new perspectives on volcanic processes. AGU, Fall Meeting 2015.

Cashman K. V., Sparks R. S. J., Blundy J. D. (2017) Vertically extensive and unstable magmatic systems: A unified view of igneous processes. Science 355, 6331. https://doi.org/10.1126/science.aag3055

Castro, J., Manga, M., Cashman, K., (2002) Dynamics of obsidian flows inferred from microstructures: insights from microlite preferred orientations. Earth and Planetary Science Letters 199, 211-226. https://doi.org/10.1016/S0012-821X(02)00559-9

Che, X., Nemchin, A., Liu, D., Long, T., Wang, C., Norman, M. D., Joy, K. H., et al. (2021) Age and composition of young basalts on the Moon, measured from samples returned by Chang'e-5. Science 374 (6569) 887-890. https://doi.org/10.1126/science.abl7957

Cherniak, D. J., Liang, Y. (2012) Ti diffusion in natural pyroxene. Geochimica et Cosmochimica Acta 98, 31-47. https://doi.org/10.1016/j.gca.2012.09.021

Cnudde, V., and Boone, M. N., (2013) High-resolution X-ray computed tomography in geosciences: A review of the current technology and applications. Earth-Science Reviews 123, 1-17, https://doi.org/10.1016/j.earscirev.2013.04.003

Cutler, K. S., Filiberto, J., Treiman, A. H., Trang, D. (2020) Experimental Investigation of Oxidation of Pyroxene and Basalt: Implications for Spectroscopic Analyses of the

Surface of Venus and the Ages of Lava Flows. The Planetary Society Journal 1, 21. https://doi.org/10.3847/PSJ/ab8faf

Davidson J. P., Morgan D. J., Charlier B. L. A., Harlou R., Hora J. M. (2007) Microsampling and Isotopic Analysis of Igneous Rocks: Implications for the Study of Magmatic Systems. Annual Reviews in Earth and Planetary Science 35, 273-311. https://doi.org/10.1146/annurev.earth.35.031306.140211

Donohue P. H., Neal C. R. (2015) Quantitative textural analysis of ilmenite in Apollo 17 high titanium mare basalts. Geochimica et Cosmochimica Acta 149, 115-130. https://doi.org/10.1016/j.gca.2014.11.002

Drake, M. J., Weill, D. F. (1971) Petrology of Apollo 11 Sample 10071. A Differentiated Mini-Igneous Complex. Earth and Planetary Science Letters 13, 61-70.

Edmonds, M., Cashman, K. V., Holness, M., Jackson, M. (2019) Architecture and dynamics of magma reservoirs. Philosophical Transactions of the Royal Society A, 377: 20180298. http://dx.doi.org/10.1098/rsta.2018.0298

Friedrich, J. M., Macke R. J., Wignarajah D. P., Rivers, M. L., Britt, D. T., Evel, D. S., (2008) Pore size distribution in an uncompacted equilibrated ordinary chondrite. Planetary and Space Science 56(7), 895-900, https://doi.org/10.1016/j.pss.2008.02.002

Gawronska, A. J., McLeod. C. L. (2022*)* Basalt. In: Cudnik, B. (eds.) *Encyclopedia of Lunar Science.* Springer, Cham. https://doi.org/10.1007/978-3-319-05546-6_135-1

Gawronska, A. J., McLeod, C. L., Blumenfeld, E. H., Hanna, R. D. Zeigler, R. A. (2022) New interpretations of lunar mare basalt flow emplacement from XCT analysis of Apollo samples. Icarus 388, 115216. https://doi.org/10.1016/j.icarus.2022.115216.

Giguere, T. A., Taylor, G. J., Hawke, B. R., Lucey, P. G. 2000. The titanium contents of lunar mare basalts. Meteoritics and Planetary Science 35, 193-200. https://doi.org/10.1111/j.1945-5100.2000.tb01985.x

Ginibre C., Worner G., Kronz A. (2002) Minor- and trace-element zoning in plagioclase: implications for magma chamber processes at Parinacota volcano, northern Chile. Contributions to Mineralogy and Petrology 143, 300-315. https://doi.org/10.1007/s00410- 002-0351-z

Ginibre C., Worner G., Kronz A. (2007) Crystal Zoning as an Archive for Magma Evolution. Elements 3, 261-266. https://doi.org/10.2113/gselements.3.4.261

Gounelle, M., Chaussidon, M., Morbidelli, A., Barrat, J.-A., Engrand, C.., Zolensky, M. E., McKeegan, K. D. (2009) A unique basaltic micrometeorite expands the inventory of solar system planetary crusts. Proceedings of the National Academy of Sciences 106 (17), 6904-6909. https://doi.org/10.1073/pnas.0900328106

Greeley, R., Spudis, P. D. (1981) Volcanism on Mars. Reviews of Geophysics 19 (1), 13-41. https://doi.org/10.1029/RG019i001p00013

Grove, T. L., Beaty, D. W. (1980) Classification, experimental petrology, and possible volcanic histories od the Apollo 11 high-K basalts. Proceedings of the 11th Lunar and Planetary Science Conference, 149-177.

Hanna, R.D., Ketcham, R.A., Zolensky, M., Behr, W., (2015) Impact-induced brittle deformation, porosity loss, and aqueous alteration in the Murchison CM chondrite:

Geochimica et Cosmochimica Acta 171, 256-282, https://doi.org/10.1016/j.gca.2015.09.005,

Hanna, R. D., and Ketcham, R. A., (2017) X-Ray computed tomography of planetary materials: A primer and review of recent studies. Chemie der Erde 77, 547-572, https://doi.org/10.1016/j.chemer.2017.01.006

Head III, J. W. 1976. Lunar Volcanism in Space and Time. Reviews of Geophysics and Space Physics 14 (2), 265-300.

Hess, W. N., and Calio, A. J. (1969) Summary of Scientific Results. In: Apollo 11 Preliminary Science Report, NASA SP-214.

Hess, P. C., Parmentier, E. M. (1995) A model for the thermal and chemical evolution of the Moon's interior: Implications for the onset of mare volcanism. Earth and Planetary Science Letters 134 (3-4), 501-514. https://doi.org/10.1016/0012-821X(95)00138-3

Hiesinger, H., Head, J. W., Wolf, U., Jaumann, R., Neukum, G. (2011) Ages and stratigraphy of lunar mare basalts: A synthesis. In: Recent Advances and Current Research Issues in Lunar Stratigraphy, Geological Society of America Special Paper 477, 1-51. https://doi.org/10.1130/2011.2477(01)

Higgins M. D. (2000) Measurement of crystal size distributions. American Mineralogist 85, 1105-1116. https://doi.org/10.2138/am-2000-8-901

Higgins M. D., Roberge J. (2007) Three magmatic components in the 1973 eruption of Eldfell volcano, Iceland: Evidence form plagioclase crystal size distribution (CSD) and geochemistry. Journal of Volcanology and Geothermal Research 161:3, 247-260. https://doi.org/10.1016/j.jvolgeores.2006.12.002

Hon, K., Kauahikaua, J., Denlinger, R., MacKay, K., 1994. Emplacement and inflation of pahoehoe sheet flows: observations and measurements of active lava flows on Kilauea Volcano, Hawaii. Geological Society of America Bulletin 106, 351–370.

Jerde, E. A., Snyder, G. A., Taylore, L. A., Liu, Y.-G., Schmitt, R. A. (1994) The origin and evolution of lunar high-Ti basalts: Periodic melting of a single source at Mare Tranquilitatis. Geochimica et Cosmochimia Acta 58, 515-527. https://doi.org/10.1016/0016-7037(94)90480-4

Jerram D. A., Davidson J. P. (2007) Frontiers in Textural and Microgeochemical Analysis. Elements 3:4, 235-238. https://doi.org/10.2113/gselements.3.4.235

Jerram D. A., Dobson K. J., Morgan D. J., Pankhurst M. J. (2018) Chapter 8 – The Petrogenesis of Magmatic Systems: Using Igneous Textures to Understand Magmatic Processes. In: Volcanic and Igneous Plumbing Systems. Elsevier, Amsterdam, Netherlands, Pp. 191-229

Johnson, T. V., Cook II, A. F., Sagan, C., Soderblom, L. A. (1979) Volcanic resurfacing rates and implications for volatiles on Io. Nature 280, 746-750. https://doi.org/10.1038/280746a0

Ketcham, R. A., and Carlson, W. D., (2001) Acquisition, optimization and interpretation of X-ray computed tomographic imagery: applications to the geosciences. Computers and Geosciences 27(1), 381-400, https://doi.org/10.1016/S0098-3004(00)00116-3

Ketcham, R. A., (2005) Computational methods for quantitative analysis of three-dimensional features in geological specimens. Geosphere 1(1), 32-41, https://doi.org/10.1130/GES00001.1

Lawrence, D. J., Elphic, R. C., Feldman, W. C., Prettyman, T. H., Gasnault, O., Maurice, S. (2002) Small-area thorium features on the lunar surface. Journal of Geophysical Research 108 (E9). https://doi.org/10.1029/2003JE002050

Lawrence, D. J., Puetter, R. C., Elphic, R. C., Feldman, W. C., Hagerty, J. J., Prettyman, T. H., Spudis, P. H. (2007) Global spatial deconvolution deconvolution of Lunar Prospector Th abundances. Geophysical Research Letters 34, L03201. https://doi.org/10.1029/2006GL028530

Lee C-T. A., Luffi P., Plank T., Dalton H., Leeman W. P. (2009) Constraints on the depths and temperatures of basaltic magma generation on Earth and other terrestrial planets using new thermobarometers for mafic magmas. Earth and Planetary Science Letters 279:1-2, 20- 33. https://doi.org/10.1016/j.epsl.2008.12.020

Li, H., Zhang, N., Liang, Y., Wu, B., Dygert, N. J., Huang, J., Parmentier, E. M. (2019) Lunar Cumulate Mantle Overturn: A Model Constrained by Ilmenite Rheology. Journal of Geophysical Research: Planets 124 (5), 1357-1378. https://doi.org/10.1029/2018JE005905

Li, S., Li, X., Zhou, J., Cao, H., Liu, L., Liu, Y., Sun, G., et al. (2022) Passive magmatism on Earth and Earth-like planets. Geosystems and Geoenvironment 1 (1), 10008. https://doi.org/10.1016/j.geogeo.2021.10.003

Lindsley, D. H. (1983) Pyroxene thermometry. American Mineralogist 68, 477-493.

Lindstrom, M. M., Haskin, L. A. (1978) Causes of compositional variations within mare basalt suites. Proceedings of the 9th Lunar and Planetary Science Conference, 465-486.

Lissenberg, C. J., MacLeod, C. J. (2016) A Reactive Porous Flow Control on Mid-ocean Ridge Magmatic Evolution. Journal of Petrology 57 (11&12), 2195-2220. https://doi.org/10.1093/petrology/egw074

Lissenberg, C. J., MacLeod, C. J., Bennett, E. N. (2019) Consequences of a crystal mush-dominated magma plumbing system: a mid-ocean ridge perspective. Philosophical Transactions of the Royal Society A 377: 20180014. http://dx.doi.org/10.1098/rsta.2018.0014

Lucey, P. G., Blewett, D. T., Taylor, G. J., Hawke, B. R. (2000) Imaging of lunar surface maturity. Journal of Geophysical Research 105 (E8), 20,377-20,386.

Lucey, P., Korotev, R. L., Gillis, J. J., Taylor, L. A., Lawrence, D., Campbell, B. A., Elphic, R., et al. (2006) Understanding the Lunar Surface and Space-Moon Interactions. Reviews in Mineralogy and Geochemistry 60 (1), 83-219. https://doi.org/10.2138/rmg.2006.60.2

The Lunar Sample Preliminary Examination Team (LSPET) (1969) Preliminary Examination of Lunar Samples from Apollo 11. Science 165, 1211-1227.

MacLellan, L., Ernst, R., El Bilali, H., Ghail, R., Bethell, E. (2021) Volcanic history of the Derceto large igneous province, Astkhik Planum, Venus. Earth-Science Reviews 220, 103619. https://doi.org/10.1016/j.earscirev.2021.103619

Magee C., O'Driscoll B., Chambers A. D. (2010) Crystallization and textural evolution of a closed system magma chamber: insights from a crystal size distribution study of the Lilloise layered intrusion, East Greenland. Geological Magazine 147:3, 363-379. https://doi.org/10.1017/S0016756809990689

Marsh B. D. (2009) Dynamics of Magmatic Systems. Elements 2:5, 287-292. https://doi.org/10.2113/gselements.2.5.287 9

McKay, D. S., Heiken, G., Basu, A., Blanford, G., Simon, S., Reedy, R., French, B. M., Papike, J. (1991) The Lunar Regolith. In: G. H. Heiken, D. T. Vaniman, B. M. French (Eds.) The Lunar Sourcebook. Cambridge University Press, Cambridge, England.

Middlemost, E. A. K. (1975) The basalt clan. Earth-Science Reviews 11 (4), 337-364. https://doi.org/10.1016/0012-8252(75)90039-2

Middlemost E. A. K. (2014) Magmas, Rocks and Planetary Development. Routlege, London. 324 pp

Mittlefehldt, D. W. (2015) Asteroid (4) Vesta: I. The howardite-eucrite-diogenite (HED) clan of meteorites. Geochemistry 75 (2), 155-183. https://doi.org/10.1016/j.chemer.2014.08.002

Morgan D. J., Jerram D. A. (2006) On estimating crystal shape for crystal size distribution analysis. Journal of Volcanoly and Geothermal Research 154, 1-7. https://doi.org/10.1016/j.jvolgeores.2005.09.016

Neal, C. R., and Taylor, L. A., 1992. Petrogenesis of mare basalts: A record of lunar volcanism. Geochimica et Cosmochimica Acta 56, 2177–2211, doi: 10.1016/0016-7037(92)90184-K

Neal C. R., Donohue P., Fagan A. L., O'Sullivan K., Oshrin J., Roberts S. (2015) Distinguishing between basalts produced by endogenic volcanism and impact processes: A non-destructive method using quantitative petrography of lunar basaltic samples. Geochimica et Cosmochimica Acta 148, 6280. https://doi.org/10.1016/j.gca.2014.08.020

Neave, D. A., Maclennan J. (2020) Clinopyroxene Dissolution Records Rapid Magma Ascent. Frontiers in Earth Science 8, 188. https://doi.org/10.3389/feart.2020.00188

Ogawa M. (2018) Magmatic differentiation and convective stirring of the mantle in early planets: the effects of the magmatism-mantle upwelling feedback. Geophysical Journal International 215:3, 2144-2155. https://doi.org/10.1093/gji/ggy413

Pankhurst M. J., Morgan D. J., Thordarson T., Loughlin S. C. (2018) Magmatic crystal records in time, space, and process, causatively linked with volcanic unrest. Earth and Planetary Science Letters 493, 231-241. https://doi.org/10.1016/j.epsl.2018.04.025

Papike, J. J., Hodges, F. N., Bence, A. E., Cameron, M., Rhodes, J. M. (1976) Mare basalts: Crystal chemistry, mineralogy, and petrology. Reviews of Geophysics 14 (4), 475-540. https://doi.org/10.1029/RG014i004p00475

Papanastassiou, D. A., DePaolo, D. J. and Wasserburg, G. J. (1977) Rb-Sr and Sm-Nd chronology and genealogy of mare basalts from the Sea of Tranquility. Proceedings of the 8th Lunar Science Conference, 1639- 1672.

Pupier E., Duchene S., Toplis M. J. (2007) Experimental quantification of plagioclase crystal size distribution during cooling of basaltic liquid. Contributions to Mineralogy and Petrology 155:5, 555-570. https://doi.org/10.1007/s00410-007-0258-9

Qian, Y., Xiao, L., Wang, Q., Head, J. W., Yang, R., Kang, Y., van der Bogert, C. H., et al. (2021) China's Chang'e-5 landing site: Geology, stratigraphy, and provenance of materials. Earth and Planetary Science Letters 561, 116855. https://doi.org/10.1016/j.epsl.2021.116855

Ringwood, A. E., Kesson, S. E. (1976) A dynamic model for mare basalt petrogenesis. Proceedings of the 7th Lunar and Planetary Science Conference (2), 1697-1722.

Roberts, S. E., Neal, C. R. (2019) Origin of lunar Very High Potassium (VHK) basalts: A combination of endogenous and exogenous processes. Geochimica et Cosmochimica Acta 266, 54-73. https://doi.org/10.1016/j.gca.2019.01.023

Sato, H., Robinson, M. S., Lawrence, S. J., Denevi, B. W., Hapke, B., Jolliff, B. L., Hiesinger, H. (2017) Lunar mare TiO2 abundances estimated from UV/Vis reflectance. Icarus, 296, 216–238. https://doi.org/10.1016/j.icarus.2017.06.013

Self, S., Keszthelyi, L. P., Thordarson, T., 1998. The importance of Pāhoehoe. Annual Reviews in Earth and Planetary Science 26, 81–110.

Shearer, C. K., Papike, J. J. (1999) Magmatic evolution of the Moon. American Mineralogist 84 (10), 1469-1494. https://doi.org/10.2138/am-1999-1001

Shearer, C., Hess, P. C., Wieczorek, M. A., Pritchard, M. E., Parmentier, E. M., Borg, L. E., Longhi, J., et al. (2006). Thermal and magmatic evolution of the Moon. Reviews in Mineralogy and Geochemistry, 60, 365-518.

Shoemaker, E. M., et al. (1969) Geologic Setting of the Lunar Samples Returned by the Apollo 11 Mission. In: Apollo 11 Preliminary Science Report, NASA SP-214.

Singer B. S., Dungan M. A., Layne G. D. (1995) Textures and Sr, Ba, Mg, Fe, K, and Ti compositional profiles in volcanic plagioclase: Clues to the dynamics of calc-alkaline magma chambers. American Mineralogist 80:7-8, 776-785. https://doi.org/10.2138/am-1995-7-815

Smith, J. V., Anderson, A. T., Newton, r. C., Olsen, E. J., Wyllie, P. J., Crewe, A. V., Isaacson, M. S., Johnson, D. (1970) Petrologic history of the moon inferred from petrography, mineralogy, and petrogenesis of Apollo 11 rocks. Proceedings of the Apollo 11 Lunar Science Conference 1, 897-925.

Snyder, G. A., Lee, D.-C., Taylor, L. A., Halliday, A. N., Jerde, E. A. (1994) Evolution of the upper mantle of the Earth's Moon: Neodymium and strontium isotopic constrains from high-Ti mare basalts. Geochimica et Cosmochimia Act 58(21), 4795-4808. https://doi.org/10.1016/0016-7037(94)90209-7

Solano, J. M. S., Jackson, M. D., Sparks, R. S. J., Blundy, J. (2014) Evolution of major and trace element composition during melt migration through crystalline mush: Implications for chemical differentiation in the crust. American Journal of Science 314 (5), 895-939. https://doi.org/10.2475/05.2014.01

Sparks, R. S. J., Annen, C., Blundy, J. D., Cashman, K. V., Rust, A. C., Jackson, D. (2019) Formation and dynamics of magma reservoirs. Philosophical Transactions of the Royal Society A 377, 20180019. http://dx.doi.org/10.1098/rsta.2018.0019

Sun, S.-s., McDonough, W. F. (1989) Chemical and isotopic systematics of oceanic basalts: implications for mantle composition and processes. In: Saunders, A. D., Norry, M. J. (Eds.) Magmatism in the Ocean Basins. Geological Society Special Publications 42, 313-345 pp.

Taylor, G. J., Keil, K., McCoy, T., Haack, H., Scott, E. R. D. (1993) Asteroid Differentiation: Pyroclastic Volcanism to Magma Oceans. Meteoritics 28, 34-52. https://doi.org/10.1111/j.1945-5100.1993.tb00247.x

Ubide, T., Kamber, B. S. (2018) Volcanic crystals as time capsules of eruption history. Nature Communications 9: 326. https://doi.org/10.1038/s41467-017-02274-w

Ubide T., Gale C., Larrea P., Arranz E., Lago M., Tierz P. (2014) The Relevance of Crystal Transefer to Magma Mixing: A Case Study in Composite Dykes from the Central Pyrenees. Journal of Petrology 55:8, 1535-1559. https://doi.org/10.1093/petrology/egu033

Ubide T., Mollo S., Zhao J., Nazzari M., Scarlato P. (2019) Sector-zoned clinopyroxene as a recorder of magma history, eruption triggers, and ascent rates. Geochimica et Cosmochimica Acta 215, 265-283. https://doi.org/10.1016/j.gca.2019.02.021

Uesugi M., Uesugi K., Oka M. (2010) Non-destructive observation of meteorite chips using quantitative analysis of optimized X-ray micro-computed tomography. Earth and Planetary Science Letters 299, 359-367. https://doi.org/10.1016/j.epsl.2010.09.016

Warren, P. H., Wasson, J. T. 1979. The Origin of KREEP. Reviews of Geophysics and Space Physics 17 (1), 73-88.

Wilding, J. D., Zhu, W., Ross, Z. E., Jackson, J. M. (2023) The magmatic web beneath Hawai'i. Science 379, 462-468. https://doi.org/10.1126/science.ade5755

Wilson, L., 2009. Volcanism in the Solar System. Nature Geoscience 2, 389-397. https://doi.org/10.1038/ngeo529

Wilson L., Head J. W. (2017) Generation, ascent and eruption of magma on the Moon: New insights into source depths, magma supply, intrusions and effusive/explosive eruptions (Part 1: Theory). Icarus 283, 146-175. https://doi.org/10.1016/j.icarus.2015.12.039

Wilson, L., and Head, J. W. (2018) Controls on Lunar Basaltic Volcanic Eruption Structure and Morphology: Gas Release Patterns in Sequential Eruption Phases. Geophysical Research Letters 45(12), 5852-5859, doi: 10.1029/2018GL078327

Withers P. J., Bouman C., Carmignato S., Cnudde V., Grimaldi D., Hagen C. K., Maire E., Manley M., Du Plessis A., Stock S. R. (2021) X-ray computed tomography. Nature Reviews: Methods and Primers 1, 18. https://doi.org/10.1038/s43586-021-00015-4 10

Wood, J. A., Dickey Jr., J. S., Marvin, U. B., Powell, B. N. 1970. Lunar anorthosites and a geophysical model of the moon. Proceedings of the Apollo 11 Lunar Science Conference 1, 965-988.

Woodcock, N. H., and Naylor, M. A., (1983) Randomness testing in three-dimensional orientation data. Journal of Structural Geology 5, 539–548.

Xue, Z., Welsh, D. F., Neal, C. R., Xiao, L. (2021) Understanding the textures of Apollo 11 high-Ti mare basalts: A quantitative petrographic approach. Meteoritics and Planetary Science 56 (12), 2211-2229. https://doi.org/10.1111/maps.13767

Zellmer, G. (2021) Gaining acuity on crystal terminology in volcanic rocks. Bulletin of Volcanology 83:77. https://doi.org/10.1007/s00445-021-01505-9

4.8. Figures and Table

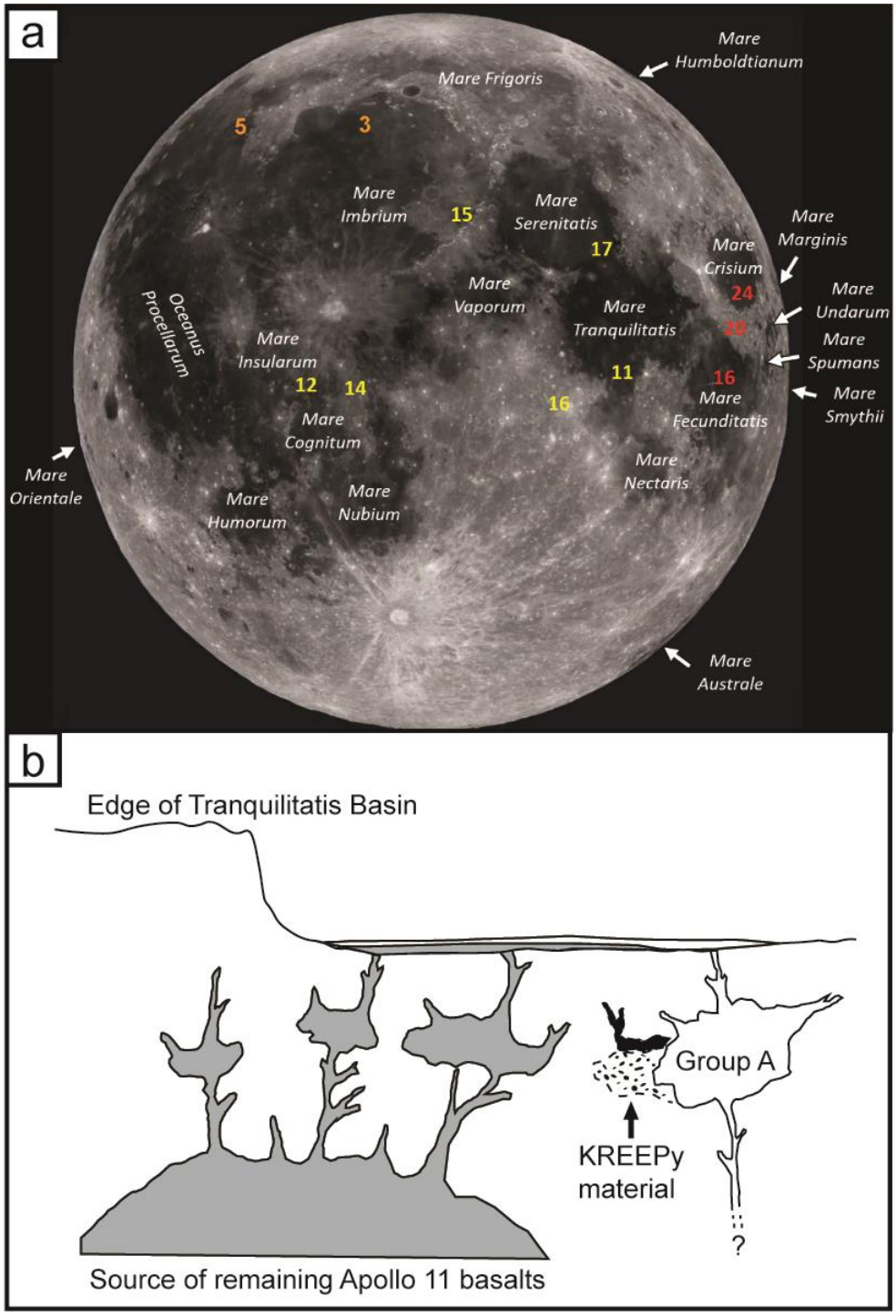

Fig. 1: a) Summary of mare basalt volcanism and surface mission landing sites; Apollo in yellow, Luna in red, Chang'e in orange. Note Apollo 11 landed on the southern edge of Mare Tranquilitatis. b) Schematic summarizing Apollo 11 basalt petrogenesis adapted from Jerde et al. (1994).

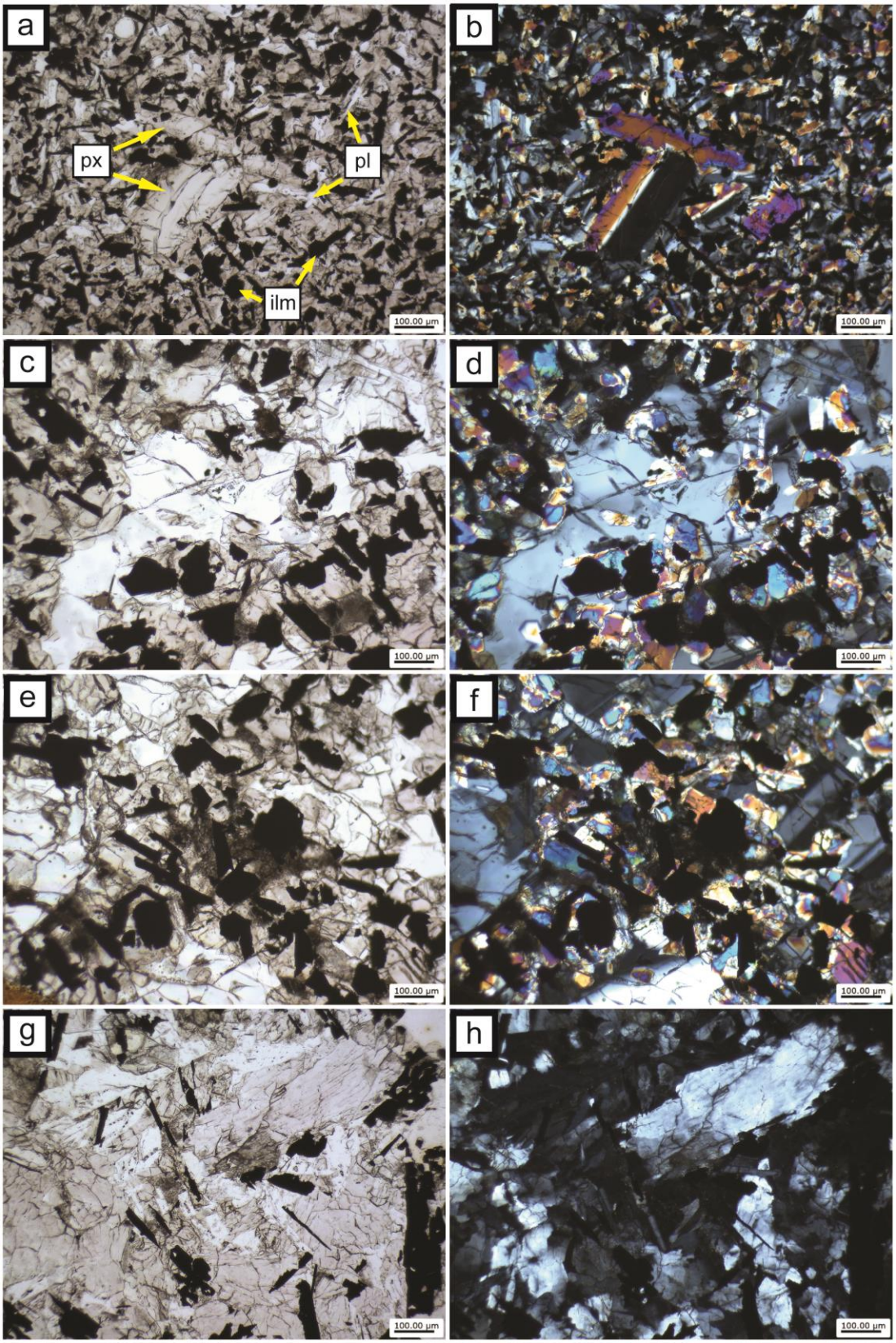
a
px
pl
ilm
100.00 µm
b
100.00 µm
c
100.00 µm
d
100.00 µm
e
100.00 µm
f
100.00 µm
g
100.00 µm
h
100.00 µm

Fig. 2.

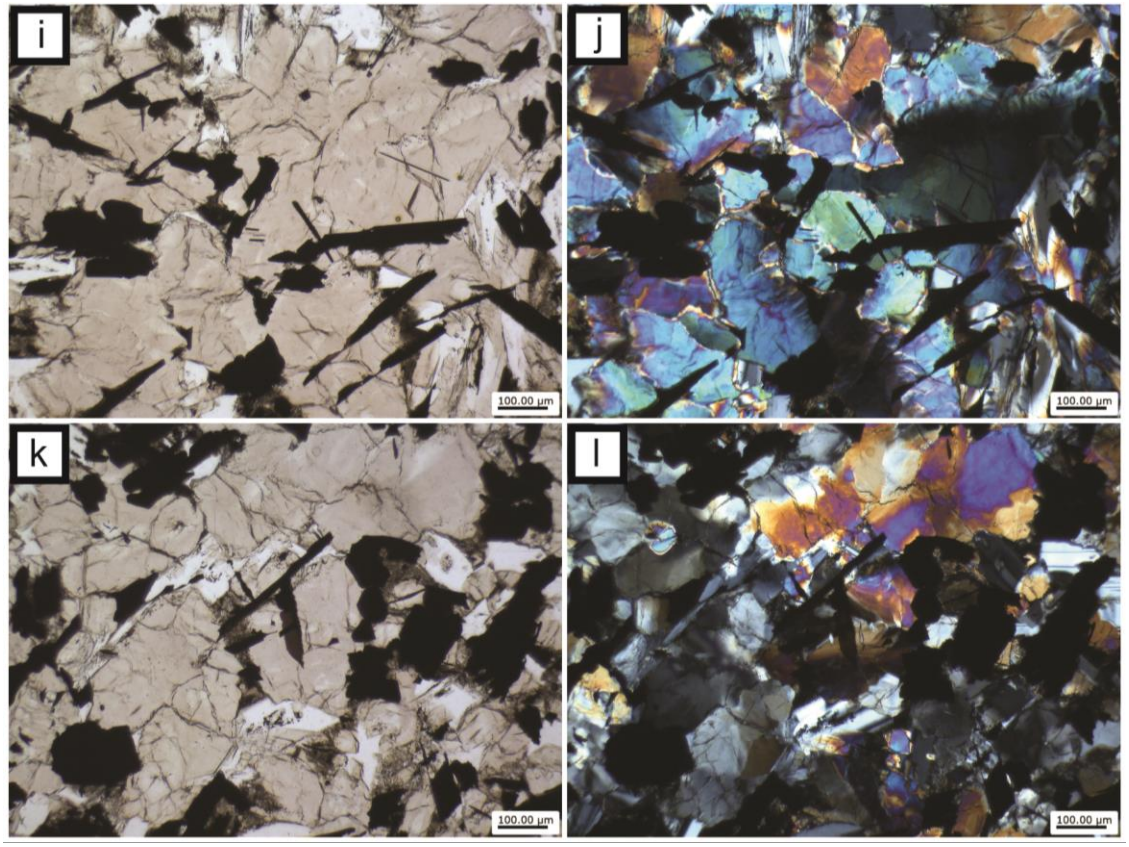

Fig. 2 (cont): Representative textures seen in the Apollo 11 group A suite. a) Plane polarized (PPL) image of relatively coarse pigeonite grains in 10049; px = pyroxene, pl = plagioclase feldspar, ilm = ilmenite. b) cross-polarized (XPL) image of the sample pyroxenes in 10049. c-d) Poikilitic plagioclase feldspar with pyroxene chadacrysts in PPL and XPL. e-f) Interstitial mesostasis in PPL and XPL. g-h) Interstitial mesostasis in PPL and XPL; notice the plastically deformed pyroxene in the top right. i-j) Coarser pyroxene poikilitically enclosing ilmenite grains in PPL and XPL. k-l) Interstitial mesostasis in PPL and XPL; the dark red tabular mineral seen in the center in PPL is tranquillityite.

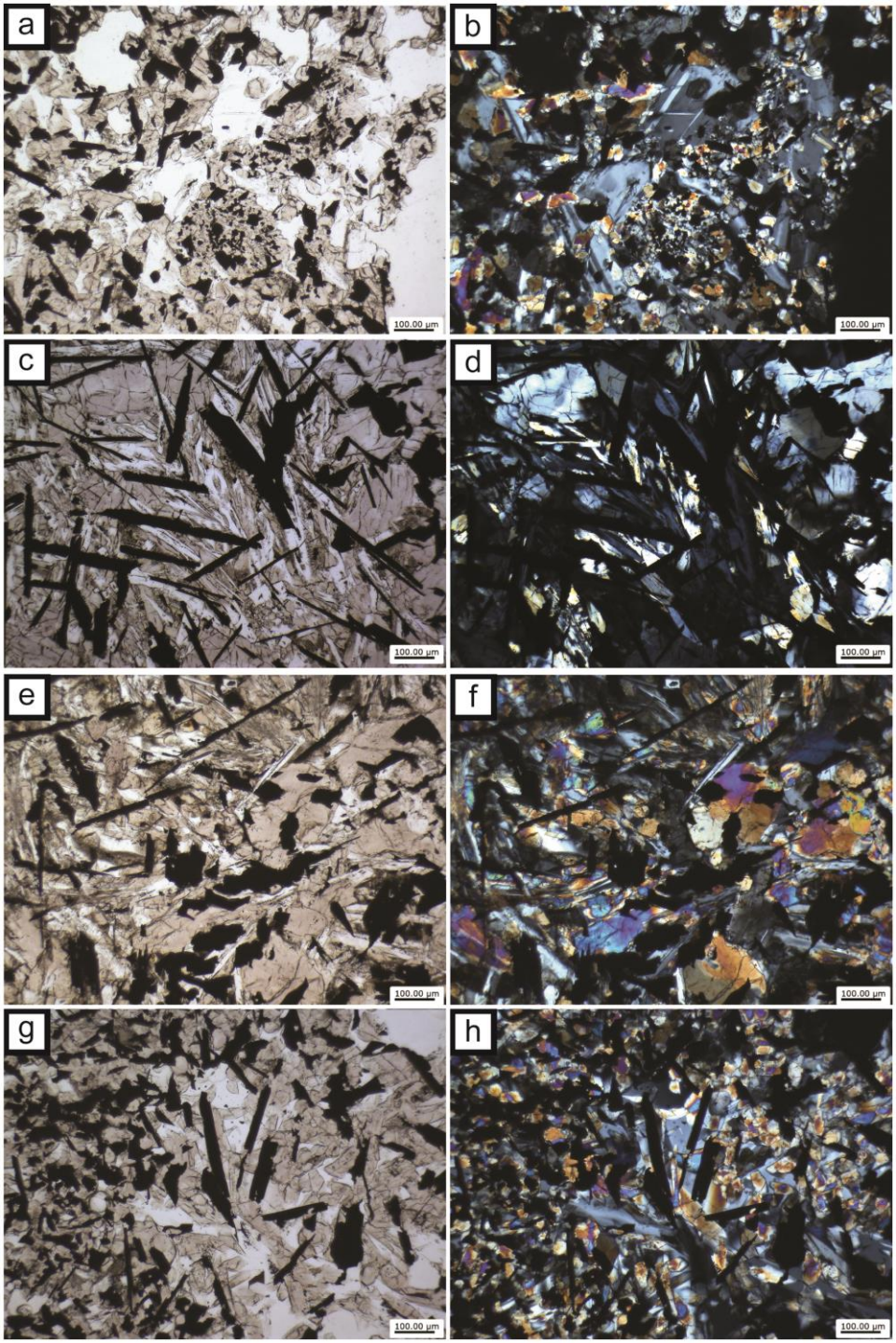

Fig. 3: Examples of texturally-distinct regions in the sample suite. a-b) Region 1 in PPL and XPL, defined by coarser-grained grains. c-d) Region 2 in PPL and XPL, defined by blady grains and greater incidence of mesostasis. e-f) Contact between region 1 (bottom) and "iota" (top; after Beaty and Albee, 1978) in 10071. g-h) Matrix domain in PPL and XPL on the left in both images, opposite to a pocket of region 1.

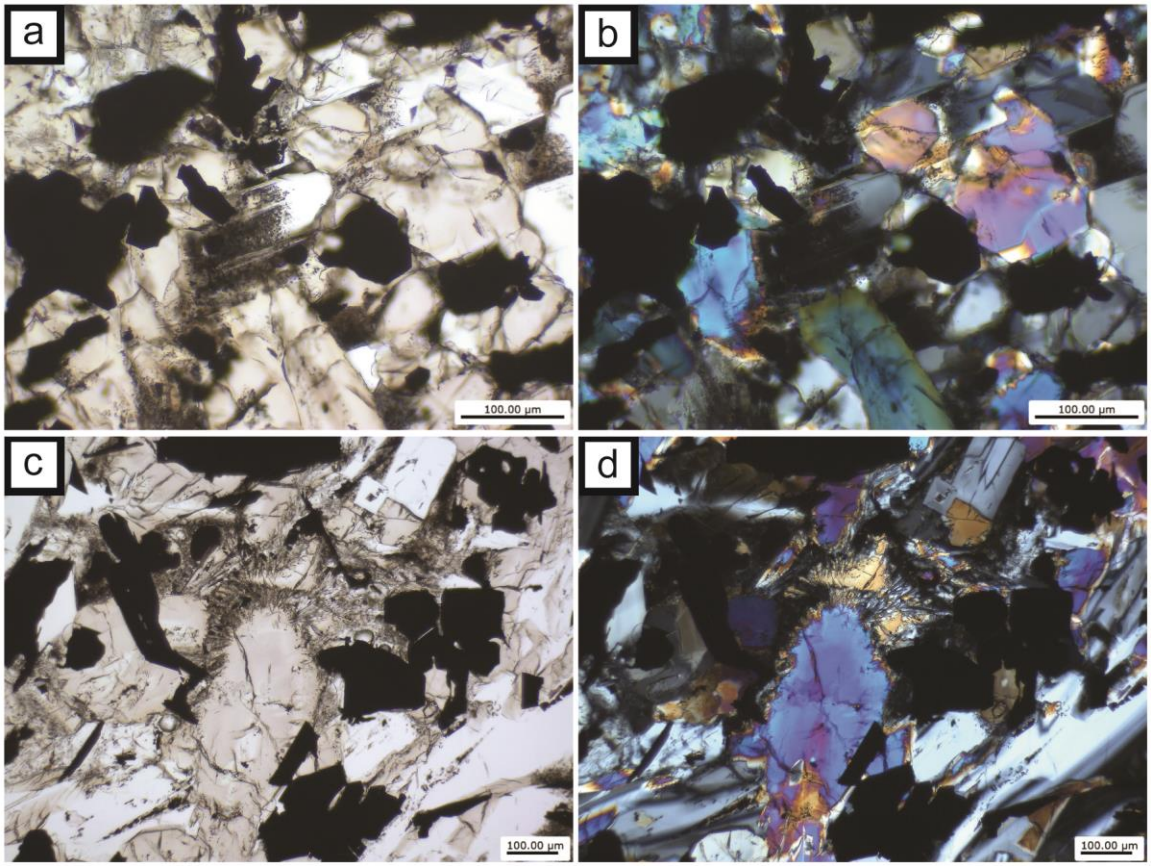

Fig. 4: Examples of reaction textures existing in Apollo 11 group A basalts. a-b) PPL and XPL of feldspar grain with numerous melt inclusions, intimately affected by nearby interstitial mesostasis. c-d) Corona of very fine grained pyroxene and feldspar on a larger pyroxene grain. Note the olivine core in the bottom left of the central large pyroxene.

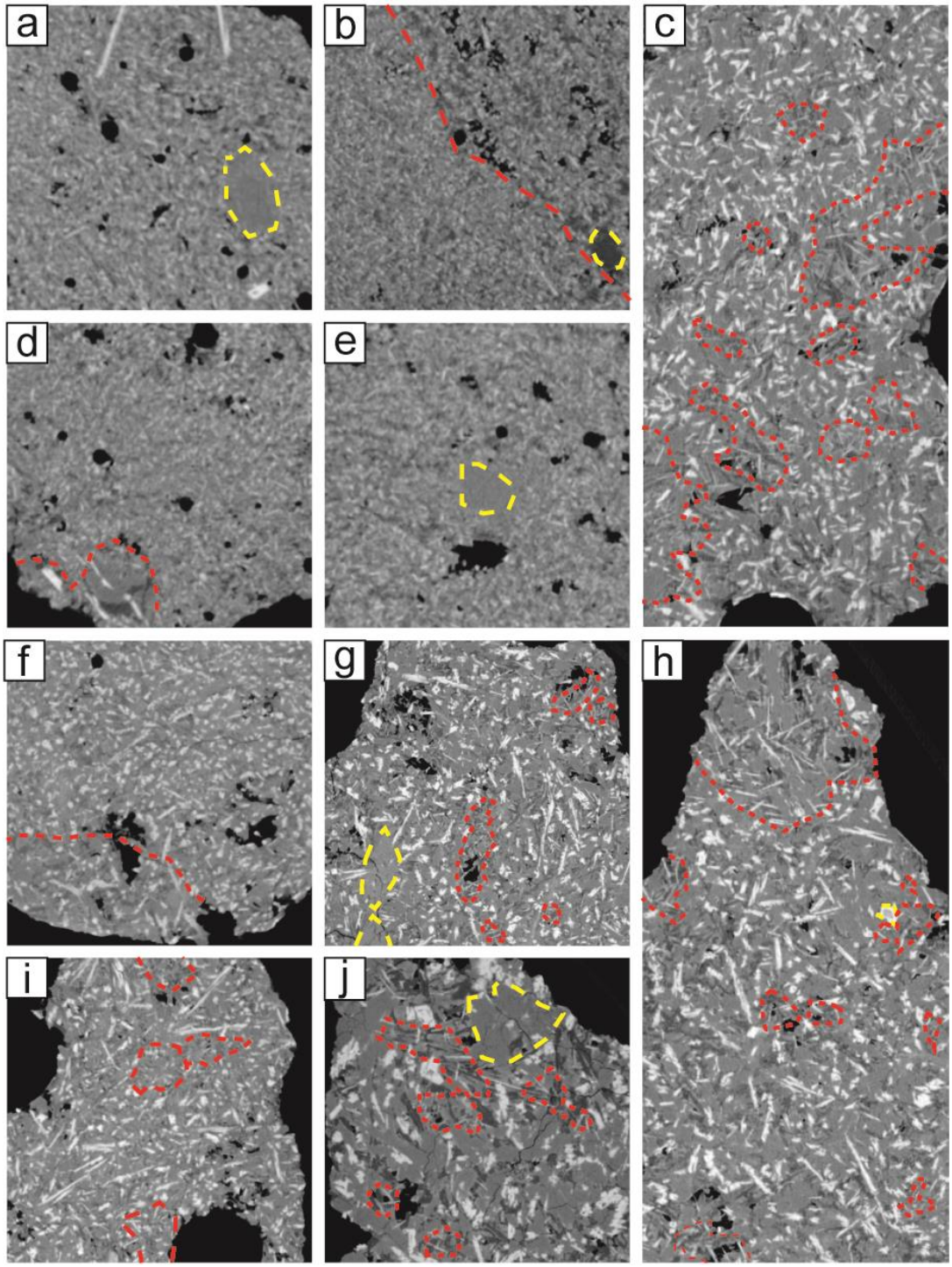

Fig. 5: Detail of XCT scans collected within the suite. Distinct grains are outlined in yellow, contacts between regions are in red. a) Coarser pyroxene in sample 10049. b) Two regions in 10069. c) Two regions in 10022. d) Two regions in 10049. e) Coarser pyroxene in 10049. f) Two regions in 10024. g) two regions in 10071. h) Two regions in 10071, where "iota" may be on top. Also, large armalcolite grain outlined. i) Two regions in 10071. j) Two regions in 10072.

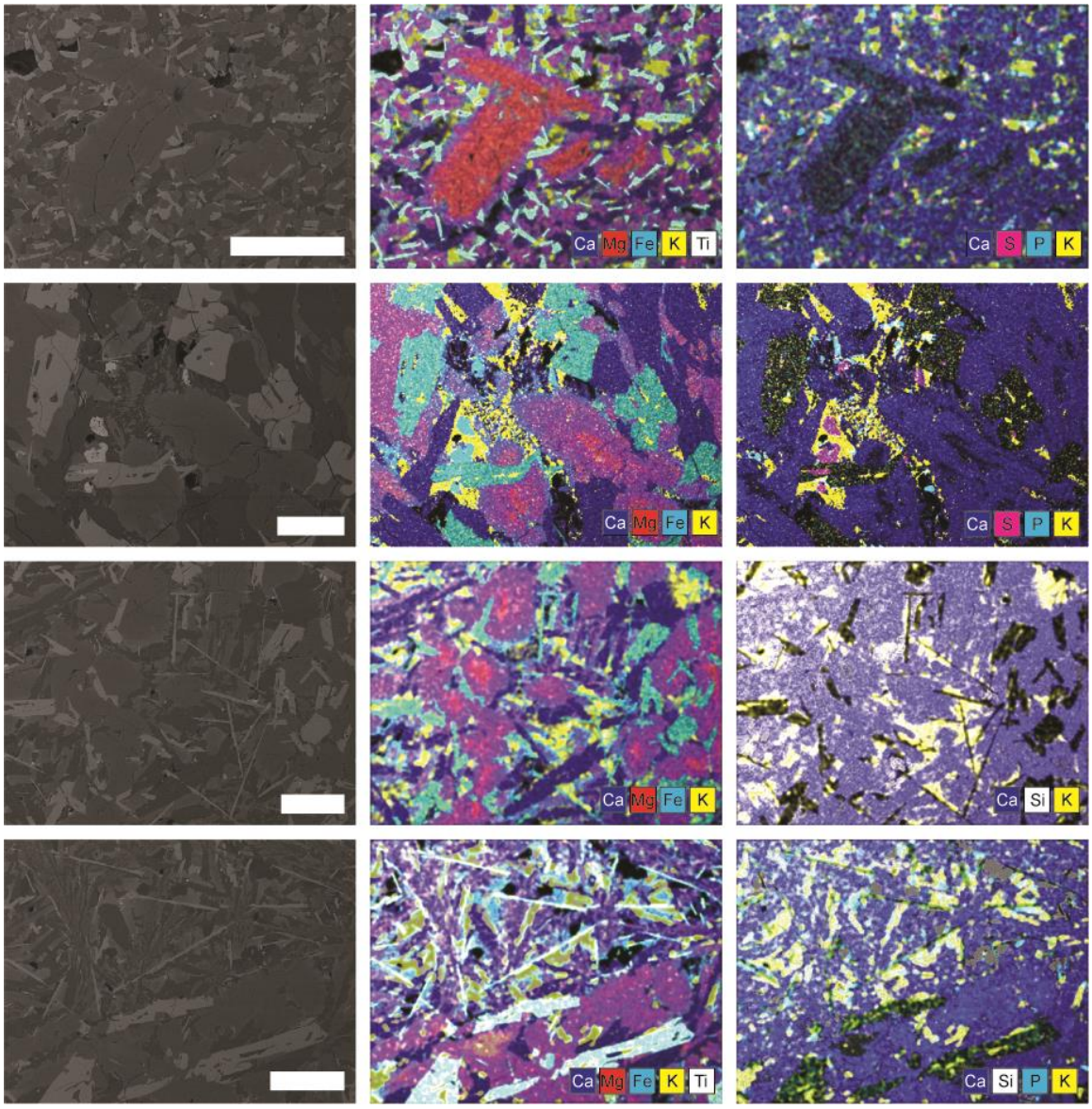

Fig. 6: SEM-EDS maps of features of interest in the Apollo 11 group A suite. Top row: pyroxene grains from Fig. 2a-b. Top middle row: pyroxene with corona, from Fig. 4c-d. Bottom middle row: contact between region 1 and 2 in sample 10022. Bottom row: contact between region 1 and "iota" in sample 10071.

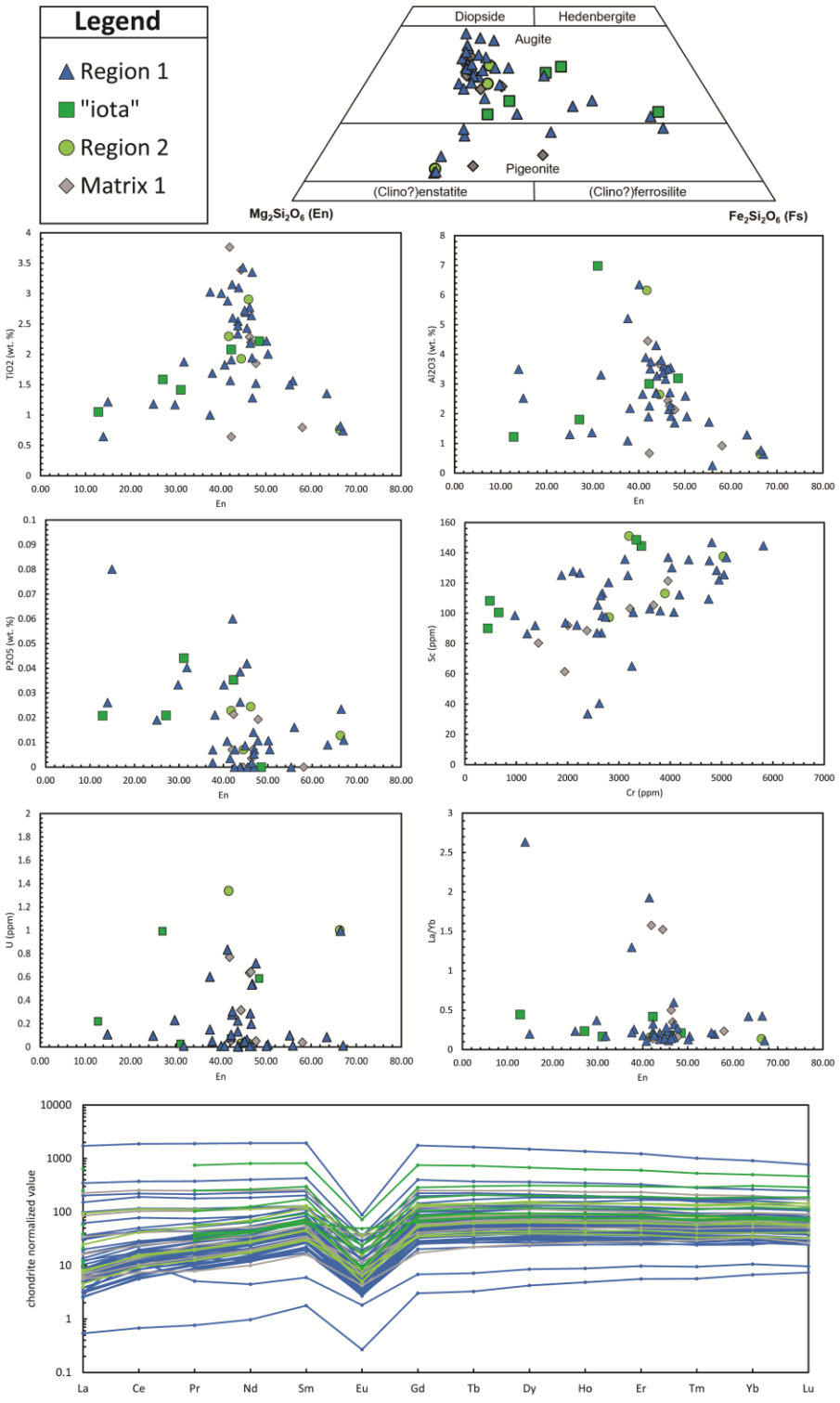

Fig. 7: Compositions of pyroxene in the Apollo 11 group a suite. All analyses represent the apparent cores of grains; for additional information regarding rim composition, see Fig. S2.

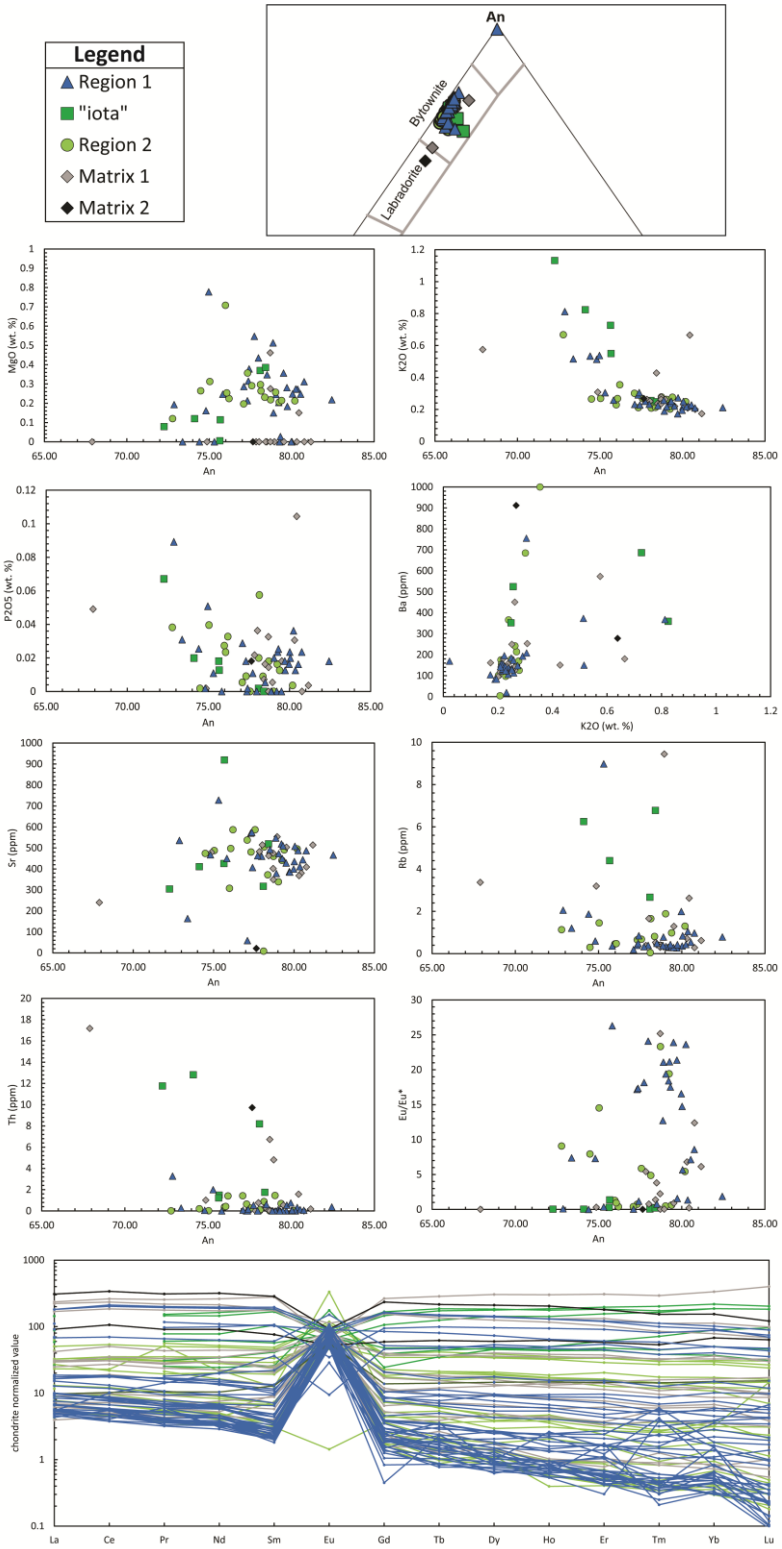

Fig. 8: Plagioclase feldspar compositions in the Apollo 11 group A basalts. All analyses represent the apparent cores of grains; for additional information regarding rim composition, see Fig. S3.

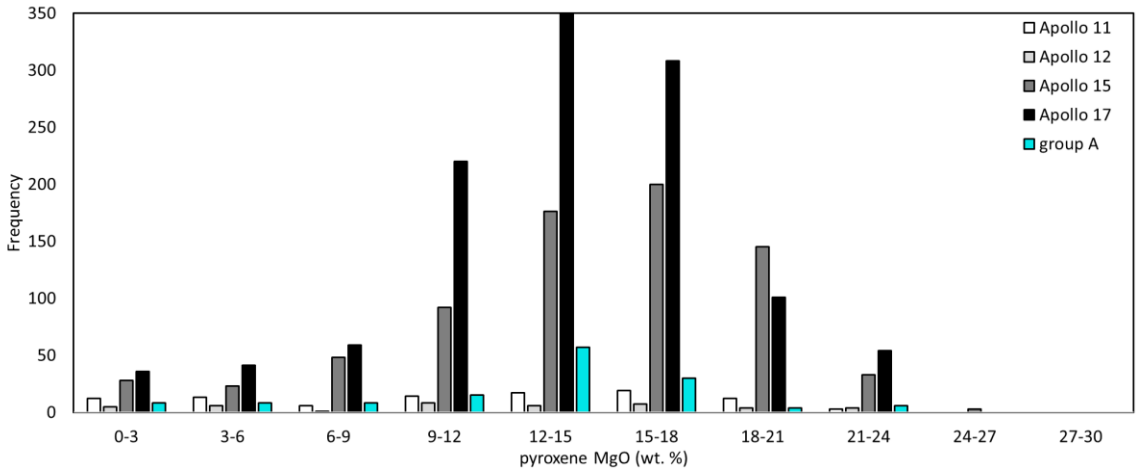
Frequency
350
300
250
200
150
100
50
0
0-3
3-6
6-9
9-12
12-15
15-18
18-21
21-24
24-27
27-30
pyroxene MgO (wt. %)
Apollo 11
Apollo 12
Apollo 15
Apollo 17
group A

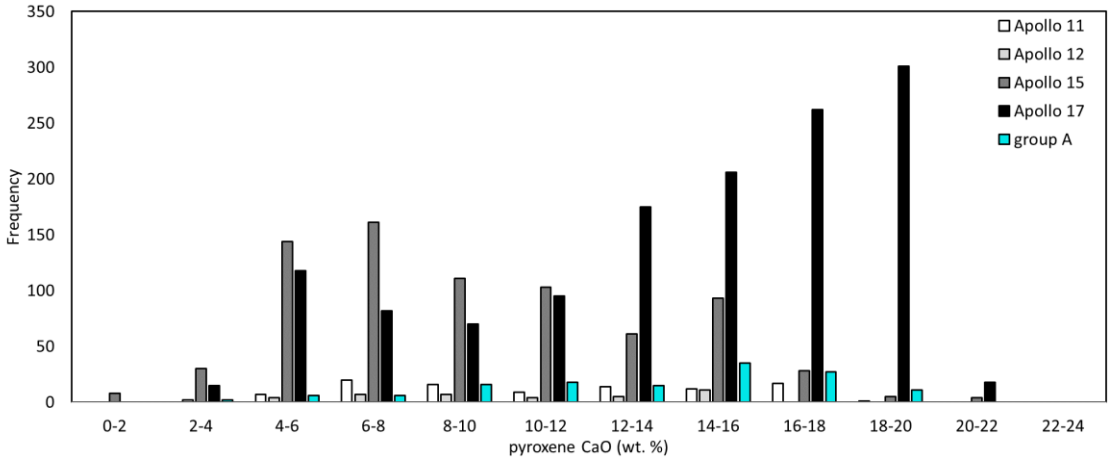
Frequency
350
300
250
200
150
100
50
0
0-2
2-4
4-6
6-8
8-10
10-12
12-14
14-16
16-18
18-20
20-22
22-24
pyroxene CaO (wt. %)
Apollo 11
Apollo 12
Apollo 15
Apollo 17
group A

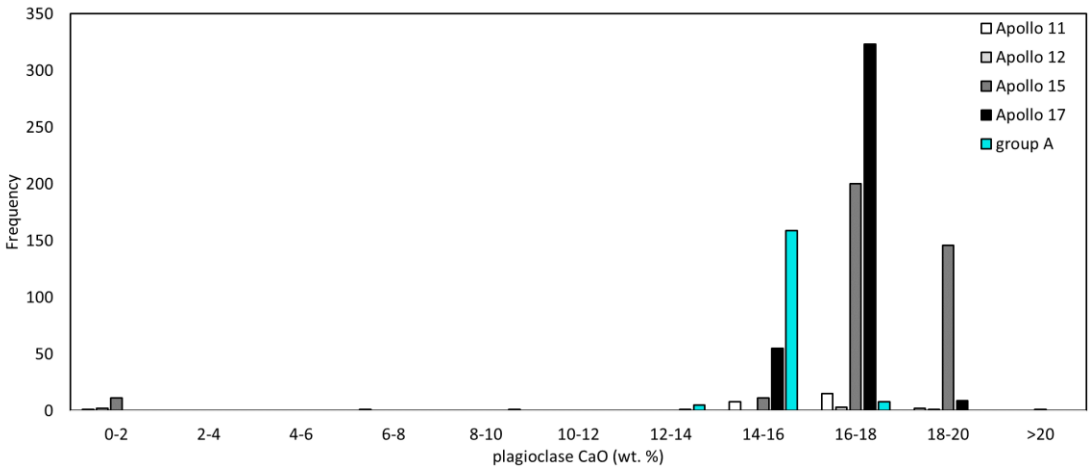
Frequency
350
300
250
200
150
100
50
0
0-2
2-4
4-6
6-8
8-10
10-12
12-14
14-16
16-18
18-20
>20
plagioclase CaO (wt. %)
Apollo 11
Apollo 12
Apollo 15
Apollo 17
group A

Fig. 9.

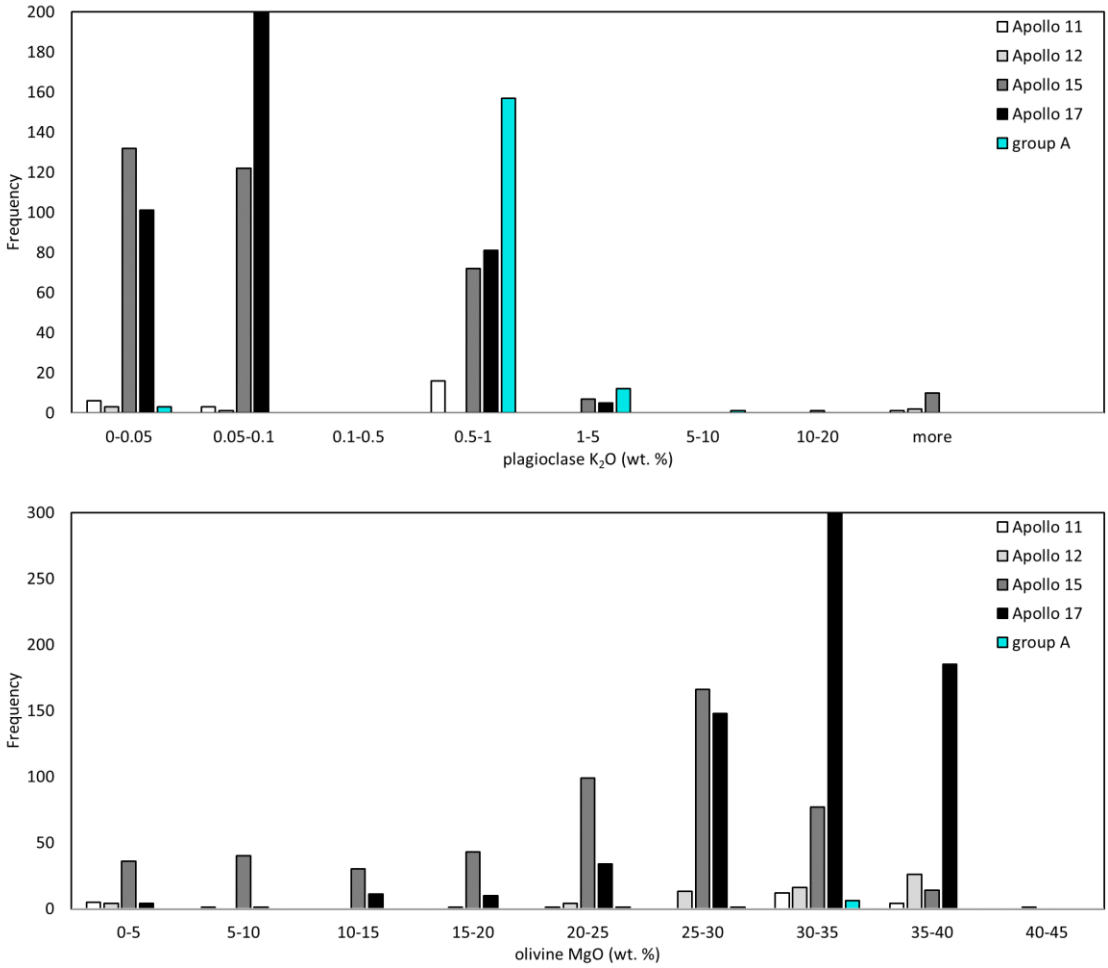

Fig. 9: (cont.) Comparison of silicate phase compositions in the Apollo 11 group A basalts against the analysis of grains from samples collected during other Apollo missions. Note that all Apollo missions landed in different locations, within different basaltic flows (see Fig. 1a).

4.9. Supplemental Figures and Tables

Table S1: Mineral modal proportions calculated from XCT data.

Sample	Pyroxene		Plagioclase Feldspar		Oxides		Silica/glass/mesostasis		Vesicles
	Here*	Previous**	Here*	Previous**	Here*	Previous**	Here*	Previous**	Here
10017	50.4	47.6 - 59.4	25.0	18 - 26.9	23.8	14.5 - 23.9	N/A	6.1 - 8.5	0.9
10022	58.9	48.9 - 55	25.6	15.6 - 29	14.9	14.1 - 26.3	N/A	~10	3.4
10024	50.2	51.4 - 52.2	15.5	16.4 - 21.7	30.7	16.4 - 21.8	3.6	~10	1.3
10049	60.1	47 - 51.0	32	18 - 24.5	7.9	14.1 - 17	N/A	8 - 18	7.1
10069	46.4	51.3 - 56	47.8	19 - 23.4	5.8	14.9 - 23.5	N/A	3.2 - 7.24	3.3
10071	61.1	47.8 - 58.3	20.6	20.6 - 23.6	18.3	14.7 - 16.8	N/A	2.7 - 9.6	0.7
10072	56.5	49.3 - 59.4	21.4	18 - 22.5	14.7	13 - 22	2.4	3.7 - 10	6.7

*These modal proportions were calculated without including vesicles for easier comparison with previous work.

**Proportions calculated in previous work were collated from the Lunar Sample Compendium.

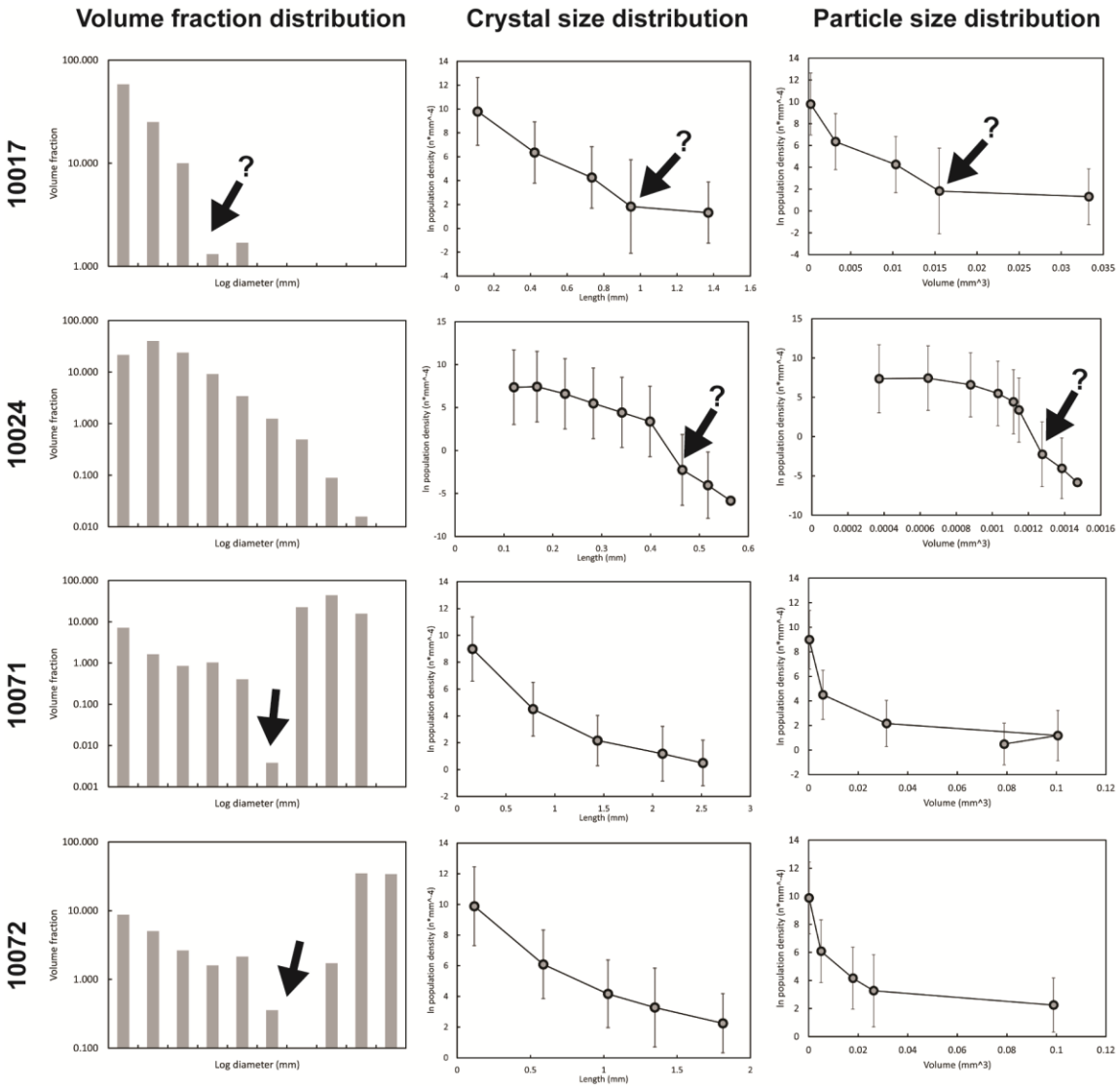

Fig. S1: Volume size fractions (VSDs), crystal size distributions (CSDs), and particle size distributions (PSDs) for ilmenite in four of the samples studied here which were large enough to successfully separate ilmenite. Note that most samples preserve some change in their ilmenite VFDs which indicates the existence of two different populations – one of larger, and one of smaller ilmenites. Including larger grains skewed bin sizes of both the CSD and PSD analyses, thus only CSD and PSD analysis of the smaller populations are reported in samples 10071 and 10072.

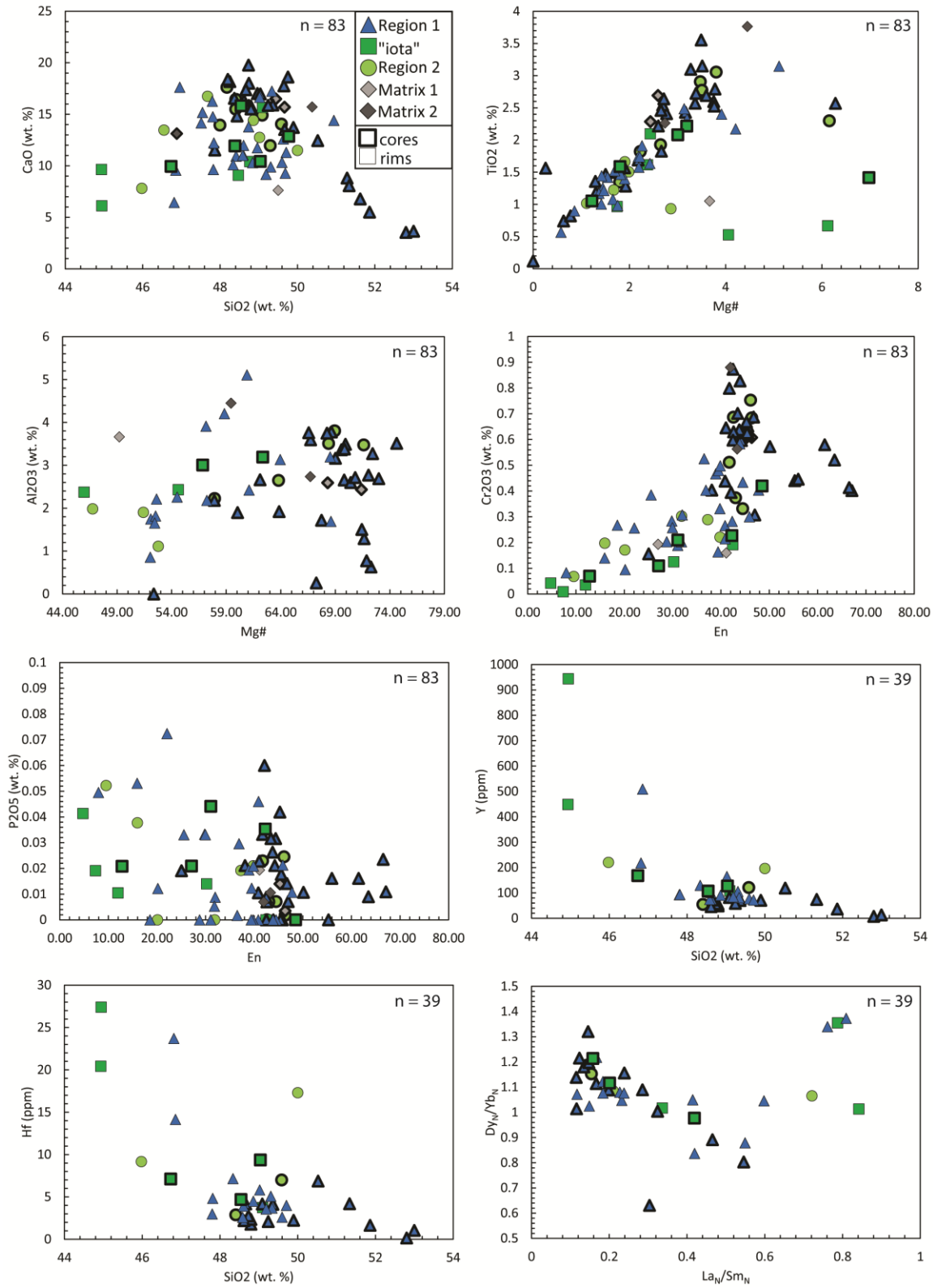

Fig. S2: Core and rim compositions of pyroxene grains in the Apollo 11 group A suite.

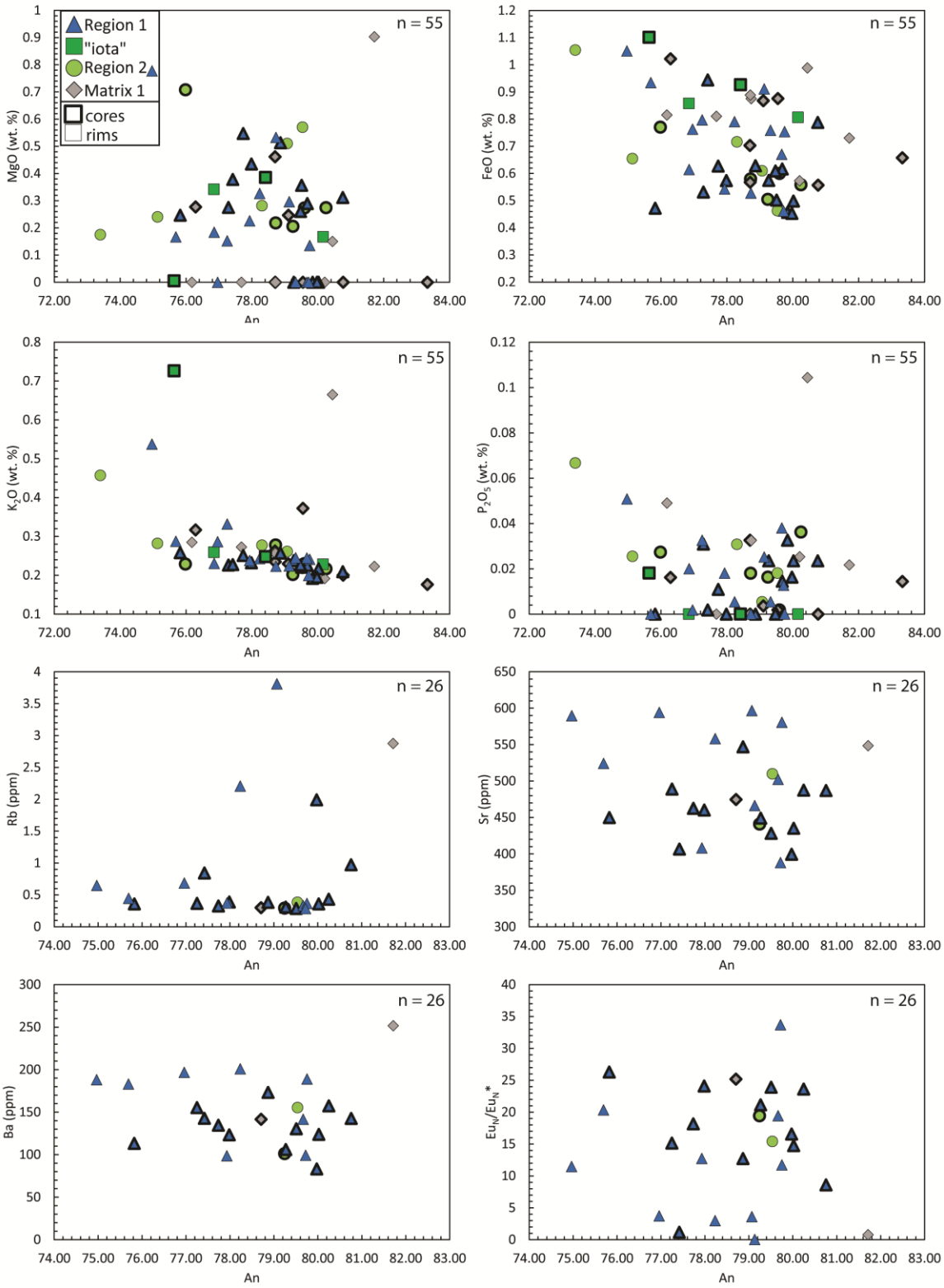

Fig. S3: Core and rim compositions of plagioclase feldspar grains in the Apollo 11 group A suite.

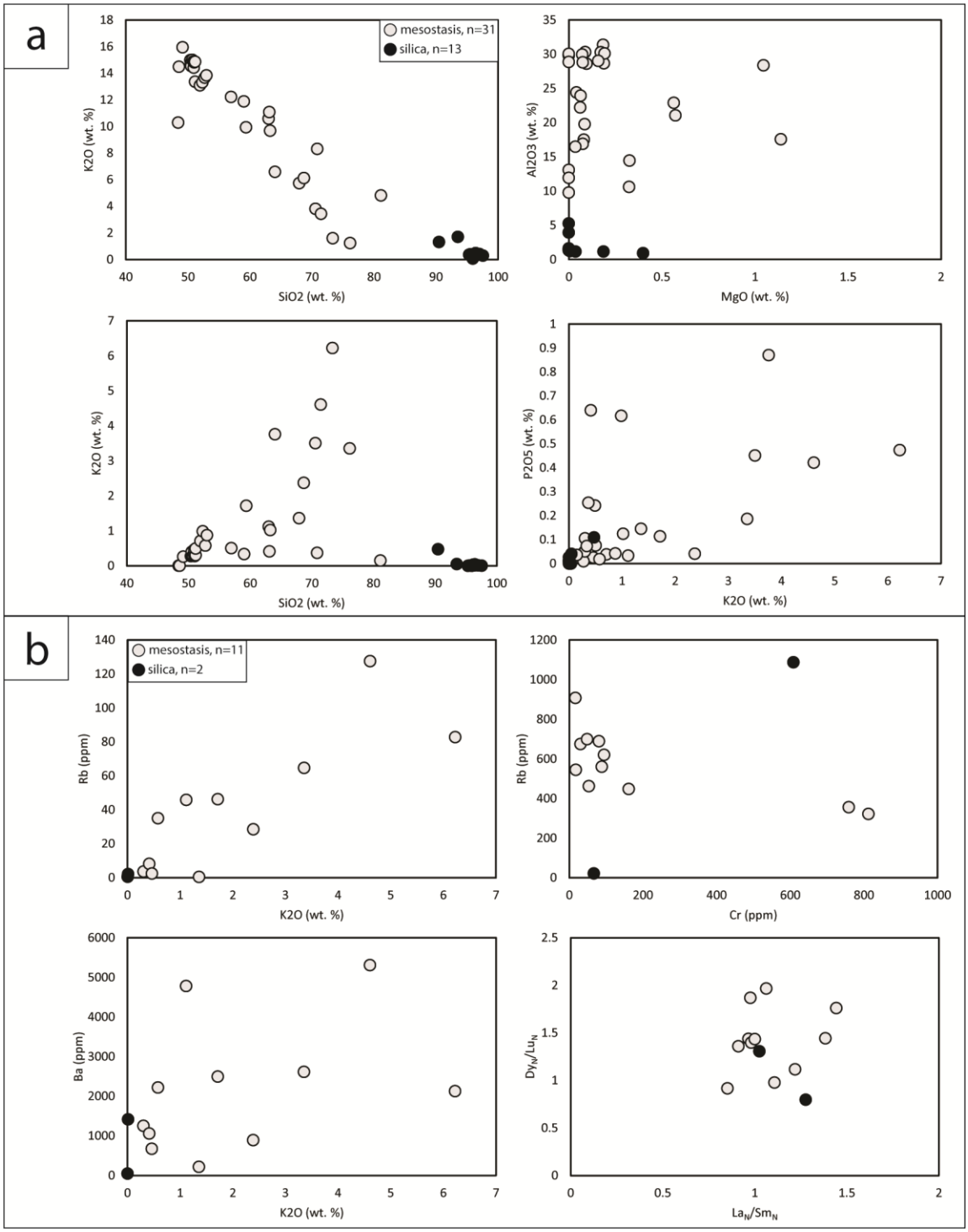

Fig. S4: a) Major element contents of mesostasis and silica phase in the Apollo 11 group A suite. b) Trace element contents of mesostasis and silica in the Apollo 11 group A suite.

Table S2: Plagioclase feldpar major element contents.

Sample	10017	10017	10017	10017	10017	10017	10017	10017
Point	1 / 1 .	3 / 1 .	5 / 1 .	7 / 1 .	8 / 1 .	10 / 1 .	17 / 1 .	18 / 1 .
SiO2	48.76	48.84	49.47	48.80	49.27	50.34	49.24	49.12
TiO2	0.16	0.11	0.10	0.13	0.08	0.09	0.12	0.14
Al2O3	31.20	30.79	30.24	31.02	31.92	29.56	30.86	31.09
Cr2O3	0.00	0.02	0.00	0.01	0.00	0.00	0.00	0.01
Fe2O3	0.00	0.00	0.00	0.00	0.00	0.00	0.00	0.00
FeO	0.45	0.44	0.59	0.52	0.54	0.87	0.76	0.46
MnO	0.03	0.00	0.01	0.03	0.03	0.00	0.02	0.00
MgO	0.15	0.27	0.20	0.27	0.03	0.00	0.00	0.00
CaO	15.38	15.47	15.29	15.73	15.48	14.61	15.39	15.47
BaO	0.00	0.00	0.00	0.00	0.00	0.00	0.00	0.00
Na2O	2.15	2.12	2.06	1.98	2.07	2.37	2.06	2.03
K2O	0.19	0.22	0.24	0.22	0.25	0.29	0.25	0.19
P2O5	0.00	0.00	0.00	0.01	0.03	0.04	0.01	0.03
Total	98.46	98.28	98.20	98.73	99.70	98.16	98.69	98.54
An	78.90	79.10	79.22	80.36	79.32	75.90	79.33	79.84
Ab	19.95	19.58	19.31	18.30	19.15	22.32	19.17	18.98
Or	1.16	1.32	1.47	1.34	1.53	1.78	1.50	1.18

Table S2 cont.: Plagioclase feldpar major element contents.

Sample	10017	10017	10017	10017	10017	10017	10017	10017
Point	19 / 1 .	24 / 1 .	27 / 1 .	31 / 1 .	38 / 1 .	39 / 1 .	40 / 1 .	41 / 1 .
SiO2	51.27	51.37	50.94	49.24	51.15	51.06	49.25	49.94
TiO2	0.06	0.10	0.05	0.11	0.05	0.06	0.10	0.14
Al2O3	29.63	29.03	29.48	31.30	29.97	30.41	30.90	30.94
Cr2O3	0.00	0.00	0.00	0.01	0.01	0.01	0.00	0.01
Fe2O3	0.00	0.00	0.00	0.00	0.00	0.00	0.00	0.00
FeO	0.76	0.83	0.84	0.51	0.76	1.05	0.50	0.48
MnO	0.02	0.01	0.01	0.00	0.00	0.01	0.00	0.00
MgO	0.00	0.03	0.16	0.65	0.00	0.78	0.00	0.39
CaO	14.44	13.81	14.30	15.73	14.33	14.47	15.65	15.27
BaO	0.00	0.00	0.00	0.00	0.00	0.00	0.00	0.00
Na2O	2.42	2.43	2.32	1.98	2.37	2.32	2.02	2.27
K2O	0.30	0.48	0.51	0.21	0.53	0.54	0.22	0.20
P2O5	0.01	0.03	0.00	0.00	0.03	0.05	0.02	0.03
Total	98.92	98.11	98.62	99.75	99.20	100.77	98.65	99.67
An	75.31	73.54	74.80	80.41	74.40	74.97	80.02	77.82
Ab	22.80	23.43	22.00	18.31	22.30	21.72	18.66	20.97
Or	1.89	3.02	3.20	1.28	3.30	3.32	1.32	1.21

Table S2 cont.: Plagioclase feldpar major element contents.

Sample	10017	10017	10017	10017	10017	10017	10017	10017
Point	42 / 1 .	43 / 1 .	52 / 1 .	53 / 1 .	57 / 1 .	59 / 1 .	61 / 1 .	64 / 1 .
SiO2	49.38	49.28	50.41	50.21	51.07	48.65	51.49	49.05
TiO2	0.10	0.08	0.05	0.07	0.06	0.13	0.09	0.09
Al2O3	30.72	30.89	30.30	30.59	29.56	31.20	30.60	30.84
Cr2O3	0.00	0.00	0.01	0.00	0.00	0.00	0.00	0.01
Fe2O3	0.00	0.00	0.00	0.00	0.00	0.00	0.00	0.00
FeO	0.57	0.75	0.76	0.63	0.92	0.39	0.87	0.67
MnO	0.00	0.00	0.02	0.04	0.02	0.00	0.00	0.02
MgO	0.00	0.14	0.00	0.51	0.00	0.28	0.47	0.00
CaO	15.31	15.44	14.80	15.29	14.11	15.68	14.57	15.48
BaO	0.00	0.00	0.00	0.00	0.00	0.00	0.00	0.00
Na2O	2.06	2.01	2.26	2.09	2.49	2.09	2.44	2.02
K2O	0.24	0.24	0.29	0.26	0.52	0.17	0.33	0.24
P2O5	0.02	0.00	0.00	0.00	0.03	0.02	0.04	0.04
Total	98.40	98.82	98.89	99.69	98.77	98.61	100.91	98.45
An	79.27	79.75	76.96	78.87	73.38	79.71	75.18	79.67
Ab	19.27	18.77	21.27	19.55	23.42	19.25	22.82	18.84
Or	1.46	1.48	1.77	1.58	3.19	1.04	2.01	1.50

Table S2 cont.: Plagioclase feldpar major element contents.

Sample	10017	10022	10022	10022	10022	10022	10022	10022
Point	65 / 1 .	6 / 1 .	7 / 1 .	9 / 1 .	19 / 1 .	28 / 1 .	31 / 1 .	32 / 1 .
SiO2	49.23	50.41	49.95	50.50	49.98	49.84	50.65	50.31
TiO2	0.08	0.14	0.11	0.11	0.11	0.13	0.21	0.21
Al2O3	30.85	29.54	30.31	29.61	29.78	30.11	29.54	29.80
Cr2O3	0.00	0.01	0.00	0.01	0.01	0.00	0.00	0.01
Fe2O3	0.00	0.00	0.00	0.00	0.00	0.00	0.00	0.00
FeO	0.50	1.00	0.72	0.85	0.80	0.66	0.77	0.65
MnO	0.00	0.00	0.01	0.01	0.03	0.00	0.01	0.00
MgO	0.36	0.24	0.11	0.25	0.36	0.30	0.71	0.24
CaO	15.57	15.01	15.03	14.93	15.27	15.25	14.77	14.58
BaO	0.00	0.00	0.00	0.00	0.00	0.00	0.00	0.00
Na2O	2.07	2.10	2.26	2.23	2.34	2.23	2.43	2.48
K2O	0.22	0.33	0.31	0.33	0.21	0.21	0.23	0.28
P2O5	0.00	0.02	0.00	0.01	0.01	0.02	0.03	0.03
Total	98.88	98.78	98.80	98.85	98.89	98.75	99.34	98.59
An	79.51	78.15	77.15	77.11	77.32	78.11	75.98	75.13
Ab	19.15	19.83	20.96	20.88	21.41	20.63	22.62	23.14
Or	1.34	2.03	1.89	2.01	1.27	1.27	1.40	1.73

Table S2 cont.: Plagioclase feldpar major element contents.

Sample	10022	10022	10022	10022	10022	10022	10022	10022
Point	35 / 1 .	37 / 1 .	41 / 1 .	47 / 1 .	51 / 1 .	54 / 1 .	55 / 1 .	60 / 1 .
SiO2	50.16	50.44	50.21	50.40	50.63	49.99	49.80	50.03
TiO2	0.15	0.05	0.11	0.12	0.14	0.12	0.15	0.07
Al2O3	29.79	29.24	29.76	29.80	29.35	30.77	29.98	29.94
Cr2O3	0.00	0.00	0.00	0.00	0.00	0.01	0.00	0.01
Fe2O3	0.00	0.00	0.00	0.00	0.00	0.00	0.00	0.00
FeO	0.96	1.14	0.78	0.87	0.59	0.70	0.85	0.93
MnO	0.00	0.00	0.01	0.00	0.03	0.01	0.00	0.04
MgO	0.69	0.22	0.66	0.29	0.26	0.27	0.34	0.15
CaO	15.04	14.60	14.98	15.10	14.34	14.64	15.01	14.92
BaO	0.00	0.00	0.00	0.00	0.00	0.00	0.00	0.00
Na2O	2.12	2.29	2.13	2.24	2.54	2.38	2.22	2.18
K2O	0.26	0.35	0.29	0.27	0.27	0.24	0.27	0.33
P2O5	0.03	0.03	0.00	0.00	0.00	0.02	0.00	0.02
Total	99.21	98.37	98.93	99.08	98.17	99.15	98.62	98.61
An	78.38	76.20	78.15	77.58	74.48	76.11	77.60	77.52
Ab	20.01	21.60	20.07	20.78	23.88	22.38	20.75	20.45
Or	1.62	2.20	1.78	1.64	1.64	1.50	1.65	2.03

Table S2 cont.: Plagioclase feldpar major element contents.

Sample	10022	10024	10024	10024	10024	10024	10024	10024
Point	62 / 1 .	4 / 1 .	5 / 1 .	10 / 1 .	11 / 1 .	12 / 1 .	13 / 1 .	14 / 1 .
SiO2	50.01	50.58	49.96	49.47	49.83	48.85	49.23	49.13
TiO2	0.15	0.09	0.15	0.12	0.13	0.14	0.12	0.10
Al2O3	30.10	29.53	30.14	30.88	30.14	30.65	30.84	31.07
Cr2O3	0.01	0.00	0.00	0.00	0.02	0.00	0.00	0.01
Fe2O3	0.00	0.00	0.00	0.00	0.00	0.00	0.00	0.00
FeO	0.85	0.93	0.63	0.54	0.57	0.62	0.53	0.59
MnO	0.00	0.02	0.00	0.04	0.00	0.01	0.00	0.00
MgO	0.30	0.17	0.55	0.23	0.43	0.29	0.53	0.27
CaO	15.13	14.67	15.24	15.40	15.30	15.57	15.55	15.84
BaO	0.00	0.00	0.00	0.00	0.00	0.00	0.00	0.00
Na2O	2.19	2.41	2.25	2.25	2.23	2.05	2.17	2.00
K2O	0.25	0.29	0.25	0.24	0.23	0.23	0.22	0.22
P2O5	0.01	0.00	0.01	0.02	0.00	0.01	0.00	0.01
Total	98.98	98.70	99.17	99.19	98.89	98.41	99.20	99.23
An	78.06	75.69	77.74	77.93	77.98	79.68	78.73	80.28
Ab	20.41	22.54	20.74	20.64	20.61	18.95	19.93	18.37
Or	1.53	1.77	1.52	1.43	1.41	1.37	1.34	1.35

Table S2 cont.: Plagioclase feldpar major element contents.

Sample	10024	10024	10024	10024	10024	10024	10024	10024
Point	24 / 1 .	25 / 1 .	26 / 1 .	27 / 1 .	28 / 1 .	33 / 1 .	35 / 1 .	36 / 1 .
SiO2	49.91	50.47	50.45	49.10	49.15	49.20	48.94	49.04
TiO2	0.08	0.11	0.14	0.15	0.06	0.13	0.05	0.11
Al2O3	30.19	30.11	30.09	30.59	30.53	31.02	30.84	30.87
Cr2O3	0.00	0.00	0.00	0.00	0.00	0.01	0.00	0.00
Fe2O3	0.00	0.00	0.00	0.00	0.00	0.00	0.00	0.00
FeO	0.71	0.72	0.47	0.61	0.80	0.68	0.61	0.56
MnO	0.01	0.01	0.00	0.00	0.01	0.02	0.02	0.00
MgO	0.21	0.31	0.25	0.26	0.15	0.29	0.51	0.27
CaO	15.07	15.10	14.89	15.77	15.16	15.71	15.56	15.76
BaO	0.00	0.00	0.00	0.00	0.00	0.00	0.00	0.00
Na2O	2.25	2.24	2.45	2.10	2.25	1.97	2.10	2.00
K2O	0.29	0.31	0.26	0.23	0.33	0.25	0.26	0.22
P2O5	0.02	0.00	0.00	0.00	0.03	0.00	0.01	0.04
Total	98.74	99.37	98.99	98.81	98.48	99.30	98.89	98.87
An	77.31	77.37	75.82	79.47	77.25	80.26	79.07	80.25
Ab	20.91	20.76	22.61	19.17	20.74	18.21	19.35	18.44
Or	1.78	1.86	1.56	1.36	2.01	1.53	1.58	1.31

Table S2 cont.: Plagioclase feldpar major element contents.

Sample	10024	10024	10024	10024	10024	10024	10024	10024
Point	42 / 1 .	43 / 1 .	49 / 1 .	50 / 1 .	51 / 1 .	53 / 1 .	58 / 1 .	59 / 1 .
SiO2	49.10	49.63	48.51	48.75	51.22	49.22	50.21	49.93
TiO2	0.11	0.07	0.11	0.12	0.05	0.08	0.10	0.06
Al2O3	30.76	29.91	31.00	31.05	29.15	31.06	30.21	30.30
Cr2O3	0.00	0.00	0.00	0.00	0.00	0.01	0.01	0.00
Fe2O3	0.00	0.00	0.00	0.00	0.00	0.00	0.00	0.00
FeO	0.60	0.72	0.46	0.50	1.28	0.49	0.59	0.61
MnO	0.00	0.02	0.01	0.00	0.02	0.01	0.02	0.00
MgO	0.27	0.28	0.57	0.21	0.12	0.25	0.18	0.18
CaO	15.67	15.34	15.85	15.61	14.20	15.59	15.04	14.97
BaO	0.00	0.00	0.00	0.00	0.00	0.00	0.00	0.00
Na2O	2.07	2.17	2.11	2.13	2.50	2.14	2.29	2.34
K2O	0.23	0.28	0.22	0.20	0.67	0.22	0.24	0.23
P2O5	0.00	0.03	0.02	0.02	0.04	0.02	0.03	0.02
Total	98.80	98.44	98.86	98.59	99.23	99.08	98.92	98.65
An	79.60	78.31	79.54	79.25	72.78	79.05	77.23	76.85
Ab	19.01	20.01	19.16	19.54	23.15	19.64	21.29	21.74
Or	1.39	1.68	1.30	1.22	4.07	1.31	1.48	1.41

Table S2 cont.: Plagioclase feldpar major element contents.

Sample	10024	10024	10024	10024	10024	10049	10049	10049
Point	60 / 1 .	62 / 1 .	65 / 1 .	70 / 1 .	80 / 1 .	2 / 1 .	3 / 1 .	5 / 1 .
SiO2	49.62	49.55	49.16	49.38	48.94	49.73	49.46	51.26
TiO2	0.13	0.16	0.11	0.05	0.11	0.16	0.06	0.70
Al2O3	30.16	30.42	30.74	30.94	31.25	30.82	30.97	1.20
Cr2O3	0.00	0.00	0.00	0.00	0.00	0.00	0.00	0.09
Fe2O3	0.00	0.00	0.00	0.00	0.00	0.00	0.00	0.00
FeO	0.53	0.66	0.56	0.44	0.72	0.67	0.87	31.74
MnO	0.04	0.00	0.00	0.03	0.01	0.00	0.02	0.45
MgO	0.28	0.30	0.28	0.19	0.20	0.23	0.18	4.58
CaO	15.16	15.20	15.40	15.47	15.67	15.32	15.45	8.19
BaO	0.00	0.00	0.00	0.00	0.00	0.00	0.00	0.00
Na2O	2.31	2.26	2.24	2.05	2.03	2.20	1.99	0.05
K2O	0.23	0.24	0.21	0.24	0.23	0.21	0.27	0.01
P2O5	0.03	0.03	0.00	0.00	0.01	0.01	0.01	0.01
Total	98.49	98.81	98.71	98.80	99.18	99.35	99.29	98.29
An	77.29	77.61	78.13	79.44	79.83	78.36	79.73	98.69
Ab	21.34	20.91	20.58	19.08	18.76	20.34	18.59	1.14
Or	1.37	1.48	1.29	1.48	1.41	1.29	1.67	0.17

Table S2 cont.: Plagioclase feldpar major element contents.

Sample	10049	10049	10049	10049	10049	10049	10049	10049
Point	8 / 1 .	9 / 1 .	14 / 1 .	17 / 1 .	18 / 1 .	19 / 1 .	23 / 1 .	24 / 1 .
SiO2	49.12	50.17	49.63	51.64	50.46	49.58	49.62	49.94
TiO2	0.15	0.19	0.12	0.26	0.28	0.17	0.17	0.11
Al2O3	30.95	30.06	30.35	29.37	29.63	30.66	30.53	30.60
Cr2O3	0.01	0.00	0.01	0.00	0.00	0.01	0.01	0.00
Fe2O3	0.00	0.00	0.00	0.00	0.00	0.00	0.00	0.00
FeO	0.91	0.94	0.96	0.99	1.02	0.90	0.87	0.85
MnO	0.01	0.04	0.00	0.04	0.01	0.00	0.04	0.00
MgO	0.30	0.38	0.18	0.15	0.28	0.28	0.32	0.25
CaO	15.46	15.09	15.17	15.04	14.78	15.22	15.24	15.36
BaO	0.00	0.00	0.00	0.00	0.00	0.00	0.00	0.00
Na2O	2.10	2.28	2.13	1.58	2.33	2.09	2.16	2.11
K2O	0.22	0.23	0.29	0.66	0.32	0.28	0.26	0.26
P2O5	0.03	0.00	0.00	0.10	0.02	0.01	0.03	0.00
Total	99.26	99.38	98.83	99.85	99.12	99.19	99.25	99.48
An	79.13	77.42	78.28	80.44	76.29	78.71	78.33	78.78
Ab	19.50	21.19	19.92	15.32	21.76	19.58	20.05	19.62
Or	1.36	1.39	1.80	4.23	1.95	1.71	1.61	1.61

Table S2 cont.: Plagioclase feldpar major element contents.

Sample	10049	10049	10049	10049	10069	10069	10069	10069
Point	31 / 1 .	34 / 1 .	37 / 1 .	40 / 1 .	1 / 1 .	2 / 1 .	7 / 1 .	8 / 1 .
SiO2	49.82	48.09	49.67	49.47	49.67	49.70	49.30	50.42
TiO2	0.20	0.10	0.10	0.15	0.15	0.16	0.12	0.11
Al2O3	31.02	31.70	30.69	30.58	31.07	31.45	31.26	31.59
Cr2O3	0.00	0.00	0.00	0.00	0.01	0.00	0.00	0.00
Fe2O3	0.00	0.00	0.00	0.00	0.00	0.00	0.00	0.00
FeO	0.84	0.64	0.76	0.80	0.66	0.68	0.56	0.57
MnO	0.05	0.00	0.00	0.04	0.05	0.02	0.02	0.03
MgO	0.26	0.22	0.26	0.29	0.00	0.00	0.00	0.00
CaO	15.53	16.35	15.35	15.20	15.72	16.05	15.85	15.77
BaO	0.00	0.00	0.00	0.00	0.00	0.00	0.00	0.00
Na2O	2.07	1.79	2.08	2.34	1.99	1.88	1.95	2.02
K2O	0.25	0.21	0.26	0.23	0.21	0.17	0.20	0.19
P2O5	0.00	0.02	0.00	0.03	0.03	0.02	0.00	0.03
Total	100.04	99.12	99.17	99.12	99.54	100.14	99.26	100.74
An	79.39	82.44	79.03	77.10	80.31	81.67	80.77	80.21
Ab	19.11	16.30	19.36	21.50	18.42	17.32	18.02	18.63
Or	1.50	1.27	1.61	1.40	1.27	1.02	1.21	1.16

Table S2 cont.: Plagioclase feldpar major element contents.

Sample	10069	10069	10069	10069	10069	10069	10069	10069
Point	13 / 1 .	15 / 1 .	16 / 1 .	19 / 1 .	21 / 1 .	26 / 1 .	27 / 1 .	31 / 1 .
SiO2	51.17	50.85	50.41	49.32	50.24	50.51	51.99	50.44
TiO2	0.10	0.17	0.15	0.14	0.12	0.15	0.22	0.13
Al2O3	29.36	29.55	30.28	31.20	31.16	30.45	29.17	30.40
Cr2O3	0.00	0.00	0.00	0.01	0.01	0.01	0.01	0.00
Fe2O3	0.00	0.00	0.00	0.00	0.00	0.00	0.00	0.00
FeO	0.98	0.87	0.73	0.68	0.76	0.76	0.76	0.88
MnO	0.01	0.01	0.00	0.00	0.01	0.01	0.01	0.00
MgO	0.00	0.00	0.00	0.00	0.00	0.00	0.00	0.00
CaO	14.30	14.62	15.74	15.75	15.30	15.31	14.73	15.37
BaO	0.00	0.00	0.00	0.00	0.00	0.00	0.00	0.00
Na2O	2.61	2.51	1.97	2.07	2.16	2.24	1.96	1.94
K2O	0.38	0.31	0.22	0.21	0.24	0.26	0.43	0.37
P2O5	0.04	0.00	0.00	0.02	0.02	0.02	0.01	0.00
Total	98.94	98.90	99.51	99.40	100.01	99.72	99.28	99.52
An	73.39	74.86	80.45	79.77	78.49	77.85	78.42	79.55
Ab	24.26	23.26	18.24	18.97	20.06	20.57	18.86	18.16
Or	2.35	1.87	1.31	1.26	1.44	1.58	2.71	2.29

Table S2 cont.: Plagioclase feldpar major element contents.

Sample	10069	10069	10069	10069	10069	10069	10069	10069
Point	32 / 1 .	35 / 1 .	36 / 1 .	37 / 1 .	39 / 1 .	43 / 1 .	44 / 1 .	45 / 1 .
SiO2	50.09	50.30	50.25	50.16	49.63	50.74	50.11	53.98
TiO2	0.09	0.12	0.17	0.23	0.15	0.15	0.12	0.15
Al2O3	30.60	30.25	30.64	30.55	30.90	30.15	30.73	28.09
Cr2O3	0.00	0.00	0.01	0.00	0.01	0.00	0.00	0.01
Fe2O3	0.00	0.00	0.00	0.00	0.00	0.00	0.00	0.00
FeO	0.88	0.84	0.98	1.05	0.94	0.91	0.62	0.80
MnO	0.04	0.00	0.00	0.01	0.03	0.01	0.01	0.01
MgO	0.00	0.00	0.00	0.00	0.00	0.00	0.00	0.00
CaO	15.47	15.11	15.43	15.30	15.55	14.89	15.76	12.59
BaO	0.00	0.00	0.00	0.00	0.00	0.00	0.00	0.00
Na2O	2.14	2.23	2.24	2.15	2.10	2.41	2.10	3.43
K2O	0.26	0.27	0.25	0.24	0.25	0.33	0.22	0.64
P2O5	0.03	0.02	0.02	0.01	0.01	0.05	0.02	0.04
Total	99.58	99.14	99.98	99.70	99.57	99.63	99.68	99.74
An	78.74	77.65	77.99	78.54	79.17	75.84	79.53	64.40
Ab	19.70	20.71	20.48	19.99	19.32	22.16	19.15	31.71
Or	1.56	1.63	1.52	1.47	1.51	2.00	1.32	3.89

Table S2 cont.: Plagioclase feldpar major element contents.

Sample	10069	10069	10069	10069	10069	10069	10069	10069
Point	48 / 1 .	50 / 1 .	55 / 1 .	61 / 1 .	64 / 1 .	65 / 1 .	68 / 1 .	69 / 1 .
SiO2	50.32	49.90	48.69	53.03	50.21	50.05	50.39	50.65
TiO2	0.15	0.10	0.06	0.22	0.17	0.22	0.17	0.11
Al2O3	30.48	31.45	31.89	28.81	30.86	30.94	31.12	30.90
Cr2O3	0.00	0.01	0.00	0.01	0.00	0.01	0.00	0.00
Fe2O3	0.00	0.00	0.00	0.00	0.00	0.00	0.00	0.00
FeO	0.83	0.70	0.64	1.00	0.75	0.81	0.67	0.57
MnO	0.00	0.01	0.00	0.00	0.01	0.00	0.00	0.00
MgO	0.00	0.00	0.51	0.00	0.00	0.00	0.33	0.00
CaO	15.58	15.98	16.31	13.31	15.43	15.61	15.87	15.44
BaO	0.00	0.00	0.00	0.00	0.00	0.00	0.00	0.00
Na2O	2.17	1.94	1.88	3.10	2.18	2.03	1.95	2.15
K2O	0.23	0.17	0.20	0.58	0.26	0.21	0.18	0.23
P2O5	0.01	0.00	0.01	0.05	0.00	0.02	0.02	0.00
Total	99.78	100.27	100.18	100.09	99.87	99.90	100.71	100.06
An	78.78	81.17	81.78	67.89	78.40	79.87	80.87	78.71
Ab	19.84	17.79	17.06	28.61	20.02	18.84	18.01	19.87
Or	1.38	1.05	1.16	3.49	1.58	1.29	1.12	1.42

Table S2 cont.: Plagioclase feldpar major element contents.

Sample	10069	10069	10069	10069	10069	10069	10069	10069
Point	70 / 1 .	74 / 1 .	81 / 1 .	82 / 1 .	86 / 1 .	87 / 1 .	88 / 1 .	91 / 1 .
SiO2	50.12	51.81	50.60	49.81	48.36	50.00	50.39	49.37
TiO2	0.08	0.11	0.09	0.14	0.09	0.19	0.18	0.11
Al2O3	31.84	29.61	30.57	31.29	32.62	31.05	31.04	31.65
Cr2O3	0.00	0.00	0.00	0.00	0.00	0.00	0.02	0.01
Fe2O3	0.00	0.00	0.00	0.00	0.00	0.00	0.00	0.00
FeO	0.73	0.96	0.74	0.75	0.70	0.89	0.87	0.57
MnO	0.01	0.02	0.00	0.03	0.00	0.00	0.02	0.00
MgO	0.90	0.06	0.00	0.00	0.00	0.00	0.25	0.00
CaO	15.74	14.41	15.17	15.62	16.63	15.45	15.72	16.02
BaO	0.00	0.00	0.00	0.00	0.00	0.00	0.00	0.00
Na2O	1.80	2.65	2.20	2.16	1.63	2.14	2.14	1.92
K2O	0.22	0.32	0.25	0.27	0.18	0.26	0.23	0.17
P2O5	0.02	0.01	0.04	0.00	0.01	0.00	0.00	0.00
Total	101.47	99.96	99.66	100.08	100.21	99.98	100.86	99.84
An	81.71	73.54	78.03	78.65	84.03	78.71	79.11	81.32
Ab	16.91	24.49	20.43	19.72	14.88	19.73	19.52	17.63
Or	1.38	1.97	1.54	1.62	1.09	1.56	1.38	1.04

Table S2 cont.: Plagioclase feldpar major element contents.

Sample	10069	10069	10069	10069	10069	10069	10069	10069
Point	93 / 1 .	94 / 1 .	99 / 1 .	100 / 1 .	106 / 1 .	108 / 1 .	109 / 1 .	110 / 1 .
SiO2	50.40	49.22	51.27	48.48	48.96	49.95	49.99	48.98
TiO2	0.07	0.06	0.14	0.06	0.09	0.14	0.15	0.10
Al2O3	30.46	30.60	30.01	32.16	32.33	31.35	31.34	31.69
Cr2O3	0.00	0.00	0.00	0.01	0.00	0.00	0.00	0.01
Fe2O3	0.00	0.00	0.00	0.00	0.00	0.00	0.00	0.00
FeO	0.81	0.73	0.82	0.66	0.77	0.45	0.46	0.72
MnO	0.00	0.00	0.01	0.00	0.00	0.01	0.00	0.01
MgO	0.00	0.11	0.00	0.00	0.00	0.00	0.00	0.00
CaO	14.92	15.43	14.91	16.60	16.43	15.84	15.82	15.87
BaO	0.00	0.00	0.00	0.00	0.00	0.00	0.00	0.00
Na2O	2.37	2.12	2.39	1.72	1.93	2.06	2.09	2.17
K2O	0.29	0.26	0.28	0.18	0.21	0.19	0.20	0.26
P2O5	0.00	0.03	0.05	0.01	0.00	0.02	0.01	0.01
Total	99.33	98.56	99.88	99.87	100.72	100.02	100.08	99.82
An	76.27	78.81	76.18	83.33	81.49	79.97	79.72	78.95
Ab	21.93	19.60	22.09	15.62	17.28	18.86	19.08	19.50
Or	1.79	1.59	1.73	1.05	1.23	1.17	1.20	1.55

Table S2 cont.: Plagioclase feldpar major element contents.

Sample	10069	10069	10069	10071	10071	10071	10071	10071
Point	112 / 1 .	113 / 1 .	114 / 1 .	3 / 1 .	4 / 1 .	5 / 1 .	6 / 1 .	11 / 1 .
SiO2	50.26	50.05	49.51	50.28	49.55	49.98	50.80	50.26
TiO2	0.09	0.15	0.24	0.10	0.15	0.15	0.16	0.14
Al2O3	29.55	30.93	31.40	30.37	31.14	30.16	30.32	30.10
Cr2O3	0.00	0.01	0.01	0.00	0.00	0.01	0.00	0.00
Fe2O3	0.00	0.00	0.00	0.00	0.00	0.00	0.00	0.00
FeO	0.70	0.81	0.84	1.02	0.79	0.79	0.72	0.80
MnO	0.01	0.03	0.03	0.03	0.04	0.00	0.01	0.01
MgO	0.46	0.00	0.18	0.18	0.31	0.33	0.35	0.27
CaO	15.47	15.19	15.60	15.29	15.91	15.35	15.14	15.25
BaO	0.00	0.00	0.00	0.00	0.00	0.00	0.00	0.00
Na2O	2.14	2.23	2.10	2.10	1.96	2.20	2.14	2.29
K2O	0.26	0.27	0.24	0.31	0.21	0.24	0.22	0.28
P2O5	0.03	0.00	0.01	0.00	0.02	0.01	0.01	0.01
Total	98.98	99.67	100.15	99.67	100.09	99.20	99.87	99.41
An	78.70	77.68	79.24	78.55	80.76	78.23	78.50	77.30
Ab	19.71	20.66	19.31	19.52	17.98	20.29	20.12	21.04
Or	1.59	1.66	1.45	1.93	1.26	1.48	1.38	1.66

Table S2 cont.: Plagioclase feldpar major element contents.

Sample	10071	10071	10071	10071	10071	10071	10071	10071
Point	18 / 1 .	19 / 1 .	25 / 1 .	26 / 1 .	29 / 1 .	30 / 1 .	31 / 1 .	32 / 1 .
SiO2	50.23	50.33	50.48	50.47	51.80	52.32	52.88	49.62
TiO2	0.20	0.15	0.20	0.17	0.21	0.12	0.29	0.10
Al2O3	30.05	29.84	29.76	29.99	29.00	28.86	27.89	31.05
Cr2O3	0.00	0.00	0.00	0.01	0.01	0.00	0.00	0.00
Fe2O3	0.00	0.00	0.00	0.00	0.00	0.00	0.00	0.00
FeO	1.11	1.36	0.86	0.93	0.69	1.46	1.78	0.81
MnO	0.03	0.02	0.00	0.01	0.01	0.01	0.03	0.00
MgO	0.37	0.11	0.34	0.39	0.26	0.12	0.08	0.17
CaO	15.26	14.85	15.04	15.28	14.32	14.35	13.52	15.68
BaO	0.00	0.00	0.00	0.00	0.00	0.00	0.00	0.00
Na2O	2.20	2.28	2.33	2.16	2.49	2.23	2.12	1.99
K2O	0.26	0.55	0.26	0.25	0.30	0.82	1.13	0.23
P2O5	0.00	0.01	0.00	0.00	0.00	0.02	0.07	0.00
Total	99.71	99.49	99.28	99.65	99.08	100.32	99.80	99.64
An	78.09	75.67	76.85	78.41	74.67	74.11	72.26	80.16
Ab	20.35	21.00	21.58	20.07	23.47	20.82	20.54	18.45
Or	1.56	3.34	1.58	1.51	1.86	5.07	7.20	1.39

Table S2 cont.: Plagioclase feldpar major element contents.

Sample	10071	10071	10071	10071	10071	10071	10071	10071
Point	33 / 1 .	35 / 1 .	42 / 1 .	43 / 1 .	47 / 1 .	51 / 1 .	55 / 1 .	56 / 1 .
SiO2	49.88	50.34	49.65	48.81	50.77	49.43	51.41	48.71
TiO2	0.07	0.09	0.73	0.56	0.17	0.11	0.19	0.39
Al2O3	29.67	30.08	29.11	28.72	30.26	30.44	28.67	30.37
Cr2O3	0.00	0.00	0.01	0.00	0.00	0.00	0.00	0.00
Fe2O3	0.00	0.00	0.00	0.00	0.00	0.00	0.00	0.00
FeO	1.10	1.15	2.61	3.30	0.76	0.87	0.81	1.36
MnO	0.01	0.01	0.05	0.00	0.00	0.01	0.01	0.01
MgO	0.01	0.17	0.53	0.15	0.32	0.16	0.33	0.19
CaO	14.82	15.24	15.17	14.68	15.02	15.44	14.54	15.53
BaO	0.00	0.00	0.00	0.00	0.00	0.00	0.00	0.00
Na2O	2.16	2.19	1.95	2.21	2.34	2.15	2.44	1.98
K2O	0.73	0.28	0.26	0.45	0.26	0.26	0.28	0.28
P2O5	0.02	0.01	0.07	0.50	0.00	0.00	0.03	0.13
Total	98.46	99.56	100.14	99.39	99.89	98.86	98.71	98.94
An	75.64	78.03	79.81	76.42	76.79	78.64	75.39	79.88
Ab	19.95	20.29	18.58	20.81	21.66	19.78	22.91	18.42
Or	4.41	1.68	1.60	2.77	1.56	1.58	1.70	1.70

Table S2 cont.: Plagioclase feldpar major element contents.

Sample	10071	10071	10071	10071	10071	10071	10071	10071
Point	68 / 1 .	69 / 1 .	74 / 1 .	80 / 1 .	82 / 1 .	83 / 1 .	84 / 1 .	85 / 1 .
SiO2	50.38	49.98	50.56	52.20	48.64	53.55	49.56	48.86
TiO2	0.14	0.19	0.14	0.17	1.51	0.29	0.16	1.70
Al2O3	30.29	31.68	30.09	29.22	1.72	27.46	30.97	2.16
Cr2O3	0.00	0.00	0.01	0.00	0.29	0.00	0.01	0.34
Fe2O3	0.00	0.00	0.00	0.00	0.00	0.00	0.00	0.00
FeO	0.72	0.89	0.85	0.56	20.76	2.04	0.70	18.22
MnO	0.00	0.01	0.02	0.00	0.33	0.01	0.01	0.25
MgO	0.22	0.36	0.24	0.27	9.54	0.19	0.25	10.08
CaO	15.11	15.17	15.08	14.16	15.18	13.30	15.65	17.48
BaO	0.00	0.00	0.00	0.00	0.00	0.00	0.00	0.00
Na2O	2.25	2.23	2.24	2.57	0.05	2.20	1.99	0.06
K2O	0.27	0.24	0.29	0.27	0.02	0.81	0.25	0.01
P2O5	0.01	0.01	0.01	0.01	0.02	0.09	0.02	0.01
Total	99.39	100.76	99.53	99.43	98.06	99.94	99.57	99.17
An	77.49	77.87	77.38	74.00	99.26	72.87	80.05	99.32
Ab	20.87	20.68	20.82	24.32	0.56	21.83	18.43	0.61
Or	1.65	1.45	1.80	1.68	0.18	5.30	1.52	0.07

Table S2 cont.: Plagioclase feldpar major element contents.

Sample	10071	10072	10072	10072	10072	10072	10072	10072
Point	94 / 1 .	3 / 1 .	5 / 1 .	10 / 1 .	12 / 1 .	13 / 1 .	17 / 1 .	20 / 1 .
SiO2	49.69	51.15	49.79	48.70	50.61	49.79	49.59	48.53
TiO2	0.11	0.16	0.11	0.11	0.19	0.12	0.19	0.16
Al2O3	32.37	30.27	31.03	31.65	30.65	31.08	31.34	31.62
Cr2O3	0.01	0.00	0.00	0.00	0.01	0.00	0.00	0.01
Fe2O3	0.00	0.00	0.00	0.00	0.00	0.00	0.00	0.00
FeO	0.91	0.61	0.67	0.65	0.83	0.63	0.70	0.70
MnO	0.03	0.02	0.00	0.00	0.03	0.01	0.01	0.02
MgO	0.32	0.31	0.26	0.21	0.28	0.27	0.26	0.25
CaO	15.30	14.69	15.40	15.84	15.14	15.40	15.55	15.92
BaO	0.00	0.00	0.00	0.00	0.00	0.00	0.00	0.00
Na2O	2.15	2.52	2.22	2.00	2.32	2.29	2.21	1.98
K2O	0.29	0.27	0.24	0.25	0.22	0.24	0.23	0.23
P2O5	0.01	0.04	0.06	0.00	0.02	0.00	0.00	0.02
Total	101.19	100.04	99.79	99.41	100.30	99.83	100.07	99.43
An	78.30	75.04	78.14	80.19	77.21	77.69	78.47	80.54
Ab	19.93	23.33	20.42	18.31	21.46	20.89	20.15	18.08
Or	1.77	1.63	1.44	1.50	1.34	1.42	1.39	1.37

Table S2 cont.: Plagioclase feldpar major element contents.

Sample	10072	10072	10072	10072	10072
Point	22 / 1 .	25 / 1 .	26 / 1 .	30 / 1 .	41 / 1 .
SiO2	49.54	51.48	49.43	50.11	50.14
TiO2	0.07	0.11	0.11	0.05	0.15
Al2O3	31.05	29.45	31.18	30.32	30.86
Cr2O3	0.01	0.00	0.00	0.00	0.00
Fe2O3	0.00	0.00	0.00	0.00	0.00
FeO	0.73	1.05	0.58	0.95	0.58
MnO	0.01	0.03	0.02	0.04	0.01
MgO	0.21	0.17	0.22	0.20	0.25
CaO	15.68	14.45	15.48	15.04	15.06
BaO	0.00	0.00	0.00	0.00	0.00
Na2O	2.07	2.59	2.13	2.27	2.44
K2O	0.28	0.46	0.28	0.30	0.27
P2O5	0.01	0.07	0.02	0.01	0.02
Total	99.66	99.86	99.44	99.29	99.79
An	79.39	73.40	78.72	77.09	76.06
Ab	18.95	23.84	19.60	21.08	22.33
Or	1.66	2.76	1.68	1.83	1.61

Table S3: Plagioclase feldspar trace element contents.

Sample	10017	10017	10017	10017	10017	10017	10017	10017
LAICPMS point*	17.1.pl.40um	17.5.pl.40um	17.7.pl.40um	17.8.pl.40um	17.19.pl.40um	17.27.pl.40um	17.38.pl.40um	17.39.pl.40um
Ca43_ppm_mean	131143.139	138987.046	130033.371	135591.973	113242.370	55800.568	197941.752	139051.641
Ca43_ppm_2SE(int)	3240.552	4091.598	2909.132	3310.331	7572.222	5219.910	19658.132	3405.311
Sc45_ppm_mean	4.722	4.629	5.471	4.828	8.918	4.679	10.170	4.742
Sc45_ppm_2SE(int)	0.305	0.258	0.597	0.283	1.891	0.265	1.027	0.276
Ti47_ppm_mean	643.793	463.749	1164.804	394.818	1244.892	646.118	929.842	437.741
Ti47_ppm_2SE(int)	25.038	113.543	292.638	15.242	276.546	23.359	682.143	25.082
V51_ppm_mean	0.691	0.474	1.004	0.557	1.801	0.283	1.165	0.699
V51_ppm_2SE(int)	0.250	0.201	0.861	0.271	0.680	0.202	0.646	0.701
Cr52_ppm_mean	3.150	3.256	9.080	2.390	49.427	7.690	32.112	21.526
Cr52_ppm_2SE(int)	0.874	0.656	2.825	0.604	24.992	1.928	3.633	24.007
Mn55_ppm_mean	47.506	52.983	84.528	53.901	200.521	32.200	261.202	58.201
Mn55_ppm_2SE(int)	1.472	2.027	15.129	1.752	62.994	3.016	32.627	2.123
Co59_ppm_mean	0.471	0.568	0.731	0.494	1.705	0.479	1.322	0.565
Co59_ppm_2SE(int)	0.108	0.100	0.202	0.083	0.484	0.168	0.156	0.105
Ni60_ppm_mean	0.090	0.300	0.300	0.108	0.665	0.228	0.688	6.374
Ni60_ppm_2SE(int)	0.204	0.189	0.246	0.121	0.292	0.108	0.223	12.129
Cu63_ppm_mean	0.448	1.928	2.708	0.430	6.673	3.886	2.774	0.326
Cu63_ppm_2SE(int)	0.214	0.434	0.356	0.154	1.974	0.352	0.427	0.137
Zn66_ppm_mean	1.019	0.804	2.424	0.855	4.041	3.404	6.663	1.021
Zn66_ppm_2SE(int)	0.738	0.530	0.720	0.477	0.872	0.690	2.114	0.590
Rb85_ppm_mean	0.784	0.296	1.043	0.432	8.978	0.596	1.868	0.649
Rb85_ppm_2SE(int)	1.028	0.054	0.386	0.202	1.770	0.162	0.349	0.460
Sr88_ppm_mean	378.663	519.294	410.888	510.178	727.991	467.278	1595.643	589.711
Sr88_ppm_2SE(int)	11.757	13.388	10.795	17.082	40.022	51.719	78.053	16.962
Y89_ppm_mean	0.807	1.182	12.786	1.190	66.176	2.900	4138.360	1.999
Y89_ppm_2SE(int)	0.108	0.109	7.587	0.087	19.561	0.408	1349.528	0.335
Zr90_ppm_mean	0.091	0.161	25.725	0.196	216.792	7.134	58.977	1.118
Zr90_ppm_2SE(int)	0.033	0.056	14.157	0.086	65.849	1.511	32.254	0.783
Nb93_ppm_mean	0.722	0.016	1.391	0.022	7.333	0.147	9.353	0.126
Nb93_ppm_2SE(int)	1.422	0.015	0.691	0.013	2.221	0.047	9.912	0.099
Ba137_ppm_mean	82.573	137.723	122.443	128.337	755.493	373.293	1321.381	188.186
Ba137_ppm_2SE(int)	3.116	5.277	12.115	4.109	131.408	45.824	40.346	7.001
Hf178_ppm_mean	0.135	0.002	0.677	0.012	6.983	0.212	3.152	0.132
Hf178_ppm_2SE(int)	0.270	0.005	0.356	0.014	2.179	0.056	1.472	0.155
Ta181_ppm_mean	0.000	0.005	0.072	0.163	0.440	0.007	0.585	0.007
Ta181_ppm_2SE(int)	0.000	0.008	0.034	0.323	0.136	0.005	0.501	0.006
Pb208_ppm_mean	0.040	0.290	0.440	0.069	1.269	0.267	13.842	0.080
Pb208_ppm_2SE(int)	0.018	0.276	0.291	0.023	0.318	0.148	8.058	0.069
Th232_ppm_mean	0.000	0.120	0.327	0.003	2.000	0.059	34.666	0.021
Th232_ppm_2SE(int)	0.000	0.232	0.184	0.005	0.637	0.045	12.970	0.015
U238_ppm_mean	0.003	0.047	0.123	0.001	8.050	0.014	3.084	1.708
U238_ppm_2SE(int)	0.006	0.096	0.080	0.002	14.944	0.006	1.207	3.363

*Point names include phase (pl) and spot size (i.e., 30 um).

Table S3: Plagioclase feldspar trace element contents.

Sample	10017	10017	10017	10017	10017	10017	10017	10017
LAICPMS point*	17.40.pl.40um	17.42.pl.40um	17.43.pl.40um	17.52.pl.40um	17.53.pl.40um	17.57.pl.40um	17.59.pl.40um	17.64.pl.40um
Ca43_ppm_mean	142903.989	141232.850	135877.933	127860.576	140502.559	23815.759	134449.701	136669.164
Ca43_ppm_2SE(int)	3662.498	4056.185	3574.189	5634.803	4370.797	1254.653	2956.674	3527.690
Sc45_ppm_mean	4.589	4.482	4.661	13.256	5.502	5.503	4.365	4.447
Sc45_ppm_2SE(int)	0.209	0.245	0.315	3.083	0.445	0.298	0.276	0.260
Ti47_ppm_mean	559.712	546.811	384.592	801.686	494.692	1607.719	664.445	419.535
Ti47_ppm_2SE(int)	18.611	18.864	14.294	154.585	20.953	153.666	18.112	12.229
V51_ppm_mean	0.594	0.440	0.785	3.323	0.862	1.258	0.849	0.496
V51_ppm_2SE(int)	0.259	0.264	0.817	1.118	0.373	0.220	0.250	0.339
Cr52_ppm_mean	4.938	3.507	1.820	156.434	22.887	54.416	4.156	3.442
Cr52_ppm_2SE(int)	1.082	0.651	0.586	57.060	10.047	9.407	0.717	0.845
Mn55_ppm_mean	51.894	53.386	56.019	469.296	98.338	48.819	45.418	54.106
Mn55_ppm_2SE(int)	2.310	1.625	1.406	141.764	18.590	5.072	1.321	1.568
Co59_ppm_mean	0.643	0.581	1.347	3.733	1.312	1.334	0.664	0.479
Co59_ppm_2SE(int)	0.088	0.089	1.433	1.038	0.329	0.601	0.113	0.079
Ni60_ppm_mean	0.177	0.221	0.217	1.468	0.507	0.816	0.348	0.130
Ni60_ppm_2SE(int)	0.164	0.152	0.112	2.433	0.193	0.293	0.193	0.125
Cu63_ppm_mean	0.317	0.271	0.962	4.434	3.255	9.154	0.925	2.003
Cu63_ppm_2SE(int)	0.101	0.153	0.299	0.541	0.437	1.622	0.155	1.174
Zn66_ppm_mean	1.036	0.777	1.222	2.526	1.564	5.189	0.803	0.717
Zn66_ppm_2SE(int)	1.091	0.387	0.696	0.623	0.479	0.643	0.579	0.366
Rb85_ppm_mean	0.359	0.310	0.368	0.687	0.384	1.200	0.271	0.334
Rb85_ppm_2SE(int)	0.083	0.066	0.071	0.624	0.054	0.421	0.055	0.057
Sr88_ppm_mean	435.209	449.100	580.701	594.137	546.934	163.500	387.152	502.354
Sr88_ppm_2SE(int)	10.892	15.998	15.632	43.223	17.971	18.633	11.788	12.177
Y89_ppm_mean	1.131	1.054	1.730	12.949	2.264	2.374	0.738	1.277
Y89_ppm_2SE(int)	0.149	0.110	0.218	3.596	0.423	0.644	0.072	0.103
Zr90_ppm_mean	0.507	0.082	0.466	12.705	0.532	17.226	0.103	0.085
Zr90_ppm_2SE(int)	0.295	0.039	0.430	17.691	0.171	1.798	0.039	0.041
Nb93_ppm_mean	0.125	0.014	0.019	0.052	0.012	0.604	0.019	0.008
Nb93_ppm_2SE(int)	0.084	0.011	0.014	0.035	0.011	0.122	0.026	0.009
Ba137_ppm_mean	123.764	106.036	188.921	196.780	173.198	150.076	103.811	141.639
Ba137_ppm_2SE(int)	4.244	3.928	5.742	13.551	6.046	21.409	3.153	4.158
Hf178_ppm_mean	0.029	0.002	0.008	0.150	0.021	0.462	0.000	0.005
Hf178_ppm_2SE(int)	0.026	0.005	0.012	0.055	0.015	0.083	0.000	0.007
Ta181_ppm_mean	0.000	0.000	0.002	0.081	0.001	0.032	0.001	0.000
Ta181_ppm_2SE(int)	0.000	0.000	0.002	0.158	0.002	0.010	0.002	0.000
Pb208_ppm_mean	0.065	0.034	0.058	0.211	0.185	0.893	0.035	0.126
Pb208_ppm_2SE(int)	0.022	0.024	0.030	0.053	0.237	0.211	0.021	0.129
Th232_ppm_mean	0.005	0.002	0.007	0.023	0.008	0.270	0.001	0.280
Th232_ppm_2SE(int)	0.006	0.003	0.007	0.009	0.007	0.219	0.002	0.560
U238_ppm_mean	0.026	0.001	0.007	0.266	0.002	0.037	0.000	0.000
U238_ppm_2SE(int)	0.040	0.001	0.011	0.515	0.003	0.015	0.000	0.000

*Point names include phase (pl) and spot size (i.e., 30 um).

Table S3: Plagioclase feldspar trace element contents.

Sample	10017	10022	10022	10022	10022	10022	10022	10024
LAICPMS point*	17.65.pl.40um	22.19.pl.30um	22.28.pl.35um	22.31.pl.35um	22.37.pl.35um	22.47.pl.35um	22.51.pl.35um	24.4.pl.40um
Ca43_ppm_mean	135475.812	129205.698	1687.962	81043.803	98624.005	142879.998	124964.039	139091.395
Ca43_ppm_2SE(int)	3668.385	5252.056	294.398	16918.676	5947.717	5829.583	6360.563	3577.654
Sc45_ppm_mean	4.498	5.834	5.148	4.867	9.012	5.163	5.170	4.595
Sc45_ppm_2SE(int)	0.252	0.537	0.355	0.598	1.453	0.487	0.537	0.249
Ti47_ppm_mean	647.426	1023.731	16.139	1070.368	1573.682	693.265	745.374	555.178
Ti47_ppm_2SE(int)	23.500	118.561	2.942	217.460	224.120	51.000	71.594	54.604
V51_ppm_mean	0.633	0.836	-0.135	0.219	0.715	0.895	0.351	0.584
V51_ppm_2SE(int)	0.249	0.292	0.193	0.917	0.451	0.626	0.683	0.274
Cr52_ppm_mean	6.300	12.006	2.097	35.699	26.220	8.101	2.127	15.307
Cr52_ppm_2SE(int)	1.041	3.588	0.730	9.160	4.222	2.065	1.503	25.920
Mn55_ppm_mean	53.631	101.288	1.742	79.285	264.112	89.865	54.431	55.267
Mn55_ppm_2SE(int)	1.612	13.295	0.459	15.225	28.034	3.532	2.449	1.224
Co59_ppm_mean	0.749	1.014	0.017	0.748	1.485	0.893	1.687	0.831
Co59_ppm_2SE(int)	0.224	0.158	0.035	0.266	0.409	0.284	1.783	0.255
Ni60_ppm_mean	0.409	0.216	0.172	0.813	0.523	0.249	0.808	0.365
Ni60_ppm_2SE(int)	0.170	0.220	0.129	0.535	0.699	0.324	0.824	0.177
Cu63_ppm_mean	5.645	0.735	1.400	1.590	1.250	0.848	1.199	0.573
Cu63_ppm_2SE(int)	0.638	0.441	2.561	0.710	0.837	0.281	0.650	0.149
Zn66_ppm_mean	1.252	0.865	0.550	12.752	3.581	1.167	4.770	0.871
Zn66_ppm_2SE(int)	0.430	0.588	0.330	15.137	1.308	0.785	2.932	0.549
Rb85_ppm_mean	0.288	0.654	0.043	0.457	35.933	0.681	0.297	0.447
Rb85_ppm_2SE(int)	0.056	0.143	0.024	0.115	2.408	0.117	0.113	0.070
Sr88_ppm_mean	428.158	480.652	8.299	307.732	587.005	587.003	473.946	524.273
Sr88_ppm_2SE(int)	10.065	22.680	1.591	63.016	40.641	31.781	31.957	11.956
Y89_ppm_mean	1.040	21.444	3.673	7.076	51.658	4.726	1.008	1.100
Y89_ppm_2SE(int)	0.111	12.082	2.036	3.533	7.020	0.633	0.190	0.103
Zr90_ppm_mean	0.179	668.988	0.106	3.676	200.367	6.740	4.286	0.111
Zr90_ppm_2SE(int)	0.066	1173.143	0.048	1.085	25.968	1.258	5.285	0.047
Nb93_ppm_mean	0.017	4.863	0.030	0.286	6.568	0.404	0.031	0.007
Nb93_ppm_2SE(int)	0.011	3.154	0.025	0.109	1.294	0.080	0.028	0.008
Ba137_ppm_mean	130.454	175.325	4.405	96.619	999.612	214.052	135.140	183.086
Ba137_ppm_2SE(int)	4.290	11.670	1.188	18.713	93.698	10.581	9.261	4.937
Hf178_ppm_mean	0.010	2.415	0.000	0.108	6.127	0.262	0.233	0.003
Hf178_ppm_2SE(int)	0.012	1.474	0.000	0.075	1.186	0.109	0.290	0.007
Ta181_ppm_mean	0.002	0.261	0.000	0.017	0.400	0.012	0.006	0.000
Ta181_ppm_2SE(int)	0.002	0.170	0.000	0.013	0.073	0.011	0.007	0.000
Pb208_ppm_mean	0.050	0.274	0.083	1.122	1.004	0.285	0.799	3.063
Pb208_ppm_2SE(int)	0.017	0.125	0.041	0.270	0.304	0.108	0.394	5.970
Th232_ppm_mean	0.005	0.646	0.029	0.372	1.411	0.261	0.209	0.049
Th232_ppm_2SE(int)	0.004	0.399	0.023	0.167	0.263	0.373	0.191	0.095
U238_ppm_mean	0.031	0.599	0.001	0.052	0.351	0.033	0.014	0.855
U238_ppm_2SE(int)	0.060	0.836	0.002	0.030	0.076	0.031	0.018	1.680

*Point names include phase (pl) and spot size (i.e., 30 um).

Table S3: Plagioclase feldspar trace element contents.

Sample	10024	10024	10024	10024	10024	10024	10024	10024
LAICPMS point*	24.5.pl.40um	24.10.pl.45um	24.11.pl.45um	24.24.pl.45um	24.25.pl.45um	24.26.pl.45um	24.28.pl.45um	24.35.pl.40um
Ca43_ppm_mean	142365.778	128265.669	133460.774	137394.321	138934.350	135692.645	142808.285	126174.384
Ca43_ppm_2SE(int)	5264.244	3175.472	4907.212	3457.245	3433.589	4387.147	3109.274	3710.902
Sc45_ppm_mean	5.127	9.785	4.474	4.422	4.354	4.398	4.446	4.651
Sc45_ppm_2SE(int)	0.331	0.899	0.323	0.280	0.268	0.238	0.238	0.264
Ti47_ppm_mean	708.065	1213.057	794.248	446.699	464.170	813.657	577.089	495.058
Ti47_ppm_2SE(int)	21.467	104.038	29.852	12.828	16.354	28.404	15.317	31.028
V51_ppm_mean	1.384	4.736	0.467	0.373	0.514	0.858	0.440	0.379
V51_ppm_2SE(int)	0.628	0.684	0.244	0.183	0.272	0.251	0.224	0.271
Cr52_ppm_mean	10.266	160.960	3.404	2.390	6.052	3.600	3.073	2.184
Cr52_ppm_2SE(int)	1.234	25.689	0.658	0.414	1.251	0.664	0.609	0.700
Mn55_ppm_mean	68.613	249.501	48.195	56.277	62.131	52.227	57.203	66.418
Mn55_ppm_2SE(int)	3.270	32.599	1.574	1.317	2.621	1.337	1.052	2.290
Co59_ppm_mean	0.647	2.613	0.613	0.655	0.771	0.616	0.624	0.547
Co59_ppm_2SE(int)	0.089	0.361	0.101	0.096	0.106	0.089	0.091	0.082
Ni60_ppm_mean	1.268	0.236	0.211	0.188	0.193	0.294	0.198	0.018
Ni60_ppm_2SE(int)	2.109	0.133	0.157	0.122	0.114	0.176	0.130	0.137
Cu63_ppm_mean	0.497	0.857	0.320	1.711	1.362	0.484	0.744	4.950
Cu63_ppm_2SE(int)	0.173	0.158	0.110	0.178	0.190	0.133	0.144	4.037
Zn66_ppm_mean	0.271	0.604	0.421	0.567	0.606	0.845	0.372	0.949
Zn66_ppm_2SE(int)	0.420	0.327	0.325	0.385	0.475	0.926	0.312	0.460
Rb85_ppm_mean	0.327	0.374	0.390	0.394	0.482	0.360	0.368	3.812
Rb85_ppm_2SE(int)	0.057	0.060	0.059	0.062	0.064	0.053	0.054	1.194
Sr88_ppm_mean	462.532	408.226	460.157	570.861	574.192	449.887	488.987	596.709
Sr88_ppm_2SE(int)	12.829	10.406	16.674	18.004	18.072	14.739	12.185	11.105
Y89_ppm_mean	1.314	3.941	0.897	1.471	1.610	0.892	1.551	7.624
Y89_ppm_2SE(int)	0.145	0.566	0.089	0.112	0.142	0.081	0.208	1.348
Zr90_ppm_mean	0.294	1.623	0.126	0.098	0.193	0.127	2.121	26.217
Zr90_ppm_2SE(int)	0.069	0.330	0.039	0.039	0.068	0.052	0.677	5.580
Nb93_ppm_mean	0.024	0.013	0.008	0.004	0.004	0.005	0.100	0.870
Nb93_ppm_2SE(int)	0.017	0.009	0.008	0.006	0.006	0.007	0.035	0.148
Ba137_ppm_mean	134.529	98.681	123.275	193.140	208.412	113.231	155.273	437.360
Ba137_ppm_2SE(int)	5.529	2.903	4.927	7.790	9.439	3.959	6.878	25.293
Hf178_ppm_mean	0.011	0.084	0.000	0.000	0.012	0.000	0.078	0.783
Hf178_ppm_2SE(int)	0.013	0.034	0.000	0.000	0.012	0.000	0.035	0.191
Ta181_ppm_mean	0.001	0.000	0.000	0.000	0.001	0.000	0.004	0.056
Ta181_ppm_2SE(int)	0.002	0.000	0.000	0.000	0.002	0.000	0.003	0.018
Pb208_ppm_mean	0.056	0.017	0.028	0.042	0.076	0.026	0.035	0.257
Pb208_ppm_2SE(int)	0.022	0.012	0.018	0.017	0.025	0.018	0.019	0.050
Th232_ppm_mean	0.534	0.000	0.001	0.000	0.000	0.000	0.045	0.179
Th232_ppm_2SE(int)	1.065	0.000	0.002	0.000	0.000	0.000	0.017	0.042
U238_ppm_mean	1.208	0.000	0.000	0.000	0.001	0.000	0.007	0.306
U238_ppm_2SE(int)	2.415	0.000	0.000	0.000	0.001	0.000	0.004	0.488

*Point names include phase (pl) and spot size (i.e., 30 um).

Table S3: Plagioclase feldspar trace element contents.

Sample	10024	10024	10024	10024	10024	10024	10049	10049
LAICPMS point*	24.36.pl.45um	24.49.pl.45um	24.50.pl.45um	24.51.pl.35um	24.53.pl.45um	24.69.olv.40um	49.2.pl.30um	49.3.pl.30um
Ca43_ppm_mean	142632.418	138110.002	139303.669	125315.267	136391.105	24282.179	127532.335	95027.804
Ca43_ppm_2SE(int)	3453.384	4511.313	4739.830	3603.641	3649.848	5261.286	7043.804	3104.916
Sc45_ppm_mean	4.427	4.326	4.152	4.721	4.381	32.106	27.706	5.347
Sc45_ppm_2SE(int)	0.338	0.214	0.253	0.306	0.241	3.860	7.470	0.355
Ti47_ppm_mean	513.992	473.769	563.918	186.450	489.810	2627.358	3300.364	690.456
Ti47_ppm_2SE(int)	19.590	20.801	25.285	13.805	17.460	486.716	741.143	55.029
V51_ppm_mean	0.433	0.434	0.580	0.011	0.514	36.615	9.216	0.175
V51_ppm_2SE(int)	0.234	0.246	0.216	0.328	0.221	4.674	3.150	0.360
Cr52_ppm_mean	5.178	3.083	2.831	1.436	2.791	1358.093	437.654	3.934
Cr52_ppm_2SE(int)	2.263	0.612	0.520	0.895	0.495	122.232	142.378	1.080
Mn55_ppm_mean	51.689	53.808	50.544	67.210	52.731	2749.185	685.789	57.153
Mn55_ppm_2SE(int)	1.942	1.565	1.815	2.175	1.240	128.150	211.528	4.216
Co59_ppm_mean	1.529	0.734	0.566	2.554	0.636	67.092	5.408	0.372
Co59_ppm_2SE(int)	1.307	0.111	0.087	0.935	0.069	3.626	1.946	0.116
Ni60_ppm_mean	0.461	0.223	0.201	23.620	0.220	11.689	0.069	0.297
Ni60_ppm_2SE(int)	0.251	0.144	0.134	11.332	0.134	0.972	0.192	0.163
Cu63_ppm_mean	2.203	0.544	0.713	21.011	1.353	1.594	0.637	1.405
Cu63_ppm_2SE(int)	0.253	0.170	0.174	3.781	0.335	0.184	0.246	1.155
Zn66_ppm_mean	0.777	0.191	0.367	4.110	0.468	5.348	0.927	1.628
Zn66_ppm_2SE(int)	0.372	0.323	0.363	0.898	0.252	0.448	0.733	0.560
Rb85_ppm_mean	0.433	0.384	0.292	1.131	0.336	0.006	0.812	0.427
Rb85_ppm_2SE(int)	0.158	0.062	0.053	0.091	0.045	0.011	0.196	0.063
Sr88_ppm_mean	487.500	509.963	440.875	1537.548	472.683	1.393	371.950	384.744
Sr88_ppm_2SE(int)	10.786	19.755	14.922	32.074	10.992	0.351	53.039	12.738
Y89_ppm_mean	1.130	1.261	0.863	4.981	1.121	9.921	46.963	12.601
Y89_ppm_2SE(int)	0.107	0.093	0.085	0.300	0.085	1.883	11.685	3.777
Zr90_ppm_mean	0.142	0.116	0.078	0.954	0.083	5.179	92.991	38.650
Zr90_ppm_2SE(int)	0.151	0.046	0.029	0.289	0.029	1.192	27.537	14.377
Nb93_ppm_mean	0.017	0.000	0.004	0.070	0.007	0.201	4.532	2.601
Nb93_ppm_2SE(int)	0.012	0.000	0.005	0.033	0.007	0.249	1.458	0.825
Ba137_ppm_mean	157.286	155.369	101.138	2414.156	131.662	0.116	154.840	147.767
Ba137_ppm_2SE(int)	5.121	7.883	4.767	53.699	3.481	0.062	15.107	10.636
Hf178_ppm_mean	0.005	0.005	0.000	0.051	0.000	0.346	3.421	1.068
Hf178_ppm_2SE(int)	0.007	0.007	0.000	0.042	0.000	0.089	0.814	0.420
Ta181_ppm_mean	0.002	0.000	0.002	0.008	0.001	0.005	0.270	0.103
Ta181_ppm_2SE(int)	0.003	0.000	0.002	0.006	0.001	0.005	0.095	0.033
Pb208_ppm_mean	0.048	0.046	0.046	0.525	0.040	0.176	0.392	0.855
Pb208_ppm_2SE(int)	0.026	0.023	0.028	0.135	0.016	0.027	0.126	0.138
Th232_ppm_mean	0.000	0.000	0.000	0.012	0.000	0.006	0.883	0.544
Th232_ppm_2SE(int)	0.000	0.000	0.000	0.007	0.000	0.004	0.274	0.178
U238_ppm_mean	0.050	0.000	0.029	0.007	0.000	0.001	0.210	0.153
U238_ppm_2SE(int)	0.096	0.000	0.056	0.014	0.000	0.001	0.069	0.061

*Point names include phase (pl) and spot size (i.e., 30 um).

Table S3: Plagioclase feldspar trace element contents.

Sample	10049	10049	10049	10049	10049	10049	10049	10069
LAICPMS point*	49.8.pl.30um	49.9.pl.30um	49.17.pl.30um	49.19.pl.30um	49.34.pl.30um	49.37.pl.30um	49.40.pl.30um	69.1.pl.30um
Ca43_ppm_mean	129784.903	128031.350	143128.307	85295.215	128048.775	59196.578	119915.525	123242.313
Ca43_ppm_2SE(int)	6620.370	3184.893	4929.817	5648.550	5214.311	6480.155	7066.309	3046.357
Sc45_ppm_mean	6.650	24.579	41.877	24.332	5.419	5.529	94.967	11.970
Sc45_ppm_2SE(int)	0.781	6.037	8.055	5.095	0.585	0.307	3.539	2.036
Ti47_ppm_mean	1144.479	10177.026	35295.623	4697.092	770.359	740.659	9164.207	1241.665
Ti47_ppm_2SE(int)	229.383	1804.432	13922.846	1254.190	26.678	39.402	442.692	190.109
V51_ppm_mean	0.816	10.568	29.334	8.547	0.524	-0.082	32.228	6.566
V51_ppm_2SE(int)	0.345	3.135	7.646	2.465	0.455	0.295	1.691	2.443
Cr52_ppm_mean	11.622	451.222	1086.229	340.162	12.851	2.722	1719.962	231.594
Cr52_ppm_2SE(int)	3.410	131.465	264.761	92.935	21.687	1.735	62.610	55.704
Mn55_ppm_mean	151.606	500.053	1003.696	675.487	64.297	60.987	1898.242	298.520
Mn55_ppm_2SE(int)	36.914	117.820	207.325	123.300	2.938	11.036	97.012	73.047
Co59_ppm_mean	1.167	4.565	27.971	21.041	0.432	0.435	18.155	3.169
Co59_ppm_2SE(int)	0.891	1.066	9.828	6.203	0.108	0.104	1.110	0.788
Ni60_ppm_mean	0.469	0.526	11.292	13.171	0.278	0.275	0.560	0.118
Ni60_ppm_2SE(int)	0.378	0.468	4.447	7.298	0.239	0.206	0.311	0.208
Cu63_ppm_mean	4.467	0.471	11.094	10.945	3.550	1.073	0.455	0.506
Cu63_ppm_2SE(int)	2.462	0.145	3.932	3.452	6.204	0.231	0.261	0.456
Zn66_ppm_mean	1.351	1.762	4.773	2.709	0.519	0.452	3.399	0.179
Zn66_ppm_2SE(int)	0.708	0.615	1.251	0.747	0.532	0.417	0.823	0.653
Rb85_ppm_mean	10.419	0.845	2.622	32.502	0.786	1.885	0.186	0.715
Rb85_ppm_2SE(int)	4.707	0.128	0.443	2.531	0.155	0.293	0.071	0.629
Sr88_ppm_mean	466.424	406.691	380.054	349.039	466.163	338.860	58.663	368.124
Sr88_ppm_2SE(int)	20.747	31.338	21.440	42.234	24.046	32.549	12.504	13.508
Y89_ppm_mean	182.495	20.360	52.054	190.312	8.639	28.061	70.533	5.682
Y89_ppm_2SE(int)	67.961	4.764	14.323	24.033	2.330	4.155	3.675	1.210
Zr90_ppm_mean	650.697	76.859	105.037	506.730	18.579	79.079	58.143	49.307
Zr90_ppm_2SE(int)	252.332	12.757	35.550	43.350	4.008	10.874	3.823	93.278
Nb93_ppm_mean	27.050	7.285	9.164	16.379	1.810	3.283	0.248	0.010
Nb93_ppm_2SE(int)	10.524	1.400	3.460	2.201	0.677	0.537	0.064	0.012
Ba137_ppm_mean	527.326	142.707	180.322	1063.611	155.488	242.070	19.691	117.364
Ba137_ppm_2SE(int)	158.329	8.275	7.799	62.616	8.760	19.155	4.607	4.627
Hf178_ppm_mean	18.357	2.637	3.355	17.177	0.470	2.360	3.701	0.139
Hf178_ppm_2SE(int)	7.099	0.520	1.128	1.541	0.116	0.338	0.361	0.056
Ta181_ppm_mean	1.404	0.400	0.561	1.250	0.128	0.189	0.023	0.000
Ta181_ppm_2SE(int)	0.564	0.079	0.218	0.199	0.100	0.035	0.012	0.000
Pb208_ppm_mean	2.408	0.134	0.450	3.456	0.242	1.276	0.296	0.228
Pb208_ppm_2SE(int)	0.882	0.034	0.107	0.326	0.071	0.949	0.434	0.394
Th232_ppm_mean	6.368	0.142	1.572	6.724	0.368	1.459	0.068	0.015
Th232_ppm_2SE(int)	2.383	0.032	1.725	0.516	0.081	0.256	0.019	0.013
U238_ppm_mean	1.873	0.042	0.197	2.136	1.588	0.576	0.033	0.005
U238_ppm_2SE(int)	0.758	0.013	0.047	0.205	2.072	0.463	0.016	0.005

*Point names include phase (pl) and spot size (i.e., 30 um).

Table S3: Plagioclase feldspar trace element contents.

Sample	10069	10069	10069	10069	10069	10069	10069	10069
LAICPMS point*	69.7.pl.30um	69.11.pl.30um	69.15.pl.30um	69.21.pl.30um	69.26.pl.30um	69.27.pl.30um	69.35.pl.25um	69.44.pl.30um
Ca43_ppm_mean	138506.238	133934.510	121793.499	134154.860	136963.279	134232.619	100635.431	132035.369
Ca43_ppm_2SE(int)	6133.881	4385.474	5355.336	7282.769	4020.517	4764.767	8200.056	4512.810
Sc45_ppm_mean	5.558	31.596	21.623	6.828	5.352	5.770	17.302	5.308
Sc45_ppm_2SE(int)	0.526	5.433	3.585	1.218	0.359	0.449	1.112	0.355
Ti47_ppm_mean	704.991	2173.941	16309.130	788.102	600.945	1126.435	4440.076	812.349
Ti47_ppm_2SE(int)	42.558	345.708	10744.251	101.404	41.357	117.522	425.432	95.541
V51_ppm_mean	1.641	14.611	15.025	1.268	1.743	0.705	3.671	0.438
V51_ppm_2SE(int)	0.509	3.223	5.599	0.756	1.352	0.704	0.466	0.460
Cr52_ppm_mean	58.112	545.915	470.293	49.318	10.959	9.599	145.218	7.345
Cr52_ppm_2SE(int)	17.096	119.109	161.743	25.975	3.177	2.073	13.380	1.312
Mn55_ppm_mean	90.719	686.431	758.028	160.561	60.351	77.653	455.531	74.116
Mn55_ppm_2SE(int)	25.595	121.772	129.367	65.561	4.175	6.149	29.256	4.354
Co59_ppm_mean	0.794	5.492	6.385	1.515	0.452	0.772	3.764	0.557
Co59_ppm_2SE(int)	0.247	0.944	1.174	0.684	0.101	0.222	0.977	0.113
Ni60_ppm_mean	0.317	0.728	0.421	0.380	0.209	0.339	1.390	0.367
Ni60_ppm_2SE(int)	0.302	0.839	0.284	0.272	0.182	0.255	0.480	0.281
Cu63_ppm_mean	0.346	0.496	1.971	0.496	0.220	0.504	1.204	0.346
Cu63_ppm_2SE(int)	0.168	0.433	0.859	0.197	0.118	0.274	0.378	0.151
Zn66_ppm_mean	0.452	1.080	2.279	0.270	0.469	0.602	2.037	0.645
Zn66_ppm_2SE(int)	0.714	0.462	1.276	0.469	0.445	0.695	0.999	0.618
Rb85_ppm_mean	0.281	3.268	3.193	0.426	0.382	0.530	21.385	1.288
Rb85_ppm_2SE(int)	0.089	0.864	0.597	0.072	0.093	0.126	2.412	0.413
Sr88_ppm_mean	409.378	485.711	479.266	474.406	482.408	462.754	440.913	503.505
Sr88_ppm_2SE(int)	17.662	31.850	21.816	24.447	18.444	16.789	26.424	18.392
Y89_ppm_mean	1.477	197.877	50.728	8.421	1.926	11.925	279.027	16.409
Y89_ppm_2SE(int)	0.230	36.397	5.733	4.975	0.700	2.613	27.793	4.396
Zr90_ppm_mean	0.547	49.602	147.495	11.157	1.961	28.152	654.109	35.964
Zr90_ppm_2SE(int)	0.229	23.425	43.217	8.245	1.276	6.828	79.110	10.514
Nb93_ppm_mean	0.020	0.509	8.671	0.516	0.060	1.277	13.966	1.172
Nb93_ppm_2SE(int)	0.022	0.173	4.370	0.413	0.072	0.282	1.534	0.407
Ba137_ppm_mean	95.042	217.109	252.862	156.251	140.415	150.434	911.804	180.488
Ba137_ppm_2SE(int)	4.255	25.966	26.990	8.510	10.053	6.496	87.144	11.575
Hf178_ppm_mean	0.029	1.740	4.241	0.395	0.062	0.866	20.439	1.158
Hf178_ppm_2SE(int)	0.020	0.205	1.197	0.277	0.058	0.224	2.674	0.357
Ta181_ppm_mean	0.003	0.114	0.576	0.033	0.001	0.087	0.981	0.090
Ta181_ppm_2SE(int)	0.005	0.090	0.304	0.025	0.003	0.030	0.161	0.032
Pb208_ppm_mean	1.220	6.143	36.430	10.505	1.412	1.197	3.754	1.571
Pb208_ppm_2SE(int)	0.974	0.959	11.991	0.875	0.400	1.801	0.405	0.313
Th232_ppm_mean	0.000	3.210	1.010	0.233	0.022	0.348	9.722	0.536
Th232_ppm_2SE(int)	0.000	0.745	0.182	0.165	0.017	0.067	1.186	0.153
U238_ppm_mean	0.001	0.449	1.401	0.094	0.004	0.078	2.818	0.144
U238_ppm_2SE(int)	0.002	0.090	2.077	0.070	0.005	0.023	0.261	0.055

*Point names include phase (pl) and spot size (i.e., 30 um).

Table S3: Plagioclase feldspar trace element contents.

Sample	10069	10069	10069	10069	10069	10069	10069	10069
LAICPMS point*	69.45.pl.25um	69.50.px.30um	69.61.pl.30um	69.69.pl.30um	69.70.pl.30um	69.81.pl.30um	69.108.pl.35um	69.109.pl.30um
Ca43_ppm_mean	36932.827	134810.495	89916.089	137493.112	131687.933	129596.331	135996.925	147102.295
Ca43_ppm_2SE(int)	3989.969	4763.222	3227.230	6275.713	3758.315	6210.623	3526.668	7426.330
Sc45_ppm_mean	57.443	7.648	230.857	5.065	5.784	7.441	5.913	7.977
Sc45_ppm_2SE(int)	9.498	1.606	19.618	0.536	0.415	0.831	0.447	1.279
Ti47_ppm_mean	176595.389	608.960	598438.137	530.007	1032.570	895.522	884.552	1073.025
Ti47_ppm_2SE(int)	29392.535	58.485	43441.667	35.376	182.007	124.389	228.070	87.826
V51_ppm_mean	96.022	1.233	294.360	0.024	0.662	3.011	3.535	4.012
V51_ppm_2SE(int)	16.603	0.569	24.442	0.428	0.425	2.058	4.486	1.301
Cr52_ppm_mean	3276.961	48.744	11005.874	7.008	7.770	57.044	43.872	153.672
Cr52_ppm_2SE(int)	547.448	17.208	986.499	4.658	2.555	17.648	4.118	72.989
Mn55_ppm_mean	1866.921	162.293	7291.029	103.967	91.583	178.014	91.371	198.976
Mn55_ppm_2SE(int)	326.565	46.725	654.568	87.643	14.009	33.610	6.012	30.352
Co59_ppm_mean	10.608	1.382	85.721	0.584	0.728	1.850	0.959	1.517
Co59_ppm_2SE(int)	1.314	0.413	30.854	0.174	0.175	0.415	0.151	0.370
Ni60_ppm_mean	0.360	0.391	18.746	1.725	0.228	0.572	7.828	1.357
Ni60_ppm_2SE(int)	0.328	0.257	11.019	3.224	0.223	0.364	12.999	0.724
Cu63_ppm_mean	3.785	0.259	40.981	2.400	0.817	1.205	0.327	0.891
Cu63_ppm_2SE(int)	0.578	0.144	11.347	4.261	0.598	0.608	0.176	0.592
Zn66_ppm_mean	13.337	0.529	43.573	0.935	0.315	0.029	0.903	-0.023
Zn66_ppm_2SE(int)	3.224	0.621	5.509	0.672	0.568	0.683	1.076	1.272
Rb85_ppm_mean	0.405	0.618	3.370	0.300	2.876	1.659	1.992	0.286
Rb85_ppm_2SE(int)	0.112	0.304	3.443	0.082	0.418	0.604	2.135	0.116
Sr88_ppm_mean	224.609	514.231	239.950	474.687	548.527	514.665	399.520	388.069
Sr88_ppm_2SE(int)	22.876	22.036	37.450	23.650	27.272	16.392	11.475	13.782
Y89_ppm_mean	80.700	5.730	395.275	7.915	21.568	22.695	1.940	3.085
Y89_ppm_2SE(int)	24.017	1.354	125.631	12.878	6.424	9.692	1.064	0.592
Zr90_ppm_mean	1113.573	4.985	7306.297	0.408	55.925	45.943	0.816	1.697
Zr90_ppm_2SE(int)	199.457	1.289	573.743	0.346	15.301	21.747	0.788	1.398
Nb93_ppm_mean	80.002	0.124	593.725	0.025	1.906	1.158	0.396	0.245
Nb93_ppm_2SE(int)	12.284	0.054	43.254	0.026	0.577	0.541	0.356	0.441
Ba137_ppm_mean	277.882	161.312	573.324	141.601	251.598	249.548	83.188	99.298
Ba137_ppm_2SE(int)	30.778	5.650	152.155	11.360	13.344	29.326	3.448	6.894
Hf178_ppm_mean	32.185	0.139	299.813	0.004	1.537	1.387	0.061	0.154
Hf178_ppm_2SE(int)	5.819	0.050	21.759	0.009	0.386	0.635	0.062	0.280
Ta181_ppm_mean	5.999	0.012	43.508	0.000	0.086	0.094	0.068	0.000
Ta181_ppm_2SE(int)	1.019	0.008	3.548	0.000	0.028	0.052	0.107	0.000
Pb208_ppm_mean	5.168	0.912	34.177	5.074	1.092	0.608	1.614	2.301
Pb208_ppm_2SE(int)	2.758	0.649	12.364	7.838	0.321	0.269	2.550	1.392
Th232_ppm_mean	1.023	0.182	17.178	0.007	0.626	0.770	0.751	0.050
Th232_ppm_2SE(int)	0.347	0.243	5.961	0.008	0.177	0.358	1.480	0.036
U238_ppm_mean	0.367	0.020	1.040	2.302	0.170	0.288	1.983	0.000
U238_ppm_2SE(int)	0.160	0.009	0.294	4.045	0.049	0.191	3.612	0.000

*Point names include phase (pl) and spot size (i.e., 30 um).

Table S3: Plagioclase feldspar trace element contents.

Sample	10069	10069	10071	10071	10071	10071	10071	10071
LAICPMS point*	69.110.pl.30um	69.112.pl.30um	71.4.pl.35um	71.5.pl.35um	71.6.pl.35um	71.18.pl.35um	71.19.pl.35um	71.26.pl.35um
Ca43_ppm_mean	121471.711	118216.223	140927.517	140221.740	129131.918	112790.703	121928.459	132861.653
Ca43_ppm_2SE(int)	4273.698	8689.268	6627.531	7357.978	7866.724	4522.902	5809.954	5990.165
Sc45_ppm_mean	8.189	21.368	4.897	4.937	13.245	64.195	9.873	5.534
Sc45_ppm_2SE(int)	0.969	4.411	0.500	0.384	1.868	5.748	1.830	0.400
Ti47_ppm_mean	1383.800	7565.632	612.568	664.270	1557.319	32537.246	4970.824	1665.089
Ti47_ppm_2SE(int)	230.001	4189.419	38.453	72.532	144.736	2970.359	913.978	174.201
V51_ppm_mean	1.100	9.776	0.203	0.273	2.364	10.094	0.883	0.401
V51_ppm_2SE(int)	0.638	3.274	0.445	0.449	0.813	0.906	0.417	0.427
Cr52_ppm_mean	34.190	387.645	1.684	3.924	131.717	446.057	37.767	7.481
Cr52_ppm_2SE(int)	17.187	119.052	1.614	1.757	23.324	36.741	11.343	9.004
Mn55_ppm_mean	161.365	803.659	79.527	77.872	396.293	2544.900	523.967	112.043
Mn55_ppm_2SE(int)	25.182	180.848	14.129	7.844	63.207	232.210	208.960	11.082
Co59_ppm_mean	1.011	7.023	0.831	0.788	4.283	14.224	2.531	0.978
Co59_ppm_2SE(int)	0.289	1.846	0.211	0.153	0.840	1.389	0.704	0.450
Ni60_ppm_mean	0.462	0.489	0.480	0.531	1.121	0.120	0.146	0.386
Ni60_ppm_2SE(int)	0.603	0.354	0.270	0.371	1.901	0.141	0.255	0.249
Cu63_ppm_mean	0.345	1.174	0.751	3.237	0.916	1.092	0.949	0.416
Cu63_ppm_2SE(int)	0.150	1.212	0.241	0.889	0.254	0.195	0.396	0.162
Zn66_ppm_mean	1.079	4.908	0.878	1.135	1.444	7.556	4.938	3.426
Zn66_ppm_2SE(int)	0.657	7.019	0.689	0.803	0.603	1.053	1.161	3.446
Rb85_ppm_mean	9.443	0.408	0.973	2.208	0.488	2.666	4.401	6.778
Rb85_ppm_2SE(int)	3.699	0.297	0.233	0.549	0.100	0.377	0.793	2.070
Sr88_ppm_mean	553.379	401.836	486.983	558.263	492.724	317.660	919.621	520.005
Sr88_ppm_2SE(int)	22.283	39.589	21.687	24.444	40.208	72.525	43.467	22.467
Y89_ppm_mean	168.923	19.594	2.903	9.368	22.355	197.880	63.168	58.557
Y89_ppm_2SE(int)	81.732	4.049	1.098	2.126	13.089	19.475	26.674	22.718
Zr90_ppm_mean	286.625	34.019	5.378	25.454	63.044	605.492	2741.302	293.170
Zr90_ppm_2SE(int)	110.451	18.645	2.576	6.859	41.631	168.059	847.474	128.086
Nb93_ppm_mean	8.222	3.212	0.123	1.503	1.135	46.616	55.389	12.645
Nb93_ppm_2SE(int)	2.527	1.906	0.092	0.472	0.702	10.316	15.643	4.562
Ba137_ppm_mean	450.699	126.183	142.553	200.952	195.236	524.926	1673.905	351.913
Ba137_ppm_2SE(int)	100.303	11.837	8.373	11.993	16.793	196.706	255.360	49.797
Hf178_ppm_mean	7.918	1.082	0.180	0.829	1.855	22.718	66.050	7.120
Hf178_ppm_2SE(int)	3.074	0.520	0.112	0.240	1.083	4.730	16.459	3.097
Ta181_ppm_mean	0.483	0.247	0.015	0.071	0.097	1.862	3.717	0.722
Ta181_ppm_2SE(int)	0.160	0.158	0.012	0.034	0.058	0.493	1.071	0.288
Pb208_ppm_mean	1.924	2.596	0.083	0.536	1.946	10.353	2.149	0.890
Pb208_ppm_2SE(int)	0.834	2.786	0.092	0.130	2.115	1.325	0.449	0.310
Th232_ppm_mean	4.812	0.078	0.063	0.519	0.592	8.196	1.485	1.759
Th232_ppm_2SE(int)	2.505	0.028	0.029	0.367	0.542	2.552	0.488	0.708
U238_ppm_mean	1.166	0.338	0.014	0.089	0.135	4.050	2.315	0.684
U238_ppm_2SE(int)	0.459	0.601	0.010	0.035	0.087	1.441	0.607	0.277

*Point names include phase (pl) and spot size (i.e., 30 um).

Table S3: Plagioclase feldspar trace element contents.

Sample	10071	10071	10071	10071	10071	10071	10072	10072
LAICPMS point*	71.30.pl.35um	71.31.pl.35um	71.33.pl.35um	71.82.pl.35um	71.83.pl.35um	71.84.pl.35um	72.3.pl.40um	72.5.pl.40um
Ca43_ppm_mean	114363.990	43818.758	113489.149	95874.491	130297.428	130509.534	133739.147	127863.350
Ca43_ppm_2SE(int)	4549.669	4804.485	4443.700	4343.252	3453.822	3521.819	5779.662	3460.452
Sc45_ppm_mean	37.062	18.927	19.141	55.834	5.923	7.285	4.792	4.817
Sc45_ppm_2SE(int)	2.358	3.293	3.757	3.012	0.609	0.521	0.254	0.272
Ti47_ppm_mean	2644.239	122413.701	1571.972	7454.097	1814.730	1216.874	774.158	663.174
Ti47_ppm_2SE(int)	156.774	30578.834	306.034	872.582	396.919	597.439	39.377	28.500
V51_ppm_mean	2.279	6.428	1.489	24.998	3.356	2.100	0.770	4.696
V51_ppm_2SE(int)	0.431	1.256	0.453	2.396	3.839	0.432	0.402	7.266
Cr52_ppm_mean	108.022	188.656	53.697	905.489	9.745	58.464	3.909	2.742
Cr52_ppm_2SE(int)	7.230	46.861	12.619	71.928	1.809	8.034	2.104	0.713
Mn55_ppm_mean	2047.550	1699.772	655.303	1796.319	122.307	147.476	54.243	56.936
Mn55_ppm_2SE(int)	119.501	470.885	158.282	68.416	10.092	11.213	3.506	1.887
Co59_ppm_mean	9.842	45.553	3.113	14.884	0.842	1.378	0.588	0.753
Co59_ppm_2SE(int)	0.762	16.500	0.683	1.178	0.186	0.198	0.103	0.242
Ni60_ppm_mean	0.296	1.172	0.200	1.184	0.226	0.236	0.274	0.647
Ni60_ppm_2SE(int)	0.227	0.774	0.171	1.441	0.306	0.253	0.183	0.307
Cu63_ppm_mean	0.941	21.051	0.530	1.586	0.930	0.611	0.598	6.231
Cu63_ppm_2SE(int)	0.537	8.732	0.146	0.373	0.270	0.135	0.247	4.579
Zn66_ppm_mean	4.906	14.430	4.232	3.220	0.888	0.352	0.422	10.142
Zn66_ppm_2SE(int)	1.053	3.535	3.431	0.586	0.659	0.427	0.455	5.557
Rb85_ppm_mean	6.251	81.829	27.160	4.881	2.056	0.839	1.452	1.652
Rb85_ppm_2SE(int)	2.391	5.946	6.285	1.077	0.392	0.607	0.332	0.246
Sr88_ppm_mean	410.694	304.726	426.030	184.295	535.606	507.744	487.681	504.872
Sr88_ppm_2SE(int)	39.874	25.332	18.745	14.281	18.494	15.012	16.754	14.237
Y89_ppm_mean	248.474	244.055	65.458	137.818	90.677	5.606	1.698	5.469
Y89_ppm_2SE(int)	74.144	33.722	20.074	9.645	15.607	0.549	0.412	0.901
Zr90_ppm_mean	251.938	2861.982	204.341	264.258	293.736	8.498	3.136	19.768
Zr90_ppm_2SE(int)	99.986	628.595	59.696	33.315	81.812	1.830	1.233	3.693
Nb93_ppm_mean	46.801	136.520	6.226	13.486	14.535	0.339	0.137	0.791
Nb93_ppm_2SE(int)	36.945	32.449	1.685	1.638	3.491	0.067	0.050	0.157
Ba137_ppm_mean	359.127	3043.164	686.845	169.364	367.964	184.555	147.363	365.955
Ba137_ppm_2SE(int)	45.311	169.673	162.868	30.923	35.972	5.739	6.285	34.047
Hf178_ppm_mean	12.885	80.749	6.887	8.020	8.851	0.294	0.126	0.581
Hf178_ppm_2SE(int)	5.315	19.646	2.124	0.856	2.153	0.064	0.060	0.140
Ta181_ppm_mean	1.324	8.468	0.305	0.666	0.897	0.012	0.009	0.053
Ta181_ppm_2SE(int)	1.075	2.018	0.082	0.091	0.225	0.006	0.008	0.018
Pb208_ppm_mean	4.554	8.038	1.227	1.285	2.030	0.259	0.158	3.231
Pb208_ppm_2SE(int)	2.696	2.083	0.312	0.220	0.543	0.291	0.087	1.633
Th232_ppm_mean	12.818	11.760	1.225	2.465	3.276	0.053	0.017	0.140
Th232_ppm_2SE(int)	8.909	1.790	0.383	0.337	0.558	0.014	0.010	0.037
U238_ppm_mean	2.058	6.210	0.370	0.754	1.018	0.031	0.007	1.049
U238_ppm_2SE(int)	1.260	1.883	0.099	0.178	0.192	0.012	0.005	1.437

*Point names include phase (pl) and spot size (i.e., 30 um).

Table S3: Plagioclase feldspar trace element contents.

Sample	10072	10072	10072	10072	10072	10072
LAICPMS point*	72.10.pl.45um	72.20.pl.40um	72.22.pl.45um	72.26.pl.40um	72.30.pl.40um	72.41.pl.40um
Ca43_ppm_mean	133314.542	134232.700	139998.982	132841.157	101539.115	130688.242
Ca43_ppm_2SE(int)	3716.700	3737.447	2760.400	6710.627	6463.314	4527.715
Sc45_ppm_mean	6.774	4.918	6.903	4.409	7.271	4.582
Sc45_ppm_2SE(int)	0.437	0.450	0.325	0.312	0.862	0.357
Ti47_ppm_mean	1044.761	828.673	1094.121	598.266	2506.704	685.291
Ti47_ppm_2SE(int)	63.942	48.068	47.546	74.909	201.170	33.025
V51_ppm_mean	5.103	1.126	2.970	0.749	1.211	0.737
V51_ppm_2SE(int)	0.596	0.351	0.363	0.364	0.340	0.269
Cr52_ppm_mean	159.171	18.033	77.979	3.715	48.400	9.943
Cr52_ppm_2SE(int)	22.902	9.535	6.926	1.150	11.936	4.192
Mn55_ppm_mean	117.438	79.075	159.767	51.432	216.602	54.684
Mn55_ppm_2SE(int)	6.519	11.488	5.745	1.943	29.445	2.263
Co59_ppm_mean	1.453	1.504	1.652	0.524	2.198	0.680
Co59_ppm_2SE(int)	0.211	1.307	0.160	0.095	1.275	0.194
Ni60_ppm_mean	0.172	0.302	0.190	0.262	0.315	0.659
Ni60_ppm_2SE(int)	0.140	0.141	0.135	0.171	0.162	0.573
Cu63_ppm_mean	0.428	0.467	0.876	5.567	1.259	12.773
Cu63_ppm_2SE(int)	0.157	0.126	0.193	9.755	0.221	13.567
Zn66_ppm_mean	0.889	0.614	1.010	0.894	1.580	3.757
Zn66_ppm_2SE(int)	0.374	0.474	0.416	0.454	0.894	3.850
Rb85_ppm_mean	1.299	0.540	0.982	0.390	22.322	0.472
Rb85_ppm_2SE(int)	0.115	0.221	0.170	0.062	3.011	0.103
Sr88_ppm_mean	495.683	443.623	490.799	459.773	537.590	497.462
Sr88_ppm_2SE(int)	18.224	11.556	10.473	25.426	22.900	14.566
Y89_ppm_mean	4.448	3.701	24.562	1.064	45.198	21.936
Y89_ppm_2SE(int)	0.782	0.607	6.573	0.123	5.928	21.372
Zr90_ppm_mean	8.471	6.784	56.802	0.102	187.726	1.410
Zr90_ppm_2SE(int)	2.137	1.664	12.076	0.038	24.025	1.004
Nb93_ppm_mean	0.272	0.511	2.341	0.003	7.545	0.250
Nb93_ppm_2SE(int)	0.070	0.135	0.611	0.005	0.766	0.201
Ba137_ppm_mean	178.263	124.007	169.630	125.401	684.918	143.829
Ba137_ppm_2SE(int)	6.798	4.230	7.811	7.583	69.723	6.386
Hf178_ppm_mean	0.282	0.254	1.806	0.002	6.450	0.135
Hf178_ppm_2SE(int)	0.082	0.130	0.380	0.005	0.875	0.181
Ta181_ppm_mean	0.013	0.026	0.150	0.001	0.503	0.013
Ta181_ppm_2SE(int)	0.005	0.011	0.043	0.002	0.066	0.021
Pb208_ppm_mean	0.264	0.443	0.733	0.209	1.169	9.017
Pb208_ppm_2SE(int)	0.057	0.047	0.113	0.072	0.177	8.800
Th232_ppm_mean	0.040	0.122	0.694	0.004	1.429	0.417
Th232_ppm_2SE(int)	0.016	0.119	0.188	0.003	0.175	0.392
U238_ppm_mean	0.021	0.017	0.185	0.005	0.379	1.649
U238_ppm_2SE(int)	0.009	0.007	0.048	0.007	0.047	3.205

*Point names include phase (pl) and spot size (i.e., 30 um).

Table S4: Plagioclase feldspar rare earth element contents.

Sample	10017	10017	10017	10017	10017	10017	10017	10017
LAICPMS point*	17.1.pl.40um	17.5.pl.40um	17.7.pl.40um	17.8.pl.40um	17.19.pl.40um	17.27.pl.40um	17.38.pl.40um	17.39.pl.40um
La139_ppm_mean	1.026	1.604	4.144	1.603	16.075	3.593	1027.746	2.328
La139_ppm_2SE(int)	0.118	0.105	1.761	0.111	3.337	0.431	322.450	0.188
Ce140_ppm_mean	3.346	3.594	10.652	3.407	42.667	8.033	2871.423	5.371
Ce140_ppm_2SE(int)	1.888	0.208	5.038	0.203	9.208	0.867	908.342	0.433
Pr141_ppm_mean	0.314	0.490	1.610	0.448	6.241	1.017	441.808	0.700
Pr141_ppm_2SE(int)	0.038	0.049	0.828	0.049	1.438	0.127	139.966	0.086
Nd146_ppm_mean	1.525	1.996	7.415	2.173	29.287	4.374	2268.457	2.982
Nd146_ppm_2SE(int)	0.193	0.260	3.745	0.209	6.860	0.539	716.474	0.469
Sm147_ppm_mean	0.383	0.503	1.979	0.448	9.226	1.081	717.092	0.739
Sm147_ppm_2SE(int)	0.103	0.121	0.989	0.116	2.434	0.178	228.273	0.151
Eu153_ppm_mean	2.789	4.875	3.290	4.685	8.756	5.921	34.435	5.504
Eu153_ppm_2SE(int)	0.183	0.251	0.195	0.244	0.454	0.696	5.537	0.243
Gd157_ppm_mean	0.171	0.396	2.167	0.509	10.630	0.806	800.123	0.601
Gd157_ppm_2SE(int)	0.054	0.104	1.117	0.098	2.919	0.145	256.846	0.112
Tb159_ppm_mean	0.032	0.050	0.355	0.053	1.881	0.131	132.456	0.075
Tb159_ppm_2SE(int)	0.013	0.015	0.193	0.014	0.524	0.051	42.027	0.015
Dy163_ppm_mean	0.183	0.263	2.303	0.285	12.509	0.657	836.745	0.519
Dy163_ppm_2SE(int)	0.045	0.083	1.441	0.062	3.640	0.125	267.639	0.177
Ho165_ppm_mean	0.030	0.054	0.454	0.054	2.648	0.105	164.126	0.122
Ho165_ppm_2SE(int)	0.012	0.015	0.270	0.013	0.781	0.023	52.667	0.102
Er166_ppm_mean	0.050	0.089	1.172	0.171	7.451	0.278	435.907	0.202
Er166_ppm_2SE(int)	0.021	0.029	0.720	0.097	2.214	0.062	140.229	0.052
Tm169_ppm_mean	0.098	0.011	0.133	0.008	0.968	0.033	52.497	0.107
Tm169_ppm_2SE(int)	0.181	0.006	0.085	0.006	0.293	0.011	16.479	0.192
Yb172_ppm_mean	0.260	0.052	0.934	0.109	6.872	0.174	320.470	0.136
Yb172_ppm_2SE(int)	0.367	0.026	0.554	0.039	2.173	0.049	101.170	0.037
Lu175_ppm_mean	0.006	0.008	0.127	0.008	0.899	0.021	36.511	0.010
Lu175_ppm_2SE(int)	0.004	0.005	0.082	0.005	0.279	0.008	11.482	0.006

*Point names include phase (pl) and spot size (i.e., 30 um).

Table S4 cont.: Plagioclase feldspar rare earth element contents.

Sample	10017	10017	10017	10017	10017	10017	10017	10017
LAICPMS point*	17.40.pl.40um	17.42.pl.40um	17.43.pl.40um	17.52.pl.40um	17.53.pl.40um	17.57.pl.40um	17.59.pl.40um	17.64.pl.40um
La139_ppm_mean	1.321	1.269	2.378	3.024	2.145	1.570	1.090	1.587
La139_ppm_2SE(int)	0.082	0.100	0.220	0.302	0.153	0.122	0.079	0.089
Ce140_ppm_mean	2.936	2.938	5.316	7.184	4.630	3.409	2.308	3.481
Ce140_ppm_2SE(int)	0.181	0.241	0.310	0.718	0.246	0.282	0.115	0.176
Pr141_ppm_mean	0.389	0.373	0.656	0.898	0.605	0.401	0.304	0.502
Pr141_ppm_2SE(int)	0.041	0.042	0.063	0.049	0.057	0.073	0.034	0.052
Nd146_ppm_mean	1.676	1.805	3.128	4.433	2.864	1.975	1.345	1.961
Nd146_ppm_2SE(int)	0.205	0.324	0.374	0.294	0.319	0.414	0.148	0.271
Sm147_ppm_mean	0.446	0.332	0.672	1.445	0.579	0.426	0.308	0.437
Sm147_ppm_2SE(int)	0.110	0.082	0.132	0.265	0.130	0.104	0.093	0.106
Eu153_ppm_mean	3.483	3.755	5.578	6.019	4.807	1.669	2.799	4.691
Eu153_ppm_2SE(int)	0.181	0.193	0.223	0.553	0.236	0.261	0.140	0.199
Gd157_ppm_mean	0.401	0.409	0.717	1.779	0.608	0.403	0.259	0.436
Gd157_ppm_2SE(int)	0.115	0.176	0.121	0.386	0.113	0.161	0.093	0.161
Tb159_ppm_mean	0.044	0.046	0.074	0.287	0.089	0.055	0.033	0.057
Tb159_ppm_2SE(int)	0.013	0.012	0.017	0.075	0.018	0.022	0.009	0.017
Dy163_ppm_mean	0.327	0.207	0.380	2.353	0.464	0.437	0.167	0.258
Dy163_ppm_2SE(int)	0.124	0.047	0.075	0.611	0.102	0.119	0.050	0.051
Ho165_ppm_mean	0.035	0.040	0.077	0.536	0.074	0.082	0.034	0.054
Ho165_ppm_2SE(int)	0.011	0.012	0.021	0.150	0.018	0.029	0.011	0.015
Er166_ppm_mean	0.113	0.097	0.178	1.600	0.231	0.279	0.073	0.112
Er166_ppm_2SE(int)	0.045	0.035	0.046	0.476	0.065	0.086	0.029	0.035
Tm169_ppm_mean	0.009	0.009	0.015	0.219	0.038	0.026	0.006	0.015
Tm169_ppm_2SE(int)	0.007	0.005	0.008	0.068	0.012	0.008	0.004	0.006
Yb172_ppm_mean	0.077	0.075	0.087	1.719	0.232	0.186	0.057	0.090
Yb172_ppm_2SE(int)	0.027	0.038	0.040	0.511	0.081	0.059	0.025	0.034
Lu175_ppm_mean	0.011	0.003	0.004	0.249	0.024	0.035	0.002	0.006
Lu175_ppm_2SE(int)	0.008	0.002	0.003	0.081	0.010	0.011	0.003	0.004

*Point names include phase (pl) and spot size (i.e., 30 um).

Table S4 cont.: Plagioclase feldspar rare earth element contents.

Sample	10017	10022	10022	10022	10022	10022	10022	10024
LAICPMS point*	17.65.pl.40um	22.19.pl.30um	22.28.pl.35um	22.31.pl.35um	22.37.pl.35um	22.47.pl.35um	22.51.pl.35um	24.4.pl.40um
La139_ppm_mean	1.301	5.504	1.008	6.830	14.945	2.764	1.746	1.800
La139_ppm_2SE(int)	0.072	2.331	0.442	5.999	2.143	0.240	0.445	0.120
Ce140_ppm_mean	2.907	13.997	N/A	N/A	N/A	N/A	N/A	4.077
Ce140_ppm_2SE(int)	0.161	6.176	N/A	N/A	N/A	N/A	N/A	0.205
Pr141_ppm_mean	0.354	4.869	0.311	2.019	5.344	0.878	0.446	0.566
Pr141_ppm_2SE(int)	0.043	5.458	0.157	1.562	0.671	0.079	0.083	0.078
Nd146_ppm_mean	1.683	10.009	1.615	7.595	24.233	3.840	2.055	2.134
Nd146_ppm_2SE(int)	0.194	4.928	0.881	4.570	2.551	0.437	0.328	0.220
Sm147_ppm_mean	0.277	3.209	0.471	2.033	7.453	1.090	1.126	0.430
Sm147_ppm_2SE(int)	0.082	1.578	0.302	0.895	1.057	0.386	1.281	0.098
Eu153_ppm_mean	3.192	3.852	0.083	2.679	6.855	5.231	4.023	4.799
Eu153_ppm_2SE(int)	0.154	0.247	0.025	0.596	0.565	0.511	0.384	0.162
Gd157_ppm_mean	0.332	3.787	0.750	1.494	8.098	0.956	0.290	0.430
Gd157_ppm_2SE(int)	0.073	2.067	0.477	0.774	1.166	0.318	0.136	0.120
Tb159_ppm_mean	0.031	0.746	0.079	0.230	1.554	0.134	0.033	0.067
Tb159_ppm_2SE(int)	0.010	0.409	0.047	0.124	0.165	0.029	0.018	0.017
Dy163_ppm_mean	0.220	4.756	0.449	1.113	9.833	0.957	0.288	0.302
Dy163_ppm_2SE(int)	0.043	2.601	0.264	0.646	1.294	0.171	0.101	0.085
Ho165_ppm_mean	0.054	0.951	0.116	0.266	2.024	0.216	0.022	0.045
Ho165_ppm_2SE(int)	0.015	0.524	0.076	0.142	0.377	0.055	0.015	0.013
Er166_ppm_mean	0.082	2.594	0.271	0.553	5.549	0.511	0.067	0.069
Er166_ppm_2SE(int)	0.040	1.491	0.147	0.328	0.999	0.158	0.065	0.035
Tm169_ppm_mean	0.014	0.368	0.024	0.094	0.774	0.067	0.009	0.010
Tm169_ppm_2SE(int)	0.005	0.211	0.015	0.060	0.130	0.023	0.010	0.006
Yb172_ppm_mean	0.082	2.396	0.232	0.541	5.038	0.626	0.061	0.260
Yb172_ppm_2SE(int)	0.029	1.362	0.150	0.305	0.809	0.197	0.057	0.374
Lu175_ppm_mean	0.008	0.371	0.025	0.369	0.675	0.053	0.009	0.003
Lu175_ppm_2SE(int)	0.004	0.209	0.016	0.599	0.098	0.025	0.008	0.003

*Point names include phase (pl) and spot size (i.e., 30 um).

Table S4 cont.: Plagioclase feldspar rare earth element contents.

Sample	10024	10024	10024	10024	10024	10024	10024	10024
LAICPMS point*	24.5.pl.40um	24.10.pl.45um	24.11.pl.45um	24.24.pl.45um	24.25.pl.45um	24.26.pl.45um	24.28.pl.45um	24.35.pl.40um
La139_ppm_mean	1.361	1.189	1.344	2.316	2.330	1.349	1.780	4.425
La139_ppm_2SE(int)	0.103	0.096	0.121	0.141	0.194	0.128	0.101	0.300
Ce140_ppm_mean	3.310	2.689	2.942	5.010	5.191	2.961	4.089	11.244
Ce140_ppm_2SE(int)	0.513	0.149	0.117	0.236	0.366	0.169	0.209	0.889
Pr141_ppm_mean	0.377	0.359	0.370	0.595	0.641	0.389	0.529	1.558
Pr141_ppm_2SE(int)	0.034	0.033	0.035	0.046	0.053	0.041	0.042	0.138
Nd146_ppm_mean	1.684	1.713	1.572	2.787	2.757	1.616	2.347	6.260
Nd146_ppm_2SE(int)	0.204	0.199	0.204	0.234	0.256	0.168	0.210	0.590
Sm147_ppm_mean	0.377	0.408	0.346	0.552	0.521	0.321	0.486	1.654
Sm147_ppm_2SE(int)	0.096	0.087	0.112	0.100	0.124	0.073	0.138	0.219
Eu153_ppm_mean	3.855	3.109	3.765	5.582	5.603	3.712	4.248	6.221
Eu153_ppm_2SE(int)	0.217	0.157	0.222	0.257	0.276	0.216	0.174	0.260
Gd157_ppm_mean	0.453	0.511	0.292	0.494	0.551	0.277	0.477	1.553
Gd157_ppm_2SE(int)	0.096	0.107	0.070	0.090	0.101	0.096	0.096	0.233
Tb159_ppm_mean	0.132	0.114	0.029	0.061	0.077	0.045	0.072	0.241
Tb159_ppm_2SE(int)	0.162	0.022	0.010	0.015	0.015	0.011	0.016	0.042
Dy163_ppm_mean	0.221	0.624	0.195	0.354	0.380	0.158	0.336	1.363
Dy163_ppm_2SE(int)	0.052	0.094	0.051	0.062	0.098	0.041	0.067	0.254
Ho165_ppm_mean	0.048	0.138	0.038	0.042	0.049	0.047	0.054	0.305
Ho165_ppm_2SE(int)	0.018	0.027	0.010	0.010	0.011	0.012	0.013	0.073
Er166_ppm_mean	0.110	0.449	0.103	0.100	0.185	0.072	0.143	0.715
Er166_ppm_2SE(int)	0.030	0.109	0.044	0.031	0.039	0.028	0.034	0.163
Tm169_ppm_mean	0.013	0.058	0.011	0.009	0.012	0.012	0.012	0.096
Tm169_ppm_2SE(int)	0.007	0.015	0.006	0.005	0.006	0.006	0.006	0.025
Yb172_ppm_mean	0.097	0.482	0.051	0.112	0.142	0.064	0.115	0.658
Yb172_ppm_2SE(int)	0.042	0.093	0.027	0.032	0.043	0.028	0.041	0.141
Lu175_ppm_mean	0.009	0.055	0.006	0.005	0.009	0.004	0.011	0.170
Lu175_ppm_2SE(int)	0.006	0.016	0.004	0.003	0.005	0.003	0.006	0.219

*Point names include phase (pl) and spot size (i.e., 30 um).

Table S4 cont.: Plagioclase feldspar rare earth element contents.

Sample	10024	10024	10024	10024	10024	10024	10049	10049
LAICPMS point*	24.36.pl.45um	24.49.pl.45um	24.50.pl.45um	24.51.pl.35um	24.53.pl.45um	24.69.olv.40um	49.2.pl.30um	49.3.pl.30um
La139_ppm_mean	1.611	1.833	1.205	10.397	1.556	0.158	7.723	4.152
La139_ppm_2SE(int)	0.125	0.127	0.089	0.441	0.071	0.037	1.548	0.807
Ce140_ppm_mean	3.417	4.083	2.831	N/A	3.478	3.535	21.607	10.998
Ce140_ppm_2SE(int)	0.173	0.234	0.187	N/A	0.164	4.940	4.492	2.247
Pr141_ppm_mean	0.489	0.517	0.352	2.409	0.452	0.289	3.346	1.579
Pr141_ppm_2SE(int)	0.130	0.052	0.040	0.160	0.038	0.230	0.719	0.372
Nd146_ppm_mean	1.981	2.233	1.532	10.322	1.954	1.097	16.361	6.918
Nd146_ppm_2SE(int)	0.201	0.249	0.190	0.809	0.232	0.254	3.601	1.723
Sm147_ppm_mean	0.355	0.545	0.379	1.893	0.398	0.574	5.123	2.052
Sm147_ppm_2SE(int)	0.083	0.118	0.087	0.315	0.085	0.163	1.261	0.618
Eu153_ppm_mean	4.298	4.567	3.645	19.298	4.122	0.071	3.070	3.925
Eu153_ppm_2SE(int)	0.185	0.268	0.197	0.711	0.122	0.082	0.450	0.389
Gd157_ppm_mean	0.375	0.424	0.351	1.801	0.408	1.039	7.092	2.126
Gd157_ppm_2SE(int)	0.091	0.097	0.090	0.217	0.097	0.278	1.805	0.595
Tb159_ppm_mean	0.071	0.039	0.036	0.224	0.063	0.222	1.285	0.422
Tb159_ppm_2SE(int)	0.036	0.010	0.010	0.035	0.016	0.054	0.342	0.125
Dy163_ppm_mean	0.244	0.279	0.219	1.210	0.216	1.615	8.882	2.448
Dy163_ppm_2SE(int)	0.053	0.064	0.046	0.158	0.051	0.359	2.295	0.708
Ho165_ppm_mean	0.041	0.040	0.032	0.202	0.041	0.383	1.872	0.497
Ho165_ppm_2SE(int)	0.013	0.011	0.010	0.031	0.011	0.081	0.458	0.140
Er166_ppm_mean	0.092	0.117	0.070	0.396	0.078	1.287	5.550	1.426
Er166_ppm_2SE(int)	0.036	0.034	0.025	0.095	0.028	0.265	1.428	0.477
Tm169_ppm_mean	0.012	0.010	0.011	0.039	0.011	0.190	0.761	0.174
Tm169_ppm_2SE(int)	0.006	0.005	0.005	0.013	0.005	0.038	0.190	0.065
Yb172_ppm_mean	0.102	0.072	0.050	0.308	0.082	1.396	5.266	1.292
Yb172_ppm_2SE(int)	0.036	0.032	0.022	0.076	0.030	0.238	1.370	0.508
Lu175_ppm_mean	0.003	0.008	0.005	0.029	0.005	0.213	0.769	0.153
Lu175_ppm_2SE(int)	0.003	0.005	0.004	0.013	0.004	0.033	0.196	0.057

*Point names include phase (pl) and spot size (i.e., 30 um).

Table S4 cont.: Plagioclase feldspar rare earth element contents.

Sample	10049	10049	10049	10049	10049	10049	10049	10069
LAICPMS point*	49.8.pl.30um	49.9.pl.30um	49.17.pl.30um	49.19.pl.30um	49.34.pl.30um	49.37.pl.30um	49.40.pl.30um	69.1.pl.30um
La139_ppm_mean	42.922	2.291	6.936	39.994	3.901	7.700	1.294	1.202
La139_ppm_2SE(int)	15.516	0.205	1.945	5.305	0.645	0.804	0.179	0.116
Ce140_ppm_mean	123.547	6.268	21.359	113.231	10.788	20.786	6.095	3.103
Ce140_ppm_2SE(int)	44.581	0.413	6.926	15.068	1.978	2.226	0.437	0.583
Pr141_ppm_mean	18.376	0.996	3.144	16.862	1.391	2.929	1.343	0.410
Pr141_ppm_2SE(int)	6.753	0.087	1.046	2.328	0.259	0.305	0.117	0.063
Nd146_ppm_mean	88.049	4.850	16.120	80.846	6.539	13.799	9.458	2.140
Nd146_ppm_2SE(int)	32.452	0.711	5.225	11.281	1.301	1.866	0.893	0.719
Sm147_ppm_mean	28.167	1.968	6.515	26.785	1.763	4.420	5.551	0.612
Sm147_ppm_2SE(int)	10.324	0.450	2.090	3.837	0.453	0.532	0.587	0.159
Eu153_ppm_mean	4.677	3.258	3.426	4.072	3.699	3.897	0.547	3.081
Eu153_ppm_2SE(int)	0.569	0.298	0.215	0.342	0.267	0.369	0.137	0.686
Gd157_ppm_mean	33.167	2.834	8.203	32.343	1.796	4.672	9.430	0.782
Gd157_ppm_2SE(int)	12.483	0.585	2.325	4.447	0.423	0.656	0.595	0.213
Tb159_ppm_mean	5.475	0.528	1.365	5.398	0.261	0.791	1.749	0.145
Tb159_ppm_2SE(int)	2.008	0.118	0.362	0.712	0.069	0.117	0.154	0.038
Dy163_ppm_mean	35.398	3.698	10.225	36.459	1.583	5.253	13.569	1.253
Dy163_ppm_2SE(int)	13.085	0.790	2.763	4.655	0.503	0.713	0.938	0.317
Ho165_ppm_mean	7.392	0.833	2.169	7.433	0.341	1.054	2.816	0.236
Ho165_ppm_2SE(int)	2.776	0.206	0.618	0.979	0.087	0.143	0.242	0.067
Er166_ppm_mean	20.129	2.393	6.216	21.924	0.790	3.360	9.005	0.547
Er166_ppm_2SE(int)	7.585	0.537	1.593	2.663	0.196	0.441	0.322	0.130
Tm169_ppm_mean	2.859	0.363	0.809	2.856	0.142	0.444	1.149	0.097
Tm169_ppm_2SE(int)	1.083	0.089	0.224	0.357	0.056	0.077	0.099	0.028
Yb172_ppm_mean	17.267	2.549	6.151	19.144	0.765	2.920	8.471	0.594
Yb172_ppm_2SE(int)	6.579	0.625	1.693	2.211	0.220	0.462	0.420	0.175
Lu175_ppm_mean	2.259	0.389	0.757	2.511	0.110	0.410	1.199	0.081
Lu175_ppm_2SE(int)	0.850	0.092	0.198	0.279	0.035	0.070	0.110	0.025

*Point names include phase (pl) and spot size (i.e., 30 um).

Table S4 cont.: Plagioclase feldspar rare earth element contents.

Sample	10069	10069	10069	10069	10069	10069	10069	10069
LAICPMS point*	69.7.pl.30um	69.11.pl.30um	69.15.pl.30um	69.21.pl.30um	69.26.pl.30um	69.27.pl.30um	69.35.pl.25um	69.44.pl.30um
La139_ppm_mean	0.934	43.034	9.980	2.351	1.625	4.123	73.212	5.890
La139_ppm_2SE(int)	0.104	9.470	1.310	0.466	0.174	0.598	6.612	1.269
Ce140_ppm_mean	2.708	129.601	30.846	5.946	4.082	11.634	207.796	16.616
Ce140_ppm_2SE(int)	0.207	28.824	3.857	1.430	0.578	1.897	20.179	3.839
Pr141_ppm_mean	0.384	19.014	4.121	0.862	0.565	1.553	29.474	2.255
Pr141_ppm_2SE(int)	0.054	4.167	0.544	0.256	0.106	0.291	2.809	0.516
Nd146_ppm_mean	1.585	91.700	20.633	4.325	2.446	7.440	148.650	10.447
Nd146_ppm_2SE(int)	0.266	20.336	2.643	1.448	0.520	1.527	14.246	2.710
Sm147_ppm_mean	0.468	29.978	6.703	1.096	1.431	2.043	43.677	3.120
Sm147_ppm_2SE(int)	0.176	6.047	1.290	0.544	1.887	0.467	4.359	0.899
Eu153_ppm_mean	3.369	5.315	4.757	4.032	4.147	3.680	5.335	4.413
Eu153_ppm_2SE(int)	0.283	0.481	0.287	0.343	0.273	0.281	0.412	0.268
Gd157_ppm_mean	0.483	33.602	7.573	1.330	0.409	2.429	48.229	3.473
Gd157_ppm_2SE(int)	0.171	6.832	1.204	0.653	0.162	0.531	5.447	1.011
Tb159_ppm_mean	0.047	5.618	1.393	0.269	0.099	0.347	8.064	0.575
Tb159_ppm_2SE(int)	0.014	1.068	0.220	0.158	0.044	0.080	0.864	0.157
Dy163_ppm_mean	0.375	36.534	9.166	1.699	0.429	2.386	53.442	3.411
Dy163_ppm_2SE(int)	0.123	6.629	1.119	0.951	0.148	0.530	5.968	0.924
Ho165_ppm_mean	0.052	7.355	1.969	0.330	0.058	0.469	11.540	0.694
Ho165_ppm_2SE(int)	0.019	1.365	0.280	0.188	0.031	0.118	1.453	0.215
Er166_ppm_mean	0.173	19.766	5.713	1.020	0.153	1.262	29.805	1.880
Er166_ppm_2SE(int)	0.065	3.476	0.922	0.610	0.058	0.274	3.062	0.556
Tm169_ppm_mean	0.021	2.546	0.836	0.152	0.023	0.162	3.911	0.245
Tm169_ppm_2SE(int)	0.010	0.446	0.119	0.098	0.015	0.046	0.454	0.078
Yb172_ppm_mean	0.123	15.657	5.551	1.046	0.144	1.146	26.241	1.460
Yb172_ppm_2SE(int)	0.056	2.291	0.880	0.679	0.087	0.298	3.415	0.442
Lu175_ppm_mean	0.014	1.762	0.827	0.097	0.018	0.125	3.080	0.220
Lu175_ppm_2SE(int)	0.009	0.251	0.165	0.059	0.012	0.047	0.409	0.076

*Point names include phase (pl) and spot size (i.e., 30 um).

Table S4 cont.: Plagioclase feldspar rare earth element contents.

Sample	10069	10069	10069	10069	10069	10069	10069	10069
LAICPMS point*	69.45.pl.25um	69.50.px.30um	69.61.pl.30um	69.69.pl.30um	69.70.pl.30um	69.81.pl.30um	69.108.pl.35um	69.109.pl.30um
La139_ppm_mean	21.696	2.154	55.803	1.461	6.954	7.343	16.508	1.186
La139_ppm_2SE(int)	7.108	0.147	28.107	0.124	1.464	2.532	31.009	0.277
Ce140_ppm_mean	65.033	5.429	160.167	3.457	18.766	18.854	N/A	2.345
Ce140_ppm_2SE(int)	19.590	0.448	77.479	0.312	4.442	6.596	N/A	0.308
Pr141_ppm_mean	8.630	0.709	24.210	0.411	2.593	2.691	0.529	0.337
Pr141_ppm_2SE(int)	2.578	0.074	11.566	0.057	0.619	0.946	0.358	0.076
Nd146_ppm_mean	42.498	2.979	122.221	2.113	14.021	13.813	1.451	1.720
Nd146_ppm_2SE(int)	14.591	0.374	54.752	0.327	3.630	5.130	0.233	0.494
Sm147_ppm_mean	11.641	0.882	42.594	0.346	3.852	3.550	0.464	0.333
Sm147_ppm_2SE(int)	3.540	0.164	16.969	0.129	0.994	1.390	0.129	0.215
Eu153_ppm_mean	3.043	4.703	3.816	4.141	5.147	4.771	3.556	2.853
Eu153_ppm_2SE(int)	0.316	0.291	0.501	0.271	0.237	0.248	0.879	0.298
Gd157_ppm_mean	12.148	1.082	54.378	0.322	4.172	4.321	0.306	0.092
Gd157_ppm_2SE(int)	4.201	0.237	18.364	0.103	1.149	1.814	0.100	0.098
Tb159_ppm_mean	2.317	0.165	10.677	0.056	0.689	0.666	0.087	0.085
Tb159_ppm_2SE(int)	0.705	0.042	3.388	0.018	0.217	0.280	0.043	0.038
Dy163_ppm_mean	15.232	1.106	77.303	0.350	4.049	4.498	0.253	0.665
Dy163_ppm_2SE(int)	5.153	0.228	23.597	0.125	1.162	1.955	0.085	0.279
Ho165_ppm_mean	3.516	0.252	17.054	0.054	0.744	0.898	0.147	0.090
Ho165_ppm_2SE(int)	1.147	0.062	5.162	0.028	0.217	0.378	0.184	0.040
Er166_ppm_mean	9.587	0.613	50.935	0.129	2.328	2.575	0.261	0.268
Er166_ppm_2SE(int)	2.789	0.183	13.738	0.071	0.722	1.084	0.187	0.189
Tm169_ppm_mean	1.361	0.142	7.473	0.032	0.277	0.318	0.040	0.061
Tm169_ppm_2SE(int)	0.363	0.075	1.934	0.022	0.080	0.141	0.047	0.030
Yb172_ppm_mean	11.528	0.771	56.884	0.133	2.040	2.008	0.601	0.277
Yb172_ppm_2SE(int)	1.983	0.221	12.430	0.083	0.676	0.843	0.976	0.159
Lu175_ppm_mean	1.610	0.105	10.171	0.026	0.254	0.237	0.087	0.025
Lu175_ppm_2SE(int)	0.253	0.041	1.897	0.016	0.089	0.101	0.121	0.028

*Point names include phase (pl) and spot size (i.e., 30 um).

Table S4 cont.: Plagioclase feldspar rare earth element contents.

Sample	10069	10069	10071	10071	10071	10071	10071	10071
LAICPMS point*	69.110.pl.30um	69.112.pl.30um	71.4.pl.35um	71.5.pl.35um	71.6.pl.35um	71.18.pl.35um	71.19.pl.35um	71.26.pl.35um
La139_ppm_mean	52.725	1.741	1.792	3.687	4.262	20.835	7.232	13.865
La139_ppm_2SE(int)	31.425	0.148	0.136	0.466	2.305	2.088	1.034	5.537
Ce140_ppm_mean	143.470	4.390	N/A	N/A	N/A	N/A	N/A	N/A
Ce140_ppm_2SE(int)	80.063	0.366	N/A	N/A	N/A	N/A	N/A	N/A
Pr141_ppm_mean	20.682	0.630	0.565	1.397	1.707	7.406	2.405	5.734
Pr141_ppm_2SE(int)	11.465	0.068	0.069	0.195	1.001	0.765	0.601	2.278
Nd146_ppm_mean	99.459	3.538	2.687	6.495	9.229	36.237	11.350	28.779
Nd146_ppm_2SE(int)	54.908	0.466	0.472	0.978	6.114	3.879	3.250	10.993
Sm147_ppm_mean	28.236	1.340	0.671	1.515	3.370	16.078	3.963	8.699
Sm147_ppm_2SE(int)	14.251	0.268	0.224	0.429	2.351	1.639	1.536	3.361
Eu153_ppm_mean	6.511	3.750	4.233	4.956	4.479	3.713	10.177	4.430
Eu153_ppm_2SE(int)	0.780	0.371	0.325	0.473	0.432	0.685	0.649	0.249
Gd157_ppm_mean	31.934	2.212	0.773	1.704	4.275	21.858	5.021	9.787
Gd157_ppm_2SE(int)	17.370	0.411	0.172	0.468	3.405	2.380	1.945	3.752
Tb159_ppm_mean	5.049	0.447	0.107	0.342	0.619	4.668	1.313	1.789
Tb159_ppm_2SE(int)	2.328	0.103	0.040	0.100	0.355	0.424	0.529	0.704
Dy163_ppm_mean	31.911	3.250	0.687	1.938	4.474	36.318	11.514	11.528
Dy163_ppm_2SE(int)	14.912	0.695	0.284	0.519	2.650	2.871	4.621	4.428
Ho165_ppm_mean	6.606	0.789	0.128	0.376	0.877	8.038	2.828	2.456
Ho165_ppm_2SE(int)	3.213	0.173	0.055	0.097	0.488	0.677	1.163	0.959
Er166_ppm_mean	17.066	2.460	0.344	0.946	2.562	25.764	10.037	7.282
Er166_ppm_2SE(int)	7.860	0.581	0.180	0.314	1.387	1.769	4.013	2.844
Tm169_ppm_mean	2.165	0.403	0.046	0.122	0.321	4.186	1.819	0.976
Tm169_ppm_2SE(int)	0.929	0.109	0.022	0.049	0.158	0.334	0.675	0.391
Yb172_ppm_mean	13.338	2.779	0.374	1.004	2.532	31.753	15.092	6.317
Yb172_ppm_2SE(int)	5.457	0.692	0.218	0.348	1.245	1.540	5.735	2.395
Lu175_ppm_mean	1.727	0.435	0.050	0.144	0.301	4.646	2.436	0.782
Lu175_ppm_2SE(int)	0.715	0.110	0.042	0.042	0.149	0.300	0.913	0.306

*Point names include phase (pl) and spot size (i.e., 30 um).

Table S4 cont.: Plagioclase feldspar rare earth element contents.

Sample	10071	10071	10071	10071	10071	10071	10072	10072
LAICPMS point*	71.30.pl.35um	71.31.pl.35um	71.33.pl.35um	71.82.pl.35um	71.83.pl.35um	71.84.pl.35um	72.3.pl.40um	72.5.pl.40um
La139_ppm_mean	34.282	34.039	6.152	21.575	26.265	2.201	1.630	3.091
La139_ppm_2SE(int)	13.740	1.686	1.340	2.509	4.365	0.137	0.126	0.369
Ce140_ppm_mean	N/A	N/A	N/A	N/A	N/A	N/A	3.567	7.425
Ce140_ppm_2SE(int)	N/A	N/A	N/A	N/A	N/A	N/A	0.227	0.841
Pr141_ppm_mean	14.541	13.906	2.956	9.213	11.115	0.766	0.472	0.968
Pr141_ppm_2SE(int)	5.675	1.058	0.744	1.038	1.862	0.073	0.049	0.115
Nd146_ppm_mean	76.381	67.844	15.874	46.388	50.985	3.185	1.874	4.143
Nd146_ppm_2SE(int)	28.995	5.849	4.181	4.925	8.639	0.335	0.281	0.557
Sm147_ppm_mean	27.379	25.602	6.307	16.308	15.670	0.990	0.466	1.085
Sm147_ppm_2SE(int)	9.316	2.184	1.806	1.623	2.898	0.194	0.130	0.226
Eu153_ppm_mean	5.192	4.426	4.282	2.013	5.225	4.547	4.172	4.516
Eu153_ppm_2SE(int)	0.478	0.330	0.217	0.117	0.246	0.288	0.247	0.266
Gd157_ppm_mean	34.344	30.039	8.020	19.393	17.366	0.938	0.543	1.043
Gd157_ppm_2SE(int)	11.150	2.634	2.462	1.509	3.001	0.174	0.131	0.222
Tb159_ppm_mean	6.954	6.471	1.650	3.710	3.003	0.186	0.061	0.201
Tb159_ppm_2SE(int)	2.179	0.781	0.499	0.265	0.540	0.026	0.020	0.051
Dy163_ppm_mean	46.652	45.073	12.017	24.477	18.601	1.085	0.363	0.983
Dy163_ppm_2SE(int)	13.835	5.925	3.669	1.857	3.192	0.167	0.124	0.205
Ho165_ppm_mean	9.988	10.509	2.500	5.326	3.644	0.230	0.055	0.240
Ho165_ppm_2SE(int)	2.954	1.636	0.795	0.428	0.620	0.041	0.019	0.047
Er166_ppm_mean	30.331	32.522	7.896	15.044	10.058	0.595	0.150	0.597
Er166_ppm_2SE(int)	8.681	5.075	2.457	1.152	1.724	0.101	0.064	0.124
Tm169_ppm_mean	4.409	5.149	1.135	2.060	1.491	0.081	0.021	0.071
Tm169_ppm_2SE(int)	1.248	0.869	0.355	0.195	0.339	0.020	0.011	0.019
Yb172_ppm_mean	31.719	37.003	8.524	14.940	8.482	0.645	0.161	0.533
Yb172_ppm_2SE(int)	8.963	6.348	2.648	1.065	1.497	0.157	0.067	0.119
Lu175_ppm_mean	4.646	5.150	1.163	1.890	1.098	0.107	0.013	0.078
Lu175_ppm_2SE(int)	1.176	0.900	0.396	0.142	0.174	0.034	0.006	0.049

*Point names include phase (pl) and spot size (i.e., 30 um).

Table S4 cont.: Plagioclase feldspar rare earth element contents.

Sample	10072	10072	10072	10072	10072	10072
LAICPMS point*	72.10.pl.45um	72.20.pl.40um	72.22.pl.45um	72.26.pl.40um	72.30.pl.40um	72.41.pl.40um
La139_ppm_mean	2.093	1.988	7.173	1.462	11.960	6.416
La139_ppm_2SE(int)	0.168	0.154	1.973	0.141	1.110	5.073
Ce140_ppm_mean	5.867	4.791	19.860	3.437	32.850	13.333
Ce140_ppm_2SE(int)	0.609	0.324	5.509	0.298	2.775	9.581
Pr141_ppm_mean	0.727	0.655	2.859	0.455	4.779	1.844
Pr141_ppm_2SE(int)	0.094	0.070	0.825	0.054	0.447	1.337
Nd146_ppm_mean	3.344	2.938	13.067	2.181	22.908	9.430
Nd146_ppm_2SE(int)	0.330	0.287	3.621	0.246	2.229	7.133
Sm147_ppm_mean	1.030	0.726	3.757	0.337	6.932	2.937
Sm147_ppm_2SE(int)	0.208	0.145	1.105	0.087	0.832	2.391
Eu153_ppm_mean	4.419	3.810	4.234	3.941	6.351	4.410
Eu153_ppm_2SE(int)	0.180	0.174	0.158	0.339	0.253	0.252
Gd157_ppm_mean	0.892	0.774	4.649	0.360	7.697	3.614
Gd157_ppm_2SE(int)	0.159	0.165	1.349	0.101	1.010	3.097
Tb159_ppm_mean	0.163	0.125	0.792	0.053	1.384	0.581
Tb159_ppm_2SE(int)	0.030	0.024	0.221	0.014	0.166	0.521
Dy163_ppm_mean	0.746	0.656	4.988	0.241	8.590	4.290
Dy163_ppm_2SE(int)	0.111	0.133	1.375	0.064	1.286	3.894
Ho165_ppm_mean	0.175	0.137	0.971	0.032	1.825	0.879
Ho165_ppm_2SE(int)	0.033	0.029	0.256	0.009	0.264	0.806
Er166_ppm_mean	0.452	0.398	2.692	0.086	4.768	2.103
Er166_ppm_2SE(int)	0.094	0.093	0.721	0.036	0.701	1.928
Tm169_ppm_mean	0.065	0.152	0.358	0.009	0.689	0.302
Tm169_ppm_2SE(int)	0.014	0.209	0.102	0.005	0.097	0.288
Yb172_ppm_mean	0.472	0.310	2.077	0.068	4.618	1.829
Yb172_ppm_2SE(int)	0.128	0.086	0.478	0.035	0.667	1.825
Lu175_ppm_mean	0.059	0.043	0.297	0.005	0.607	0.177
Lu175_ppm_2SE(int)	0.026	0.014	0.072	0.005	0.100	0.166

*Point names include phase (pl) and spot size (i.e., 30 um).

Table S5: Pyroxene major element contents.

Sample	10017	10017	10017	10017	10017	10017	10017	10017
Point	14 / 1 .	21 / 1 .	22 / 1 .	29 / 1 .	32 / 1 .	33 / 1 .	45 / 1 .	48 / 1 .
SiO2	49.77	46.86	49.89	49.47	49.62	50.10	50.62	49.10
TiO2	1.87	1.01	1.57	2.34	2.21	2.18	2.04	2.15
Al2O3	2.49	1.42	1.90	2.58	2.43	2.15	2.45	2.94
Cr2O3	0.47	0.27	0.39	0.60	0.60	0.61	0.57	0.57
Fe2O3	0.00	0.00	0.00	0.00	0.00	0.00	0.00	0.00
FeO	13.72	33.14	16.48	10.22	11.07	10.26	10.93	12.18
MnO	0.21	0.47	0.26	0.14	0.18	0.17	0.17	0.23
MgO	14.37	5.80	13.89	14.87	16.30	15.91	16.37	14.29
CaO	15.94	9.58	13.72	17.85	15.96	17.41	16.32	16.66
Na2O	0.07	0.00	0.05	0.10	0.07	0.09	0.09	0.09
K2O	0.01	0.01	0.00	0.00	0.00	0.00	0.00	0.01
P2O5	0.00	0.00	0.06	0.02	0.00	0.00	0.04	0.00
Total	98.92	98.55	98.22	98.18	98.45	98.88	99.60	98.21
Mg# (Mg/(Mg+Fe))	65.13	23.78	60.04	72.18	72.40	73.42	72.75	67.65
En	42.87	18.55	42.10	44.48	47.96	46.54	47.83	43.18
Fs	22.96	59.44	28.01	17.15	18.29	16.85	17.91	20.65
Wo	34.17	22.01	29.89	38.37	33.76	36.61	34.26	36.18

Table S5 cont.: Pyroxene major element contents.

Sample	10017	10017	10017	10022	10022	10022	10022	10022
Point	55 / 1 .	62 / 1 .	63 / 1 .	2 / 1 .	4 / 1 .	10 / 1 .	12 / 1 .	13 / 1 .
SiO2	50.17	49.65	48.59	48.95	46.95	49.78	48.74	46.96
TiO2	2.34	2.41	1.25	2.62	3.03	0.11	3.10	3.15
Al2O3	2.71	2.77	1.45	2.82	5.21	30.21	3.27	5.11
Cr2O3	0.59	0.62	0.31	0.79	0.59	0.00	0.83	0.53
Fe2O3	0.00	0.00	0.00	0.00	0.00	0.00	0.00	0.00
FeO	9.89	10.22	25.87	11.29	12.04	0.72	9.82	13.21
MnO	0.14	0.16	0.39	0.15	0.16	0.00	0.14	0.23
MgO	14.69	14.78	10.57	16.49	12.05	0.00	14.46	11.55
CaO	18.54	17.76	11.08	14.84	18.38	15.03	18.01	17.63
Na2O	0.10	0.09	0.01	0.08	0.11	2.22	0.13	0.10
K2O	0.00	0.00	0.00	0.00	0.00	0.30	0.00	0.00
P2O5	0.04	0.03	0.01	0.00	0.01	0.01	0.00	0.00
Total	99.22	98.49	99.52	98.02	98.52	98.38	98.50	98.46
Mg# (Mg/(Mg+Fe))	72.59	72.05	42.13	72.24	64.06	0.00	72.42	60.91
En	43.77	44.41	31.97	49.23	37.62	0.00	43.94	36.51
Fs	16.53	17.23	43.92	18.92	21.11	3.59	16.73	23.43
Wo	39.70	38.36	24.11	31.86	41.27	96.41	39.33	40.06

Table S5 cont.: Pyroxene major element contents.

Sample	10022	10022	10022	10022	10022	10022	10022	10022
Point	14 / 1 .	16 / 1 .	27 / 1 .	33 / 1 .	39 / 1 .	40 / 1 .	42 / 1 .	43 / 1 .
SiO2	46.86	49.79	49.21	53.05	45.98	49.59	48.74	47.55
TiO2	1.22	1.86	1.43	0.76	0.93	1.93	2.57	2.17
Al2O3	2.52	2.47	1.67	0.64	2.86	2.65	3.37	4.21
Cr2O3	0.12	0.44	0.23	0.36	0.07	0.33	0.65	0.47
Fe2O3	0.00	0.00	0.00	0.00	0.00	0.00	0.00	0.00
FeO	34.36	13.90	22.38	16.14	37.71	15.01	11.73	15.63
MnO	0.49	0.20	0.36	0.25	0.49	0.27	0.18	0.24
MgO	4.54	15.72	14.12	23.66	2.82	14.85	15.05	12.53
CaO	9.21	14.05	8.94	4.09	7.82	14.04	15.86	15.18
Na2O	0.09	0.05	0.03	0.01	0.13	0.04	0.09	0.09
K2O	0.12	0.00	0.00	0.00	0.11	0.00	0.00	0.00
P2O5	0.08	0.02	0.00	0.01	0.05	0.01	0.02	0.02
Total	99.62	98.50	98.38	98.98	98.98	98.71	98.27	98.08
Mg# (Mg/(Mg+Fe))	19.08	66.84	52.92	72.33	11.77	63.81	69.57	58.84
En	14.93	46.76	42.65	66.36	9.53	44.50	45.55	38.91
Fs	63.32	23.20	37.94	25.39	71.48	25.24	19.93	27.22
Wo	21.76	30.04	19.41	8.25	18.98	30.25	34.52	33.87

Table S5 cont.: Pyroxene major element contents.

Sample	10022	10022	10022	10022	10024	10024	10024	10024
Point	44 / 1 .	46 / 1 .	56 / 1 .	59 / 1 .	1 / 1 .	19 / 1 .	20 / 1 .	21 / 1 .
SiO2	49.68	51.97	54.58	47.48	50.50	49.60	48.80	49.75
TiO2	0.95	1.30	0.23	3.23	2.01	0.90	2.43	2.54
Al2O3	8.27	1.06	25.29	4.55	1.90	0.86	3.17	2.69
Cr2O3	0.14	0.38	0.00	0.66	0.53	0.21	0.62	0.64
Fe2O3	0.00	0.00	0.00	0.00	0.00	0.00	0.00	0.00
FeO	25.90	14.76	2.34	11.03	12.06	23.26	12.15	9.66
MnO	0.31	0.25	0.04	0.15	0.24	0.33	0.22	0.16
MgO	4.02	19.63	0.11	13.03	17.59	14.17	15.18	14.64
CaO	9.29	9.27	12.14	18.17	14.62	10.34	15.52	18.62
Na2O	0.67	0.03	2.09	0.11	0.07	0.02	0.10	0.14
K2O	0.13	0.00	1.48	0.00	0.00	0.00	0.00	0.00
P2O5	0.05	0.00	0.06	0.01	0.01	0.05	0.00	0.03
Total	99.42	98.64	98.38	98.42	99.53	99.74	98.17	98.86
Mg# (Mg/(Mg+Fe))	21.66	70.33	8.02	67.81	72.23	52.04	69.01	72.99
En	15.92	56.77	1.13	40.37	50.45	40.88	45.79	43.78
Fs	57.61	23.95	12.94	19.17	19.40	37.67	20.56	16.20
Wo	26.47	19.28	85.93	40.47	30.15	21.45	33.65	40.02

Table S5 cont.: Pyroxene major element contents.

Sample	10024	10024	10024	10024	10024	10024	10024	10024
Point	22 / 1 .	30 / 1 .	31 / 1 .	41 / 1 .	45 / 1 .	56 / 1 .	61 / 1 .	63 / 1 .
SiO2	48.41	47.82	48.25	49.06	46.74	48.79	48.75	49.63
TiO2	1.17	0.67	2.57	2.78	0.65	1.00	1.57	1.64
Al2O3	1.37	14.00	6.28	2.98	3.50	1.09	1.78	2.42
Cr2O3	0.28	0.08	0.65	0.82	0.10	0.23	0.38	0.43
Fe2O3	0.00	0.00	0.00	0.00	0.00	0.00	0.00	0.00
FeO	26.45	22.35	11.28	9.89	37.14	26.17	20.44	16.87
MnO	0.36	0.21	0.15	0.13	0.52	0.40	0.34	0.27
MgO	9.65	1.68	13.50	15.23	4.31	12.35	13.24	14.87
CaO	10.94	9.64	18.18	17.25	8.03	8.08	12.29	12.61
Na2O	0.03	1.36	0.10	0.10	0.00	0.04	0.02	0.05
K2O	0.00	1.17	0.00	0.00	0.02	0.01	0.00	0.01
P2O5	0.03	0.05	0.02	0.04	0.03	0.00	0.01	0.00
Total	98.70	99.03	100.98	98.27	101.03	98.16	98.82	98.81
Mg# (Mg/(Mg+Fe))	39.39	11.83	68.07	73.31	17.12	45.67	53.59	61.10
En	29.81	7.96	41.03	45.91	13.93	37.59	39.48	44.52
Fs	45.88	59.29	19.25	16.72	67.40	44.72	34.19	28.34
Wo	24.31	32.76	39.72	37.37	18.67	17.69	26.33	27.14

Table S5 cont.: Pyroxene major element contents.

Sample	10024	10024	10024	10024	10024	10024	10024	10024
Point	64 / 1 .	67 / 1 .	68 / 1 .	7 / 1 .	73 / 1 .	75 / 1 .	76 / 1 .	77 / 1 .
SiO2	48.97	48.79	49.67	48.72	50.94	48.53	48.80	47.80
TiO2	2.46	0.13	2.22	2.51	1.52	2.19	1.69	1.58
Al2O3	2.66	30.75	2.60	3.65	1.69	3.51	2.18	2.20
Cr2O3	0.60	0.00	0.57	0.62	0.40	0.58	0.40	0.38
Fe2O3	0.00	0.00	0.00	0.00	0.00	0.00	0.00	0.00
FeO	11.38	0.53	12.67	10.50	13.31	12.49	16.37	22.03
MnO	0.15	0.00	0.22	0.16	0.20	0.19	0.27	0.32
MgO	14.77	0.42	16.91	13.89	16.32	14.68	12.64	8.25
CaO	17.02	15.48	13.52	18.79	14.42	15.88	15.79	16.27
Na2O	0.08	2.23	0.07	0.12	0.07	0.07	0.06	0.03
K2O	0.03	0.22	0.00	0.01	0.00	0.00	0.00	0.01
P2O5	0.02	0.00	0.01	0.02	0.01	0.02	0.02	0.03
Total	98.14	98.55	98.46	98.97	98.89	98.13	98.24	98.91
Mg# (Mg/(Mg+Fe))	69.82	58.32	70.41	70.23	68.60	67.69	57.92	40.04
En	44.24	3.54	50.13	41.73	47.78	44.35	38.10	25.54
Fs	19.12	2.53	21.06	17.69	21.87	21.17	27.69	38.26
Wo	36.64	93.93	28.81	40.58	30.34	34.48	34.21	36.20

Table S5 cont.: Pyroxene major element contents.

Sample	10024	10024	10049	10049	10049	10049	10049	10049
Point	79 / 1 .	8 / 1 .	1 / 1 .	6 / 1 .	7 / 1 .	10 / 1 .	11 / 1 .	12 / 1 .
SiO2	49.33	48.18	50.50	47.84	47.86	48.96	51.28	47.84
TiO2	0.72	1.61	1.85	1.42	1.18	1.08	1.50	1.21
Al2O3	0.56	2.20	2.13	1.55	1.30	1.66	1.72	1.41
Cr2O3	0.18	0.39	0.50	0.19	0.16	0.16	0.44	0.19
Fe2O3	0.00	0.00	0.00	0.00	0.00	0.00	0.00	0.00
FeO	29.27	19.40	12.04	24.54	28.20	21.59	16.14	26.52
MnO	0.47	0.25	0.17	0.37	0.43	0.40	0.23	0.38
MgO	11.35	10.50	16.15	10.15	8.06	13.36	19.02	8.64
CaO	7.22	15.87	15.14	12.22	11.54	11.75	8.81	11.83
Na2O	0.00	0.04	0.09	0.04	0.02	0.00	0.04	0.02
K2O	0.00	0.01	0.00	0.00	0.00	0.00	0.00	0.00
P2O5	0.02	0.04	0.02	0.00	0.02	0.00	0.00	0.02
Total	99.13	98.50	98.59	98.32	98.77	98.96	99.17	98.08
Mg# (Mg/(Mg+Fe))	40.88	49.10	70.52	42.45	33.73	52.45	67.74	36.73
En	34.44	32.01	47.80	31.05	25.04	39.38	55.27	26.98
Fs	49.82	33.19	19.99	42.10	49.19	35.71	26.32	46.47
Wo	15.74	34.79	32.21	26.86	25.77	24.90	18.41	26.55

Table S5 cont.: Pyroxene major element contents.

Sample	10049	10049	10049	10049	10049	10049	10049	10049
Point	13 / 1 .	15 / 1 .	16 / 1 .	20 / 1 .	21 / 1 .	26 / 1 .	27 / 1 .	28 / 1 .
SiO2	49.66	49.44	49.50	49.02	51.86	48.58	52.80	48.61
TiO2	2.69	2.29	1.05	2.33	1.36	0.98	0.74	1.22
Al2O3	2.59	2.44	3.67	3.20	1.29	1.76	0.63	1.47
Cr2O3	0.61	0.61	0.16	0.58	0.52	0.20	0.40	0.26
Fe2O3	0.00	0.00	0.00	0.00	0.00	0.00	0.00	0.00
FeO	12.56	11.19	25.11	11.95	15.60	26.37	16.31	25.57
MnO	0.17	0.18	0.38	0.18	0.25	0.39	0.26	0.34
MgO	15.18	15.67	13.65	14.60	22.11	9.17	23.85	9.82
CaO	15.70	16.49	7.62	16.66	5.51	11.01	3.54	11.99
Na2O	0.06	0.09	0.07	0.06	0.03	0.05	0.00	0.01
K2O	0.00	0.00	0.02	0.01	0.01	0.01	0.00	0.00
P2O5	0.01	0.00	0.02	0.00	0.01	0.00	0.01	0.03
Total	99.23	98.39	101.23	98.59	98.55	98.52	98.55	99.31
Mg# (Mg/(Mg+Fe))	68.30	71.40	49.20	68.53	71.64	38.27	72.27	40.64
En	45.30	46.36	41.09	43.87	63.49	28.77	67.10	29.95
Fs	21.03	18.57	42.42	20.15	25.14	46.41	25.74	43.76
Wo	33.67	35.07	16.49	35.97	11.37	24.82	7.16	26.29

Table S5 cont.: Pyroxene major element contents.

Sample	10049	10049	10049	10049	10049	10049	10069	10069
Point	29 / 1 .	30 / 1 .	33 / 1 .	35 / 1 .	38 / 1 .	39 / 1 .	10 / 1 .	12 / 1 .
SiO2	51.62	53.00	48.23	50.18	50.52	46.81	51.08	49.47
TiO2	1.46	0.82	3.45	1.94	1.28	0.57	0.64	3.39
Al2O3	1.51	0.77	3.68	2.27	1.92	0.58	0.67	3.67
Cr2O3	0.58	0.41	0.80	0.51	0.31	0.10	0.18	0.94
Fe2O3	0.00	0.00	0.00	0.00	0.00	0.00	0.00	0.00
FeO	15.33	16.45	12.19	11.57	16.06	37.12	27.30	10.58
MnO	0.27	0.28	0.20	0.18	0.27	0.48	0.35	0.17
MgO	21.50	23.58	15.22	15.93	15.92	6.43	14.10	14.33
CaO	6.79	3.65	14.95	16.05	12.45	6.44	5.44	16.62
Na2O	0.04	0.00	0.09	0.09	0.02	0.00	0.01	0.11
K2O	0.00	0.00	0.00	0.00	0.00	0.01	0.01	0.00
P2O5	0.02	0.02	0.02	0.01	0.01	0.01	0.02	0.00
Total	99.11	99.00	98.82	98.74	98.76	98.54	99.80	99.29
Mg# (Mg/(Mg+Fe))	71.43	71.87	69.00	71.05	63.86	23.60	47.93	70.71
En	61.47	66.54	46.40	46.91	46.99	20.17	42.30	44.48
Fs	24.59	26.05	20.84	19.12	26.60	65.31	45.96	18.43
Wo	13.95	7.41	32.76	33.97	26.41	14.52	11.73	37.09

Table S5 cont.: Pyroxene major element contents.

Sample	10069	10069	10069	10069	10069	10069	10069	10069
Point	14 / 1 .	17 / 1 .	20 / 1 .	22 / 1 .	30 / 1 .	40 / 1 .	41 / 1 .	42 / 1 .
SiO2	50.13	49.85	49.87	49.32	49.83	50.67	50.50	50.90
TiO2	2.33	1.96	2.20	2.88	1.54	2.04	2.50	2.09
Al2O3	2.89	2.02	2.28	3.90	1.85	2.54	2.38	2.39
Cr2O3	0.54	0.50	0.69	0.82	0.35	0.54	0.49	0.53
Fe2O3	0.00	0.00	0.00	0.00	0.00	0.00	0.00	0.00
FeO	13.72	19.90	14.49	12.42	19.39	12.29	12.41	12.12
MnO	0.17	0.31	0.22	0.17	0.30	0.22	0.19	0.22
MgO	11.56	13.65	15.40	13.38	10.78	15.91	15.35	16.47
CaO	16.97	11.97	13.17	16.55	14.72	15.52	15.35	15.41
Na2O	0.09	0.07	0.09	0.10	0.04	0.06	0.11	0.10
K2O	0.00	0.01	0.00	0.00	0.01	0.01	0.00	0.00
P2O5	0.01	0.00	0.01	0.00	0.02	0.01	0.00	0.00
Total	98.40	100.24	98.41	99.54	98.83	99.80	99.29	100.23
Mg# (Mg/(Mg+Fe))	60.02	55.01	65.45	65.76	49.78	69.75	68.78	70.78
En	36.75	40.84	46.67	41.50	33.45	46.84	46.03	47.96
Fs	24.48	33.41	24.64	21.61	33.75	20.31	20.89	19.80
Wo	38.78	25.75	28.69	36.89	32.81	32.85	33.09	32.25

Table S5 cont.: Pyroxene major element contents.

Sample	10069	10069	10069	10069	10069	10069	10069	10069
Point	49 / 1 .	51 / 1 .	62 / 1 .	66 / 1 .	85 / 1 .	95 / 1 .	96 / 1 .	119 / 1 .
SiO2	49.71	52.11	50.18	50.03	53.56	96.42	55.81	50.38
TiO2	2.27	0.80	1.89	0.20	1.18	0.38	0.31	2.26
Al2O3	4.25	0.92	2.55	31.24	1.01	1.99	24.02	2.74
Cr2O3	0.55	0.25	0.47	0.00	0.48	0.01	0.02	0.56
Fe2O3	0.00	0.00	0.00	0.00	0.00	0.00	0.00	0.00
FeO	12.24	20.06	15.70	0.86	16.73	0.35	1.15	12.43
MnO	0.17	0.32	0.25	0.02	0.24	0.01	0.02	0.22
MgO	12.34	19.83	10.85	0.00	22.76	0.00	0.00	13.97
CaO	18.11	4.26	16.34	15.74	4.48	0.59	14.07	15.71
Na2O	0.12	0.03	0.08	2.08	0.02	0.27	1.99	0.08
K2O	0.00	0.00	0.01	0.24	0.00	0.03	0.29	0.02
P2O5	0.01	0.00	0.01	0.04	0.00	0.00	2.17	0.01
Total	99.77	98.58	98.32	100.46	100.46	100.05	99.87	98.37
Mg# (Mg/(Mg+Fe))	64.24	63.80	55.20	0.00	70.81	0.00	0.00	66.71
En	38.29	58.08	34.56	0.00	64.36	0.00	0.00	43.34
Fs	21.32	32.96	28.05	4.10	26.53	31.96	6.00	21.63
Wo	40.40	8.97	37.40	95.90	9.11	68.04	94.00	35.03

Table S5 cont.: Pyroxene major element contents.

Sample	10069	10071	10071	10071	10071	10071	10071	10071
Point	120 / 1 .	1 / 1 .	2 / 1 .	7 / 1 .	8 / 1 .	9 / 1 .	12 / 1 .	14 / 1 .
SiO2	46.88	49.04	44.95	49.77	48.77	49.54	48.44	48.84
TiO2	3.76	2.22	0.53	1.41	2.10	1.72	2.69	1.91
Al2O3	4.45	3.19	4.06	6.98	2.43	2.36	3.60	2.26
Cr2O3	0.88	0.42	0.01	0.21	0.19	0.12	0.63	0.28
Fe2O3	0.00	0.00	0.00	0.00	0.00	0.00	0.00	0.00
FeO	16.37	17.63	39.60	17.92	21.11	21.36	13.47	20.88
MnO	0.25	0.27	0.47	0.28	0.29	0.35	0.21	0.34
MgO	13.46	16.39	2.11	8.71	14.25	12.50	15.17	14.03
CaO	13.13	10.43	6.12	12.86	10.41	12.02	14.84	10.31
Na2O	0.10	0.04	0.11	0.47	0.02	0.06	0.12	0.05
K2O	0.04	0.00	0.07	0.34	0.01	0.02	0.01	0.02
P2O5	0.01	0.00	0.02	0.04	0.00	0.01	0.00	0.23
Total	99.32	99.63	98.04	99.00	99.59	100.05	99.18	99.15
Mg# (Mg/(Mg+Fe))	59.44	62.36	8.67	46.41	54.62	51.05	66.74	54.50
En	41.96	48.52	7.34	31.09	42.44	37.73	45.42	42.32
Fs	28.63	29.28	77.35	35.90	35.27	36.18	22.64	35.33
Wo	29.41	22.20	15.31	33.00	22.29	26.09	31.94	22.35

Table S5 cont.: Pyroxene major element contents.

Sample	10071	10071	10071	10071	10071	10071	10071	10071
Point	15 / 1 .	16 / 1 .	17 / 1 .	27 / 1 .	28 / 1 .	37 / 1 .	38 / 1 .	39 / 1 .
SiO2	47.51	48.20	48.37	48.47	48.39	48.54	49.10	59.35
TiO2	2.40	3.55	2.53	0.67	2.08	1.59	1.61	0.23
Al2O3	3.91	3.49	3.76	6.12	3.01	1.81	2.38	23.16
Cr2O3	0.48	0.80	0.60	0.04	0.23	0.11	0.12	0.00
Fe2O3	0.00	0.00	0.00	0.00	0.00	0.00	0.00	0.00
FeO	17.37	10.48	12.50	33.07	19.12	22.58	20.81	2.89
MnO	0.30	0.14	0.20	0.47	0.31	0.31	0.32	0.03
MgO	13.00	13.67	13.97	3.41	14.14	8.94	9.94	0.06
CaO	14.16	18.39	16.55	9.08	11.93	15.82	15.67	10.66
Na2O	0.09	0.16	0.11	0.56	0.08	0.04	0.07	1.59
K2O	0.00	0.00	0.00	0.07	0.01	0.02	0.01	2.52
P2O5	0.01	0.03	0.01	0.01	0.04	0.02	0.01	0.09
Total	99.25	98.92	98.59	101.97	99.32	99.78	100.04	100.59
Mg# (Mg/(Mg+Fe))	57.15	69.94	66.57	15.53	56.86	41.38	45.98	3.58
En	39.48	41.73	42.48	11.97	42.28	27.11	30.22	0.64
Fs	29.60	17.94	21.33	65.12	32.08	38.40	35.51	17.37
Wo	30.92	40.34	36.19	22.91	25.64	34.49	34.26	81.99

Table S5 cont.: Pyroxene major element contents.

Sample	10071	10071	10071	10071	10071	10071	10071	10071
Point	40 / 1 .	41 / 1 .	44 / 1 .	45 / 1 .	46 / 1 .	49 / 1 .	50 / 1 .	57 / 1 .
SiO2	48.66	49.19	47.68	48.18	49.04	44.94	46.73	49.31
TiO2	2.60	1.74	1.46	3.06	2.79	0.97	1.05	1.60
Al2O3	3.75	2.18	1.81	3.80	3.78	1.74	1.22	1.75
Cr2O3	0.63	0.30	0.17	0.69	0.70	0.04	0.07	0.27
Fe2O3	0.00	0.00	0.00	0.00	0.00	0.00	0.00	0.00
FeO	11.76	20.31	24.78	11.33	11.76	39.69	35.86	22.06
MnO	0.15	0.32	0.34	0.18	0.20	0.50	0.48	0.41
MgO	14.18	15.25	6.53	14.11	14.45	1.46	4.01	13.46
CaO	17.38	9.17	16.75	17.61	16.98	9.65	9.95	9.89
Na2O	0.10	0.03	0.04	0.10	0.12	0.00	0.00	0.04
K2O	0.00	0.01	0.00	0.00	0.00	0.01	0.00	0.06
P2O5	0.01	0.02	0.00	0.00	0.03	0.04	0.02	0.00
Total	99.23	98.53	99.56	99.06	99.85	99.04	99.40	98.84
Mg# (Mg/(Mg+Fe))	68.24	57.23	31.96	68.95	68.65	6.17	16.62	52.09
En	42.62	45.88	20.11	42.60	43.45	4.77	12.82	40.84
Fs	19.84	34.29	42.82	19.18	19.85	72.61	64.32	37.57
Wo	37.55	19.83	37.08	38.22	36.70	22.62	22.86	21.59

Table S5 cont.: Pyroxene major element contents.

Sample	10071	10071	10071	10071	10071	10071	10071	10071
Point	58 / 1 .	63 / 1 .	64 / 1 .	71 / 1 .	73 / 1 .	77 / 1 .	95 / 1 .	97 / 1 .
SiO2	49.36	48.34	51.33	47.82	50.34	46.38	47.49	48.40
TiO2	2.64	1.44	1.56	3.68	2.01	2.58	1.88	2.30
Al2O3	2.72	1.42	0.26	3.86	3.23	6.84	3.31	6.16
Cr2O3	0.69	0.20	0.45	0.75	0.54	0.57	0.48	0.51
Fe2O3	0.00	0.00	0.00	0.00	0.00	0.00	0.00	0.00
FeO	11.54	26.05	16.80	11.44	13.86	10.95	20.29	13.28
MnO	0.19	0.42	0.27	0.16	0.27	0.20	0.29	0.21
MgO	15.72	10.22	19.37	13.56	16.95	13.06	10.06	13.32
CaO	15.90	10.12	8.07	17.83	13.11	17.57	14.20	15.50
Na2O	0.08	0.00	0.03	0.09	0.08	0.12	0.17	0.15
K2O	0.01	0.17	0.02	0.01	0.01	0.02	0.04	0.03
P2O5	0.01	0.01	0.02	0.00	0.01	0.00	0.04	0.02
Total	98.85	98.39	98.17	99.20	100.41	98.29	98.24	99.89
Mg# (Mg/(Mg+Fe))	70.83	41.14	67.26	67.87	68.54	68.01	46.92	64.13
En	46.75	31.82	55.98	41.34	49.62	41.03	31.79	41.74
Fs	19.26	45.53	27.25	19.57	22.78	19.30	35.96	23.35
Wo	33.99	22.65	16.77	39.09	27.60	39.68	32.24	34.91

Table S5 cont.: Pyroxene major element contents.

Sample	10071	10071	10072	10072	10072	10072	10072	10072
Point	98 / 1 .	99 / 1 .	2 / 1 .	6 / 1 .	7 / 1 .	8 / 1 .	14 / 1 .	15 / 1 .
SiO2	46.27	48.62	48.49	46.55	49.09	48.86	49.02	49.30
TiO2	5.35	3.00	2.47	1.22	2.77	1.50	1.66	1.82
Al2O3	26.80	6.35	4.30	1.67	3.51	1.99	1.91	2.23
Cr2O3	0.06	0.62	0.59	0.20	0.68	0.30	0.29	0.37
Fe2O3	0.00	0.00	0.00	0.00	0.00	0.00	0.00	0.00
FeO	5.77	10.49	13.18	30.21	12.73	21.02	20.93	18.59
MnO	0.04	0.14	0.21	0.42	0.19	0.33	0.33	0.31
MgO	1.82	13.15	14.30	5.06	15.45	10.36	12.43	14.37
CaO	13.00	19.13	15.27	13.46	14.91	14.41	12.76	11.96
Na2O	2.27	0.12	0.11	0.04	0.09	0.06	0.06	0.06
K2O	0.44	0.00	0.00	0.02	0.00	0.01	0.00	0.00
P2O5	0.13	0.03	0.00	0.04	0.00	0.00	0.02	0.01
Total	101.95	101.67	98.92	98.89	99.43	98.84	99.40	99.03
Mg# (Mg/(Mg+Fe))	36.04	69.08	65.91	22.98	68.39	46.76	51.41	57.94
En	12.66	40.11	43.77	15.96	46.38	31.86	37.27	43.03
Fs	22.47	17.95	22.64	53.49	21.44	36.27	35.22	31.23
Wo	64.87	41.94	33.59	30.54	32.18	31.87	27.51	25.74

Table S5 cont.: Pyroxene major element contents.

Sample	10072	10072	10072	10072	10072	10072	10072	10072
Point	18 / 1 .	19 / 1 .	31 / 1 .	32 / 1 .	35 / 1 .	37 / 1 .	38 / 1 .	39 / 1 .
SiO2	48.62	47.81	50.00	48.41	48.59	48.73	49.34	48.74
TiO2	2.73	1.40	1.02	2.91	3.35	3.15	2.49	1.74
Al2O3	3.38	1.90	1.11	3.48	3.55	3.51	3.14	2.22
Cr2O3	0.67	0.26	0.22	0.75	0.88	0.87	0.50	0.40
Fe2O3	0.00	0.00	0.00	0.00	0.00	0.00	0.00	0.00
FeO	11.64	25.48	21.36	10.83	11.05	8.50	13.16	19.61
MnO	0.17	0.34	0.30	0.18	0.19	0.11	0.20	0.32
MgO	15.13	7.05	13.39	15.33	15.50	14.02	13.10	12.22
CaO	16.35	14.76	11.49	16.44	15.76	19.77	17.25	13.79
Na2O	0.11	0.06	0.12	0.15	0.16	0.18	0.15	0.12
K2O	0.00	0.01	0.00	0.01	0.00	0.01	0.01	0.01
P2O5	0.04	0.07	0.02	0.02	0.00	0.00	0.02	0.03
Total	98.84	99.16	99.04	98.51	99.05	98.86	99.34	99.18
Mg# (Mg/(Mg+Fe))	69.84	33.02	52.78	71.62	71.44	74.63	63.95	52.62
En	45.28	22.05	39.82	46.14	46.93	42.49	39.84	36.88
Fs	19.55	44.74	35.62	18.29	18.76	14.44	22.45	33.21
Wo	35.17	33.21	24.56	35.57	34.31	43.07	37.71	29.91

Table S5 cont.: Pyroxene major element contents.

Sample	10072	10072	10072	10072
Point	42 / 1 .	43 / 1 .	44 / 1 .	46 / 1 .
SiO2	71.93	49.71	49.24	48.36
TiO2	0.58	1.47	1.83	3.43
Al2O3	13.23	1.82	2.66	3.81
Cr2O3	0.02	0.33	0.44	1.01
Fe2O3	0.00	0.00	0.00	0.00
FeO	5.08	21.43	14.80	9.74
MnO	0.09	0.33	0.27	0.17
MgO	0.45	13.31	13.61	14.60
CaO	5.10	11.31	15.87	17.33
Na2O	0.94	0.15	0.16	0.18
K2O	1.93	0.00	0.00	0.01
P2O5	0.15	0.00	0.01	0.01
Total	99.50	99.86	98.90	98.64
Mg# (Mg/(Mg+Fe))	13.69	52.54	62.11	72.75
En	6.49	39.77	40.85	44.88
Fs	40.89	35.93	24.92	16.81
Wo	52.62	24.30	34.23	38.31

Table S6: Pyroxene trce element contents.

Sample	10017	10017	10017	10017	10022	10022	10022	10022
LAICPMS point	17.21.px.40um	17.22.px.40um	17.33.px.40um	17.55.px.40um	22.4.px.40um	22.12.px.40um	22.14.px.40um	22.33.px.35um
Ca43_ppm_mean	124079.166	132793.099	138899.611	136409.006	160182.950	128809.608	147545.553	171951.598
Ca43_ppm_2SE(int)	3232.578	4215.998	5640.368	5178.395	5491.134	3903.907	3088.199	12784.666
Sc45_ppm_mean	107.166	105.498	113.399	98.531	135.758	100.760	125.203	137.628
Sc45_ppm_2SE(int)	3.050	4.468	3.144	3.507	5.239	3.346	3.178	7.683
Ti47_ppm_mean	6404.181	8636.490	24902.899	8969.421	13329.095	12372.013	11334.460	17587.038
Ti47_ppm_2SE(int)	266.195	433.284	4154.023	331.667	493.576	431.374	263.918	1044.444
V51_ppm_mean	50.580	77.158	81.557	80.120	79.529	126.908	36.907	147.886
V51_ppm_2SE(int)	3.316	7.728	4.454	3.594	5.212	4.176	1.276	6.733
Cr52_ppm_mean	1899.216	2585.849	2678.651	2672.654	3117.260	4071.448	1883.690	5034.970
Cr52_ppm_2SE(int)	88.384	139.060	127.416	109.975	130.333	119.966	55.990	269.117
Mn55_ppm_mean	2545.218	2015.762	2574.111	2035.981	1790.549	1570.516	2476.694	1891.992
Mn55_ppm_2SE(int)	136.980	116.257	142.647	93.745	68.731	52.128	165.557	128.485
Co59_ppm_mean	19.172	17.916	24.194	19.118	17.337	20.807	19.491	21.885
Co59_ppm_2SE(int)	1.459	0.819	6.235	1.546	0.725	0.964	0.743	2.559
Ni60_ppm_mean	0.819	0.750	1.386	7.743	0.640	1.690	1.055	1.528
Ni60_ppm_2SE(int)	0.425	0.231	1.147	11.190	0.149	0.486	1.073	0.481
Cu63_ppm_mean	3.204	0.515	3.800	1.665	0.551	0.768	0.554	5.067
Cu63_ppm_2SE(int)	0.469	0.136	0.505	0.404	0.078	0.120	0.089	3.862
Zn66_ppm_mean	6.756	3.775	15.289	3.505	3.829	2.167	4.136	10.494
Zn66_ppm_2SE(int)	1.744	1.047	2.856	0.547	1.350	0.339	0.551	3.811
Rb85_ppm_mean	1.412	1.296	1.093	0.698	1.727	0.010	0.165	0.015
Rb85_ppm_2SE(int)	0.343	1.043	0.397	0.216	3.256	0.009	0.058	0.025
Sr88_ppm_mean	33.048	12.088	57.307	28.024	29.926	8.370	14.205	10.914
Sr88_ppm_2SE(int)	8.141	0.936	14.012	4.996	5.264	0.317	0.458	0.770
Y89_ppm_mean	508.916	70.762	159.816	63.348	115.041	38.171	149.081	62.716
Y89_ppm_2SE(int)	169.895	6.343	16.190	2.668	3.224	1.029	5.218	2.878
Zr90_ppm_mean	348.106	49.987	225.030	36.527	118.142	54.334	135.108	45.942
Zr90_ppm_2SE(int)	88.617	15.826	36.038	2.606	10.704	57.590	7.161	2.088
Nb93_ppm_mean	13.492	0.613	19.186	1.103	1.392	0.160	0.825	0.231
Nb93_ppm_2SE(int)	4.080	0.311	4.346	0.775	0.383	0.225	0.231	0.144
Ba137_ppm_mean	78.979	35.340	71.444	48.470	14.235	1.838	3.851	0.368
Ba137_ppm_2SE(int)	12.315	5.608	20.088	13.122	4.081	3.388	1.529	0.210
Hf178_ppm_mean	14.154	2.242	9.419	1.899	6.392	1.563	7.528	2.978
Hf178_ppm_2SE(int)	2.680	0.171	1.422	0.137	0.427	0.116	0.386	0.356
Ta181_ppm_mean	0.802	0.060	1.104	0.038	0.089	0.018	0.072	0.017
Ta181_ppm_2SE(int)	0.218	0.043	0.262	0.014	0.034	0.014	0.025	0.010
Pb208_ppm_mean	5.233	0.337	1.269	0.325	0.258	0.105	0.412	25.683
Pb208_ppm_2SE(int)	4.776	0.287	0.418	0.230	0.073	0.058	0.064	41.954
Th232_ppm_mean	8.650	0.117	2.021	0.131	0.425	0.023	0.210	0.020
Th232_ppm_2SE(int)	2.855	0.031	0.297	0.076	0.140	0.027	0.080	0.018
U238_ppm_mean	2.027	0.088	0.287	0.133	0.150	0.003	0.108	1.000
U238_ppm_2SE(int)	1.022	0.050	0.055	0.165	0.087	0.002	0.118	1.987

*Point names include phase (px) and spot size (i.e., 30 um).

Table S6 cont.: Pyroxene trce element contents.

Sample	10022	10022	10024	10024	10024	10024	10024	10024
LAICPMS point	22.39.px.25um	22.40.px.35um	24.1.px.45um	24.19.px.45um	24.20.px.45um	24.21.px.45um	24.22.px.45um	24.45.pyx.45um
Ca43_ppm_mean	111105.489	168119.519	177953.749	114100.734	140485.338	177831.427	138803.475	127500.662
Ca43_ppm_2SE(int)	6296.718	7761.062	3982.372	2384.246	2758.306	4055.666	3019.566	5521.829
Sc45_ppm_mean	89.332	151.138	125.560	98.661	103.013	130.129	126.667	98.637
Sc45_ppm_2SE(int)	6.491	9.620	3.899	2.808	2.342	3.428	3.656	4.923
Ti47_ppm_mean	6276.154	17465.583	15113.416	7330.463	11643.536	13582.982	8318.288	5207.780
Ti47_ppm_2SE(int)	366.513	1216.658	412.998	209.780	212.538	318.051	177.298	233.670
V51_ppm_mean	15.761	71.811	180.424	56.307	117.628	135.262	60.530	17.154
V51_ppm_2SE(int)	1.725	5.605	4.118	1.601	3.295	2.793	1.371	1.817
Cr52_ppm_mean	790.692	3196.925	5048.298	1973.154	3603.767	4033.193	2241.372	975.144
Cr52_ppm_2SE(int)	81.234	207.760	138.158	53.015	94.676	86.330	47.627	74.806
Mn55_ppm_mean	3155.159	2063.431	1468.451	2383.474	1765.339	1507.628	2504.138	3384.659
Mn55_ppm_2SE(int)	262.551	97.487	39.647	54.953	36.429	35.058	49.530	100.699
Co59_ppm_mean	19.451	18.650	17.551	21.480	18.456	16.057	20.792	22.120
Co59_ppm_2SE(int)	1.577	0.621	0.728	1.115	0.457	0.392	0.503	0.984
Ni60_ppm_mean	0.137	0.780	1.114	0.478	0.676	0.625	0.513	0.562
Ni60_ppm_2SE(int)	0.145	0.279	0.173	0.098	0.138	0.125	0.118	0.142
Cu63_ppm_mean	1.383	0.558	0.391	0.750	0.516	0.930	0.887	2.617
Cu63_ppm_2SE(int)	0.415	0.186	0.129	0.103	0.097	0.482	0.197	0.811
Zn66_ppm_mean	6.129	2.936	1.727	3.094	2.143	1.932	3.446	7.127
Zn66_ppm_2SE(int)	1.506	0.583	0.301	0.404	0.487	0.289	0.331	0.490
Rb85_ppm_mean	1.384	0.154	0.047	0.233	0.021	0.235	0.568	8.351
Rb85_ppm_2SE(int)	0.355	0.115	0.058	0.273	0.011	0.062	0.144	3.305
Sr88_ppm_mean	52.626	14.759	14.577	18.828	7.946	18.443	19.764	116.579
Sr88_ppm_2SE(int)	17.237	1.522	0.862	2.370	0.311	1.065	2.168	29.789
Y89_ppm_mean	220.103	120.988	53.487	77.038	48.685	72.850	176.232	1909.666
Y89_ppm_2SE(int)	32.595	6.122	1.618	1.949	1.463	2.130	13.521	471.824
Zr90_ppm_mean	196.295	124.245	33.813	42.713	27.633	56.193	154.848	1113.576
Zr90_ppm_2SE(int)	30.933	6.041	1.109	1.173	1.179	1.835	35.406	380.090
Nb93_ppm_mean	2.358	0.815	0.058	0.355	0.072	0.284	3.249	26.719
Nb93_ppm_2SE(int)	0.619	0.551	0.023	0.153	0.021	0.049	1.516	7.676
Ba137_ppm_mean	70.979	7.795	0.372	5.624	0.473	30.630	56.694	380.571
Ba137_ppm_2SE(int)	18.687	5.025	0.178	0.997	0.475	8.508	15.122	120.264
Hf178_ppm_mean	9.171	7.001	2.353	2.606	1.773	3.639	7.365	43.346
Hf178_ppm_2SE(int)	1.904	0.376	0.131	0.126	0.108	0.181	1.184	13.166
Ta181_ppm_mean	0.124	0.051	0.010	0.016	0.022	0.020	0.164	1.731
Ta181_ppm_2SE(int)	0.043	0.018	0.004	0.005	0.028	0.004	0.077	0.548
Pb208_ppm_mean	0.467	0.080	0.163	0.287	0.039	0.088	0.560	8.778
Pb208_ppm_2SE(int)	0.164	0.029	0.227	0.090	0.014	0.059	0.196	2.357
Th232_ppm_mean	0.596	0.126	0.008	0.193	0.008	0.056	0.896	22.924
Th232_ppm_2SE(int)	0.185	0.033	0.005	0.099	0.003	0.010	0.449	5.913
U238_ppm_mean	0.202	0.031	0.022	0.074	0.063	0.226	0.231	3.465
U238_ppm_2SE(int)	0.079	0.016	0.038	0.065	0.076	0.399	0.098	0.949

*Point names include phase (px) and spot size (i.e., 30 um).

Table S6 cont.: Pyroxene trce element contents.

Sample	10024	10024	10024	10024	10024	10024	10049	10049
LAICPMS point	24.56.px.45um	24.68.px.45um	24.73.px.45um	24.74.px.45um	24.76.px.45um	24.77.px.45um	49.1.px.30um	49.11.px.30um
Ca43_ppm_mean	114577.290	133603.311	127647.800	96085.564	136939.949	124195.013	106128.313	144444.991
Ca43_ppm_2SE(int)	2841.271	8076.268	3478.557	2033.191	4267.405	6470.157	4264.426	3717.819
Sc45_ppm_mean	92.005	101.654	127.742	75.578	100.615	107.048	80.375	111.774
Sc45_ppm_2SE(int)	2.336	4.103	2.767	2.363	2.076	5.174	3.346	3.525
Ti47_ppm_mean	6152.611	12334.512	7810.330	8099.899	10772.777	8105.733	6117.072	15266.917
Ti47_ppm_2SE(int)	114.288	554.987	197.490	187.470	188.979	322.012	299.584	1646.684
V51_ppm_mean	28.653	130.821	50.299	77.457	108.338	69.629	33.446	65.661
V51_ppm_2SE(int)	1.032	5.847	1.589	1.971	3.697	2.959	3.000	4.040
Cr52_ppm_mean	1370.038	3806.619	2106.893	2430.389	3279.795	2288.122	1434.384	2647.044
Cr52_ppm_2SE(int)	43.213	124.715	42.949	48.619	103.122	93.390	102.290	128.781
Mn55_ppm_mean	2898.532	1681.072	2978.031	1272.773	1795.737	2277.191	2487.327	2300.736
Mn55_ppm_2SE(int)	86.924	42.824	65.850	29.358	41.733	74.674	108.704	72.572
Co59_ppm_mean	21.247	19.849	22.910	13.626	18.507	19.890	20.743	20.568
Co59_ppm_2SE(int)	0.556	0.742	0.563	0.547	0.581	0.794	0.839	0.769
Ni60_ppm_mean	0.521	0.931	1.005	0.527	0.723	0.703	0.653	0.604
Ni60_ppm_2SE(int)	0.179	0.166	0.185	0.117	0.165	0.142	0.183	0.183
Cu63_ppm_mean	2.856	1.146	4.052	0.792	1.064	0.387	0.459	0.915
Cu63_ppm_2SE(int)	0.390	0.418	0.593	0.094	0.178	0.084	0.120	0.222
Zn66_ppm_mean	4.715	2.072	4.650	1.459	2.054	2.982	3.978	3.923
Zn66_ppm_2SE(int)	0.424	0.266	0.373	0.198	0.203	0.414	0.634	0.558
Rb85_ppm_mean	3.698	0.008	0.522	0.168	0.605	0.022	1.340	0.218
Rb85_ppm_2SE(int)	0.971	0.007	0.079	0.066	0.103	0.011	0.857	0.063
Sr88_ppm_mean	40.371	8.073	47.403	6.557	13.031	9.932	55.202	24.210
Sr88_ppm_2SE(int)	7.249	0.705	4.764	0.228	1.125	0.830	13.526	5.153
Y89_ppm_mean	273.426	43.692	254.569	41.039	55.659	92.751	73.071	102.670
Y89_ppm_2SE(int)	36.903	2.244	7.511	1.138	1.820	6.440	4.131	5.828
Zr90_ppm_mean	257.719	26.376	504.327	27.283	42.551	49.618	48.131	91.130
Zr90_ppm_2SE(int)	43.992	1.553	87.684	0.884	2.554	3.944	6.152	7.057
Nb93_ppm_mean	5.919	0.049	8.615	0.224	0.694	0.090	0.465	3.159
Nb93_ppm_2SE(int)	1.755	0.013	1.455	0.065	0.124	0.016	0.163	0.904
Ba137_ppm_mean	96.027	0.022	86.064	3.392	10.395	0.337	46.564	21.834
Ba137_ppm_2SE(int)	27.127	0.020	25.291	1.261	1.852	0.124	20.054	7.504
Hf178_ppm_mean	10.697	1.720	21.715	1.696	2.351	2.982	2.591	4.129
Hf178_ppm_2SE(int)	1.317	0.170	2.324	0.083	0.145	0.251	0.280	0.206
Ta181_ppm_mean	0.414	0.006	0.452	0.015	0.046	0.011	0.044	0.161
Ta181_ppm_2SE(int)	0.118	0.003	0.068	0.005	0.012	0.005	0.018	0.047
Pb208_ppm_mean	1.532	0.056	0.905	0.084	0.108	0.042	0.394	0.169
Pb208_ppm_2SE(int)	0.226	0.013	0.164	0.015	0.026	0.033	0.499	0.038
Th232_ppm_mean	3.452	0.005	1.658	0.034	0.122	0.015	0.145	0.225
Th232_ppm_2SE(int)	0.641	0.003	0.483	0.012	0.021	0.006	0.050	0.035
U238_ppm_mean	0.601	0.008	0.718	0.076	0.052	0.038	0.051	0.100
U238_ppm_2SE(int)	0.137	0.007	0.211	0.113	0.019	0.048	0.017	0.016

*Point names include phase (px) and spot size (i.e., 30 um).

Table S6 cont.: Pyroxene trce element contents.

Sample	10049	10049	10049	10049	10049	10049	10049	10049
LAICPMS point	49.15.px.30um	49.20.px.30um	49.21.px.30um	49.26.px.30um	49.27.px.30um	49.28.px.30um	49.30.px.30um	49.35.px.30um
Ca43_ppm_mean	123490.840	143697.353	70495.573	124742.638	35379.091	117816.982	42597.190	133457.535
Ca43_ppm_2SE(int)	8101.758	4523.006	5327.484	4168.253	1887.461	4203.961	1634.850	3967.187
Sc45_ppm_mean	88.548	104.336	65.164	88.648	33.569	86.059	40.513	92.226
Sc45_ppm_2SE(int)	6.740	2.982	3.079	4.541	1.617	3.515	1.608	2.891
Ti47_ppm_mean	51149.479	19762.993	8800.980	8569.351	4080.709	7683.730	4877.414	18163.675
Ti47_ppm_2SE(int)	9383.446	2115.404	527.355	351.864	252.434	382.909	204.210	904.396
V51_ppm_mean	59.539	79.376	84.174	55.449	46.541	47.397	57.423	54.081
V51_ppm_2SE(int)	8.597	3.671	7.319	3.473	2.615	2.054	2.679	2.172
Cr52_ppm_mean	2378.801	3064.381	3253.301	2224.868	2391.072	1930.867	2620.742	2181.888
Cr52_ppm_2SE(int)	338.669	137.589	115.163	130.261	129.453	87.566	106.441	66.857
Mn55_ppm_mean	2457.544	1936.774	2093.007	2004.995	1964.888	2004.015	2062.161	2213.214
Mn55_ppm_2SE(int)	96.160	83.850	54.319	98.073	99.253	82.442	57.273	116.533
Co59_ppm_mean	21.559	20.270	29.962	19.690	30.481	18.201	30.544	19.585
Co59_ppm_2SE(int)	1.588	0.699	1.077	1.555	1.768	1.116	1.065	1.156
Ni60_ppm_mean	2.528	1.290	4.059	1.302	3.895	1.455	3.830	0.661
Ni60_ppm_2SE(int)	2.334	0.301	0.929	0.356	0.545	0.553	0.444	0.188
Cu63_ppm_mean	2.577	1.060	1.471	0.641	0.578	1.429	1.275	1.062
Cu63_ppm_2SE(int)	0.373	0.519	0.643	0.278	0.133	0.347	1.266	0.158
Zn66_ppm_mean	6.583	3.785	4.078	2.214	3.696	3.589	3.763	4.811
Zn66_ppm_2SE(int)	0.945	0.452	0.601	0.373	0.641	0.573	1.063	0.845
Rb85_ppm_mean	7.445	3.938	0.660	0.357	0.054	6.642	0.605	5.879
Rb85_ppm_2SE(int)	2.222	0.734	0.185	0.104	0.024	1.493	0.374	0.771
Sr88_ppm_mean	155.007	20.883	8.539	56.249	1.057	85.877	5.651	104.546
Sr88_ppm_2SE(int)	25.489	2.128	1.383	17.823	0.502	3.327	1.677	6.293
Y89_ppm_mean	125.012	164.476	36.082	74.117	7.320	101.605	13.302	106.271
Y89_ppm_2SE(int)	10.518	8.770	2.206	3.139	0.675	9.274	1.325	15.795
Zr90_ppm_mean	342.266	149.113	40.597	51.869	2.737	91.857	15.131	167.945
Zr90_ppm_2SE(int)	36.105	25.191	3.930	2.779	0.595	13.621	7.580	11.593
Nb93_ppm_mean	26.751	5.318	0.785	0.810	0.078	2.725	0.552	7.538
Nb93_ppm_2SE(int)	4.490	1.199	0.127	0.265	0.032	0.722	0.199	0.555
Ba137_ppm_mean	297.392	134.788	21.277	32.396	2.077	211.695	30.470	213.870
Ba137_ppm_2SE(int)	78.590	29.247	4.166	7.705	1.033	51.501	7.116	21.599
Hf178_ppm_mean	11.607	5.818	1.647	2.585	0.150	3.916	1.046	6.027
Hf178_ppm_2SE(int)	1.114	0.881	0.193	0.200	0.034	0.458	1.092	0.543
Ta181_ppm_mean	1.583	0.395	0.073	0.053	0.159	0.238	0.065	0.396
Ta181_ppm_2SE(int)	0.274	0.098	0.047	0.018	0.289	0.162	0.076	0.046
Pb208_ppm_mean	1.522	1.315	0.188	0.128	0.144	0.809	0.126	0.904
Pb208_ppm_2SE(int)	1.466	0.283	0.034	0.046	0.175	0.200	0.037	0.623
Th232_ppm_mean	1.853	2.320	0.293	0.184	0.010	0.732	0.197	1.127
Th232_ppm_2SE(int)	0.421	0.210	0.062	0.047	0.007	0.179	0.181	0.279
U238_ppm_mean	0.635	0.406	0.085	1.454	0.011	0.284	0.997	0.535
U238_ppm_2SE(int)	0.131	0.049	0.018	2.790	0.014	0.055	1.912	0.338

*Point names include phase (px) and spot size (i.e., 30 um).

Table S6 cont.: Pyroxene trce element contents.

Sample	10049	10049	10049	10069	10069	10069	10069	10069
LAICPMS point	49.38.px.30um	49.39.px.30um	49.7.px.30um	69.10.px.30um	69.12.px.30um	69.20.px.30um	69.22.px.30um	69.51.px.25um
Ca43_ppm_mean	121884.177	70214.600	85681.732	106903.521	143387.871	128688.243	134422.691	56703.402
Ca43_ppm_2SE(int)	5842.258	5047.076	2685.178	3573.832	4499.387	4727.370	6054.800	3113.641
Sc45_ppm_mean	93.823	65.515	86.589	91.983	105.390	103.194	97.594	61.444
Sc45_ppm_2SE(int)	5.006	5.159	2.762	4.189	3.964	3.648	3.766	3.743
Ti47_ppm_mean	7535.842	3541.137	5822.231	6344.425	12118.880	30231.992	13423.068	5658.769
Ti47_ppm_2SE(int)	582.789	195.094	184.986	210.479	772.680	7746.176	1635.573	245.570
V51_ppm_mean	45.522	10.855	27.674	49.881	112.207	97.720	83.463	43.991
V51_ppm_2SE(int)	4.171	1.083	1.290	2.253	9.208	5.232	5.567	2.294
Cr52_ppm_mean	1959.674	594.514	1213.642	2004.799	3676.599	3217.076	2740.442	1945.111
Cr52_ppm_2SE(int)	146.272	55.711	48.759	78.060	289.057	118.115	170.720	99.467
Mn55_ppm_mean	2423.380	2655.394	2866.875	2717.057	1828.413	2228.615	2063.847	2777.994
Mn55_ppm_2SE(int)	111.592	245.159	95.409	116.197	112.701	133.930	84.403	104.705
Co59_ppm_mean	21.115	16.383	22.127	21.451	19.677	20.912	16.879	26.568
Co59_ppm_2SE(int)	1.291	1.485	0.679	1.216	1.107	1.107	0.662	1.327
Ni60_ppm_mean	0.593	0.284	0.534	0.498	1.417	2.382	1.113	0.642
Ni60_ppm_2SE(int)	0.201	0.136	0.124	0.239	0.418	2.837	0.718	0.374
Cu63_ppm_mean	0.952	0.682	0.228	0.306	1.404	1.393	0.658	0.491
Cu63_ppm_2SE(int)	0.201	0.129	0.075	0.163	0.508	0.636	0.141	0.251
Zn66_ppm_mean	4.542	5.180	4.872	4.636	2.501	4.510	4.137	3.661
Zn66_ppm_2SE(int)	1.164	0.547	0.538	2.485	0.576	0.883	0.860	1.178
Rb85_ppm_mean	2.610	27.794	0.677	0.782	0.243	4.183	6.845	0.112
Rb85_ppm_2SE(int)	0.632	6.266	0.451	1.371	0.161	7.502	1.806	0.076
Sr88_ppm_mean	16.498	83.781	17.417	16.566	12.966	15.420	44.544	25.380
Sr88_ppm_2SE(int)	2.489	10.027	1.767	1.895	1.913	6.708	8.849	6.055
Y89_ppm_mean	118.734	217.863	98.443	98.009	142.264	99.252	277.806	39.060
Y89_ppm_2SE(int)	7.667	10.635	4.585	3.678	57.456	10.296	110.674	2.895
Zr90_ppm_mean	146.950	621.038	184.473	51.835	46.380	121.261	159.030	23.143
Zr90_ppm_2SE(int)	18.086	104.682	237.412	3.141	7.400	31.701	29.027	4.412
Nb93_ppm_mean	3.914	20.069	2.303	0.138	0.203	8.316	3.911	0.334
Nb93_ppm_2SE(int)	0.722	4.105	1.472	0.053	0.077	3.215	1.373	0.138
Ba137_ppm_mean	51.468	452.797	24.685	5.721	6.293	16.756	246.009	17.306
Ba137_ppm_2SE(int)	9.419	68.522	4.506	1.637	4.704	4.990	60.754	3.240
Hf178_ppm_mean	6.875	23.710	3.404	2.675	2.862	4.377	6.703	1.112
Hf178_ppm_2SE(int)	0.780	3.695	0.275	0.246	0.402	0.870	1.044	0.259
Ta181_ppm_mean	0.235	1.197	0.071	0.016	0.061	0.502	0.363	0.012
Ta181_ppm_2SE(int)	0.052	0.254	0.021	0.009	0.063	0.199	0.111	0.016
Pb208_ppm_mean	0.654	2.887	0.317	1.514	60.040	30.054	12.433	10.638
Pb208_ppm_2SE(int)	0.138	0.571	0.057	0.656	7.935	4.759	2.029	0.893
Th232_ppm_mean	1.424	7.286	0.550	0.116	1.694	0.342	3.645	0.127
Th232_ppm_2SE(int)	0.233	1.502	0.115	0.031	1.136	0.091	1.700	0.051
U238_ppm_mean	0.542	2.542	0.097	0.055	0.315	0.644	0.835	0.038
U238_ppm_2SE(int)	0.220	0.631	0.030	0.034	0.330	1.059	0.321	0.015

*Point names include phase (px) and spot size (i.e., 30 um).

Table S6 cont.: Pyroxene trce element contents.

Sample	10069	10071	10071	10071	10071	10071	10071	10071
LAICPMS point	69.120.px.30um	71.1.px.35um	71.2.px.35um	71.7.px.35um	71.12.px.45um	71.14.px.45um	71.28.px.35um	71.37.px.35um
Ca43_ppm_mean	132785.691	169004.502	99802.482	167220.386	152682.454	166262.599	132309.188	132558.536
Ca43_ppm_2SE(int)	4759.896	7350.568	6771.641	4043.158	4772.630	2836.579	4164.926	6006.323
Sc45_ppm_mean	121.353	144.479	53.340	148.574	135.541	125.119	108.344	100.510
Sc45_ppm_2SE(int)	5.864	6.332	1.868	3.839	3.534	3.649	2.885	6.243
Ti47_ppm_mean	50532.465	20866.070	7352.220	19705.867	16516.090	14239.736	6579.098	7468.794
Ti47_ppm_2SE(int)	14973.039	954.770	805.896	456.551	544.355	646.209	218.564	449.038
V51_ppm_mean	112.610	77.705	3.846	71.269	129.543	87.890	11.490	18.685
V51_ppm_2SE(int)	5.861	3.589	0.359	2.913	3.873	3.773	1.127	1.840
Cr52_ppm_mean	3956.739	3437.272	211.282	3340.662	4362.355	3176.925	485.779	659.204
Cr52_ppm_2SE(int)	189.822	139.608	8.496	118.900	109.374	140.630	36.230	49.267
Mn55_ppm_mean	2359.782	1856.051	3285.552	2046.913	1799.464	1884.260	3187.180	2319.286
Mn55_ppm_2SE(int)	180.867	69.049	144.460	50.773	45.922	72.515	122.554	164.477
Co59_ppm_mean	20.952	19.814	18.762	18.754	18.529	18.794	20.016	16.227
Co59_ppm_2SE(int)	1.246	0.951	0.816	0.871	0.736	0.726	0.779	1.740
Ni60_ppm_mean	1.238	1.322	0.505	4.297	0.986	0.675	0.653	0.375
Ni60_ppm_2SE(int)	1.465	0.310	0.174	6.915	0.245	0.171	0.901	0.232
Cu63_ppm_mean	1.401	7.050	1.531	1.772	0.767	0.796	0.385	8.968
Cu63_ppm_2SE(int)	0.606	8.857	0.281	0.607	0.420	0.161	0.134	16.275
Zn66_ppm_mean	7.224	4.916	8.823	5.656	2.280	2.831	5.526	4.025
Zn66_ppm_2SE(int)	1.892	2.553	1.000	3.165	0.448	0.526	0.516	0.876
Rb85_ppm_mean	2.437	1.183	3.420	1.189	0.156	0.569	0.328	0.144
Rb85_ppm_2SE(int)	0.713	2.096	0.354	2.093	0.041	0.162	0.274	0.070
Sr88_ppm_mean	22.451	14.870	179.315	16.772	14.332	17.955	23.493	78.727
Sr88_ppm_2SE(int)	4.148	0.770	23.150	1.256	0.827	0.793	2.707	19.351
Y89_ppm_mean	329.776	127.084	943.601	132.132	81.047	114.283	278.613	106.766
Y89_ppm_2SE(int)	120.360	6.173	137.811	3.579	1.856	5.164	34.107	4.570
Zr90_ppm_mean	456.862	153.156	670.517	148.017	73.794	112.559	234.519	84.478
Zr90_ppm_2SE(int)	133.655	5.931	100.724	4.208	2.310	7.105	17.973	5.372
Nb93_ppm_mean	23.756	3.720	34.613	2.152	0.752	2.137	0.726	0.579
Nb93_ppm_2SE(int)	8.896	5.201	8.140	0.947	0.187	0.538	0.163	0.290
Ba137_ppm_mean	134.260	3.192	261.098	5.060	13.965	27.110	10.304	26.055
Ba137_ppm_2SE(int)	24.534	1.718	30.711	0.759	3.894	10.010	4.048	7.263
Hf178_ppm_mean	16.265	9.355	27.395	8.640	4.520	6.010	12.607	4.685
Hf178_ppm_2SE(int)	4.222	0.571	3.874	0.414	0.204	0.267	1.140	0.339
Ta181_ppm_mean	1.488	0.135	1.779	0.227	0.055	0.136	0.051	0.046
Ta181_ppm_2SE(int)	0.515	0.038	0.443	0.201	0.014	0.034	0.014	0.029
Pb208_ppm_mean	3.870	0.492	15.209	1.523	0.141	0.444	0.392	3.458
Pb208_ppm_2SE(int)	1.251	0.166	1.514	0.287	0.022	0.275	0.130	1.944
Th232_ppm_mean	4.519	0.140	14.618	0.136	0.136	0.278	0.458	0.143
Th232_ppm_2SE(int)	1.714	0.036	3.297	0.069	0.025	0.095	0.193	0.081
U238_ppm_mean	0.771	0.587	3.685	0.026	0.035	0.105	0.072	0.992
U238_ppm_2SE(int)	0.222	1.098	0.878	0.007	0.010	0.035	0.020	1.119

*Point names include phase (px) and spot size (i.e., 30 um).

Table S6 cont.: Pyroxene trce element contents.

Sample	10071	10071	10071	10071	10071	10071	10071	10071
LAICPMS point	71.38.px.35um	71.40.px.35um	71.41.px.35um	71.49.px.35um	71.50.px.35um	71.57.35um	71.58.px.35um	71.63.px.40um
Ca43_ppm_mean	123328.781	170925.486	107844.239	86241.184	108499.884	132642.250	177266.602	120339.748
Ca43_ppm_2SE(int)	4683.396	5114.972	5591.774	3147.629	2914.988	5645.602	4707.514	2628.646
Sc45_ppm_mean	61.712	136.954	65.242	77.461	90.037	99.429	144.745	95.185
Sc45_ppm_2SE(int)	3.726	4.534	5.706	4.145	5.569	3.465	4.629	1.969
Ti47_ppm_mean	3803.096	18038.572	5795.734	4621.648	5486.790	10589.058	21068.483	9006.625
Ti47_ppm_2SE(int)	243.009	575.564	435.003	212.646	309.043	385.766	655.131	181.763
V51_ppm_mean	6.020	140.501	27.494	7.999	11.639	62.545	165.579	49.690
V51_ppm_2SE(int)	0.618	5.284	2.368	0.520	1.179	2.447	4.246	1.345
Cr52_ppm_mean	259.165	5096.553	1177.610	331.347	447.319	2479.577	5816.419	1888.522
Cr52_ppm_2SE(int)	20.605	146.202	111.029	16.046	37.525	86.101	160.088	41.210
Mn55_ppm_mean	1999.230	1553.908	1845.800	3733.202	2805.709	2100.099	1572.561	2297.414
Mn55_ppm_2SE(int)	70.409	44.631	147.330	113.286	161.012	81.317	44.482	69.526
Co59_ppm_mean	11.121	17.517	15.504	17.634	17.775	22.852	18.473	19.873
Co59_ppm_2SE(int)	0.679	0.672	1.296	0.537	3.464	2.261	0.808	0.524
Ni60_ppm_mean	0.259	1.167	0.258	0.105	0.252	0.974	1.280	0.444
Ni60_ppm_2SE(int)	0.143	0.513	0.136	0.096	0.150	0.222	0.255	0.132
Cu63_ppm_mean	0.923	0.897	0.674	0.422	0.888	0.468	0.822	0.413
Cu63_ppm_2SE(int)	0.350	0.176	0.174	0.121	0.394	0.131	0.123	0.063
Zn66_ppm_mean	5.204	2.907	4.241	8.045	4.918	2.867	2.619	3.119
Zn66_ppm_2SE(int)	2.648	0.604	1.152	0.827	0.501	0.528	0.408	0.357
Rb85_ppm_mean	0.624	0.030	5.598	0.423	1.142	0.716	0.023	4.109
Rb85_ppm_2SE(int)	0.245	0.019	0.926	0.062	0.334	0.390	0.015	0.275
Sr88_ppm_mean	259.997	11.638	183.490	26.977	98.829	20.003	12.546	42.655
Sr88_ppm_2SE(int)	11.535	0.523	28.354	3.434	23.805	2.096	0.459	1.379
Y89_ppm_mean	107.536	71.826	84.233	448.191	167.593	105.273	70.190	129.864
Y89_ppm_2SE(int)	9.266	2.276	7.471	44.848	8.392	6.805	2.084	2.912
Zr90_ppm_mean	69.850	65.206	82.182	485.772	155.753	92.520	67.394	170.718
Zr90_ppm_2SE(int)	3.769	2.109	12.051	64.441	34.168	8.847	1.913	20.021
Nb93_ppm_mean	0.381	0.138	1.408	23.858	4.540	1.065	0.156	3.088
Nb93_ppm_2SE(int)	0.070	0.032	0.310	6.234	2.844	0.245	0.033	0.463
Ba137_ppm_mean	124.314	0.434	177.460	140.728	72.827	17.422	0.029	87.788
Ba137_ppm_2SE(int)	12.583	0.843	17.359	29.969	23.049	2.961	0.028	7.760
Hf178_ppm_mean	3.742	4.176	3.563	20.422	7.113	5.076	4.121	7.166
Hf178_ppm_2SE(int)	0.261	0.218	0.512	2.420	0.894	0.382	0.266	0.520
Ta181_ppm_mean	0.026	0.027	0.076	0.890	0.156	0.113	0.054	0.249
Ta181_ppm_2SE(int)	0.008	0.009	0.023	0.254	0.090	0.075	0.053	0.050
Pb208_ppm_mean	0.590	0.302	1.758	3.008	1.219	0.851	2.330	0.640
Pb208_ppm_2SE(int)	0.246	0.186	0.718	0.797	0.480	1.211	4.011	0.063
Th232_ppm_mean	0.398	0.186	0.501	7.366	0.816	0.356	0.028	0.841
Th232_ppm_2SE(int)	0.212	0.322	0.123	2.011	0.470	0.163	0.008	0.127
U238_ppm_mean	0.069	0.308	0.092	1.279	0.220	0.075	0.198	0.476
U238_ppm_2SE(int)	0.029	0.597	0.032	0.446	0.151	0.023	0.344	0.288

*Point names include phase (px) and spot size (i.e., 30 um).

Table S6 cont.: Pyroxene trce element contents.

Sample	10071	10071	10071	10071	10072	10072	10072	10072
LAICPMS point	71.64.px.40um	71.95.px.40um	71.97.px.40um	71.99.px.45um	72.2.px.45um	72.7.px.45um	72.8.px.45um	72.18.px.45um
Ca43_ppm_mean	164243.922	160779.231	119982.673	157629.586	155259.447	156101.541	137506.596	94484.956
Ca43_ppm_2SE(int)	4499.546	4415.790	5832.725	7755.835	3261.255	3020.602	2585.569	2793.329
Sc45_ppm_mean	146.885	134.823	97.352	120.431	112.333	137.027	124.432	87.050
Sc45_ppm_2SE(int)	4.763	4.006	4.075	7.762	2.913	2.991	3.141	2.645
Ti47_ppm_mean	19628.183	18462.416	10410.775	12092.372	13827.748	14761.468	13783.840	9379.533
Ti47_ppm_2SE(int)	535.253	666.454	411.432	510.753	265.595	368.769	371.121	247.396
V51_ppm_mean	151.371	136.284	82.344	80.950	146.870	136.982	113.625	94.713
V51_ppm_2SE(int)	3.952	4.650	7.328	4.858	4.229	3.049	4.167	2.561
Cr52_ppm_mean	4810.626	4764.469	2811.399	2800.103	4181.944	3960.738	3596.370	2661.184
Cr52_ppm_2SE(int)	139.674	162.470	150.672	156.817	124.825	91.547	119.810	66.938
Mn55_ppm_mean	1855.008	1623.998	2248.920	2234.615	1587.527	1654.790	1980.958	1941.340
Mn55_ppm_2SE(int)	50.971	52.828	78.424	136.792	38.382	32.939	64.696	49.349
Co59_ppm_mean	20.331	16.981	20.368	18.488	17.239	16.983	18.193	20.889
Co59_ppm_2SE(int)	0.723	0.632	0.649	1.400	0.525	0.492	0.506	0.672
Ni60_ppm_mean	1.110	0.912	0.801	1.904	0.919	0.865	0.662	0.768
Ni60_ppm_2SE(int)	0.225	0.175	0.223	1.799	0.164	0.200	0.147	0.268
Cu63_ppm_mean	0.494	1.428	1.153	1.321	0.488	0.855	0.954	1.364
Cu63_ppm_2SE(int)	0.083	0.724	0.221	0.283	0.076	0.641	0.126	0.398
Zn66_ppm_mean	2.752	2.773	3.072	4.292	1.787	2.158	2.321	2.674
Zn66_ppm_2SE(int)	0.358	1.059	0.374	0.478	0.269	0.300	0.335	0.492
Rb85_ppm_mean	0.358	0.031	0.566	0.049	0.106	0.052	0.023	0.210
Rb85_ppm_2SE(int)	0.597	0.028	0.333	0.031	0.181	0.041	0.010	0.072
Sr88_ppm_mean	12.729	11.278	10.348	14.366	10.119	18.604	11.010	9.742
Sr88_ppm_2SE(int)	0.853	0.396	0.810	0.939	0.328	1.632	0.813	1.000
Y89_ppm_mean	74.041	74.000	88.822	106.067	55.015	81.663	90.695	45.705
Y89_ppm_2SE(int)	2.494	2.211	6.989	6.514	1.682	1.567	5.902	2.331
Zr90_ppm_mean	66.701	54.805	71.483	81.097	34.443	64.477	92.004	43.465
Zr90_ppm_2SE(int)	2.062	1.986	4.972	5.724	1.223	1.253	18.542	3.898
Nb93_ppm_mean	0.341	0.161	1.729	0.145	0.072	0.161	1.253	0.768
Nb93_ppm_2SE(int)	0.051	0.047	0.428	0.046	0.017	0.044	0.642	0.072
Ba137_ppm_mean	2.271	0.277	21.492	0.381	0.293	2.968	12.239	13.853
Ba137_ppm_2SE(int)	0.523	0.236	3.219	0.339	0.144	0.698	6.327	1.604
Hf178_ppm_mean	4.195	3.614	3.648	4.816	2.372	4.162	4.493	2.200
Hf178_ppm_2SE(int)	0.182	0.182	0.251	0.219	0.122	0.188	0.552	0.132
Ta181_ppm_mean	0.038	0.027	0.090	0.023	0.010	0.021	0.080	0.047
Ta181_ppm_2SE(int)	0.008	0.007	0.021	0.014	0.004	0.005	0.035	0.011
Pb208_ppm_mean	0.026	0.100	0.525	1.594	0.125	0.153	0.201	1.420
Pb208_ppm_2SE(int)	0.012	0.024	0.441	0.303	0.148	0.082	0.096	0.414
Th232_ppm_mean	0.050	0.026	0.284	0.053	0.009	0.015	0.283	0.214
Th232_ppm_2SE(int)	0.009	0.007	0.052	0.047	0.004	0.004	0.145	0.052
U238_ppm_mean	0.013	0.010	1.339	0.009	0.005	0.009	0.123	0.048
U238_ppm_2SE(int)	0.005	0.004	2.366	0.005	0.002	0.006	0.072	0.008

*Point names include phase (px) and spot size (i.e., 30 um).

Table S6 cont.: Pyroxene trce element contents.

Sample	10072	10072	10072	10072	10072	10072	10072	10072	10072
LAICPMS point	72.19.px.40um	72.31.px.40um	72.32.px.40um	72.35.px.40um	72.37.px.40um	72.38.px.40um	72.43.px.35um	72.44.px.40um	72.46.px.40um
Ca43_ppm_mean	132518.370	104895.245	143387.081	151019.626	182806.614	146695.305	61727.314	92545.872	131921.013
Ca43_ppm_2SE(int)	3182.778	4261.641	4686.202	5369.421	4680.215	8857.067	2039.960	3207.219	9621.837
Sc45_ppm_mean	114.826	74.293	113.155	122.151	128.389	105.617	59.092	87.115	109.478
Sc45_ppm_2SE(int)	2.802	4.581	3.677	4.601	4.720	6.242	2.048	2.378	6.620
Ti47_ppm_mean	11519.320	6899.748	13735.849	16207.414	16172.185	10606.595	4247.496	8092.197	13674.839
Ti47_ppm_2SE(int)	303.485	376.301	414.814	579.356	348.160	613.260	191.069	278.739	1244.410
V51_ppm_mean	95.815	36.589	133.447	145.568	159.997	82.950	31.162	82.312	151.019
V51_ppm_2SE(int)	3.006	4.944	4.670	6.495	5.197	5.263	2.005	4.483	12.904
Cr52_ppm_mean	2665.297	1315.575	3896.696	4951.897	4904.871	2645.556	1082.012	2573.039	4751.034
Cr52_ppm_2SE(int)	79.673	150.296	117.413	177.406	128.172	158.133	47.840	111.820	332.240
Mn55_ppm_mean	2034.001	2221.210	1551.696	1577.599	1302.670	1464.785	3177.734	2159.127	1632.968
Mn55_ppm_2SE(int)	43.578	99.912	51.390	57.718	34.573	104.364	106.555	80.326	92.063
Co59_ppm_mean	19.215	18.524	17.473	19.011	16.471	15.106	27.268	21.927	19.346
Co59_ppm_2SE(int)	1.532	1.227	0.672	1.497	0.655	1.095	0.900	0.836	0.950
Ni60_ppm_mean	1.000	1.514	2.656	1.371	1.798	0.890	0.738	1.076	1.556
Ni60_ppm_2SE(int)	0.509	0.631	2.229	0.345	0.731	0.303	0.310	0.413	0.446
Cu63_ppm_mean	1.809	4.505	1.969	1.917	1.967	6.755	2.471	3.824	1.333
Cu63_ppm_2SE(int)	1.037	2.087	0.521	0.583	0.231	4.617	0.533	2.299	0.672
Zn66_ppm_mean	3.170	5.422	3.083	2.337	2.587	4.900	5.912	5.773	2.579
Zn66_ppm_2SE(int)	0.401	1.107	0.699	0.390	0.395	2.191	0.698	2.095	0.550
Rb85_ppm_mean	0.569	11.562	0.209	0.064	0.117	0.113	0.528	0.074	0.018
Rb85_ppm_2SE(int)	0.173	2.298	0.078	0.091	0.216	0.035	0.141	0.044	0.016
Sr88_ppm_mean	15.708	124.526	17.505	11.862	14.158	77.805	5.415	7.225	8.093
Sr88_ppm_2SE(int)	0.968	19.585	2.773	2.776	0.390	5.478	0.789	1.061	1.143
Y89_ppm_mean	93.639	195.918	54.187	53.467	56.876	81.182	71.817	58.540	43.178
Y89_ppm_2SE(int)	3.867	20.560	1.441	1.941	1.686	5.035	5.712	2.094	2.940
Zr90_ppm_mean	84.020	484.827	42.762	41.535	42.839	61.733	87.769	36.265	31.061
Zr90_ppm_2SE(int)	11.210	82.160	3.172	1.603	1.484	3.828	9.770	1.650	2.990
Nb93_ppm_mean	2.112	21.398	0.647	0.234	0.080	0.182	4.643	0.190	0.143
Nb93_ppm_2SE(int)	0.798	4.117	0.237	0.128	0.026	0.051	0.924	0.108	0.062
Ba137_ppm_mean	10.644	388.173	14.334	0.885	0.101	21.133	13.705	1.505	0.775
Ba137_ppm_2SE(int)	2.759	79.901	4.912	0.176	0.061	1.896	2.161	0.625	0.230
Hf178_ppm_mean	4.829	17.300	2.883	2.774	2.754	3.689	3.996	2.088	2.037
Hf178_ppm_2SE(int)	1.016	2.461	0.558	0.159	0.151	0.284	0.453	0.134	0.293
Ta181_ppm_mean	0.283	1.100	0.030	0.020	0.018	0.204	0.249	0.018	0.026
Ta181_ppm_2SE(int)	0.254	0.202	0.012	0.013	0.007	0.260	0.071	0.008	0.014
Pb208_ppm_mean	2.455	3.720	0.779	1.019	0.917	3.202	0.861	1.305	0.960
Pb208_ppm_2SE(int)	2.389	0.648	0.109	0.615	0.166	2.798	0.085	1.199	0.827
Th232_ppm_mean	0.311	5.188	0.044	0.035	0.017	0.046	0.882	0.023	0.085
Th232_ppm_2SE(int)	0.124	1.419	0.015	0.013	0.006	0.018	0.169	0.013	0.113
U238_ppm_mean	0.902	6.373	0.029	0.008	0.278	0.014	0.191	0.009	0.039
U238_ppm_2SE(int)	1.168	6.938	0.008	0.003	0.545	0.006	0.045	0.008	0.064

*Point names include phase (px) and spot size (i.e., 30 um).

Table S7: Pyroxene rare earth element contents.

Sample	10017	10017	10017	10017	10022	10022	10022	10022
LAICPMS point	17.21.px.40um	17.22.px.40um	17.33.px.40um	17.55.px.40um	22.4.px.40um	22.12.px.40um	22.14.px.40um	22.33.px.35um
La139_ppm_mean	82.089	1.598	3.833	1.355	2.811	0.601	3.231	0.940
La139_ppm_2SE(int)	37.307	0.412	0.462	0.208	0.309	0.059	0.304	0.134
Ce140_ppm_mean	228.564	7.099	15.899	7.430	14.078	3.667	16.243	N/A
Ce140_ppm_2SE(int)	100.114	0.995	1.435	0.963	0.934	0.290	0.895	N/A
Pr141_ppm_mean	35.625	1.399	3.146	1.354	2.868	0.788	3.578	1.217
Pr141_ppm_2SE(int)	15.244	0.163	0.284	0.121	0.109	0.056	0.186	0.153
Nd146_ppm_mean	188.048	9.044	20.949	8.642	19.231	5.510	25.310	8.565
Nd146_ppm_2SE(int)	80.554	0.899	1.971	0.577	0.619	0.280	1.320	0.927
Sm147_ppm_mean	65.467	5.198	11.377	4.806	9.793	2.987	12.892	4.814
Sm147_ppm_2SE(int)	25.980	0.527	1.013	0.383	0.520	0.218	0.580	0.798
Eu153_ppm_mean	2.042	0.378	0.927	0.437	0.559	0.265	0.462	0.465
Eu153_ppm_2SE(int)	0.726	0.181	0.186	0.139	0.070	0.195	0.051	0.444
Gd157_ppm_mean	82.042	8.324	18.130	7.435	15.524	5.208	20.498	7.465
Gd157_ppm_2SE(int)	31.138	0.813	1.601	0.382	0.558	0.363	0.962	0.500
Tb159_ppm_mean	13.882	1.703	3.744	1.538	3.154	1.009	3.943	1.593
Tb159_ppm_2SE(int)	4.838	0.177	0.342	0.087	0.111	0.068	0.189	0.131
Dy163_ppm_mean	92.393	12.655	29.035	11.486	21.395	6.843	28.520	11.099
Dy163_ppm_2SE(int)	31.209	1.175	2.913	0.545	0.710	0.423	1.305	0.571
Ho165_ppm_mean	19.605	2.852	6.399	2.540	4.741	1.537	6.052	2.470
Ho165_ppm_2SE(int)	6.433	0.266	0.616	0.110	0.150	0.099	0.230	0.229
Er166_ppm_mean	54.198	8.380	19.438	7.310	13.637	4.388	17.379	7.502
Er166_ppm_2SE(int)	16.962	0.845	1.894	0.347	0.550	0.213	0.682	0.638
Tm169_ppm_mean	7.199	1.185	2.929	1.021	1.803	0.617	2.399	1.030
Tm169_ppm_2SE(int)	2.111	0.136	0.316	0.057	0.067	0.049	0.100	0.112
Yb172_ppm_mean	45.047	7.782	20.151	7.206	13.042	4.184	16.219	6.832
Yb172_ppm_2SE(int)	12.174	0.779	2.323	0.329	0.592	0.208	0.745	0.616
Lu175_ppm_mean	6.242	1.139	2.947	1.027	1.805	0.741	2.274	1.044
Lu175_ppm_2SE(int)	1.598	0.109	0.351	0.056	0.087	0.355	0.117	0.096

*Point names include phase (px) and spot size (i.e., 30 um).

Table S7 cont.: Pyroxene rare earth element contents.

Sample	10022	10022	10024	10024	10024	10024	10024	10024
LAICPMS point	22.39.px.25um	22.40.px.35um	24.1.px.45um	24.19.px.45um	24.20.px.45um	24.21.px.45um	24.22.px.45um	24.45.pyx.45um
La139_ppm_mean	5.844	2.361	0.918	1.221	0.609	1.575	7.218	406.963
La139_ppm_2SE(int)	1.530	0.214	0.072	0.110	0.041	0.110	1.939	113.378
Ce140_ppm_mean	25.731	N/A	5.129	6.169	3.509	8.577	27.607	1148.174
Ce140_ppm_2SE(int)	4.912	N/A	0.369	0.343	0.193	0.518	5.487	305.089
Pr141_ppm_mean	5.042	2.753	1.114	1.415	0.838	1.762	4.929	179.876
Pr141_ppm_2SE(int)	0.930	0.160	0.053	0.067	0.047	0.068	0.795	49.402
Nd146_ppm_mean	32.637	19.757	8.224	9.812	5.860	11.751	30.125	903.625
Nd146_ppm_2SE(int)	5.750	0.862	0.286	0.403	0.330	0.349	3.991	244.267
Sm147_ppm_mean	17.969	10.630	4.373	5.298	3.416	6.482	15.125	296.901
Sm147_ppm_2SE(int)	2.626	0.841	0.297	0.260	0.192	0.280	1.375	77.554
Eu153_ppm_mean	0.914	0.486	0.271	0.316	0.184	0.394	0.520	5.134
Eu153_ppm_2SE(int)	0.197	0.067	0.027	0.039	0.025	0.037	0.049	1.301
Gd157_ppm_mean	26.357	16.547	6.929	9.113	5.892	9.692	23.264	359.936
Gd157_ppm_2SE(int)	3.644	0.782	0.331	0.352	0.328	0.488	2.076	92.625
Tb159_ppm_mean	5.241	3.303	1.412	1.898	1.208	1.977	4.831	61.222
Tb159_ppm_2SE(int)	0.652	0.240	0.069	0.087	0.054	0.071	0.415	15.168
Dy163_ppm_mean	40.069	23.459	9.719	13.884	9.058	14.135	33.843	379.934
Dy163_ppm_2SE(int)	4.817	1.439	0.345	0.547	0.271	0.539	2.737	91.925
Ho165_ppm_mean	7.948	5.013	2.128	3.046	1.954	2.993	7.312	76.918
Ho165_ppm_2SE(int)	1.186	0.275	0.092	0.139	0.079	0.095	0.603	18.467
Er166_ppm_mean	23.786	14.473	5.956	8.769	5.437	8.345	20.387	202.777
Er166_ppm_2SE(int)	3.547	0.773	0.298	0.358	0.174	0.333	1.566	47.191
Tm169_ppm_mean	3.501	2.036	0.776	1.293	0.798	1.106	2.890	25.792
Tm169_ppm_2SE(int)	0.605	0.157	0.043	0.073	0.040	0.039	0.243	5.916
Yb172_ppm_mean	24.713	13.230	5.362	9.068	5.325	7.442	19.469	154.596
Yb172_ppm_2SE(int)	4.499	0.906	0.258	0.379	0.228	0.276	1.614	34.280
Lu175_ppm_mean	3.710	1.795	0.712	1.262	0.740	0.988	2.689	19.573
Lu175_ppm_2SE(int)	0.590	0.073	0.041	0.052	0.037	0.055	0.203	4.137

*Point names include phase (px) and spot size (i.e., 30 um).

Table S7 cont.: Pyroxene rare earth element contents.

Sample	10024	10024	10024	10024	10024	10024	10049	10049
LAICPMS point	24.56.px.45um	24.68.px.45um	24.73.px.45um	24.74.px.45um	24.76.px.45um	24.77.px.45um	49.1.px.30um	49.7.px.30um
La139_ppm_mean	36.067	0.622	8.600	0.683	1.567	1.276	1.415	2.945
La139_ppm_2SE(int)	8.630	0.064	2.185	0.074	0.209	0.144	0.234	0.614
Ce140_ppm_mean	117.061	3.432	30.802	3.511	7.126	7.548	6.300	10.745
Ce140_ppm_2SE(int)	28.702	0.314	5.513	0.237	0.855	0.892	0.562	1.768
Pr141_ppm_mean	17.094	0.820	5.881	0.751	1.320	1.774	1.339	2.113
Pr141_ppm_2SE(int)	3.829	0.081	0.658	0.038	0.111	0.193	0.132	0.317
Nd146_ppm_mean	86.634	5.570	37.371	5.676	8.775	12.331	9.115	13.664
Nd146_ppm_2SE(int)	17.663	0.492	2.855	0.228	0.680	1.311	0.839	1.744
Sm147_ppm_mean	31.243	3.085	19.260	3.142	4.237	7.037	5.208	6.710
Sm147_ppm_2SE(int)	5.464	0.214	0.807	0.164	0.249	0.759	0.393	0.587
Eu153_ppm_mean	1.353	0.156	0.920	0.158	0.251	0.278	0.686	0.423
Eu153_ppm_2SE(int)	0.211	0.025	0.105	0.028	0.025	0.030	0.137	0.074
Gd157_ppm_mean	40.479	5.136	29.775	5.065	6.870	11.725	8.417	11.785
Gd157_ppm_2SE(int)	6.678	0.325	0.794	0.226	0.311	1.099	0.601	0.812
Tb159_ppm_mean	7.749	1.100	6.415	1.046	1.418	2.400	1.793	2.404
Tb159_ppm_2SE(int)	1.093	0.062	0.201	0.046	0.070	0.208	0.112	0.133
Dy163_ppm_mean	50.867	7.991	47.256	7.443	10.536	16.791	12.613	17.627
Dy163_ppm_2SE(int)	6.576	0.501	1.225	0.235	0.448	1.353	0.735	0.918
Ho165_ppm_mean	10.724	1.732	10.479	1.613	2.228	3.693	2.839	4.018
Ho165_ppm_2SE(int)	1.316	0.092	0.325	0.066	0.089	0.280	0.184	0.222
Er166_ppm_mean	30.032	4.953	30.835	4.685	6.345	10.569	8.384	11.875
Er166_ppm_2SE(int)	3.729	0.310	0.902	0.160	0.240	0.689	0.462	0.590
Tm169_ppm_mean	4.223	0.717	4.495	0.678	0.908	1.551	1.232	1.763
Tm169_ppm_2SE(int)	0.477	0.038	0.144	0.030	0.045	0.109	0.077	0.086
Yb172_ppm_mean	27.793	4.943	31.649	4.488	6.100	10.488	8.712	12.580
Yb172_ppm_2SE(int)	2.864	0.283	0.862	0.173	0.316	0.662	0.569	0.692
Lu175_ppm_mean	3.663	0.685	4.524	0.609	0.833	1.460	1.295	1.852
Lu175_ppm_2SE(int)	0.345	0.036	0.122	0.025	0.041	0.096	0.095	0.109

*Point names include phase (px) and spot size (i.e., 30 um).

Table S7 cont.: Pyroxene rare earth element contents.

Sample	10049	10049	10049	10049	10049	10049	10049	10049
LAICPMS point	49.11.px.30um	49.15.px.30um	49.20.px.30um	49.21.px.30um	49.26.px.30um	49.27.px.30um	49.28.px.30um	49.30.px.30um
La139_ppm_mean	2.462	8.199	23.563	1.902	2.144	0.128	8.684	0.769
La139_ppm_2SE(int)	0.157	2.308	1.608	0.320	0.357	0.095	3.611	0.191
Ce140_ppm_mean	11.069	25.272	71.281	7.161	8.801	0.414	25.888	7.145
Ce140_ppm_2SE(int)	0.540	5.821	4.207	1.477	1.054	0.146	5.221	5.704
Pr141_ppm_mean	2.542	4.272	10.974	1.291	1.746	0.072	4.128	0.484
Pr141_ppm_2SE(int)	0.304	0.811	0.719	0.449	0.131	0.023	0.789	0.144
Nd146_ppm_mean	16.238	24.433	56.977	5.804	11.165	0.453	21.742	2.083
Nd146_ppm_2SE(int)	0.984	3.872	3.940	0.615	0.684	0.123	3.869	0.454
Sm147_ppm_mean	8.343	10.604	19.976	2.639	5.817	0.271	9.376	0.910
Sm147_ppm_2SE(int)	0.625	1.149	1.386	0.339	0.393	0.085	1.262	0.163
Eu153_ppm_mean	0.463	1.972	0.737	0.163	0.667	0.016	1.134	0.105
Eu153_ppm_2SE(int)	0.071	0.346	0.054	0.035	0.162	0.008	0.094	0.071
Gd157_ppm_mean	13.349	15.237	24.703	4.142	9.023	0.621	13.810	1.403
Gd157_ppm_2SE(int)	0.834	1.452	1.473	0.517	0.485	0.138	1.953	0.262
Tb159_ppm_mean	2.686	3.120	4.536	0.824	1.849	0.123	2.515	0.268
Tb159_ppm_2SE(int)	0.172	0.246	0.238	0.066	0.115	0.025	0.270	0.036
Dy163_ppm_mean	19.259	22.852	31.206	6.021	13.569	1.073	18.006	2.160
Dy163_ppm_2SE(int)	1.082	1.960	1.482	0.421	0.632	0.144	1.699	0.254
Ho165_ppm_mean	4.299	5.121	6.324	1.396	2.924	0.275	3.907	0.498
Ho165_ppm_2SE(int)	0.225	0.484	0.297	0.100	0.178	0.038	0.328	0.051
Er166_ppm_mean	11.979	16.125	18.222	4.084	8.721	0.926	11.253	1.616
Er166_ppm_2SE(int)	0.710	1.441	0.897	0.322	0.433	0.093	0.971	0.166
Tm169_ppm_mean	1.694	2.245	2.378	0.639	1.207	0.144	1.596	0.242
Tm169_ppm_2SE(int)	0.112	0.159	0.140	0.052	0.067	0.019	0.149	0.027
Yb172_ppm_mean	11.447	16.430	15.591	4.523	8.440	1.139	11.527	1.801
Yb172_ppm_2SE(int)	0.649	1.286	0.996	0.346	0.417	0.124	1.026	0.189
Lu175_ppm_mean	1.641	2.313	2.045	0.622	1.184	0.187	1.526	0.245
Lu175_ppm_2SE(int)	0.108	0.199	0.135	0.052	0.071	0.016	0.137	0.025

*Point names include phase (px) and spot size (i.e., 30 um).

Table S7 cont.: Pyroxene rare earth element contents.

Sample	10049	10049	10049	10069	10069	10069	10069	10069
LAICPMS point	49.35.px.30um	49.38.px.30um	49.39.px.30um	69.10.px.30um	69.12.px.30um	69.20.px.30um	69.22.px.30um	69.51.px.25um
La139_ppm_mean	7.463	4.733	14.693	1.598	20.304	3.862	48.298	1.319
La139_ppm_2SE(int)	3.949	0.654	1.934	0.207	13.842	0.847	32.324	0.463
Ce140_ppm_mean	27.189	17.515	47.754	8.448	63.353	14.679	134.998	4.556
Ce140_ppm_2SE(int)	15.877	1.916	7.851	0.428	41.368	2.724	85.759	1.295
Pr141_ppm_mean	4.244	3.293	7.150	2.307	9.908	2.760	20.371	0.750
Pr141_ppm_2SE(int)	1.857	0.326	0.631	0.763	6.264	0.451	12.424	0.197
Nd146_ppm_mean	22.028	19.201	38.654	13.015	52.748	16.128	106.791	4.668
Nd146_ppm_2SE(int)	7.612	1.576	3.019	1.192	31.100	2.411	62.166	1.093
Sm147_ppm_mean	10.020	9.422	17.268	6.951	18.784	8.292	37.145	2.461
Sm147_ppm_2SE(int)	2.474	0.694	1.076	0.637	9.760	1.140	19.258	0.321
Eu153_ppm_mean	1.682	0.501	1.650	0.395	0.534	0.290	1.974	0.245
Eu153_ppm_2SE(int)	0.297	0.261	0.746	0.151	0.209	0.040	1.678	0.074
Gd157_ppm_mean	13.441	14.569	25.052	11.658	25.158	12.283	46.022	3.532
Gd157_ppm_2SE(int)	2.602	1.210	1.663	0.874	12.180	1.544	22.078	0.600
Tb159_ppm_mean	2.690	3.037	5.217	2.576	4.552	2.404	8.426	0.827
Tb159_ppm_2SE(int)	0.444	0.218	0.309	0.191	2.017	0.277	3.629	0.129
Dy163_ppm_mean	20.087	22.282	39.621	18.569	28.699	17.338	54.321	6.354
Dy163_ppm_2SE(int)	3.351	1.594	2.059	1.058	12.193	1.870	22.479	0.739
Ho165_ppm_mean	4.227	4.803	8.745	4.084	5.955	3.996	11.372	1.552
Ho165_ppm_2SE(int)	0.603	0.342	0.447	0.252	2.395	0.421	4.342	0.191
Er166_ppm_mean	12.746	14.779	27.788	11.843	16.687	11.570	30.769	4.617
Er166_ppm_2SE(int)	1.815	0.958	1.325	0.802	6.340	1.292	11.015	0.571
Tm169_ppm_mean	1.726	2.054	4.202	1.749	2.207	1.613	3.975	0.746
Tm169_ppm_2SE(int)	0.224	0.145	0.202	0.139	0.815	0.197	1.288	0.108
Yb172_ppm_mean	12.489	14.854	30.182	11.529	13.336	11.040	25.073	5.665
Yb172_ppm_2SE(int)	1.333	1.073	1.589	0.586	4.592	1.285	7.082	0.586
Lu175_ppm_mean	1.751	2.277	4.398	1.712	1.778	1.505	3.171	0.674
Lu175_ppm_2SE(int)	0.180	0.237	0.237	0.122	0.578	0.171	0.772	0.081

*Point names include phase (px) and spot size (i.e., 30 um).

Table S7 cont.: Pyroxene rare earth element contents.

Sample	10069	10071	10071	10071	10071	10071	10071	10071
LAICPMS point	69.120.px.30um	71.1.px.35um	71.2.px.35um	71.7.px.35um	71.12.px.45um	71.14.px.45um	71.28.px.35um	71.37.px.35um
La139_ppm_mean	53.709	2.789	152.000	2.310	2.041	3.835	13.389	2.909
La139_ppm_2SE(int)	28.633	0.316	22.336	0.156	0.166	0.910	5.274	0.632
Ce140_ppm_mean	155.464	N/A	N/A	N/A	9.336	16.081	N/A	N/A
Ce140_ppm_2SE(int)	79.038	N/A	N/A	N/A	0.418	2.754	N/A	N/A
Pr141_ppm_mean	23.728	3.206	71.030	3.515	2.026	3.185	9.768	2.749
Pr141_ppm_2SE(int)	11.589	0.280	11.658	1.510	0.103	0.407	2.476	0.233
Nd146_ppm_mean	116.010	20.680	376.725	19.327	13.089	19.909	58.815	19.102
Nd146_ppm_2SE(int)	54.940	0.811	66.259	0.604	0.420	1.794	12.207	1.350
Sm147_ppm_mean	40.015	11.389	124.614	10.868	7.016	10.213	26.616	9.343
Sm147_ppm_2SE(int)	17.500	0.745	21.316	0.667	0.313	0.685	4.237	0.792
Eu153_ppm_mean	0.877	0.514	4.191	0.556	0.356	0.438	0.888	1.018
Eu153_ppm_2SE(int)	0.321	0.063	0.590	0.115	0.038	0.050	0.154	0.250
Gd157_ppm_mean	51.765	16.838	154.287	17.585	10.792	14.933	37.649	14.431
Gd157_ppm_2SE(int)	21.138	0.976	23.648	0.852	0.461	0.719	5.152	0.971
Tb159_ppm_mean	9.329	3.473	27.344	3.543	2.193	3.118	7.732	2.913
Tb159_ppm_2SE(int)	3.618	0.155	4.479	0.194	0.091	0.158	0.879	0.171
Dy163_ppm_mean	63.474	24.142	171.702	23.945	15.573	21.358	51.370	20.675
Dy163_ppm_2SE(int)	24.058	1.143	25.861	1.056	0.505	0.908	5.639	1.072
Ho165_ppm_mean	13.335	5.171	35.364	5.303	3.312	4.624	11.123	4.248
Ho165_ppm_2SE(int)	4.828	0.220	5.126	0.199	0.134	0.196	1.238	0.225
Er166_ppm_mean	38.878	14.447	99.494	14.782	9.438	12.838	32.219	12.496
Er166_ppm_2SE(int)	13.949	0.717	13.948	0.767	0.476	0.497	3.609	0.775
Tm169_ppm_mean	5.311	2.220	13.482	2.142	1.346	1.772	4.634	1.754
Tm169_ppm_2SE(int)	1.765	0.478	1.875	0.126	0.055	0.083	0.516	0.121
Yb172_ppm_mean	34.087	13.319	84.851	13.903	8.779	11.743	32.045	12.404
Yb172_ppm_2SE(int)	11.454	0.701	10.806	0.572	0.321	0.478	3.299	0.765
Lu175_ppm_mean	4.465	1.838	11.833	1.929	1.178	1.621	4.810	1.734
Lu175_ppm_2SE(int)	1.442	0.133	1.459	0.075	0.057	0.092	0.539	0.108

*Point names include phase (px) and spot size (i.e., 30 um).

Table S7 cont.: Pyroxene rare earth element contents.

Sample	10071	10071	10071	10071	10071	10071	10071	10071
LAICPMS point	71.38.px.35um	71.40.px.35um	71.41.px.35um	71.49.px.35um	71.50.px.35um	71.57.35um	71.58.px.35um	71.63.px.40um
La139_ppm_mean	5.008	1.374	4.547	59.543	9.284	2.730	1.374	3.973
La139_ppm_2SE(int)	1.841	0.345	0.631	12.750	3.821	0.382	0.080	0.217
Ce140_ppm_mean	N/A	N/A	N/A	N/A	N/A	N/A	N/A	16.300
Ce140_ppm_2SE(int)	N/A	N/A	N/A	N/A	N/A	N/A	N/A	0.722
Pr141_ppm_mean	3.800	1.514	2.740	23.920	5.428	2.215	1.621	3.032
Pr141_ppm_2SE(int)	0.997	0.077	0.273	4.488	1.418	0.241	0.085	0.108
Nd146_ppm_mean	20.866	11.113	15.191	123.494	30.699	14.377	11.344	20.341
Nd146_ppm_2SE(int)	3.754	0.479	1.412	22.343	6.006	1.532	0.516	0.698
Sm147_ppm_mean	9.604	6.015	7.077	45.643	14.298	7.760	6.582	11.038
Sm147_ppm_2SE(int)	1.200	0.379	0.707	6.579	1.654	0.644	0.462	0.500
Eu153_ppm_mean	2.826	0.318	2.175	1.328	1.374	0.491	0.532	0.733
Eu153_ppm_2SE(int)	0.166	0.036	0.339	0.188	0.288	0.077	0.498	0.056
Gd157_ppm_mean	13.367	9.258	10.364	58.962	21.348	12.775	9.589	16.360
Gd157_ppm_2SE(int)	1.272	0.541	1.193	7.098	1.656	0.991	0.433	0.610
Tb159_ppm_mean	2.855	2.001	2.022	11.288	4.349	2.611	2.021	3.235
Tb159_ppm_2SE(int)	0.238	0.081	0.235	1.238	0.225	0.164	0.098	0.117
Dy163_ppm_mean	20.229	13.716	15.127	79.170	30.448	18.603	13.549	23.742
Dy163_ppm_2SE(int)	1.511	0.655	1.630	7.970	1.673	1.236	0.434	0.645
Ho165_ppm_mean	4.329	3.128	3.272	17.407	6.628	4.055	2.898	5.301
Ho165_ppm_2SE(int)	0.372	0.316	0.337	1.622	0.290	0.228	0.125	0.162
Er166_ppm_mean	12.832	8.034	9.680	49.550	18.915	11.894	8.171	15.481
Er166_ppm_2SE(int)	0.919	0.360	0.954	4.437	0.864	0.702	0.322	0.407
Tm169_ppm_mean	1.843	1.130	1.355	7.387	2.823	1.614	1.136	2.235
Tm169_ppm_2SE(int)	0.128	0.071	0.141	0.636	0.125	0.110	0.067	0.084
Yb172_ppm_mean	13.316	7.668	9.645	52.307	20.865	11.535	7.685	15.174
Yb172_ppm_2SE(int)	0.837	0.376	1.160	4.529	0.847	0.649	0.426	0.449
Lu175_ppm_mean	1.926	1.023	1.347	7.319	2.890	1.616	0.995	2.063
Lu175_ppm_2SE(int)	0.141	0.065	0.155	0.576	0.121	0.087	0.063	0.076

*Point names include phase (px) and spot size (i.e., 30 um).

Table S7 cont.: Pyroxene rare earth element contents.

Sample	10071	10071	10071	10071	10072	10072	10072	10072
LAICPMS point	71.64.px.40um	71.95.px.40um	71.97.px.40um	71.99.px.45um	72.2.px.45um	72.7.px.45um	72.8.px.45um	72.18.px.45um
La139_ppm_mean	1.585	1.328	1.781	2.075	0.775	1.234	1.941	1.493
La139_ppm_2SE(int)	0.088	0.082	0.137	0.150	0.044	0.055	0.506	0.197
Ce140_ppm_mean	7.689	6.970	9.662	12.041	4.221	6.724	9.018	5.235
Ce140_ppm_2SE(int)	0.292	0.286	0.766	0.842	0.151	0.226	1.802	0.386
Pr141_ppm_mean	1.708	1.675	1.918	2.571	1.001	1.564	1.832	1.066
Pr141_ppm_2SE(int)	0.083	0.147	0.120	0.163	0.037	0.056	0.222	0.102
Nd146_ppm_mean	11.354	10.932	13.277	17.404	7.245	11.313	12.529	6.385
Nd146_ppm_2SE(int)	0.554	0.538	2.067	1.665	0.243	0.301	1.368	0.328
Sm147_ppm_mean	6.147	6.213	7.129	10.191	4.109	6.464	6.826	3.375
Sm147_ppm_2SE(int)	0.353	0.315	0.658	0.898	0.179	0.304	0.632	0.265
Eu153_ppm_mean	0.340	0.300	0.293	0.374	0.206	0.349	0.283	0.184
Eu153_ppm_2SE(int)	0.089	0.028	0.047	0.061	0.018	0.027	0.037	0.021
Gd157_ppm_mean	9.779	9.848	11.282	13.937	6.641	10.266	10.797	5.518
Gd157_ppm_2SE(int)	0.510	0.388	0.863	1.174	0.303	0.458	0.767	0.404
Tb159_ppm_mean	1.920	1.928	2.291	3.032	1.369	2.138	2.317	1.162
Tb159_ppm_2SE(int)	0.097	0.080	0.205	0.188	0.075	0.070	0.181	0.058
Dy163_ppm_mean	13.418	14.148	16.166	20.442	10.381	15.656	16.900	8.593
Dy163_ppm_2SE(int)	0.528	0.516	1.220	0.896	0.409	0.487	1.017	0.592
Ho165_ppm_mean	2.949	3.023	3.510	4.475	2.193	3.217	3.623	1.852
Ho165_ppm_2SE(int)	0.138	0.111	0.273	0.220	0.080	0.115	0.244	0.116
Er166_ppm_mean	8.425	8.412	10.194	12.320	6.223	9.163	10.573	5.291
Er166_ppm_2SE(int)	0.404	0.352	0.929	0.726	0.255	0.277	0.744	0.277
Tm169_ppm_mean	1.137	1.144	1.441	1.877	0.901	1.298	1.468	0.795
Tm169_ppm_2SE(int)	0.065	0.053	0.127	0.335	0.046	0.066	0.111	0.057
Yb172_ppm_mean	8.063	7.783	11.260	11.615	5.970	8.626	10.085	5.281
Yb172_ppm_2SE(int)	0.381	0.305	2.331	0.914	0.245	0.277	0.872	0.284
Lu175_ppm_mean	1.118	1.019	1.425	1.646	0.816	1.101	1.398	0.746
Lu175_ppm_2SE(int)	0.054	0.053	0.102	0.140	0.043	0.037	0.117	0.041

*Point names include phase (px) and spot size (i.e., 30 um).

Table S7 cont.: Pyroxene rare earth element contents.

Sample	10072	10072	10072	10072	10072	10072	10072	10072	10072
LAICPMS point	72.19.px.40um	72.31.px.40um	72.32.px.40um	72.35.px.40um	72.37.px.40um	72.38.px.40um	72.43.px.35um	72.44.px.40um	72.46.px.40um
La139_ppm_mean	2.095	22.401	1.076	0.899	1.157	1.764	3.029	0.726	0.750
La139_ppm_2SE(int)	0.269	4.996	0.101	0.066	0.107	0.205	0.679	0.089	0.082
Ce140_ppm_mean	10.423	68.895	5.786	5.073	6.030	8.384	N/A	3.963	12.160
Ce140_ppm_2SE(int)	1.823	14.572	0.473	0.608	0.168	0.673	N/A	0.344	17.074
Pr141_ppm_mean	2.028	10.581	1.189	1.392	1.282	1.840	1.682	0.952	0.875
Pr141_ppm_2SE(int)	0.145	2.023	0.088	0.652	0.071	0.150	0.328	0.065	0.140
Nd146_ppm_mean	13.175	53.032	8.174	7.789	9.282	12.937	9.606	6.782	6.035
Nd146_ppm_2SE(int)	0.650	9.465	0.472	0.413	0.486	0.938	1.710	0.448	0.611
Sm147_ppm_mean	7.355	20.048	4.501	4.339	5.132	6.805	4.661	4.046	3.192
Sm147_ppm_2SE(int)	0.413	2.902	0.325	0.274	0.299	0.541	0.723	0.324	0.364
Eu153_ppm_mean	0.347	2.108	0.369	0.215	0.281	0.808	0.188	0.188	0.171
Eu153_ppm_2SE(int)	0.032	0.384	0.096	0.027	0.033	0.080	0.041	0.030	0.034
Gd157_ppm_mean	11.918	28.416	7.076	7.091	7.674	11.094	7.474	6.755	5.517
Gd157_ppm_2SE(int)	0.660	3.560	0.359	0.405	0.549	0.847	1.036	0.442	0.457
Tb159_ppm_mean	2.348	5.345	1.402	1.367	1.525	2.063	1.525	1.334	0.996
Tb159_ppm_2SE(int)	0.129	0.595	0.063	0.067	0.082	0.156	0.136	0.090	0.094
Dy163_ppm_mean	16.707	36.628	10.076	10.070	10.879	15.097	11.927	10.374	7.530
Dy163_ppm_2SE(int)	0.731	3.902	0.363	0.415	0.447	0.962	0.979	0.575	0.590
Ho165_ppm_mean	3.577	8.321	2.171	2.162	2.375	3.299	2.797	2.384	1.609
Ho165_ppm_2SE(int)	0.159	0.911	0.093	0.098	0.104	0.215	0.248	0.106	0.099
Er166_ppm_mean	10.668	23.338	6.163	6.250	6.395	9.348	8.869	6.810	5.023
Er166_ppm_2SE(int)	0.525	2.518	0.285	0.267	0.361	0.616	0.744	0.298	0.344
Tm169_ppm_mean	1.548	3.301	0.845	0.875	0.828	1.257	1.305	0.979	0.691
Tm169_ppm_2SE(int)	0.097	0.332	0.057	0.042	0.045	0.091	0.079	0.068	0.070
Yb172_ppm_mean	10.395	23.021	5.853	5.831	5.516	8.296	9.540	6.850	5.102
Yb172_ppm_2SE(int)	0.549	2.213	0.221	0.290	0.257	0.575	0.594	0.353	0.693
Lu175_ppm_mean	1.431	3.257	0.822	0.819	0.747	1.097	1.491	0.951	0.619
Lu175_ppm_2SE(int)	0.081	0.314	0.063	0.062	0.057	0.085	0.128	0.054	0.050

*Point names include phase (px) and spot size (i.e., 30 um).

Table S8: Olivine major element contents.

Sample	10024	10071	10071	10071	10072	10072	10072	10072
Point	74 / 1 .	13 / 1 .	65 / 1 .	67 / 1 .	33 / 1 .	34 / 1 .	36 / 1 .	45 / 1 .
SiO2	34.82	37.67	37.10	36.59	37.33	37.47	36.25	37.33
Na2O	0.00	0.00	0.01	0.00	0.05	0.08	0.08	0.08
MgO	24.36	33.34	32.94	31.19	32.70	33.16	26.98	32.52
Al2O3	0.00	0.05	0.04	0.05	0.06	0.04	0.05	0.05
CaO	0.29	0.37	0.34	0.35	0.35	0.37	0.42	0.35
TiO2	0.12	0.13	0.09	0.16	0.21	0.16	0.19	0.15
Cr2O3	0.08	0.16	0.16	0.13	0.17	0.18	0.13	0.17
MnO	0.35	0.29	0.26	0.30	0.27	0.24	0.32	0.24
FeO	39.49	27.97	29.43	31.36	29.06	27.96	36.02	28.63
K2O	0.00	0.00	0.01	0.01	0.00	0.00	0.01	0.00
P2O5	0.00	0.00	0.01	0.02	0.04	0.05	0.03	0.01
Total	99.52	99.99	100.37	100.15	100.25	99.71	100.49	99.52
Mg# (Mg/(Mg+Fe))	52.37	67.99	66.61	63.94	66.73	67.88	57.18	66.93

Table S9: Olivine trace element contents.

Sample	10071	10072	10072	10072
LAICPMS point	71.65.olv.40um	72.34.ol.40um	72.36.olv.40um	72.45.olv.25um
Ca43_ppm_mean	5011.748	5757.731	88597.701	9971.343
Ca43_ppm_2SE(int)	1649.366	1187.233	7882.236	1397.744
Sc45_ppm_mean	13.422	16.287	76.569	19.550
Sc45_ppm_2SE(int)	1.406	1.331	6.759	1.734
Ti47_ppm_mean	892.531	7227.312	20541.768	4518.888
Ti47_ppm_2SE(int)	292.774	2486.270	3438.370	703.207
V51_ppm_mean	17.726	33.444	91.874	22.020
V51_ppm_2SE(int)	1.094	5.987	8.195	3.125
Cr52_ppm_mean	1060.822	1345.931	3003.289	978.551
Cr52_ppm_2SE(int)	43.278	153.076	259.977	122.173
Mn55_ppm_mean	2131.654	2151.716	1636.453	2776.599
Mn55_ppm_2SE(int)	80.300	71.863	135.924	141.121
Co59_ppm_mean	71.131	68.099	25.553	59.910
Co59_ppm_2SE(int)	2.808	2.198	3.297	2.694
Ni60_ppm_mean	27.949	21.725	1.652	10.766
Ni60_ppm_2SE(int)	2.025	1.185	0.447	1.371
Cu63_ppm_mean	0.712	2.436	0.939	3.489
Cu63_ppm_2SE(int)	0.352	0.337	0.194	0.819
Zn66_ppm_mean	3.385	6.807	4.700	10.861
Zn66_ppm_2SE(int)	0.532	0.773	0.658	1.865
Rb85_ppm_mean	0.032	0.548	0.248	1.285
Rb85_ppm_2SE(int)	0.037	0.451	0.123	0.416
Sr88_ppm_mean	3.108	3.467	9.791	21.703
Sr88_ppm_2SE(int)	1.469	1.094	0.959	4.660
Y89_ppm_mean	4.347	5.084	41.265	36.235
Y89_ppm_2SE(int)	1.710	1.490	2.420	7.790
Zr90_ppm_mean	5.471	13.000	41.257	50.646
Zr90_ppm_2SE(int)	3.161	4.256	4.555	12.228
Nb93_ppm_mean	0.415	0.884	1.427	2.148
Nb93_ppm_2SE(int)	0.385	0.307	0.258	0.655
Ba137_ppm_mean	2.990	6.249	8.806	45.579
Ba137_ppm_2SE(int)	1.496	2.117	2.852	10.656
Hf178_ppm_mean	0.216	0.467	1.939	1.476
Hf178_ppm_2SE(int)	0.123	0.156	0.233	0.369
Ta181_ppm_mean	0.017	0.064	0.128	0.148
Ta181_ppm_2SE(int)	0.011	0.024	0.033	0.045
Pb208_ppm_mean	0.721	1.970	1.261	3.520
Pb208_ppm_2SE(int)	1.263	0.607	0.278	0.612
Th232_ppm_mean	0.014	0.152	0.128	0.789
Th232_ppm_2SE(int)	0.009	0.158	0.042	0.226
U238_ppm_mean	0.076	0.353	0.063	0.217
U238_ppm_2SE(int)	0.143	0.515	0.016	0.062

*Point names include phase (ol) and spot size (i.e., 30 um).

Table S10: Olivine rare earth element contents.

Sample	10071	10072	10072	10072
LAICPMS point	71.65.olv.40um	72.34.ol.40um	72.36.olv.40um	72.45.olv.25um
La139_ppm_mean	0.3141643	0.650495283	1.532257053	5.967487266
La139_ppm_2SE(int)	0.277048454	0.212926661	0.253282745	1.822666936
Ce140_ppm_mean	0.96591951	1.775383418	6.126185488	18.12039681
Ce140_ppm_2SE(int)	0.659846047	0.589767702	0.805618804	5.788041733
Pr141_ppm_mean	0.094843691	0.337380005	1.125487783	2.681578033
Pr141_ppm_2SE(int)	0.053125647	0.148754074	0.107359478	0.82333168
Nd146_ppm_mean	0.585315236	1.243452486	6.808743705	12.66623314
Nd146_ppm_2SE(int)	0.29430749	0.428598598	0.550996372	3.658561178
Sm147_ppm_mean	0.272452875	0.409939189	3.373507763	4.185528506
Sm147_ppm_2SE(int)	0.143010273	0.15049478	0.307417655	1.272869223
Eu153_ppm_mean	0.131401548	0.067676366	0.213528732	0.284338355
Eu153_ppm_2SE(int)	0.173964011	0.04095242	0.037531218	0.069772193
Gd157_ppm_mean	0.487491327	0.662807787	5.567073121	5.083291616
Gd157_ppm_2SE(int)	0.242996314	0.227146751	0.518332942	1.286621347
Tb159_ppm_mean	0.090756785	0.127297279	1.060123441	0.944986123
Tb159_ppm_2SE(int)	0.044253314	0.045477957	0.094048253	0.215561605
Dy163_ppm_mean	0.690722001	0.825852017	7.982267843	6.101219787
Dy163_ppm_2SE(int)	0.300316114	0.242206922	0.544705594	1.47195856
Ho165_ppm_mean	0.178514777	0.18966669	1.691575627	1.223019721
Ho165_ppm_2SE(int)	0.076106105	0.053844661	0.10440892	0.259815681
Er166_ppm_mean	0.556166839	0.697091092	4.899245964	3.54972932
Er166_ppm_2SE(int)	0.202943188	0.192629234	0.363934021	0.783849584
Tm169_ppm_mean	0.11074072	0.095021562	0.662103357	0.522640426
Tm169_ppm_2SE(int)	0.03633888	0.018978354	0.052264711	0.115116796
Yb172_ppm_mean	0.719018888	0.735816954	4.367624735	3.281691672
Yb172_ppm_2SE(int)	0.231463407	0.153075305	0.278256346	0.636988521
Lu175_ppm_mean	0.129986678	0.124460184	0.664562027	0.432363578
Lu175_ppm_2SE(int)	0.037470524	0.019615849	0.046909216	0.062798943

*Point names include phase (ol) and spot size (i.e., 30 um).

Table S11: Glass major element compositions.

Sample	10017	10017	10017	10017	10017	10022	10022	10022
Point	36 / 1 .	47 / 1 .	49 / 1 .	51 / 1 .	60 / 1 .	5 / 1 .	8 / 1 .	17/1
SiO2	95.33	50.53	51.01	52.73	93.52	51.17	30.96	59.37
Na2O	0.29	2.50	2.27	2.49	0.15	2.35	0.26	1.47
MgO	0.00	0.00	0.19	0.00	0.00	0.16	0.27	0.57
Al2O3	1.38	29.84	30.10	28.85	5.26	29.01	4.74	21.06
CaO	0.36	14.54	14.81	13.67	1.70	13.36	28.61	9.93
TiO2	0.32	0.05	0.08	0.06	0.24	0.08	0.38	0.50
Cr2O3	0.00	0.00	0.00	0.00	0.00	0.00	0.02	0.00
MnO	0.03	0.03	0.00	0.02	0.01	0.06	0.16	0.05
FeO	0.35	1.01	0.84	0.97	0.44	1.42	9.83	4.39
K2O	0.00	0.40	0.28	0.58	0.05	0.49	1.92	1.72
P2O5	0.01	0.05	0.01	0.02	0.04	0.24	21.19	0.11
Total	98.07	98.95	99.59	99.39	101.42	98.34	98.33	99.16

Table S11 cont.: Glass major element compositions.

Sample	10022	10022	10022	10024	10024	10024	10024	10049
Point	38 / 1 .	45 / 1 .	52 / 1 .	3 / 1 .	9 / 1 .	18 / 1 .	23 / 1 .	32 / 1 .
SiO2	56.95	70.85	50.49	76.15	52.33	51.95	63.01	68.70
Na2O	1.65	1.10	2.05	0.74	2.63	3.04	2.04	1.01
MgO	0.04	0.08	0.19	0.04	1.05	0.10	0.56	0.08
Al2O3	24.41	16.88	28.66	16.49	28.36	28.61	22.90	17.50
CaO	12.22	8.31	14.76	1.23	13.31	13.09	10.58	6.12
TiO2	0.21	0.31	0.30	0.53	0.20	0.08	0.11	0.44
Cr2O3	0.01	0.01	0.00	0.01	0.00	0.01	0.01	0.00
MnO	0.05	0.01	0.01	0.01	0.02	0.01	0.00	0.04
FeO	2.27	1.42	1.98	1.67	1.49	0.96	1.03	2.04
K2O	0.51	0.37	0.31	3.36	0.99	0.71	1.12	2.37
P2O5	0.08	0.25	0.11	0.19	0.62	0.04	0.03	0.04
Total	98.40	99.60	98.86	100.40	100.98	98.59	101.39	98.35

Table S11 cont.: Glass major element compositions.

Sample	10049	10069	10069	10069	10069	10069	10069	10069
Point	36 / 1 .	6 / 1 .	11 / 1 .	25 / 1 .	54 / 1 .	75 / 1 .	83 / 1 .	103 / 1 .
SiO2	95.53	51.15	50.70	73.36	50.88	71.46	90.47	70.57
Na2O	0.33	2.49	2.31	0.68	2.40	1.11	0.38	0.89
MgO	0.00	0.00	0.00	0.00	0.09	0.00	0.00	0.00
Al2O3	1.52	30.03	29.81	11.92	30.30	13.08	3.94	9.78
CaO	0.39	14.86	15.00	1.60	14.88	3.43	1.31	3.81
TiO2	0.29	0.04	0.09	1.50	0.30	1.11	1.15	0.74
Cr2O3	0.01	0.00	0.00	0.02	0.00	0.01	0.00	0.00
MnO	0.00	0.00	0.02	0.01	0.03	0.05	0.03	0.12
FeO	0.25	0.79	0.94	2.28	1.05	4.16	1.68	8.45
K2O	0.01	0.30	0.29	6.22	0.35	4.61	0.47	3.50
P2O5	0.00	0.05	0.05	0.47	0.02	0.42	0.11	0.45
Total	98.34	99.73	99.22	98.07	100.31	99.43	99.55	98.30

Table S11 cont.: Glass major element compositions.

Sample	10071	10071	10072	10072	10072	10072	10072	10072
Point	48 / 1 .	92	4 / 1 .	9 / 1 .	11 / 1 .	27 / 1 .	24 / 1 .	29
SiO2	49.15	67.94	63.26	50.94	64.03	63.13	59.02	60.04
Na2O	1.98	1.22	1.89	2.54	1.09	1.42	1.58	1.70
MgO	0.18	1.14	0.06	0.07	0.33	0.09	0.06	0.14
Al2O3	31.36	17.57	22.21	29.94	14.45	19.77	23.93	21.95
CaO	15.95	5.73	9.67	14.41	6.58	11.07	11.88	9.84
TiO2	0.10	0.49	0.22	0.20	1.05	0.38	0.14	0.30
Cr2O3	0.01	0.01	0.00	0.00	0.01	0.01	0.01	0.00
MnO	0.04	0.11	0.04	0.01	0.09	0.04	0.01	0.01
FeO	0.71	4.83	1.85	1.49	6.33	2.51	1.11	2.35
K2O	0.26	1.36	1.02	0.46	3.76	0.41	0.34	2.39
P2O5	0.03	0.14	0.12	0.03	0.87	0.64	0.07	0.06
Total	99.78	100.54	100.34	100.10	98.60	99.47	98.15	98.77

Table S12: Mesostasis trace element contents.

Sample	10017	10022	10022	10024	10024	10069
LAICPMS point	17.51.meso.40um	22.17.meso.40um	22.52.meso.25um	24.3.meso.45um	24.23.meso.45um	69.25.meso.30um
Ca43_ppm_mean	75097.045	78986.135	87624.506	96401.790	66707.357	88177.010
Ca43_ppm_2SE(int)	2201.158	7560.195	3530.125	2314.325	2059.808	11505.208
Sc45_ppm_mean	14.606	10.802	12.024	12.638	28.727	59.124
Sc45_ppm_2SE(int)	0.973	1.337	0.970	0.441	5.241	9.901
Ti47_ppm_mean	5014.012	49402.786	1613.135	4202.390	4121.147	11086.911
Ti47_ppm_2SE(int)	704.673	10299.273	208.829	215.702	322.255	665.933
V51_ppm_mean	0.923	1.233	1.054	0.522	3.144	21.122
V51_ppm_2SE(int)	0.218	0.386	0.777	0.186	0.745	6.039
Cr52_ppm_mean	30.796	94.709	53.366	16.868	80.894	812.675
Cr52_ppm_2SE(int)	7.706	23.747	5.798	1.243	19.821	214.268
Mn55_ppm_mean	486.573	925.330	624.801	526.942	780.331	1556.498
Mn55_ppm_2SE(int)	46.389	207.550	58.776	20.091	134.228	255.169
Co59_ppm_mean	2.111	4.951	3.799	1.501	3.904	16.445
Co59_ppm_2SE(int)	0.256	1.075	0.524	0.149	0.666	2.447
Ni60_ppm_mean	0.454	0.219	0.642	0.249	0.864	11.564
Ni60_ppm_2SE(int)	0.147	0.157	0.406	0.116	0.491	2.278
Cu63_ppm_mean	2.849	4.538	3.616	3.585	5.024	16.647
Cu63_ppm_2SE(int)	0.527	1.072	1.012	0.449	1.151	6.552
Zn66_ppm_mean	5.145	8.980	7.244	5.517	6.190	4.902
Zn66_ppm_2SE(int)	0.805	1.302	2.025	0.818	0.552	0.653
Rb85_ppm_mean	34.982	46.190	3.634	64.643	45.775	82.778
Rb85_ppm_2SE(int)	3.907	2.978	0.562	3.084	1.608	8.871
Sr88_ppm_mean	674.576	620.028	461.956	907.584	689.245	321.979
Sr88_ppm_2SE(int)	26.750	30.525	28.840	22.290	29.467	36.181
Y89_ppm_mean	313.663	1173.843	108.681	419.420	368.916	809.818
Y89_ppm_2SE(int)	33.429	215.640	12.186	70.515	36.756	59.266
Zr90_ppm_mean	1083.257	1768.958	270.337	1243.050	1149.884	1932.888
Zr90_ppm_2SE(int)	112.459	273.966	37.573	126.089	44.378	274.402
Nb93_ppm_mean	33.337	150.613	7.589	47.874	28.637	52.824
Nb93_ppm_2SE(int)	2.473	23.223	1.370	8.966	1.210	8.744
Ba137_ppm_mean	2219.171	2494.783	1250.887	2614.777	4780.679	2127.295
Ba137_ppm_2SE(int)	171.340	259.952	90.503	133.820	127.071	217.717
Hf178_ppm_mean	34.918	52.152	12.310	41.820	40.903	57.786
Hf178_ppm_2SE(int)	3.321	8.000	2.094	4.150	2.212	7.912
Ta181_ppm_mean	2.217	8.607	0.472	2.449	1.651	3.757
Ta181_ppm_2SE(int)	0.215	1.288	0.113	0.310	0.073	0.633
Pb208_ppm_mean	4.348	12.376	5.574	5.619	3.744	22.695
Pb208_ppm_2SE(int)	0.408	1.687	1.561	0.977	0.179	1.529
Th232_ppm_mean	9.572	20.469	1.952	12.359	7.010	29.862
Th232_ppm_2SE(int)	1.157	3.719	0.332	2.515	0.305	4.298
U238_ppm_mean	2.454	3.276	0.553	3.884	1.796	9.336
U238_ppm_2SE(int)	0.330	0.485	0.088	1.228	0.099	2.725

*Point names include phase (meso) and spot size (i.e., 30 um).

Table S12 cont.: Mesostasis trace element contents.

Sample	10069	10071	10072	10072	10072
LAICPMS point	69.75.meso.30um	71.92.pl.40um	72.9.meso.35um	72.27.meso.40um	72.29.pl.35um
Ca43_ppm_mean	39461.713	188236.524	96466.709	76322.381	133966.645
Ca43_ppm_2SE(int)	2879.770	5728.557	7246.886	5195.661	3937.054
Sc45_ppm_mean	19.318	8.320	59.276	15.061	8.394
Sc45_ppm_2SE(int)	1.338	0.839	12.628	1.531	0.882
Ti47_ppm_mean	10239.600	984.080	26117.445	2061.759	1211.186
Ti47_ppm_2SE(int)	2625.975	81.976	1378.427	216.728	72.326
V51_ppm_mean	3.260	2.206	19.588	1.666	0.661
V51_ppm_2SE(int)	1.672	0.472	3.848	0.443	0.351
Cr52_ppm_mean	161.479	48.526	759.148	88.610	17.985
Cr52_ppm_2SE(int)	73.357	9.691	156.648	16.489	5.905
Mn55_ppm_mean	342.425	181.315	2111.491	652.063	252.346
Mn55_ppm_2SE(int)	33.711	30.714	311.312	89.982	11.383
Co59_ppm_mean	6.354	1.602	157.244	3.616	1.182
Co59_ppm_2SE(int)	0.662	0.245	35.924	0.505	0.160
Ni60_ppm_mean	10.436	0.349	97.028	0.634	0.489
Ni60_ppm_2SE(int)	1.737	0.193	26.890	0.199	0.298
Cu63_ppm_mean	2.465	0.856	56.388	4.418	3.359
Cu63_ppm_2SE(int)	0.355	0.165	16.246	1.070	0.728
Zn66_ppm_mean	5.250	0.833	10.639	4.387	2.299
Zn66_ppm_2SE(int)	0.838	0.466	4.718	0.815	0.993
Rb85_ppm_mean	127.465	0.442	2.401	8.141	28.500
Rb85_ppm_2SE(int)	5.711	0.089	0.527	0.971	3.336
Sr88_ppm_mean	447.941	699.581	356.141	560.456	544.353
Sr88_ppm_2SE(int)	34.143	23.837	56.201	42.318	18.033
Y89_ppm_mean	565.268	10.413	367.231	202.005	449.165
Y89_ppm_2SE(int)	75.939	3.557	47.999	32.988	122.851
Zr90_ppm_mean	2886.865	27.858	954.944	962.335	499.374
Zr90_ppm_2SE(int)	267.180	14.053	450.752	401.142	85.187
Nb93_ppm_mean	62.512	1.116	52.928	38.235	15.907
Nb93_ppm_2SE(int)	6.096	0.553	12.086	9.632	2.219
Ba137_ppm_mean	5306.467	216.460	673.983	1056.585	890.771
Ba137_ppm_2SE(int)	268.128	11.029	182.384	74.864	141.243
Hf178_ppm_mean	85.781	0.731	26.243	29.505	15.487
Hf178_ppm_2SE(int)	7.233	0.291	7.067	10.696	2.620
Ta181_ppm_mean	4.817	0.051	3.028	1.847	0.909
Ta181_ppm_2SE(int)	0.360	0.033	0.702	0.538	0.146
Pb208_ppm_mean	21.829	0.226	6.115	5.275	7.261
Pb208_ppm_2SE(int)	3.081	0.104	1.437	1.215	1.050
Th232_ppm_mean	47.328	0.166	6.799	10.400	9.276
Th232_ppm_2SE(int)	5.339	0.094	1.647	3.443	2.326
U238_ppm_mean	16.040	0.160	1.385	2.321	1.815
U238_ppm_2SE(int)	1.677	0.147	0.478	0.686	0.364

*Point names include phase (meso) and spot size (i.e., 30 um).

Table S13: Mesostasis rare earth element contents.

Sample	10017	10022	10022	10024	10024	10069
LAICPMS point	17.51.meso.40um	22.17.meso.40um	22.52.meso.25um	24.23.meso.45um	24.3.meso.45um	69.25.meso.30um
La139_ppm_mean	66.485	277.300	17.652	72.154	130.675	173.451
La139_ppm_2SE(int)	7.752	51.351	2.577	4.823	25.690	13.847
Ce140_ppm_mean	190.187	772.648	54.436	197.280	330.853	502.680
Ce140_ppm_2SE(int)	20.770	137.095	7.572	10.825	66.069	38.741
Pr141_ppm_mean	27.926	115.859	7.986	28.462	45.756	73.325
Pr141_ppm_2SE(int)	3.095	21.061	1.049	1.906	9.856	5.783
Nd146_ppm_mean	138.803	577.110	38.502	134.617	207.556	344.776
Nd146_ppm_2SE(int)	16.056	103.347	4.948	8.588	40.710	26.235
Sm147_ppm_mean	44.442	183.441	13.380	47.509	60.957	111.987
Sm147_ppm_2SE(int)	4.962	33.124	1.977	4.350	11.363	9.124
Eu153_ppm_mean	9.376	11.209	5.430	12.010	13.515	6.250
Eu153_ppm_2SE(int)	0.348	0.925	0.502	0.530	0.387	0.467
Gd157_ppm_mean	51.092	216.152	16.500	55.809	68.096	127.929
Gd157_ppm_2SE(int)	5.838	41.796	2.415	5.350	11.750	9.905
Tb159_ppm_mean	8.895	36.985	2.894	10.432	11.830	22.791
Tb159_ppm_2SE(int)	1.021	6.937	0.371	1.033	2.008	1.674
Dy163_ppm_mean	57.668	222.337	19.463	69.081	76.260	149.814
Dy163_ppm_2SE(int)	6.459	40.140	2.371	6.737	12.842	11.383
Ho165_ppm_mean	12.150	45.449	4.300	14.355	15.580	31.462
Ho165_ppm_2SE(int)	1.302	8.222	0.534	1.523	2.488	2.406
Er166_ppm_mean	34.595	124.506	12.724	40.666	45.747	87.573
Er166_ppm_2SE(int)	3.891	22.656	1.742	4.321	8.291	6.420
Tm169_ppm_mean	4.765	15.938	2.125	5.727	6.327	12.161
Tm169_ppm_2SE(int)	0.522	2.949	0.232	0.627	1.086	0.901
Yb172_ppm_mean	30.916	95.709	14.672	37.827	41.787	79.081
Yb172_ppm_2SE(int)	3.012	17.330	1.978	4.041	7.020	6.462
Lu175_ppm_mean	4.010	11.895	2.124	4.941	5.284	10.440
Lu175_ppm_2SE(int)	0.384	2.088	0.305	0.563	0.822	0.924

*Point names include phase (meso) and spot size (i.e., 30 um).

Table S13 cont.: Mesostasis rare earth element contents.

Sample	10069	10071	10072	10072	10072
LAICPMS point	69.75.meso.30um	71.92.pl.40um	72.27.meso.40um	72.29.pl.35um	72.9.meso.35um
La139_ppm_mean	123.816	3.525	38.599	123.890	60.940
La139_ppm_2SE(int)	15.211	0.476	8.352	31.450	16.698
Ce140_ppm_mean	345.401	8.529	104.181	N/A	N/A
Ce140_ppm_2SE(int)	43.636	1.306	20.583	N/A	N/A
Pr141_ppm_mean	46.077	1.151	14.950	51.688	25.380
Pr141_ppm_2SE(int)	5.814	0.189	2.824	13.000	6.405
Nd146_ppm_mean	204.294	5.446	71.371	244.747	124.678
Nd146_ppm_2SE(int)	25.450	0.961	13.823	61.127	28.272
Sm147_ppm_mean	65.584	1.577	22.506	75.275	43.205
Sm147_ppm_2SE(int)	8.757	0.365	3.789	19.768	8.691
Eu153_ppm_mean	6.954	6.612	7.502	7.154	5.321
Eu153_ppm_2SE(int)	0.411	0.339	0.639	0.899	0.850
Gd157_ppm_mean	74.315	1.672	28.130	82.929	53.868
Gd157_ppm_2SE(int)	9.722	0.466	4.419	22.735	8.792
Tb159_ppm_mean	14.464	0.297	5.177	13.803	10.142
Tb159_ppm_2SE(int)	1.781	0.096	0.741	3.739	1.563
Dy163_ppm_mean	102.046	2.100	35.211	86.402	69.296
Dy163_ppm_2SE(int)	13.695	0.711	5.692	23.948	9.474
Ho165_ppm_mean	21.821	0.370	7.884	17.008	14.235
Ho165_ppm_2SE(int)	2.847	0.111	1.332	4.609	1.740
Er166_ppm_mean	67.207	1.100	24.429	44.315	40.888
Er166_ppm_2SE(int)	8.532	0.400	4.540	12.040	4.740
Tm169_ppm_mean	10.029	0.163	3.535	5.843	5.683
Tm169_ppm_2SE(int)	1.345	0.072	0.678	1.538	0.604
Yb172_ppm_mean	68.184	1.230	25.848	35.364	39.367
Yb172_ppm_2SE(int)	9.577	0.475	4.992	9.627	3.885
Lu175_ppm_mean	9.134	0.119	3.604	4.395	5.097
Lu175_ppm_2SE(int)	1.197	0.051	0.720	1.163	0.386

*Point names include phase (meso) and spot size (i.e., 30 um).

Table S14: Silica major element contents.

Sample	10017	10017	10022	10069	10069	10069	10069	10069
Point	25 / 1 .	58 / 1 .	29 / 1 .	46 / 1 .	60 / 1 .	73 / 1 .	92 / 1 .	97 / 1 .
SiO2	95.92	96.19	95.93	96.39	90.69	96.89	97.56	81.13
Na2O	0.32	0.29	0.00	0.31	0.36	0.29	0.24	1.04
MgO	0.00	0.00	0.40	0.00	0.00	0.00	0.19	0.32
Al2O3	1.34	1.38	0.93	1.55	2.10	1.62	1.17	10.61
CaO	0.31	0.36	0.07	0.47	0.38	0.41	0.29	4.81
TiO2	0.29	0.30	0.22	0.45	0.36	0.45	0.44	0.39
Cr2O3	0.01	0.00	0.00	0.01	0.01	0.02	0.00	0.01
MnO	0.00	0.00	0.02	0.00	0.00	0.01	0.03	0.01
FeO	0.12	0.09	0.60	0.38	0.33	0.47	0.21	0.69
K2O	0.00	0.01	0.00	0.01	0.02	0.02	0.01	0.15
P2O5	0.00	0.02	0.01	0.00	0.04	0.00	0.00	0.04
Total	98.32	98.64	98.18	99.57	100.37	100.17	100.13	99.19

Table S14: Silica major element contents.

Sample	10069	10071	10071	10071	10071	10071	10071
Point	111 / 1 .	20 / 1 .	24 / 1 .	75 / 1 .	86 / 1 .	87 / 1 .	91 / 1 .
SiO2	97.00	96.44	52.99	50.39	48.42	48.55	51.05
Na2O	0.36	0.29	2.11	2.26	0.00	0.06	2.46
MgO	0.00	0.04	0.08	0.17	9.59	13.84	0.19
Al2O3	1.61	1.17	28.80	30.28	1.32	3.78	32.54
CaO	0.41	0.30	13.84	14.99	10.28	14.49	14.70
TiO2	0.33	0.31	0.07	0.09	1.12	2.14	0.12
Cr2O3	0.00	0.00	0.00	0.00	0.24	0.50	0.00
MnO	0.01	0.01	0.04	0.01	0.44	0.25	0.00
FeO	0.23	0.19	1.53	0.70	27.52	15.72	0.68
K2O	0.01	0.04	0.88	0.28	0.01	0.00	0.29
P2O5	0.00	0.00	0.03	0.03	0.00	0.00	0.01
Total	99.96	98.32	99.20	98.97	99.33	98.77	99.11

Table S15: Silica trace element contents.

Sample	10017	10069	10069
LAICPMS point	17.25.si.40um	69.60.si.25um	69.111.si.30um
Ca43_ppm_mean	6252.844	23075.729	175717.861
Ca43_ppm_2SE(int)	648.689	4445.810	16500.207
Sc45_ppm_mean	10.179	29.877	50.455
Sc45_ppm_2SE(int)	0.531	4.539	15.940
Ti47_ppm_mean	2072.800	30773.696	3738.268
Ti47_ppm_2SE(int)	196.610	16654.708	786.978
V51_ppm_mean	2.238	19.928	15.101
V51_ppm_2SE(int)	0.414	5.781	6.422
Cr52_ppm_mean	66.873	714.865	608.892
Cr52_ppm_2SE(int)	10.224	228.531	258.196
Mn55_ppm_mean	61.081	711.026	1214.134
Mn55_ppm_2SE(int)	8.728	135.779	470.869
Co59_ppm_mean	0.694	5.033	8.415
Co59_ppm_2SE(int)	0.144	0.972	2.983
Ni60_ppm_mean	0.668	0.940	2.097
Ni60_ppm_2SE(int)	0.277	0.906	0.994
Cu63_ppm_mean	5.958	2.774	0.718
Cu63_ppm_2SE(int)	0.943	1.332	0.343
Zn66_ppm_mean	3.823	6.793	2.938
Zn66_ppm_2SE(int)	1.280	3.098	1.571
Rb85_ppm_mean	0.504	0.134	2.092
Rb85_ppm_2SE(int)	0.174	0.055	0.295
Sr88_ppm_mean	21.638	35.103	1087.301
Sr88_ppm_2SE(int)	2.030	4.065	83.377
Y89_ppm_mean	2.980	144.483	227.345
Y89_ppm_2SE(int)	0.559	10.683	47.969
Zr90_ppm_mean	17.492	371.248	634.024
Zr90_ppm_2SE(int)	2.153	203.847	98.328
Nb93_ppm_mean	0.510	25.876	14.321
Nb93_ppm_2SE(int)	0.141	14.050	1.475
Ba137_ppm_mean	46.572	26.466	1416.987
Ba137_ppm_2SE(int)	8.963	4.721	91.737
Hf178_ppm_mean	0.715	12.864	20.324
Hf178_ppm_2SE(int)	0.156	7.329	2.536
Ta181_ppm_mean	0.027	2.470	1.081
Ta181_ppm_2SE(int)	0.014	1.455	0.202
Pb208_ppm_mean	0.174	199.027	38.377
Pb208_ppm_2SE(int)	0.054	199.833	33.907
Th232_ppm_mean	0.106	1.337	22.366
Th232_ppm_2SE(int)	0.022	0.156	19.034
U238_ppm_mean	0.154	0.227	3.148
U238_ppm_2SE(int)	0.138	0.056	0.403

*Point names include phase (si) and spot size (i.e., 30 um).

Table S16: Silica rare earth element contents.

Sample	10017	10069	10069
LAICPMS point	17.25.si.40um	69.60.si.25um	69.111.si.30um
La139_ppm_mean	0.766	34.224	42.223
La139_ppm_2SE(int)	0.302	2.815	5.073
Ce140_ppm_mean	3.673	108.399	112.119
Ce140_ppm_2SE(int)	1.728	8.162	12.237
Pr141_ppm_mean	0.289	15.607	15.647
Pr141_ppm_2SE(int)	0.066	1.496	1.683
Nd146_ppm_mean	1.583	78.309	77.912
Nd146_ppm_2SE(int)	0.855	5.773	9.367
Sm147_ppm_mean	0.387	24.418	26.596
Sm147_ppm_2SE(int)	0.142	2.387	4.399
Eu153_ppm_mean	0.338	0.729	14.755
Eu153_ppm_2SE(int)	0.056	0.182	1.413
Gd157_ppm_mean	0.521	28.053	32.402
Gd157_ppm_2SE(int)	0.161	3.215	6.335
Tb159_ppm_mean	0.072	4.586	6.474
Tb159_ppm_2SE(int)	0.022	0.393	1.179
Dy163_ppm_mean	0.716	28.824	44.171
Dy163_ppm_2SE(int)	0.209	2.925	8.759
Ho165_ppm_mean	0.156	6.374	9.721
Ho165_ppm_2SE(int)	0.049	0.707	1.944
Er166_ppm_mean	0.322	15.378	27.498
Er166_ppm_2SE(int)	0.103	1.119	5.478
Tm169_ppm_mean	0.049	1.883	4.888
Tm169_ppm_2SE(int)	0.017	0.216	2.077
Yb172_ppm_mean	0.313	12.767	27.454
Yb172_ppm_2SE(int)	0.085	1.349	5.637
Lu175_ppm_mean	0.090	1.640	3.381
Lu175_ppm_2SE(int)	0.076	0.174	0.694

*Point names include phase (si) and spot size (i.e., 30 um).

5. Synthesis

This work represents a multidimensional, integrated study of sample microstructural and geochemical characteristics. Samples were investigated in two and three dimensions with the help of traditional thin section analysis, and x-ray computed analysis (XCT), respectively. XCT was applied to evaluate sample textures in a way never before seen within lunar samples – this work was the first to decisively evaluate structural components of lunar mare basalts such as mineral phase orientations and size distributions using all three dimensions. Through XCT work, eruption styles of mare basalts across the lunar surface were constrained, indicating that samples cooled as pahoehoe lava flows of low viscosity. This was followed by detailed geochemical analysis of the same mare samples to better understand their formation at depth. Elemental signatures of individual grains preserve a record of the magmatic environments they grew in, and provide evidence for magmatic system architectures at depth which allow for magma storage, and/or mixing between distinct magma batches. Through this work, it was found that many lunar magmas preserve evidence of evolution in magmatic systems more complex than originally thought, where mechanisms like mixing, mingling, assimilation, and storage can occur. In this way, this dissertation collectively evaluated the mechanisms involved in the emplacement of secondary basaltic crusts on planetary objects across the Solar System in the first chapter, and the generation, storage, and travel of basaltic magmas at depth prior to eruption in the second chapter. The third chapter combined these techniques to evaluate in detail the petrogenetic history of a specific sample suite. This work thus began to address remining questions regarding magma generation, storage, and eruption in extraterrestrial systems, within the context of recent advancements in terrestrial igneous petrology. Through this work it was found that at least some lunar magmatic systems are open in nature, and are thus not so different from their open-system terrestrial counterparts, suggesting that extraterrestrial magmatic systems on other planetary objects have the potential to operate in this way.

Future directions should include comprehensive investigation of other lunar basaltic suites in a similar multidisciplinary and multidimensional framework to that presented in chapter 4. Additional evaluation of isotopic signatures at the crystal scale would provide further constraints on melt evolution, while geothermobarometric analysis could provide detailed constrains regarding phase crystallization depths and system evolution. Finally, detailed modeling of melt composition could provide additional information regarding melt and phase evolution, starting from the generation of partial melts and ending with solidification on the lunar surface. Such directions would greatly benefit from detailed, systematic evaluation of the entire lunar suite to support comparative analysis of lunar basalt petrogenesis across the Moon.